

Science and Technology of Nuclear Installations

# Safety Features of High Temperature Gas Cooled Reactor

Lead Guest Editor: Chao Fang

Guest Editors: Robert Morris and Fu Li





---

# **Safety Features of High Temperature Gas Cooled Reactor**

Science and Technology of Nuclear Installations

---

## **Safety Features of High Temperature Gas Cooled Reactor**

Lead Guest Editor: Chao Fang

Guest Editors: Robert Morris and Fu Li



---

Copyright © 2017 Hindawi. All rights reserved.

This is a special issue published in “Science and Technology of Nuclear Installations.” All articles are open access articles distributed under the Creative Commons Attribution License, which permits unrestricted use, distribution, and reproduction in any medium, provided the original work is properly cited.

---

## Editorial Board

Nusret Aksan, Switzerland  
Won Pil Baek, Republic of Korea  
Stephen M. Bajorek, USA  
George Bakos, Greece  
Leon Cizelj, Slovenia  
Alejandro Clausse, Argentina  
Francesco D' Auria, Italy  
Mark Deinert, USA  
Cesare Frepoli, USA  
Michel Giot, Belgium  
Valerio Giusti, Italy

Tim Haste, France  
Keith E. Holbert, USA  
Tomasz Kozlowski, USA  
Tomoaki Kunugi, Japan  
H.-Y. Lee, Republic of Korea  
Jiri Macek, Czech Republic  
Borut Mavko, Slovenia  
Oleg Melikhov, Russia  
Rafael Miró, Spain  
Michael I. Ojovan, UK  
Domenico Paladino, Switzerland

Manmohan Pandey, India  
Luca Podofillini, Switzerland  
Carlo Sborchia, France  
Arkady Serikov, Germany  
James F. Stubbins, USA  
Iztok Tiselj, Slovenia  
Rizwan Uddin, USA  
Eugenijus Ušpuras, Lithuania  
Hidemasa Yamano, Japan  
Enrico Zio, Italy  
Massimo Zucchetti, Italy

# Contents

---

## **Safety Features of High Temperature Gas Cooled Reactor**

Chao Fang, Robert Morris, and Fu Li

Volume 2017, Article ID 9160971, 3 pages

## **Dynamic Behavior Analysis of Touchdown Process in Active Magnetic Bearing System Based on a Machine Learning Method**

Zhe Sun, Xunshi Yan, Jingjing Zhao, Xiao Kang, Guojun Yang, and Zhengang Shi

Volume 2017, Article ID 1839871, 11 pages

## **Oxidation Behavior of Matrix Graphite and Its Effect on Compressive Strength**

Xiangwen Zhou, Cristian I. Contescu, Xi Zhao, Zhenming Lu, Jie Zhang, Yutai Katoh, Yanli Wang, Bing Liu, Yaping Tang, and Chunhe Tang

Volume 2017, Article ID 4275375, 6 pages

## **The Optimization of Radiation Protection in the Design of the High Temperature Reactor-Pebble-Bed Module**

Sida Sun, Hong Li, and Sheng Fang

Volume 2017, Article ID 3984603, 15 pages

## **Analysis of Precooling Injection Transient of Steam Generator for High Temperature Gas Cooled Reactor**

Yan Wang, Lei Shi, and Yanhua Zheng

Volume 2017, Article ID 8521410, 8 pages

## **Design and Development Framework of Safety-Critical Software in HTR-PM**

Chao Guo, Huasheng Xiong, Xiaojin Huang, and Duo Li

Volume 2017, Article ID 2981943, 9 pages

## **Analysis of Seismic Soil-Structure Interaction for a Nuclear Power Plant (HTR-10)**

Xiaoxin Wang, Qin Zhou, Kaixin Zhu, Li Shi, Xiaotian Li, and Haitao Wang

Volume 2017, Article ID 2358403, 13 pages

## **FM-DBEM Simulation of 3D Microvoid and Microcrack Graphite Models**

Houdi Lu, Hongtao Wang, Haitao Wang, Lie Jin, Xinxin Wu, and Yu Zhou

Volume 2017, Article ID 1071709, 14 pages

## **Three Design Basis Accidents' Analysis on the HTR-10GT**

Minggang Lang, Heng Xie, and Yujie Dong

Volume 2017, Article ID 1686291, 13 pages

## **Using Wireless Sensor Networks to Achieve Intelligent Monitoring for High-Temperature Gas-Cooled Reactor**

Jianghai Li, Jia Meng, Xiaojing Kang, Zhenhai Long, and Xiaojin Huang

Volume 2017, Article ID 3721578, 8 pages

## **Dynamic Modeling and Control Characteristics of the Two-Modular HTR-PM Nuclear Plant**

Zhe Dong, Yifei Pan, Maoxuan Song, Xiaojing Huang, Yujie Dong, and Zuoyi Zhang

Volume 2017, Article ID 6298037, 19 pages

**The Electric Current Effect on Electrochemical Deconsolidation of Spherical Fuel Elements**

Xiaotong Chen, Zhenming Lu, Hongsheng Zhao, Bing Liu, Junguo Zhu, and Chunhe Tang  
Volume 2017, Article ID 2126876, 6 pages

**A New Method to Measure Crack Extension in Nuclear Graphite Based on Digital Image Correlation**

Shigang Lai, Li Shi, Alex Fok, Haiyan Li, Libin Sun, and Zhengming Zhang  
Volume 2017, Article ID 2416545, 10 pages

**Research on the Computed Tomography Pebble Flow Detecting System for HTR-PM**

Xin Wan, Ximing Liu, Jichen Miao, Peng Cong, Yuai Zhang, and Zhifang Wu  
Volume 2017, Article ID 5403701, 13 pages

**Physical Analysis of the Initial Core and Running-In Phase for Pebble-Bed Reactor HTR-PM**

Jingyu Zhang, Fu Li, and Yuliang Sun  
Volume 2017, Article ID 8918424, 6 pages

**Source Term Analysis of the Irradiated Graphite in the Core of HTR-10**

Xuegang Liu, Xin Huang, Feng Xie, Fuming Jia, Xiaogui Feng, and Hong Li  
Volume 2017, Article ID 2614890, 6 pages

**Adsorption Behaviors of Cobalt on the Graphite and SiC Surface: A First-Principles Study**

Wenyi Wang, Chuan Li, Jianzhu Cao, and Chao Fang  
Volume 2017, Article ID 8296387, 8 pages

**3D Nondestructive Visualization and Evaluation of TRISO Particles Distribution in HTGR Fuel Pebbles Using Cone-Beam Computed Tomography**

Gongyi Yu, Yi Du, Xincheng Xiang, Yuan Liu, Ziqiang Li, and Xiangang Wang  
Volume 2017, Article ID 3857075, 6 pages

## Editorial

# Safety Features of High Temperature Gas Cooled Reactor

**Chao Fang,<sup>1,2,3</sup> Robert Morris,<sup>4</sup> and Fu Li<sup>1,2,3</sup>**

<sup>1</sup>*Institute of Nuclear and New Energy Technology, Tsinghua University, Beijing 100084, China*

<sup>2</sup>*Collaborative Innovation Center of Advanced Nuclear Energy Technology, Beijing 100084, China*

<sup>3</sup>*The Key Laboratory of Advanced Reactor Engineering and Safety, Ministry of Education, Beijing 100084, China*

<sup>4</sup>*Oak Ridge National Laboratory, Fusion and Materials for Nuclear Systems Division, Oak Ridge, TN 37831, USA*

Correspondence should be addressed to Chao Fang; [fangchao@tsinghua.edu.cn](mailto:fangchao@tsinghua.edu.cn)

Received 19 October 2017; Accepted 19 October 2017; Published 9 November 2017

Copyright © 2017 Chao Fang et al. This is an open access article distributed under the Creative Commons Attribution License, which permits unrestricted use, distribution, and reproduction in any medium, provided the original work is properly cited.

Most of current operating nuclear power plants (NPPs) are light-water reactors (LWR). LWR features, as ceramic fuel, metallic fuel cladding, and core structure, use water as coolant and moderator. The safety of NPPs relies on three basic methodologies: reactivity control, residual heat removal, radioactive retention. For NPP, high safety is achieved by proper design, good quality components, different types of safety systems, and engineering safety features, such as reactor trip, emergency core cooling system, safety injection, decay heat removal system, and containment. In the case of LWR, all accidents, even the design extension condition with core melt (before being named as severe accident), can be controlled and mitigated. For this purpose, reliable cooling of the core and removal of residual decay heat are crucial to preventing core melt, and additional measures must be provided to mitigate the consequences of core melt. In this case, containment plays very important roles. Containment provide many functions, such as radiation shielding, physical protection, radioactive retention, maintaining of coolant inventory (which is crucial to cooling the core and removing the decay heat).

High Temperature Gas Cooled Reactor (HTGR) provides another solution. HTGR uses TRISO coated particle fuel, full ceramic core structure, and helium as coolant. The fuel, core structure, and coolant in HTGR can all withstand high temperature. Therefore HTGR can provide high temperature output for high efficiency electricity generation and wide range of process heat applications, including hydrogen production. Furthermore, modular HTGR can provide inherent safety features.

Although it is based on the same safety function requirements, such as reactivity control, residual heat removal, and radioactive retention, modular HTGR achieved the safety in different way.

The reactivity control is very simple for HTGR. Although reactor trip with control rod drop is equipped, the trip of helium circulator is enough for trip reactor, because the negative temperature feedback provides enough reactivity compensation even for large reactivity insertion accident, taking into account the following fact of residual decay removal mechanism.

For the residual heat removal in modular HTGR, after accident, no forced cooling for the core is required; residual heat is removed from core through the core, reflector, and core barrel and then out of pressure vessel, by means of heat conductivity, radiation, and convection, along the temperature gradient. In this case, availability of coolant is not necessary and external power is not required. Of course, the core will be heated up to some degree to provide the temperature gradient for heat transfer and provide the negative temperature feedback for automatic reactor trip for reactivity control. The maximum core temperature after accident is limited by the accumulation of residual heat, which is proportional to the power density during normal operation and to the temperature limit that the integrity of TRISO fuel is ensured to retain all fission products in all accident conditions, with enough margin. Therefore it is a very simple solution. Neither massive fuel degradation nor core melt will be possible. Therefore it provides a very good foundation for radioactive retention.

For radioactive retention, it is also very straightforward for modular HTGR. Because the possibility of massive fuel degradation is physically eliminated, almost all the fission products are retained inside the coating of TRISO particle in normal operation and accident condition. The failure rate of TRISO particle is very low for all accident conditions. Then the maximum plausible radioactive release into environment for all accidents is limited to the extent that no off-site emergency action is needed. The goal of catastrophe-free can be achieved by modular HTGR. For modular HTGR, the most important barrier to radioactive retention is TRISO particle, compared to the containment in LWR, although next barriers of primary pressure boundary and containment (usually named as vented lower pressure containment) are also provided in modular HTGR to reduce the radioactive release as low as reasonably achievable.

These safety phenomena and safety features of modular HTGR depend on the high quality of TRISO particle fuel, proper design of core geometry to disperse the residual heat, the selected power density in order to limit the maximum fuel temperature after accident, ceramic core structure and coolant which can withstand very high temperature, and all the measures required to mitigate the consequences of accident and to reduce the radioactive release as low as reasonably achievable. The research on the modular HTGR have many different features, compared to LWR, because of different fuel type (TRISO coated particle), different core structure (graphite), different coolant (helium), different type of components (such as helium circulator), different type of systems (such as fuel handling system for pebble fuel), different operation dynamic behavior, different accident scenario, different applications (such as process heat application and cogeneration), and so forth. This special issue provides some new information and recent progress. Understanding of the safety features of the HTGR has greatly increased especially after the design and construction of Chinese modular HTGR demonstration plant (High Temperature Reactor-Pebble-Bed Module, HTR-PM).

There are a lot of academic achievements related to the safety features of HTGR emerging in the recent years, including, beyond design basis accident (BDBA), multiscale source term analysis, behavior of tritium in the primary and secondary circuit, and minimizing emergency response for the modular HTGR, which is essential for the future improvements in the design, operation, and maintenance of the modular HTGR. The recent progress in this field is addressed in the following:

- (1) performance of HTGR fuel
- (2) safety and accident analysis of HTGR (including reactor physics analysis, thermal-hydraulics analysis)
- (3) source term analysis of HTGR
- (4) control of multimodular HTGRs and related human factor analysis
- (5) optimizing radiation protection of HTGR

The paper "Oxidation Behavior of Matrix Graphite and Its Effect on Compressive Strength" studies the oxidation

behavior of newly developed A3-3 MG in the temperature range from 500 to 950°C in air and the effect of oxidation on the compressive strength of oxidized MG specimens. Microstructure images of SEM and porosity measurement indicate that the significant compressive strength loss of MG oxidized at 550°C may be attributed to both the uniform pore formation throughout the bulk and the preferential oxidation of the binder.

The paper "Analysis of Precooling Injection Transient of Steam Generator for High Temperature Gas Cooled Reactor" simulates several postulated precooling injection transients and evaluates their effects, which will provide support for the precooling design. The analysis results show that enough precooling injection must be available to satisfy the precooling requirements, and larger mass flow rate of precooling water injection will accelerate the precooling process.

The paper "Adsorption Behaviors of Cobalt on the Graphite and SiC Surface: A First-Principles Study" presents the adsorption behavior of the activation product cobalt (Co) on graphite and SiC surfaces which have been studied with first-principle calculations, including the adsorption energy, charge density difference, density of states, and adsorption ratios. The results show that the SiC layer in a fuel element could obstruct the diffusion of Co effectively in normal and accidental operation conditions, but the graphite may become a carrier of Co nuclide radioactivity in the primary circuit of HTR-PM.

The paper "Dynamic Modeling and Control Characteristics of the Two-Modular HTR-PM Nuclear Plant" summarizes the study of the proposed power control system for a two-modular HTR-PM plant and gives the verification results based on numerical simulation. The simulation examines the cases of plant power steps and ramps and shows that the plant control characteristics are satisfactory.

The paper "The Optimization of Radiation Protection in the Design of the High Temperature Reactor-Pebble-Bed Module" proposes a methodology that jointly optimizes the system design and radiation protection of the High Temperature Reactor-Pebble-Bed Module (HTR-PM) within the confines of the "as low as reasonably achievable (ALARA)" principle. It demonstrates that the annual collective dose of HTR-PM is reduced from 0.490 man-Sv/a before optimization to 0.445 man-Sv/a after optimization, which complies with the requirements of the Chinese regulatory guide and proves the effectiveness of the proposed routine and framework.

The paper "A New Method to Measure Crack Extension in Nuclear Graphite Based on Digital Image Correlation" introduces a new method based on digital image correlation (DIC) for measuring crack extension in brittle materials. Cross-correlation of the displacements measured by DIC with a step function is employed to identify the advancing crack tip in a graphite beam specimen under three-point bending. The load-crack extension curve, which is required for analyzing the R-curve and tension softening behavior, is obtained for this material. Furthermore, a sensitivity analysis of the threshold value employed for the cross-correlation parameter in the crack identification process is conducted.

The paper "Research on the Computed Tomography Pebble Flow Detecting System for HTR-PM" constructs

a computed tomography pebble flow detecting (CT-PFD) system to study pebble dynamics in which a three-dimensional model is simulated, scaled to the ratio of 1:5 based on the core of HTR-PM. A multislice helical CT is utilized to acquire the reconstructed cross-sectional images of simulated pebbles, among which special tracer pebbles are used to indicate pebble flow. The proposed pebble-detecting and tracking technique described in this paper will be implemented in the near future.

Overall, the main purpose of this special issue is to provide a platform for sharing the latest and significant research achievements on the safety features of the HTGR. We believe that this special issue will supply interesting information on the safety features of HTGR.

### **Acknowledgments**

We would like to express gratitude to all those who helped us during organizing this special issue and express heartfelt gratitude to Mr. Liguozhang, who supplied abundant materials about HTGRs for reference in the process of writing this editorial.

*Chao Fang*  
*Robert Morris*  
*Fu Li*

## Research Article

# Dynamic Behavior Analysis of Touchdown Process in Active Magnetic Bearing System Based on a Machine Learning Method

Zhe Sun,<sup>1,2,3</sup> Xunshi Yan,<sup>1,2,3</sup> Jingjing Zhao,<sup>1,2,3</sup> Xiao Kang,<sup>4</sup>  
Guojun Yang,<sup>1,2,3</sup> and Zhengang Shi<sup>1,2,3</sup>

<sup>1</sup>*Institute of Nuclear and New Energy Technology, Tsinghua University, Beijing 100084, China*

<sup>2</sup>*Collaborative Innovation Center of Advanced Nuclear Energy Technology, Beijing 100084, China*

<sup>3</sup>*The Key Laboratory of Advanced Reactor Engineering and Safety, Ministry of Education, Beijing 100084, China*

<sup>4</sup>*Mechanical Engineering, Texas A&M University, College Station, TX 77843, USA*

Correspondence should be addressed to Zhe Sun; [sun\\_zhe@tsinghua.edu.cn](mailto:sun_zhe@tsinghua.edu.cn)

Received 30 December 2016; Revised 28 August 2017; Accepted 14 September 2017; Published 18 October 2017

Academic Editor: Eugenijus Ušpuras

Copyright © 2017 Zhe Sun et al. This is an open access article distributed under the Creative Commons Attribution License, which permits unrestricted use, distribution, and reproduction in any medium, provided the original work is properly cited.

Magnetic bearings are widely applied in High Temperature Gas-cooled Reactor (HTGR) and auxiliary bearings are important backup and safety components in AMB systems. The performance of auxiliary bearings significantly affects the reliability, safety, and serviceability of the AMB system, the rotating equipment, and the whole reactor. Research on the dynamic behavior during the touchdown process is crucial for analyzing the severity of the touchdown. In this paper, a data-based dynamic analysis method of the touchdown process is proposed. The dynamic model of the touchdown process is firstly established. In this model, some specific mechanical parameters are regarded as functions of deformation of auxiliary bearing and velocity of rotor firstly; furthermore, a machine learning method is utilized to model these function relationships. Based on the dynamic model and the Kalman filtering technique, the proposed method can offer estimation of the rotor motion state from noisy observations. In addition, the estimation precision is significantly improved compared with the method without learning. The proposed method is validated by the experimental data from touchdown experiments.

## 1. Introduction

Magnetic bearings are widely applied in High Temperature Gas-cooled Reactor (HTGR), where the rotating machines are running under highly purified helium environment. Compared with conventional bearings, Active Magnetic Bearings (AMBs) possess several attractive advantages, such as no friction, no need of lubrication, and the ability of long-term high speed running. Some types of essential rotating equipment in HTGR are supported by AMBs, that is, the main helium circulator and the helium blower in the fuel circulation system. The reliability of this equipment, especially in accident condition, plays a crucial role in the safety of the whole nuclear plant.

In an AMB system, the rotating rotor is suspended by electromagnetic forces and there is no contact between the

rotor and the stator. An AMB system is a complex mechatronic system and consists of a large number of structural, electronic components and sophisticated control software. AMB systems are usually equipped with a series of control, protection, backup, and safety components and software to ensure the reliability and the safety of the whole rotating equipment. The control and protection software of an AMB system is designed to suspend the rotor within a wide range of operating conditions. Some abnormal operation conditions, for example, long-term overload, unexpected impact, and slight failure of components, are sustainable and can hardly affect the suspension. However, in the worst case, the magnetic suspension will fail and the rotor will touch down. To avoid damage to the rotor and the stator during the touchdown process, the so-called auxiliary bearings are necessary for AMB systems. The auxiliary bearings bear the rotating

rotor during the touchdown process. They are important backup and safety components in AMB systems and can be regarded as the “last stand” for the safety of an AMB system.

In the applications associated with HTGR, the performance of auxiliary bearings significantly affects the reliability, safety, and serviceability of the AMB system, the rotating equipment, and the whole reactor. Research on the dynamic behavior during the touchdown process is crucial for analyzing the severity of the touchdown. Evaluating the contact forces between the rotor and the auxiliary bearings plays a central role of dynamic analysis of a touchdown process. However, due to the restrictions in structure design, it is difficult to equip force sensors in engineering rotating equipment. Thus these forces can hardly be measured directly and should be estimated from the acceleration and velocity of the rotor. On the other hand, only the displacements of the rotor are recorded in AMB systems. As is well known, estimating the velocity and acceleration from noisy displacement data is hardly realizable. Therefore this paper focuses on the estimation of velocities and accelerations of the rotor based on the dynamic model and the measured data.

Many remarkable achievements have been accomplished in the literature to estimate the highly nonlinear dynamic process associated with rotor touchdown. In 1991, Ishii and Kirk [1] built the touchdown model of the Jeffcott rotor, gained the transient response of the touchdown process by a numerical method, and obtained the optimal damping to reduce the displacement and the contact force. In 1994, Fumagali and Schweitzer [2] analyzed the influence of the air gap, friction coefficient, supporting damping, and stiffness on the dynamic behavior of rotors touchdown process. Fang and Barrett [3] added the Coulomb friction to Kirks mathematical model and gained the transient response using the Newmark- $\beta$  method. In 2003, Zeng [4] studied the dynamic behavior of the rotor drop onto the auxiliary bearing with different supporting conditions, found out the critical friction coefficient causing the backward whirling, and claimed the low friction coefficient and soft support can reduce the contact force and the possibility of occurring backward whirl. Sun et al. [5–7] considered rotor drop simulation of a flywheel energy storage system, numerically and experimentally. The results suggested therefore that the life of the auxiliary bearing can be extended by reducing auxiliary bearing clearance, dropping velocity, contact friction, and support stiffness, applying static side-loads and increasing support. Keogh and Yong [8] indicated that the rotor drop procedure can be treated as a combination of bounce and rub. They simulated transient thermal response for a series of contact conditions. Moreover, an active recovery strategy was also obtained to make the rotor return from a persistent contact state back to a contact-free state [9]. The majority of reported research involves horizontal rotor drop. However, in vertical rotor drop tests forward whirl is prevalent. In 2008, Tan et al. [10] built a finite element model of vertical arranged rotor drop onto the auxiliary bearings and got the equivalent stress distribution of the rotor and auxiliary bearings. In 2011, Zhao et al. [11] used ABAQUS to analyze stress and deformation in an auxiliary bearing. However, this paper lacks consideration of the dynamic behavior of the rotor. In 2013, Xiao et al. [12] analyzed the load characteristics of the ceramic ball

auxiliary bearing and established a finite element model in ANSYS applied in the transient response of the dropped rotor. However, this work did not consider the friction between the rotor and auxiliary bearing. Sun et al. [13] estimated the displacements, velocities, and accelerations of the rotor during touchdown from both the dynamic model and noisy data, the dynamic model of the rotor is introduced, and Kalman filtering technique is applied. Most papers in this region emphasize the dynamic behavior of the rotor touchdown process and the influence of different factors such as the air gap, rotational speed, and the eccentricity. Only a few works pay attention to the process of data acquired by the experiments.

On the other hand, rapidly developing machine learning techniques offer an attractive solution for data process. In the region of motion control of mechatronic systems, soft sensing [14–16] is an important application of machine learning technique. Soft sensing is an approach to estimate hard-to-measure variables of a dynamic system from easy-to-measure variables. The soft sensing technique can also be applied to improve the measurement quality of some variables by incorporating information from various sources. Many achievements of soft sensing based on Neural Network (NN) [17–21] and Support Vector Regression (SVR) [22, 23] are reported. These applications of soft sensing technique are closely related to the motion data process. However, to our best knowledge, no achievement of learning-based data process in the region of touchdown process is published.

In this paper, a novel touchdown process analysis method based on prior knowledge based learning technique is proposed. Similar to some above-mentioned literature, the presented work mainly utilizes a data-based design verification strategy. In other words, the proposed method depends on the actual data and will be implemented in the machine which is already designed and built and when touchdown incident or test has occurred.

More specifically, this paper is an extension of [13] and the dynamical model proposed in [13] is utilized. In [13], some mechanical parameters, such as stiffness, damping ratio, and friction coefficient, are introduced and regarded as known constants. In this paper, however, these parameters are modeled as functions of deformation of auxiliary bearing and velocity of the rotor. These functions are mathematically modeled by a prior knowledge based machine learning method. Kalman filtering technique is then applied to estimate the velocity and accelerator of the rotor. The learning-based model is trained by minimizing the error between measured and estimated motion states of the rotor. The proposed method is validated by the results of touchdown experiments.

The proposed method can be utilized to evaluate the operational state and residual life of the auxiliary bearings [7, 24] after touchdown. The improvement in designing auxiliary bearing can be expected thereby.

## 2. An Introduction to Prior Knowledge Based Kernel Regression

Prior Knowledge Based Kernel Regression (PKBKR) [25] is an extension of SVR [26, 27]. Similar to SVR, PKBKR

is a sample-based modeling method. When some input-output relationship has to be modeled, some training samples (input-output pairs  $(\mathbf{s}, \zeta)$ ) should be observed firstly, and then the model can be established. The process of establishing the model based on the training samples is usually called "training." PKBKR is also a kernel method; that is, a kernel function is applied to evaluate the relationship between various samples. A kernel function  $Q : \mathbb{R}^n \times \mathbb{R}^n \mapsto \mathbb{R}$  is a bivariable real-valued function defined by the user. In this paper we use the notation  $Q$  rather than conventional  $K$  to avoid confusing with stiffness. For a sample  $s$  and a sample set  $T = \{\mathbf{t}_1, \dots, \mathbf{t}_m\}$ , we use the following notation:

$$Q(\mathbf{s}, T) = \mathbf{Q}_{s,T} = [Q(\mathbf{s}, \mathbf{t}_1) \ \cdots \ Q(\mathbf{s}, \mathbf{t}_m)]. \quad (1)$$

Suppose that  $m$  samples  $T = \{\mathbf{t}_k, \zeta_k\}_{k=1}^m$  are obtained; the PKBKR model is in the following form:

$$\tilde{\zeta} = \sum_{k=1}^m \alpha_k Q(\mathbf{t}_k, \mathbf{s}) = \mathbf{Q}_{s,T} \boldsymbol{\alpha}, \quad (2)$$

where  $\alpha_k$  is coefficients,  $\boldsymbol{\alpha} = [\alpha_1, \dots, \alpha_m]^T$ . The parameter  $\alpha_k$  will be determined in the training procedure. The main difference between PKBKR and standard SVR is that the PKBKR algorithm allows introducing an initial guess  $f_0$  of the known model. The regularization term in SVR, which is introduced to control the model complexity, is replaced by the distance between the estimated model and the initial guess in the function space. Compared with standard SVR, the incorporation of initial guess may produce a more reasonable model. The detailed implementation of PKBKR can be found in [25] and is ignored here due to the limitation of space.

In this paper, the output  $\zeta$  is physically a mechanical quantity and cannot be measured directly, thus we use a function of  $\zeta$  to train the model. Because of this and computational considerations, model (2) is slightly modified in this paper. The following model is used:

$$\tilde{\zeta} = \mathbf{Q}_{s,T'} \boldsymbol{\alpha}, \quad (3)$$

where  $T'$  is a sample set defined by the user and can be differed from the observed sample set  $T$ . The particularity in modeling and training of PKBKR models will be discussed in the following sections.

### 3. Dynamic Model of Touchdown Process

**3.1. Basic Assumptions of Model.** In this paper, auxiliary bearing in the form of angular contact rolling-element bearing and vertically arranged AMB system is studied. A bearing of this type can bear both radial and axial load. In other words, it can be utilized as a radial-axial auxiliary bearing.

The touchdown process is quite complicated, which involves highly nonlinear and coupled interactions between the rotor, inner ring, balls, and outer ring of auxiliary bearings. Among these interactions, the impact between the rotor and the inner ring of auxiliary bearing plays a dominant role. Thus, for simplicity, in this paper the interaction between the rotor and a radial-axial auxiliary bearing is considered,

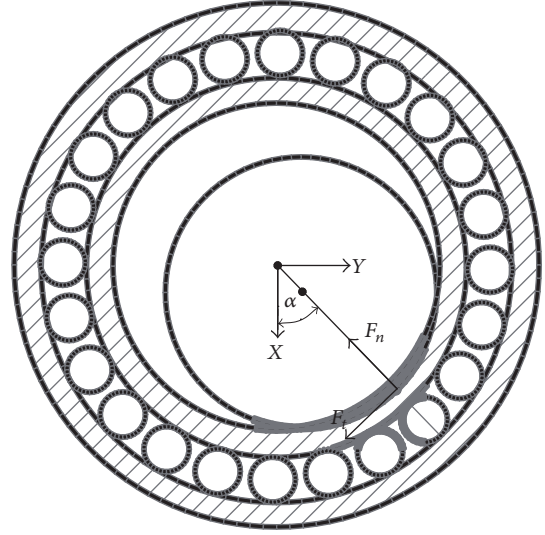


FIGURE 1: Sketch of auxiliary bearing and contact forces.

the auxiliary bearing is regarded as a whole, and the dynamic characteristics of auxiliary bearing parts and interactions between these parts are presented by the contact model with variable mechanical parameters, which will be discussed in this section.

On the other hand, as discussed in [28, 29] and this paper, the major impact forces occur at the first few impacts, this procedure usually takes only about one-tenth of a second, and the variation of the rotational speed of the rotor is neglectable. In this procedure, the motion state of the rotor is mainly affected by the impact forces, and the speed-dependent forces, such as centrifugal and gyroscopic forces, play relatively minor roles. Therefore this paper concentrates on the impact forces between rotor and auxiliary bearing.

The rotor motion can be described by its displacements in three directions, namely,  $x$ ,  $y$ ,  $z$ , where  $x$  and  $y$  are the radial displacements and  $z$  is the axial displacement. The inclination of the rotor is ignored in this paper.

**3.2. Dynamic Model.** Figure 1, which is a sketch of the auxiliary bearing, reveals contact forces. Throughout this paper, we assume that the rotor rotates in the anticlockwise direction.

The dynamic behavior of the rotor can be described by the following equations [13]:

$$\ddot{x} = -\frac{F_n}{m} \cos \alpha + \frac{F_t}{m} \sin \alpha + e\omega^2 \cos \theta, \quad (4a)$$

$$\ddot{y} = -\frac{F_n}{m} \sin \alpha - \frac{F_t}{m} \cos \alpha + e\omega^2 \sin \theta, \quad (4b)$$

$$\ddot{z} = \frac{F_z}{m} - g, \quad (4c)$$

$$\theta = \theta_0 + \omega t, \quad (4d)$$

$$\alpha = \arctan \frac{y}{x}. \quad (4e)$$

The definitions of notations are listed in the nomenclature.

In the touchdown process, the dynamic behaviors of the rotor can be divided into a few classes according to the contact situations between the rotor and the auxiliary bearing. In the following part we divide the contact forces into two parts. The subscripts  $R$  and  $Z$  are utilized to denote the source of the contact force, namely,  $F_z = F_{zR} + F_{zZ}$ , for example. In this paper, the normal contact forces are described by the stiffness-damping model and the tangential contact forces by the friction model. Moreover, this paper assumes that the radial and the axial contact phenomena are decoupled. The detailed discussions of contact forces are given as follows:

(1) Radial contact

(a) No radial contact exists: the criterion of this case is  $r \leq r_0$ . The contact forces resulting by radial contact are all zero; namely,

$$\begin{aligned} F_{nR} &= 0, \\ F_{tR} &= 0, \\ F_{zR} &= 0. \end{aligned} \quad (5)$$

(b) Radial contact occurs: in this case, the radial force is given by the stiffness-damping model, and the tangent and axial forces are given by the friction model; namely,

$$F_{nR} = k_R (r - r_0) + c_R \dot{r}, \quad (6a)$$

$$F_{tR} = \mu F_{nR}, \quad (6b)$$

$$F_{zR} = \mu \text{sign}(\dot{z}) F_{nR}. \quad (6c)$$

(2) Axial contact

(a) No axial contact exists: the criterion of this case is  $z \geq -z_0$ . The contact forces resulting by axial contact are all zero; namely,

$$\begin{aligned} F_{nZ} &= 0, \\ F_{tZ} &= 0, \\ F_{zZ} &= 0. \end{aligned} \quad (7)$$

(b) Axial contact occurs: in this case, the axial force is obtained by the stiffness-damping model, and the radial force is zero. The tangent force, estimated by theoretical derivations and experiments, is proportional to the axial positive pressure due to friction. It is important to notice the positive pressure is exactly  $F_{zZ}$ . The force  $F_{zR}$  resulted by the friction and will not lead to tangent force. From this discussion,

$$F_{nZ} = 0, \quad (8a)$$

$$F_{tZ} = k_{ZR} F_{zZ}, \quad (8b)$$

$$F_{zZ} = -k_Z (z + z_0) - c_Z \dot{z}. \quad (8c)$$

**3.3. Learning-Based Model of Parameters.** The model discussed in the above subsection involves some mechanical parameters, such as  $k_R, c_R$ . In [13], these parameters are regarded as constants and these values are determined theoretically or empirically. However, in this paper, these parameters are modeled as functions of auxiliary bearing deformation and rotor velocity. These function relationships can hardly be determined theoretically or experimentally. Thus this paper uses PKBKR technique to model these relationships. To be more specific, we use the PKBKR to model the following parameters:

$$k_R(\rho) = \mathbf{Q}_{\rho, T_R} \boldsymbol{\alpha}_1, \quad (9a)$$

$$c_R(\rho) = \mathbf{Q}_{\rho, T_R} \boldsymbol{\alpha}_2, \quad (9b)$$

$$\mu(\rho) = \mathbf{Q}_{\rho, T_R} \boldsymbol{\alpha}_3, \quad (9c)$$

$$k_Z(\zeta) = \mathbf{Q}_{\zeta, T_Z} \boldsymbol{\alpha}_4, \quad (9d)$$

$$c_Z(\zeta) = \mathbf{Q}_{\zeta, T_Z} \boldsymbol{\alpha}_5, \quad (9e)$$

$$k_{ZR}(\zeta) = \mathbf{Q}_{\zeta, T_Z} \boldsymbol{\alpha}_6, \quad (9f)$$

where

$$\begin{aligned} \boldsymbol{\rho} &= \begin{bmatrix} r - r_0 \\ \dot{r} \end{bmatrix}, \\ \boldsymbol{\zeta} &= \begin{bmatrix} z + z_0 \\ \dot{z} \end{bmatrix} \end{aligned} \quad (10)$$

refer to the radial and axial deformation of auxiliary bearing and velocity of the rotor, respectively. Moreover,  $T_R$  and  $T_Z$  are predefined sample sets. The nominal values of these parameters are regarded as constant functions and utilized as the initial guesses of the models in (9a), (9b), (9c), (9d), (9e), and (9f). We formally denote these constant functions by  $f_{0,1}, \dots, f_{0,6}$ , respectively. Their values can be found in [13]. The parameters  $\boldsymbol{\alpha}_1, \dots, \boldsymbol{\alpha}_6$  will be determined in the training process discussed in Section 4.3.

## 4. State Estimation and Model Training

Kalman filtering is an effective algorithm for state estimation based on system model and observations. Nonlinear extended Kalman filtering can be applied to deal with the nonlinear discrete-time system.

**4.1. State Space Description of Touchdown Process.** To apply Kalman filtering the state space description should be established firstly. Define the state variable as

$$\boldsymbol{\xi} = [x \ y \ z \ \theta \ \dot{x} \ \dot{y} \ \dot{z}]^T. \quad (11)$$

Then through the discussions in the next section, the derivative of  $\xi$  is

$$\begin{aligned} \dot{\xi} &= \varphi(\xi) \\ &= \begin{bmatrix} \dot{x} \\ \dot{y} \\ \dot{z} \\ \omega \\ m^{-1}(-F_n \cos \alpha + F_t \sin \alpha) + e\omega^2 \cos \theta \\ m^{-1}(-F_n \sin \alpha - F_t \cos \alpha) + e\omega^2 \sin \theta \\ m^{-1}F_z - g \end{bmatrix}, \end{aligned} \quad (12)$$

where  $\varphi$  is the state transfer function. The observations are given by the displacement sensors. The observation variable is defined as  $\eta = [x \ y \ z]^T$ .

The derivative matrix of  $\varphi$  with respect to the state variable  $\xi$ , denoted by  $\Phi$ , is also necessary for applying Kalman filtering. This procedure is quite tedious and the computation result is quite complex. Hence we only give a few components of this matrix as examples, and the others can be computed in a similar way

$$\begin{aligned} \Phi_{(5,1)} &= \frac{\partial \dot{x}}{\partial x} = \frac{1}{m} \left( -\frac{\partial F_n}{\partial x} \cos \alpha - F_n \frac{\partial \cos \alpha}{\partial x} \right. \\ &\quad \left. + \frac{\partial F_t}{\partial x} \sin \alpha + F_t \frac{\partial \sin \alpha}{\partial x} \right), \end{aligned} \quad (13a)$$

$$\Phi_{(5,5)} = \frac{\partial \dot{x}}{\partial \dot{x}} = \frac{1}{m} \left( -\frac{\partial F_n}{\partial \dot{x}} \cos \alpha + \frac{\partial F_t}{\partial \dot{x}} \sin \alpha \right), \quad (13b)$$

$$\begin{aligned} &\frac{\partial F_{nR}}{\partial x} \\ &= \begin{cases} 0, & r \leq r_0, \\ k_R \frac{\partial r}{\partial x} + \frac{\partial k_R}{\partial x} (r - r_0) + c_R \frac{\partial \dot{r}}{\partial x} + \frac{\partial c_R}{\partial x} \dot{r}, & r > r_0, \end{cases} \end{aligned} \quad (13c)$$

$$\frac{\partial F_{tR}}{\partial x} = \mu \frac{\partial F_{nR}}{\partial x} + F_{nR} \frac{\partial \mu}{\partial x}, \quad (13d)$$

$$\frac{\partial F_{nZ}}{\partial x} = \frac{\partial F_{tZ}}{\partial x} = 0,$$

$$\dot{r} = \frac{x}{r} \dot{x} + \frac{y}{r} \dot{y} = \cos \alpha \dot{x} + \sin \alpha \dot{y}, \quad (13e)$$

$$\frac{\partial r}{\partial x} = \frac{x}{r} = \cos \alpha, \quad (13f)$$

$$\frac{\partial \dot{r}}{\partial x} = \frac{y^2}{r^3} \dot{x} - \frac{xy}{r^3} \dot{y},$$

$$\frac{\partial \cos \alpha}{\partial x} = \frac{y^2}{r^3}, \quad (13g)$$

$$\frac{\partial \sin \alpha}{\partial x} = \frac{-xy}{r^3},$$

$$\frac{\partial F_{nR}}{\partial \dot{x}} = \begin{cases} 0, & r \leq r_0, \\ \frac{\partial k_R}{\partial \dot{x}} (r - r_0) + c_R \frac{\partial \dot{r}}{\partial \dot{x}} + \dot{r} \frac{\partial c_R}{\partial \dot{x}}, & r > r_0, \end{cases} \quad (13h)$$

$$\frac{\partial F_{tR}}{\partial \dot{x}} = \mu \frac{\partial F_{nR}}{\partial \dot{x}} + F_{nR} \frac{\partial \mu}{\partial \dot{x}}, \quad (13i)$$

$$\frac{\partial \dot{r}}{\partial \dot{x}} = \cos \alpha, \quad (13j)$$

$$\frac{\partial k_R}{\partial x} = \left( \frac{\partial r}{\partial x} \left( \frac{\partial}{\partial r} \mathbf{Q}_{\rho, T_R} \right) + \frac{\partial \dot{r}}{\partial x} \left( \frac{\partial}{\partial \dot{r}} \mathbf{Q}_{\rho, T_R} \right) \right) \alpha_1, \quad (13k)$$

$$\frac{\partial k_R}{\partial \dot{x}} = \frac{\partial \dot{r}}{\partial \dot{x}} \left( \frac{\partial}{\partial \dot{r}} \mathbf{Q}_{\rho, T_R} \right) \alpha_1, \quad (13l)$$

$$\frac{\partial c_R}{\partial x} = \left( \frac{\partial r}{\partial x} \left( \frac{\partial}{\partial r} \mathbf{Q}_{\rho, T_R} \right) + \frac{\partial \dot{r}}{\partial x} \left( \frac{\partial}{\partial \dot{r}} \mathbf{Q}_{\rho, T_R} \right) \right) \alpha_2, \quad (13m)$$

$$\frac{\partial c_R}{\partial \dot{x}} = \frac{\partial \dot{r}}{\partial \dot{x}} \left( \frac{\partial}{\partial \dot{r}} \mathbf{Q}_{\rho, T_R} \right) \alpha_2, \dots \quad (13n)$$

**4.2. Nonlinear Extended Kalman Filtering.** In the last subsection, the system is described by the following time-invariant continuous-time state space description:

$$\dot{\xi} = \varphi(\xi), \quad (14a)$$

$$\eta = \mathbf{H}\xi, \quad (14b)$$

where  $\xi$  and  $\eta$  are the state variable and the observation variable,  $\varphi$  is the state transfer function, and  $\mathbf{H}$  is the observation matrix. In order to discretize the model (14a) and (14b) to a discrete-time model, the Runge-Kutta [30] method is utilized, and then the discrete-time model is in the following iterative form:

$$\xi_{k+1} = \mathbf{f}(\xi_k) = \xi_k + \frac{1}{6} (\mathbf{k}_1 + 2\mathbf{k}_2 + 2\mathbf{k}_3 + \mathbf{k}_4), \quad (15a)$$

$$\mathbf{k}_1 = h\varphi(\xi_k), \quad (15b)$$

$$\mathbf{k}_2 = h\varphi\left(\xi_k + \frac{1}{2}\mathbf{k}_1\right), \quad (15c)$$

$$\mathbf{k}_3 = h\varphi\left(\xi_k + \frac{1}{2}\mathbf{k}_2\right), \quad (15d)$$

$$\mathbf{k}_4 = h\varphi(\xi_k + \mathbf{k}_3), \quad (15e)$$

$$\eta_k = \mathbf{H}\xi_k, \quad (15f)$$

where  $h$  is the sampling period.

The first-order derivative matrix of  $\mathbf{f}$  should be evaluated to apply Kalman filtering. Through tedious computations, the

derivative matrix  $\Phi_k = (\partial \mathbf{f} / \partial \mathbf{z})|_{(\xi_k)}$  can be written in the iterative form [23]:

$$\Phi_k = \mathbf{I} + \frac{1}{6} \left( \frac{\partial \mathbf{k}_1}{\partial \xi} + 2 \frac{\partial \mathbf{k}_2}{\partial \mathbf{z}} + 2 \frac{\partial \mathbf{k}_3}{\partial \xi} + \frac{\partial \mathbf{k}_4}{\partial \xi} \right) \Big|_{(\xi_k)}, \quad (16a)$$

$$\frac{\partial \mathbf{k}_1}{\partial \xi} \Big|_{(\xi_k)} = h \frac{\partial \varphi}{\partial \xi} \Big|_{(\xi_k)}, \quad (16b)$$

$$\frac{\partial \mathbf{k}_2}{\partial \xi} \Big|_{(\xi_k)} = h \frac{\partial \varphi}{\partial \xi} \Big|_{(\xi_k + (1/2)\mathbf{k}_1)} \left( \mathbf{I} + \frac{1}{2} \frac{\partial \mathbf{k}_1}{\partial \xi} \Big|_{(\xi_k)} \right), \quad (16c)$$

$$\frac{\partial \mathbf{k}_3}{\partial \xi} \Big|_{(\xi_k)} = h \frac{\partial \varphi}{\partial \xi} \Big|_{(\xi_k + (1/2)\mathbf{k}_2)} \left( \mathbf{I} + \frac{1}{2} \frac{\partial \mathbf{k}_2}{\partial \xi} \Big|_{(\xi_k)} \right), \quad (16d)$$

$$\frac{\partial \mathbf{k}_4}{\partial \xi} \Big|_{(\xi_k)} = h \frac{\partial \varphi}{\partial \xi} \Big|_{(\xi_k + \mathbf{k}_3)} \left( \mathbf{I} + \frac{\partial \mathbf{k}_3}{\partial \xi} \Big|_{(\xi_k)} \right), \quad (16e)$$

where  $\mathbf{I}$  is the identity matrix.

Then extended Kalman filtering can be applied to compute the rotor displacement estimation  $\tilde{\xi}_k$ . The detailed estimation program is standard, and we write down it here for completeness

$$\tilde{\xi}_{k,-} = \mathbf{f}(\tilde{\xi}_{k-1}), \quad (17a)$$

$$\tilde{\eta}_k = \mathbf{H} \tilde{\xi}_{k,-}, \quad (17b)$$

$$\tilde{\xi}_k = \tilde{\xi}_{k,-} + \mathbf{K}_k (\eta_k - \tilde{\eta}_k), \quad (17c)$$

$$\mathbf{P}_{k,-} = \Phi_k \mathbf{P}_{k-1} \Phi_k^\top + \mathbf{Q}, \quad (17d)$$

$$\mathbf{K}_k = \mathbf{P}_{k,-} (\mathbf{H} \mathbf{P}_{k,-} \mathbf{H}^\top + \mathbf{R})^{-1}, \quad (17e)$$

$$\mathbf{P}_k = (\mathbf{I} - \mathbf{K}_k \mathbf{H}) \mathbf{P}_{k,-}, \quad (17f)$$

where  $\tilde{\xi}_0, \mathbf{P}_0, \mathbf{Q}, \mathbf{R}$  are predefined parameters.

**4.3. Model Training.** Suppose that all mechanical parameters are given and a measured data set  $\{\eta_k\}_{k=1}^l$  is available, given the coefficients  $\alpha_1, \dots, \alpha_6$ , and then the system state and output  $\{\tilde{\xi}, \tilde{\eta}_k\}_{k=1}^l$  can be estimated based on the dynamic model and the state estimation technique discussed in the above subsections. Therefore the estimated output  $\{\tilde{\eta}_k\}_{k=1}^l$  depends on the coefficients  $\alpha_1, \dots, \alpha_6$  and can be utilized to evaluate the precision of PKBKR model. More specifically, we use the following minimization problem to train these parameters:

$$\begin{aligned} \min_{\alpha_1, \dots, \alpha_6} & \sum_{k=1}^l \|\tilde{\eta}_k - \eta_k\|^2 \\ & + \lambda \left( \sum_{k=1}^3 \|\mathbf{Q}_{\rho, T_R} \alpha_k - f_{0,k}\|_{\mathcal{H}}^2 + \sum_{k=4}^6 \|\mathbf{Q}_{\zeta, T_Z} \alpha_k - f_{0,k}\|_{\mathcal{H}}^2 \right), \end{aligned} \quad (18)$$

where  $\lambda$  is the regularization parameter and  $\mathcal{H}$  is the reproducing kernel Hilbert space [31, 32] associated with the kernel function  $Q$ . The regularization term  $\lambda(\sum \|\mathbf{Q}_{\rho, T_R} \alpha_k - f_{0,k}\|_{\mathcal{H}}^2 + \sum \|\mathbf{Q}_{\zeta, T_Z} \alpha_k - f_{0,k}\|_{\mathcal{H}}^2)$  represents the distance between

PKBKR models and initial guesses. The prior knowledge carried by the initial guesses is incorporated by introducing this term.

## 5. Experiments

**5.1. Experiment Setup.** Experiments are performed to validate the proposed method. The data in the experiments are attained from 21 touchdown experiments on the backup helium circulator system of HTR-10. A detailed description of this system can be found in [11, 13, 33]. These experiments are performed with various conditions; for example, the brake of drive motor will be applied and an additional axial load (about 2000 N) will be applied by an axial loader [29]. The experiment conditions are summarized in Table 1.

In the analysis, the data in the first 0.15 seconds after the touchdown is used. The proposed method is utilized to estimate the state of the system. Moreover, the results in [13], which are produced by a method without machine learning modeling, are also illustrated for comparison.

**5.2. Results of Displacement Estimation.** Firstly, the results of rotor displacement estimation in experiment #11 are shown in Figures 2–4. In these figures, the measured displacements are denoted by  $x, y, z$ . Notations  $x_{\text{est}}, y_{\text{est}}, z_{\text{est}}$  refer to the displacements estimated by the method in [13] and  $x_{\text{est,PKBKR}}, y_{\text{est,PKBKR}}, z_{\text{est,PKBKR}}$  stand for estimation results of the proposed method.

Moreover, the displacement estimation errors of all 21 experiments are shown in Figure 5, where the estimation error is evaluated by the root mean square error as

$$x_{\text{err}} = \sqrt{\frac{1}{l} \sum_{k=1}^l (x_{\text{est},k} - x_k)^2}, \quad (19a)$$

$$\begin{aligned} x_{\text{err,PKBKR}} &= \sqrt{\frac{1}{l} \sum_{k=1}^l (x_{\text{est,PKBKR},k} - x_k)^2}, \\ y_{\text{err}} &= \sqrt{\frac{1}{l} \sum_{k=1}^l (y_{\text{est},k} - y_k)^2}, \end{aligned} \quad (19b)$$

$$\begin{aligned} y_{\text{err,PKBKR}} &= \sqrt{\frac{1}{l} \sum_{k=1}^l (y_{\text{est,PKBKR},k} - y_k)^2}, \\ z_{\text{err}} &= \sqrt{\frac{1}{l} \sum_{k=1}^l (z_{\text{est},k} - z_k)^2}, \end{aligned} \quad (19c)$$

$$z_{\text{err,PKBKR}} = \sqrt{\frac{1}{l} \sum_{k=1}^l (z_{\text{est,PKBKR},k} - z_k)^2},$$

where  $l$  denotes the size of data set,  $x_k, x_{\text{est},k}, x_{\text{est,PKBKR},k}$  denote  $k$ -th sample of  $x, x_{\text{est}}, x_{\text{est,PKBKR},k}$ , respectively, and other notations are self-explanatory.

TABLE 1: Summation of touchdown experiments.

Number of experiments	Touchdown speed (rpm)	Brake?	Additional axial load?	Auxiliary bearing type
1	5000	No	No	Ceramic ball
2	5000	No	No	Ceramic ball
3	5000	No	No	Ceramic ball
4	5000	No	No	Ceramic ball
5	5000	No	No	Ceramic ball
6	5000	Yes	No	Ceramic ball
7	5000	Yes	No	Ceramic ball
8	5000	Yes	Yes	Ceramic ball
9	5000	Yes	Yes	Ceramic ball
10	5000	Yes	Yes	Ceramic ball
11	5000	Yes	Yes	Ceramic ball
12	5000	Yes	Yes	Ceramic ball
13	5000	Yes	No	Ceramic ball
14	5000	Yes	No	Ceramic ball
15	5000	Yes	Yes	Ceramic ball
16	5000	Yes	Yes	Ceramic ball
17	5000	Yes	Yes	Ceramic ball
18	5000	Yes	Yes	Ceramic ball
19	5000	Yes	Yes	Ceramic ball
20	5000	Yes	Yes	Ceramic ball
21	5000	No	No	Steel ball

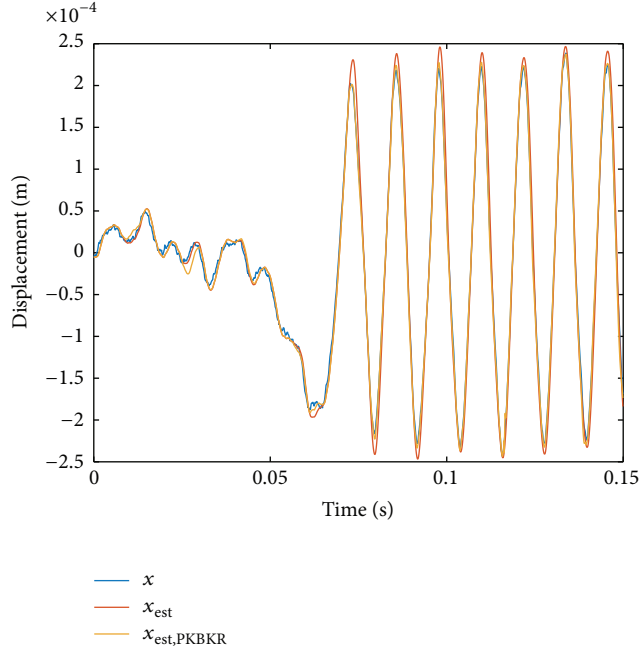


FIGURE 2: Measured and estimated displacements. X-direction, experiment #11.

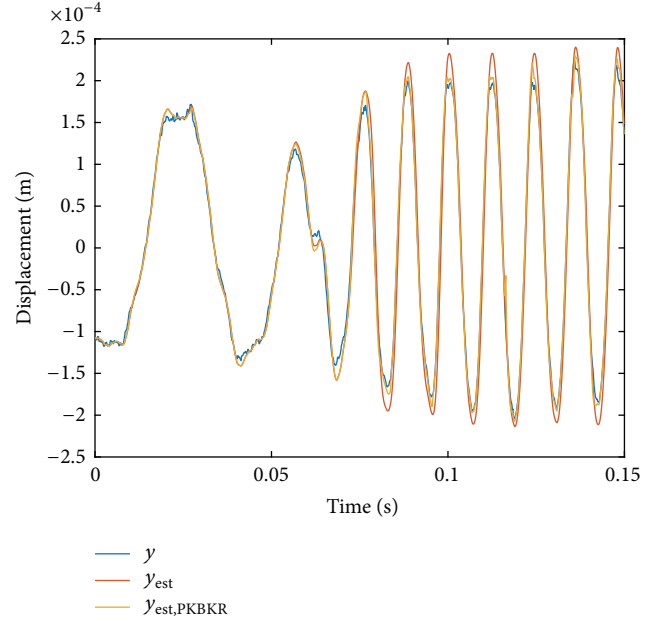


FIGURE 3: Measured and estimated displacements. Y-direction, experiment #11.

As shown in Figure 5, precise estimations of the displacement of the rotor can be achieved by the proposed method under various conditions in all 21 experiments, and the root mean square errors in all three directions are less

than 0.02 mm. Thus the proposed method is suitable for analyzing the touchdown process under various conditions.

It is obvious that the proposed method makes an excellent estimation of rotor displacement and outperforms the

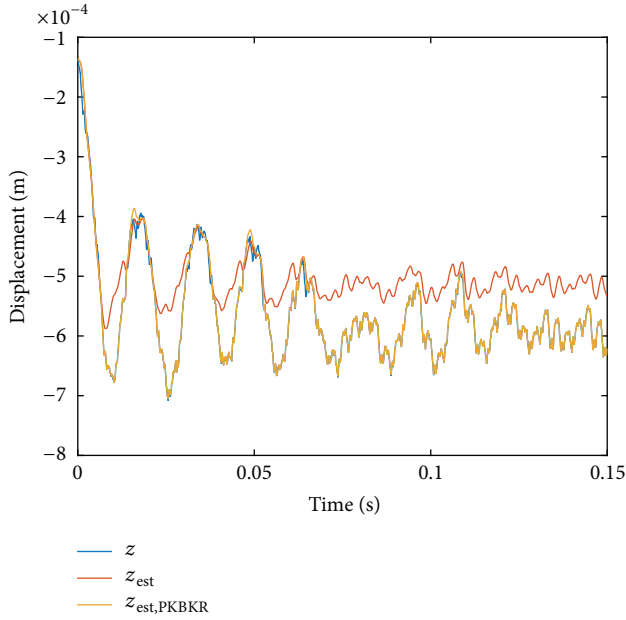


FIGURE 4: Measured and estimated displacements. Z-direction, experiment #11.

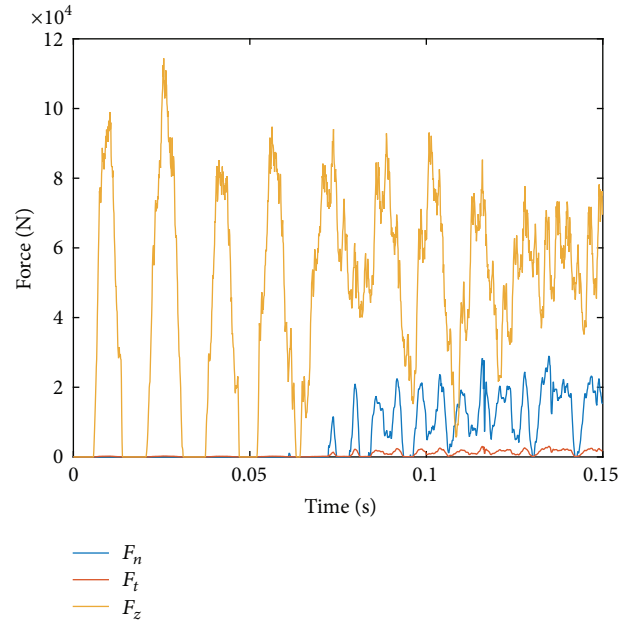


FIGURE 6: Estimated force. Experiment #11.

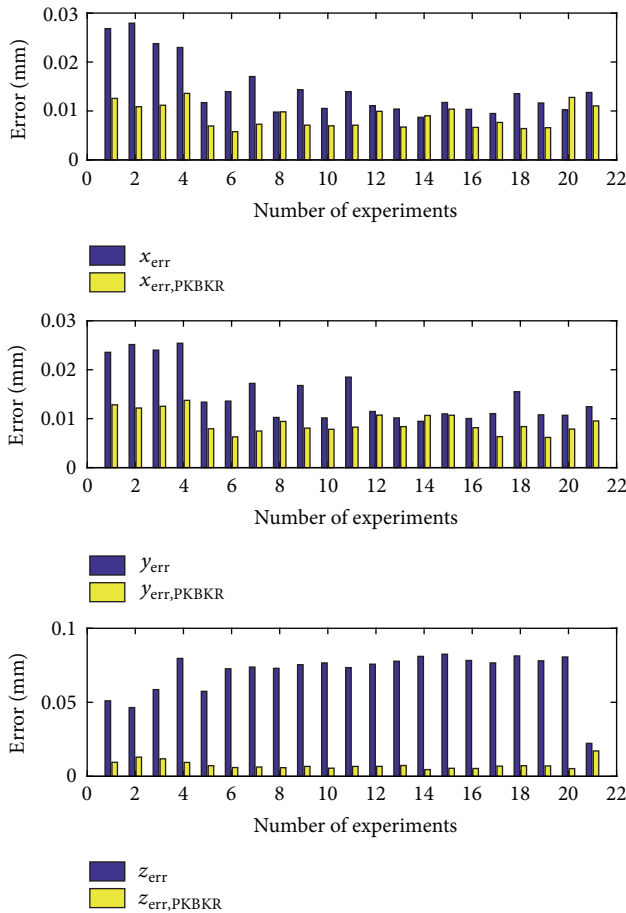


FIGURE 5: Displacement estimation errors. All directions and all 21 experiments.

method without learning, especially in the estimation of  $z$ -displacement.

The main reason is that, in the original dynamic model, some mechanical parameters are assumed to be constant, but in practice these parameters may be affected by the motion of rotor and auxiliary bearing. By introducing learning method, these parameters are allowed to vary with respect to rotor motion and the quality of the dynamic model is significantly improved. Moreover, the relationship between these parameters and the rotor motion is determined by the measured data; thus precise estimations are achieved. On the other hand, as for the precision of radial displacement estimation, both methods (with and without learning) are similar, shown in Figure 5. The main reason is that, compared with complicated axial motion, the radial motion of the rotor is relatively simpler and smoother. As shown in Figure 5, the rotor carries out circular motion after first few impacts and radial displacements in  $X$ - and  $Y$ -direction are sinusoidal. The radial acceleration, velocity, and deformation of the auxiliary bearing are relatively smaller; thus the radial mechanical parameters do not vary significantly and the estimation method with constant methods also achieves satisfactory performance.

**5.3. Results of Force Estimation.** The estimated contact force in experiment #11 is shown in Figure 6. The maximal impact occurs at the first touchdown. The touchdown process can be divided into two stages: in the first six bounces, no radial contact between the rotor and auxiliary bearing occurs and the radial forces can be neglected; after the sixth bounces, the rotor clings to the auxiliary bearing and large radial forces emerge. The radial force is dominated by the normal force.

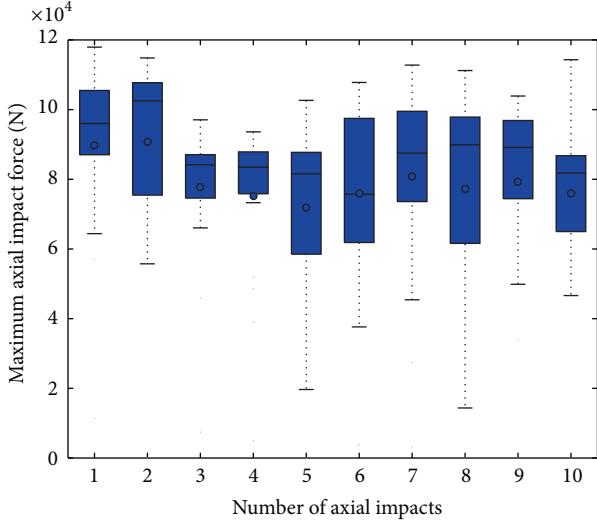


FIGURE 7: Estimated axial force. All 21 experiments.

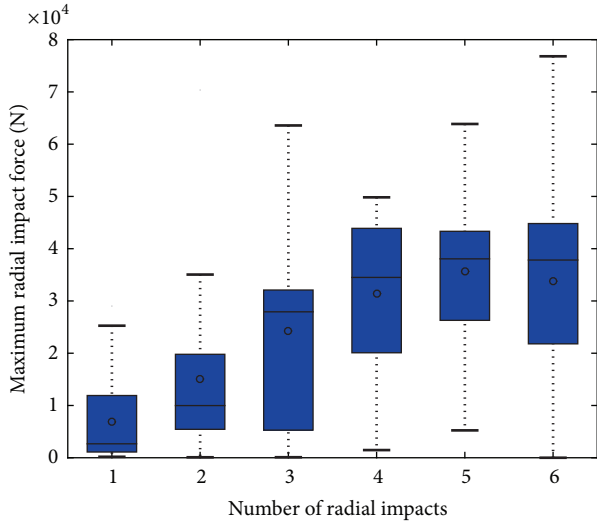


FIGURE 8: Estimated normal force. All 21 experiments.

The experiment results have shown the validity of the proposed method in estimating the motion state of the rotor during the touchdown process.

Furthermore, in order to visualize the force estimations in all 21 experiments, the peak values of axial and radial forces are extracted. The peak values are grouped according to the number of impacts. The statistical distributions are illustrated in the form of boxplot, shown in Figures 7 and 8. From these figures, a similar pattern can be found; namely, the maximal axial impact occurs at the first two touchdowns and the peak values of axial force decrease slowly in the following touchdowns and bounces. As above mentioned, the radial forces emerge after the first radial contact between rotor and bearing, and the peak values of radial force increase at the first several radial impacts. The maximal radial force is about one-third to one-half of the maximal axial force.

## 6. Conclusions and Discussions

Magnetic bearings are widely applied in High Temperature Gas-cooled Reactor (HTGR) and auxiliary bearings are important backup and safety components in AMB systems. In the applications associated with HTGR, the performance of auxiliary bearings significantly affects the reliability, safety, and serviceability of the AMB system, the rotating equipment, and the whole reactor. The dynamic model of the touchdown process is firstly established. In this model, some mechanical parameters are regarded as functions of deformation of auxiliary bearing and velocity of the rotor and a machine learning technique is utilized to model these function relationships. Based on the dynamic model and Kalman filtering technique, the proposed method can offer estimations of rotor's motion state from noisy observations and estimation precision is significantly improved compared with the method without learning. The proposed method is validated by the experimental data from touchdown experiments.

The proposed method in this paper provides a novel data processing method for the touchdown process and is a foundation for further researches.

The future work includes the following:

(1) As above mentioned, this paper depends on the actual touchdown data, which cannot be directly utilized in the design stage of the whole rotating equipment. In order to evaluate the severity of touchdown and improve the auxiliary bearing design, analysis of strain and stress in the auxiliary bearing will be performed based on the estimated force. Moreover, the operational state and remaining life of auxiliary bearings can be estimated as well, as discussed in [7, 24]. Together with these works, the design-verification-validation loop can be completed.

(2) In this paper, a relatively simple motion model is applied. Only one axial-radial auxiliary bearing and three degree-of-freedom of the rotor are considered, the eccentricity is constant, and the gyroscopic force is ignored. In the future work, we intend to apply the proposed method to the five degree-of-freedom rotor-bearing model [28]. Furthermore, the overall motion model considering the interaction between the rotor, inner ring, balls, and outer ring of the auxiliary bearing will be analyzed in the future.

(3) In this paper, 21 experiments are analyzed and conclusions are plotted in a statistical sense. In the future, more touchdown experiments are planned to make more precise statistical analyses of the performance of auxiliary bearings, touchdown conditions, and their effect on the whole reactor under accident conditions.

## Nomenclature

- $\alpha$ : Contact angle between the rotor and the auxiliary bearing
- $\ddot{x}, \ddot{y}, \ddot{z}$ : Second-order derivatives of displacements, namely, the accelerations of the rotor
- $\dot{x}, \dot{y}, \dot{z}$ : Derivatives of displacements, namely, the velocities of the rotor

$\rho$ :	Vector of auxiliary bearing radial deformation and rotor radial velocity
$\zeta$ :	Vector of auxiliary bearing axial deformation and rotor axial velocity
$\mu$ :	Friction coefficient between the rotor and the auxiliary bearing
$\omega$ :	Rotational speed of the rotor
sign:	Signum function
$\theta$ :	Rotational angle of the rotor
$\theta_0$ :	Rotational angle of the rotor at the instant of the shutdown of magnetic bearings
$c_R, c_Z$ :	Radial and axial damping coefficient
$e$ :	Eccentricity between the mass center and the rotational center of the rotor
$F_n, F_t, F_z$ :	Radial, tangential, and axial contact forces between the rotor and the auxiliary bearing
$F_{nR}, F_{tR}, F_{zR}$ :	Contact forces caused by radial contact
$F_{nZ}, F_{tZ}, F_{zZ}$ :	Contact forces caused by axial contact
$g$ :	Acceleration due to gravity
$k_R, k_Z$ :	Radial and axial stiffness
$k_{ZR}$ :	Coefficient between tangential force and axial positive pressure
$m$ :	Mass of the rotor
$Q$ :	Kernel function
$r$ :	Radial displacement of the rotor
$r_0, z_0$ :	Nominal radial and axial clearance between the rotor and the auxiliary bearing at operation position
$t$ :	Time elapsed since the shutdown of magnetic bearings
$T_R, T_Z$ :	Sample sets
$x, y, z$ :	Displacements of the rotor in three directions
$\alpha_1, \dots, \alpha_6$ :	Coefficients in learning models.

## Conflicts of Interest

The authors declare that there are no conflicts of interest regarding the publication of this paper.

## Acknowledgments

This paper is financially supported by the National Science and Technology Major Project of China (2011ZX069) and Project 61305065 and Project 51275261 supported by NSFC.

## References

- [1] T. Ishii and R. G. Kirk, "Transient response technique applied to active magnetic bearing machinery during rotor drop," *Journal of Rotating Machinery and Vehicle Dynamics*, pp. 191–199, 1991.
- [2] M. Fumagalli and G. Schweitzer, "Measurements on a rotor contacting its housing," in *Proceedings of the in Imech Conference Transactions*, vol. 6, pp. 779–788, 1996.
- [3] Z. Fang and L. E. Barrett, "Transient response of single disk rotor with active magnetic bearings during rotor drop," *Journal of Shanghai Jiaotong University*, p. 7, 1996.
- [4] S. Zeng, "Modelling and experimental study of the transient response of an active magnetic bearing rotor during rotor drop on back-up bearings," *Proceedings of the Institution of Mechanical Engineers, Part I: Journal of Systems and Control Engineering*, vol. 217, no. 6, pp. 505–517, 2003.
- [5] G. Sun, A. B. Palazzolo, A. Provenza, and G. Montague, "Detailed ball bearing model for magnetic suspension auxiliary service," *Journal of Sound and Vibration*, vol. 269, no. 3–5, pp. 933–963, 2004.
- [6] G. Sun, "Rotor drop and following thermal growth simulations using detailed auxiliary bearing and damper models," *Journal of Sound and Vibration*, vol. 289, no. 1–2, pp. 334–359, 2006.
- [7] J. G. Lee and A. Palazzolo, "Catcher bearing life prediction using a rainflow counting approach," *Journal of Tribology*, vol. 134, no. 3, Article ID 031101, 2012.
- [8] P. S. Keogh and W. Y. Yong, "Thermal assessment of dynamic rotor/auxiliary bearing contact events," *Journal of Tribology*, vol. 129, no. 1, pp. 143–152, 2007.
- [9] M. Schlotter and P. S. Keogh, "Synchronous position recovery control for flexible rotors in contact with auxiliary bearings," *Journal of Vibration and Acoustics*, vol. 129, no. 5, pp. 550–558, 2007.
- [10] Z.-W. Tan, L. Wan, and S.-Y. He, "Impact simulation of HTR-10 vertical magnetic suspension rotor dropping into catcher bearings in early design phase," *Hedongli Gongcheng/Nuclear Power Engineering*, vol. 29, no. 5, pp. 5–8, 2008.
- [11] J.-X. Zhao, G.-J. Yang, Y. Li, and S.-Y. Yu, "Numerical analysis of magnetically suspended rotor in htr-10 helium circulator being dropped into auxiliary bearings," *Nuclear Power Engineering*, vol. 33, no. 3, pp. 61–64, 2012.
- [12] Z. Xiao, G. Yang, Z. Shi, and S. Yu, "Behavior of a magnetically suspended rotor dropped into auxiliary bearings," in *Proceedings of the 2013 21st International Conference on Nuclear Engineering, ICONE 2013*, August 2013.
- [13] Z. Sun, X. Kang, J. Zhao, G. Yang, and Z. Shi, "Dynamic behavior analysis of touchdown process in active magnetic bearing system based on Kalman filtering," in *Proceedings of the 2014 22nd International Conference on Nuclear Engineering, ICONE 2014*, July 2014.
- [14] W. Yan, H. Shao, and X. Wang, "Soft sensing modeling based on support vector machine and Bayesian model selection," *Computers & Chemical Engineering*, vol. 28, no. 8, pp. 1489–1498, 2004.
- [15] J. Luo and H. Shao, "Soft sensing modeling using neurofuzzy system based on rough set theory," in *Proceedings of the 2002 American Control Conference*, pp. 543–548, May 2002.
- [16] S. C. Patwardhan, J. Prakash, and S. L. Shah, "Soft sensing and state estimation: review and recent trends," *IFAC Proceedings Volumes*, vol. 40, no. 19, pp. 65–72, 2007.
- [17] K. Worden, W. J. Staszewski, and J. J. Hensman, "Natural computing for mechanical systems research: A tutorial overview," *Mechanical Systems and Signal Processing*, vol. 25, no. 1, pp. 4–111, 2011.
- [18] F. Wu and T. Chai, "Soft sensing method for magnetic tube recovery ratio via fuzzy systems and neural networks," *Neurocomputing*, vol. 73, no. 13–15, pp. 2489–2497, 2010.
- [19] E. Terzic, R. Nagarajah, and M. Alamgir, "A neural network approach to fluid quantity measurement in dynamic environments," *Mechatronics*, vol. 21, no. 1, pp. 145–155, 2011.
- [20] Y. Çaya, A. Çiçekb, F. Karac, and S. Sağıroğlu, "Prediction of engine performance for an alternative fuel using artificial

- neural network,” *Applied Thermal Engineering*, vol. 37, pp. 217–225, 2012.
- [21] E. Kilic, C. U. Dogruer, M. Dolen, and A. B. Koku, “Position estimation for timing belt drives of precision machinery using structured neural networks,” *Mechanical Systems and Signal Processing*, vol. 29, pp. 343–361, 2012.
- [22] Z. Sun, J. Zhao, and S. Yu, “Nonlinear nonparametric identification of magnetic bearing system based on support vector regression,” in *Proceedings of the 13th International Symposium on Magnetic Bearings*, 2012.
- [23] Z. Sun, J. Zhao, Z. Shi, and S. Yu, “Soft sensing of magnetic bearing system based on support vector regression and extended Kalman filter,” *Mechatronics*, vol. 24, no. 3, pp. 186–197, 2014.
- [24] G. Sun, “Auxiliary bearing life prediction using Hertzian contact bearing model,” *Journal of Vibration and Acoustics*, vol. 128, no. 2, pp. 203–209, 2006.
- [25] Z. Sun, Z.-K. Zhang, and H.-G. Wang, “Incorporating prior knowledge into kernel based regression,” *Acta Automatica Sinica*, vol. 34, no. 12, pp. 1515–1521, 2008.
- [26] A. J. Smola and B. Schölkopf, “A tutorial on support vector regression,” *Statistics and Computing*, vol. 14, no. 3, pp. 199–222, 2004.
- [27] N. Cristianini and J. Shawe-Taylor, *An Introduction to Support Vector Machines*, Cambridge University Press, Cambridge, UK, 2000.
- [28] Y. Zhao, G. Yang, X. Liu, Z. Shi, and L. Zhao, “Research on dynamics and experiments about auxiliary bearings for the helium circulator of the 10 MW high temperature gas-cooled reactor,” *Annals of Nuclear Energy*, vol. 95, pp. 176–187, 2016.
- [29] Y. Zhao, G. Yang, P. Keogh, and L. Zhao, “Dynamic Analysis for the Rotor Drop Process and Its Application to a Vertically Levitated Rotor/Active Magnetic Bearing System,” *Journal of Tribology*, vol. 139, no. 4, p. 041701, 2017.
- [30] F. E. Cellier and E. Kofman, *Continuous System Simulation*, Springer Science+Business Media, Boston, Mass, USA, 2006.
- [31] H. Meschkowski, *Hilbertsche Räume mit Kernfunktion*, Die Grundlehren der mathematischen Wissenschaften, Bd. 113, Springer, Berlin, Germany, 1962.
- [32] B. Schölkopf and A. J. Smola, *Learning with Kernels: Support Vector Machines, Regularization, Optimization, and beyond*, The MIT Press, Cambridge, Mass, USA, 2003.
- [33] X. Kang, G. Yang, and S. Yu, “Dynamic behavior of the AMB’s vertical arranged rotor during its drop process,” in *Proceedings of the 2014 22nd International Conference on Nuclear Engineering, ICONE 2014*, July 2014.

## Research Article

# Oxidation Behavior of Matrix Graphite and Its Effect on Compressive Strength

Xiangwen Zhou,<sup>1</sup> Cristian I. Contescu,<sup>2</sup> Xi Zhao,<sup>1</sup> Zhenming Lu,<sup>1</sup> Jie Zhang,<sup>1</sup> Yutai Katoh,<sup>2</sup> Yanli Wang,<sup>2</sup> Bing Liu,<sup>1</sup> Yaping Tang,<sup>1</sup> and Chunhe Tang<sup>1</sup>

<sup>1</sup>Institute of Nuclear and New Energy Technology of Tsinghua University, Collaborative Innovation Center of Advanced Nuclear Energy Technology, The Key Laboratory of Advanced Reactor Engineering and Safety, Ministry of Education, Beijing 100084, China

<sup>2</sup>Oak Ridge National Laboratory, UT-Battelle Inc., P.O. Box 2008, Oak Ridge, TN 37831, USA

Correspondence should be addressed to Xiangwen Zhou; [xiangwen@tsinghua.edu.cn](mailto:xiangwen@tsinghua.edu.cn)

Received 22 December 2016; Revised 15 June 2017; Accepted 4 July 2017; Published 1 August 2017

Academic Editor: Eugenijus Ušpuras

Copyright © 2017 Xiangwen Zhou et al. This is an open access article distributed under the Creative Commons Attribution License, which permits unrestricted use, distribution, and reproduction in any medium, provided the original work is properly cited.

Matrix graphite (MG) with incompletely graphitized binder used in high-temperature gas-cooled reactors (HTGRs) is commonly suspected to exhibit lower oxidation resistance in air. In order to reveal the oxidation performance, the oxidation behavior of newly developed A3-3 MG at the temperature range from 500 to 950°C in air was studied and the effect of oxidation on the compressive strength of oxidized MG specimens was characterized. Results show that temperature has a significant influence on the oxidation behavior of MG. The transition temperature between Regimes I and II is ~700°C and the activation energy ( $E_a$ ) in Regime I is around 185 kJ/mol, a little lower than that of nuclear graphite, which indicates MG is more vulnerable to oxidation. Oxidation at 550°C causes more damage to compressive strength of MG than oxidation at 900°C. Comparing with the strength of pristine MG specimens, the rate of compressive strength loss is 77.3% after oxidation at 550°C and only 12.5% for oxidation at 900°C. Microstructure images of SEM and porosity measurement by Mercury Porosimetry indicate that the significant compressive strength loss of MG oxidized at 550°C may be attributed to both the uniform pore formation throughout the bulk and the preferential oxidation of the binder.

## 1. Introduction

Graphite offers numerous advantages for in-core nuclear applications because of its thermomechanical properties and chemical inertness in nonoxidizing environments. Therefore, it is widely used in HTGRs as the moderating, reflector, structural, and fuel element matrix materials [1–3]. However, graphite is easily oxidized by air at temperatures greater than 450°C [4]. In low probability, yet imaginable off-normal events, air or water ingress accidents would cause fast graphite corrosion that may affect the core and fuel integrity in HTGRs. Many studies related to the oxidation behavior and its impact on the mechanical properties of nuclear graphite materials have been reported in recent years [5–8]. Contescu [8] studied the effect of the oxidation temperature on the compressive strength of PCEA graphite. Samples in the direction of grain were oxidized in air at two temperatures (600

and 700°C) and three levels of weight loss. Results showed that oxidation at 600°C was more damaging on strength than oxidation at 700°C, at comparable levels of weight loss which was due to the differences in the distribution of oxidation layer and mechanism of development of porosity. Whereas a block reactor core consists mainly of highly graphitized nuclear graphite and contains only a small amount of fuel element matrix graphite (MG); the active pebble-bed core consists of a large part of fuel element matrix graphite [9]. The MG contains around 10% of incompletely graphitized resin-derived carbon because of temperature limit restriction (<2000°C) during the fabrication process of pebble fuel elements [3]. Because of its incompletely graphitized binder content, the activation energy of historic matrix-grade graphitic materials is lower than that of most modern nuclear graphite [9–12]. The activation energies of filler and binder for A3-27 were reported separately by Moormann et al. [9].

The activation energy of the filler (165 kJ/mol) is larger than that of the binder (123 kJ/mol). Lee et al. studied the oxidation rate of graphitic matrix material GKrS produced by ORNL thermogravimetrically with temperatures from 873 to 1873 K [10]. The activation energy for GKrS was determined to be 111.5 kJ/mol in the kinetic regime, from 873 to 1023 K. It is supposed that the lower activation energy of GKrS matrix graphite could be attributed to the preferential oxidation of the binder phase in the kinetic regime [10]. Many researchers have observed the preferential binder oxidation in their studies as well [11–13]. The preferential oxidation of binder often has a significant influence on the degradation of mechanical properties of graphite in the kinetic regime of graphite oxidation that may lead to severe consequences such as failure of pebble fuel elements and subsequent release of large amounts of radioactive fission products. Comparing with the large amount of reported researches on the oxidation behavior of nuclear graphite, oxidation experiments and basic kinetic data for matrix-grade graphite in air are sparse because the historic grades of A3-3 or A3-27 from Germany are no longer commercially available and modern candidate grades are still being developed and difficult to obtain [10]. In this study, the A3-3 MG composing approximately 71% natural flake graphite, 18% artificial graphite, and 11% phenol resin was newly developed and manufactured in INET, Tsinghua University of Beijing, China [3]. Chinese domestic producers produced all the raw materials used in the preparation of the newly developed A3-3 MG. The oxidation performance of the MG is very crucial for the integrity evaluation and safety analysis of pebble fuel elements in normal and off-normal conditions. In order to reveal the oxidation performance of the MG, the oxidation behavior of MG in air in the temperature range from 500°C to 950°C was studied, and the effect of oxidation at two typical temperatures on the compressive strength of MG was characterized.

## 2. Experimental

**2.1. MG Specimens.** All MG specimens covered by this report were machined from the MG pebbles manufactured by the Institute of Nuclear and New Energy Technology (INET) [3]. In order to meet the specimen requirements of standard test method for compressive strength of carbon and graphite (ASTM C-695) [14], a compromise had to be made to machine the specimens into cylindrical shape with 2:1 ratio between length (25.4 mm) and diameter (12.7 mm). This exceeds the recommended minimum specimen size of 9.5 mm diameter and 19 mm length for compressive strength test. Meanwhile, as the maximum grain size in MG is 0.16 mm, the specimens with diameter of 12.7 mm were in compliance with the requirement that the diameter of test specimens for compressive strength measurements should be at least five times larger than the maximum grain size in graphite. As shown in Figure 1, 6 specimens were machined from a MG pebble, in parallel orientation to the molding direction during fabrication. Five pebbles were used to machine 30 cylindrical specimens. The machined specimens were then heat-treated at 1900°C in vacuum for 2 hours to remove any trace of metallic impurities that might be

TABLE I: Physical properties of specimens before oxidation.

	Length (mm)	Diameter (mm)	Weight (g)	Density (g/cm <sup>3</sup> )
Average	25.308	12.627	5.506	1.737
St. dev.	0.033	0.023	0.032	0.004

introduced during machining. Then the specimens were supersonically cleaned with acetone and ethanol and dried at 120°C for 24 hours. Physical measurements showed that the specimens were uniform. The average dimension and density values with standard deviation of these specimens before oxidation are shown in Table 1.

**2.2. Oxidation Measurements.** The MG specimens were oxidized in air using the protocol recommended by ASTM D7542-09 [15]. A home-made experimental equipment build at Oak Ridge National Laboratory (ORNL) was used for MG oxidation studies [8, 16]. Basically, the oxidation setup consists of a three-zone vertical tube furnace and an analytical balance with weight-below port feature on the top of the furnace. The graphite specimen is suspended by a Pt wire in the central zone, of uniform temperature, of the furnace. The weight loss caused by oxidation is automatically recorded by computer in isothermal conditions. The oxidation temperatures at 500, 550, 600, 650, 700, 750, 800, 860, 900, and 950°C were selected and at each temperature 2 or 3 specimens were oxidized to around 15% weight loss with the air flow rate of 10 L/min to test repeatability. According to the ASTM D7542-09, the oxidation rate at a given temperature is determined by a linear fit of the weight loss plotted against time in the range from 5% to 10% loss of original specimen weight. The activation energy ( $E_a$ ) and preexponential factor are calculated from the slope and intercept of the linear Arrhenius plot of the logarithm of oxidation rate versus the reciprocal of absolute temperature [15, 16].

**2.3. Testing of Compressive Strength.** In order to reveal the effect of oxidation on the mechanical properties of MG, the compressive strengths of the specimens oxidized at two typical temperatures were tested. The two selected temperatures are 550°C located in the kinetic regime and 900°C in the boundary layer control regime, respectively. For comparison, the compressive strengths of pristine (unoxidized) MG specimens were measured as well. Because the MG specimens oxidized at 550°C to around 15% weight loss were too weak to be handled in the strength test, specimens were oxidized to approximately 10% weight loss before the compressive strength test. Three specimens were tested for each oxidation condition. An Instron Model 1322 Electromechanical Test System was used for performing the compressive strength tests. An MTS servohydraulic machine with a 25 kN load cell and a 407 controller was used for performing the compressive strength test at a crosshead speed of 0.00762 mm/s using LabView program. Irregular fracture behavior of the oxidized specimens may be caused by uncontrolled failure under compression of the oxidized layer at the contact surface between the parallel faces of the cylindrical specimen and the

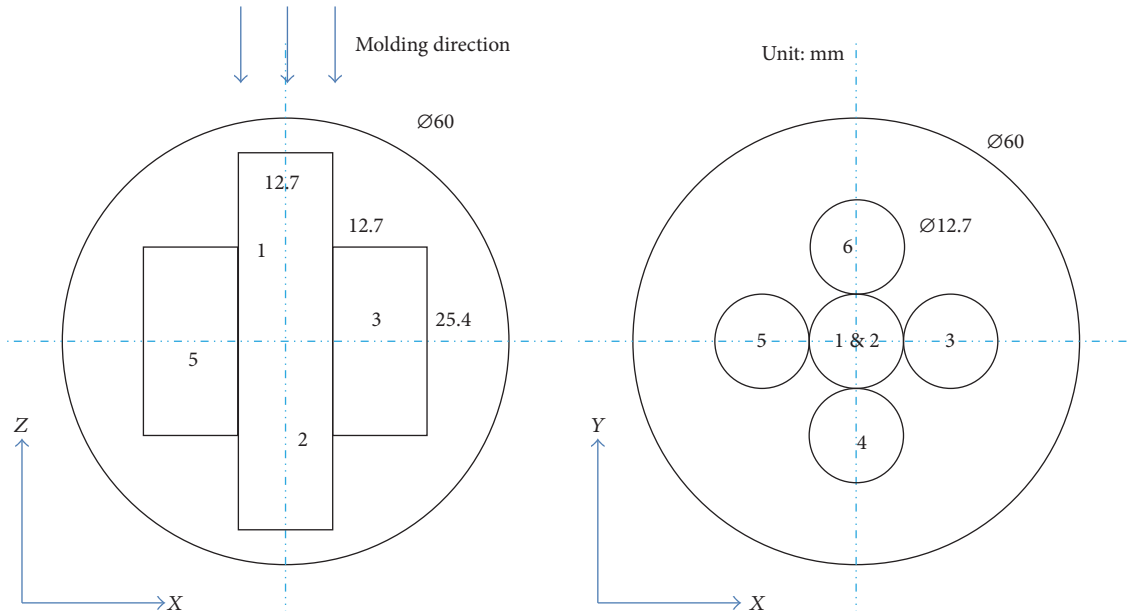


FIGURE 1: Schematic for the machining of specimens from a MG pebble.

loading fixtures. In order to avoid the uncontrolled failure, a 1 mm thick layer of oxidized layer was machined from both parallel faces of all the oxidized cylindrical specimens, and this surface preparation process does not reduce the strength according to literature reported results [8].

**2.4. Microstructure Characterizations.** The MG specimens (both oxidized and pristine) were cut at 1/3 of the length for scanning microscopy examination and test of Mercury porosimetry. The shorter pieces were encased in resin and then the exposed surface after cutting was polished using several different grades of alumina powder (from coarse to fine) that allows for an optically flat surface. The microstructure of MG specimens was investigated at 1500x magnification by Hitachi S-3000N Scanning Electron Microscope (SEM) system. The larger pieces were used in the Mercury Porosimetry to measure the porosity of MG. The volume of the pores in MG was determined by measuring the volume of mercury intruding the MG at various pressures. The value of the parameters applied in the Mercury Porosimetry measurement is as follows: the surface tension of the mercury ( $\gamma$ ) is 485 dynes/cm and the contact angle between mercury and MG ( $\theta$ ) is  $130.0^\circ$ , respectively.

### 3. Results and Discussions

The relationships between the residual weight and oxidation time of MG at different temperatures in air were shown in Figure 2. It can be seen that the oxidizing temperature has a remarkable influence on the oxidation of MG. The oxidation rate accelerates significantly with the increasing temperature when the oxidizing temperatures are below  $800^\circ\text{C}$ . At  $500^\circ\text{C}$ , it takes more than 200 hours to reach the weight loss of 15%. When the oxidizing temperatures are  $700^\circ\text{C}$  and  $900^\circ\text{C}$ , the oxidation time for 15% weight loss is 0.9 and 0.2 hours,

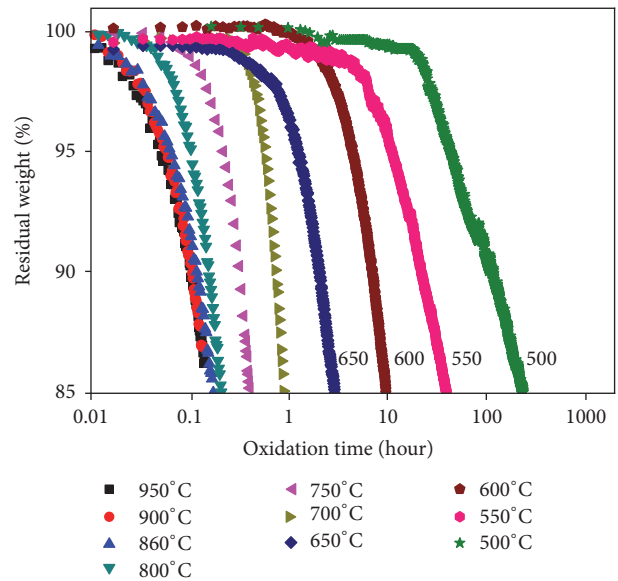


FIGURE 2: The relationship between the weight loss and oxidation time at different temperatures.

respectively. The average oxidation rate of MG at  $900^\circ\text{C}$  is more than 1000 times faster than that at  $500^\circ\text{C}$ . However, with further increases in oxidizing temperature above  $800^\circ\text{C}$ , the oxidation rates remain almost constant, showing that the oxidation control mechanisms at relatively low and high oxidizing temperatures are different.

Based on the average oxidation rate in the range from 5% to 10% loss of original specimen weight, the Arrhenius plot of MG in the temperature range of  $500\text{--}950^\circ\text{C}$  is shown in Figure 3. The slopes and intercepts of the best-fit lines for three regimes were presented in Figure 3 as well. The

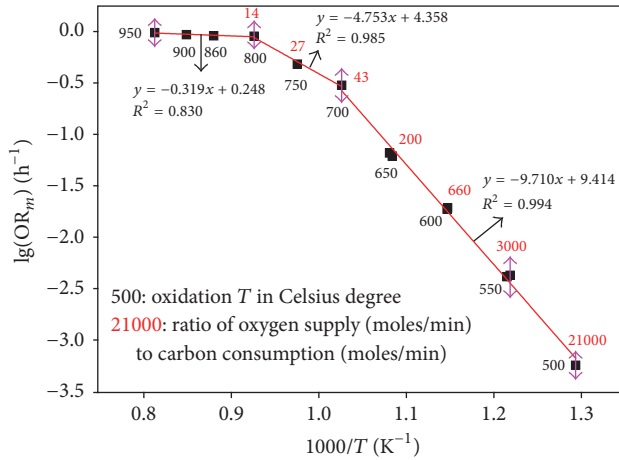


FIGURE 3: Arrhenius plot of MG oxidized in air at 500–950°C.

procedure recommended in ASTM D7542-09 was adopted to calculate the  $E_a$  for each regime from the Arrhenius plot. The  $E_a$  of MG was determined to be 185.83 kJ/mol in the chemical kinetics control regime, Regime I, at temperatures below 700°C; 90.96 kJ/mol in the in-pore controlled diffusion regime, Regime II, from 700 to 800°C; and 6.10 kJ/mol in the boundary layer control regime, Regime III, from 800 to 950°C. The  $E_a$  in Regime II is around one-half of that in Regime I and  $E_a$  in Regime III is very close to zero, in good agreement with the  $E_a$  variation trend in the three regimes mentioned elsewhere [11]. As the  $E_a$  for most graphite materials was in the range of 190–210 kJ/mol [11], the slightly smaller  $E_a$  for MG was probably due to the existence of incompletely graphitized binder in the MG. The mass-normalized oxidation rate ( $OR_m$ ) for MG in Regime I can be described as

$$OR_m = 2.59 \times 10^9 \times \exp\left(\frac{-22362.13}{T}\right) \text{ h}^{-1}, \quad (1)$$

where  $T$  is the temperature in Kelvin units.

The ratio of oxygen supply rate (moles/min) to carbon loss rate (moles/min) at relatively low temperatures is also shown in Figure 3. A previous report suggested that Arrhenius plots of standard size specimens (diameter = length = 25.4 mm) were linear as long as this ratio was larger than ~10, indicating oxidation in Regime I [11]. For the MG specimens with the diameter of 12.7 mm, the plot was linear between 500 and 700°C. As the oxidation rate increased with the increase in temperature and the ratio declined gradually. When the ratio dropped to ~43 at 700°C, the plot started to bend, which apparently does not agree with the rule mentioned above. However, considering that the oxidation is uniform throughout the graphite specimens in Regime I and the MG specimens have only 1/4 mass of the standard specimens, the carbon loss rate should be four times larger than the currently observed rate if the standard size specimens were used with the same air flow rate of 10 L/min. Accordingly, the ratio should be reduced four times, from 43 to 11.75, which is very close to the empirically estimated threshold ratio of ~10.

The average dimensional and corresponding density changes of specimens oxidized to ~10% weight loss at 550 and

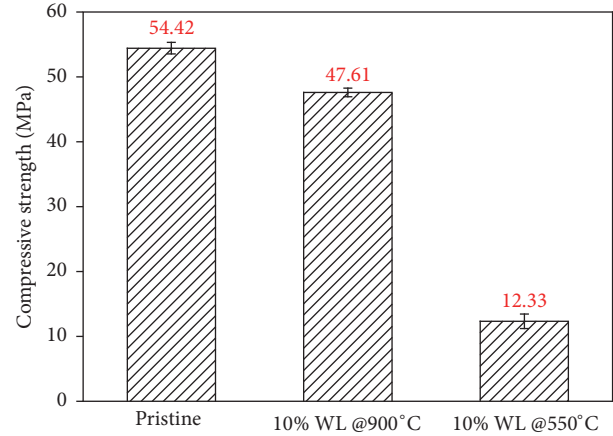


FIGURE 4: Average values for compressive strength of MG specimens oxidized to ~10% weight loss at 550 and 900°C.

900°C for compressive strength testing are shown in Table 2. The dimension did not change (within the experimental errors) after oxidation at 550°C. However, the length and diameter of specimens oxidized at 900°C shrank by 1.3% and 3.2%, respectively. As a result, the average density of the specimens oxidized at 550 and 900°C declined by 10.8% and 3.45%, respectively, showing the effect of different oxidation regimes. When the specimens were oxidized at 550°C (in Regime I) the oxidation was uniform throughout the specimens, which slightly changed their size but significantly decreased their density. When the oxidation temperature increased to 900°C (in Regime III), oxidation occurred mainly on the surface, which changed the dimensions but had only slight influence on the density.

Figure 4 indicates the average values of compressive strength for MG specimens oxidized to ~10% weight loss at 550 and 900°C. With the comparative weight loss of ~10%, the compressive strength of the specimens oxidized at 900°C is about four times larger than of those oxidized at 550°C. Comparing with the strength of pristine specimens, the reduction in compressive strength is 77.3% after oxidation at 550°C in the kinetic regime and only 12.5% for oxidation at 900°C. The average rate of strength loss for oxidation at 550°C is 7.63% of the initial compressive strength value per each percentage of weight loss. Meanwhile, after oxidation at 900°C the figure is only 1.17% of initial strength value for every 1% of weight loss. It is obvious that oxidation at 550°C causes more degradations to compressive strength of MG than oxidation at 900°C. Figures 5–7 show the SEM images of the pristine MG and MG specimens oxidized at 550°C and 900°C in air to about 10% weight loss. Table 3 reports the value of porosity for MG specimens and corresponding oxidation conditions. From Figures 5 and 7, it can be seen that the microstructure difference between the pristine MG and MG specimens oxidized at 900°C is too insignificant to be observed by eye. As shown in Table 3, the porosity of MG specimens oxidized at 900°C is slightly lower than that of the pristine MG, which is in good agreement with the SEM investigation results. However, as shown in Figure 6, the microstructure of MG specimens oxidized at 550°C dramatically changed after the oxidation

TABLE 2: Average physical property changes before and after oxidation to around 10% weight loss.

Oxidation $T$ ( $^{\circ}\text{C}$ )	Weight loss (%)		Length (%)		Diameter (%)		Density (%)	
	Average	St. dev.	Average	St. dev.	Average	St. dev.	Average	St. dev.
550	-10.13	0.35	+0.35	0.02	+0.20	0.01	-10.79	0.28
900	-10.73	0.51	-1.29	0.03	-3.22	0.05	-3.45	0.12

TABLE 3: Porosity of MG specimens (both pristine and oxidized) measured by Mercury Porosimetry.

Samples	Porosity (%)
Pristine	18.09
Oxidized at $550^{\circ}\text{C}$ to 10% WL	30.87
Oxidized at $900^{\circ}\text{C}$ to 10% WL	19.74

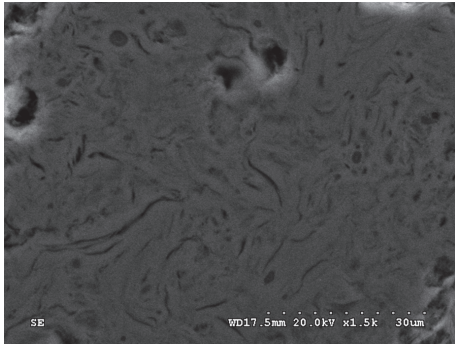
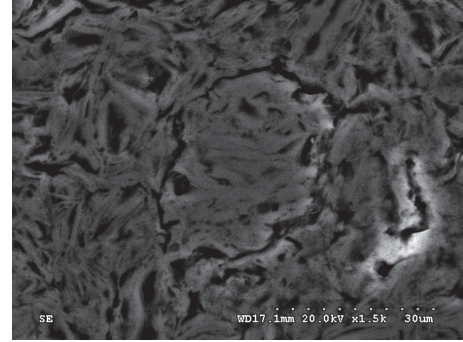
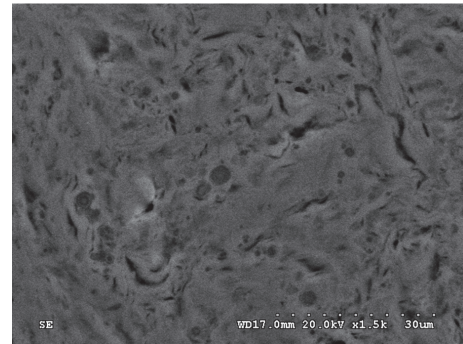


FIGURE 5: SEM image of pristine A3-3 MG at 1500x Mag.

where a large amount of pores were developed and formed. Its porosity value increases remarkably from 18.09% of the porosity of pristine MG to 30.87%. The different development and formation of pores between the specimens oxidized at 550 and  $900^{\circ}\text{C}$  are due to the different oxidation mechanism: oxidation at  $550^{\circ}\text{C}$  in the kinetic regime spreads uniformly in the bulk, while oxidation at  $900^{\circ}\text{C}$  in the boundary layer control regime is limited to a narrow surface layer and bulk is not apparently affected. Comparing with the microstructure of the pristine MG shown in Figure 5, the binder material of the MG specimens oxidized at  $550^{\circ}\text{C}$  in Figure 6 shrinks or even disappears around the filler grains, which indicates the weaker oxidation resistance of the binder phase [10]. In a previous report, it was found that the compressive strength of PCEA graphite oxidized at  $600^{\circ}\text{C}$  in the kinetic regime to around 10% weight loss, dropping only by  $\sim 26\%$  [8]. From the microstructure images and porosity measurement results, it can be concluded that the significant strength loss of the MG specimens oxidized at  $550^{\circ}\text{C}$  in the kinetic regime may be ascribed to both the pore formation throughout the bulk after oxidation and the preferential binder phase oxidation.

#### 4. Conclusion

Oxidation behavior of MG in air in the temperature range from 500 to  $950^{\circ}\text{C}$  was investigated. The activation energy

FIGURE 6: SEM image of A3-3 MG oxidized at  $550^{\circ}\text{C}$  to 10% weight loss at 1500x Mag.FIGURE 7: SEM image of A3-3 MG oxidized at  $900^{\circ}\text{C}$  to 10% weight loss at 1500x Mag.

in the chemical kinetic control regime calculated from the Arrhenius plot was  $\sim 185$  kJ/mol, slightly lower than that of nuclear graphite, which indicates that MG was more vulnerable to oxidation. Oxidizing temperature also played an important role in the degradation of compressive strength of MG. Oxidation at  $900^{\circ}\text{C}$  caused less damage on the compressive strength than oxidation at  $550^{\circ}\text{C}$ . At the same weight loss of  $\sim 10\%$ , the compressive strength of specimens oxidized at  $900^{\circ}\text{C}$  was about 4 times larger than after oxidation at  $550^{\circ}\text{C}$ . The average rates of strength loss for oxidation at  $550^{\circ}\text{C}$  and  $900^{\circ}\text{C}$  are 7.63% and 1.17% of the initial compressive strength value for every 1% of weight loss, respectively. The significant strength loss of MG induced by the oxidation at  $550^{\circ}\text{C}$  in the kinetic regime was probably due to both the uniform pores formation throughout the bulk of MG and the preferential oxidation of binder phase. This conclusion was supported by the measurements on the compressive strength and rationalized by the SEM examinations and porosity measurements of the pristine and oxidized MG specimens.

## Disclosure

This manuscript has been authored by UT-Battelle, LLC under Contract no. DE-AC05-00OR22725, with the U.S. Department of Energy. The United States Government retains and the publisher, by accepting the article for publication, acknowledges that the United States Government retains a nonexclusive, paid-up, irrevocable, worldwide license to publish or reproduce the published form of this manuscript, or allow others to do so, for United States Government purposes. The Department of Energy will provide public access to these results of federally sponsored research in accordance with the DOE Public Access Plan (<https://energy.gov/downloads/doe-public-access-plan>).

## Conflicts of Interest

The authors declare that they have no conflicts of interest.

## Acknowledgments

Supports from the State Scholarship Foundation of China (201406215002), the Chinese National S&T Major Project (ZX06901), Chinese National Natural Science Foundation (51420105006), and Key Program for International S&T Cooperation Projects of China (2016YFE0100700) are acknowledged. The work performed at Oak Ridge National Laboratory was supported partially by the Advanced Reactor Technologies program of U.S. Department of Energy, Office of Nuclear Energy.

## References

- [1] T. L. Albers, "High-temperature properties of nuclear graphite," *Journal of Engineering for Gas Turbines and Power*, vol. 131, no. 6, Article ID 064501, pp. 1-2, 2009.
- [2] Z. Zhang, Z. Wu, D. Wang et al., "Current status and technical description of Chinese  $2 \times 250$  MWth HTR-PM demonstration plant," *Nuclear Engineering and Design*, vol. 239, no. 7, pp. 1212–1219, 2009.
- [3] Z. Xiangwen, L. Zhenming, Z. Jie et al., "Preparation of spherical fuel elements for HTR-PM in INET," *Nuclear Engineering and Design*, vol. 263, pp. 456–461, 2013.
- [4] W.-K. Choi, B.-J. Kim, E.-S. Kim, S.-H. Chi, and S.-J. Park, "Oxidation behavior of IG and NBG nuclear graphites," *Nuclear Engineering and Design*, vol. 241, no. 1, pp. 82–87, 2011.
- [5] C. I. Contescu, T. Guldan, R. P. Wichner, and T. D. Burchell, *Oxidation resistance of NNGP graphite materials*, NNGP program, Oak Ridge, TN, USA, 2008.
- [6] S. Chi and G. Chan Kim, "Effects of air flow rate on the oxidation of NBG-18 and NBG-25 nuclear graphite," *Journal of Nuclear Materials*, vol. 491, pp. 37–42, 2017.
- [7] X. Luo, J.-C. Robin, and S. Yu, "Comparison of oxidation behaviors of different grades of nuclear graphite," *Nuclear Science and Engineering*, vol. 151, no. 1, pp. 121–127, 2005.
- [8] C. I. Contescu, *Effect of air oxidation on pore structure development and mechanical properties of nuclear graphite*, Oak Ridge, TN, USA, 2010.
- [9] R. Moormann, H.-K. Hinssen, and K. Kühn, "Oxidation behaviour of an HTR fuel element matrix graphite in oxygen compared to a standard nuclear graphite," *Nuclear Engineering and Design*, vol. 227, no. 3, pp. 281–284, 2004.
- [10] J. J. Lee, T. K. Ghosh, and S. K. Loyalka, "Oxidation rate of graphitic matrix material in the kinetic regime for VHTR air ingress accident scenarios," *Journal of Nuclear Materials*, vol. 451, no. 1-3, pp. 48–54, 2014.
- [11] C. I. Contescu, S. Azad, D. Miller, M. J. Lance, F. S. Baker, and T. D. Burchell, "Practical aspects for characterizing air oxidation of graphite," *Journal of Nuclear Materials*, vol. 381, no. 1-2, pp. 15–24, 2008.
- [12] H.-K. Hinssen, K. Kühn, R. Moormann, B. Schlögl, M. Fechter, and M. Mitchell, "Oxidation experiments and theoretical examinations on graphite materials relevant for the PBMR," *Nuclear Engineering and Design*, vol. 238, no. 11, pp. 3018–3025, 2008.
- [13] R. P. Wichner, T. D. Burchell, and C. I. Contescu, "Penetration depth and transient oxidation of graphite by oxygen and water vapor," *Journal of Nuclear Materials*, vol. 393, no. 3, pp. 518–521, 2009.
- [14] "Standard test method for compressive strength of carbon and graphite. ASTM C695-91," 2010.
- [15] "Standard test method for air oxidation of carbon and graphite in the kinetic regime. ASTM D7542-09".
- [16] C. I. Contescu and T. D. Burchell, *ASTM activities on standard method for graphite oxidation. ORNL/GEN4/LTR-09-002*, Oak Ridge, TN, USA, 2009.

## Research Article

# The Optimization of Radiation Protection in the Design of the High Temperature Reactor-Pebble-Bed Module

**Sida Sun, Hong Li, and Sheng Fang**

*Key Laboratory of Advanced Reactor Engineering and Safety of the Ministry of Education, Collaborative Innovation Center of Advanced Nuclear Energy Technology, Institute of Nuclear and New Energy Technology, Tsinghua University, Beijing 100084, China*

Correspondence should be addressed to Sheng Fang; [fangsheng@tsinghua.edu.cn](mailto:fangsheng@tsinghua.edu.cn)

Received 29 December 2016; Revised 20 April 2017; Accepted 16 May 2017; Published 31 July 2017

Academic Editor: Arkady Serikov

Copyright © 2017 Sida Sun et al. This is an open access article distributed under the Creative Commons Attribution License, which permits unrestricted use, distribution, and reproduction in any medium, provided the original work is properly cited.

The optimization of radiation protection is an important task in both the design and operation of a nuclear power plant. Although this topic has been considerably investigated for pressurized water reactors, there are very few public reports on it for pebble-bed reactors. This paper proposes a routine that jointly optimizes the system design and radiation protection of High Temperature Reactor-Pebble-Bed Module (HTR-PM) towards the As Low As Reasonably Achievable (ALARA) principle. A systematic framework is also established for the optimization of radiation protection for pebble-bed reactors. Typical calculations for the radiation protection of radioactivity-related systems are presented to quantitatively evaluate the efficiency of the optimization routine, which achieve 23.3%~90.6% reduction of either dose rate or shielding or both of them. The annual collective doses of different systems are reduced through iterative optimization of the dose rates, designs, maintenance procedures, and work durations and compared against the previous estimates. The comparison demonstrates that the annual collective dose of HTR-PM is reduced from 0.490 man-Sv/a before optimization to 0.445 man-Sv/a after optimization, which complies with the requirements of the Chinese regulatory guide and proves the effectiveness of the proposed routine and framework.

## 1. Introduction

Optimization is one of the three basic principles of radiation protection recommended by the International Commission on Radiological Protection (ICRP). Since its first formal introduction in ICRP publication 26 [1], the concept of optimization of radiation protection was continuously improved and interpreted in a series of successive ICRP publications [1–5]. A widely used interpretation is as follows: the likelihood of incurring exposures, the number of people exposed, and the magnitude of their individual doses should be kept As Low As Reasonably Achievable (ALARA), taking into account economic and societal factors [5]. In some contexts, the optimization of radiation protection is also known as the ALARA principle.

With respect to a nuclear power plant, there are continuous efforts in the optimization of radiation protection for both design and operation. For those power plants in operation, the radiation dose management has been successively improved following the principle of optimization and has achieved significant dose reduction in the past decades [6–11]. For recently developed Generation III nuclear reactors,

the optimization of radiation protection has been integrated deeply into the design. The European Pressurized Water Reactor (EPR) has established the ALARA principle as one of the main objectives in the design and made a large effort to reduce both individual and collective dose to an acceptable level [12]. Another typical Generation III nuclear reactor, AP1000, takes the advantages of both operating plant experience and advanced techniques to reduce maintenance duration and doses, so as to achieve the optimization of radiation protection [13].

As one of the potential candidates for the fourth-generation nuclear reactors, the gas-cooled pebble-bed reactor also emphasizes the optimization of radiation protection. The pioneer 15 MWe AVR experimental high temperature reactor has achieved an average collective dose between 0.5 and 0.6 Sv per year during its 21 years of successful operation [14], which is considerably low. The 300 MWe thorium high temperature reactor (THTR-300) has continued to optimize its radiation protection during both operation and decommissioning [15]. For the latest 200 MWe High Temperature Reactor-Pebble-bed Module (HTR-PM)

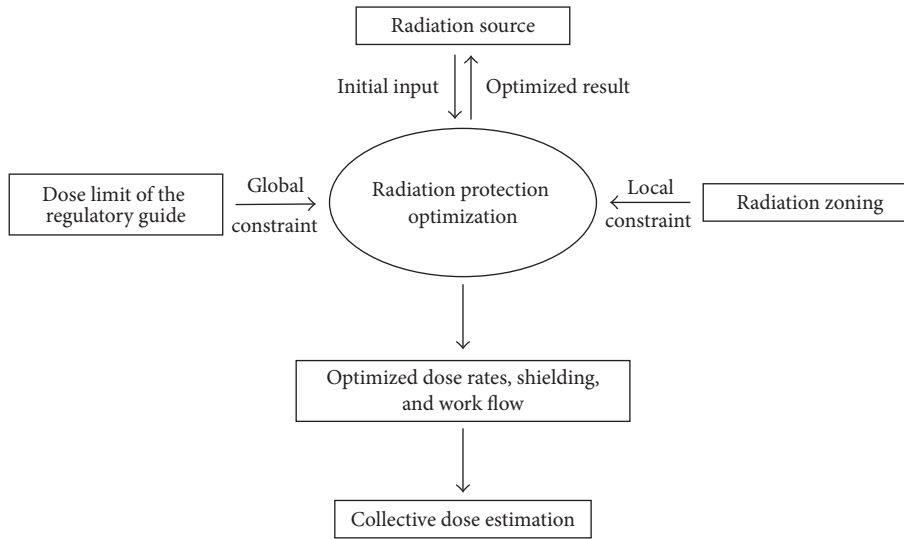


FIGURE 1: Framework of the radiation protection optimization in the HTR-PM design.

demonstration power plant, the optimization of radiation protection is not only an important goal in design [16], but also a licensing requirement demanded by the national nuclear safety administration of China.

However, compared with abundant experiences and reports on the radiation protection optimization of pressurized water reactors (PWR), there are only few reports on that of pebble-bed reactors, and even fewer on a systematic optimization of radiation protection. Given the potential deployment of pebble-bed reactors in China and other places around the world, it is necessary to build up a tailored guideline of the radiation protection optimization for industrial pebble-bed reactors. HTR-PM, which is currently under construction, provides an opportunity for this purpose.

In this study, a framework of the radiation protection optimization is proposed for HTR-PM in the design stage. In this framework, the radiation source is analyzed and a routine is formed for the joint optimization of the system design and the radiation protection of HTR-PM. The application of this routine in the HTR-PM design provides optimized dose rates, radiation protection design, and work flow of each system. Based on this optimization, the annual collective dose of HTR-PM is estimated for every radioactivity-related work and compared with the previous estimate before optimization. The presented framework may provide useful information and experiences for the optimization of radiation protection for future pebble-bed reactors.

## 2. Framework of the Radiation Protection Optimization in the HTR-PM Design

The radiation protection optimization is a comprehensive process that involves multiple aspects of the HTR-PM design. As shown in Figure 1, the dose limit demanded by the regulatory guide is the global constraint of the optimization, while the radiation zoning serves as a local constraint for

specific radiation protection tasks. The radiation source is the initial input for the first iteration of the optimization. As the iteration continues, the system design is gradually refined and the radiation source changes accordingly. At each iteration, the dose rates of the refined design and updated source term are computed and checked with the dose limit of the regulatory guide and the radiation zoning requirement. When the above two criteria are met, a series of radiation protection schemes are provided as candidates for the final design. These schemes are discussed with the designers of the involved systems and further optimized to practical issues such as the space layout of different equipment, the support of shielding structures, the accessibility of maintenance, and the cost. This iteration continues until an optimal solution that both the designers of systems and radiation protection agree on has been found.

## 3. Dose Limit of the Regulatory Guide and Radiation Zoning

**3.1. Dose Limit of the Regulatory Guide.** According to the HAD102/12 regulatory guide in China [17], the individual dose limit for a nuclear power plant is 20 mSv/a (five-year average) and the individual dose constraint is 15 mSv/a. To be compliant with this, the individual dose limit for HTR-PM is set to 15 mSv/a, and the collective dose limit is set to 0.5 man-Sv/a. These two limits are global constraints for the radiation protection optimization, because they affect all radioactivity-related systems in HTR-PM and affect all aspects of the radiation protection. They provide criteria for the overall evaluation of the whole radiation protection efficiency of HTR-PM.

**3.2. Radiation Zoning.** Radiation zoning of HTR-PM is determined based on the possible distribution of radiation sources, the accessible requirement, and the operation and maintenance activities in certain areas. The classification of radiation

TABLE 1: Classification of radiation zones for the HTR-PM's operation.

Number	Name	Dose rate (mSv/h)	Airborne radioactivity concentration	Residence characteristics
I	Supervised area	$0.0005 < d \leq 0.0025$	negligible	40 h per week
II	Conventional work area	$0.0025 < d \leq 0.0075$	$\leq 0.1$ DAC*	Less than 40 h per week
III	Intermittent work area	$0.0075 < d \leq 0.03$	$\leq 1$ DAC	Usually less than 10 h per week, which accordingly determines the dose rate upper limit
	Controlled area			Determined by the staff in charge of radiation protection
IV	Limited work area	$0.03 < d \leq 3$	$\leq 10$ DAC	
V	Chartered work area	$d > 3$	—	Temporarily chartered

\* Airborne radioactivity concentration is represented by derived air concentration (DAC).

TABLE 2: Level of radioactive pollution control (Bq/cm<sup>2</sup>).

Surface type	$\alpha$ radioactive material		$\beta$ radioactive material
	Extremely toxic	Others	
Workbench, equipment, wall, and floor			
Controlled area	4	40	40
Supervised area	0.4	4	4
Work clothes, gloves, and work shoes			
Controlled area	0.4	0.4	4
Supervised area			
Hand, skin, underwear, and work socks	0.04	0.04	0.4

zones for HTR-PM in power operation stage is presented in Table 1. A controlled area is designated in which specific measures for protection and safety are or could be required for (a) controlling exposures or preventing the spread of contamination in normal operation and (b) preventing or limiting the likelihood and magnitude of exposures in anticipated operational occurrences and accident conditions. An area is designated as a supervised area, on condition that specific measures for protection and safety are not normally needed [18]. But occupational exposure conditions are still kept under review for a supervised area. The controlled area is further classified into four areas: the green, the yellow, the orange, and the red area. Each of these areas is physically separated from others by concrete walls.

Since the radiation sources at some areas may change in the outage of HTR-PM, the radiation zoning of these areas is slightly different from that in plant operation. However, the classification criteria for outage are still the same ones listed in Table 1.

Besides the radiation level, the surface contamination level is also taken into consideration. The corresponding classification is provided in Table 2. Compared to the dose limit, the radiation zoning is more specific and operable for a single radiation protection task.

## 4. Radiation Source

**4.1. Fission Product.** According to the calculation of the reactor core inventory at equilibrium, the orders of magnitude of

noble gases (Kr and Xe) and iodine are both  $10^{16}$  Bq per MW of HTR-PM, while that of the primary metal fission products ( $^{89}\text{Sr}$ ,  $^{90}\text{Sr}$ ,  $^{134}\text{Cs}$ ,  $^{137}\text{Cs}$ , and  $^{110\text{m}}\text{Ag}$ ) is  $10^{15}$  Bq per MW of HTR-PM. The majority of these fission products are retained inside the coated particles in the spherical fuel elements of HTR-PM.

Because HTR-PM uses an online refueling strategy, the irradiated spherical fuel elements keep cycling between the reactor pressure vessel (RPV) and the pipes of HTR-PM's fuel handling system which are outside the reactor cavity. Because the irradiated fuel elements carry fission products, they can temporarily increase local radiation level along their path. Thus, these mobile fuel elements are dynamic sources in a spatiotemporal transient state, which is a unique feature of HTR-PM.

When the reactor is shut down, the fuel elements in RPV and the pipes of HTR-PM's fuel handling system will be discharged, except for a few shielded devices. Thus, for the reactor cavity and the rooms near the fuel transportation pipes, the radiation level will be significantly reduced so that these rooms can be accessible for maintenance.

Another carrier of fission products is the graphite dust that is mainly produced by the abrasion between fuel elements in the reactor core or between fuel elements and the fuel transportation pipes. Its radioactivity primarily results from a very limited leakage of fission products from defective/failed coated particles in the fuel elements. Among these fission products, the gaseous radionuclides can be removed

by the helium purification system. The solid radionuclides may be adsorbed on the fuel element surfaces by the graphite matrix. HTR-PM uses a purge system to remove such graphite dust, which is collected in shielded containers.

**4.2. Activation Product.** The activation products can come from the impurities in the structural material, helium coolant, and graphite matrix of fuel elements. For components in the reactor cavity, the activation level can be high due to the strong neutron flux. However, the radiation contributed by the activation products is still much lower than that of the reactor core during power operation. But in the maintenance stage, the reactor is shut down and the radiation from the reactor core drastically decreases. The  $\gamma$  rays from the activation products become the primary radiation sources for the maintenance work. The activation products in the primary coolant after 40-year lifetime of HTR-PM include noble gases (Kr and Xe), iodine, metals with long half-lives ( $^{89}\text{Sr}$ ,  $^{90}\text{Sr}$ ,  $^{134}\text{Cs}$ ,  $^{137}\text{Cs}$ ,  $^{110\text{m}}\text{Ag}$ ,  $^{60}\text{Co}$ , and  $^{55}\text{Fe}$ ),  $^{14}\text{C}$ , and  $^3\text{H}$ . And their orders of magnitude are  $10^9$ ,  $10^7$ ,  $10^3$ ,  $10^6$ , and  $10^8$  Bq per MW of HTR-PM, respectively.

## 5. Dose Calculation and Optimization Routine

**5.1. Dose Calculation.** For the primary shielding, the 1D ANISN [19] and 2D DOT codes [20] are used to calculate the distribution of the neutron flux and  $\gamma$  rays.

For various secondary shieldings,  $\gamma$  radiation sources can be a primary concern, which are calculated using KORIGEN code [21], a Karlsruhe version of the Oak Ridge Lab's ORIGEN [22]. Because of the moving feature of the fuel elements, there can be multiple radiation sources in a single radiation protection task. To deal with this spatiotemporal complexity, an in-house software tool that calculates the dynamic dose field for multiple radiation sources is developed, which uses multidimensional point kernel and buildup factor methods to estimate gamma transport in room scale. A 3D visualization module has been developed to better model complex structures and radiation source movement [16, 23].

**5.2. Optimization Routine.** Although the movement of fuel elements makes the radiation protection complex, it also brings the freedom of changing the spatiotemporal distribution of radiation sources through careful transport path design. To take advantage of this freedom, an iterative optimization routine (Figure 2) is formed and applied to all radioactivity-related systems in HTR-PM. During the iteration, the dose reduction scheme and the system design are jointly optimized to achieve the ALARA goal with consideration of the maintenance procedures, dose rates, and work durations. The iteration continues until both the dose constraint in Figure 1 and the ALARA principle is met. Typical examples using the routine in Figure 2 for optimization of radiation protection will be described in the next section.

## 6. Radiation Optimization in System Design

**6.1. Reactor Cavity.** The activation of equipment inside the reactor cavity is a key concern of the radiation protection

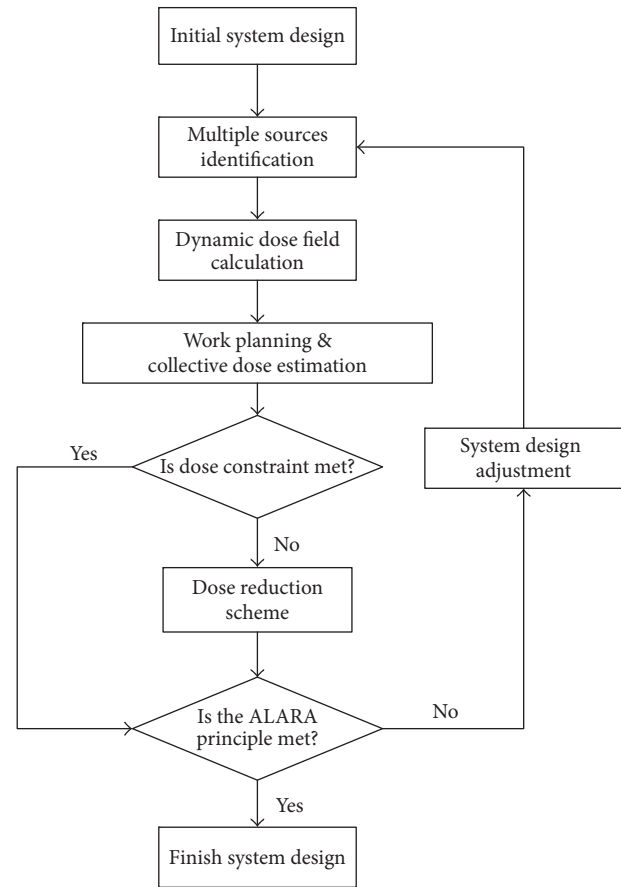


FIGURE 2: Flowchart of the radiation protection optimization routine for HTR-PM.

for the maintenance work after the reactor is shut down. Therefore, the cobalt impurities are required to be less than 0.02% in the design of HTR-PM, while the sample analysis result reveals that the actual percentage of the cobalt impurities is even lower.

Because staff receive radiation from different equipment, a joint consideration of work flow and the radiation contribution from all related equipment is necessary for optimizing the radiation protection. Figure 3(a) shows the dose reduction design for the maintenance work on top of RPV, which receives the radiation from the steel plates on the cavity cap and the cavity wall, the drivers of both control rods, and absorber balls, and the steel maintenance platform and the dose limit are 1 mSv/h for this maintenance. Before optimization, both the drivers of control rods and the steel plate on the cap contribute high dose rates to the position of interest (Figure 3(b)). During the optimization process, several dose reduction methods have been compared. The first dose reduction method, in which the boron-containing polyethylene plate is installed for reducing neutron flux, works for all the radiation sources in Figure 3(a). However, the dose rate of the drivers of control rods still exceeds the dose limit (Figure 3(c)), and the installation requires additional support structures which may not be available. The second method is the cobalt impurity control. But it is so

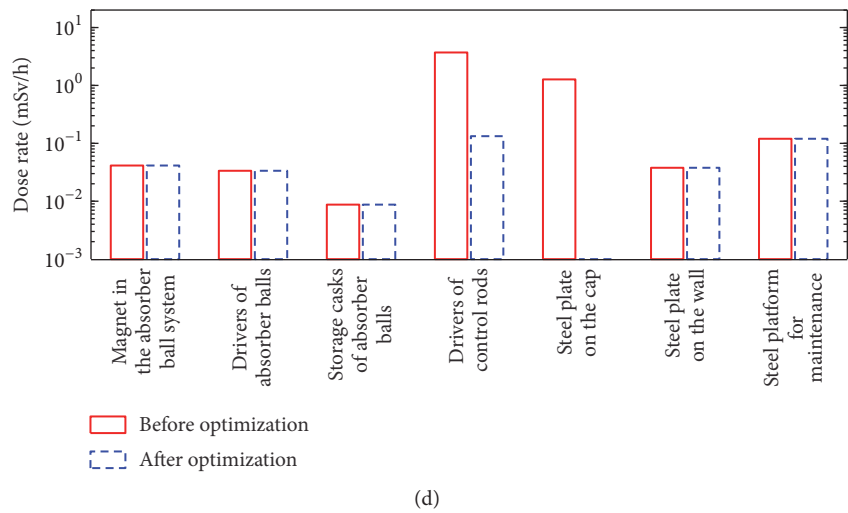
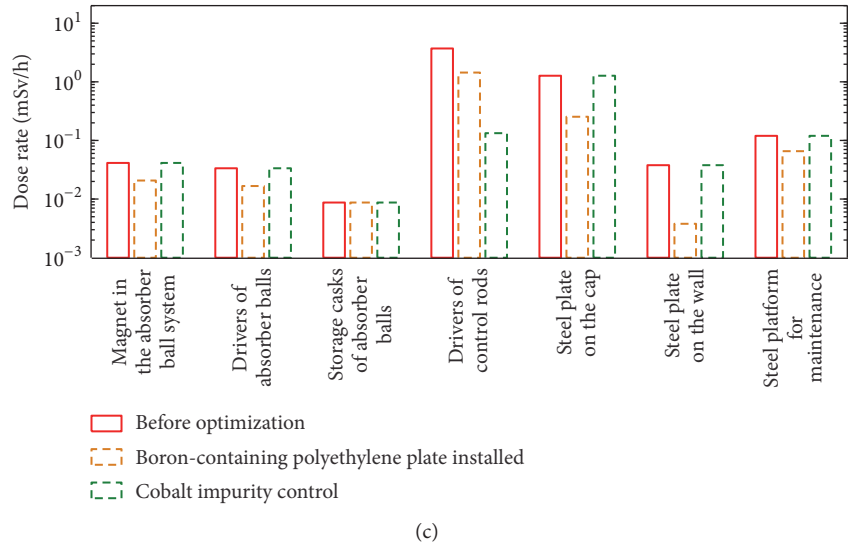
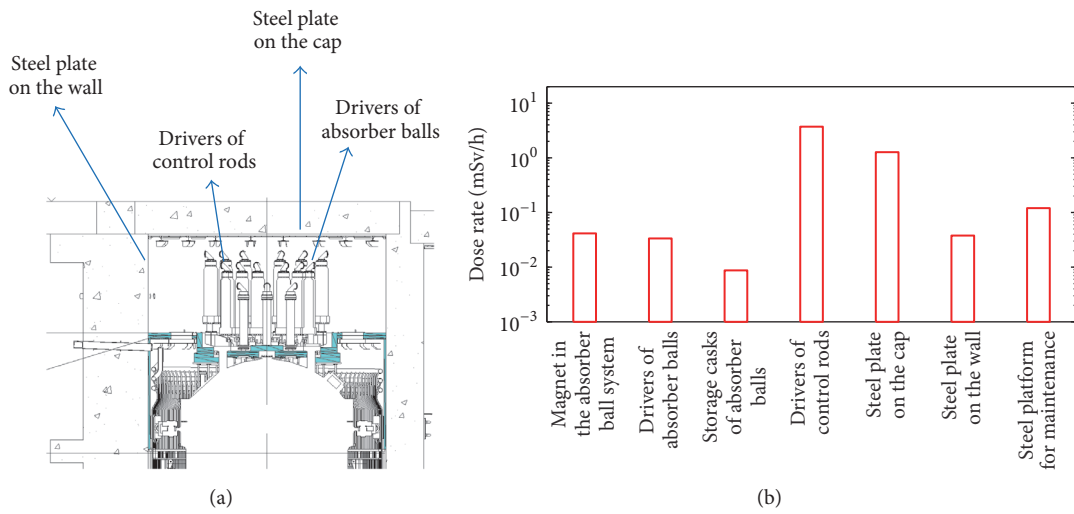


FIGURE 3: (a) The dose reduction design for the maintenance work on top of RPV; (b) dose rates of different equipment for the maintenance work on top of RPV; (c) dose rates before optimization and after boron-containing polyethylene plate installed or cobalt impurity control; (d) dose rates before and after optimization.

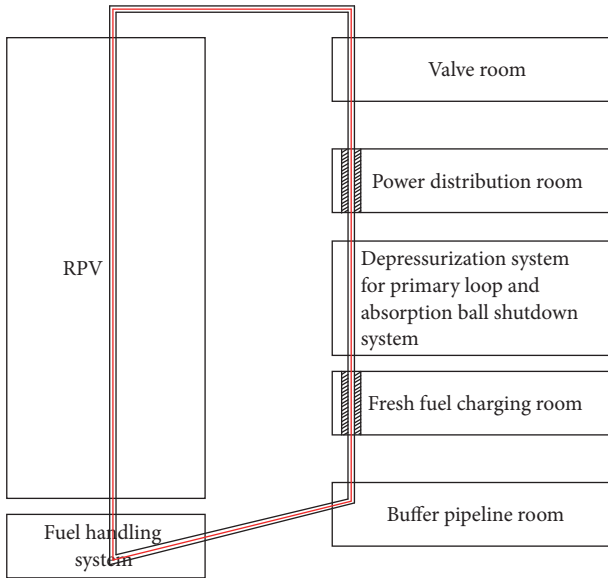


FIGURE 4: Simplified sketch of the fuel transportation path and the related room layout. The red line indicates the primary fuel transportation path and the shaded block indicates the concrete shielding wall.

expensive that it is only affordable to implement the cobalt control on the drivers of control rods. Therefore, the cobalt control does not reduce the radiation from steel plate on the cap (Figure 3(c)), of which the contributed dose rate exceeds the dose limit. In order to round this dilemma, the work flow of the maintenance is modified so that the cap together with the steel plate will be removed first before the maintenance work starts. This removes a critical radiation source in the maintenance and makes it only necessary to implement the cobalt control on the drivers of control rods, which saves a lot of expenses. As the final result, the collective dose rate is reduced to 0.49 mSv/h, with affordable cost (Figure 3(d)).

**6.2. Fuel Handling System.** Two features of the fuel handling system are the moving fuels and its large pipe loop for fuel transferring, which passes several rooms as shown in Figure 4. For those rooms that require the access of staff, a thick concrete shielding wall is used to lower the radiation to an acceptable level (shaded block in Figure 4). In the related radiation protection design, the dynamic dose rate evaluation is performed to avoid inappropriate overestimation in traditional static evaluation, so that the radiation protection is optimized toward a good balance between costs and benefits.

Figure 5 shows one typical example, in which the position of interest receives the radiation from three different fuel elements that are moving downwards in three nearby pipes, respectively (Figure 5(a)). The dynamic evaluation reveals that the instant dose rate varies considerably as the fuels move to different heights (Figure 5(b)). Given the dose limit (0.0075 mSv/h), the daily averaged dose rates are evaluated with both dynamic calculation and static calculation (which

uses the peak values of the instant dose rates in Figure 5(b)). As shown in Figure 5(c), the static evaluation is so conservative that it suggests a 30% growth of the density of the concrete wall to meet the dose limit. This density growth will significantly increase the cost, weight, and requirement for supporting structures. In comparison, the dynamic method provides a more realistic dose rate estimate which proves that the dose rate can meet the dose limit with current concrete shielding and avoid the unnecessary cost.

**6.3. Spent Fuel Storage System.** The spent fuel storage system transfers the spent fuel elements and graphite spheres for reactor starting from the different storage casks and stores these casks in silos underground. The spent fuel elements are highly radioactive, so the spent fuel storage casks are equipped with very thick shielding.

But the graphite spheres are only mildly radioactive and their number is much less than that of the spent fuel elements, which makes it inefficient to use the same shielding as the spent fuel cask. Therefore, both shielding and increasing distance strategies are utilized, in order to reduce the shielding thickness and the related cost (Figure 6(a)). Figure 6(b) shows the calculated dose rate contour for different combination of the steel shielding thickness and the distance prohibited to access, together with the dose limit plane. The dose rate contour under the dose limit plane corresponds to the combinations that meet the requirement. Based on these combinations, the layout of equipment around the graphite sphere casks is adjusted accordingly, in order to achieve an optimal combination that reduces both the prohibited distance and shielding thickness. Figure 6(c) compares the combination before and after optimization. The thickness of the shielding is reduced from 20 cm to 15 cm. The prohibited distance mildly increases from 30 cm to 130 cm. However, this increase has no substantial influences on the maintenance of different equipment, because no maintenance work is required within this distance.

When loading the spent fuel elements to the storage cask, both the cask and the moving fuels are radiation sources that can potentially threat staff. In this case, a joint design with consideration of multiple sources and shielding is necessary to achieve the optimal combination. Figure 7(a) shows an optimization example for the spent fuel storage system, which consists of two moving sources, one static source and two shielding structures. The aim of this calculation is to ensure that the dose rate under the concrete floor is within the requirement of the radiation zoning. Using the routine in Figure 2, different combinations of these two shielding structures are calculated as the candidates for optimization. The dose contour under the plane of the dose limit in Figure 7(b) shows all the available combinations that meet the given dose limit (0.03 mSv/h). With consideration of other aspects, such as maintenance requirements and support structures, a final optimized result is selected from the available choices shown in Figure 7(b). Compared to traditional separate design before optimization, the combination after optimization reduces the thickness of concrete and

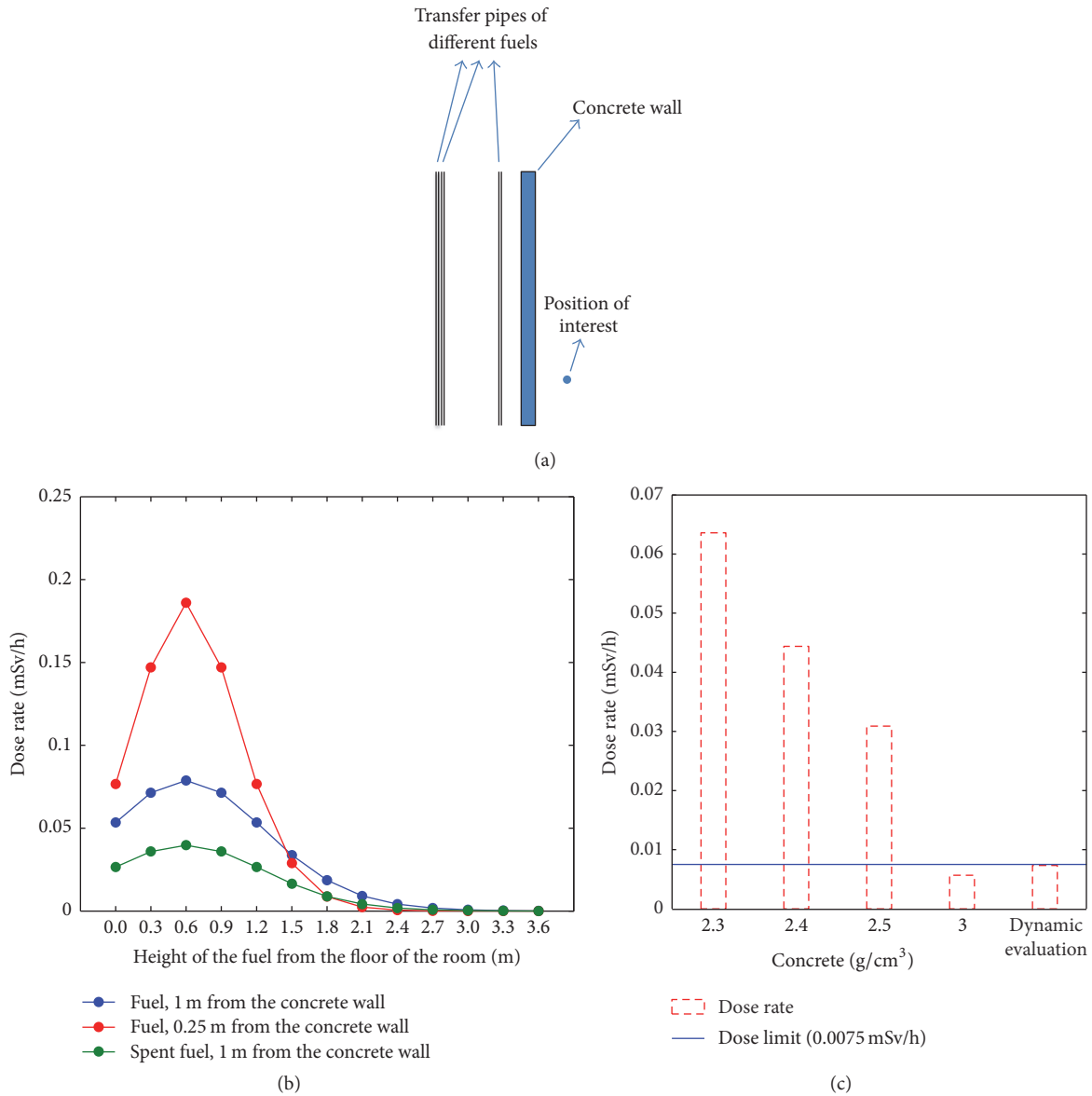


FIGURE 5: (a) An example of fuels moving and irradiating a position of interest; (b) the dynamic evaluation of dose rates; (c) dose rates with different densities of the concrete and dynamic evaluation.

the shielding for the pipe by 62.5% and 45.0%, respectively (Figure 7(c)).

6.4. Other Strategies for Radiation Optimization

6.4.1. Layout Aspect. Compartments of different radiation zonings are physically separated by shielding or concrete walls. The access to these rooms is provided by independent corridors, in which the maximum dose rate is lower than 0.0075 mSv/h. Nonradioactive equipment is physically separated from radioactive equipment, so as to avoid radiation damage and unnecessary occupational exposure in nonradioactive work. And the ventilation system ensures that the air only flows from the nonradioactive area to the radioactive

area. Radioactive equipment is usually concentrated in a single room, in order to make the best of the shielding walls.

6.4.2. Radiation Source Reduction. The fresh fuel elements of HTR-PM are vacuumized to remove N-14 before being charged into the reactor core, so that the corresponding activation product C-14 is reduced. The helium purification system of HTR-PM removes the radionuclides and other contaminations in the primary coolant. The metal and iodine in the coolant are filtered by the dust filter. H-3 and C-14 are oxidized into tritium water and <sup>14</sup>CO<sub>2</sub>, respectively, which are retained by the molecular sieve. Gaseous contaminations are absorbed by the activated carbon.

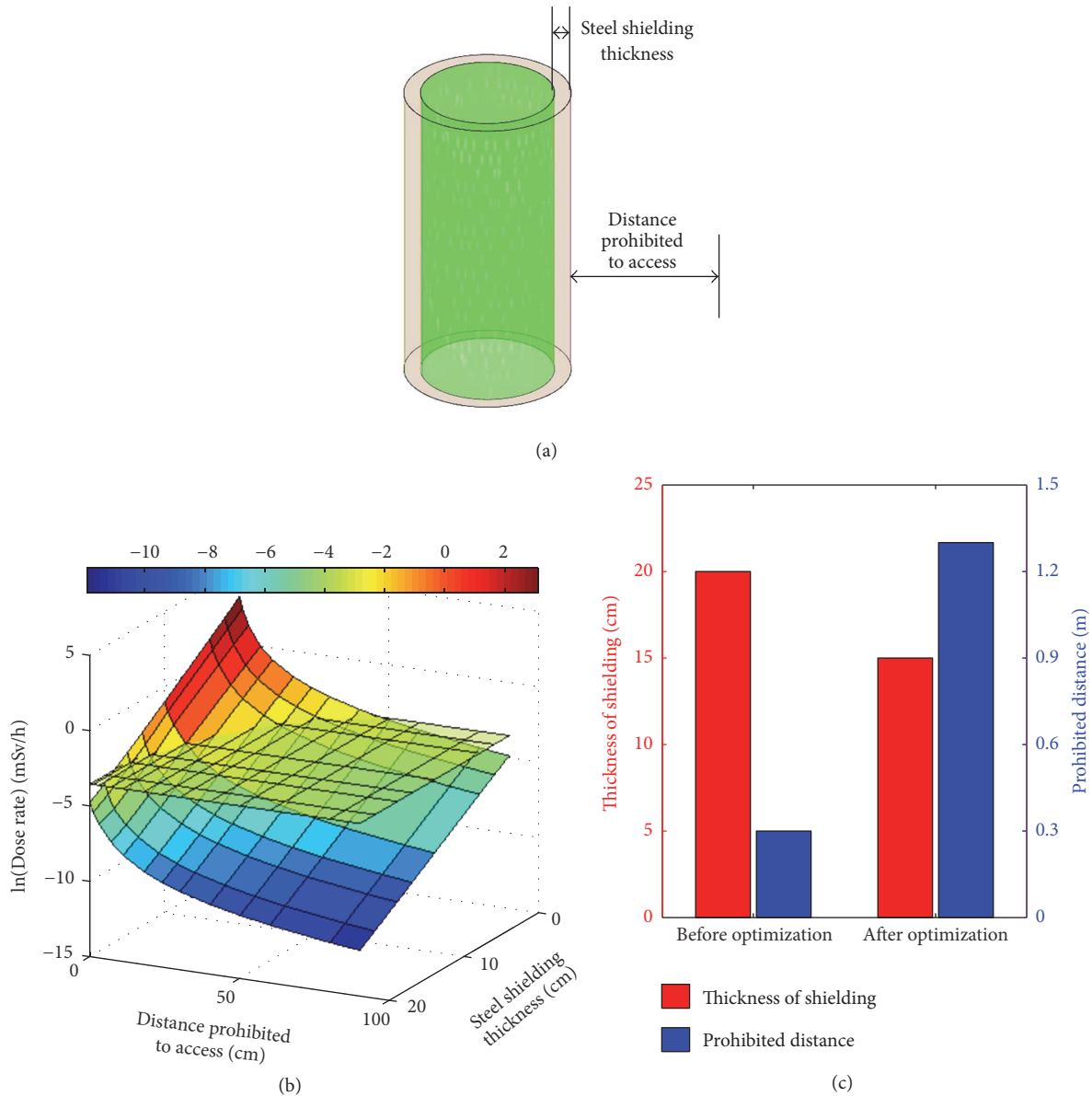


FIGURE 6: (a) Sketch of the graphite sphere cask; (b) the dose limit plane (0.03 mSv/h) and the dose rate contour of the graphite sphere storage cask with respect to distance and the thickness of shielding; (c) the dose rate and prohibited distance before and after optimization.

**6.4.3. Radiation Tolerance.** The tolerance of radiation damage is another important concern with respect to the reliability of components. By calculating the cumulative dose, the radiation damage is evaluated with different shielding designs and spatial arrangements. The design that best matches the IAEA-provided thresholds for radiation damage to materials [24] and ALARA principle is chosen.

## 7. Annual Collective Dose Estimate Optimization

With the optimization of radiation protection, a refined annual collective dose is estimated and compared with the previous rough estimate before optimization for each system.

**7.1. Fuel Handling System.** The primary maintenance work of the fuel handling system takes place in several rooms, most of which is done in the fuel handling system room and the buffer pipeline room.

Before optimization, no maintenance details were considered for the fuel handling system room. Consequently, there were only very rough estimates, for which the total annual work duration was 140 man-hours and the average dose rate was 0.03 mSv/h. During optimization, the maintenance work is broken down into very specific tasks such as the repair of the fuel discharging equipment, the replacement of its motor, and the ultrasonic measurement of the thickness of pipe elbows. And the intervals between two maintenances have also been established for these tasks, which are two years

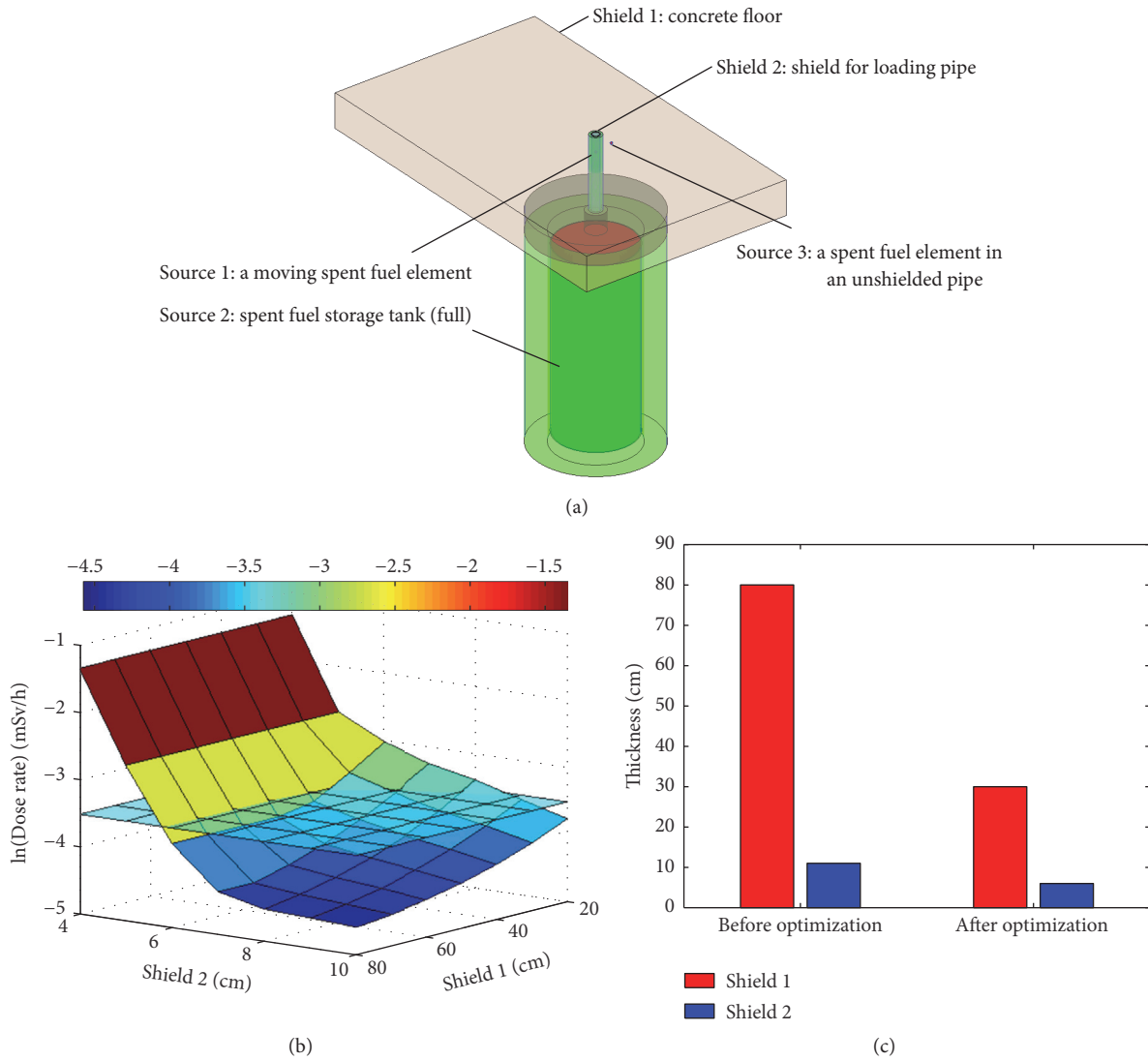


FIGURE 7: The optimization of the concrete floor and the shielding for the loading pipe. (a) The radiation computation model generated by the in-house tool; (b) dose rate contour and dose limit (the transparent plane); (c) the comparison between the designs before and after optimization.

for most tasks and four years for others. The establishment of these maintenance cycles provides a more realistic estimate of the work duration (total 29 man-hours), which is much less than the previous estimate. The dose rates are also replaced with spatially varying calculation results, for which the maximum exceeds 1 mSv/h and the minimum is 0.0046 mSv/h (Figure 8(a), work positions 1 and 6).

For the buffer pipeline room, the annual work duration and the average dose rate were estimated to be 70 man-hours and 0.03 mSv/h, respectively, before optimization, in the absence of detailed maintenance information. During optimization, the analysis of work contents reveals that the maintenance intervals of the equipment in this room can be quite long, which are two, four, six, or even ten years. This significantly reduces the annual average work durations, for

tasks like the inspection of magnetic buffer components, the ultrasonic measurement of the thickness of pipe elbows, the repair of the fuel charging equipment, the replacement of the server system, and so on. As a result, the optimized total annual work duration is 28 man-hours. The dose rates at most maintenance work positions are generally below 0.001 mSv/h (Figure 8(b)), because most radioactive fuel elements in this room are removed in advance and the only remaining radiation source (i.e., the container of graphite dust which is far away from work positions) is well-shielded. However, for the ultrasonic thickness measurement and the inspection of magnetic buffer components, the work positions are difficult to identify and the dose rates are unable to be calculated consequently. Thus, the dose rates of these two tasks are set to the maximal dose rate (0.03 mSv/h) allowed by the radiation

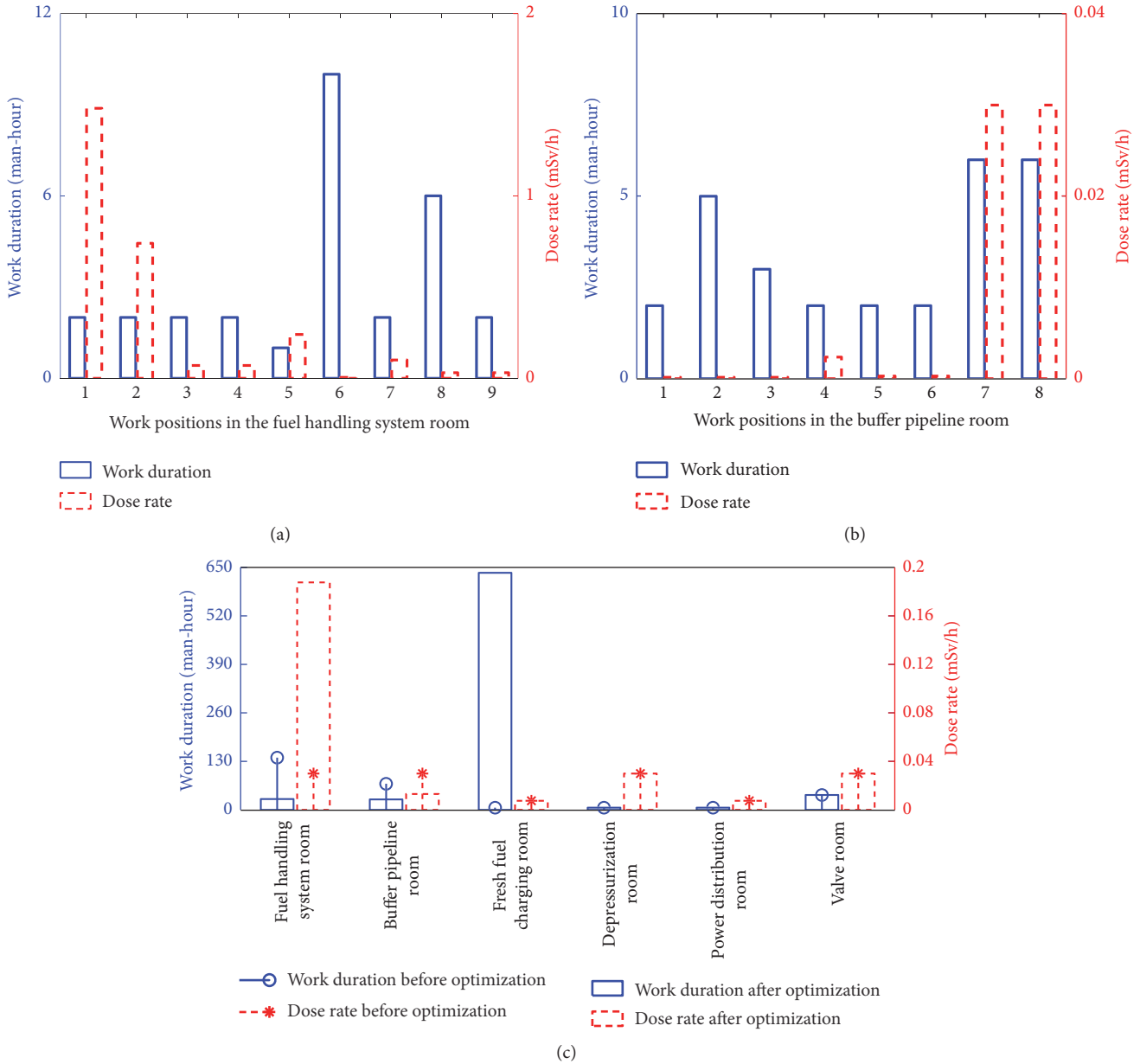


FIGURE 8: Dose rates and work durations in (a) the fuel handling system room; (b) the buffer pipeline room; and (c) different rooms of the fuel handling system.

zone for this room (Figure 8(b), work positions 7 and 8), which is a conservative estimate. In a real case, the dose rates for these two tasks may be lower than the estimate.

Figure 8(c) summarizes the dose rates and work durations in different rooms of the fuel handling system before and after optimization, respectively. The work duration in the fuel handling system room is reduced after the refined estimation, while the corresponding average dose rate is increased after optimization. For the buffer pipeline room, both the work duration and the average dose rate are reduced after optimization. For the other four rooms, the ultrasonic thickness measurements every two years are the major radioactive tasks, for which the dose rates are 0.03 mSv/h or 0.0075 mSv/h

according to the upper limits of the corresponding radiation zones. Although this estimation is a little conservative, it can handle the uncertainties in the identification of work positions and corresponding dose rates well.

7.2. Control Rod System, Air Circulator, and Hoist. Before optimization, the annual maintenance work duration and dose rate related to the control rod system were 4 man-hours and 3 mSv/h, respectively. According to the experience in HTR-10, the maintenance work mainly involves the disassembly and replacement of the electrical penetrations, the drivers, and different equipment of the control rod system, which are implemented every 10 years. Based on this maintenance cycle,

TABLE 3: The annual work durations and dose rates of RPV, SG, and helium circulator.

	Work position	Work duration (man-hours)	Dose rate (mSv/h)	Collective dose (man-Sv/a)
RPV	1	15	3.50	199.05
	2	15	3.63	
	3	30	1.78	
	4	10	3.87	
SG	1	50	0.91	62.82
	2	50	0.23	
	3	50	$3.89 \times 10^{-4}$	
	4	50	0.12	
Helium circulator	1	20	0.95	54.02
	2	10	1.75	
	3	10	1.75	

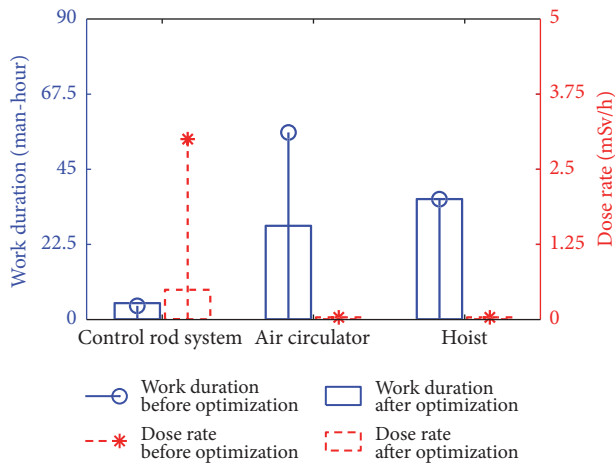


FIGURE 9: Dose rates and work durations of the control rod system, air circulator, and hoist.

the annually average work duration for the control rod system is estimated to be 4.8 man-hours (Figure 9). And the dose rate at the work position is 0.49 mSv/h, after the work flow optimization in Figure 3.

As for the air circulator and hoist, their maintenances do not involve radioactivity. But in order to be appropriately conservative, the dose rates are set to the upper limit (0.03 mSv/h) of the reactor maintenance hall, where the maintenance work takes place. Before optimization, the annual work duration of the air circulator was conservatively estimated as 56 man-hours with no consideration of the detailed work contents. During optimization, the maintenance work of the air circulator is specified as the inspection and cleaning which are conducted every two years. Based on the maintenance schedule, the final annual work duration is 28 man-hours (Figure 9).

7.3. RPV, Steam Generator (SG), and Helium Circulator. The maintenance work of these three components contributes the majority of the annual collective dose estimate, of which the

dose rates and annual work durations are summarized in Table 3. For RPV and SG, the annual work durations and dose rates are estimated according to the experiences of similar maintenance work on other advanced reactors in China. For the helium circulator, the experiences of the maintenance work on HTR-10 [25] are referred to estimate the annual work duration and dose rate.

For RPV, four representative positions are chosen for the collective dose estimation, including the top head and bottom head of RPV (work positions 1 and 4) and the positions above and below the hot gas duct (work positions 2 and 3). The dose rates at these positions are all above 1 mSv/h, which are considerably high. Therefore, the robotic and remote flaw detection equipment is widely used to reduce the work duration and occupational dose. The optimized work durations at these four positions are 15, 15, 30, and 10 man-hours. The corresponding collective dose is estimated to be 199.05 man-Sv/a. However, this estimate does not take the effect of personal radiation protection into consideration. Therefore, it can be viewed as the upper limit of the collective dose.

For SG, its dose rates show variations between chosen representative positions, from lower than 0.001 mSv/h to almost 1 mSv/h (Table 3). The helium leakage detection and pressure test every two years are identified as the primary maintenance work and the total estimated work duration is 200 man-hours. Because of the uncertainties of work positions, the total estimated work duration is divided equally into four parts for the four representative positions. The resultant collective dose estimate is lower than 1/3 of that of RPV.

With respect to the helium circulator, the maintenance work involves the inspection and repair of the internal components every five years and the replacement of vulnerable parts of the helium circulator and its electrical penetrations every ten years. The representative dose rates near the helium circulator are lower than RPV but higher than SG (Table 3). The corresponding work durations are estimated based on recent experiences on the helium circulator of HTR-10 [25]. Because the interval between two maintenances of

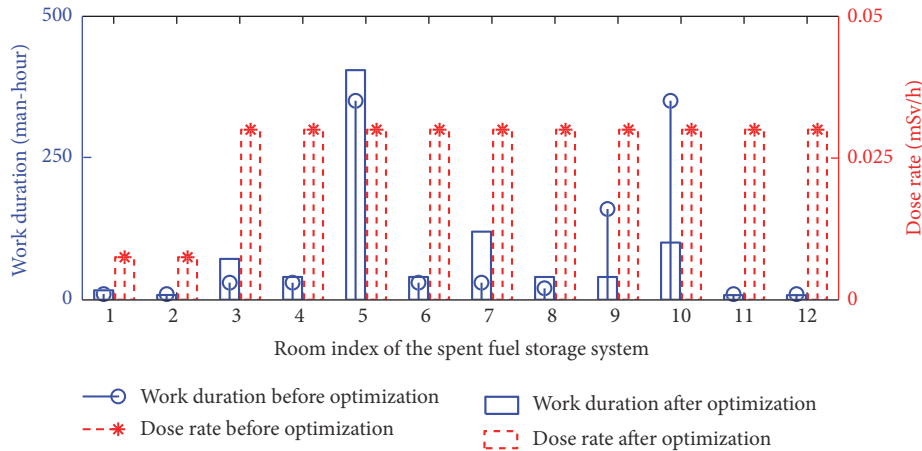


FIGURE 10: Dose rates and work durations of rooms of the spent fuel storage system.

the helium circulator is much longer than RPV and SG, the corresponding annual work duration and the collective dose are lower than those of RPV and SG.

**7.4. Spent Fuel Storage System.** The maintenance work of the spent fuel storage system involves 12 rooms. In the maintenance stage, the fuels in these rooms are removed so that the dose rates are quite low. However, the maintenance work can take place at any corner of any room, which makes it difficult to choose representative work positions. In order to deal with the uncertainties, the upper limits of radiation zones for these rooms are used as the representative dose rates (Figure 10). Meanwhile, the investigation of work contents shows that the major tasks in the ventilation equipment room mainly involve the inspection of the bearing lubrication every two years and the replacement of the bearings and electrical components every ten years (Figure 10, room 9). These long maintenance cycles reduce the annual work duration from 160 man-hours to 40 man-hours. For the electrical equipment room, the robotic and remote detection techniques are intensively used to replace the manual inspection on site, which greatly reduces the work duration in the radioactive environment by 71.3% (Figure 10, room 10). For rooms 5 and 7, the work durations slightly increase. After optimization, the annual average collective dose for the whole spent fuel storage system decreases by 4.41 man-mSv/a, compared to that before optimization.

**7.5. Helium Purification System.** For the helium purification system, the maintenance work details were not specified before optimization. Therefore, the dose rate was set to the upper limit of the radiation zone which is 3 mSv/h and the annual work duration was 36 man-hours for conservative considerations. During optimization, the major work that involves radioactivity is identified as the maintenance of the compressors, valves, and instruments every two years. For them, the upper limit of the radiation zone is used as the representative dose rate and the work duration is estimated to be 2.5 man-hours. Another task that might need radiation protection is the replacement of the dust filter every twenty years. For this task, the refined dose rate estimate is

0.54 mSv/h and the annual work duration is estimated to be 1 man-hour after optimization.

**7.6. Liquid/Solid Waste Disposal System and Ventilation System.** These three systems only involve very limited radioactivity, for which the work durations remain much the same as those before optimization. But the dose rate calculation is further refined for better estimation of collective dose rates.

For the liquid waste disposal system, the dose rates of the maintenance work were all set to the upper limits of the corresponding radiation zones before optimization. To get optimized estimates, the dose rate calculation is improved with the developed software. For example, the dose rate at the work position near the evaporator is estimated to be 0.0035 mSv/h after optimization (Figure 11, position 1 of the liquid waste disposal system), when the evaporator is fully loaded with liquid waste. If the radioactive liquid in the evaporator is removed before maintenance, the dose rate can be even lower than the above estimate. Dose rates near the liquid waste storage cask and evaporator equipment are estimated to be 0.0055 mSv/h and 0.0056 mSv/h, respectively, after optimization (Figure 11, positions 2 and 3 of the liquid waste disposal system). The work durations are estimated to be equal at all these three positions, which are the same as those before optimization.

For the solid waste disposal system, the dose rates at primary work positions are 0.021 and 0.025 mSv/h, respectively, after refined dose estimation, which are more realistic than previous estimates before optimization.

As for the ventilation system, the radiation zone is changed from the green zone in the previous design to the yellow zone in the current design. Therefore, the dose rate estimate which is the upper limit of the radiation zone increases from 0.0075 mSv/h to 0.03 mSv/h. Besides, the work duration estimate is slightly increased to 8 man-hours with the consideration of the additional preparation stages.

**7.7. Absorber Ball System.** The absorber ball system was not analyzed in the previous estimate. According to the experiences on HTR-10, the maintenance work of the absorber ball

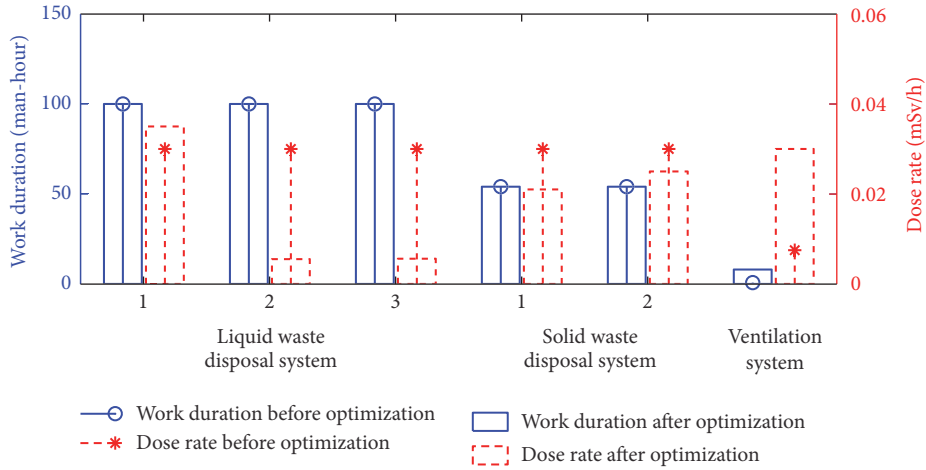


FIGURE 11: Dose rates and work durations of the liquid/solid waste disposal system and ventilation system.

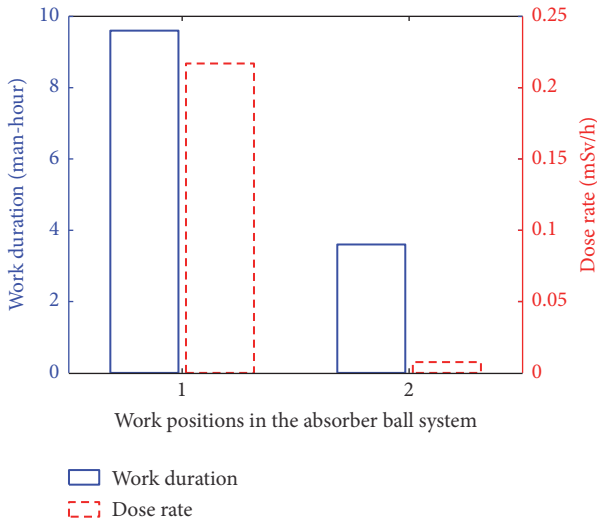


FIGURE 12: Dose rates and work durations of the absorber ball system.

system also involves radioactivity. The primary radioactive maintenance work of this system is the replacement of its drivers and other components. For the replacement of the drivers, the dose rate is 0.217 mSv/h and the work duration is 9.6 man-hours (Figure 12, work position 1). For the maintenance work of other components, the dose rate is 0.0075 mSv/h and the work duration is estimated to be 3.6 man-hours (Figure 12, work position 2).

**7.8. Total Annual Collective Dose.** The optimized annual collective dose estimates for primary systems are compared with the estimates before optimization in Figure 13. The total annual collective dose after optimization is 0.445 man-Sv/a, which is reduced by 9.18% from the previous 0.490 man-Sv/a before optimization. The annual collective dose of the helium purification system shows the most significant decrease after optimization, due to the refined dose rates and more realistic

work duration estimates than those before optimization. For the control rod system, its annual collective dose is reduced by 9.65 man-mSv/a (80.4%), as a result of the optimized work flow and radiation protection practices. There are also decreases of the annual collective dose for the air circulator, spent fuel storage system, and liquid/solid waste disposal system. It is noticeable that the annual collective doses may not always decrease for every system, because the optimization aims at the ALARA principle, instead of a sole decrease of the dose. For example, the annual collective dose of the fuel handling system increases by 54.5% after optimization, because of a more detailed investigation on the work flow. The collective dose of the ventilation system also increases, because the radiation zoning is adjusted for its room. And the absorber ball system which is neglected in the previous estimate is also added to the analysis. This demonstrates that the presented framework not only optimizes the quantities such as dose rate and work duration but also completes the radiation protection design.

## 8. Conclusion

The optimization of radiation protection in the HTR-PM's design stage is reviewed and presented as a systematic framework in this study. A routine that jointly optimizes system design and radiation protection is proposed and presented with typical calculations of optimization tasks for the radioactivity-related systems, including the control rod and absorber ball system in the reactor cavity, fuel handling system, and spent fuel storage system. The optimization using this routine quantitatively achieves the reduction of either the dose rate or the shielding or both for these systems by about 23.3%~90.6%. Based on the refined dose rate estimation and work flow, the annual collective doses of different systems are optimized and compared against the previous estimates. The comparison reveals that the annual collective dose of HTR-PM is reduced from 0.490 man-Sv/a before optimization to 0.445 man-Sv/a after optimization, which complies with the requirements of the Chinese regulatory guide.

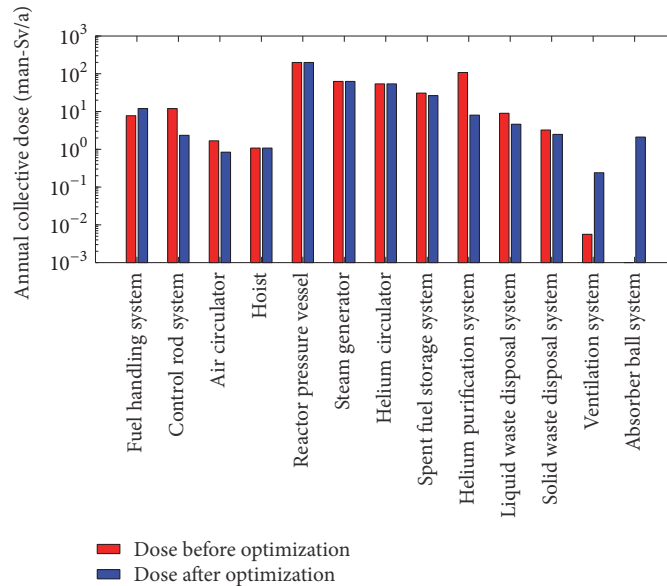


FIGURE 13: Collective dose of HTR-PM before and after optimization.

## Conflicts of Interest

The authors declare that they have no conflicts of interest.

## Acknowledgments

The authors greatly acknowledge the financial support from the National Natural Science Foundations of China (Grant no. 11475100), the Education Ministry Foundation of China (Grant no. 20151080400), and the Foundation of Key Laboratory of Advanced Reactor Engineering and Safety of the Ministry of Education (Grant no. ARES201410).

## References

- [1] ICRP, "Recommendations of the ICRP," *Annals of the ICRP*, vol. 1, no. 3, 1977.
- [2] ICRP, "A compilation of the major concepts and quantities in use by ICRP," *Annals of the ICRP*, vol. 14, no. 4, 1985.
- [3] ICRP, "1990 Recommendations of the international commission on radiological protection," *Annals of the ICRP*, vol. 21, no. 1–3, 1991.
- [4] ICRP, "The optimisation of radiological protection: broadening the process," *Annals of the ICRP*, vol. 36, no. 3, pp. 69–87, 2006.
- [5] ICRP, "The 2007 recommendations of the international commission on radiological protection," *Annals of the ICRP*, vol. 37, no. 2–4, 2007.
- [6] J. Baum, *Occupational Exposures and Practices in Nuclear Power Plants*, Brookhaven National Lab., New York, NY, USA.
- [7] A. Gauvenet, "Radiation protection practices and experience in French operating reactors," *Nuclear Technology*, vol. 72, no. 3, pp. 246–253, 1986.
- [8] J. Hildebrand, "Experience in the optimization of radiation protection practices during the cleanup of Three Mile Island Unit 2," *Optimization of Radiation Protection*, 1986.
- [9] G. Vivian and K. Donnelly, *A Canadian Nuclear Power Producer's Approach to The Optimization of Design for Radiation Protection*, IAEA, 1986.
- [10] R. Wilson, G. A. Vivian, W. J. Chase et al., "Occupational dose reduction Experience in Ontario Hydro nuclear power stations," *Nuclear Technology*, vol. 72, no. 3, pp. 231–245, 1986.
- [11] M.-S. Yim and H. Ocken, "Radiation dose management in nuclear power plants," *Progress in Nuclear Energy*, vol. 39, no. 1, pp. 31–51, 2001.
- [12] E. Baumann and I. R. Terry, "The EPR: a clear step forward in dose reduction and radiation protection," *Nuclear Engineering and Design*, vol. 236, no. 14, pp. 1720–1727, 2006.
- [13] B. Doehnert, "Design of the Ap 1000 power reactor," in *Proceedings of the International Conference on Nuclear Energy for New Europe Portorož*, September, 2006.
- [14] R. Bäumer, H. Barnert, E. Baust et al., *AVR-Experimental High-Temperature Reactor, 21 Years of Successful Operation for a Future Energy Technology*, VDI-Verlag GmbH, Düsseldorf, Germany, 1990.
- [15] H. Wahsweiler and I. Kalinowski, "Experience in Optimization of Operational Radiation Protection in The THTR 300," in *SVA further education course: Optimization of the radiation protection from the design to the decommissioning of nuclear installations*, 1987.
- [16] S. Fang, H. Li, J. Cao, W. Li, F. Xie, and J. Tong, "γ dose rate estimation and operation management suggestions for decommissioning the reactor pressure vessel of htr-pm," in *Proceedings of the 15th International Conference on Environmental Remediation and Radioactive Waste Management*, p. V002T03A005, Brussels, Belgium.
- [17] N. N. S. Administration, *Radiation Protection Design for Nuclear Power Plants*, National Nuclear Safety Administration, 1990.
- [18] I. A. E. Agency, *Radiation Protection and Safety of Radiation Sources*, International Basic Safety Standards, 2014.
- [19] W. W. Engle Jr, *A users manual for anisn: a one dimensional discrete ordinates transport code with anisotropic scattering*, Oak Ridge Gaseous Diffusion Plant, Tennessee, Tenn, USA, 1967.

- [20] F. Mynatt, "DOT III two-dimensional discrete ordinates transport code," Tech. Rep., Oak Ridge National Laboratory, Tennessee, Tenn, SA, 1973.
- [21] U. Fischer and H. W. Wiese, *Verbesserte konsistente Berechnung des nuklearen Inventars abgebrannter DWR-Brennstoffe auf der Basis von Zell-Abbrand-Verfahren mit KORIGEN*, Ber./KFK, 1983.
- [22] M. Bell, "ORIGEN-The Oak Ridge Isotope Generation and Depletion Code," *ORNL*, p. 4628, 1973.
- [23] S. Sun, S. Fang, and H. Li, "Radiation Shielding Design of High Temperature Reactor Pebble-Bed Module (HTR-PM)," in *Proceedings of the 24th International Conference on Nuclear Engineering*, American Society of Mechanical Engineers, 2016.
- [24] H. Ullmaier and W. Schilling, *Radiation Damage in Metallic Reactor Materials*, 1980.
- [25] C. Guo, L. Wei, H. Li, J. Cao, and S. Fang, "Radiation protection practices during the helium circulator maintenance of the 10 mw high temperature gas-cooled reactor-test module (HTR-10)," *Science and Technology of Nuclear Installations*, vol. 2016, Article ID 5967831, 13 pages, 2016.

## Research Article

# Analysis of Precooling Injection Transient of Steam Generator for High Temperature Gas Cooled Reactor

**Yan Wang, Lei Shi, and Yanhua Zheng**

*Institute of Nuclear and New Energy Technology, Tsinghua University, Collaborative Innovation Centre of Advanced Nuclear Energy Technology, Key Laboratory of Advanced Reactor Engineering and Safety, Ministry of Education, Beijing 100084, China*

Correspondence should be addressed to Yan Wang; wangyanfcw@tsinghua.edu.cn

Received 19 December 2016; Revised 8 May 2017; Accepted 23 May 2017; Published 27 July 2017

Academic Editor: Hidemasa Yamano

Copyright © 2017 Yan Wang et al. This is an open access article distributed under the Creative Commons Attribution License, which permits unrestricted use, distribution, and reproduction in any medium, provided the original work is properly cited.

After a postulated design basis accident leads high temperature gas cooled reactor to emergency shutdown, steam generator still remains with high temperature level and needs to be cooled down by a precooling before reactor restarts with clearing of fault. For the large difference of coolant temperature between inlet and outlet of steam generator in normal operation, the temperature distribution on the components of steam generator is very complicated. Therefore, the temperature descending rate of the components in steam generator needs to be limited to avoid the potential damage during the precooling stage. In this paper, a pebble-bed high temperature gas cooled reactor is modeled by thermal-hydraulic system analysis code and several postulated precooling injection transients are simulated and compared to evaluate their effects, which will provide support for the precooling design. The analysis results show that enough precooling injection is necessary to satisfy the precooling requirements, and larger mass flow rate of precooling water injection will accelerate the precooling process. The temperature decrease of steam generator is related to the precooling injection scenarios, and the maximal mass flow rate of the precooling injection should be limited to avoid the excessively quick temperature change of the structures in steam generator.

## 1. Introduction

Emergency shutdown system will be tripped to start up after a postulated accident is detected, and the decay heat will be removed by the residual heat removal system. Steam generator (SG) still remains with high temperature level after emergency shutdown, and it needs to be cooled down to a certain temperature level before the reactor restarts with faults clearing. In high temperature gas cooled reactor (HTGR), due to the larger temperature difference of coolant between inlet and outlet of SG in normal operation, the temperature distribution on SG is very complicated. Therefore, the temperature descending rate of the SG components during the cooling transient should be controlled to avoid potential damage on the mechanical structure resulting from an excessively quick temperature change.

A precooling design where the SG will be cooled down by a precooling water injection into SG is presented in this paper. Because the mixture of water and steam with high

pressure remains in SG after emergency shutdown, it needs to be drained out of SG to decrease the SG pressure for the following cooling water injection into SG. Therefore, the precooling design is composed of two main stages: the first stage defined as pressure relief is the prearrangements including draining the water in SG and decreasing the SG pressure, which will be achieved by the actions of draining-emptier system and pressure relief system. The second stage defined as the precooling water injection is aimed at cooling the SG down with a cooling water injected into the SG. Not only does the SG temperature change obviously during the precooling water injection stage, but also the temperature distribution of the SG structures will also be affected due to heat convection during the pressure relief stage to certain extent. Some relevant discussion on the pressure relief transient could be found in the early study [1], where the effects on the SG temperature under different pressure relief design were compared and the analysis result could provide some support for the pressure relief setting of the current precooling design.

TABLE 1: Design parameters of HTR-PM.

Parameters	Designed value
Reactor power (MWth)	$2 \times 250$
Power density (MW/m <sup>3</sup> )	3.22
Helium pressure of primary loop (MPa)	7
Helium mass flow rate (kg/s)	96
Inlet helium temperature (°C)	250
Outlet helium temperature (°C)	750
Main steam pressure (MPa)	13.9
Main feedwater temperature (°C)	205
Main steam temperature (°C)	571
Feedwater flow rate for one reactor steam generator (kg/s)	98

In this paper, a further study focuses on the precooling water injection stage to evaluate the precooling design. Several postulated precooling water injections are simulated and compared to evaluate if the precooling water injection designs could cool down the SG to the expected temperature level within the stipulated time and the temperature decrease of SG during the precooling water injection could satisfy the accepted limitation. The high temperature gas cooled reactor pebble-bed module (HTR-PM) is selected for the study on the precooling transient of SG. For better understanding, brief descriptions on the HTR-PM are given in the next section.

## 2. The HTR-PM Reactor

The HTGR as one candidate for the Generation IV nuclear energy system technology [2] is well known with its inherent safety features which has the capability to realize the safety target where the consequences of all conceivable assumed severe accidents should not result in notable offsite radiation impacts [3]. The study on the modular HTGR is developed in China, including the HTR-10 [4] and HTR-PM [5, 6], which consists of  $2 \times 250$  MWth module pebble-bed reactor with standardization and modularization technology. The general design parameters on HTR-PM are shown in Table 1.

The single reactor module is illustrated as in Figure 1, which consists of the reactor pressure vessel (RPV), the steam generator pressure vessel (SGPV), and the connecting horizontal coaxial hot-gas duct pressure vessel. The reactor core in the RPV is a one-zone cylindrical loose packed bed with an average height of 11 m and a diameter of 3 m, which consists of about 420,000 spherical fuel elements in the equilibrium state. The cold helium with an average temperature of 250°C is circulated into the RPV through the outer annular channel of the hot-gas duct by the helium blower installed on the top space of the SGPV. The main part of the helium flows upwards to the top of the core through 30 coolant boreholes in the side reflector and is collected in the cold helium plenum located in the upper part of the top reflector, and then it flows down

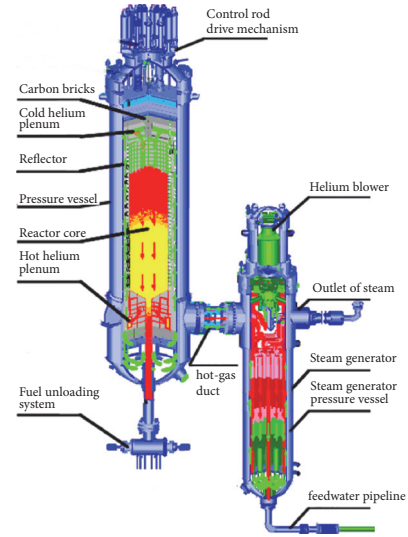


FIGURE 1: Illustration of the HTR-PM.

through the pebble bed and is heated up to an average temperature of 750°C. The 750°C hot helium out of the RPV is fed into the SGPV through the central channel of the hot-gas duct and flows around the outside of the steam generator heat-exchange tubes (SGHT) from the upside to the downside to have a heat transfer with the secondary side of the SG. Then, the cooled helium turns reversely at the bottom of the SGPV, flowing upwards between the steam generator shroud and the SGPV and back to the top space of the SGPV.

A simplified schematic diagram of the SG secondary loop of the HTR-PM is illustrated as in Figure 2. The SG is designed as a once-through assembly type of helical tube steam generator placed below the core in elevation. The 205°C subcooled feedwater in the secondary side of the SG flows in the helical tubes from the bottom to the top. The 750°C hot helium from reactor fed into the SG flows around the SGHT and transfers its heat to the subcooled feedwater in the SGHT to produce a 571°C superheated steam at the SG outlet, whereby its temperature decreases from 750°C to 250°C. Then all the superheated steam is collected at the upper plenum and passes through the live-steam pipeline (LP) to the turbine hall. The secondary loop isolation system including the isolation valves on the feedwater pipeline (FP) and the LP is designed to isolate the secondary loop timely after emergency shutdown. To ensure credible isolation, two different feedwater isolation valves (FIV), as well as two main steam isolation valves (SIV), are installed. The draining-emptier system is designed to drain the residual water in the SG after emergency shutdown. An airtight draining storage tank installed inside the reactor building below the SGPV is connected to the FP via two parallel and independent draining pipelines with two draining valves (DV) on each draining pipeline.

## 3. Description on the Precooling Injection

When some postulated accident of HTGR occurs, the reactor safety protection system is tripped to start emergency

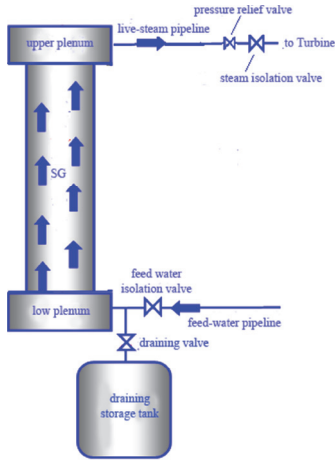


FIGURE 2: Illustration of the HTR-PM secondary loop.

shutdown. A sequence of protective actions is carried out, including dropping of all reflector rods, shutdown of blower and close of blower flaps, and isolation of the SG secondary side. SG which remains with high temperature level after emergency shutdown will be cooled down by the precooling. In this paper, a postulated precooling solution is proposed to study. A series of actions will be carried out as the following: the water in SG will be discharged by the draining-emptier system, and the pressure relief valve (PRV) installed on the LP will be opened to decrease the secondary side pressure of the SG for the precooling injection. Then, the precooling water in the form of superheated steam is pumped into the secondary side of the SG to cool down the SG.

The SGHT has a very complicated temperature distribution, whose minimal temperature is less than 250°C and maximal temperature exceeds 570°C in the normal steady-state operation. During the water-discharge and the pressure relief, the mixture of water and steam in the secondary side of the SG will flow through the SGHT and the LP and transfer heat with them; thus, the temperature distribution of the structures will be affected, whose effect had been analyzed in the early study [1, 7]. With the following precooling water injection, the SGHT and the LP will be cooled down and the temperature decrease during the transient will have a stress effect on the structures. The excessive change of temperature which may result in the potential damage should be avoided. Therefore, the study on the precooling injection is significant for HTGR and it will be focused in the following sections.

#### 4. Analysis of the Precooling Injection Transient

**4.1. Analysis Model.** A system code PCNHR developed by Tsinghua University and used for transient thermal-hydraulic analysis of flow systems is used to simulate the precooling transient. The PCNHR [8] code had been benchmarked by the comparison with the famous general analysis code of RETRAN-02 [9], which is widely used in the plant design for pressurized water reactor (PWR).

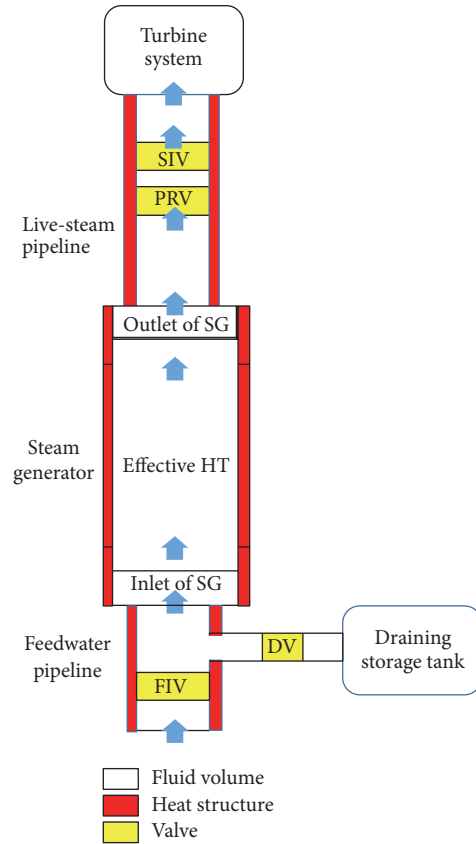


FIGURE 3: Secondary loop model of the HTR-PM.

The analysis model for the secondary loop of the HTR-PM is shown as in Figure 3.

The secondary loop of HTR-PM consists mainly of the FP, the SGHT, and the LP. The SGHT bundles are simplified as one pipe with equivalent thermal-hydraulic diameter in the model. It includes the inlet part, the outlet part, and the effective heat transfer part which transfers heat between the primary side and the secondary side, and the total SGHT is divided into 72 meshes in its length direction. The FP is divided into 2 meshes in length direction and the LP is divided into 54 meshes in length direction. The DV on the draining pipeline, the FIV on the FP, and the PRV and the SIV on the LP are all represented by control function in the model. The components, such as the SGHT, the FP, and the LP, are modeled with “heat structure” in the model, whose temperature is affected by heat transfer between the wall surface of the components and the fluid in the secondary loop during the transient. Because the helium circulation in the primary loop stops after emergency shutdown, the heat transfer from the primary side of SG to the secondary side through the SGHT by heat conduction and natural convection is weak. Therefore, the outside wall surface of the SGHT is assumed as adiabatic boundary in model. The outside wall surfaces of the FP and the LP are also treated as adiabatic boundary for the heat insulating material wrapped outside them.

The precooling fluid is injected from the LP as input source and transfers heat with the “heat structures” when it

passed through the SG. The heat transfer coefficient correlation will be automatically chosen in the code according to flow condition. In this code, Dittus-Boelter correlation is used for forced convection heat transfer with single-phase vapor flow.

$$\text{Nu} = 0.023\text{Re}^{0.8} * \text{Pr}^{0.4}, \quad (1)$$

where Nu is Nusselt number, Re is Reynolds number, and Pr is Prandtl number.

**4.2. Assumptions and Claims.** For the operation of nuclear power plant with higher efficiency, the SG is expected to be cooled down as soon as possible. On the other side, the temperature descending rate of SG during the precooling transient must be controlled below the acceptable limitation to avoid potential damage on the mechanical structure from an excessively quick temperature change. In this analysis, the SG is required to be cooled down to 200°C within 8 hours by the precooling injection for the next actions of reactor system. According to a conservative stress evaluation on the SG components, the limitation on the maximal temperature descending rate of SG components during the cooling transient is defined as 3°C/min in this analysis.

A postulated scenario is defined in this analysis: the reactor in normal operation is led to emergency shutdown for some certain reason; a sequence of protection actions are triggered. After the protection actions are completed, the PRV is opened to control the pressure decrease of the secondary side to approx. 1 MPa. Then, the precooling water is injected into the secondary side of the SG to cool down the components. The superheated steam injection is designed to avoid sudden cold shock from phase transition of fluid during the transient, and the support system for precooling injection could supply a stable steam below 200°C. Therefore, several postulated precooling injection cases are designed and compared to study their effect on the components during the transient.

*Case 1.* It includes a 200°C/1.1 MPa precooling injection with a constant mass flow rate of 1 t/h.

*Case 2.* It includes a 200°C/1.1 MPa precooling injection with a constant mass flow rate of 5 t/h.

*Case 3.* It includes a 200°C/1.1 MPa precooling injection with a variable mass flow rate as shown in Figure 4.

*Case 4.* It includes a variable precooling steam injection as shown in Table 2.

The larger the mass flow rate of precooling injection, the faster the cooling of steam generator. Also because of more and more uniform temperature distribution on the SG components with continuous precooling injection, the transient could be accelerated by increasing the mass flow rate of precooling injection and decreasing the temperature of precooling fluid. However, the precooling injection with constant mass flow rate and temperature has better feasibility for the real precooling system design than that with variable mass flow rate and temperature. Hence, an expected

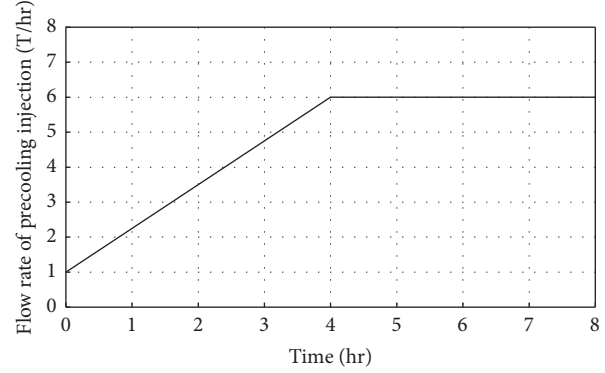


FIGURE 4: Mass flow rates of Case 3.

TABLE 2: Precooling injection in Case 4.

Time (hr)*	Flow rate (T/hr)	Temperature (°C)	Pressure (MPa)
0–2	1	190	1.1
2–4	4	170	0.7
4–6	6	170	0.7
6–8	6	150	0.3

\*The time is calculated from the beginning of the precooling injection.

precooling design should have a good balance of the cooling effect and the feasibility of the design. In this analysis, by comparison with Cases 1 and 2, the cooling effect is studied for the precooling design with constant mass flow rate in the range from 1 t/h to 5 t/h, and Cases 3 and 4 with variable flow rate and temperature are designed for the study on the acceleration of the precooling.

**4.3. Analysis Results.** The fluid temperatures at different locations with different cooling water injections are shown in Figure 5. The results show that, under the case with 1 t/h precooling water injection, the fluid temperature at the SGHT outlet is approx. 345°C at the 8th hour after the precooling injection, while the fluid temperature at the PRV in the LP is about 400°C. In Case 2 with 5 t/h precooling water injection, both of the fluid temperatures at the SGHT outlet and at the PRV decrease to 200°C within 5 hours, which indicates that the SGHT and the LP had been well cooled down by the precooling water injection.

The wall temperatures of the SGHT at the outlet and the LP at the PRV under different cooling water injections are shown in Figure 6. The wall temperature at the SG outlet descends to approx. 347°C in 8 hours in Case 1; meanwhile, the wall temperature at the PRV is 408°C. But in the case with 5 t/h precooling water injection, the wall temperature of the SGHT and the LP had almost decreased to 200°C in 5 hours. The SGHT and the LP are also cooled down to 200°C in Case 3, although it needs more time than that in Case 2. In Case 4, the SGHT and the LP are cooled down below 200°C within 6 hours; then their temperatures decrease continuously with the temperature decrease of the precooling water.

Figure 7 shows the temperature distribution of the SGHT and the LP at different time points. The total length of the SGHT and the LP is normalized and the SGHT inlet is

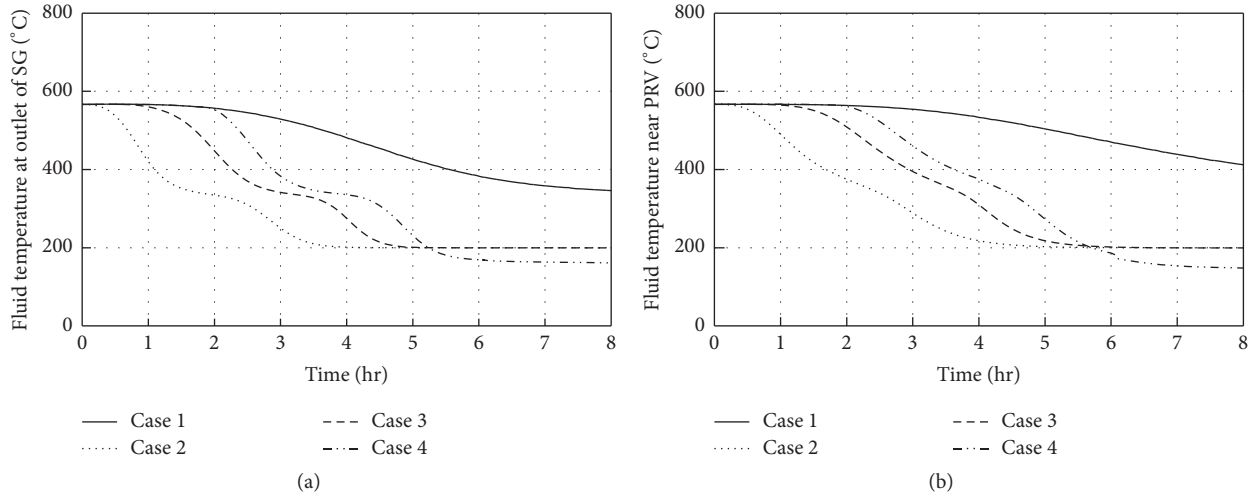


FIGURE 5: Fluid temperature at different locations during precooling injection.

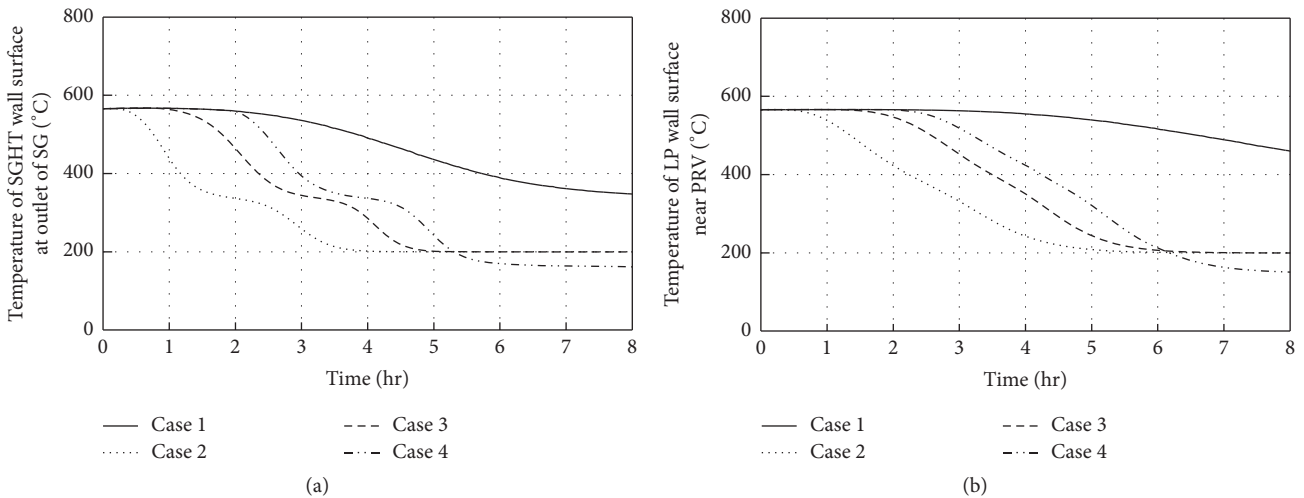


FIGURE 6: Wall surface temperature at different locations during precooling injection.

set as the start point. It is observed that the temperature distribution on the SGHT is uneven before the precooling water injection and its temperature decreases continuously with the precooling water injection. In both Cases 3 and 4, the SGHT and the LP could be cooled down to 200°C in 6 hours after the precooling injection. Larger flow rate of the precooling water injection will accelerate the transient, and the precooling process will finish in 5 hours under the case with 5 t/h precooling injection. But the maximal wall temperature still remains above 400°C after 8 hours of the precooling injection under Case 1, which indicates that the 1 t/h precooling injection is not enough to satisfy the precooling requirements.

The temperature descending rates at some typical locations of the SGHT during the transient are shown in Figure 8. The temperature descending rate of the SGHT in Case 2 is obviously higher than that in other cases at the early stage of the precooling injection, which indicates that higher flow rate of the precooling injection results in faster temperature

decrease. Although the precooling transient could be accelerated by flow rate increase or temperature decrease of the precooling injection for more uniform temperature distribution on the SGHT with continuous precooling, the temperature descending rate at the outlet of SGHT in Case 4 exceeds 3°C/min after 2 hours, which indicates that the flow rate increase of the precooling injection in Case 4 is a little faster than the limitation. The location where the maximal descending rate of SGHT temperature occurs during the transient is also related to the precooling injection scenario; the maximal descending rate of SGHT occurs at the inlet of SGHT in Case 1, while it occurs at the outlet of SGHT in Case 3.

**4.4. Comparison Results.** With the above results, it can be known that the SG in Cases 2–4 can be cooled down to the expected temperature level in 8 hours but Case 1 cannot satisfy the requirement. In the other side, the maximal temperature descending rates in Cases 1 and 3 are controlled below 3°C/min, but those in Cases 2 and 4 exceed the

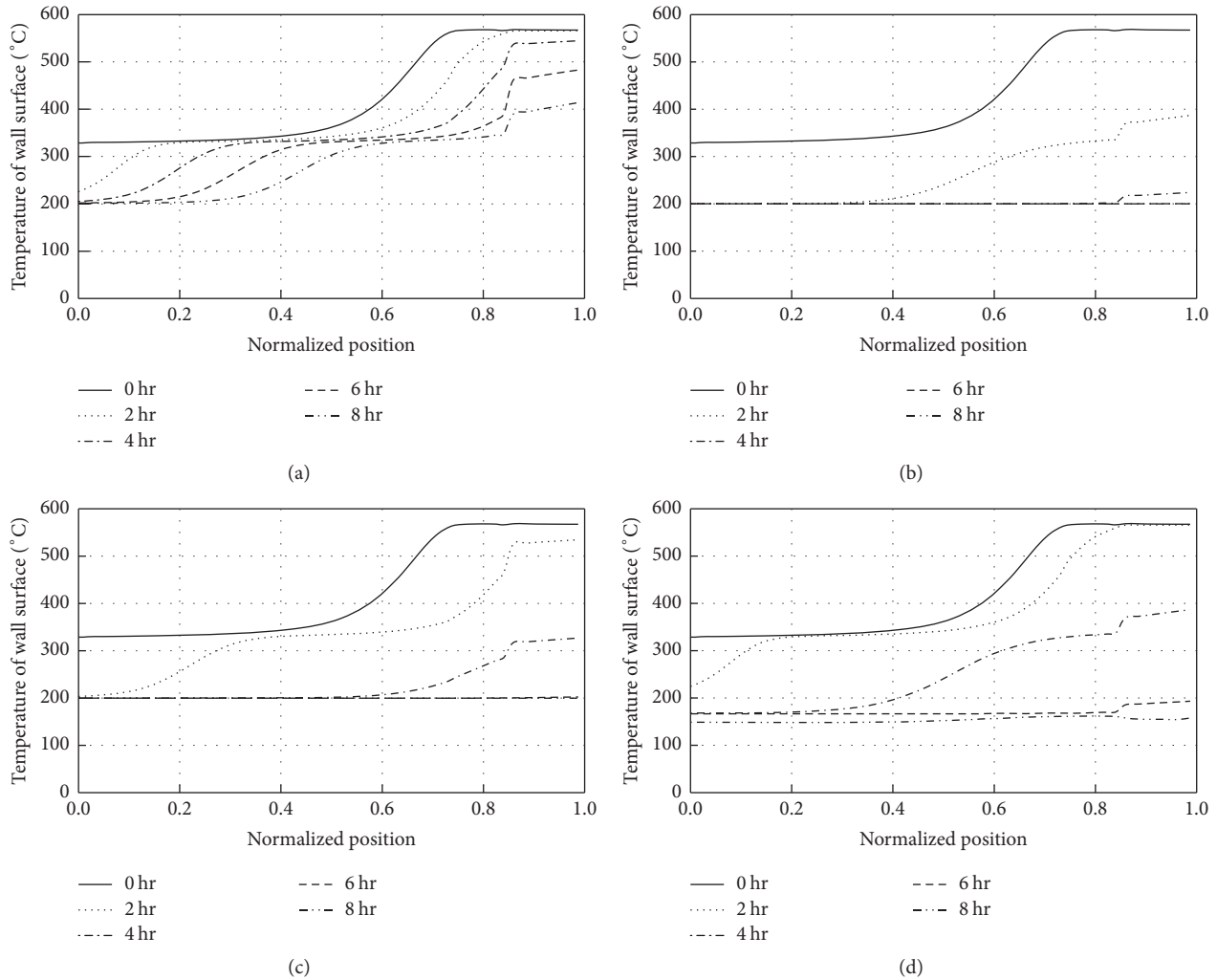


FIGURE 7: Temperature distribution of SGHT and LP during precooling injection.

limitation. Therefore, it can be concluded that Case 3 is better in all the current provided precooling cases. Because the SG in Case 3 has been cooled down to  $200^{\circ}\text{C}$  only within 6 hours, the temperature descending rate could be decreased further by decreasing the flow rate of the precooling injection.

## 5. Conclusions

A precooling injection is needed to cool down the steam generator, which remains with high pressure and high temperature level after emergency shutdown of high temperature gas cooled reactor. Larger mass flow rate of precooling water injection will accelerate the precooling process, but the temperature descending rate of the structures should also be limited to avoid the potential damage on the components from excessively quick temperature change. Some different precooling injection scenarios for a 200 MWe high temperature gas cooled reactor are analyzed and compared. The analysis results show that enough precooling water injection is necessary for the cooling of steam generator to satisfy

the precooling target in the stipulated time. The time when the maximal temperature descending rate of SGHT occurs and the location where the maximal temperature descending rate of SGHT occurs are related to the precooling injection scenario. Based on the analysis result of the HTR-PM, it is concluded that the SG could be cooled down to the expected temperature level with a reasonable precooling injection. For the reason that the temperature distributions of the SGHT get more uniform with the continuous precooling injection, the precooling transient could be accelerated by gradually increasing the flow rate of the precooling injection.

## Initialisms

- DV: Draining valve
- FIV: Feedwater isolation valve
- FP: Feedwater pipeline
- HTGR: High temperature gas cooled reactor
- LP: Live-steam pipeline
- PRV: Pressure relief valve

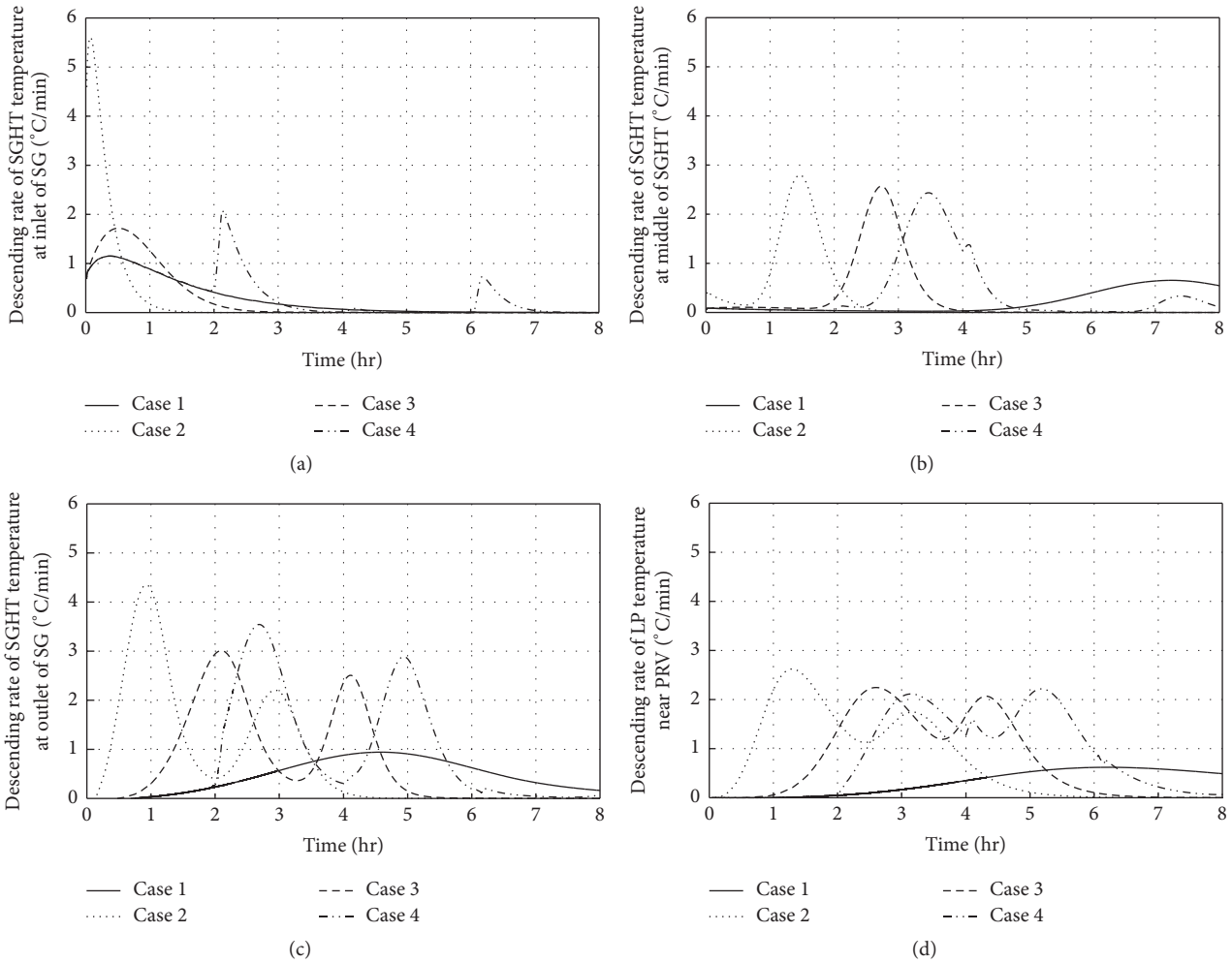


FIGURE 8: Temperature descending rate at different locations during precooling injection.

RPV: Reactor pressure vessel  
 SG: Steam generator  
 SGHT: Steam generator heat-exchange tubes  
 SGPV: Steam generator pressure vessel  
 SIV: Steam isolation valves.

**Conflicts of Interest**

The authors declare that they have no conflicts of interest.

**Acknowledgments**

This work was supported by the National Science and Technology Major Project (no. ZX06908) and the National High Technology Research and Development Program of China (863) (2014AA052701).

**References**

[1] W. Yan, "Study on pressure relief system design for high temperature gas cooled reactor," *Progress in Nuclear Energy*, vol. 77, pp. 344–351, 2014.

[2] M. A. Fütterer, L. Fu, C. Sink et al., "Status of the very high temperature reactor system," *Progress in Nuclear Energy*, vol. 77, pp. 266–281, 2014.

[3] G. H. Lohnert, "Technical design features and essential safety-related properties of the HTR-module," *Nuclear Engineering and Design*, vol. 121, no. 2, pp. 259–275, 1990.

[4] Y. Xu and K. Zuo, "Overview of the 10 MW high temperature gas cooled reactor - Test module project," *Nuclear Engineering and Design*, vol. 218, no. 1-3, pp. 13–23, 2002.

[5] Z. Zhang, Z. Wu, Y. Sun, and F. Li, "Design aspects of the Chinese modular high-temperature gas-cooled reactor HTR-PM," *Nuclear Engineering and Design*, vol. 236, no. 5-6, pp. 485–490, 2006.

[6] Z. Zhang, Y. Dong, F. Li et al., "The Shandong Shidao Bay 200 MWe high-temperature gas-cooled reactor pebble-bed module (HTR-PM) demonstration power plant: an engineering and technological innovation," *Engineering*, vol. 2, no. 1, pp. 112–118, 2016.

[7] Y. Wang, "Study on Pressure Relief Transient for High Temperature Gas Cooled Reactor," in *Proceedings of the 2012 20th International Conference on Nuclear Engineering and the ASME 2012 Power*, p. 269, Anaheim, Calif, USA.

- [8] J. Liu, Z. Zhang, D. Lu, Z. Shi, X. Chen, and Y. Dong, "Personal computer-based simulator for nuclear-heating reactors," *Nuclear Technology*, vol. 129, no. 2, pp. 175–186, 2000.
- [9] Anon, "RETRAN02-A Program for Transient Thermal Hydraulic Analysis of Complex Fluid Flow Systems," *Electric Power Research Institute (Report) EPRI NP*, vol. 1, 1981.

## Research Article

# Design and Development Framework of Safety-Critical Software in HTR-PM

**Chao Guo, Huasheng Xiong, Xiaojin Huang, and Duo Li**

*Institute of Nuclear and New Energy Technology, Collaborative Innovation Center of Advanced Nuclear Energy Technology, Key Laboratory of Advanced Reactor Engineering and Safety of Ministry of Education, Tsinghua University, Beijing 100084, China*

Correspondence should be addressed to Duo Li; [liduo@tsinghua.edu.cn](mailto:liduo@tsinghua.edu.cn)

Received 29 December 2016; Revised 19 May 2017; Accepted 28 May 2017; Published 28 June 2017

Academic Editor: Luca Podofillini

Copyright © 2017 Chao Guo et al. This is an open access article distributed under the Creative Commons Attribution License, which permits unrestricted use, distribution, and reproduction in any medium, provided the original work is properly cited.

With the development of information technology, the instrumentation and control system of nuclear power plant nowadays rely heavily on the massive and complex software to ensure the safe and efficient operation of the power plant. The improvement of the software design and development for the safety systems has been a research focus for its decisive impact on the nuclear safety. The framework of the software design and development for reactor protection system in High Temperature Gas-Cooled Reactor-Pebble bed Module was introduced in this paper. Firstly, during the design period, in addition to multichannel redundancy, grouping of protection variables and diverse 2-out-of-4 logics were adopted by different subsystems of each channel in case of common cause failure. Then a series of development characteristics together with strict software verification and validation were performed. Thirdly, during the software test period, an improved software reliability growth model based on the Goel-Okumoto model according to the analysis of fault severity was proposed to help in estimating the reliability of the software product and identifying the software release time.

## 1. Introduction

The analog instrumentation and control (I&C) systems are being replaced by the digital ones in the nuclear power plants (NPPs) during the last decade as the rapid development of computer science. Although providing a series of advantages such as better accuracy of monitor and control, more friendly human-machine interface, and higher automation level, digital I&C systems are still facing challenges connected with the modern information technologies [1]. The digital system also brings challenges to the probability safety assessment (PSA) of the NPP as there is no mature and widely used method for software reliability evaluation.

The improvement and evaluation of software reliability for the digital I&C system have been a research focus and the Nuclear Regulatory Commission of America also referred to this research topic in its five-year research plan for digital I&C system proposed in 2010 [2]. This issue is even critical for the safety-related systems like the reactor protection system (RPS) and the software failure could be unacceptable.

The design and development of digital I&C systems are different from the analog ones. For example, the redundancy arrangement of multiple channels is widely used to reduce the failure rate effectively for the analog RPS, while the digital component brings common cause failure (CCF) possibility which cannot be overcome by redundancy as all redundant channels are of the identical software and hardware. The regulatory authority emphasizes quality, diversity, and defense-in-depth as procedures against CCF of digital RPS [3].

Besides quality control (QC) process, the safety-critical software of an NPP has to undertake independent verification and validation (V&V) process following the requirement of the IEEE 1012 [4], which guarantees the software quality by enforcing rigorous V&V activities. Documentation audit is the major activity taken during the early period of the V&V process while the software unit test and the integrated test play a crucial role in the software coding and system integration.

Software reliability growth models (SRGMs) are commonly used to assess the software reliability. The SRGMs

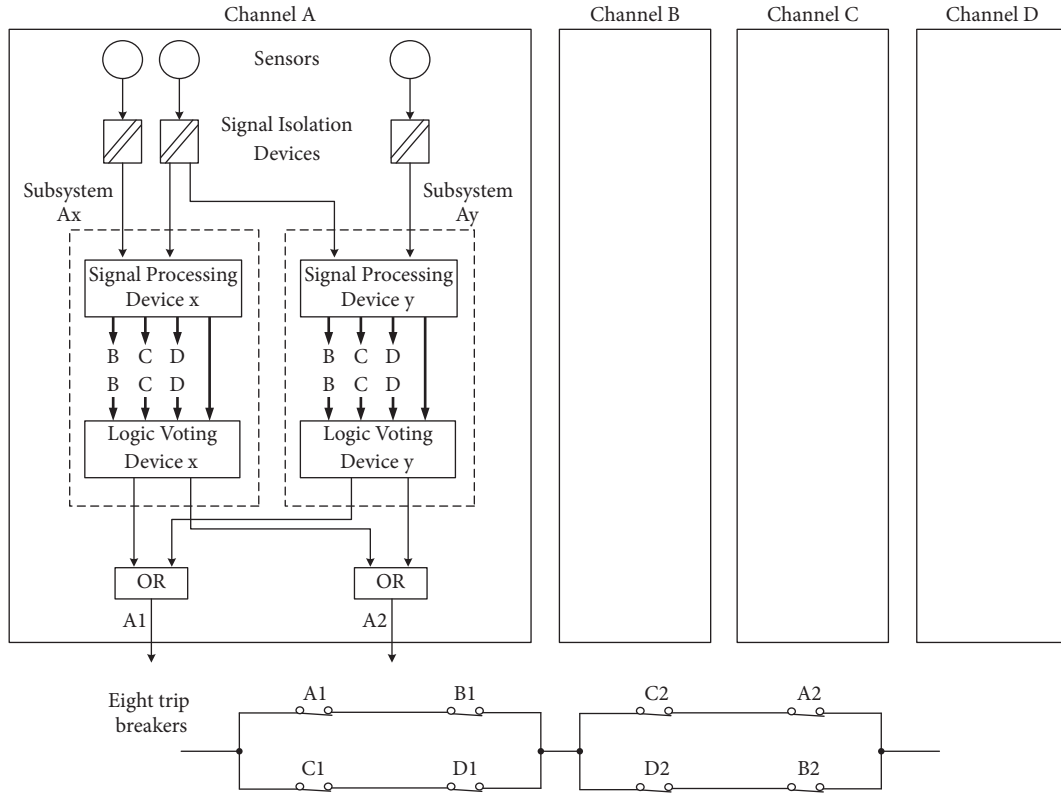


FIGURE 1: Architecture of the reactor protection system (RPS) in HTR-PM.

are able to track the reliability growth curve during the test process which helps the development group to evaluate the number of residual faults and the development cost and to make decisions for the software release time and the test resource allocation [5–8]. During the last four decades, hundreds of software reliability models have been developed for different kinds of applications, and the available models are usually based on certain assumptions and limitations [9, 10]. With the particularity of safety-critical software of the RPS, the severity of the software fault should be studied and the critical faults should be paid more attention.

High Temperature Gas-Cooled Reactor-Pebble bed Module (HTR-PM) is the first HTGR to be commercially operated in the world, and the RPS of HTR-PM is the first digital RPS domestically designed, developed, and commercially operated in China. There are several characteristics for the software design and development process of RPS in HTR-PM. For example, it employs two groups of protection variables and diverse 2-out-of-4 voting logics for two subsystems in each channel in case of CCF. In addition, it is a custom-made system which only serves the HTR-PM, and the software is independently developed and is not based on the configuration of function modules on a platform; thus the software has been simplified effectively [11].

In this paper, the architecture of the RPS in HTR-PM is first introduced in Section 2. Section 3 shows the software design and development features, including the voting logic diversity, development optimization, and the software V&V.

A novel software reliability growth model based on the analysis of fault severity is derived in Section 4. At last, the conclusion of this paper is given in Section 5.

## 2. Architecture of Reactor Protection System

The RPS of HTR-PM can generate the reactor trip signal and the engineered safety featured actuation signal (ESFAS) in case of design basis accidents. The RPS has four redundant channels, A, B, C, and D, together with eight trip breakers as shown in Figure 1. Each channel includes several sensors, several Signal Isolation Devices, two Signal Processing Devices, and two Logic Voting Devices. They can fulfil the functions including signal measurement and isolation, unit transformation, setpoint comparison, and the first-step 2-out-of-4 (2/4) logic. The second-step 2/4 voting logic is performed by eight trip breakers.

Only Signal Processing Devices and Logic Voting Devices are the digital ones among these devices, and others are all analog ones. The Signal Processing Device x and the Logic Voting Device x in one channel are defined as subsystem x. Similarly, the Signal Processing Device y and the Logic Voting Device y in one channel are defined as subsystem y. Both subsystems in one channel can achieve the unit transformation and 2/4 voting functions. The hardware and software of subsystems Ax, Bx, Cx, and Dx in four channels are identical, and the hardware and software of subsystems

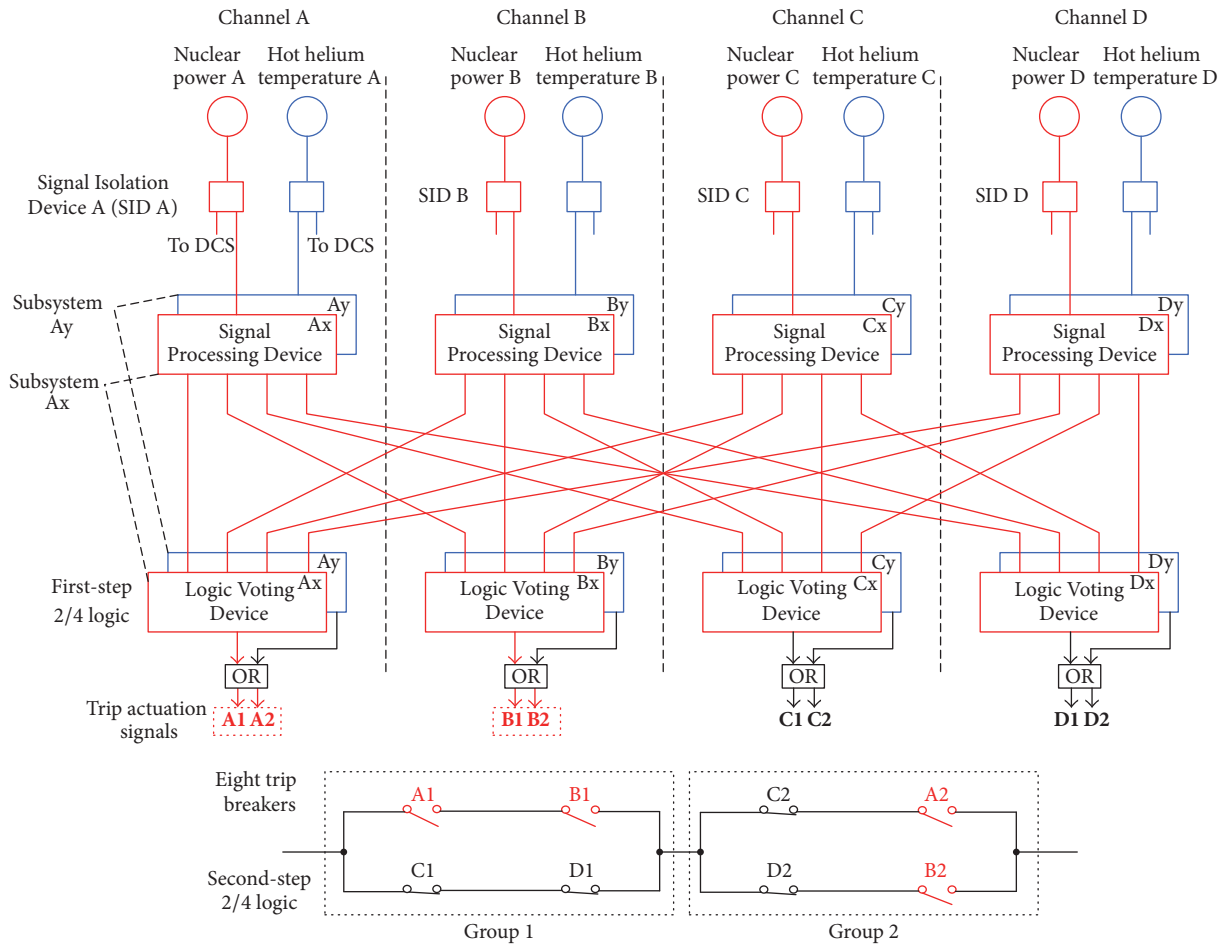


FIGURE 2: An example for the grouping of protection variables in two subsystems of one channel.

Ay, By, Cy, and Dy in four channels are identical, too. But the software of subsystems x and y is different in case of CCF.

Each channel receives dozens of hardwired analog signals from the sensors including the nuclear power, hot/cold helium temperature, helium pressure, and steam pressure. Some other switch signals like the status of the nuclear instrumentation system are also collected by the RPS for certain logic decision. It should be noted that there are a set of independent sensors for each channel which is subject to the principles of the redundancy requirement and the entity separation requirement.

The Signal Isolation Devices in each channel allocate the input signals to subsystems x and y of the same channel, the distributed control system (DCS), and the postaccident monitoring system if necessary. These signals are isolated electrically to ensure that the single fault in any equipment will not affect others.

Each design basis accident of HTR-PM corresponds at least two protection variables which are then divided into two groups. Subsystems x and y are used to deal with these two groups of protection variables, respectively, in order to decrease the risk of CCF. Figure 2 shows an example for the grouping diversity. When the design basis accident

“false removal of control rods in power operation condition of HTR-PM” happens, there are two consequences: (1) abnormal increase of nuclear power; (2) abnormal increase of hot helium temperature. Two protection variables “nuclear power” and “hot helium temperature” are then assigned to subsystems x and y, respectively. As the protection variables that two subsystems deal with are different, the corresponding software for unit transformation and protection logics is also different. Each subsystem outputs reactor trip signals and ESFAS signals independently, so subsystems x and y act as the grouping diversity for safety functions. In addition, the voting logic diversity of two subsystems will be introduced in Section 3.1.

Figure 2 also shows the topological relations between four channels: every Signal Processing Device x sends information to four Logic Voting Devices x simultaneously, and the first-step 2/4 logic is realized by the Logic Voting Devices x. Similar processes are taken for four subsystems y. Taking Channel A as an example, the Logic Voting Devices Ax and Ay each generate a reactor trip signal according to the 2/4 voting results and these two signals then perform “OR” logic to generate two trip actuation signals A1 and A2 to actuate trip breakers A1 and A2, respectively. Thus even if one subsystem

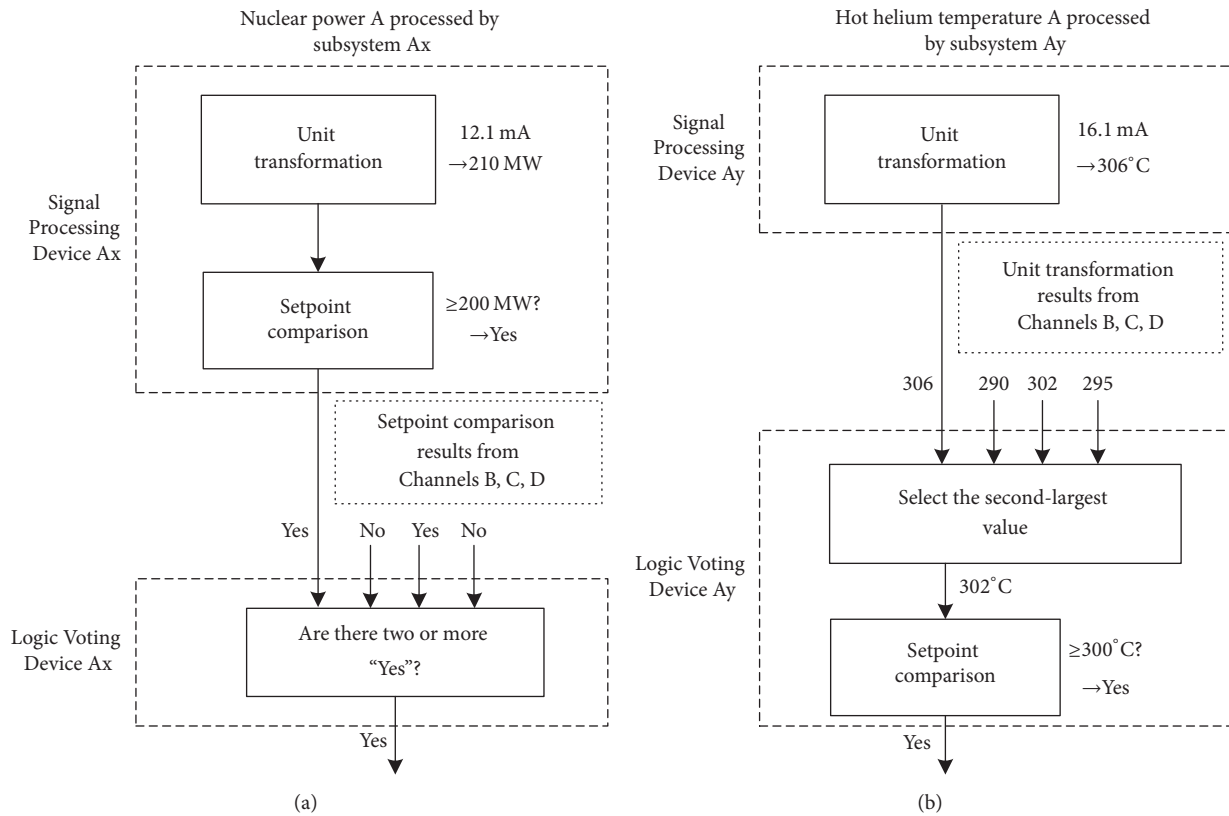


FIGURE 3: An example of diversity of 2/4 voting logic for (a) subsystem Ax and (b) subsystem Ay in Channel A.

fails to generate reactor trip actuation signal in the case of a design basis accident, the diverse subsystem can also ensure the reactor trip.

Eight trip breakers with series-parallel structure are used to cut off the power supply of control rod system. They are assigned to two groups as shown in Figure 2. Each channel of RPS controls two trip breakers belonging to different groups. If any 2-out-of-4 channels output the trip actuation signals, the reactor trip is realized. In Figure 2, Channels C and D are supposed to fail to work and only trip breakers A1, A2, B1, and B2 controlled by Channels A and B are successfully opened. It can be found that the power supply of the control rod can still be cut off under such circumstance, so the second-step 2/4 logic is achieved.

### 3. Software Design and Development

**3.1. Voting Logic Diversity.** In addition to the grouping diversity of protection variables proposed in Section 2, the voting logic diversity is also employed against CCF in the RPS of HTR-PM. Specifically, the 2/4 logic in subsystem x and subsystem y of each channel is achieved using different ways. The design basis accident "false removal of control rods in power operation condition" and two related protection variables are also taken as an example to illustrate this diversity, which is shown in Figure 3.

Either subsystem in each channel consists of two devices, that is, a Signal Processing Device and a Logic Voting Device.

Every subsystem is able to realize the unit transformation and the logic voting functions separately. For example, the unit transformation processes of "nuclear power" and "hot helium temperature" are performed by the Signal Processing Devices Ax and Ay in two subsystems, respectively, as shown in Figure 3. The corresponding software codes for unit transformation of these two variables in two Signal Processing Devices are naturally different.

The 2/4 logic of two subsystems is also designed to be different. In subsystem Ax, the Signal Processing Device Ax identifies whether the value of protection variable is larger than the setpoint. If so, a "Yes" signal is generated and sent to Logic Voting Devices Ax, Bx, Cx, and Dx of four channels simultaneously. On the other hand, each Logic Voting Device x receives four "Yes" or "No" comparison results from Signal Processing Devices Ax, Bx, Cx, and Dx and then performs 2/4 logic. For the example in Figure 3(a), the Logic Voting Device Ax receives two "Yes" signals so a reactor trip signal is generated according to the 2/4 logic. The same processing operations are implemented on other channels at the same time.

For subsystem y, however, after unit transformation in Signal Processing Device Ay, the value of protection variable is directly sent to four Logic Voting Devices y of four channels without setpoint comparison. Then every Logic Voting Device y chooses the second largest value from four protection variables. And the setpoint comparison is performed only for this second largest value. Take the case in

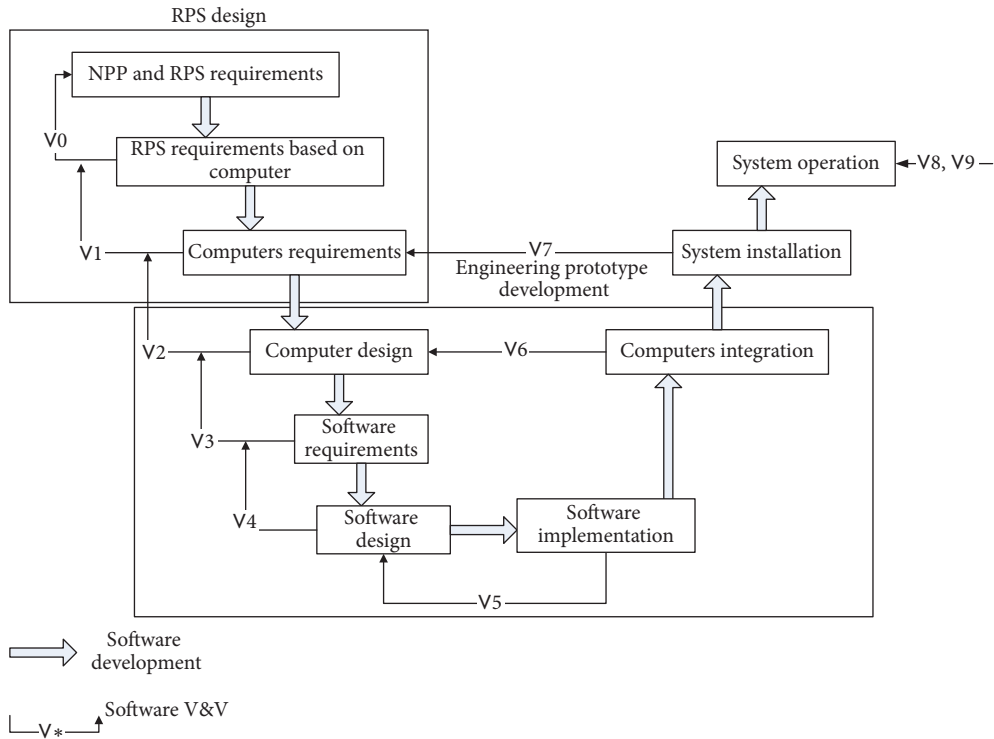


FIGURE 4: Software verification and validation model of RPS in HTR-PM.

Figure 3(b) as an example; as the second largest value of the hot helium temperature is greater than the setpoint, it can be derived that the largest value should also be greater than the setpoint, so the 2/4 logic is fulfilled and a reactor trip signal is generated by the Logic Voting Device Ay.

Grouping of protection variables and diverse voting logic achieve software difference between two subsystems which can effectively reduce the probability of CCF.

**3.2. Software Development Characteristics.** The introduction in Section 3.1 refers to the software design optimization based on voting logic diversity. In this section, the approaches taken during the software development process of the RPS in HTR-PM will be discussed.

**3.2.1. No Configuration Platform.** Software development based on a configuration platform is a common method for the coding of RPS, and most well-known RPSs in the world are developed in this way. The famous platforms include the Common Q platform of Westinghouse and the TELEPERM XS platform of AREVA. The platform modules are selected and configured for a specific project. One of the problems for this kind of configuration is that the reliability of the whole platform and the complex configuration tool is difficult to validate. Furthermore, the configuration process may introduce undesired functions because of functional relevance of the platform modules.

The software for the RPS of HTR-PM is not developed based on a platform. Every line of the software code is written in demand rather than being selected from the platform

library. The advantage for this development method is that there is no need to prove the reliability of the configuration platform and configuration tool to the regulatory agency as no platform or configuration tool is used. This simplification reduces the difficulty for the design audit of the RPS in HTR-PM. On the other hand, all software is newly developed and only used for this project. There is no application precedent for the software code. So the software verification and validation process should be paid special attention to ensure the software reliability.

**3.2.2. Customized Software.** Without a configuration platform and a configuration tool, the RPS in HTR-PM is developed totally by customized software, which means that the drivers of the hardware, the database, the application functions, and the displays were all developed from the beginning. In this way, the software of the RPS in HTR-PM could be simplified effectively. The decrease in the amount of software code is an important guarantee for software reliability.

**3.3. Software Verification and Validation.** Software V&V for the RPS is a mandatory activity required by the related standards like the IEEE 1012 and this process should be carried out during every development period, which can ensure that the objectives "do things right" and "do the right things" [4].

Figure 4 illustrates the software V&V model [12] that the RPS in HTR-PM employed during the development process. This V-shaped model shows both the development

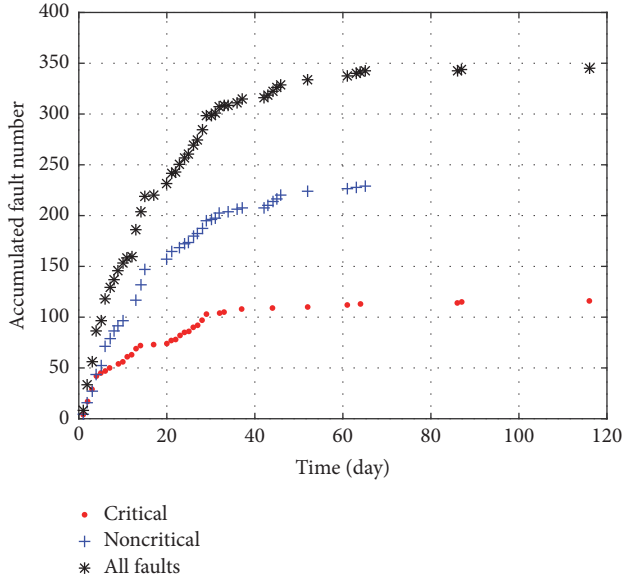


FIGURE 5: Accumulated fault numbers during software test.

and the V&V processes, and the output of the software development process is the input of the V&V process. For example, the output of the “software design” is the software design specification, and the output of the “software implementation” process is the software code, so the duty of the V&V process “V5” is software testing based on the software design specification. In addition to software testing, there are two main activities for the software V&V: in the early stages of development, the major V&V activity is document audit; in the later part of software development, the major V&V activity is integrated testing and system testing. It should be noted that every V&V process should be taken under strict rules, and a series of reports are expected to prove the effectiveness of the V&V activities.

According to the requirement of the related standard, an independent software V&V should be taken. The RPS of HTR-PM was developed by China Techenergy Co., Ltd., and the software V&V is taken charge of by the Institute of Nuclear and New Energy Technology of Tsinghua University, so the V&V group is organizationally independent of the development group in technical, management, personnel, and financial aspects which ensures the effectiveness of the V&V process.

## 4. Software Reliability Modelling

**4.1. Software Test Data Analysis.** A novel software reliability model based on the fault severity analysis was proposed. Figure 5 shows the accumulated fault numbers during the software test process of a processing module of the RPS in HTR-PM. The  $x$ -axis means the date to detect the fault and the  $y$ -axis means the accumulated fault number. The faults are classified to critical and noncritical faults according to the severity recorded in the fault report. It can be found that the accumulated faults increase quickly at the beginning of the test and around 90% of the faults were detected during the

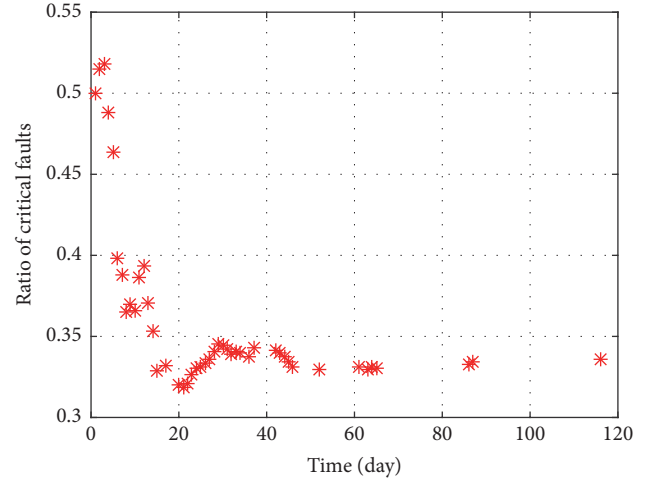


FIGURE 6: Ratio of critical faults to total accumulated faults.

first 1/3 of test period. As the critical faults have more severe effects on the safety functions of the RPS and have a greater impact on software reliability, the critical fault was specially studied in this paper.

The ratio of the critical faults to total faults was analyzed and the ratio curve is shown in Figure 6. It can be found that, during the first 20% of the test period, the proportion of critical fault declines rapidly; during the remaining 80% of the test period, the proportion of the critical fault basically remains unchanged. This trend is related to many factors, such as the testers’ experience and the test strategies. By including more parameters related to the testing process in the SRGM, the model is closer to reality and the precision of the model can be improved. Specifically, the ratio trend in Figure 6 can be fitted with an exponential function.

**4.2. Proposed Software Reliability Model.** Suppose that  $\{N(t), t \geq 0\}$  is a counting process, where  $N$  is the total detected faults in time  $t$ . A mean value function (MVF)  $m(t)$  is used to express the expected number of accumulated faults by time  $t$ , and the general form of the SRGM based on a nonhomogeneous Poisson process (NHPP) that has Poisson distribution with mean  $m(t)$  is described as

$$P\{N(t) = n\} = \frac{m(t)^n}{n!} e^{-m(t)}, \quad n = 0, 1, 2, \dots \quad (1)$$

and  $m(t)$  can be expressed in terms of the failure intensity function  $\lambda(t)$ :

$$m(t) = \int_0^t \lambda(x) dx. \quad (2)$$

Goel-Okumoto (G-O) model is a common and effective SRGM [13] and  $m(t)$  for the G-O model is

$$m(t) = a(1 - e^{-bt}). \quad (3)$$

Here  $a$  is the expected total number of faults in the software and  $b$  is the detection rate per fault. The corresponding failure intensity function  $\lambda(t)$  is expressed as

$$\lambda(t) = abe^{-bt}. \quad (4)$$

In this paper, the faults are classified to critical and noncritical faults as illustrated in Figure 5. The ratios of accumulated critical and noncritical faults to total fault are supposed to be  $r_c$  and  $r_n$ , respectively. It is easy to get the expression of the MVFs of the critical and noncritical faults:

$$\begin{aligned} m_c(t) &= a \cdot r_c(t) \cdot (1 - e^{-bt}) \quad (0 \leq r_c \leq 1), \\ m_n(t) &= a \cdot r_n(t) \cdot (1 - e^{-bt}) \quad (0 \leq r_n \leq 1). \end{aligned} \quad (5)$$

And, according to the definition, the relationship of  $r_c$  and  $r_n$  is given by

$$r_c + r_n = 1. \quad (6)$$

Based on the analysis in Section 4.1, the ratio of critical fault can be regarded as an exponential function. So  $r_c$  is supposed to have the form as follows:

$$r_c(t) = xe^{-yt} + z, \quad (x > 0, y > 0, z > 0), \quad (7)$$

where  $x$  and  $y$  are defined as the proportional and exponential decrease rate of the critical-fault ratio, respectively, and  $z$  is defined as the stable value of critical-fault ratio.  $r_c(t)$  approaches  $z$  when the time  $t$  is large enough. So the MVF of critical and noncritical faults can be derived by (5), (6), and (7) as follows:

$$\begin{aligned} m_c(t) &= a \cdot (xe^{-yt} + z) \cdot (1 - e^{-bt}), \\ m_n(t) &= a \cdot (1 - xe^{-yt} - z) \cdot (1 - e^{-bt}). \end{aligned} \quad (8)$$

The modelling process is shown as follows: firstly, the software fault data is classified to critical and noncritical faults according to the severity information of the test report; secondly, the ratio of critical faults to total accumulated faults is calculated; then the ratio is fitted with (7), and the parameters  $x$ ,  $y$ , and  $z$  are estimated during this process; thirdly, the accumulated fault numbers are applied to fit (8), and the parameters  $a$  and  $b$  are estimated.

**4.3. Experimental Results and Discussion.** The software reliability model proposed above was validated with the data of software fault obtained during the development of RPS in HTR-PM illustrated in Section 4.1.

The ratio in Figure 6 was first fitted with (7) and the parameters were estimated with the Least Square Estimation (LSE) method. The data with  $t \leq 40$  d was used for fitting and other data were used to validate the prediction ability of the model. The fitted result is shown in Figure 7, and the specific fitting values of parameters in (7) are listed in Table 1.

This fitting result was then used to estimate the parameters in (8) and LSE was applied for parameter estimation. Let  $N_i^c$  and  $N_i^n$ ,  $i = 1, 2, \dots, k$ , denote the observed cumulative

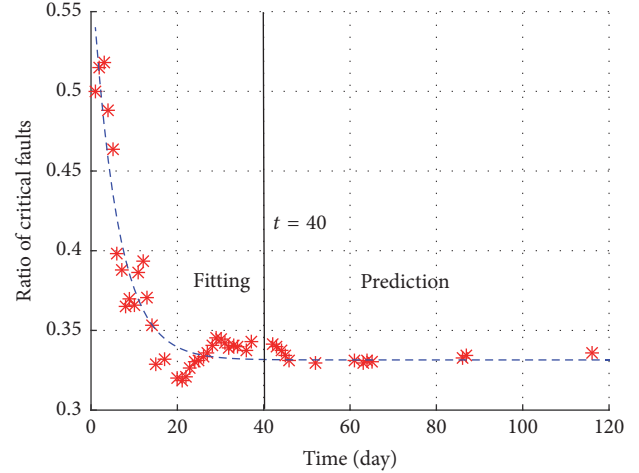


FIGURE 7: Fitted curve of ratio of critical faults to total accumulated faults.

TABLE 1: Estimated parameters of the proposed model, G-O model, and inflection S-shaped model.

Model	$a$	$b$	$x/\beta$	$y$	$z$
Our model	345.4856	0.0613	0.2477	0.1712	0.3315
G-O model	356.6320	0.0569	—	—	—
ISS model	486.5345	0.0004	-0.9913	—	—

TABLE 2: Fitting and prediction results of three models.

Model	RMSE	
	Fitting	Prediction
Our model	8.8251	2.2758
G-O model	8.5034	7.3072
ISS model	8.0388	32.6790

numbers of critical faults and noncritical faults by time  $t_i$ , respectively, where  $N_i^c + N_i^n = N_i$ . The parameters  $a$  and  $b$  in (8) can be estimated by solving

$$\min_{a,b} S^2 = \sum_{i=1}^k [(N_i^c - m_c(t_i))^2 + (N_i^n - m_n(t_i))^2]. \quad (9)$$

The G-O model and the inflection S-shaped (ISS) model [14] were also adopted for reliability modelling as a comparison to the proposed model. The fitting results and the prediction effects are shown in Table 1 and Table 2, respectively. Figures 8 and 9 illustrate the fitting and prediction results of these three models.

From Table 2 it can be easily found that the fitting effects of three models are similar while the model proposed in this paper gives the best prediction effect compared with the other two models. This conclusion can also be arrived at from Figure 9 where the proposed model gives the most accurate fitting results, which means that this proposed model is more effective in evaluating the residual faults, assessing the release time of the software, allocating the test resource, and so on.

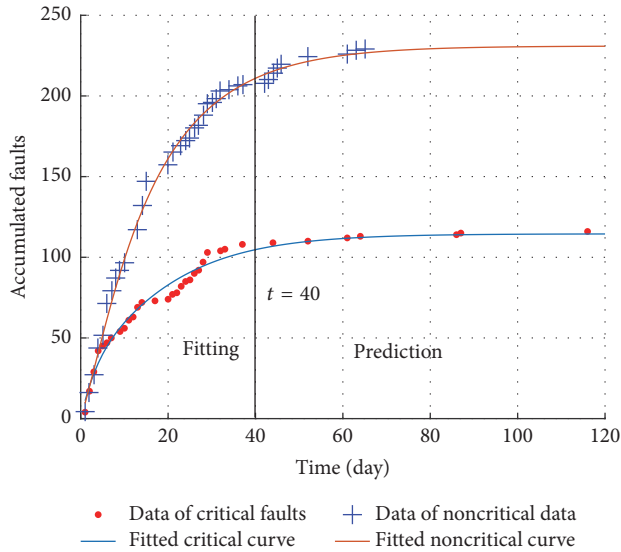


FIGURE 8: Fitted curves of the critical and noncritical faults.

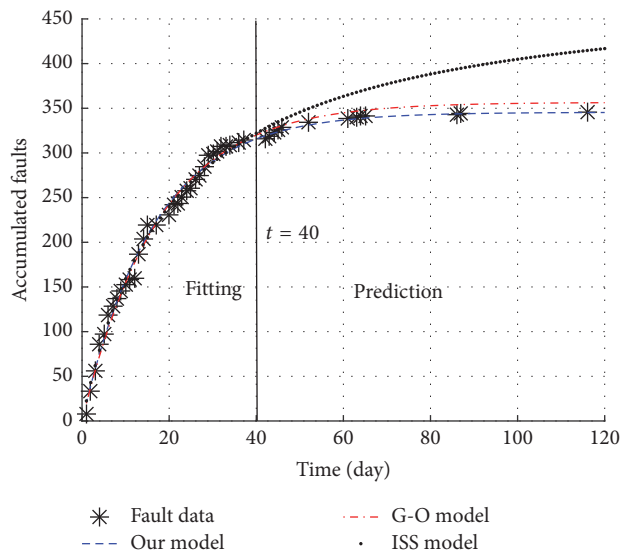


FIGURE 9: Fitted curves of three models for total accumulated faults.

It should be noted that the proposed model is closely related to the shape of the ratio curve. The ratio curve is affected by multiple factors, such as test case design, test strategies, and test experience of the testers. One of the premises when using the proposed model may be that the testers already have sufficient testing experience to locate the critical faults more quickly than the noncritical ones. If the accumulated fault data is collected at the beginning of the whole test project when the testers are not yet familiar with the testing tool, the tested software, and the test techniques, the shape of the ratio curve may be different. For example, the ratio of the critical faults to total faults may be small at the beginning; with the continuous progress of the testing process, the ratio may gradually increase. Then a new function should be chosen for ratio curve fitting, while

the modelling approaches are similar to that proposed in this paper.

## 5. Conclusion

Digital instrumentation and control systems play an important role in the safe and efficient operation of the nuclear power plants. Due to the severe consequence of software failure, the design and development of safety-critical software should be paid special attention. In this paper, the software design and development framework of reactor protection system in High Temperature Gas-Cooled Reactor-Pebble bed Module were studied.

Firstly, the protection variables corresponding to every design basis accident were grouped and dealt with in two subsystems, respectively, in each channel. The 2/4 logic performed by two subsystems of each channel was also designed to be different. The grouping of protection variables and the 2/4 voting logic diversity can be effective approaches against CCF of four-channel redundancy.

A series of characteristics during the software development process were also introduced, including no configuration platform and the customized software function. Together with the software development, an independent software verification and validation activity was carried out to ensure the software reliability. At last, a novel software reliability growth model based on the G-O model was developed by considering the fault severity to estimate the reliability of the software product. This model has better prediction effect than the G-O and the ISS models. The influencing factors of the ratio curve and the processing method for a different shape of ratio curve were also discussed.

## Conflicts of Interest

The authors declare that there are no conflicts of interest regarding the publication of this paper.

## Acknowledgments

This work was supported by the National Science and Technology Major Project (Grant no. ZX06901) and Tsinghua University Initiative Scientific Research Program (Grant no. 20151080380).

## References

- [1] M. Yastrebenetsky and V. Kharchenko, "Reliability and safety of nuclear power plant instrumentation and control systems: New challenges and solutions," in *Proceedings of the 2nd International Symposium on Stochastic Models in Reliability Engineering, Life Science, and Operations Management (SMRLO '16)*, pp. 47–55, February 2016.
- [2] U.S. Nuclear Regulatory Commission, in *NRC Digital System Research Plan FY 2010-FY 2014*, 2010.
- [3] NUREG-0800 Chapter 7 BTP 7-14, *Guidance on Software Reviews for Digital Computer-Based Instrumentation and Control Systems*, Chapter 7, 2016.

- [4] IEEE 1012-2004, "IEEE Standard for Software Verification and Validation," 2016.
- [5] X. Li, M. Xie, and S. H. Ng, "Sensitivity analysis of release time of software reliability models incorporating testing effort with multiple change-points," *Applied Mathematical Modelling. Simulation and Computation for Engineering and Environmental Systems*, vol. 34, no. 11, pp. 3560–3570, 2010.
- [6] C.-Y. Huang and M. R. Lyu, "Optimal release time for software systems considering cost, testing-effort, and test efficiency," *IEEE Transactions on Reliability*, vol. 54, no. 4, pp. 583–591, 2005.
- [7] K.-C. Chiu, J.-W. Ho, and Y.-S. Huang, "Bayesian updating of optimal release time for software systems," *Software Quality Journal*, vol. 17, no. 1, pp. 99–120, 2009.
- [8] M. Xie and B. Yang, "A study of the effect of imperfect debugging on software development cost," *IEEE Transactions on Software Engineering*, vol. 29, no. 5, pp. 471–473, 2003.
- [9] Y. Yang and R. Sydnor, "Multi-threads software reliability estimation based on test results and software structure," in *Proceedings of the 10th International Conference on Probabilistic Safety Assessment and Management 2010 (PSAM '10)*, pp. 2326–2336, June 2010.
- [10] NUREG/CR-6942, *Dynamic Reliability Modeling of Digital Instrumentation and Control Systems for Nuclear Reactor Probabilistic Risk Assessments The Ohio State University U. S. Nuclear Regulatory Commission Office of Nuclear Regulatory Research Dynamic Reliability Modeli*, 2007.
- [11] D. Li, H. Xiong, and C. Guo, "Design and Development of HTR-PM Reactor Protection System," in *Proceedings of the 21st International Conference on Nuclear Engineering*, Chengdu, China, 2013.
- [12] National Nuclear Safety Administration of China, *HAD 102/16 Software for computer based systems important to safety in nuclear power plants*, 2004.
- [13] A. L. Goel and K. Okumoto, "Time-dependent error-detection rate model for software reliability and other performance measures," *IEEE Transactions on Reliability*, vol. 28, no. 3, pp. 206–211, 1979.
- [14] M. Ohba, "Inflection S-shaped software reliability growth model," in *Stochastic models in reliability theory*, vol. 235, pp. 144–162, Springer, 1984.

## Research Article

# Analysis of Seismic Soil-Structure Interaction for a Nuclear Power Plant (HTR-10)

**Xiaoxin Wang, Qin Zhou, Kaixin Zhu, Li Shi, Xiaotian Li, and Haitao Wang**

*Institute of Nuclear and New Energy Technology, Collaborative Innovation Center of Advanced Nuclear Energy Technology, Tsinghua University, Beijing 100084, China*

Correspondence should be addressed to Li Shi; [shili@tsinghua.edu.cn](mailto:shili@tsinghua.edu.cn)

Received 30 December 2016; Revised 25 April 2017; Accepted 18 May 2017; Published 13 June 2017

Academic Editor: Michael I. Ojovan

Copyright © 2017 Xiaoxin Wang et al. This is an open access article distributed under the Creative Commons Attribution License, which permits unrestricted use, distribution, and reproduction in any medium, provided the original work is properly cited.

The response of nuclear power plants (NPPs) to seismic events is affected by soil-structure interactions (SSI). In the present paper, a finite element (FE) model with transmitting boundaries is used to analyse the SSI effect on the response of NPP buildings subjected to vertically incident seismic excitation. Analysis parameters that affect the accuracy of the calculations, including the dimension of the domain and artificial boundary types, are investigated through a set of models. A numerical SSI analysis for the 10 MW High Temperature Gas Cooled Test Reactor (HTR-10) under seismic excitation was carried out using the developed model. The floor response spectra (FRS) produced by the SSI analysis are compared with a fixed-base model to investigate the SSI effect on the dynamic response of the reactor building. The results show that the FRS at foundation level are reduced and those at higher floor levels are altered significantly when taking SSI into account. The peak frequencies of the FRS are reduced due to the SSI, whereas the acceleration at high floor levels is increased at a certain frequency range. The seismic response of the primary system components, however, is reduced by the analysed SSI for the HTR-10 on the current soil site.

## 1. Introduction

The structural integrity of nuclear power plants (NPPs) built on medium or soft soil sites during an earthquake has been a focus of research in recent years [1–7]. Soil-Structure Interactions (SSI) may greatly amplify the seismic response of the NPP's reactor building and increase the safety requirements [1, 2, 8]. Given their inherent safety features such as meltdown-proof safety, negative temperature reactivity coefficients, and passive decay heat removal [9, 10], High Temperature Gas Cooled Reactors (HTGRs) present advantages for construction on various soil sites when compared to Pressurized Water Reactors (PWRs). The seismic design of safety related nuclear structures and facilities on soil sites is built upon SSI analysis. Hence, SSI is of significant importance for nuclear safety and therefore the future development of commercial HTGR. The 10 MW High Temperature Gas Cooled Test Reactor (HTR-10) was constructed on a soil site in Beijing, China. Although SSI have been considered during the reactor design, a simplified model was adopted due to the lack of required computing

capabilities. A more comprehensive SSI analysis will enhance the understanding of the dynamic response of the reactor building in seismic events.

A variety of SSI effects on the seismic response of NPPs have been investigated by recent studies. The floor response spectra (FRS) of the AP1000 nuclear island on five generic soil type sites as well as a hard rock site were compared by Tuñón-Sanjur et al. [1]. Chen and Maslenikov [3] calculated the SSI response of a nuclear reactor building and showed that FRS of the structure were highly sensitive to soil stiffness. Farahani et al. [4] carried out an SSI analysis of NPP buildings and concluded that the seismic responses were dependent on the subsurface profile. Saxena et al. [5] observed that slip and separation at the soil-foundation interface due to SSI have significant effect on the response of the reactor building. Politopoulos et al. [2] focused on a partially embedded NPP on a layered soil site and demonstrated that the base rocking excitation induced by SSI may amplify the seismic response.

Two groups of methods, namely, the substructure method and the direct method, are commonly used to study SSI. In the substructure method [11, 12], the SSI problem is divided

into several subproblems which are solved separately based on the assumption of linear model and the solutions are superposed to give the complete results of the SSI problem. In the direct method, the combined soil-structure system is analysed in a single step. The interaction problem can be calculated using numerical methods such as the finite element method (FEM) [13], the boundary element method (BEM) [14], and their coupling procedures (BEM/FEM) [15, 16]. Comprehensive literature reviews can be found in papers and books [17–19]. Several computer codes designed for SSI analysis, such as SASSI [20] and CLASSI [21], have been developed. Compared to these codes, SSI analysis by general purpose commercial FE software provides advantages including modelling flexibility via the choice of element, improved nonlinear solvers, and postprocessing capabilities. When SSI is analysed using FEM, special handling, for instance, through transmitting boundaries, is required to simulate the wave propagation from the finite element mesh to the far field of infinite soil [22–25]. In this way, waves are artificially transmitted to the far field rather than reflected by the boundary. Among the various transmitting boundaries developed and implemented in SSI analysis, the most widely used one is the viscous boundary [22] which replaces the far field with viscous damping. Also widely used is the viscoelastic boundary [24] which employs springs to the viscous boundary to improve the accuracy. Since these artificial boundaries are approximate representation of infinite soil, modelling parameters such as size and shape of calculation domain and the artificial boundary type are expected to affect the reliability of the SSI analysis.

In this paper, a numerical model to simulate SSI was developed using commercial FE code. The model has been verified and the requirements for the modelling parameters are investigated. The seismic SSI of the HTR-10 NPP building is then analysed using the validated model. The FRS, which affect directly the design of nuclear components to withstand seismic events, are calculated to investigate the SSI effect.

## 2. Numerical Modelling

*2.1. Dynamic Response Function in Frequency Domain.* The SSI analysis was performed in frequency domain using a complex frequency response method. The calculation procedure is as follows.

- (1) The input acceleration of a seismic event,  $\ddot{u}_i(t)$ , in time domain is converted to frequency domain by Fourier transformation

$$\ddot{u}_i(\omega) = \int_{-\infty}^{+\infty} \ddot{u}_i(t) e^{-i\omega t} dt. \quad (1)$$

- (2) The response function  $\mathbf{T}(\omega)$  of the structure is calculated in frequency domain.
- (3) The response function in frequency domain is converted to time domain via inverse Fourier transformation

$$\ddot{u}_r(t) = \frac{1}{2\pi} \int_{-\infty}^{+\infty} \mathbf{T}(\omega) \ddot{u}_i(\omega) e^{i\omega t} d\omega. \quad (2)$$

$\mathbf{T}(\omega)$  in step (2) is derived from a three-dimensional FE model of the soil and the structure. The accuracy of the response function depends on the validity of the soil-structure model.

For a three-directional earthquake input, the acceleration input  $\ddot{u}_i(t)$  in formula (1) can be decomposed for each direction; that is,  $\ddot{u}_i(t) = [\ddot{u}_{ix} \ \ddot{u}_{iy} \ \ddot{u}_{iz}]^T$ , so the frequency response function  $\mathbf{T}(\omega)$  is written as

$$\mathbf{T}(\omega) = \begin{bmatrix} T_{xx}(\omega) & T_{yx}(\omega) & T_{zx}(\omega) \\ T_{xy}(\omega) & T_{yy}(\omega) & T_{zy}(\omega) \\ T_{xz}(\omega) & T_{yz}(\omega) & T_{zz}(\omega) \end{bmatrix}. \quad (3)$$

The component  $T_{ij}(\omega)$  represents the response along  $j$  direction when subjected to simple harmonic acceleration with unit amplitude in  $i$  direction. The response corresponding to excitation in each of the three directions is decoupled and calculated separately.

### 2.2. FE Model for Calculation of Frequency Response Function

*2.2.1. Modelling of Structure and Soil.* A three-dimensional FE model representing the structure and soil with truncated boundaries as illustrated in Figure 1 is constructed to obtain the frequency response function  $\mathbf{T}(\omega)$  in (3) for a soil-structure system subjected to vertically incident seismic excitation. As the nonvertically incident excitations have influence mainly on structures with large spans, such as dams, bridges, and pipes, the current method is considered adequate for the SSI analysis for NPPs. The subsurface soil is modelled as viscoelastic layered deposits with different shear modulus. The bottom of the model is set at the surface of the bedrock which has a shear wave velocity of 2400 m/s. The soil domain is meshed using structured hexahedral elements. The element size in  $Z$  direction is smaller than 1/5 of the local shear wave length for a cut-off frequency of 25 Hz according to the requirements of ASCE Standard 4-98 [26]. Input acceleration, that is, simple harmonic acceleration with unit amplitude, is applied to the nodes at the bottom surface of the model.

*2.2.2. Artificial Boundary Conditions.* In order to account for the infinite soil, viscous and viscoelastic boundaries have been implemented in the FE model in Figure 1.

For models with viscous boundaries, the wave propagation in the far field is modelled as viscous damping following Lysmer and Kuhlemeyer [22]. The equivalent damping constant is calculated as

$$\begin{aligned} c_s &= \rho V_s, \\ c_p &= \rho V_p, \end{aligned} \quad (4)$$

where  $c$  is a viscous damping constant,  $\rho$  is the soil density, and  $V$  is the shear wave velocity. The subscriptions  $s$  and  $p$  correspond to shear and compression wave, respectively.

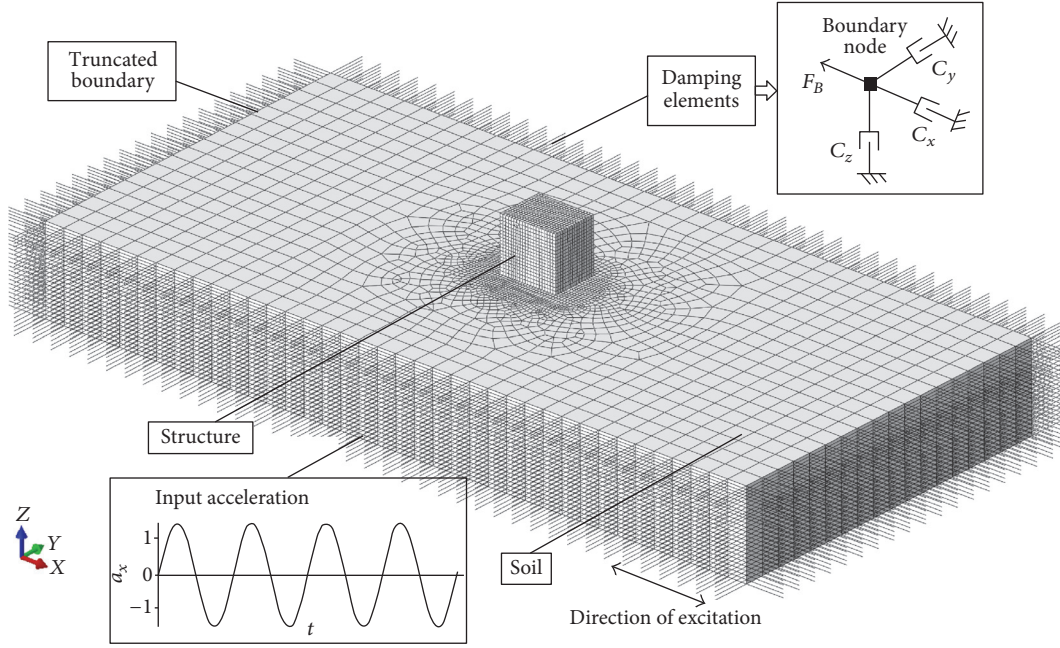


FIGURE 1: Illustration of the FE model for SSI analysis.

For models with viscoelastic boundaries, springs are added to the viscous model following Deeks and Randolph [24]. The spring constant for axisymmetric shear wave propagation problems is determined as

$$k_s = \frac{G}{2r}, \quad (5)$$

where  $G$  is the soil shear modulus and  $r$  is the distance between the boundary and the symmetry axis. Liu et al. [27] reported that satisfactory results can be obtained using this damping-spring approach for both compression and shear waves' propagation modelling. Therefore, this approach is adopted in this study, with

$$\begin{aligned} k_s &= \alpha_s \frac{G}{r}, \\ k_p &= \alpha_p \frac{G}{r}. \end{aligned} \quad (6)$$

The coefficients  $\alpha_s$  and  $\alpha_p$  are set to be 2/3 and 4/3, and  $r$  is approximately the distance between the truncated boundary and the structure, as recommended by Liu et al. [27].

The viscous damping and spring constant in (4) and (6) are discretized in dashpot and spring elements connected to the nodes of the truncated boundary following Liu et al. [27]. To simulate viscous boundary, 3 dashpots with orthogonal degrees of freedom are connected to each boundary node as illustrated in Figure 1. For viscoelastic boundary, 3 dashpots and 3 springs are connected to each boundary node. Fixed boundary conditions are applied to the dashpot and spring elements.

The earthquake motions at the truncated boundaries are applied as equivalent forces to the boundary nodes. For

vertically incident seismic excitation, the equivalent force  $F_B$  is calculated as [28]

$$\begin{aligned} F_B(t) &= F_f(x, y, z, t) + c\dot{u}_f(x, y, z, t) \\ &\quad + ku_f(x, y, z, t), \end{aligned} \quad (7)$$

where  $c$  is the damping constant of the dashpot elements and  $k$  is the spring constant.  $F_f$ ,  $u_f$ ,  $\dot{u}_f$  are force, displacement, and velocity, respectively, corresponding to free-field motion. The damping constant  $c_s$  (4) and spring constant  $k_s$  (6) are used to calculate the force,  $F_{Bs}$ , caused by the shear wave. Similarly, damping constant  $c_p$  (4) and spring constant  $k_p$  (6) are used to calculate the force,  $F_{Bp}$ , caused by the compression wave.

In (7),  $F_f$ ,  $u_f$ ,  $\dot{u}_f$  are commonly derived based on one-dimensional theory of wave propagation. In this study, a method based on FE modelling is proposed to calculate these parameters directly. When free-field soil is subjected to one-dimensional input, the responses are the same at any position in the direction perpendicular to the excitation. Therefore, a long slice of soil represented by one layer of elements is used to model the free-field response as shown in Figure 2. Symmetry boundary conditions are applied to the side surfaces of the model by constraining the motion perpendicular to the excitation. Soil properties, mesh sizes in  $Z$  direction, and the input acceleration at the bottom of the model are the same as the soil-structure model in Figure 1.

In the first step of the analysis, free boundary conditions are applied to both ends of the model. The slice model is sufficiently long (>1000 m) in the direction of excitation so that the reflected waves from both ends are attenuated significantly to affect the middle of the soil slice model. The

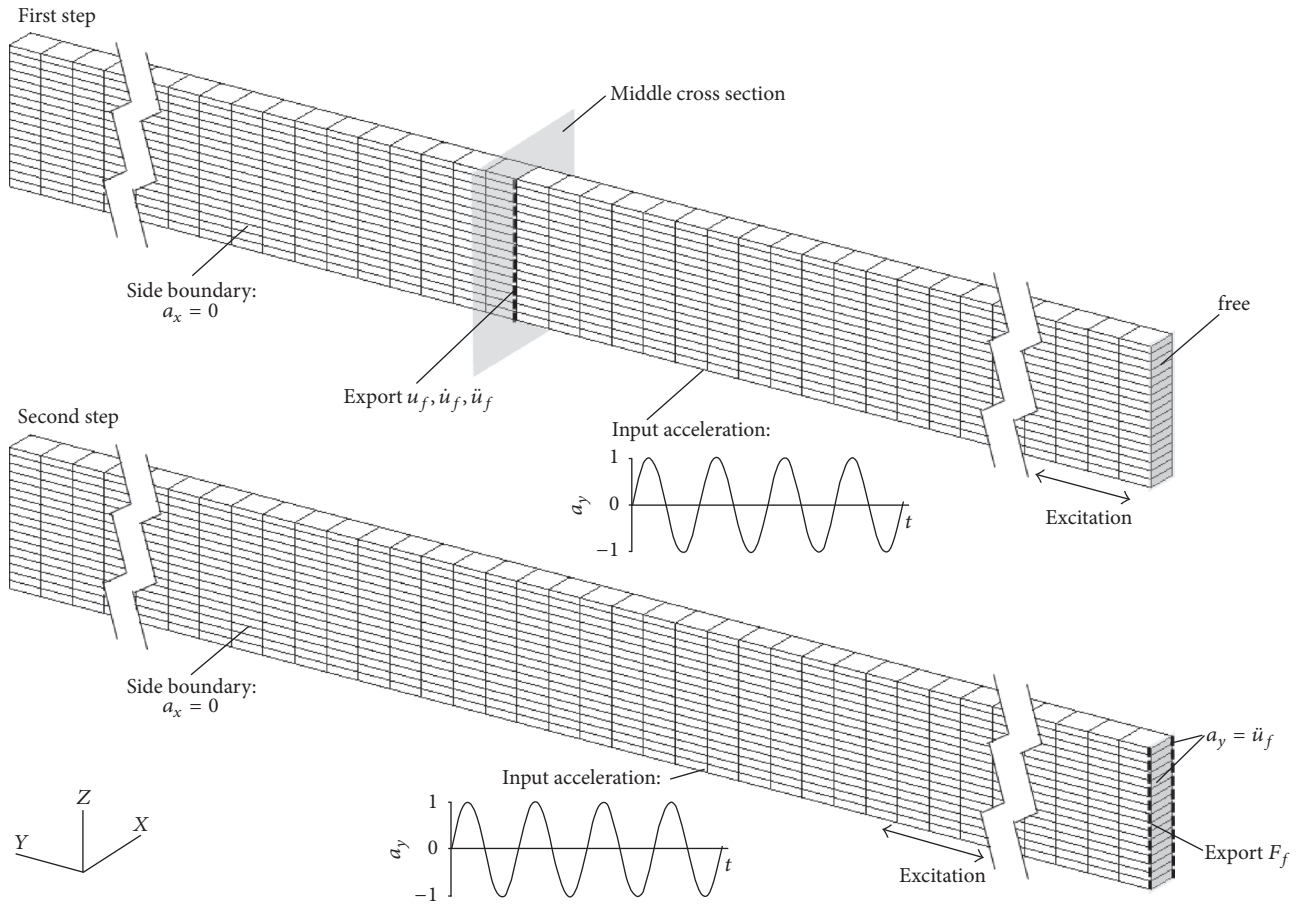


FIGURE 2: FE model to derive the required variables for the equivalent force in (7).

motion in this part of the model can be considered as free-field motion of infinite soil. The required  $u_f$ ,  $\dot{u}_f$ , and  $\ddot{u}_f$  can be calculated for the nodes in the middle cross section.

In the second step of the analysis,  $\ddot{u}_f$  is applied to both ends of the slice to replace the free boundary in the first step. The boundary conditions on the sides and the input motion at the bottom of the model remain the same as these in the first step above. The reaction forces,  $F_f$ , at the boundary nodes of the model are calculated and extracted.

From the two-step analysis, the free-field variables required to calculate the equivalent forces in (7) are obtained. This method facilitates the modelling of the artificial boundary.

### 3. Validation of the Numerical Model

**3.1. Method and Model.** The model validation is carried out by a simplified model of an NPP building with dimensions of 56 m  $\times$  50 m and 27 m height, as shown in Figure 3(a). The building is modelled using shell and beam elements with a size below 2 m. Distributed mass is added to the floor of the structure to represent the reactor and other major facilities in the building. The step profile soil type proposed by Tuñón-Sanjur et al. [1], which is based on a survey of 22 commercial NPPs in the United States, is used. The soil parameters for

each layer are listed in Table 1. The damping ratios of all layers are assumed to be 5%, which is approximately an average value for the adopted soil profile. The thickness of the calculation domain in  $Z$  direction is 40 m, including layer 1 through 3 in Table 1. Vertical ( $Z$  direction) size of each layer is also shown in Table 1. The horizontal ( $X$  and  $Y$  direction) element size is restricted to be less than 10 m. Sensitivity analysis was conducted and the results indicated that further refinement of the mesh in either horizontal or vertical direction would have negligible effects on the results.

The NPP model is subjected to one-directional excitation along  $y$  axis. The FE model is shown in Figure 3(b). With this model, the components  $[T_{yx} \ T_{yy} \ T_{yz}]$  in (3) are calculated. Due to the symmetry of the NPP building, only half of the model is analysed.

In order to test the SSI model, 8 cases with varied sizes and artificial boundary types (see Table 2) were studied. Figure 4 is a diagram of the soil-structure calculation domain. To validate the models, an extended model with a size of 1600  $\times$  800 m was also studied for comparison. Free boundary conditions were applied to the sides of the extended model. Most of the wave energy reflected from the truncated boundaries would be absorbed before reaching the building again. The results of the extended model can be regarded as more representative solution.

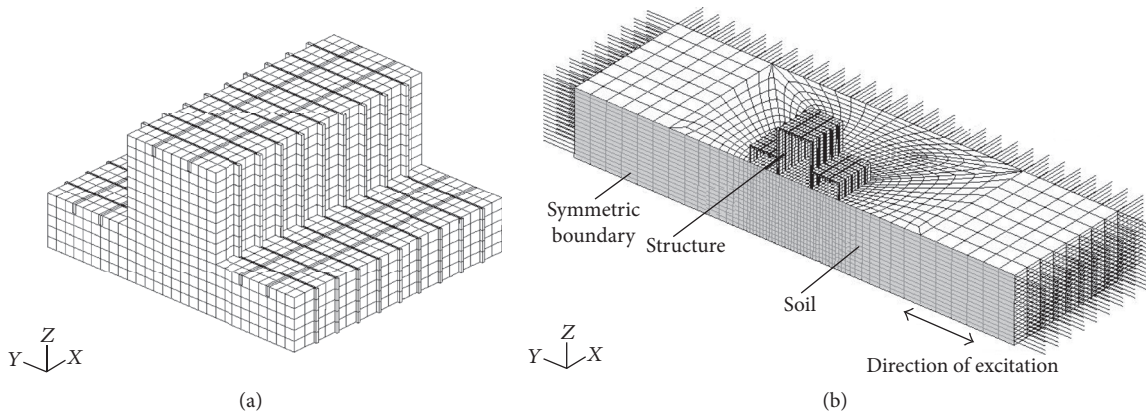


FIGURE 3: FE models of (a) simplified NPP structure and (b) soil-structure model for analysis.

TABLE 1: Parameters and element sizes of each layer for step profile soil.

Layer number	Depth (m)	Shear wave velocity (m/s)	Shear wave length (m)	Finite element height (z direction) (m)
1	0–11.5	304.8	12.19	2–2.375
2	11.5–23.38	548.6	21.95	2.375
3	23.38–40	1310.6	52.43	2.375
Bedrock	>40	>2400		

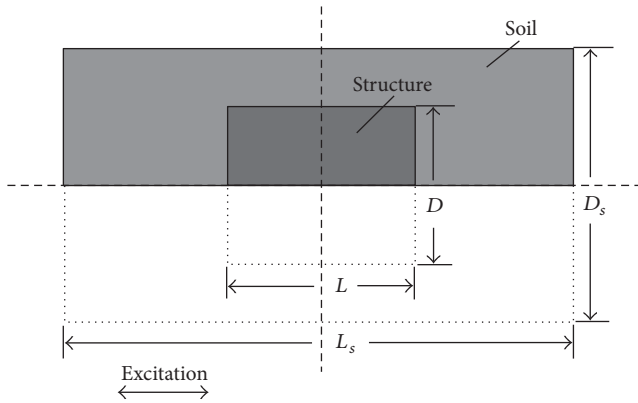


FIGURE 4: Diagram of SSI calculation domain.

TABLE 2: Size of calculation domain and boundary type.

Case number	Size of calculation domain $L_s \times D_s$ (m)	Boundary type
1	96 × 70	Viscous
2	160 × 160	Viscous
3	280 × 160	Viscous
4	280 × 260	Viscous
5	400 × 200	Viscous
6	520 × 260	Viscous
7	96 × 70	Viscoelastic
8	160 × 160	Viscoelastic
Extended	1600 × 800	Free

### 3.2. Results

3.2.1. *Effect of Calculation Domain Size and Shape.* Figures 5(a)–5(c) show the frequency response at the floor level (FL) +0.0 m in three orthogonal directions, Y direction (along the excitation), X direction (perpendicular to the excitation), and in Z direction for cases 1, 2, 3, and 5 in Table 2. The accuracy of all 6 cases in Table 2 with viscous boundaries is summarised in Table 3.

As shown in Figure 5(a), significant differences are observed in the frequency response peaks corresponding to the natural frequencies of the soil-structure system. The smallest model in size (case 1, 96 × 70 m) is characterized by a peak value 52% less than the extended model. As the size

of the model increases, the response curve changes to match closer that of the extended model. A model with a size of 280 × 160 m shows almost no difference in the peak values. Comparison between cases 1, 2, 3, 5, and 6 in Table 3 indicates that models with large size along the direction of excitation produce better results than small models. The maximum relative error is less than 10% over the whole frequency range when the size of the model along Y direction is 400 m; that is, the distance between the truncated boundary and the building is about 3 times the dimension of the building.

In X and Z directions, as shown in Figures 5(b) and 5(c), the acceleration is smaller than that in Y direction. For models with dimensions of 96 × 70 m and 160 × 160 m, the responses in X and Z directions differ from those of the extended model. A good agreement is observed between the

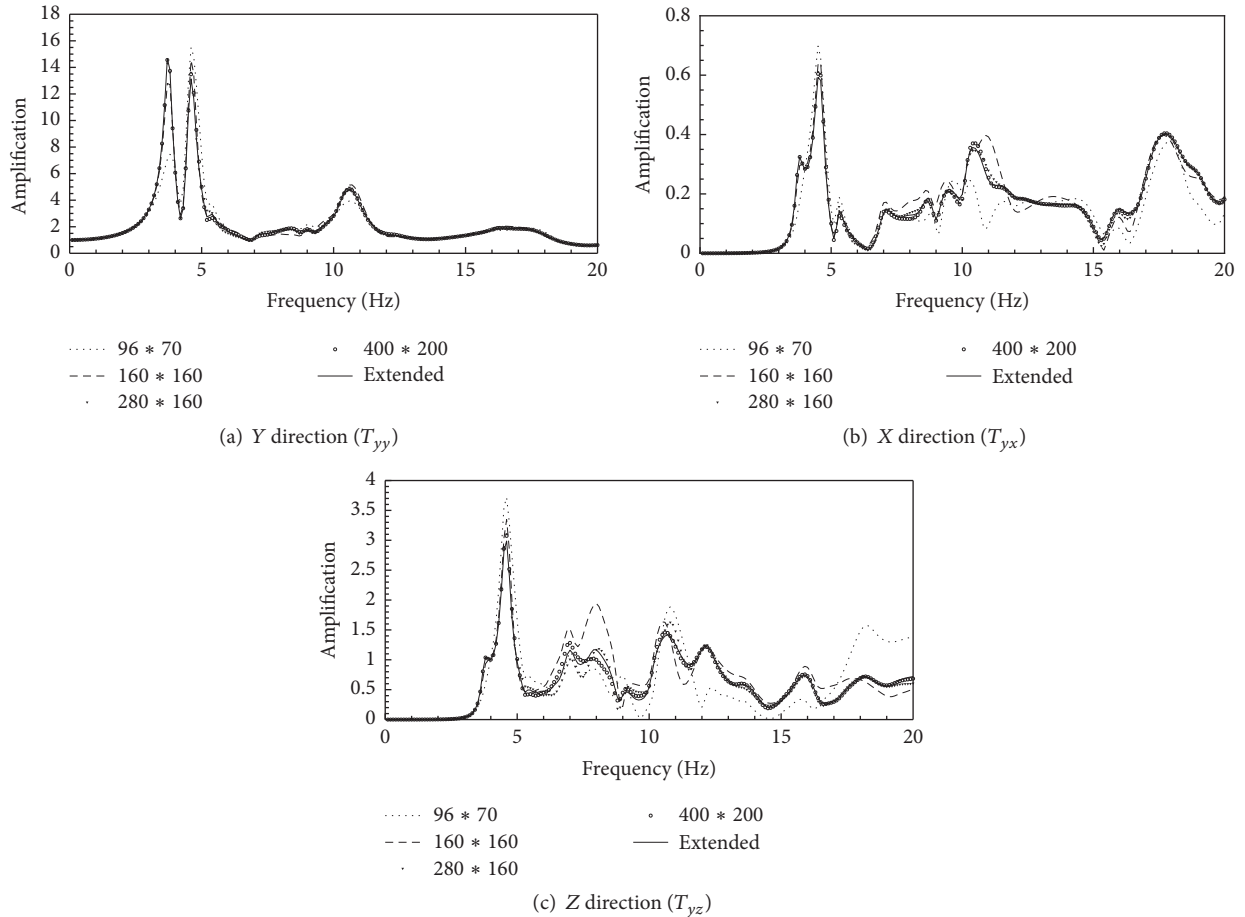


FIGURE 5: Frequency response curves in orthogonal directions at FL +0 m for cases 1, 2, 3, and 5 when excited in Y direction.

TABLE 3: Calculation errors for cases 1 through 6 in comparison with the extended model.

Case number	1	2	3	4	5	6
Size of the calculation domain $L_s \times D_s$ (m)	96 × 70	160 × 160	280 × 160	280 × 260	400 × 200	520 × 260
Maximum relative error of frequency response function ( $T_{yy}$ )	59.8%	21.7%	17.6%	17.2%	8.5%	9.0%

response curve of the extended model and models with Y dimension greater than 280 m. Since motions perpendicular to the excitation are much smaller than that along excitation, their contribution to the overall seismic response is negligible.

Based on the results in Figure 5, when the distance between the truncated boundary and the structure is  $\sim 3$  times the length of the structure, the response function is calculated with acceptable accuracy. This model size is adopted in the HTR-10 study described in Section 4.

Figures 6(a)–6(c) illustrate the frequency responses at FL +0.0 m in three orthogonal directions for cases 3 and 4 when excited in Y direction. Comparison between case 4 (280 × 260 m) and case 3 (280 × 160 m) shows that excessively enlarging the calculation domain in the direction

perpendicular to excitation has limited effect on the accuracy of the response curve.

The dynamic response of the soil-structure model subjected to a simple harmonic acceleration with unit amplitude at a typical frequency of 4.7 Hz, corresponding to the fundamental frequency in Y direction, is shown in Figure 7 in order to illustrate the appropriate shape of soil model in the X-Y plane. The dimension of the soil influenced by the structure along the excitation to that perpendicular to the excitation is about 2:1. In this sense, for a square-based structure, a soil model with an aspect ratio (i.e., model size along the excitation to that perpendicular to the excitation) of 2 is reasonable to represent the response in the soil. This aspect ratio is adopted to determine the model size perpendicular to the excitation in the following study.

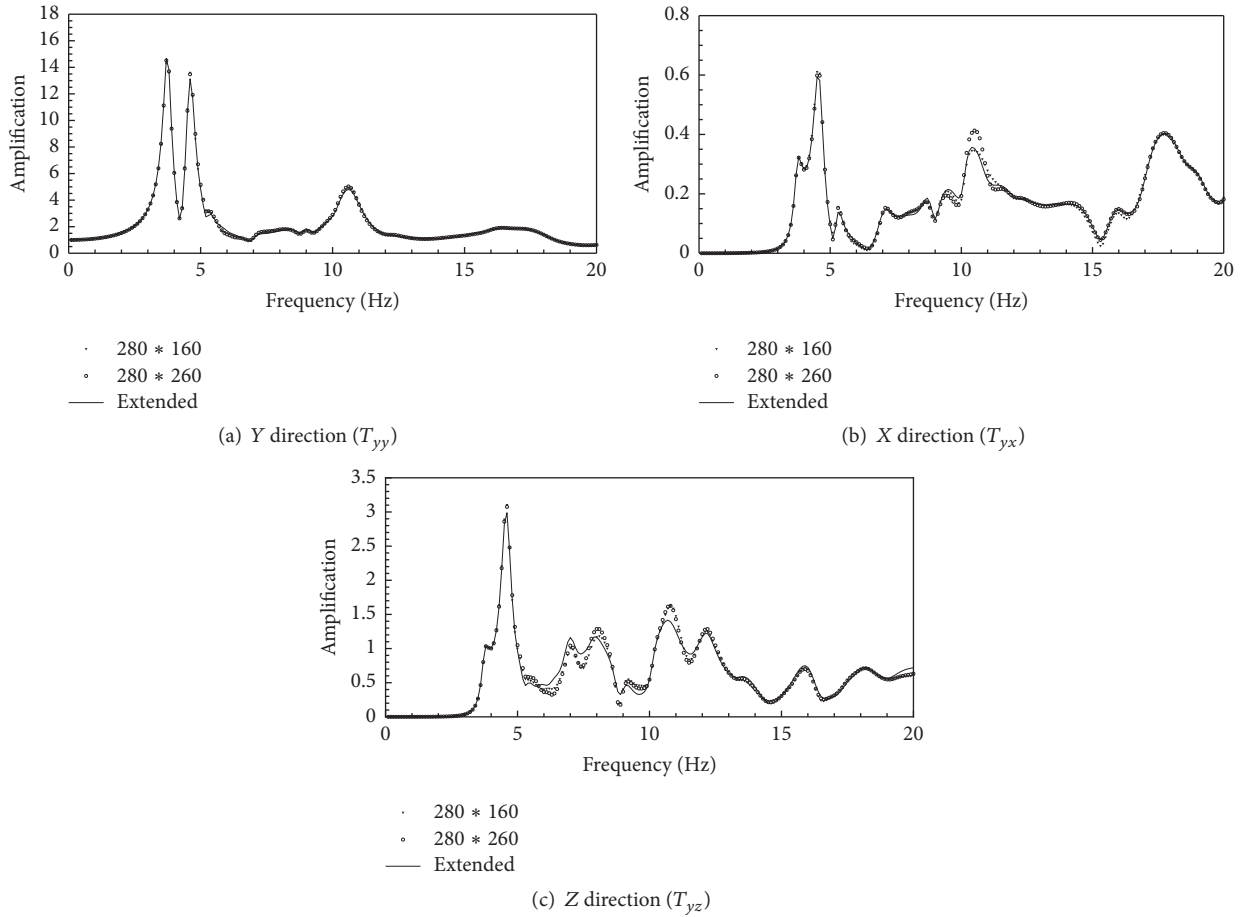


FIGURE 6: Frequency response curves in orthogonal directions at FL +0 m for cases 3 and 4 when excited in Y direction.

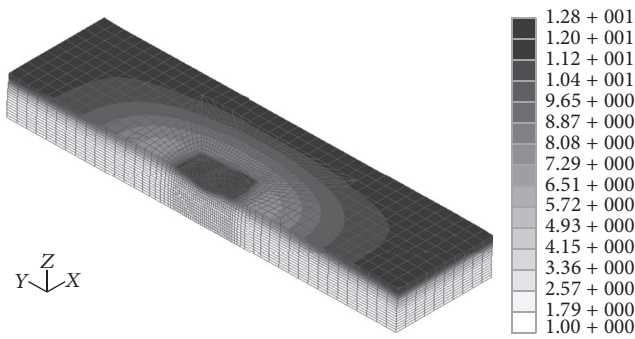


FIGURE 7: Contour of acceleration in the soil in Y direction ( $L_s \times D_s = 400 \times 200$  m, frequency of the simple harmonic input motion is 4.7 Hz).

3.2.2. *Effect of the Artificial Boundary Type.* To investigate the effect of viscoelastic boundary on the soil-structure model, the results of cases 7 and 8 are compared to those of cases 1 and 2. The amplification factors for viscoelastic and viscous boundaries of the  $90 \times 70$  m models are presented in Figure 8. As the model dimension is not long enough in the direction of excitation, the result from case 1 is not acceptable (see Section 3.2.1). The same conclusion is valid for the model with viscoelastic boundaries. As the

model dimensions increase, the difference between the two boundary types was observed to decrease (2.5% for  $160 \times 160$  m model). As illustrated by Deeks and Randolph [24], the viscoelastic boundary improves the results related to rigid body displacement and response in the low frequency range. In the current study, because the natural frequencies of the NPP structures are usually relatively high (between 4 Hz and 6 Hz), the advantages of the viscoelastic boundary are not significant.

In summary, the artificial boundary type has little effect on the accuracy of SSI analysis for NPP buildings when using complex frequency response method. Both of viscous and viscoelastic artificial boundaries provide satisfactory results when compared with an extended model following the recommended dimension in Section 3.2.1. Since the viscous boundary provides implementation benefits, it is adopted in the HTR-10 study.

#### 4. SSI Study for HTR-10

The numerical model as described in Sections 2 and 3 was used for seismic SSI analysis of HTR-10 NPP.

4.1. *SSI Model of HTR-10.* The HTR-10 NPP building consists of a reactor hall and an annex building. The reactor hall (30 m

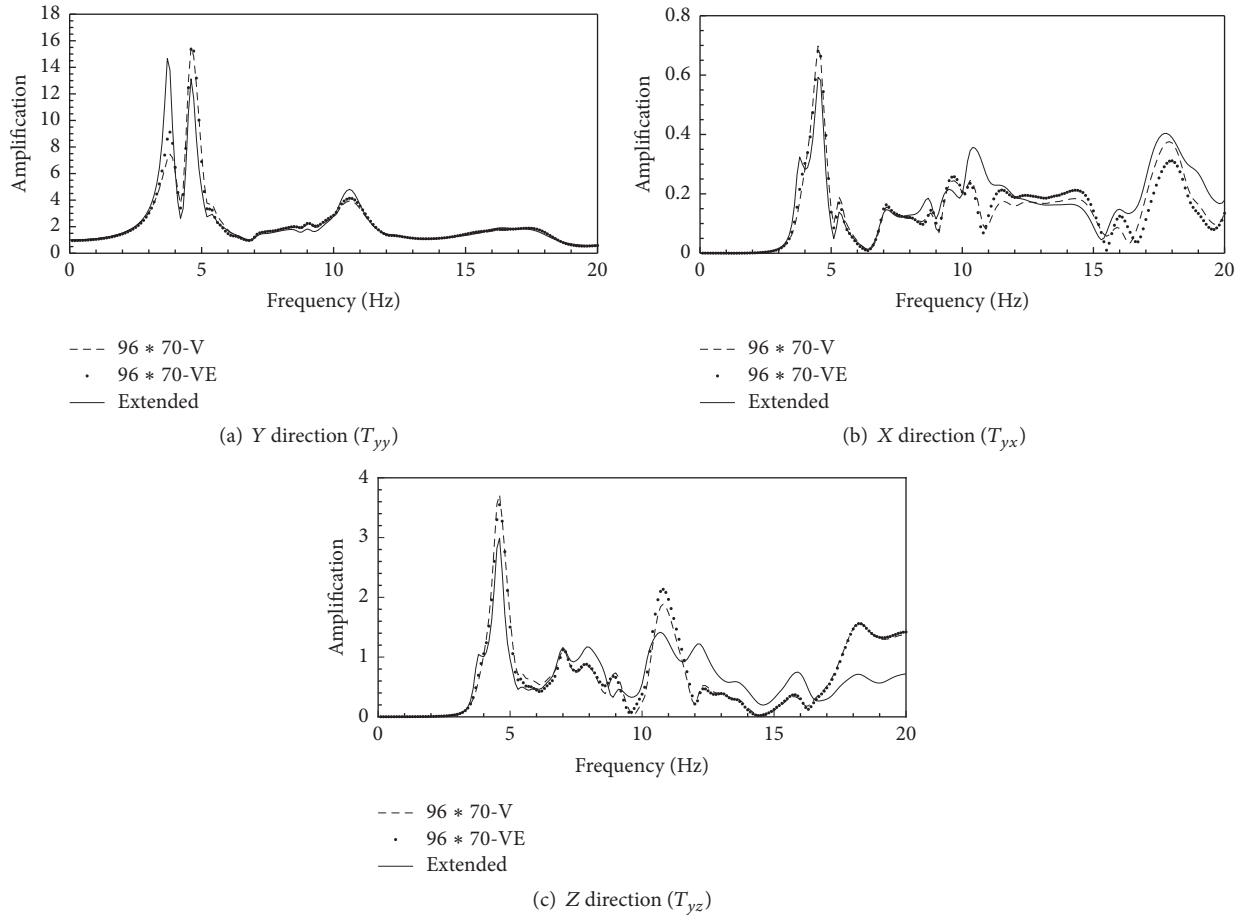


FIGURE 8: Frequency response curves in orthogonal directions at FL +0 m for cases 1 and 7 when excited in Y direction.

TABLE 4: Soil parameters and element size of each layer for HTR-10.

Layer	Depth(m)	Shear wave velocity (m/s)	Shear wave length (m)	Damping ratio	Vertical element size (m)
1	0–6	310.9	12.4	4.6%	1.5
2	6–12	412.7	16.5	5.8%	2.0
3	12–15	680.9	27.2	4.6%	3.0
4	15–25	834.8	33.4	3.6%	5.0
5	25–34	782.4	31.3	7.8%	4.5
6	34–37.8	434.3	17.4	12.8%	1.9
7	37.8–41.9	374.6	15.0	15.0%	2.1
8	41.9–44	362.1	14.5	15.4%	1.1
9	44–52.1	722.7	28.9	4.2%	4.1
Bedrock	>52.1	>2400			

long, 24 m wide) rests on soil at elevation  $-17.0$  m and rises to an elevation of  $+28.0$  m. The 5 m high annex building (46 m long, 34 m wide) surrounds the reactor hall with a foundation at elevation of  $+0.0$  m. The primary system cabin inside the reactor hall is a shaft structure stretching from the  $-17.0$  m level to the  $+11.0$  m level. The NPP is constructed on a soil site in Beijing, China. The parameters of the soil layers based on geological surveys are listed in Table 4. The soil layers above the bedrock are 52.1 m in thickness.

The HTR-10 building is subjected to a two-directional seismic input in the  $X$ - $Y$  plane. The standard spectrum recommended by NRC Regulatory Guides 1.60 [29] was normalised to 0.32 g zero period acceleration (ZPA) and adopted as design spectrum. Synthetic earthquake time histories developed from the design spectrum in strict conformance to the requirements in ASCE 4-98 [26] and Standard Review Plan [30] as shown in Figure 11 were applied to the ground surface as the design free-field motions. This earthquake

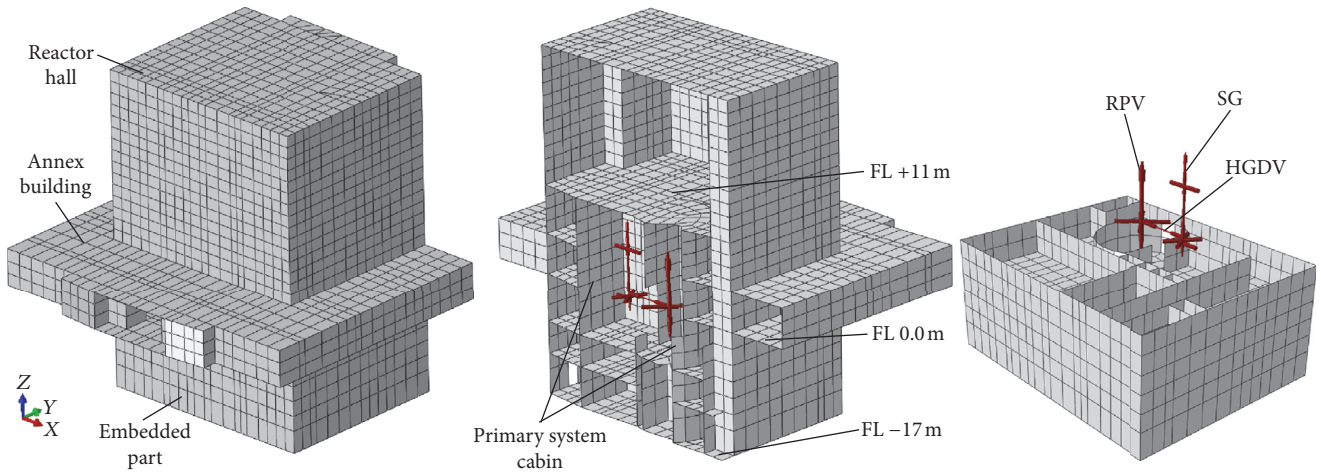


FIGURE 9: Model of the HTR-10 building.

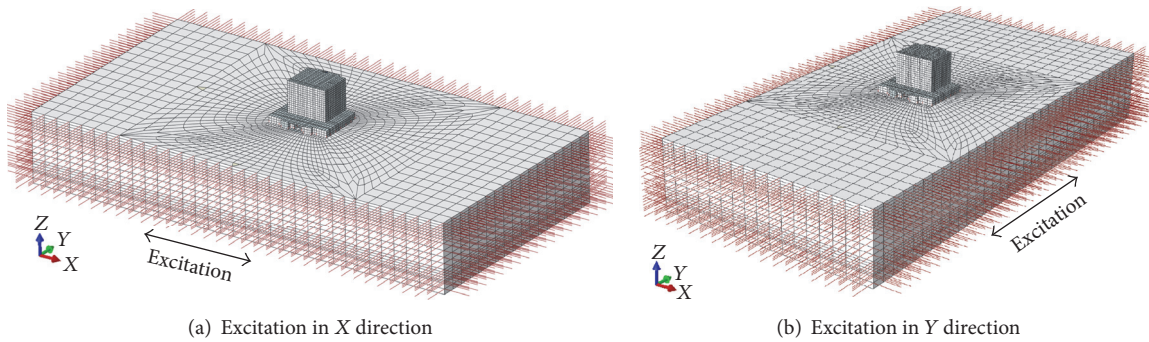


FIGURE 10: Joint mesh of structure and soil of the HTR-10 SSI analysis.

motion was then deconvoluted to the bottom layer of soil (-52.1 m) using computer program SHAKE [31] to calculate the acceleration input  $\ddot{u}_i(t)$  used in (1).

The HTR-10 building is modelled using shell and beam elements as shown in Figure 9. The Reactor Pressure Vessel (RPV), Steam Generator (SG), and Hot Gas Conduct Vessel (HGCV) are simplified to a lumped-mass model which captures the essential features of the structures. Other facilities and components are modelled by distributed mass on the floor.

The responses corresponding to excitation in each direction are calculated separately according to Section 2.1. The soil-structure models used to calculate the frequency response function when subjected to excitation in X and Y directions are shown in Figures 10(a) and 10(b), respectively. FE models with dimensions of  $330 \times 170$  m and viscous boundaries are adopted for the SSI analysis (see Section 3). The equivalent forces at the truncated boundaries were obtained by the method in Section 2.2 using the soil properties in Table 4. The results in the two directions are combined using (1) through (3) to produce the response of the structure. The FRS with damping ratio of 5% were calculated at all floor levels and the locations of the supports of the RPV and SG.

In order to investigate the effect of SSI, a fixed-base model assuming that the NPP building is sitting on the rigid rock was also analysed and the FRS were generated for comparison. In the fixed-base model, the design free-field motions are directly applied to the nodes that connect to the rock, including the floor at -17.0 m, the embedded walls of the reactor hall, and the floor of the annex building at +0.0 m.

**4.2. SSI Effect of HTR-10.** In order to investigate the effects of SSI on the reactor building and the main components, the FRS were investigated at three different floor levels, including the bottom of the building (FL -17.0 m), top floor (FL +11.0 m), and RPV and SG supports (FL -0.29 m). The FRS at these floor levels are shown in Figure 12. The results of the SSI model (solid lines) are compared with those of the fixed-base model (dashed lines). At all floor levels, the spectrum curves in both X and Y directions are clearly different for the SSI and fixed-base results.

Figures 12(a) and 12(b) are the FRS at FL -17.0 m in X and Y directions, respectively. The dashed lines represent the fixed-base results at FL -17.0 m, which are the same as the design spectra (i.e., free-field response spectra at FL +0.0 m). The free-field response spectra at FL -17.0 m obtained from the soil slice model are also presented in Figures 12(a) and

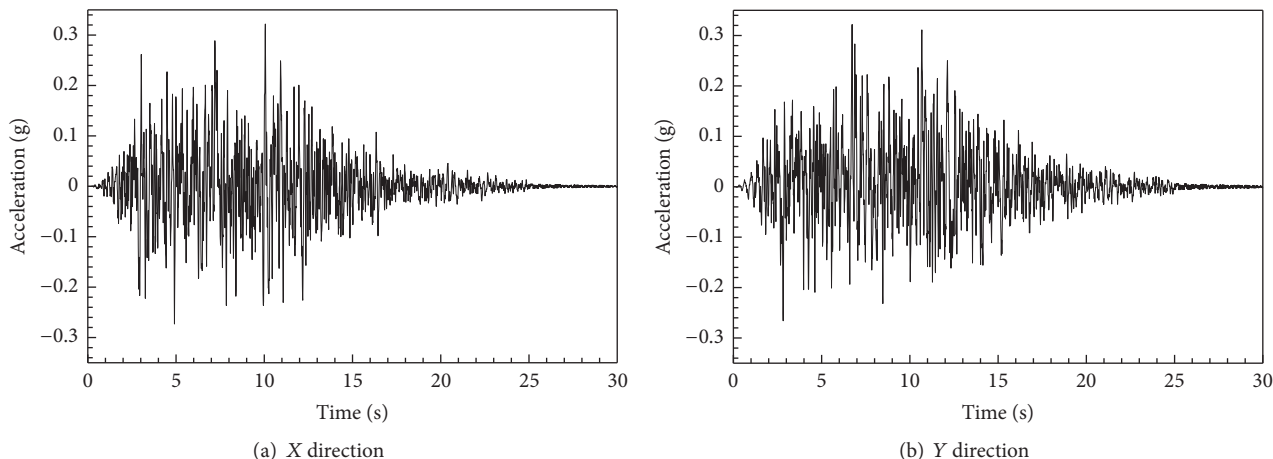


FIGURE 11: Design free-field motions at the ground surface.

12(b) as long dashed lines. The results show that the free-field response is amplified from  $-17$  m (long dashed lines) to  $0$  m (dashed lines) by the soil layers. The embedded structure resting on the  $-17.0$  m soil layer is subjected to lower level of excitation than that at  $0$  m. It can be concluded that using fixed-base model is conservative at lower floors for HTR-10.

The FRS for FL  $+11.0$  m is illustrated in Figures 12(c) and 12(d), demonstrating that the FRS is substantially altered because of the SSI. The peak frequency is reduced from over  $10$  Hz to less than  $5$  Hz due to the SSI. The relatively high frequencies in the range from  $6$  Hz to  $30$  Hz are suppressed by the SSI. The responses in the relatively low frequencies ranging from  $3$  Hz to  $5$  Hz are amplified by a maximum of  $2.5$  times. Thus, the SSI effect should be considered in calculating FRS at floors above the ground surface, especially at high floor levels.

Figures 12(e) and 12(f) present the FRS at the supports of RPV and SG in the primary system cabin at FL  $-0.29$  m. The acceleration in the high frequency range between  $6$  Hz and  $30$  Hz is reduced by the SSI for both  $X$  and  $Y$  directions. At lower frequency ranges, the SSI model produces larger responses in both  $X$  and  $Y$  directions. However, the increase is not as obvious as that in FL  $+11.0$  m. Since the fundamental frequencies of the integrated structure of primary system components (i.e., RPV, SG, and HGCV) in both  $X$  and  $Y$  directions are around  $10$  Hz, seismic responses of these components are reduced when taking SSI into consideration for the current soil sites.

## 5. Conclusions

In this study, a numerical method for seismic SSI analysis with commercial code is developed. Three-dimensional FE models composed of upper structure and subsurface soil with transmitting boundaries were solved in the frequency domain to determine the frequency response function of an NPP under vertically incident seismic excitation. A comprehensive investigation of this numerical method is carried out and the modelling parameters which produce reliable results were determined. Several recommendations are provided for

the SSI analysis of NPP subjected to horizontal earthquake ground motion.

- (1) The distance between the truncated boundary of the soil model and the building should be at least 3 times the length of the structure in the direction of excitation.
- (2) Soil model with an aspect ratio (size along the excitation to that perpendicular to the excitation) of  $2:1$  produces satisfactory results for a square-based structure.
- (3) SSI analysis in the frequency domain with viscous boundary is adequate to produce satisfactory results for NPP.

The seismic response of the HTR-10 reactor building subjected to horizontal ground motion was analysed. The results show that the SSI do not amplify significantly the dynamic response of HTR-10 for the particular soil profile. The following conclusions are made by comparing the FRS results from SSI and fixed-base models.

- (1) The response at lower floor levels is reduced due to SSI.
- (2) The FRS curve is substantially changed at higher floor levels. The peak frequency of the FRS is reduced due to the soil flexibility and the spectral acceleration increases at certain frequency range. SSI analysis is essential for the seismic designs of the safety related components installed at these floors.

The above results are valid for a broad range of earthquakes with ground motion that can be represented by the standard spectrum of RG 1.60 [29]. The analyses performed in this study may be used for seismic design of NPPs based on codes and regulations. However, SSI effect under a wider range of seismic excitations, such as near-source ground motions characterized by large ground velocity and displacement pulses with long-periods [32] should be investigated separately in order to obtain a more comprehensive conclusion about the SSI effect on NPPs.

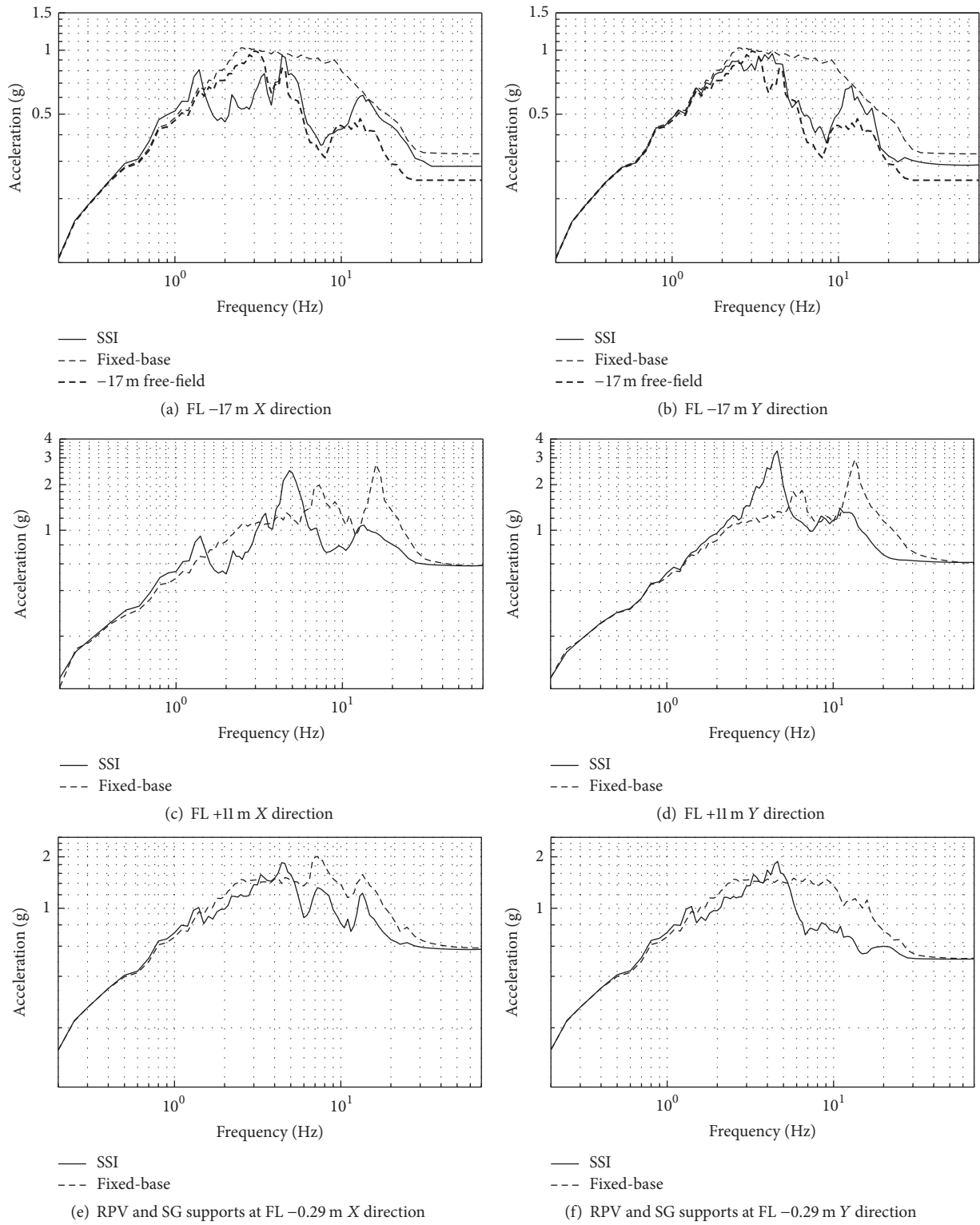


FIGURE 12: FRS results at typical floor levels in X and Y directions.

## Conflicts of Interest

The authors declare that they have no conflicts of interest.

## Acknowledgments

This work is supported by the National Natural Science Foundation of China under Grant no. 11302116. The authors wish to express their thanks for the support.

## References

- [1] L. Tuñón-Sanjur, R. S. Orr, S. Tinic, and D. P. Ruiz, "Finite element modeling of the AP1000 nuclear island for seismic analyses at generic soil and rock sites," *Nuclear Engineering and Design*, vol. 237, no. 12-13, pp. 1474–1485, 2007.
- [2] I. Politopoulos, I. Sergis, and F. Wang, "Floor response spectra of a partially embedded seismically isolated nuclear plant," *Soil Dynamics and Earthquake Engineering*, vol. 78, pp. 213–217, 2015.
- [3] J. C. Chen and O. R. Maslenikov, "Seismic soil-structure interaction responses of N-reactor facility," *Journal of Pressure Vessel Technology, Transactions of the ASME*, vol. 126, no. 1, pp. 25–33, 2004.
- [4] R. V. Farahani, T. M. Dessalegn, N. R. Vaidya, and E. Bazan-Zurita, "Seismic soil-structure interaction analysis of a nuclear power plant building founded on soil and in degraded concrete stiffness condition," *Nuclear Engineering and Design*, vol. 297, pp. 320–326, 2016.
- [5] N. Saxena, D. K. Paul, and R. Kumar, "Effects of slip and separation on seismic SSI response of nuclear reactor building," *Nuclear Engineering and Design*, vol. 241, no. 1, pp. 12–17, 2011.
- [6] A. L. Halbritter, N. J. Krutzik, Z. Boyadjiev, and T. Katona, "Dynamic analysis of VVER type nuclear power plants using different procedures for consideration of soil-structure interaction effects," *Nuclear Engineering and Design*, vol. 182, no. 1, pp. 73–92, 1998.
- [7] D. M. Ghiocel and R. G. Ghanem, "Stochastic finite-element analysis of seismic soil-structure interaction," *Journal of Engineering Mechanics*, vol. 128, no. 1, pp. 66–77, 2002.
- [8] B. Fatahi, S. H. R. Tabatabaiefar, and B. Samali, "Soil-structure interaction vs Site effect for seismic design of tall buildings on soft soil," *Geomechanics and Engineering*, vol. 6, no. 3, pp. 293–320, 2014.
- [9] Z. Wu, D. Lin, and D. Zhong, "The design features of the HTR-10," *Nuclear Engineering and Design*, vol. 218, pp. 25–32, 2002.
- [10] G. Brinkmann, J. Pirson, S. Ehster et al., "Important viewpoints proposed for a safety approach of HTGR reactors in Europe: Final results of the EC-funded HTR-L project," *Nuclear Engineering and Design*, vol. 236, no. 5-6, pp. 463–474, 2006.
- [11] R. J. Apsel and J. E. Luco, "Impedance functions for foundations embedded in a layered medium: An integral equation approach," *Earthquake Engineering & Structural Dynamics*, vol. 15, no. 2, pp. 213–231, 1987.
- [12] E. Kausel, R. V. Whitman, J. P. Morray, and F. Elsabee, "The spring method for embedded foundations," *Nuclear Engineering and Design*, vol. 48, no. 2-3, pp. 377–392, 1978.
- [13] J. P. Wolf, *Soil-Structure Interaction Analysis in Time Domain*, Prentice Hall, Englewood Cliffs, NJ, USA, 1988.
- [14] J. Dominguez and J. M. Roesset, "Dynamic stiffness of rectangular foundations," Tech. Rep. R78 20, Department of Civil Engineering, Massachusetts Institute of Technology, Cambridge, 1978.
- [15] M. Yazdchi, N. Khalili, and S. Valliappan, "Dynamic soil-structure interaction analysis via coupled finite-element-boundary-element method," *Soil Dynamics and Earthquake Engineering*, vol. 18, no. 7, pp. 499–517, 1999.
- [16] O. Von Estorff and M. Firuziaan, "Coupled BEM/FEM approach for nonlinear soil/structure interaction," *Engineering Analysis with Boundary Elements*, vol. 24, no. 10, pp. 715–725, 2000.
- [17] J. M. Roesset, "A review of soil-structure interaction," in *Soil-Structure Interaction The Status of Current Analysis Methods And Research*, J. J. Johnson, Ed., NUREG/CR-1780 and UCRL-53011, US Nuclear Regulatory Commission and Lawrence Livermore Laboratory, 1980.
- [18] E. Kausel, "Early history of soil-structure interaction," *Soil Dynamics and Earthquake Engineering*, vol. 30, no. 9, pp. 822–832, 2010.
- [19] D. Clouteau, R. Cottureau, and G. Lombaert, "Dynamics of structures coupled with elastic media—a review of numerical models and methods," *Journal of Sound and Vibration*, vol. 332, no. 10, pp. 2415–2436, 2013.
- [20] J. Lysmer, F. Ostadan, and C. Chin, *SASSI2000—System for Analysis of Soil-Structure Interaction*, University of California, Berkeley, Calif, USA, 1999.
- [21] H. L. Wong and J. E. Luco, *Soil-Structure Interaction: A Linear Continuum Mechanics Approach (CLASSI)*, Dept. of Civil Engineering, University of Southern, Los Angeles, Calif, USA, 1980.
- [22] J. Lysmer and R. L. Kuhlemeyer, "Finite dynamic model for infinite media," *Journal of the Engineering Mechanics Division*, vol. 95, no. EM4, pp. 859–877, 1969.
- [23] Z. P. Liao and H. L. Wong, "A transmitting boundary for the numerical simulation of elastic wave propagation," *International Journal of Soil Dynamics and Earthquake Engineering*, vol. 3, no. 4, pp. 174–183, 1984.
- [24] A. J. Deeks and F. M. Randolph, "Axisymmetric time-domain transmitting boundaries," *Journal of Engineering Mechanics*, vol. 120, no. 1, pp. 25–42, 1994.
- [25] L. Kellezi, "Local transmitting boundaries for transient elastic analysis," *Soil Dynamics and Earthquake Engineering*, vol. 19, no. 7, pp. 533–547, 2000.
- [26] ASCE Standard, *Seismic Analysis of Safety-Related Nuclear Structures and Commentary (4-98)*, American Society of Civil Engineers, Reston, Va, USA, 2000.
- [27] J. B. Liu, Z. Y. Wang, X. L. Du, and Y. X. Du, "Three-dimensional visco-elastic artificial boundaries in time domain for wave motion problems," *Engineering Mechanics*, vol. 22, no. 6, pp. 46–51, 2005.
- [28] J. B. Liu and Y. D. Lu, "A direct method for analysis of dynamic soil-structure interaction based on interface idea," in *Proceedings of the Chinese-Swiss Workshop on Soil-Structure Interaction Location*, Beijing, China, 1997.
- [29] NRC Regulatory Guides 1.60, *Design Response Spectra for Seismic Design of Nuclear Power Plants*, U.S. Nuclear Regulatory Commission, Washington, DC, USA, 2014.
- [30] *Stand Review Plan for Review of Safety Analysis Reports for Nuclear Power Plants: LWR Edition—Design of Structures, Components, Equipment, and Systems*, Chapter 3, U.S. Nuclear Regulatory Commission, Washington, DC, USA, 2014.

- [31] P. B. Schnabel, J. Lysmer, and H. B. Seed, "SHAKE—A Computer Program for Earthquake Response Analysis of Horizontally Layered Sites," Tech. Rep. EERC 72-12, Earthquake Engineering Research Center, UCB, December 1972.
- [32] P. Somerville and R. Graves, "Conditions that give rise to unusually large long period ground motions," *The Structural Design of Tall Buildings*, vol. 2, no. 3, pp. 211–232, 1993.

## Research Article

# FM-DBEM Simulation of 3D Microvoid and Microcrack Graphite Models

**Houdi Lu, Hongtao Wang, Haitao Wang, Lie Jin, Xinxin Wu, and Yu Zhou**

*Key Laboratory of Advanced Reactor Engineering and Safety of Ministry of Education, Collaborative Innovation Center of Advanced Nuclear Energy Technology, Institute of Nuclear and New Energy Technology, Tsinghua University, Beijing 100084, China*

Correspondence should be addressed to Hongtao Wang; wanghongtao@tsinghua.edu.cn

Received 30 December 2016; Revised 12 April 2017; Accepted 10 May 2017; Published 6 June 2017

Academic Editor: Leon Cizelj

Copyright © 2017 Houdi Lu et al. This is an open access article distributed under the Creative Commons Attribution License, which permits unrestricted use, distribution, and reproduction in any medium, provided the original work is properly cited.

The graphite is porous medium, and the geometry and size distribution of its structural deficiencies such as microcracks and microvoids at different oxidation degrees have a great influence on the overall performance. In this paper, we adopt the FM-DBEM to study 3D models which contain spheroidal microvoids and circular microcracks. The accuracy of this method is tested by a comparison to the theoretical solution to the problem of 2D microcrack and microvoid interaction problem. Two simulations are conducted: the simulation of graphite model containing a large number of randomly distributed microcracks and microvoids and the simulation of graphite model containing microcracks and growing microvoids. The simulations investigate the effective moduli versus the two microstructures' density and the effect of microvoid's growth on the SIF of microcrack.

## 1. Introduction

Nuclear graphite is widely used as fuel blocks and reactor internals in high-temperature gas-cooled reactors (HTR) because of its high-temperature resistance and neutron moderation [1, 2]. As the structural material of HTR, the mechanical property and structural integrity of graphite structure have a great impact on HTR's safe operation. The oxide gas and possible accidents will lead to the oxidation of graphite and influence its mesostructure and mechanical parameter. As a kind of porous media, there exist structural deficiencies such as microcracks and microvoids in graphite. During the oxidation process, the microvoids in the graphite will grow, and the microcrack tip often fractures first during the fracture process. Therefore, it is of great value to study the interaction between microcracks and microvoids in the graphite.

Many researchers have developed continuum damage micromechanical models to study graphite as a kind of brittle material. Kachanov [3, 4] and Ju [5] discussed the loss of moduli in terms of evolution of the microstructure, but their research did not involve material parameters.

Hu and Chandra [6] and Huang et al. [7] adopted a unit cell approach and obtained the stress intensity factors by modeling a finite number of defects. Hu et al. [8] developed an integral equation to model interactions between voids and microcracks of 2D elastic fracture mechanics. The local behavior of such defective material has been studied by many other researchers [9–12] using theoretical approaches, but the theoretical solutions are obtained for simple cases, such as a void among several regularly spaced cracks or a crack among several regularly spaced voids embedded in an infinite plate subjected to remote loading. Another characteristic of graphite is its anisotropy. The anisotropy of the coefficient of thermal expansion in crystallites and the generation of internal stresses beyond the elastic limit of graphite crystals cause the cracking in graphite [13, 14]. Yan et al. [15] developed a 2D micromechanistic model which considered intergranular cracks and intragranular cracks to predict the response of graphite under temperature changes and irradiation, and this model was appropriate for generalized plane strain condition. At present, much less literature has been focused on 3D theoretical solutions and the 3D simulation of the interaction between microvoids and microcracks.

The finite element method (FEM) is also widely used to solve the microvoid and microcrack problems in some practical structures. In order to ensure the accuracy of simulation, a large number of elements are used, which largely reduces the computational efficiency. Even under such a condition, the accuracy is not that satisfactory because the assumed displacement functions do not satisfy the dominance conditions at the free boundary. In order to solve such problems, some modified methods [16, 17] are applied, but these methods need to model the vicinity of microvoids and microcracks with a mass of elements; besides, special elements are also defined to tackle the problem [18, 19].

The boundary element method (BEM) is an effective method in solving microvoid and microcrack problems, since only the boundary of the analyzed domain needs to be discretized [20]. The advantages of BEM are that it can not only reduce the initial preparation data and the degrees of freedom, but also simplify the microcrack meshing process; thus, much fewer elements are needed than in FEM. When dealing with fracture problems, the dual boundary element method (DBEM) is applied to overcome the degeneration difficulty when the two surfaces of the same crack coincide [21]. In the research on the DBEM, Portela et al. [22, 23] first used this method for the analysis of 2D crack problem, and then this method was extended to 3D crack analysis by Mi and Aliabadi [24], Cisilino and Aliabadi [25], and Wilde and Aliabadi [26]. Meanwhile, many researchers [27–30] have adopted the fast multipole method (FMM) (Rokhlin [31]) in their BEM because of FMM's ability to reduce memory requirement and calculation scale. Another fast algorithm widely adopted for crack problems is hierarchical matrices. The hierarchical matrices method is an algebraic method, and its approximation is based only on the knowledge of individual matrix entries. Research on hierarchical matrices DBEM for 3D general elastic crack problems has been reported by Benedetti et al. [32–34]. The hierarchical matrices method has better computational speed than FMM, but FMM is more capable for large scale problem than the former because FMM's cost of storing is smaller. So far, 3D microcrack problem has been studied by several researchers. Lai and Rodin [35] presented a fast BEM for analyzing 3D linear elastic solids containing many cracks. Nishimura et al. [36] discussed a three-dimensional fast multipole boundary integral equation method for crack problems for Laplace's equation. Wang and Yao [37] adopted fast multipole-dual boundary element method (FM-DBEM) to analyze the 3D crack problems. Lu [38] introduced a modeling method based on Python and ABAQUS/CAE to get microvoid and microcrack models. However, the interaction of microvoid and microcrack still needs intensive research.

In this paper, we adopt the FM-DBEM to explore 3D graphite models which contain spheroidal microvoids and circular microcracks and study their interaction. The 3D models' effective moduli are evaluated in several conditions. A FM-DBEM solver written by C++ code is used and its accuracy is tested by a comparison to the theoretical solution to the 2D problem of the interaction between microcrack and microvoid. This method shows high accuracy and efficiency,

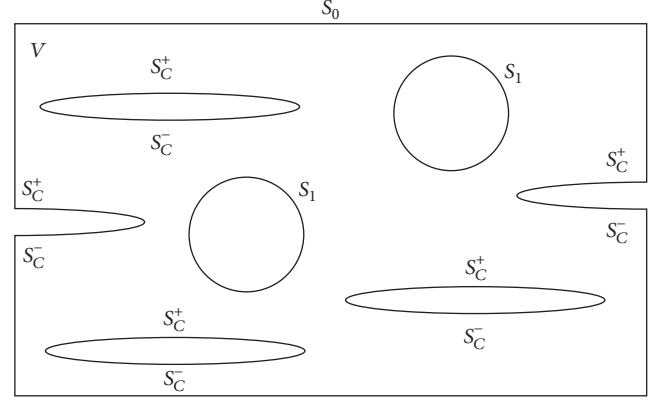


FIGURE 1: An elastic solid containing edge and embedded cracks.

and it can be applied to simulate complex structures and components containing microvoids and microcracks.

## 2. Models and Methods

*2.1. Dual Boundary Element Method for 3D Microcrack and Microvoid Interaction.* Figure 1 shows the model of an elastic structure containing edge, embedded voids, and cracks.  $V$  and  $S_0$  represent the domain and outer boundary of the solid.  $S_1$  represent the inner boundary of the voids.  $S_C^+$  and  $S_C^-$  represent the two coinciding surfaces of the cracks.

The dual boundary integral equations for 3D elastic fracture mechanics without body force are shown as

$$c_{ij}(x) u_j(x) + \int_{S_0} [T_{ij}^*(x, y) u_j(y) - U_{ij}^*(x, y) t_j(y)] dS(y) \quad (1)$$

$$= - \int_{S_C^+} T_{ij}^*(x, y) \Delta u_j(y) dS(y) \quad (x \in S_0, S_1)$$

$$\frac{1}{2} [u_i^+(x) + u_i^-(x)] + \int_{S_0} [T_{ij}^*(x, y) u_j(y) - U_{ij}^*(x, y) t_j(y)] dS(y) \quad (2)$$

$$= - \int_{S_C^-} T_{ij}^*(x, y) \Delta u_j(y) dS(y), \quad (x \in S_C^-)$$

$$\frac{1}{2} [t_i^+(x) - t_i^-(x)] + \int_{S_0} [S_{ij}^*(x, y) u_j(y) - D_{ij}^*(x, y) t_j(y)] dS(y) \quad (3)$$

$$= - \int_{S_C^+} S_{ij}^*(x, y) \Delta u_j(y) dS(y), \quad (x \in S_C^+),$$

where  $x$  and  $y$  represent the source and field point;  $u_i$  and  $t_i$  are the boundary displacement and traction vectors;  $c_{ij}(x)$  is a free term related to the shape of boundary at point  $x$ ;

$\Delta u_i = u_i^+ - u_i^-$  is the relative displacement between  $S_C^+$  and  $S_C^-$ . The kernel functions  $U_{ij}^*(x, y)$  and  $T_{ij}^*(x, y)$  are shown as

$$\begin{aligned} U_{ij}^*(x, y) &= \frac{1}{16\pi G(1-\nu)r} \left[ (3-4\nu)\delta_{ij} + \frac{r_i r_j}{r^2} \right] \\ T_{ij}^*(x, y) &= \frac{1}{8\pi(1-\nu)r} \left\{ (1-2\nu) \left( \frac{n_i r_j - n_j r_i}{r} \right) \right. \\ &\quad \left. - \frac{\partial r}{\partial n} \left[ (1-2\nu)\delta_{ij} + \frac{3r_i r_j}{r^2} \right] \right\}, \end{aligned} \quad (4)$$

where  $r$  represents the distance between  $x$  and  $y$ ;  $G$  and  $\nu$  represent the shear modulus and Poisson's ratio.  $D_{ij}^*(x, y)$  and  $S_{ij}^*(x, y)$  are obtained from  $U_{ij}^*(x, y)$  and  $T_{ij}^*(x, y)$ :

$$\begin{aligned} D_{ij}^*(x, y) &= n_k(x) \left[ \lambda \delta_{ki} \frac{\partial U_{lj}^*(x, y)}{\partial x_l} + G \left( \frac{\partial U_{kj}^*(x, y)}{\partial x_i} \right. \right. \\ &\quad \left. \left. + \frac{\partial U_{ij}^*(x, y)}{\partial x_k} \right) \right] = \frac{1}{8\pi(1-\nu)r^2} \left\{ (1-2\nu) \right. \\ &\quad \cdot \left[ \delta_{ij} \frac{r_k n_k(x)}{r} + \frac{r_i n_j(x) - r_j n_i(x)}{r} \right] + 3 \frac{r_i r_j r_k}{r^3} \\ &\quad \left. \cdot n_k(x) \right\} \\ S_{ij}^*(x, y) &= n_k(x) \left[ \lambda \delta_{ki} \frac{\partial T_{lj}^*(x, y)}{\partial x_l} + G \left( \frac{\partial T_{kj}^*(x, y)}{\partial x_i} \right. \right. \\ &\quad \left. \left. + \frac{\partial T_{ij}^*(x, y)}{\partial x_k} \right) \right] \quad (5) \\ &= -\frac{G}{4\pi(1-\nu)r^3} \left\{ 3 \frac{\partial r}{\partial n} \left[ 5r_i r_j r_k n_k(x) \right. \right. \\ &\quad \left. \left. - (1-2\nu)r_j n_i(x) \right] + (1-4\nu)n_j(y)n_i(x) \right. \\ &\quad \left. - 3\nu \left[ r_i r_j n_k(y)n_k(x) + r_k r_j n_i(y)n_k(x) \right. \right. \\ &\quad \left. \left. + \delta_{ij} r_k n_k(x) \frac{\partial r}{\partial n} + r_i n_j(x) \frac{\partial r}{\partial n} \right] - (1-2\nu) \right. \\ &\quad \cdot \left[ n_i(y)n_j(x) + n_k(y)n_k(x)\delta_{ij} \right. \\ &\quad \left. \left. + 3r_i r_k n_j(y)n_k(x) \right] \right\}, \end{aligned}$$

where  $n_k(x)$  and  $n_k(y)$  represent the outward normal vectors at points  $x$  and  $y$ ;  $\lambda$  is the Lamé constant.

Collocation and eight-node quadratic are used to discretize the dual boundary integral equations. The concept of finite part integral is used to deal with the strongly singular and hypersingular integrals, and it requires that the traction and displacement derivatives should be Hölder continuous. Besides, discontinuous elements are adopted for crack modeling and edge-discontinuous elements on surfaces

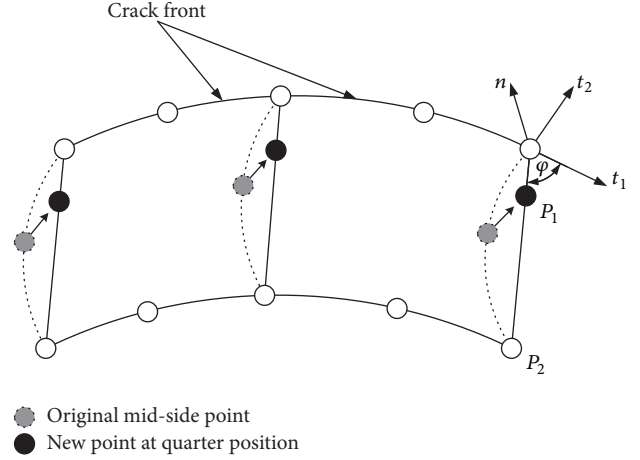


FIGURE 2: Generation of quarter point element.

are adopted for approaching the corner or intersecting the crack surface. Continuous elements are adopted on all other surfaces.

The two-point crack opening displacement formulas are used to calculate the stress intensity factors. The relative displacement of two surfaces of the crack at the collocation points  $\Delta u$  is obtained by the DBEM analysis. The SIFs at geometry point  $Q$  are given:

$$\begin{aligned} K_I^Q &= \frac{4K_I^{P_1} - K_I^{P_2}}{3} \\ K_I^P &= \frac{G}{2(1-\nu)\sqrt{\cos\varphi}} \sqrt{\frac{\pi}{2l_{PQ}}} \Delta u_n^P \\ K_{II}^Q &= \frac{4K_{II}^{P_1} - K_{II}^{P_2}}{3} \\ K_{II}^P &= \frac{G}{2(1-\nu)\sqrt{\cos\varphi}} \sqrt{\frac{\pi}{2l_{PQ}}} \Delta u_{t_2}^P \\ K_{III}^Q &= \frac{4K_{III}^{P_1} - K_{III}^{P_2}}{3} \\ K_{III}^P &= \frac{G}{2\sqrt{\cos\varphi}} \sqrt{\frac{\pi}{2l_{PQ}}} \Delta u_{t_1}^P, \end{aligned} \quad (6)$$

where  $l_{PQ}$  represents the distance between  $P$  and  $Q$ ;  $\Delta u_n$  and  $\Delta u_{t_i}$  are the normal and tangent components of  $\Delta u$  at  $P$  under the local coordinate system defined at  $Q$  (see Figure 2).

**2.2. Fast Multipole-Dual Boundary Element Method.** Considering a reference point  $O$  close to  $y$ , if a threshold of  $|\overrightarrow{Oy}| < |\overrightarrow{Ox}|$  is satisfied, the integrals in (1) and (2) can be expanded around  $O$  as

$$\begin{aligned}
\int_{S_0} U_{ij}^*(x, y) t_j(y) dS(y) &= \frac{1}{8\pi G} \\
&\cdot \sum_{n=0}^{\infty} \sum_{m=-n}^n \left( \overline{F_{ij,n,m}^S}(\vec{Ox}) M_{j,n,m}^{U1}(O) \right. \\
&+ \left. \overline{G_{i,n,m}^S}(\vec{Ox}) M_{n,m}^{U2}(O) \right) \\
\int_{S_0} T_{ij}^*(x, y) u_j(y) dS(y) &= \frac{1}{8\pi G} \\
&\cdot \sum_{n=0}^{\infty} \sum_{m=-n}^n \left( \overline{F_{ij,n,m}^S}(\vec{Ox}) M_{j,n,m}^{T1}(O) \right. \\
&+ \left. \overline{G_{i,n,m}^S}(\vec{Ox}) M_{n,m}^{T2}(O) \right) \\
\int_{S_c^+} T_{ij}^*(x, y) \Delta u_j(y) dS(y) &= \frac{1}{8\pi G} \\
&\cdot \sum_{n=0}^{\infty} \sum_{m=-n}^n \left( \overline{F_{ij,n,m}^S}(\vec{Ox}) M_{j,n,m}^{T1,S_c}(O) \right. \\
&+ \left. \overline{G_{i,n,m}^S}(\vec{Ox}) M_{n,m}^{T2,S_c}(O) \right),
\end{aligned} \tag{7}$$

where

$$\begin{aligned}
F_{ij,n,m}^S(\vec{Ox}) &= \frac{\lambda + 3G}{\lambda + 2G} \delta_{ij} S_{n,m}(\vec{Ox}) \\
&\quad - \frac{\lambda + G}{\lambda + 2G} (\vec{Ox})_j \frac{\partial}{\partial x_i} S_{n,m}(\vec{Ox}) \\
G_{i,n,m}^S(\vec{Ox}) &= \frac{\lambda + G}{\lambda + 2G} \frac{\partial}{\partial x_i} S_{n,m}(\vec{Ox}) \\
S_{n,m}(\vec{Oy}) &= (n-m)! P_n^m(\cos \theta) e^{im\phi} \frac{1}{r^{n+1}}.
\end{aligned} \tag{8}$$

$M_{j,n,m}^{U1}(O)$ ,  $M_{n,m}^{U2}(O)$ ,  $M_{j,n,m}^{T1}(O)$ ,  $M_{n,m}^{T2}(O)$ ,  $M_{j,n,m}^{T1,S_c}(O)$ , and  $M_{n,m}^{T2,S_c}(O)$  are called multipole moments presented by Wang and Yao [37];  $S_{n,m}$  is called solid spherical harmonic function [39].

Equation (3) can be expanded as

$$\begin{aligned}
\int_{S_0} D_{ij}^*(x, y) t_j(y) dS(y) &= \frac{1}{8\pi G} \\
&\cdot \sum_{n=0}^{\infty} \sum_{m=-n}^n n_k \left[ \lambda \delta_{ki} \frac{\partial \overline{F_{ij,n,m}^S}(\vec{Ox})}{\partial x_i} \right.
\end{aligned}$$

$$\begin{aligned}
&+ G \left( \frac{\partial \overline{F_{kj,n,m}^S}(\vec{Ox})}{\partial x_i} + \frac{\partial \overline{F_{ij,n,m}^S}(\vec{Ox})}{\partial x_k} \right) \\
&\cdot M_{j,n,m}^{U1}(O) + \frac{1}{8\pi G} \sum_{n=0}^{\infty} \sum_{m=-n}^n n_k \left[ \lambda \delta_{ki} \frac{\partial \overline{G_{l,n,m}^S}(\vec{Ox})}{\partial x_i} \right. \\
&+ G \left( \frac{\partial \overline{G_{k,n,m}^S}(\vec{Ox})}{\partial x_i} + \frac{\partial \overline{G_{i,n,m}^S}(\vec{Ox})}{\partial x_k} \right) \left. \right] M_{n,m}^{U2}(O)
\end{aligned}$$

$$\begin{aligned}
\int_{S_0} S_{ij}^*(x, y) u_j(y) dS(y) &= \frac{1}{8\pi G} \\
&\cdot \sum_{n=0}^{\infty} \sum_{m=-n}^n n_k \left[ \lambda \delta_{ki} \frac{\partial \overline{F_{lj,n,m}^S}(\vec{Ox})}{\partial x_i} \right. \\
&+ G \left( \frac{\partial \overline{F_{kj,n,m}^S}(\vec{Ox})}{\partial x_i} + \frac{\partial \overline{F_{ij,n,m}^S}(\vec{Ox})}{\partial x_k} \right) \\
&\cdot M_{j,n,m}^{T1}(O) + \frac{1}{8\pi G} \sum_{n=0}^{\infty} \sum_{m=-n}^n n_k \left[ \lambda \delta_{ki} \frac{\partial \overline{G_{l,n,m}^S}(\vec{Ox})}{\partial x_i} \right. \\
&+ G \left( \frac{\partial \overline{G_{k,n,m}^S}(\vec{Ox})}{\partial x_i} + \frac{\partial \overline{G_{i,n,m}^S}(\vec{Ox})}{\partial x_k} \right) \left. \right] M_{n,m}^{T2}(O)
\end{aligned}$$

$$\begin{aligned}
\int_{S_c^+} S_{ij}^*(x, y) \Delta u_j(y) dS(y) &= \frac{1}{8\pi G} \\
&\cdot \sum_{n=0}^{\infty} \sum_{m=-n}^n n_k \left[ \lambda \delta_{ki} \frac{\partial \overline{F_{lj,n,m}^S}(\vec{Ox})}{\partial x_i} \right. \\
&+ G \left( \frac{\partial \overline{F_{kj,n,m}^S}(\vec{Ox})}{\partial x_i} + \frac{\partial \overline{F_{ij,n,m}^S}(\vec{Ox})}{\partial x_k} \right) \\
&\cdot M_{j,n,m}^{T1,S_c}(O) + \frac{1}{8\pi G} \sum_{n=0}^{\infty} \sum_{m=-n}^n n_k \left[ \lambda \delta_{ki} \frac{\partial \overline{G_{l,n,m}^S}(\vec{Ox})}{\partial x_i} \right. \\
&+ G \left( \frac{\partial \overline{G_{k,n,m}^S}(\vec{Ox})}{\partial x_i} + \frac{\partial \overline{G_{i,n,m}^S}(\vec{Ox})}{\partial x_k} \right) \\
&\cdot M_{n,m}^{T2,S_c}(O) \left. \right].
\end{aligned} \tag{9}$$

Considering another reference point  $O'$  close to  $x$ , if a threshold  $|\vec{Ox}| < |\vec{O'x}|$  is satisfied, the integrals in (1), (2), and (3) can be expanded around  $O'$  in a local expansion form:

$$\begin{aligned}
\int_{S_0} U_{ij}^*(x, y) t_j(y) dS(y) &= \frac{1}{8\pi G} \\
&\cdot \sum_{n=0}^{\infty} \sum_{m=-n}^n \left( F_{ij,n,m}^R(\vec{O'x}) L_{j,n,m}^{U1}(O') \right.
\end{aligned}$$

$$\begin{aligned}
& + G_{i,n,m}^R \left( \overrightarrow{O'x} \right) L_{n,m}^{U2} (O') \\
\int_{S_0} T_{ij}^* (x, y) u_j (y) dS (y) & = \frac{1}{8\pi G} \\
& \cdot \sum_{n=0}^{\infty} \sum_{m=-n}^n \left( F_{ij,n,m}^R \left( \overrightarrow{O'x} \right) L_{j,n,m}^{T1} (O') \right. \\
& + G_{i,n,m}^R \left( \overrightarrow{O'x} \right) L_{n,m}^{T2} (O') \left. \right) \\
& \cdot L_{j,n,m}^{T1} (O') + \frac{1}{8\pi G} \\
& \cdot \sum_{n=0}^{\infty} \sum_{m=-n}^n n_k \left[ \lambda \delta_{ki} \frac{\partial G_{i,n,m}^R \left( \overrightarrow{O'x} \right)}{\partial x_l} \right. \\
& + G \left( \frac{\partial G_{k,n,m}^R \left( \overrightarrow{O'x} \right)}{\partial x_i} + \frac{\partial G_{i,n,m}^R \left( \overrightarrow{O'x} \right)}{\partial x_k} \right) \left. \right] \\
\int_{S_c^+} T_{ij}^* (x, y) \Delta u_j (y) dS (y) & = \frac{1}{8\pi G} \\
& \cdot \sum_{n=0}^{\infty} \sum_{m=-n}^n \left( F_{ij,n,m}^R \left( \overrightarrow{O'x} \right) L_{j,n,m}^{T1,S_c} (O') \right. \\
& + G_{i,n,m}^R \left( \overrightarrow{O'x} \right) L_{n,m}^{T2,S_c} (O') \left. \right) \\
& \cdot L_{n,m}^{T2} (O') \\
\int_{S_0} D_{ij}^* (x, y) t_j (y) dS (y) & = \frac{1}{8\pi G} \\
& \cdot \sum_{n=0}^{\infty} \sum_{m=-n}^n n_k \left[ \lambda \delta_{ki} \frac{\partial F_{lj,n,m}^R \left( \overrightarrow{O'x} \right)}{\partial x_l} \right. \\
& + G \left( \frac{\partial F_{kj,n,m}^R \left( \overrightarrow{O'x} \right)}{\partial x_i} + \frac{\partial F_{ij,n,m}^R \left( \overrightarrow{O'x} \right)}{\partial x_k} \right) \left. \right] \\
& \cdot L_{j,n,m}^{T1,S_c} (O') + \frac{1}{8\pi G} \\
& \cdot \sum_{n=0}^{\infty} \sum_{m=-n}^n n_k \left[ \lambda \delta_{ki} \frac{\partial G_{l,n,m}^R \left( \overrightarrow{O'x} \right)}{\partial x_l} \right. \\
& + G \left( \frac{\partial G_{k,n,m}^R \left( \overrightarrow{O'x} \right)}{\partial x_i} + \frac{\partial G_{i,n,m}^R \left( \overrightarrow{O'x} \right)}{\partial x_k} \right) \left. \right] \\
& \cdot L_{n,m}^{T2,S_c} (O'), \\
& \cdot L_{n,m}^{U1} (O') + \frac{1}{8\pi G} \\
& \cdot \sum_{n=0}^{\infty} \sum_{m=-n}^n n_k \left[ \lambda \delta_{ki} \frac{\partial G_{l,n,m}^R \left( \overrightarrow{O'x} \right)}{\partial x_l} \right. \\
& + G \left( \frac{\partial G_{k,n,m}^R \left( \overrightarrow{O'x} \right)}{\partial x_i} + \frac{\partial G_{i,n,m}^R \left( \overrightarrow{O'x} \right)}{\partial x_k} \right) \left. \right] \\
& \cdot L_{n,m}^{U2} (O') \\
\int_{S_0} S_{ij}^* (x, y) u_j (y) dS (y) & = \frac{1}{8\pi G} \\
& \cdot \sum_{n=0}^{\infty} \sum_{m=-n}^n n_k \left[ \lambda \delta_{ki} \frac{\partial F_{lj,n,m}^R \left( \overrightarrow{O'x} \right)}{\partial x_l} \right. \\
& + G \left( \frac{\partial F_{kj,n,m}^R \left( \overrightarrow{O'x} \right)}{\partial x_i} + \frac{\partial F_{ij,n,m}^R \left( \overrightarrow{O'x} \right)}{\partial x_k} \right) \left. \right]
\end{aligned} \tag{10}$$

where

$$\begin{aligned}
F_{ij,n,m}^R \left( \overrightarrow{O'x} \right) & = \frac{\lambda + 3G}{\lambda + 2G} \delta_{ij} R_{n,m} \left( \overrightarrow{O'x} \right) \\
& - \frac{\lambda + G}{\lambda + 2G} \left( \overrightarrow{O'x} \right)_j \frac{\partial}{\partial x_i} R_{n,m} \left( \overrightarrow{O'x} \right) \\
G_{i,n,m}^R \left( \overrightarrow{O'x} \right) & = \frac{\lambda + G}{\lambda + 2G} \frac{\partial}{\partial x_i} R_{n,m} \left( \overrightarrow{O'x} \right) \\
R_{n,m} \left( \overrightarrow{Oy} \right) & = \frac{1}{(n+m)!} P_n^m (\cos \theta) e^{im\phi} r^n.
\end{aligned} \tag{11}$$

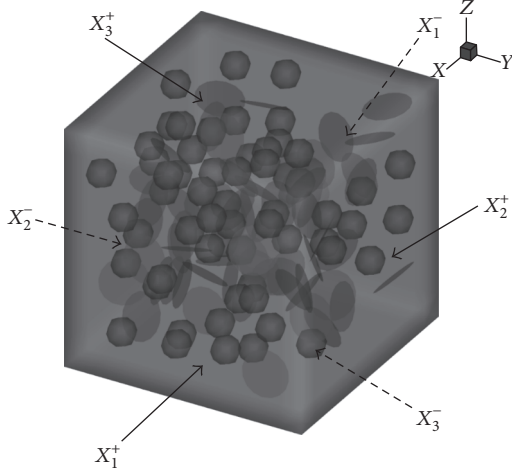


FIGURE 3: An isotropic cube containing randomly located spheroidal microvoids and circular microcracks.

$L_{j,n,m}^{U1}(O')$ ,  $L_{n,m}^{U2}(O')$ ,  $L_{j,n,m}^{T1}(O')$ ,  $L_{n,m}^{T2}(O')$ ,  $L_{j,n,m}^{T1,S_c}(O')$ , and  $L_{n,m}^{T2,S_c}(O')$  are called local moments. Instead of being evaluated directly, the local moments are derived by a linear mapping acting on the multipole moments in the FM framework.  $R_{n,m}$  is another solid spherical harmonic function.

Based on the geometry information of the boundary element, an adaptive tree is constructed. By introducing an exponential expansion, three operators, namely, the multipole to local translation, exponential to exponential translation, and exponential to local translation, are carried out recursively throughout the tree in order to obtain both the multipole moments and local moments for the tree nodes of various levels. Yoshida [39] presented the formulas of the translation operators for 3D elastostatics problems.

In the iterative solution of DBEM, GMRES is adopted. A left preconditioner matrix with block diagonal forms presented by Nishimura et al. [36] is used in this paper. Each diagonal block corresponds to one tree leaf, and entries of the block are evaluated by the collocation nodes contained in the leaf directly. In this paper, multipole, local, and exponential expansions are all of eighteenth order, and the 2-norm of the error in the FMM approximation presented by Greengard and Rokhlin [40] is less than  $10^{-6}$ . When the multipole and local expansion are of twenty-fourth order and the exponential expansion is of twenty-seventh order, the value difference of SIF [37] between this expansion order and the eighteenth order is within 0.5% of analytical value, showing the adequacy of the eighteenth order.

**2.3. 3D Microvoid and Microcrack Graphite Model Simulated Using FM-DBEM.** Considering a representative elastic solid cube with spheroidal microvoids and circular microcracks, see Figure 3. Based on previous circular and elliptical microcrack studies in BEM [41], this paper inherits most of the symbols and characters from previous research.

The formula for the constitutive relation of elastic problem without body force is

$$\sigma_{ij} = C_{ijkl}\varepsilon_{kl}, \quad (12)$$

where  $\varepsilon_{kl}$  is the elastic strain,  $C_{ijkl}$  is the elastic coefficients, and the elastic strain field  $\varepsilon_{kl}$  is defined by

$$\varepsilon_{kl} = \frac{1}{2}(u_{i,j} + u_{j,i}), \quad (13)$$

where  $u_i$  is the elastic displacement.

The boundary conditions are given by mechanical boundary conditions:

$$t_i = \sigma_{ij}n_j = \bar{t}_i \quad (14)$$

$$u_i = \bar{u}_i,$$

where  $t_i$  is the surface traction and  $n_i$  is the component of the unit outward normal vector of the surface.

The side length of the cubic is  $L$ . For the spheroidal microvoid in this solid, if its radius is  $R_v$ , then its volume is defined as  $V_v = 4/3\pi R_v^3$ . If the number of spheroidal microvoids is  $N_v$ , the spheroidal microvoid density parameter in the solid is defined by  $\omega_1 = 4\pi R_v^3 N_v / 3L^3$ . Similarly, the radius of the circular microcrack is  $R_c$  and the number of elliptical microcracks is  $N_c$ . Following Budiansky and O'Connell [42] and Kachanov [43], the microcrack density parameter is defined as  $\omega_2 = R_c^3 N_c / L^3$ . Young's modulus  $E_0$  and Poisson's ratio  $\nu_0$  of the matrix are 9.8 Gpa and 0.14, respectively.

The weakened solid model shows similar behaviors as an isotropic elastic medium when the amount of microvoids and microcracks is large enough. The procedure can be used to obtain the effective Young's modulus  $E^{\text{eff}}$ . The average strain and stress in the solid are defined by

$$\begin{aligned} \bar{\varepsilon}_{ij} &= \frac{1}{V} \int_V \varepsilon_{ij} dV \\ \bar{\sigma}_{ij} &= \frac{1}{V} \int_V \sigma_{ij} dV. \end{aligned} \quad (15)$$

When different boundary conditions are applied, the material constants and effective moduli can be obtained.

Applying the boundary condition as in

$$\begin{aligned} \text{Surface } x_1^+: \quad & \bar{u}_1 = u_0, \\ & \bar{t}_2 = \bar{t}_3 = 0 \end{aligned} \quad (u_0 \neq 0)$$

$$\begin{aligned} \text{Surface } x_1^-: \quad & \bar{u}_1 = 0, \\ & \bar{t}_2 = \bar{t}_3 = 0 \end{aligned}$$

$$\text{Surface } x_2^+: \quad \bar{t}_1 = \bar{t}_2 = \bar{t}_3 = 0$$

$$\begin{aligned} \text{Surface } x_2^-: \quad & \bar{t}_1 = 0, \\ & \bar{u}_2 = 0, \end{aligned}$$

$$\bar{t}_3 = 0$$

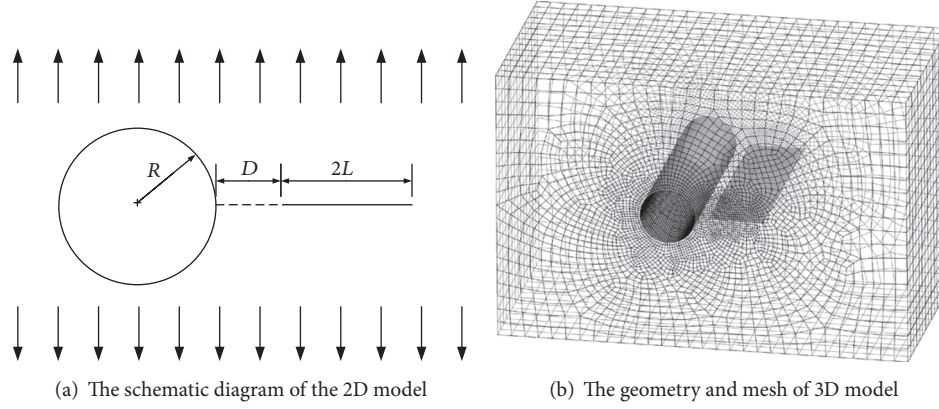


FIGURE 4: The schematic diagram of a crack aligned along the center of the hole.

$$\begin{aligned}
 \text{Surface } x_3^+ : \quad & \bar{t}_1 = \bar{t}_2 = \bar{t}_3 = 0 \\
 \text{Surface } x_3^- : \quad & \bar{t}_1 = \bar{t}_2 = 0, \\
 & \bar{u}_3 = 0
 \end{aligned} \tag{16}$$

then effective Young's modulus in direction  $X_1$  can be obtained by

$$E_1^{\text{eff}} = \frac{\overline{\sigma_{11}}}{\overline{\varepsilon_{11}}} \tag{17}$$

Applying the boundary condition as in

$$\begin{aligned}
 \text{Surface } x_1^+ : \quad & \bar{u}_1 = u_0, \\
 & \bar{t}_2 = \bar{t}_3 = 0 \\
 & (u_0 \neq 0) \\
 \text{Surface } x_1^- : \quad & \bar{u}_1 = 0, \\
 & \bar{t}_2 = \bar{t}_3 = 0 \\
 \text{Surface } x_2^+ : \quad & \bar{t}_1 = 0, \\
 & \bar{u}_2 = u_0, \\
 & \bar{t}_3 = 0 \\
 \text{Surface } x_2^- : \quad & \bar{t}_1 = 0, \\
 & \bar{u}_2 = 0, \\
 & \bar{t}_3 = 0 \\
 \text{Surface } x_3^+ : \quad & \bar{t}_1 = \bar{t}_2 = 0, \\
 & \bar{u}_3 = u_0 \\
 \text{Surface } x_3^- : \quad & \bar{t}_1 = \bar{t}_2 = 0, \\
 & \bar{u}_3 = 0.
 \end{aligned} \tag{18}$$

we can obtain

$$K^{\text{eff}} = \frac{\overline{\sigma_{11}} + \overline{\sigma_{22}} + \overline{\sigma_{33}}}{3(\overline{\varepsilon_{11}} + \overline{\varepsilon_{22}} + \overline{\varepsilon_{33}})}. \tag{19}$$

**2.4. A Computational Test of Microcrack and Microvoid Interaction under Plane Strain State.** The current literature on the theoretical analysis of the microcrack-microvoid interaction model is based on the 2D model [8, 11, 44, 45], and there is less research on the theoretical solution of the 3D microcrack-microvoid interaction. Therefore, the test algorithm in this section adopts a model with a large thickness to approximate the 2D plane strain state.

The 2D crack and hole model and 3D meshing schematic diagram of BEM are shown in Figures 4 and 6. In Figure 4, the centers of the single crack and the single hole are located on the same horizontal axis, and there is balanced vertical tensile stress in the up and down direction. The radius of the 2D circular hole is  $R$ , the crack length is  $2L$ ,  $R = L$ , and the vertical distance from the crack tip to the hole's margin is  $D$ . In the simulated model, a large external matrix is established. The thickness of the circular hole and the crack is much larger than the sizes of the hole and the crack. The midsection in the model can be equaled to the approximate plane strain state.

Figure 5 shows the comparison between the simulation result of this test model and the 2D theoretical approximate solution. The crack tips' SIFs from FM-DBEM conform to the theoretical approximate solution, especially when distance  $D$  is small. The crack tip to the left of the hole enlarges fast with the decrease of distance  $D$ . The tip's stress intensity factor  $K_1$  shall become 2-3 times larger than when there is no hole and but only the single crack.

Moreover, if we spin the crack in the above model with an  $\alpha$  angle, a 2D inclined crack and hole model is formed. In Figure 6, the hole's radius is  $R$ , the crack's length maintains  $2L$ , and their distance is  $D_1 = 2.2R$ , which is equivalent to  $D = 1.2R$  in the above model.

Figure 7 shows the comparison between the simulation result and the 2D theoretical approximate solution. In this inclined crack and hole model, because of the existence of crack's inclined angle, its tip's SIFs  $K_1$  and  $K_2$  shall change.

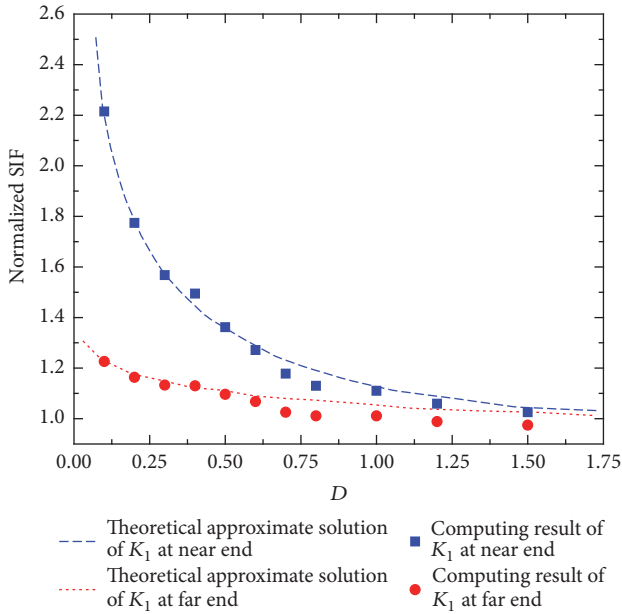


FIGURE 5: The comparison between the result from the 3D model in Figure 4 and the 2D theoretical solution.

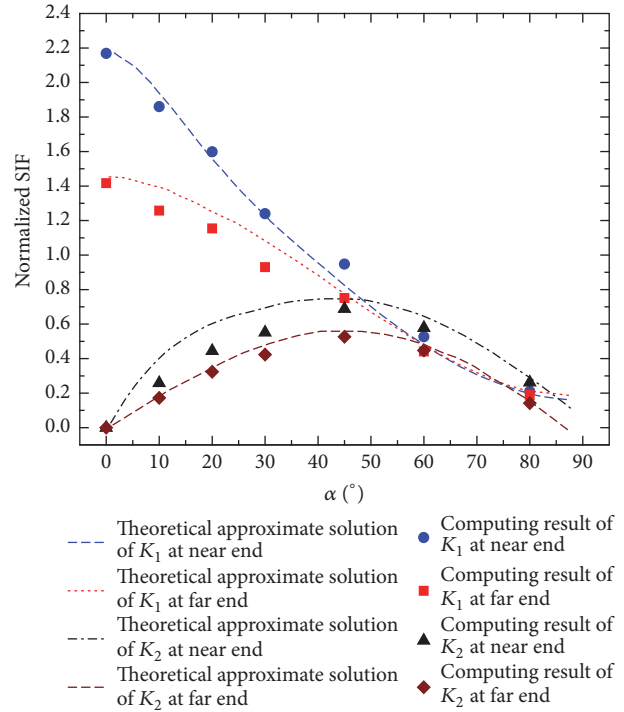


FIGURE 7: The comparison between the result from the 3D model in Figure 6 and the 2D theoretical solution.

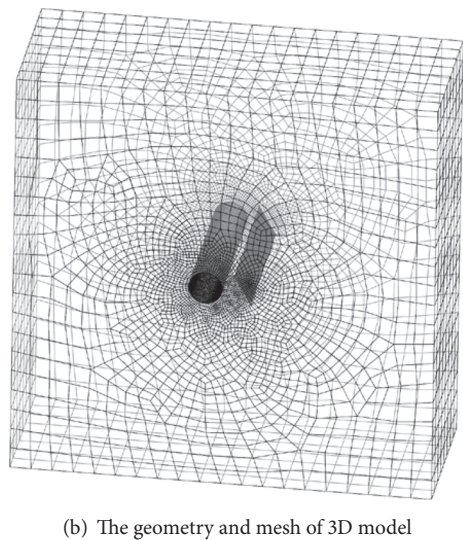
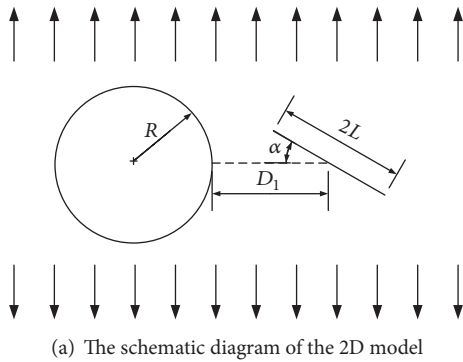


FIGURE 6: The schematic diagram of the inclined crack and hole model.

When we keep the distance between centers of the crack and the hole to  $D_1$  and change the crack's inclined angle  $\alpha$  from  $0^\circ$  to  $90^\circ$ , the  $K_1$  value shall decrease to 0 with the increase in the angle and there is no apparent difference between the two  $K_2$  values. Besides, they both increase first and then decrease. When the loading direction is vertical to the crack's plane, the  $K_1$  value is the largest and the crack is most likely to start cracking. When the loading direction is parallel to the crack's plane, there is basically no stress concentration.

### 3. Results and Discussion

3.1. *The Simulation of Graphite Model Containing a Large Number of Randomly Distributed Microcracks and Microvoids.* Related research on graphite's microstructure has shown that there are obvious microvoids and microcracks in nuclear graphite's microstructure, especially the oxidized graphite material.

In this section, we study the model where there are a large number of microvoids and microcracks in the elastic matrix. The influence of microvoids' and microcracks' distribution, size, density, and so forth on the performance of the overall damage model is studied. A graphite model containing 50 randomly distributed microcracks and 50 randomly distributed microvoids is built, as in Figure 8. By changing the sizes of microvoids and microcracks, the damage model's effective elastic modulus decreases almost linearly as  $\omega_1$  and  $\omega_2$  increase. Figures 9 and 10 show the relations between the normalized effective moduli  $E^{eff}/E_0$ ,  $K^{eff}/K_0$ , and  $\omega_2$ , with  $\omega_1$  fixed.

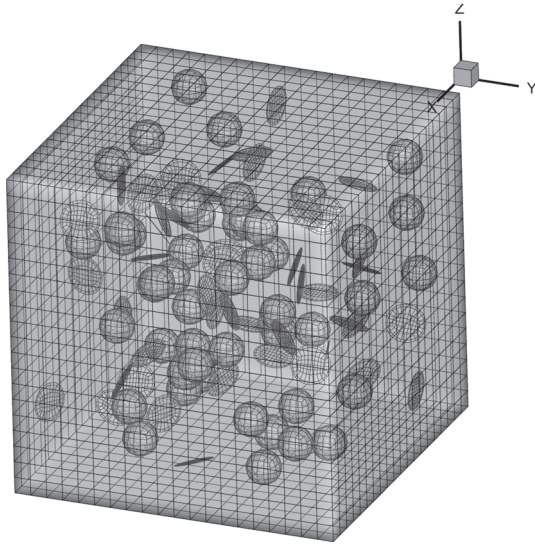


FIGURE 8: A global translucent view of element distribution in a cube containing randomly distributed microcracks and microvoids.

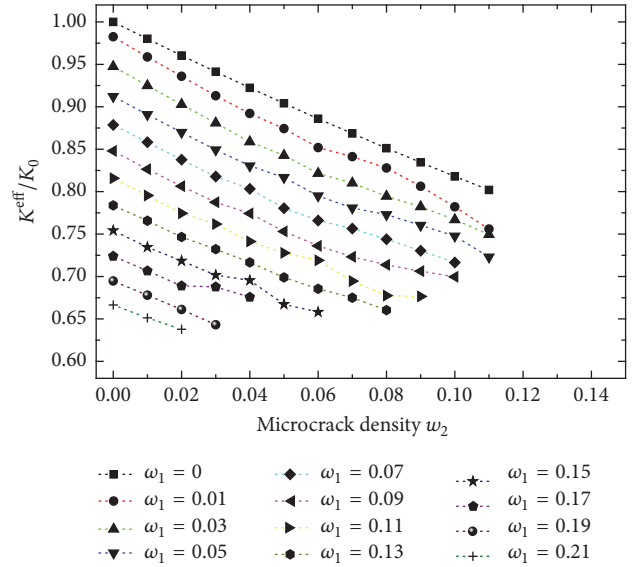


FIGURE 10:  $K^{eff}/K_0$  versus the microcrack's and microvoid's density.

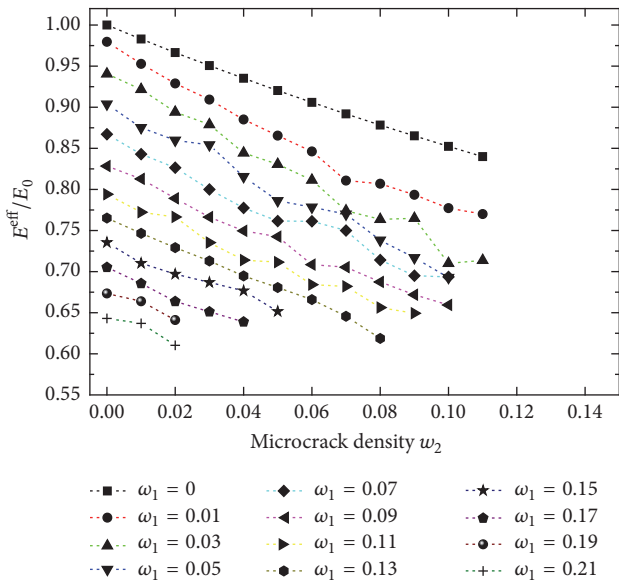


FIGURE 9:  $E^{eff}/E_0$  versus the microcrack's and microvoid's density.

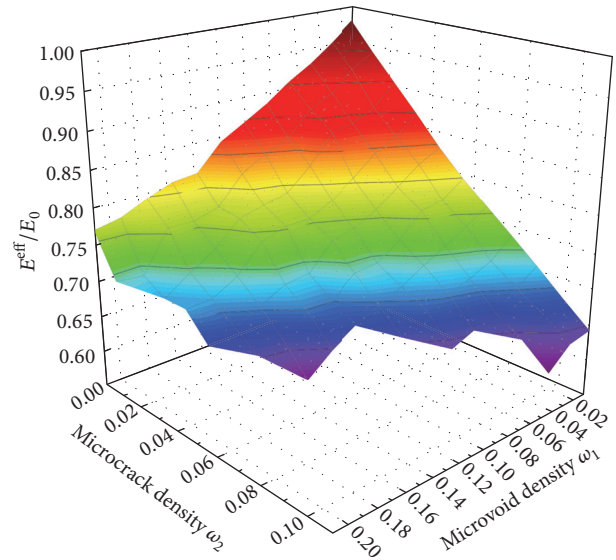


FIGURE 11:  $E^{eff}/E_0$  versus the microcrack's and microvoid's density.

From this simulation, we can see that, under different microvoid densities, the two effective moduli  $E^{eff}$  and  $K^{eff}$  decrease linearly with the increase in the microcrack's density.

Figures 11 and 12 show  $\omega_1$  and  $\omega_2$ 's combined influence on the microvoid and microcrack model. The two independent variables on the horizontal axes are  $\omega_1$  and  $\omega_2$ , while two normalized effective moduli  $E^{eff}/E_0$  and  $K^{eff}/K_0$  are on the vertical axis. Both figures show that, due to the different definitions of the microcrack and the microvoid, the decreasing rate of  $E^{eff}$  and  $K^{eff}$  with the microcrack density increase is about twice as fast as that with microvoid density increase. In other words, under the same density increase, the increase

in microcrack density shall make the whole model's moduli decrease faster.

3.2. The Simulation of Graphite Model Containing Microcracks and Growing Microvoids. On the basis of the simulated analysis of the graphite model containing randomly distributed microcracks and microvoids, the simulation of graphite model with the growing microvoids is conducted in order to study the effect of the microvoid's growth on the existing microcrack during the graphite's oxidation process.

The model in Figure 13 also contains 50 microcracks and 50 microvoids with random locations and directions. The microcrack keeps its geometrical parameters during the

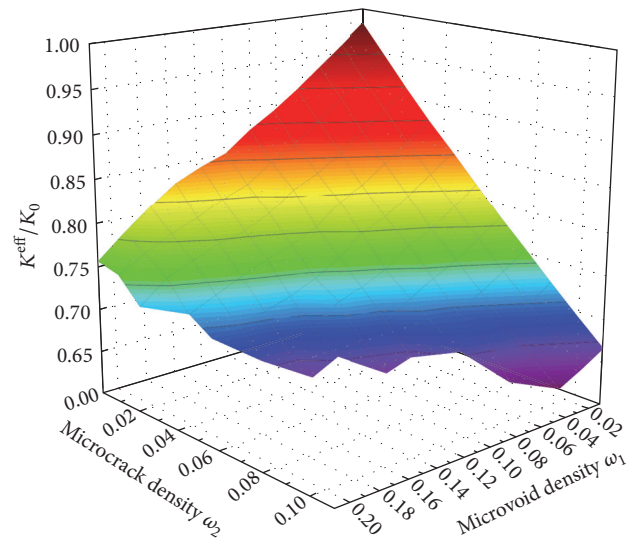


FIGURE 12:  $K^{\text{eff}}/K_0$  versus the microcrack's and microvoid's density.

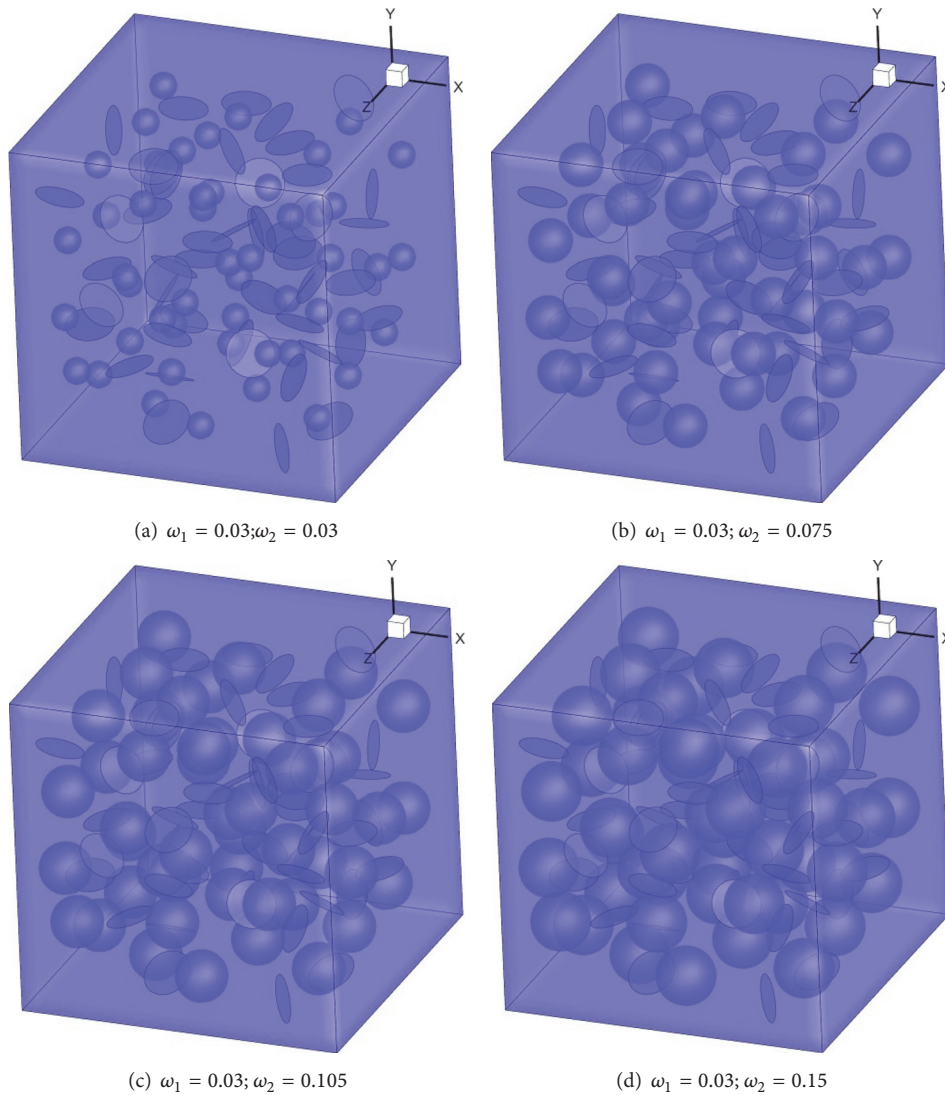


FIGURE 13: A model with a fixed microcrack density and growing microvoids.

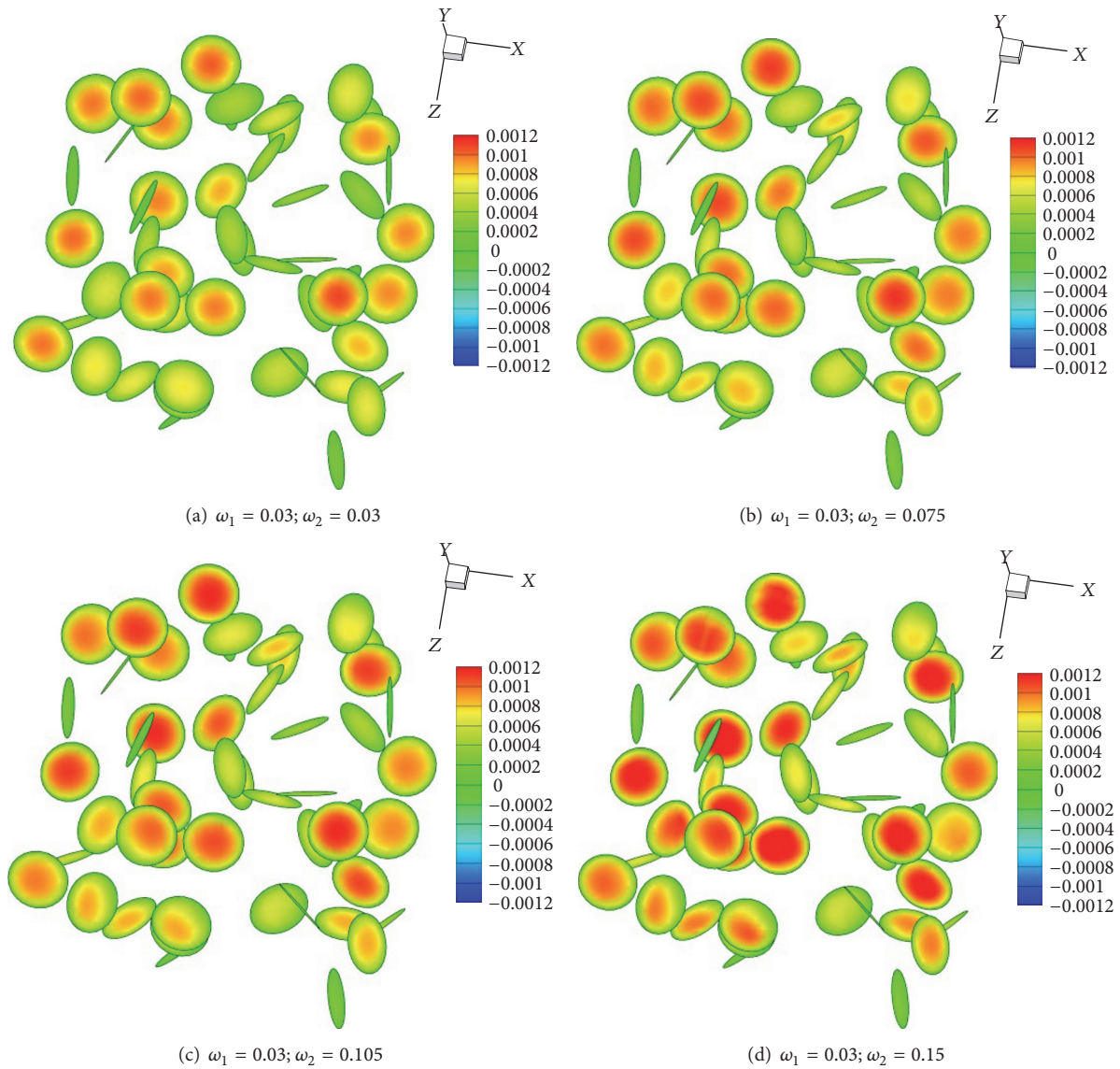


FIGURE 14: The microcracks' opening displacement.

microvoid's size change. The microvoid's density  $\omega_1$  and the microcrack's density  $\omega_2$  are shown in Figure 13.

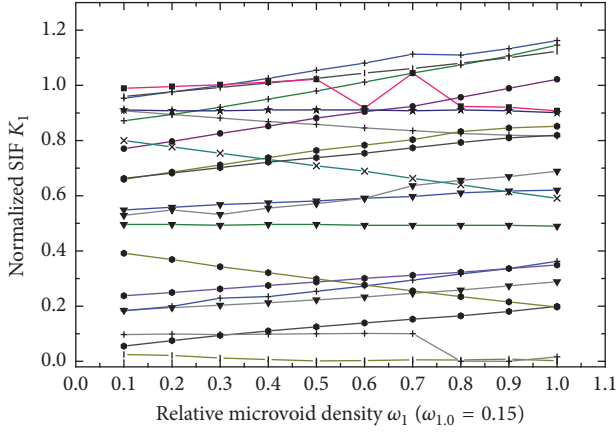
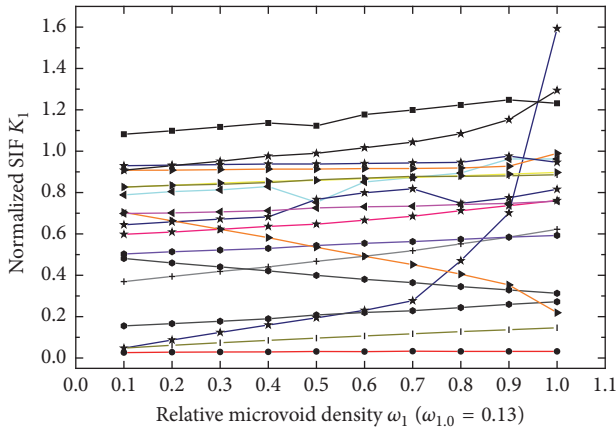
In order to study the effect of growing microvoids on the microcracks' opening displacement and the tips' SIFs under the same force boundary conditions, we simulate models with different  $\omega_2$ . All microcracks' opening displacement is drawn in Figure 14. With the microvoid's growth, most microcracks' opening distances are gradually increasing, which means that with the increase in the microvoid's size the microcrack bears more local stress concentration and is easier to be damaged, especially those microcracks with relatively coincident normal direction and loading direction. Their opening distances show a more apparent increasing tendency.

In this series of models, we partly select every microcrack tip node's stress intensity factor  $K_1$  randomly. Figures 15 and 16 show that the value of  $K_1$  changes with the increase in the

microvoid's size.  $\omega_{1,0}$  represents the maximal value of  $\omega_1$  in a certain simulation.

From the above models, it is clear that under single axis tension, the microcrack tips'  $K_1$  values are located in the range between 0 and 1 basically, which is also a result of the randomness of microcrack directions and microvoid distributions. With the increase in the microvoid's size, the changing tendency of microcrack tip nodes' SIFs also shows a large randomness: some microcrack tips' SIFs shall increase in a relatively large scale because the distance between the microcrack and the microvoid decreases and the microcrack plane is vertical to the loading direction; some microcrack tips' SIFs shall decrease or change randomly; many relatively normal microcrack tips'  $K_1$  values shall remain or slowly increase.

If we average all microcrack tip nodes'  $K_1$  values in the models with different microvoid sizes, the  $K_1$  values versus

FIGURE 15:  $K_I$  versus relative microvoid density when  $\omega_2 = 0.02$ .FIGURE 16:  $K_I$  versus relative microvoid density when  $\omega_2 = 0.06$ .

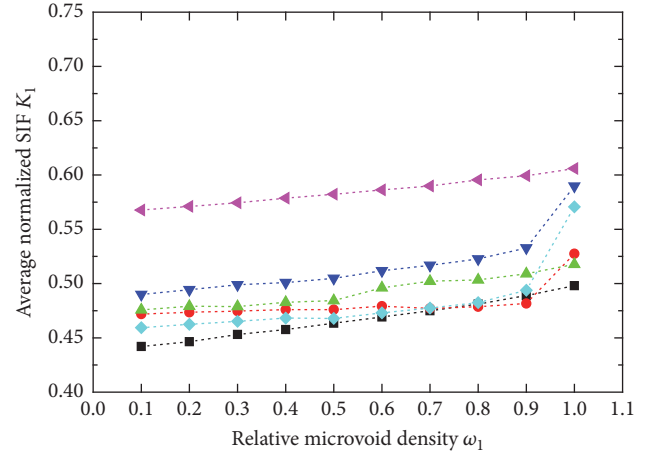
the increase in microvoids' sizes are shown in Figure 17. This figure shows that the microcrack tips' SIFs slowly increase with the microvoid growing.

#### 4. Conclusions

This paper adopted the 3D FM-DBEM to simulate the graphite model containing a large quantity of microvoids and microcracks. By the simulation under the approximate 3D equivalent plane strain state and the comparison to several existing theoretical approximate solutions, we have ensured the effectiveness and accurateness of the solver and proved that a result with high precision can be guaranteed by using this FM-DBEM to simulate the structural model containing microvoids and microcracks.

There is an obvious strengthening effect at the microcrack tip nearest the microvoid's edge, and the SIFs of the microcrack tips increase rapidly with the decrease in the distance between the microcrack and the microvoid, whereas the microcrack tips far from the microvoids' edge are influenced slightly and the SIFs remain with the original values.

Through the 3D simulation of the graphite model containing a large number of microvoids and microcracks, we



-■-  $\omega_{1,0} = 0.15, \omega_2 = 0.02$     -▼-  $\omega_{1,0} = 0.13, \omega_2 = 0.05$   
 -●-  $\omega_{1,0} = 0.15, \omega_2 = 0.03$     -◆-  $\omega_{1,0} = 0.13, \omega_2 = 0.06$   
 -▲-  $\omega_{1,0} = 0.14, \omega_2 = 0.04$     -▽-  $\omega_{1,0} = 0.11, \omega_2 = 0.07$

FIGURE 17: Average  $K_I$  versus relative microvoid density.

find that the whole model's two effective moduli  $E^{\text{eff}}$  and  $K^{\text{eff}}$  both decrease with the increase in the two microstructures' density. The decreasing rate of  $E^{\text{eff}}$  and  $K^{\text{eff}}$  with microcrack density increasing is about twice as fast as that with microvoid density. Meanwhile, with the growth of the microvoid, the microcrack shall bear more local stress concentration under the same load condition; therefore, there shall be larger crack opening displacement and the graphite is more likely to be damaged.

#### Conflicts of Interest

The authors declare that there are no conflicts of interest regarding the publication of this paper.

#### Acknowledgments

This research is supported by Tsinghua University Initiative Scientific Research Program (Grant no. 20131089332). Additional funds were also provided by the National Natural Science Foundation of China (Grant no. 11002080) and the China Scholarship Council.

#### References

- [1] Z. Wu, D. Lin, and D. Zhong, "The design features of the HTR-10," *Nuclear Engineering and Design*, vol. 218, pp. 25–32, 2002.
- [2] Z. Zhang, J. Liu, S. He, Z. Zhang, and S. Yu, "Structural design of ceramic internals of HTR-10," *Nuclear Engineering and Design*, vol. 218, no. 1-3, pp. 123–136, 2002.
- [3] M. L. Kachanov, "A microcrack model of rock inelasticity part I: Frictional sliding on microcracks," *Mechanics of Materials*, vol. 1, no. 1, pp. 19–27, 1982.
- [4] M. L. Kachanov, "A microcrack model of rock inelasticity part II: Propagation of microcracks," *Mechanics of Materials*, vol. 1, no. 1, pp. 29–41, 1982.

- [5] J. W. Ju, "On two-dimensional self-consistent micromechanical damage models for brittle solids," *International Journal of Solids and Structures*, vol. 27, no. 2, pp. 227–258, 1991.
- [6] K. X. Hu and A. Chandra, "A fracture-mechanics approach to modeling strength degradation in ceramic grinding processes," *Journal of Engineering for Industry-Transactions of the ASME*, vol. 115, no. 1, pp. 73–84, 1993.
- [7] Y. Huang, K. X. Hu, and A. Chandra, "Damage evaluation of solids containing dilute inclusions and microcracks," AME Report 92-30, 1992.
- [8] K. X. Hu, A. Chandra, and Y. Huang, "Multiple void-crack interaction," *International Journal of Solids and Structures*, vol. 30, no. 11, pp. 1473–1489, 1993.
- [9] M. Isida and H. Igawa, "Analysis of a zig-zag array of circular holes in an infinite solid under uniaxial tension," *International Journal of Solids and Structures*, vol. 27, no. 7, pp. 849–864, 1991.
- [10] C. Yi-Zhou, "General case of multiple crack problems in an infinite plate," *Engineering Fracture Mechanics*, vol. 20, no. 4, pp. 591–597, 1984.
- [11] Y. Z. Chen, "A special boundary-element formulation for multiple-circular-hole problems in an infinite plate," *Computer Methods in Applied Mechanics and Engineering*, vol. 50, no. 3, pp. 263–273, 1985.
- [12] S.-X. Gong and H. Horii, "General solution to the problem of microcracks near the tip of a main crack," *Journal of the Mechanics and Physics of Solids*, vol. 37, no. 1, pp. 27–46, 1989.
- [13] P. J. Hacker, G. B. Neighbour, and B. McEnaney, "Coefficient of thermal expansion of nuclear graphite with increasing thermal oxidation," *Journal of Physics D: Applied Physics*, vol. 33, no. 8, pp. 991–998, 2000.
- [14] L. Delannay, P. Yan, J. F. B. Payne, and N. Tzelepi, "Predictions of inter-granular cracking and dimensional changes of irradiated polycrystalline graphite under plane strain," *Computational Materials Science*, vol. 87, pp. 129–137, 2014.
- [15] P. Yan, L. Delannay, J. F. B. Payne, and A. Tzelepi, "Micromechanistic modelling of the polycrystalline response of graphite under temperature changes and irradiation," *Carbon*, vol. 96, pp. 827–835, 2016.
- [16] A. K. Soh, "An improved method for determining free boundary stresses," *The Journal of Strain Analysis for Engineering Design*, vol. 27, no. 2, pp. 93–99, 1992.
- [17] A. K. Soh, "Development of special finite elements for free boundaries," *International Journal of Solids and Structures*, vol. 36, no. 6, pp. 899–917, 1999.
- [18] R. Piltner, "Special finite elements with holes and internal cracks," *International Journal for Numerical Methods in Engineering*, vol. 21, no. 8, pp. 1471–1485, 1985.
- [19] A. K. Soh and Z. F. Long, "A high precision element with a central circular hole," *International Journal of Solids and Structures*, vol. 36, no. 35, pp. 5485–5497, 1999.
- [20] T. A. Cruse, "BIE fracture mechanics analysis: 25 years of developments," *Computational Mechanics*, vol. 18, no. 1, pp. 1–11, 1996.
- [21] T. A. Cruse, "Boundary Element Analysis in Computational Fracture Mechanics," *Mechanics Computational Mechanics*, vol. 55, no. 192, pp. 799–806, 1988.
- [22] A. Portela, M. H. Aliabadi, and D. P. Rooke, "The dual boundary element method: Effective implementation for crack problems," *International Journal for Numerical Methods in Engineering*, vol. 33, no. 6, pp. 1269–1287, 1992.
- [23] A. Portela, M. H. Aliabadi, and D. P. Rooke, "Dual boundary element incremental analysis of crack propagation," *Computers and Structures*, vol. 46, no. 2, pp. 237–247, 1993.
- [24] Y. Mi and M. H. Aliabadi, "Dual boundary element method for three-dimensional fracture mechanics analysis," *Engineering Analysis with Boundary Elements*, vol. 10, no. 2, pp. 161–171, 1992.
- [25] A. P. Cislino and M. H. Aliabadi, "Three-dimensional BEM analysis for fatigue crack growth in welded components," *International Journal of Pressure Vessels and Piping*, vol. 70, no. 2, pp. 135–144, 1997.
- [26] A. J. Wilde and M. H. Aliabadi, "3-D dual BEM formulation for the analysis of crack growth," *Computational Mechanics*, vol. 23, no. 3, pp. 250–257, 1999.
- [27] Y. Fu, K. J. Klimkowski, G. J. Rodin et al., "A fast solution method for three-dimensional many-particle problems of linear elasticity," *International Journal for Numerical Methods in Engineering*, vol. 42, no. 7, pp. 1215–1229, 1998.
- [28] V. Popov and H. Power, "O(N) Taylor series multipole boundary element method for three-dimensional elasticity problems," *Engineering Analysis with Boundary Elements*, vol. 25, no. 1, pp. 7–18, 2001.
- [29] T. Takahashi, N. Nishimura, and S. Kobayashi, "A fast BIEM for three-dimensional elastodynamics in time domain," *Engineering Analysis with Boundary Elements*, vol. 27, no. 5, pp. 491–506, 2003.
- [30] Y. J. Liu, N. Nishimura, Y. Otani, T. Takahashi, X. L. Chen, and H. Munakata, "A fast boundary element method for the analysis of fiber-reinforced composites based on a rigid-inclusion model," *Journal of Applied Mechanics, Transactions ASME*, vol. 72, no. 1, pp. 115–128, 2005.
- [31] V. Rokhlin, "Rapid solution of integral equations of classical potential theory," *Journal of Computational Physics*, vol. 60, no. 2, pp. 187–207, 1985.
- [32] I. Benedetti, M. H. Aliabadi, and G. Davi, "A fast 3D dual boundary element method based on hierarchical matrices," *International Journal of Solids and Structures*, vol. 45, no. 7-8, pp. 2355–2376, 2008.
- [33] I. Benedetti, A. Milazzo, and M. H. Aliabadi, "A fast dual boundary element method for 3D anisotropic crack problems," *International Journal for Numerical Methods in Engineering*, vol. 80, no. 10, pp. 1356–1378, 2009.
- [34] I. Benedetti and M. H. Aliabadi, "A fast hierarchical dual boundary element method for three-dimensional elastodynamic crack problems," *International Journal for Numerical Methods in Engineering*, vol. 84, no. 9, pp. 1038–1067, 2010.
- [35] Y.-S. Lai and G. J. Rodin, "Fast boundary element method for three-dimensional solids containing many cracks," *Engineering Analysis with Boundary Elements*, vol. 27, no. 8, pp. 845–852, 2003.
- [36] N. Nishimura, K.-I. Yoshida, and S. Kobayashi, "A fast multipole boundary integral equation method for crack problems in 3D," *Engineering Analysis with Boundary Elements*, vol. 23, no. 1, pp. 97–105, 1999.
- [37] H. T. Wang and Z. H. Yao, "A new fast multipole boundary element method for large scale analysis of mechanical properties in 3D particle-reinforced composites," *Cmes-Computer Modeling in Engineering & Sciences*, vol. 7, no. 1, pp. 85–95, 2005.
- [38] H. D. Lu, "FM-BEM Simulation of 3-D Microvoid and Microcrack Graphite Models with Python and Abaqus/CAE Pre-Processing," *2016 ANS Winter Meeting and Nuclear Technology Expo*, 2016.

- [39] K. I. Yoshida, *Applications of Fast Multipole Method to Boundary Integral Equation Method*, Dept. of Global Environment Eng., Kyoto Univ, 2001.
- [40] L. Greengard and V. Rokhlin, "A new version of the fast multipole method for the Laplace equation in three dimensions," in *Acta numerica*, 1997, vol. 6 of *Acta Numer.*, pp. 229–269, Cambridge Univ. Press, Cambridge, 1997.
- [41] H. Wang, H. Wang, L. Jin, and Z. Yao, "Numerical determination on effective elastic moduli of 3-D solid with a large number of microcracks using FM-DBEM," *CMES - Computer Modeling in Engineering and Sciences*, vol. 94, no. 6, pp. 529–552, 2013.
- [42] B. Budiansky and R. J. O'connell, "Elastic moduli of a cracked solid," *International Journal of Solids and Structures*, vol. 12, no. 2, pp. 81–97, 1976.
- [43] M. Kachanov, "Effective elastic properties of cracked solids: critical review of some basic concepts," *Applied Mechanics Reviews*, vol. 45, no. 8, pp. 304–335, 1992.
- [44] C. Atkinson, "Interaction between a crack and an inclusion," *International Journal of Engineering Science*, vol. 10, no. 2, pp. 127–136, 1972.
- [45] Y. K. Cheung and Y. Z. Chen, "Solutions of branch crack problems in plane elasticity by using a new integral equation approach," *Engineering Fracture Mechanics*, vol. 28, no. 1, pp. 31–41, 1987.

## Research Article

# Three Design Basis Accidents' Analysis on the HTR-10GT

Minggang Lang, Heng Xie, and Yujie Dong

*Institute of Nuclear and New Energy Technology of Tsinghua University, Collaborative Innovation Center of Advanced Nuclear Energy Technology, The Key Laboratory of Advanced Reactor Engineering and Safety, Ministry of Education, Beijing, China*

Correspondence should be addressed to Yujie Dong; [dongyj@tsinghua.edu.cn](mailto:dongyj@tsinghua.edu.cn)

Received 23 December 2016; Revised 14 April 2017; Accepted 7 May 2017; Published 5 June 2017

Academic Editor: Hidemasa Yamano

Copyright © 2017 Minggang Lang et al. This is an open access article distributed under the Creative Commons Attribution License, which permits unrestricted use, distribution, and reproduction in any medium, provided the original work is properly cited.

The study simulated the design basis accidents (DBAs) sequences of the HTR-10GT core with THERMIX. When a DBA happens, the protection system will receive a scram signal which shall lead to active measures to shut down the reactor following it. In the paper, three typical DBA cases were studied. They include an accident induced by station blackout, a case caused by the withdrawal of one control rod out of the core by a mistake, and a case resulting from an earthquake, respectively. The simulation results illustrate that the fuel peak temperatures in the core during these accidents are 1066°C, 1201°C and 1067°C, respectively. It is shown that the HTR-10GT has a good safety characteristic.

## 1. Introduction

Since Lohnert and Reutler proposed the concept of modular high-temperature gas-cooled reactor (HTGR) in the end of the 1970s, various countries have put a lot of attention on development of modular HTGR for its high degree of passive safety and the potential to provide high-temperature fluid for process heat applications [1, 2]. Several reactors of various power levels have been constructed in the 20th century, such as AVR and THTR-300 in Germany, Peach Bottom (as the smaller test reactor) and Fort St. Vrain (as the demo plant) in USA, HTTR (30 MW thermal) in Japan, and HTR-10 (the 10 MW high-temperature gas-cooled test reactor) in China. At present, all HTGRs except for HTTR and HTR-10 are in decommissioning since many years. China is designing and constructing its commercial demonstration HTGR plant which is called HTR-PM (high-temperature gas-cooled reactor-pebble-bed module) now.

China's HTR-10 was a pebble-bed modular test HTR, which was designed, constructed, and operated by Institute of Nuclear and New Energy Technology (INET) of Tsinghua University. In December of 2000, the HTR-10 reached criticality for the first time and in January of 2003 it achieved full power operation with a thermal power output of 10 MW and a coolant outlet temperature of 700°C [3]. As time goes on, many planned commissioning tests have been performed

on HTR-10 to test the performance of the spherical fuel elements and to demonstrate its passive safety characteristics. The designing codes used for the HTR-10 were also validated against the test results at the same time [4–7].

The HTR with a gas turbine in direct cycle mode promises higher electricity generation efficiency. To verify the technology, INET first plans to raise the outlet temperature to 750°C in the HTR-10 core with the same sphere fuels and to replace the steam generator with a gas turbine power conversion unit. The new designed reactor is named HTR-10GT, and its main operating parameters are listed in Table 1.

The preliminary scheme of the HTR-10GT is to replace the steam generator with a helium gas turbine, while keeping pressure boundary of the primary loop system and the layout of the reactor pressure vessel (RPV) unchanged. Figure 1 shows the layout and schematic of the HTR-10GT. The key parameters of the protection system of the HTR-10GT are similar to those of the HTR-10, but the parameters related to the secondary loop, such as flow rate of feedwater and steam fraction, do not apply. The limiting temperature of helium flow passing through the core inlet and outlet is increased by 50°C and 80°C, respectively. In addition, the ratio between flow rates of the primary loop and the secondary loop in the HTR-10 is changed to a normalized value between the flow rate of the primary loop and the power of the gas turbine in the HTR-10GT. The detailed parameters of the

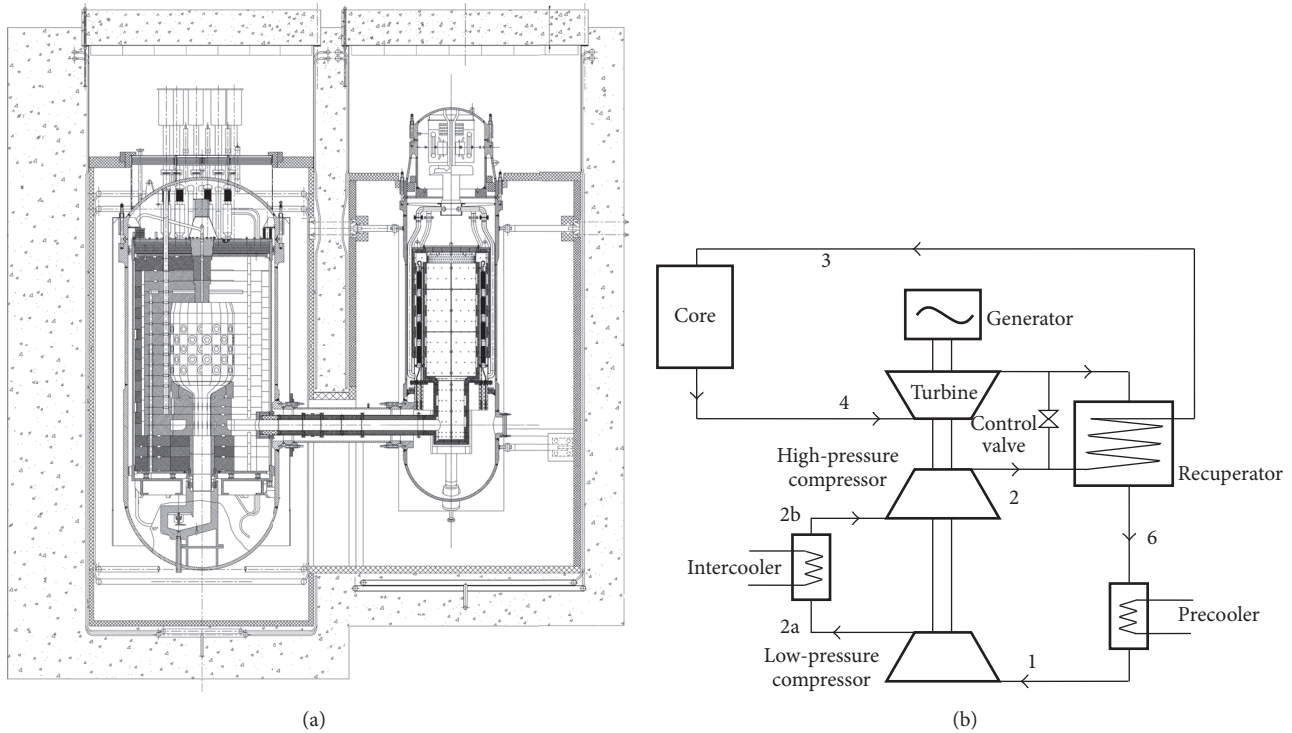


FIGURE 1: (a) Layout of HTR-10GT. (b) Schematic of HTR-10GT.

TABLE 1: Main operation parameters of HTR-10GT in comparison with HTR-10 and HTR-PM.

Core	HTR-10GT	HTR-10	HTR-PM
Thermal power, MW	10	10	250/unit
Coolant inlet/outlet temperature, °C	330/750	250/700	250/750
System pressure, MPa	1.59	3.0	7.0
Helium flow rate, kg/s	4.56	4.32	96

protection system of the HTR-10GT are illustrated in Table 2. The operating temperatures of the components contained in reactor pressure vessel and hot gas duct rise as the helium temperatures at the core inlet and outlet increase. However, these temperatures remain well below the components design temperatures of the HTR-10, as a large safety margin has been taken into account.

The passive safety characteristics of the HTR-10 have been approved by the National Nuclear Safety Administration (NNSA) of China, after analysis of design basis accidents (DBAs) and beyond design basis accidents (BDBAs) was completed [8]. However, because of the differences between the main operating parameters of the HTR-10 and HTR-10GT, China's nuclear regulations require that new safety analysis of the HTR-10GT be performed at operating and accidental states and certified. The paper studied three DBA cases induced by station blackout, by one control rod withdrawal out of the core by mistake, and by earthquake. Transient analysis of the three cases was performed using the THERMIX code, and safety characteristics of the HTR-10GT

are discussed in detail in the paper. The results will be meaningful to the HTR-PM, as the helium temperature at the core outlet of the HTR-PM is similar to the HTR-10GT.

## 2. Analysis Tools and Models

The design basis accidents of HTR-10 were analysed with THERMIX, a thermal hydraulic code system developed by KFA-Jülich (now FZJ) of Germany. The THERMIX code has been applied for the simulation of the helium circulator trip ATWS test. THERMIX has been validated and verified against data from experiments performed at KFA [9], benchmark calculations for the GT-MHR [10], and extensive experimental programs carried out on the THTR-300 [11]. At present, the code is under further validation in INET through data of the tests on the HTR-10 to improve the design methodology for future HTGRs. In the study, THERMIX was used to analyse the DBAs of the HTR-10GT.

The general code structure of THERMIX adopts a two-dimensional cylindrical geometry and consists of a general-purpose steady-state or transient heat conduction code and a quasi-steady-state convection code. The code system consists of a two-dimensional transient solid temperature model (Thermix), a quasi-stationary gas flow model (Konvek), a primary loop model (Kismet), a point-neutron kinetics model (Kinex), and a graphite corrosion model. THERMIX is able to analyse the thermal hydraulic performance of pebble-bed HTGRs under normal operation and accident conditions, including the pebble-bed reactor core as well as the primary loop, the helium blower, and the steam generator. Brief descriptions on the four modules are introduced in the

TABLE 2: Parameters of protection system.

Protection parameters	Triggering value	Triggering error	Delay time
Neutron flux of full power level	$\geq 120\%$	3%	1 s
Neutron flux of middle power level	$\geq 200\%$	10%	1–30 s
Reactor period	$\leq 20$ s	6%	1 s
Temperature of hot helium	$\geq 790^\circ\text{C}$	$10^\circ\text{C}$	8 s
Temperature of cold helium	$\geq 345^\circ\text{C}$	$4^\circ\text{C}$	8 s
Relative variation of the primary flow rate	$\leq 0.75$ or $\geq 1.3$	3%	1 s
Absolute sliding rate of the primary loop pressure	$\geq .03$ MPa/min	0.053 MPa/h	1 s
Negative relative varying of the turbine power	$\geq 25\%$ /min	3%	1 s

following part and some detailed description of the equations used in the modules can be seen in [12].

**2.1. Neutron Kinetics Module.** Nuclear physical characteristics are predicted by a conventional point kinetics model with six groups of delayed neutrons in this module. Fission power is estimated through a balance of feedback reactivity and external reactivity. The former reactivity results from temperature variation of fuel, moderator, and reflector as well as change of xenon concentration, while the latter one is induced by movement of control rods or external inserted reactivity such as water ingress. In addition, decay heat is calculated by kinetic equations of the fission products.

**2.2. Solid Heat Conduction Module.** The conduction module includes a two-dimensional transient temperature model for solid materials and a one-dimensional transient temperature model for spherical fuel elements. Time-dependent general heat conduction equation is solved with temperature-dependent material properties in this module. In the simulation, a two-dimensional rotation symmetrical model in  $r$ ,  $z$  geometry is established for heat conduction of the HTR-10GT. The computational model consists of 35 radial and 61 axial mesh points, as shown in Figure 2. It describes most of the HTR-10GT components such as pebble-bed core, graphite reflectors, carbon bricks, and reactor pressure vessel with 44 different material regions.

**2.3. Gas Convection Module.** A quasi-stationary gas flow model is used in the convection module to simulate the complex flow conditions inside a pebble-bed HTGR. This module solves steady-state continuity, momentum, and energy equations of gas in the reactor, coupled with a given time-dependent temperature profile of solid structures. The computational model covers main flow passages in the HTR-10GT, for example, reactor core, cold helium channels, cold and hot helium plenums, and control rod channels.

**2.4. Primary Circuit Module.** In this module, pressure, temperature, and mass flow rate of coolant in the primary loop are calculated. A quasi-stationary model, consisting of steady-state continuity, momentum, and energy equations of fluid, is used to predict the above-mentioned parameters. The calculating model of the HTR-10GT primary loop contains

hot gas duct, power conversion unit in steam generator vessel, and so forth.

### 3. Description of the Accidents

All transients of the HTR-10GT, including DBA and BDBA, have been described in the “final safety analysis report” by the INET. Three typical accidents will be presented to illustrate the safety characteristics of the HTR-10GT in the following. In accident analyses, we always assume conservatively that the first scram signal fails to work. The protection system will scram the reactor when the second protective parameter reaches its limiting value.

The simulation study comprises three DBA cases of the HTR-10GT. The first one is induced by station blackout. Once a station blackout occurs, the helium blower and the steam turbine will shut down immediately, leading to a loss of coolant flow and a decrease of heat exchange from the primary loop. As the core continues to be heated up, the fuel temperature will rise and the pressure and temperature in the primary loop will increase, too. The core power declines due to negative temperature feedback. As soon as the offsite power is lost, the control rods drop automatically by gravity. On the other hand, the protection system would detect a scram signal when the pressure, the flow rate of the primary loop, or the turbine power reaches specified values.

The second case is induced by a control rod withdrawal out of core by mistake. The positive reactivity inserted is determined by location of the control rod in the reflectors and operating state. The performed analysis is for typical operating conditions with full rated power of an equilibrium core and with reactivity of a control rod less than 1%. The total reactivity inserted by a control rod withdrawal is shown in Figure 3. In this case, the protection system receives three scram signals: too high neutron flux in the relative power level referenced to the rated power ( $\geq 1.23$ ), too high helium temperature at core outlet ( $\geq 800^\circ\text{C}$ ), and too large absolute sliding rate of the primary system pressure ( $\geq 0.031$  MPa/min).

The last case calculated is caused by earthquake. When an earthquake occurs in the HTR-10GT, the compactness of the pebble bed will increase due to violent shaking, which will lead to a decreasing neutron leakage rate. There is also a relative shift between the top of the active core and the control rods in the reflectors. This results in a positive

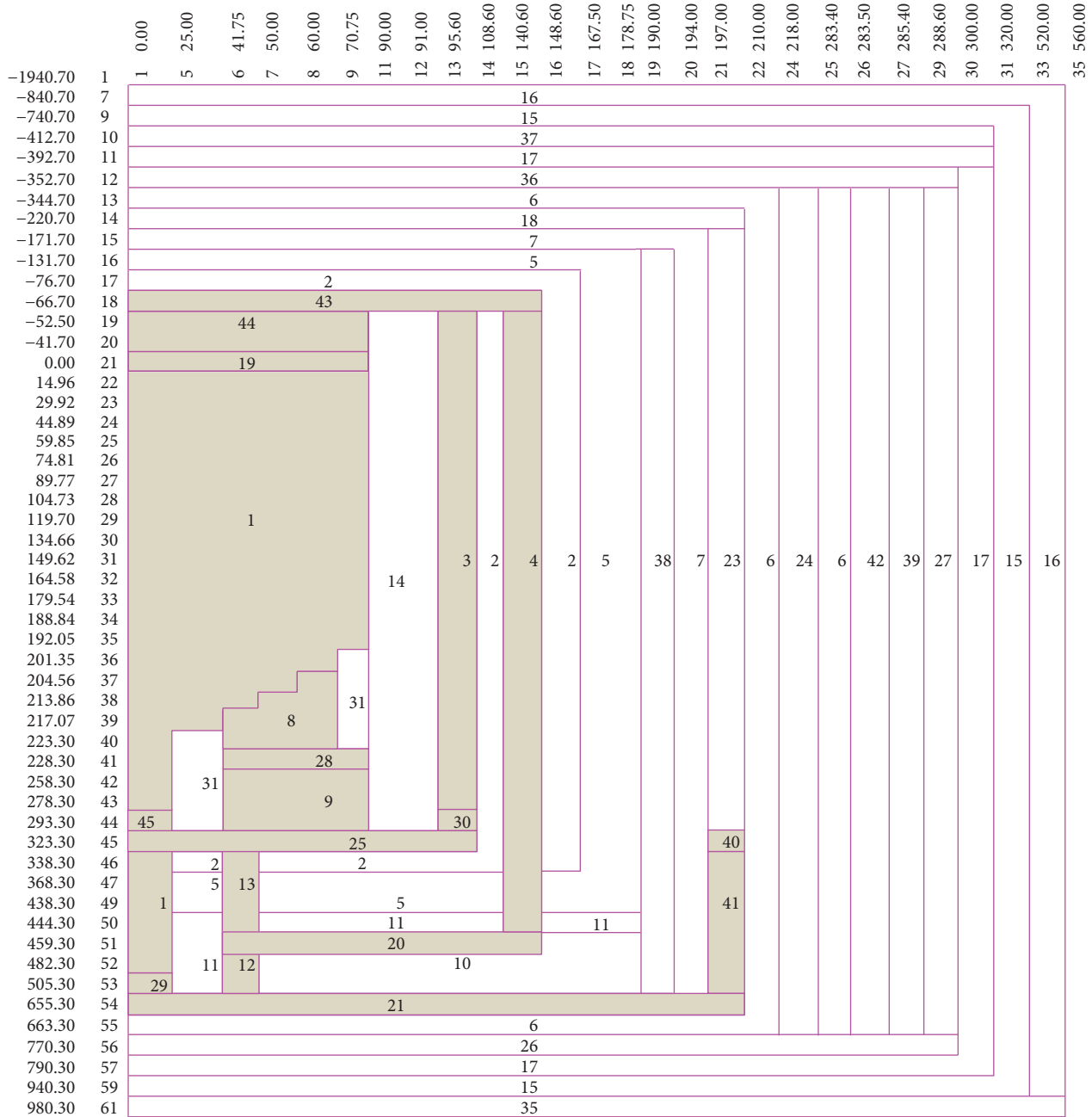


FIGURE 2: THERMIX model of the HTR-10GT core. 1, core; 2, 14, and 31, side reflectors without channels; 3, side reflectors within control rod channels; 4, side reflectors within cooling channels; 5, carbon brick; 6, reactor pressure vessel; 7, core shell; 8, top part of the bottom reflector within flow channels; 9, lower part of the bottom reflector within flow channels; 10 and 11, steel support in the core bottom; 12, annulus passage of cold helium at the core bottom; 13, leakage inside the metal internals; 15, concrete; 16, side boundary of flow; 17, thermal insulation; 18, top helium cavity in the RPV; 19, core inlet cavity; 20, flow passages around the core bottom; 21, bottom helium cavity in RPV; 23, helium gap between the RPV and the core shell; 24, side air cavity outside the RPV; 25, outlet cavity at the core bottom; 26, bottom air cavity outside the RPV; 27, side part of the reactor cavity; 28, cavity inside the bottom reflectors; 29, inlet throttle of the refueling pipe; 30, outlet throttle of control rod channels; 35, bottom boundary of flow; 36, top air cavity outside the RPV; 37, air cavity in the top of the reactor cavity; 38, side helium gap inside the core shell; 39, cavity cooling system; 40, helium inlet channel in the core shell; 41, annular flow passage inside the core shell; 42, air gap outside the thermal insulation of the reactor cavity; 43, helium cavity in the top reflectors; 44, helium passage in the top reflectors.

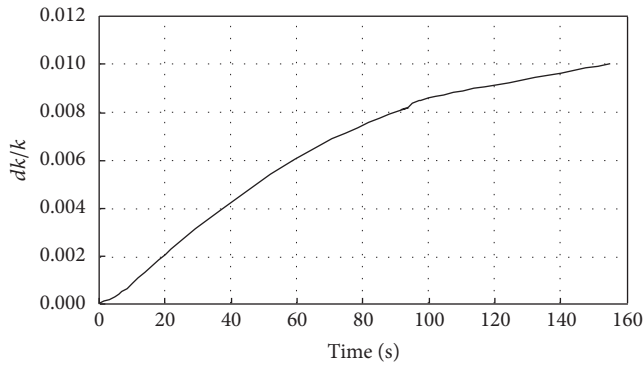


FIGURE 3: Reactivity inserted by a control rod withdrawal.

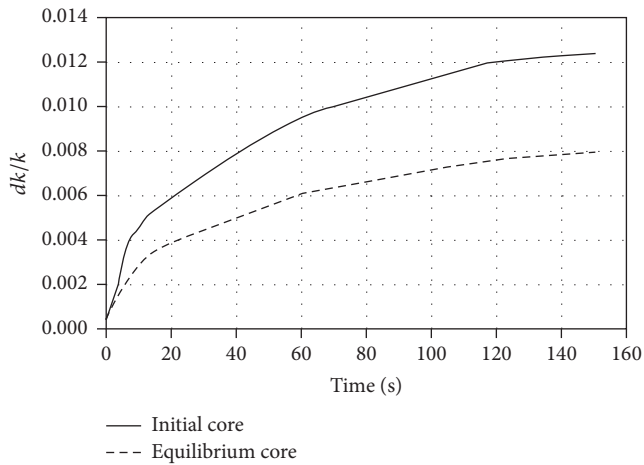


FIGURE 4: Reactivity inserted by an earthquake.

reactivity insertion. The horizontal acceleration at the surface of the earth induced by an earthquake is  $2.0 \text{ m/s}^2$  during normal operation. The shaking experiments on pebble beds in Germany showed that horizontal forces caused by an earthquake would result in a densification of the pebble-bed core, reaching a peak after 3~4 minutes as earthquake forces continue. The initial packing fraction of a randomly composed pebble-bed core is 0.61. If the surface horizontal acceleration increases from  $2.0 \text{ m/s}^2$  to  $10 \text{ m/s}^2$ , the peak packing fraction of the bed increases from 0.615 to 0.64, as specified in the HTR-10 final safety analysis report. In our analysis, a conservative hypothesis is taken demonstrating that the packing fraction of the HTR-10GT core increases during the earthquake from 0.61 to 0.64—the maximum value attainable in a random packing of spheres. The total reactivity inserted by an earthquake is 1.24% and 0.788%, calculated by VSOP, for an initial core and an equilibrium core, respectively, which can be seen in Figure 4. The time-dependent variation of reactivity in the plot will be used in the analysis. After an earthquake, the HTR-10GT protection system will receive two scram signals: too high neutron flux in relative power level referenced to the rated power ( $\geq 1.23$ ) and too short reactor period ( $\leq 20 \text{ s}$ ).

The accident detection and protection system of the HTR-10GT is triggered by scram signals. As mentioned above, the

first scram signal is assumed to be skipped in the analysis. After the second scram signal, the protection system takes actions to shut down the reactor, which include dropping the control rods into the reflectors by gravity, shutting down the primary circuit blower, stopping the gas turbine, and isolating the primary circuit. The accidents mentioned above are classified to level II accidents [8], which may happen once a year, and the reactor can restore normal operation after shutdown and taking some measures. During these accidents, the reactor can scram and residual decay heat will be removed from the reactor vessel by the reactor cavity cooling system through heat transfer in form of conduction, convection, and radiation among in-vessel structures and the core.

#### 4. Hypothesis and Calculating Conditions

The spherical fuel elements containing coated TRISO particles can effectively retain all relevant radioactive fission products up to the temperature of  $1620^\circ\text{C}$ . In the first phase of the HTR-10 project, the coated particle fuel was experimentally proven to keep its integrity and retain the radioactive fission products effectively up to  $1250^\circ\text{C}$ . So the maximum temperature of fuel elements is set as  $1230^\circ\text{C}$  under all accident conditions for HTR-10. For the HTR-10GT, the peak fuel temperature permitted in accidents is set to be  $1230^\circ\text{C}$  in the beginning. After more tests on spherical fuel elements, the setting point of fuel peak temperature in accidents is increased to  $1620^\circ\text{C}$ , which is used in the HTR-PM and the second phase of the HTR-10GT designing.

The study analyses typical operating cases of the HTR-10GT in full power for the three accidents consequences. The assumed conditions when the accidents occur are the following:

- (i) The core operating power is the rated power with an addition of 5% due to measuring error.
- (ii) The cooling flow passing through the core is 86% of the rated pump flow.
- (iii) The core is in an equilibrium state and the total reactivity inserted by a control rod withdrawal is 1%.
- (iv) One control rod in the reflector is drawn up at a speed of  $1 \text{ cm/s}$ .
- (v) The first scram signal is skipped and the protecting system takes actions following the second signal.
- (vi) The worst effect of instruments measuring error is considered when scram signals are triggered.
- (vii) Longest time delay before the protecting measures action is considered.
- (viii) When the reactor scrams, the flow rate in the primary loop decreases to  $0.0 \text{ kg/s}$  in 0.25 seconds and the gas turbine is bypassed in 0.25 s (which is an extremely conservative condition).

#### 5. Computational Results

For the HTR-10GT, the initial core and the equilibrium core have different physical characteristics. In fact, there is no truly

TABLE 3: Accident sequence of an initial core induced by station blackout.

Events	HTR-10GT	HTR-10
Station blackout occurs, helium blower and turbine shut down	0.0 s	0.0 s
Absolute sliding rate of the turbine power $\geq 28\%/min$	20.0	20.0
Absolute sliding rate of the system pressure $\geq 0.031 MPa/min$	38.2 s	35.8 s
Protection system takes actions to scram	39.2 s	36.8 s
Time at which fuel temperature reaches a peak	31.2 s	0.0 s
Peak fuel temperature	1066°C	1033°C
Time at which system pressure reaches a peak	13.2 s	78.8 s
Peak system pressure	1.6 Mpa	3.18 MPa

TABLE 4: Accident sequence of an equilibrium core induced by station blackout.

Events	HTR-10GT	HTR-10
Station blackout occurs, the helium blower and turbine shut down	0.0 s	0.0 s
Absolute sliding rate of the turbine power $\geq 28\%/min$	20.0 s	20.0 s
Absolute sliding rate of system pressure $\geq 0.031 MPa/min$	66.9 s	36.0 s
Protection system takes actions to scram	67.9 s	37.0 s
Time at which fuel temperature reached a peak	68.0 s	0.0 s
Peak fuel temperature	989.0	944°C
Time at which system pressure reached a peak	15.2 s	78.7 s
Peak system pressure	1.6 MPa	3.18 MPa

initial core for the HTR-10GT, as the HTR-10 will have been operating for years. However, the three cases studied here are based on an initial core similar to that of the HTR-10 in order to better compare the accident consequences. Of course, the cases for an equilibrium core were simulated, too.

*5.1. Accident Induced by Station Blackout.* Tables 3 and 4 indicate the key events following a station blackout of the HTR-10GT. The accident consequences of the HTR-10 induced by station blackout are compared in Tables 3 and 4, too. Figures 5–10 show the plots of important parameters of HTR-10GT in accident for both the startup core and the equilibrium core, which consist of reactor power, peak fuel temperature, average fuel temperature, temperature feedback reactivity, total reactivity, and primary system pressure.

Once a station blackout occurs, the helium blower and the gas turbine would shut down quickly. 20 seconds later, the first scram signal “absolute sliding rate of the turbine power” reaches its setting value of 28%/min, but it is skipped.

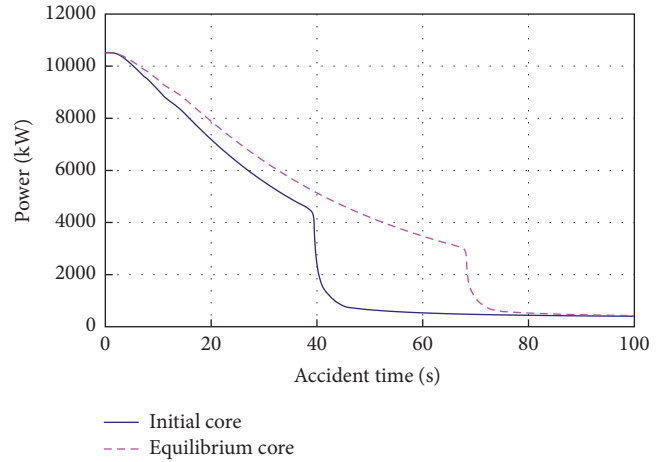


FIGURE 5: Power in station blackout accident of the HTR-10GT.

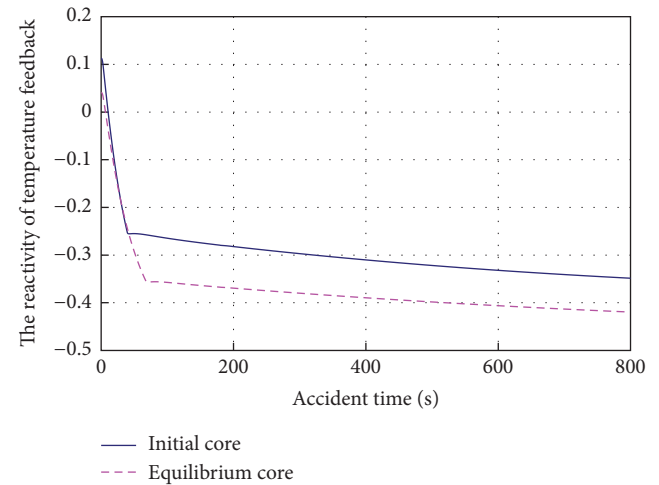


FIGURE 6: Temperature feedback reactivity in station blackout accident of the HTR-10GT.

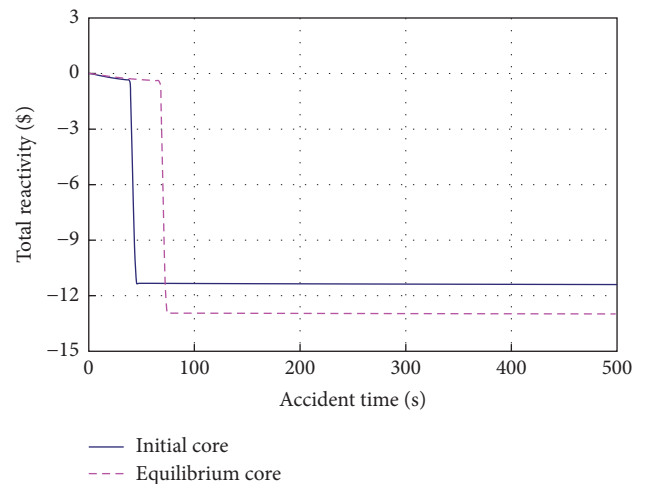


FIGURE 7: Total reactivity in station blackout accident of the HTR-10GT.

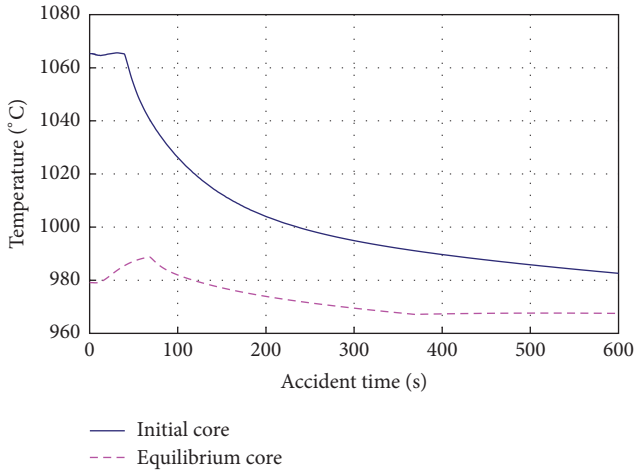


FIGURE 8: Peak fuel temperature in station blackout accident of the HTR-10GT.

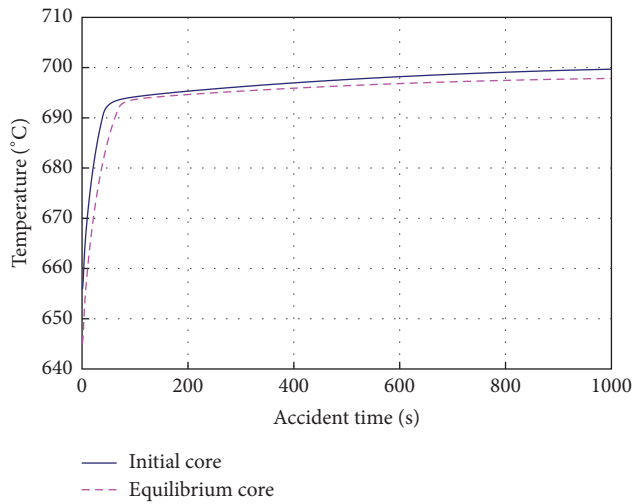


FIGURE 9: Fuel average temperature in station blackout accident of the HTR-10GT.

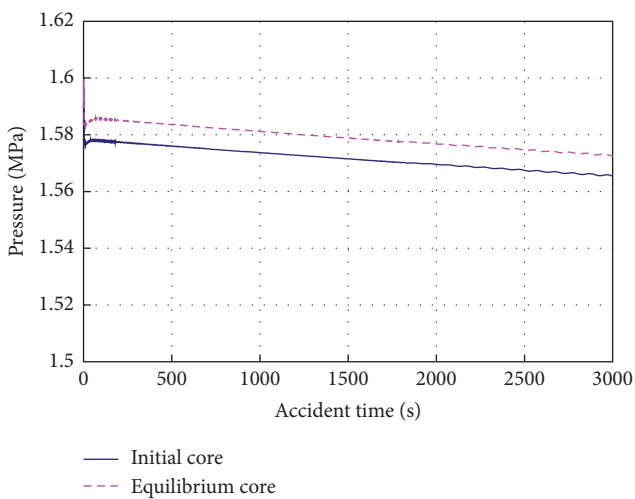


FIGURE 10: System pressure in station blackout accident of the HTR-10GT.

TABLE 5: Accident sequence of an initial core induced by a control rod withdrawal by mistake.

Events	HTR-10GT	HTR-10
A control rod begins to withdraw out of the reflectors at a speed of 1 cm/s	0.0 s	0.0 s
Neutron flux of power level $\geq 1.23$	8.85 s	11.3 s
Core power reaches a peak	37.8 s (24.3 MW)	36.4 s (23.5 MW)
Hot helium temperature exceeds its setting point	80.1 s (800°C)	84.9 s (750°C)
Time at which control rods begin to drop	88.1 s	92.9 s
Fuel temperature reaches a peak	83.5 s (1201°C)	93.3 s (1170°C)
Time at which the accident rod is withdrawn out of the reflectors	155.0 s	155.0 s

The second signal is detected after 38.2 s and 66.9 s for the initial core and the equilibrium core, respectively. Then the protection system takes actions to scram and the HTR-10GT shuts down immediately. The peak fuel temperature in the accident is calculated to be 1066°C and 989°C for the startup core and the equilibrium core, respectively. For the HTR-10, the corresponding temperatures are 1033°C and 944°C. The peak fuel temperature of the HTR-10GT is about 45°C higher than that of the HTR-10. The difference between the peak fuel temperatures of the HTR-10GT and HTR-10 is consistent with the difference in the steady-state core outlet temperatures.

From Table 3, we can see that the second scram signal “absolute sliding rate of the system pressure” of the HTR-10GT reaches its setting value later than the HTR-10. This is due to the fact that the system pressure of the HTR-10GT is lower than the HTR-10. Figure 10 shows a plot of the transient system pressures during the accident. From the corresponding plots of the temperature feedback reactivity and the total reactivity in Figures 6 and 7, one can see that the second signal is detected much later for an equilibrium core than an initial core. The shutdown in an initial core takes place earlier and its power decreases more quickly than in an equilibrium core, as shown in Figure 5. Figures 8 and 9 depict the peak and average fuel temperatures. As the peak fuel temperature is lower than 1230°C, it can be concluded that the HTR-10GT remains in a safe condition in a station blackout accident scenario.

5.2. Accident Induced by a Control Rod Withdrawal out of the Reflectors. Tables 5 and 6 show the important events since a control rod is withdrawn out of the reflectors at a speed of 1 cm/s by mistake. The accident consequences of the HTR-10 are also compared in Tables 5 and 6. Figures 11–18 depict plots of important parameters of the HTR-10GT in accident for both an initial core and an equilibrium core, which consist of reactor power, peak fuel temperature, average fuel temperature, temperature feedback reactivity,

TABLE 6: Accident sequence of an equilibrium core induced by a control rod withdrawal by mistake.

Events	HTR-10GT	HTR-10
A control rod begins to withdraw out of the reflectors at a speed of 1 cm/s	0.0 s	0.0 s
Neutron flux of power level $\geq 1.23$	10.5 s	10.5 s
Core power reaches a peak	39.4 s (31.1 MW)	37.9 s (30.3 MW)
Hot helium temperature exceeds its setting point	54.9 s (800°C)	54.9 s (750°C)
Time at which control rods begin to drop	62.9 s	62.9 s
Fuel temperature reaches a peak	55.7 s (1066°C)	64.0 s (1041°C)
Time at which the accident rod is withdrawn out of the reflectors	155.0 s	155.0 s

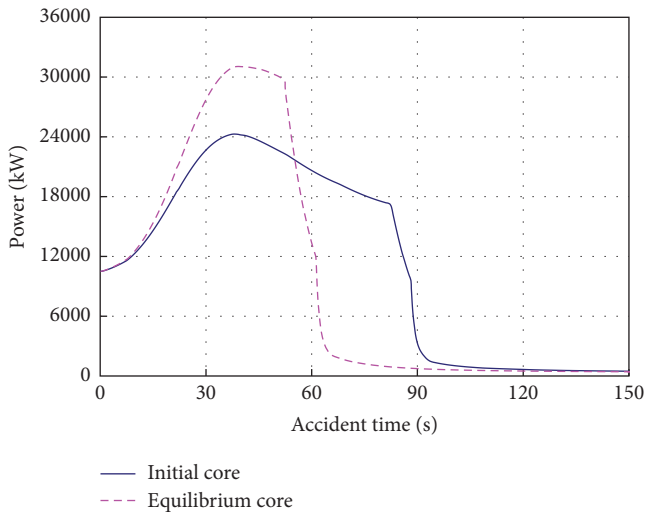


FIGURE 11: Core power in a control rod withdrawal accident of the HTR-10GT.

total reactivity, flow rate of primary loop, system pressure, and helium temperature at core inlet and outlet.

When a control rod is withdrawn out of the reflectors in 155 seconds by mistake, core power increases quickly due to a positive reactivity inserted. The reactivity worth of one control rod of the HTR-10GR is shown in Figure 3, which is larger than that of the HTR-10. As core power increases, the first scram signal triggered by high flux is ignored in the simulation. The second signal triggered by high helium temperature occurs about half a minute later. Then all control rods begin to drop due to the shutting down actions taken by the protection system, which leads to the HTR-10GT shutting down safely.

From Table 5, we can see that neutron flux of the HTR-10GT core increases more quickly than that of the HTR-10, because the absolute value of its feedback coefficient of reactivity caused by temperature change becomes smaller as

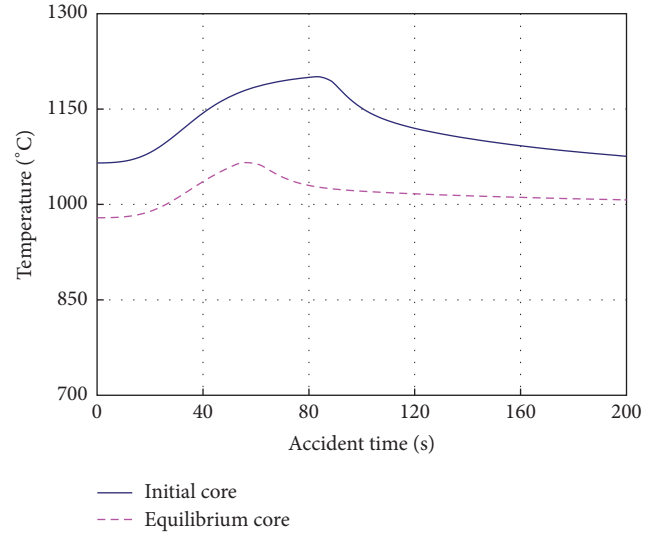


FIGURE 12: Peak fuel temperature in a control rod withdrawal accident of the HTR-10GT.

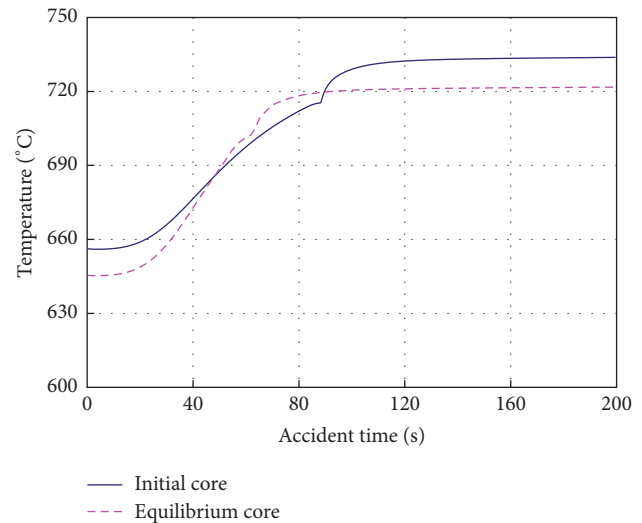


FIGURE 13: Fuel average temperature in a control rod withdrawal accident of the HTR-10GT.

the core operating temperature increases. Thus, for the HTR-10GT, the power increases rapidly and the peak power is higher, which leads to an earlier scram signal for the second time. The peak fuel temperature increases in the accident by about 30°C, which is smaller than 50°C—the helium temperature increased at the core outlet.

The plot in Figure 11 shows that the power of an initial core in accident increases slower than an equilibrium core, so the peak power is lower, which results in a higher peak fuel temperature. This is due to the fact that the initial core has a small value of absolute temperature reactivity feedback coefficient, as shown in Figure 17. One can also see in Figure 12 that the initial core of the HTR-10GT has a higher peak of fuel temperature, while the equilibrium core has a higher average temperature of fuel, as shown in Figure 13. This

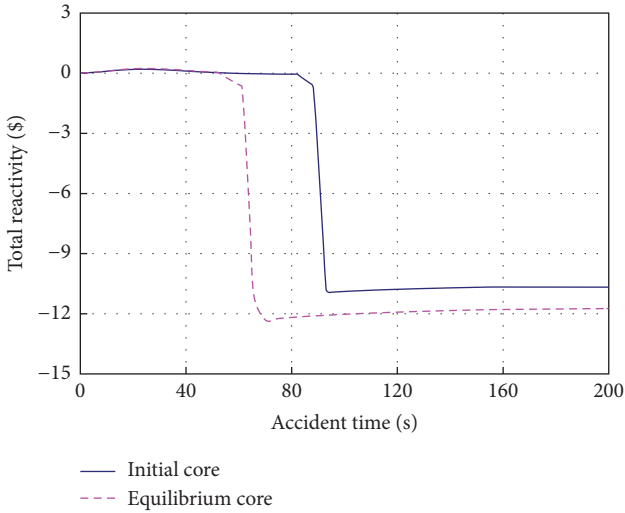


FIGURE 14: Total reactivity in a control rod withdrawal accident of the HTR-10GT.

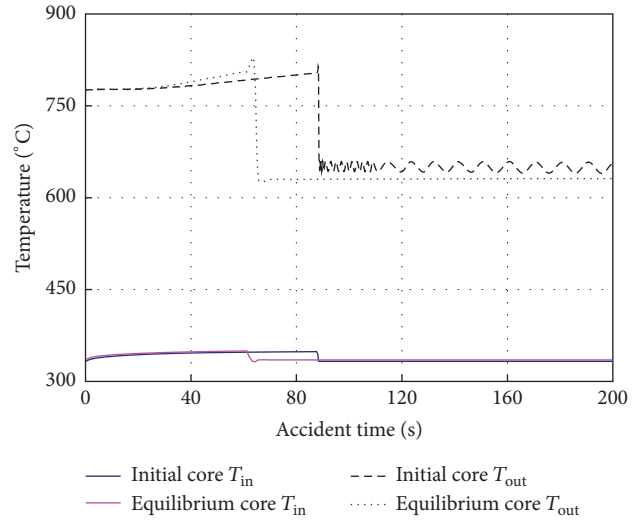


FIGURE 16: Core helium temperature in a control rod withdrawal accident of the HTR-10GT.

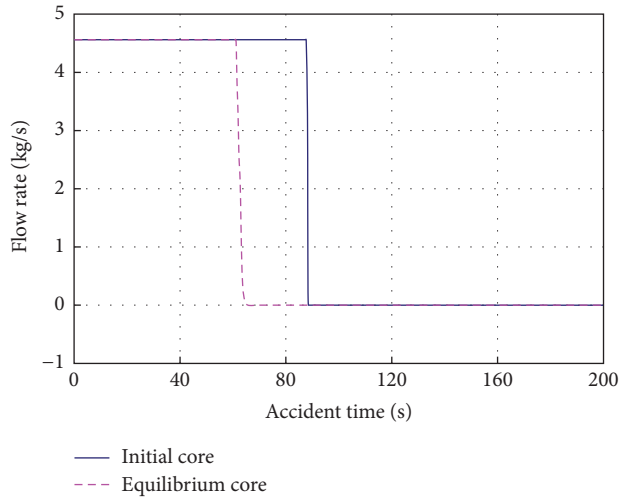


FIGURE 15: Flow rate of the primary loop in a control rod withdrawal accident of the HTR-10GT.

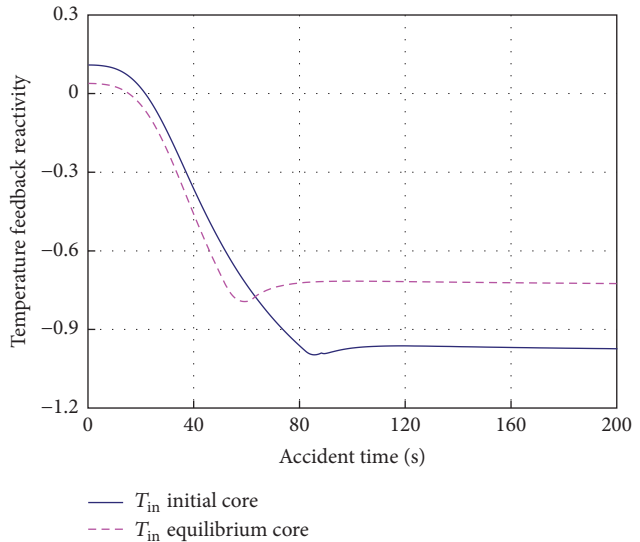


FIGURE 17: Temperature feedback reactivity in a control rod withdrawal accident of the HTR-10GT.

is also a result of the reactivity characteristics of the HTR-10GT core. Figure 16 shows the helium temperature at the core inlet and outlet.

When the second scram signal is detected, the protection system takes shutdown actions. Dropping control rods leads total reactivity to decrease quickly, as shown in Figure 14. In Figure 15, we can see that isolating the primary loop makes the helium flow in it nearly stop. The curves in Figure 18 show that the system pressure remains almost unchanged for both cores during the accident. The peak fuel temperature in accident is calculated to be 1201°C and 1066°C for the initial core and the equilibrium core, respectively, while for the HTR-10 the temperatures are 1170°C and 1041°C, respectively. The peak fuel temperature of the HTR-10GT is higher than that of the HTR-10, but both are lower than 1230°C. The HTR-10GT remains in safe conditions in a control rod withdrawal accident scenario [13–15].

5.3. *Accident Induced by Earthquake.* Tables 7 and 8 depict the important events in the HTR-10GT following an earthquake. The accident consequences of the HTR-10 are also compared in Tables 7 and 8. Figures 19–26 show the plots of key parameters of the HTR-10GT in accident for both an initial core and an equilibrium core, which consist of reactor power, peak fuel temperature, average fuel temperature, temperature feedback reactivity, total reactivity, flow rate of primary loop, system pressure, and helium temperatures at core inlet and outlet.

In less than 150 seconds after an earthquake occurs, a total reactivity of 1.24% is inserted into the startup up core and 0.788% is inserted into the equilibrium core. Core power begins to go up as soon as the positive reactivity insertion starts. Then the core temperature increases and the reactor

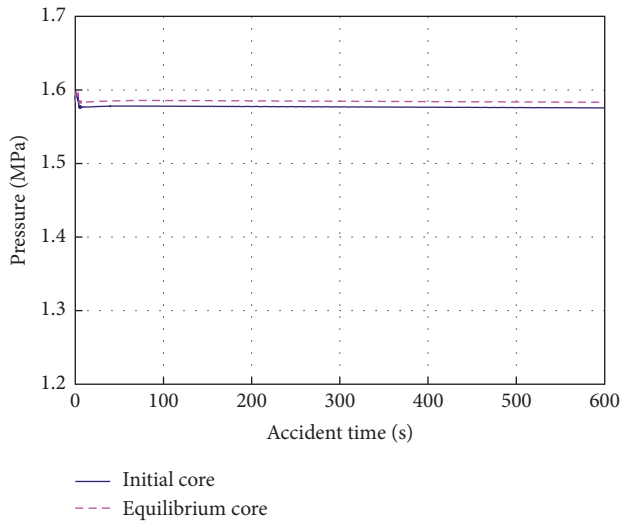


FIGURE 18: System pressure in a control rod withdrawal accident of the HTR-10GT.

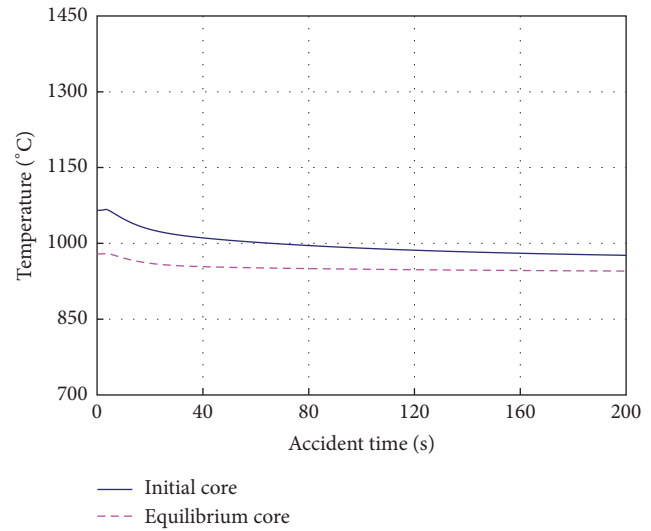


FIGURE 20: Fuel peak temperature in an earthquake accident of the HTR-10GT.

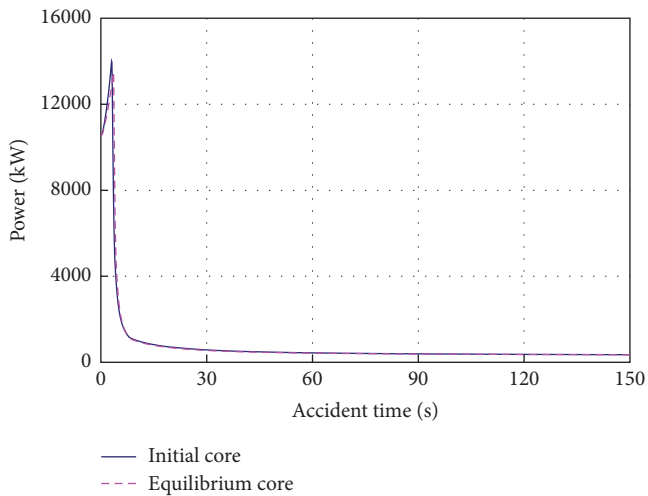


FIGURE 19: Core power in an earthquake accident of the HTR-10GT.

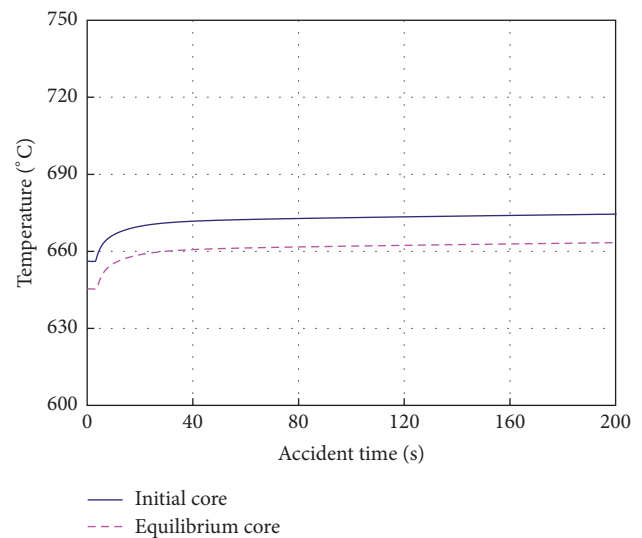


FIGURE 21: Average fuel temperature in an earthquake accident of the HTR-10GT.

will shut down by itself due to negative temperature reactivity feedback, even though there is no shutdown action. The first scram signal triggered by a short period measurement is soon received but is ignored as assumed. Two seconds later, the second signal (high flux) is detected and the protection system scrams the reactor. The peak fuel temperatures in the accident are  $1067^{\circ}\text{C}$  and  $980^{\circ}\text{C}$  for the initial core and the equilibrium core, respectively, while for HTR-10 the temperatures are  $1038^{\circ}\text{C}$  and  $945^{\circ}\text{C}$ , respectively. The peak fuel temperature of HTR-10GT in accident is about  $30^{\circ}\text{C}$  higher than that of HTR-10. Shortly afterwards, the HTR-10GT reactor shuts down safely. Both fuel peak temperatures are lower than  $1230^{\circ}\text{C}$ . The HTR-10GT remains in a safe condition in an earthquake accident scenario.

Tables 7 and 8 tell us that the earthquake accident consequences in the HTR-10GT progress more quickly than in the HTR-10, because the HTR-10GT operates at a higher

temperature and it has a faster temperature feedback. The peak fuel temperature of the HTR-10GT is higher than that of HTR-10, which leads to a fast reactivity feedback that causes the peak power of HTR-10GT less than that of HTR-10. The peak fuel temperature increase in the accident is about  $30^{\circ}\text{C}$ , which is lower than  $50^{\circ}\text{C}$ —the helium temperature increased at core outlet.

Comparing Figures 11 and 19, one can find that the core power increases more quickly in the earthquake accident than in the control rod withdrawal case for different positive insertion speeds. Because of the temperature negative feedback of reactivity, the peak and average fuel temperatures only rise a little as shown in Figures 20 and 21. Total reactivity plotted in Figure 22 and temperature feedback reactivity plotted in Figure 25 illustrate a relatively short time to reach

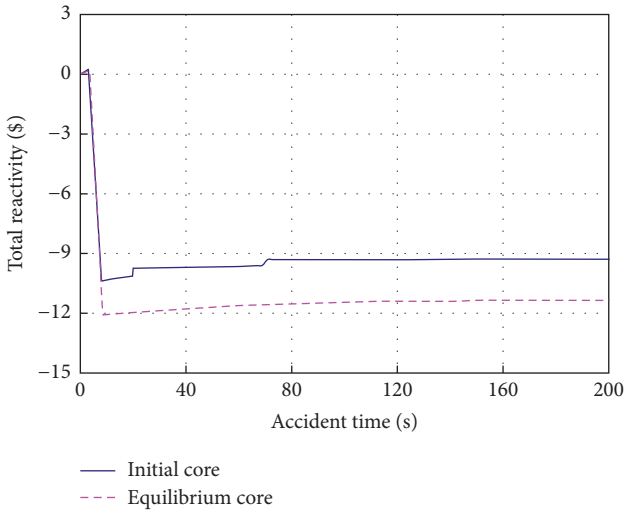


FIGURE 22: Total reactivity in an earthquake accident of the HTR-10GT.

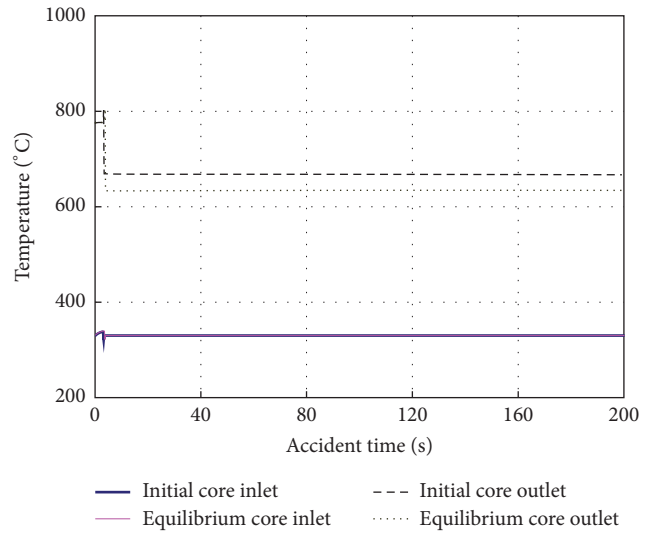


FIGURE 24: Temperature of core helium in an earthquake accident of the HTR-10GT.

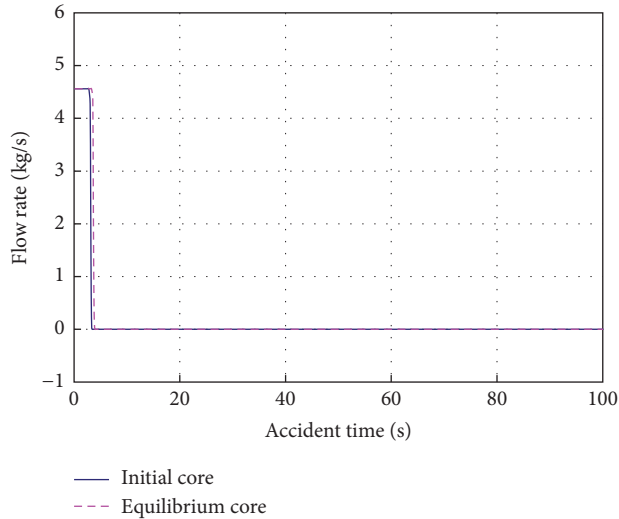


FIGURE 23: Flow rate of primary loop in an earthquake accident of the HTR-10GT.

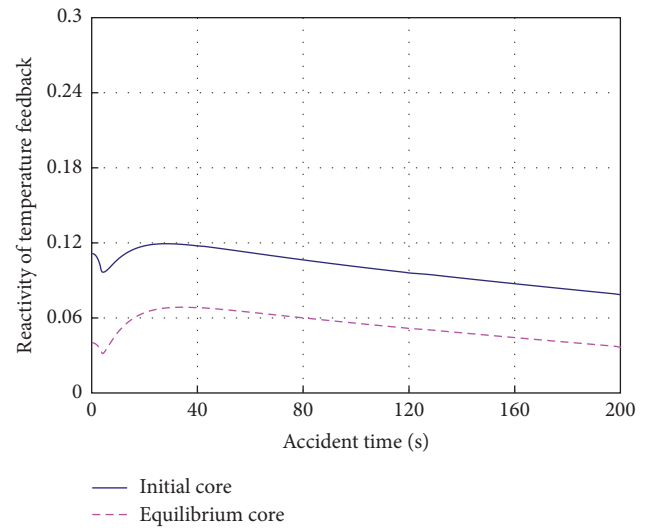


FIGURE 25: Temperature feedback reactivity in an earthquake accident of the HTR-10GT.

peaks of power and temperature. One can also see that in the earthquake accident the flow rate in the primary loop as shown in Figure 23 and the helium temperature of core as plotted in Figure 24 proceed smoothly. In the scram, the system remains in a high pressure condition, which can be seen in Figure 26, and it shows a similar behavior to that in a control rod withdrawal accident. In an earthquake accident, protection system takes measures to scram and leads to safe shutting down, which is similar to a control rod withdrawal accident.

## 6. Conclusions

The HTR-10GT is the second phase of HTGR technology development in China. It is based upon the reactor core of HTR-10 and replaces the steam generator with a helium

turbine generator. Although its physical core remains the same as HTR-10, the HTR-10GT has different operating parameters and its core runs at a higher temperature. So thermal hydraulic safety analysis must be performed for the final safety analysis report. Under the new operating parameters, three design basis accidents were simulated with the THERMIX code system.

From the preceding analysis, it can be concluded that, in the simulated DBAs of the HTR-10GT, there is no chemical reaction in the core and the peak fuel temperature is 1201°C, which has a tolerance to the safe margin of 1230°C. As the spherical fuel elements containing TRISO coated particles can effectively retain radioactive fission products up to the temperature of 1620°C under the given normal operating conditions, there is negligible additional radioactivity release

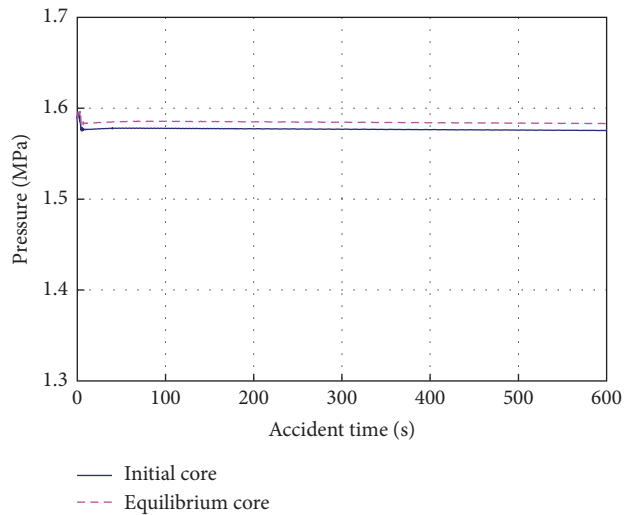


FIGURE 26: System pressure in an earthquake accident of the HTR-10GT.

TABLE 7: Accident sequence of an initial core induced by earthquake.

Events	HTR-10GT	HTR-10
Densification of pebble bed and positive reactivity is induced	0.0 s	0.0 s
Reactor cycle $\leq 20$ s	0.54 s	0.54 s
Neutron flux of power level $\geq 1.23$	2.04 s	2.54 s
Control rods begin to drop	3.04 s	3.54 s
Time at which reactor power reaches a peak	3.04 s (14.0 MW)	4.04 s (15.2 MW)
Time at which fuel temperature reaches a peak	3.34 s (1067°C)	5.68 s (1038°C)
Time at which total positive reactivity reaches a peak ( $dk/k$ )	150.0 s (1.24%)	150.0 s (1.24%)

TABLE 8: Accident sequence of an equilibrium core induced by earthquake.

Events	HTR-10GT	HTR-10
Densification of the pebble bed and positive reactivity is induced	0.0 s	0.0 s
Reactor cycle $\leq 20$ s	0.54 s	0.54 s
Neutron flux of power level $\geq 1.23$	2.54 s	3.03 s
Control rods begin to drop	3.54 s	4.03 s
Time at which reactor power reaches a peak	3.54 s (13.5 MW)	4.29 s (14.0 MPa)
Time at which fuel temperature reaches a peak	3.74 s (980°C)	5.47 s (945°C)
Time at which total positive reactivity reaches a peak ( $dk/k$ )	150.0 s (0.788%)	150.0 s (0.788%)

expected and no fuel element damage in DBAs induced by either a station blackout, an inadvertent control rod withdrawal, or an earthquake. The HTR-10GT remains in safe condition in all three cases.

## Conflicts of Interest

The authors declare that there are no conflicts of interest regarding the publication of this paper.

## Acknowledgments

The authors would like to thank Professor Zhou Zhiwei and Dr. Zheng Yanhua for kindly contributing to the study. This work has been supported by the National S&T Major Project (Grant no. ZX06901).

## References

- [1] G. H. Lohnert and H. Reutler, "Modular HTR—a new design of high-temperature pebble-bed reactor," *Nuclear Energy*, vol. 22, no. 3, pp. 197–201, 1982.
- [2] H. Reutler and G. H. Lohnert, "Advantages of going modular in HTRs," *Nuclear Engineering and Design*, vol. 78, no. 2, pp. 129–136, 1984.
- [3] Y. Xu, "High temperature gas-cooled reactor programme in China," in *Proceedings of International Symposia Energy Future in the Asia/Pacific Region*, Taipei, Taiwan, 1999.
- [4] S. Hu, R. Wang, and Z. Gao, "Safety demonstration tests on HTR-10," in *Proceedings of 2nd International Topical Meeting on High Temperature Reactor Technology*, Beijing, China, 2004.
- [5] Z. Gao, S. He, and M. Zhang, "Afterheat removal for HTR-10 test module under accident conditions," in *Proceedings of Specialists Meeting on Decay Heat Removal and Heat Transfer under Normal and Accident Conditions in Gas Cooled Reactors*, Juelich, Germany, 1992.
- [6] Y. Dong, F. Chen, Z. Zhang et al., "Simulation and analysis of helium circulator trip ATWS test at full power on the HTR-10," in *Proceedings of the 4th International Topical Meeting on High Temperature Reactor Technology*, Washington, DC, USA, 2008.
- [7] S. Jiang, "High temperature gas-cooled reactor project in Tsinghua University," in *Proceedings of 21st-Century-COE Workshop on Energy and Environmental Issues in Asia*, Kyoto, Japan, 2006.
- [8] Z. Gao and L. Shi, "Thermal hydraulic transient analysis of the HTR-10," *Nuclear Engineering and Design*, vol. 218, no. 1–3, pp. 65–80, 2002.
- [9] H. Haque, W. Feltes, M. Wickert, N. Kohtz, and J. Lukaszewicz, "Thermal response of a modular HTR under accident conditions," *Nuclear Energy*, vol. 22, no. 3, pp. 201–210, 1982.
- [10] H. Haque, W. Feltes, and G. Brinkmann, "Thermal response of a modular high temperature reactor during passive cooldown under pressurized and depressurized conditions," *Nuclear Engineering and Design*, vol. 236, no. 5–6, pp. 475–484, 2006.
- [11] L. Wolf, W. Scherer, W. Giesser, and W. Feltes, "High temperature reactor core physics and reactor dynamics," *Nuclear Engineering and Design*, vol. 121, no. 2, pp. 227–240, 1990.
- [12] Y. Zheng, J. Lapins, E. Laurien, L. Shi, and Z. Zhang, "Thermal hydraulic analysis of a pebble-bed modular high temperature

gas-cooled reactor with ATTICA3D and THERMIX codes,” *Nuclear Engineering and Design*, vol. 246, pp. 286–297, 2012.

- [13] M. Lang, “The ATWS analysis of one control rod withdrawal out of the HTR-10GT core under the loss of the system pressure,” in *Proceedings of 22nd International Conference on Nuclear Engineering*, Prague, Czech Republic, 2014.
- [14] M. Lang and Y. Dong, “The ATWS analysis of one control rod withdraw out of the HTR-10GT core in addition with bypass valve failure,” *Nuclear Engineering and Design*, vol. 271, pp. 459–464, 2014.
- [15] M. Lang and Y. Dong, “The ATWS analysis of one control rod withdrawal out of the HTR-10GT core,” in *Proceedings of 18th International Conference on Nuclear Engineering, ICONE18*, Xi’an, China, 2010.

## Research Article

# Using Wireless Sensor Networks to Achieve Intelligent Monitoring for High-Temperature Gas-Cooled Reactor

Jianghai Li,<sup>1</sup> Jia Meng,<sup>2</sup> Xiaojing Kang,<sup>2</sup> Zhenhai Long,<sup>2</sup> and Xiaojin Huang<sup>1</sup>

<sup>1</sup>*Institute of Nuclear and New Energy Technology, Collaborative Innovation Centre of Advanced Nuclear Energy Technology, Key Laboratory of Advanced Reactor Engineering and Safety of Ministry of Education, Tsinghua University, Beijing, China*

<sup>2</sup>*Chinergy Co., Ltd., Beijing, China*

Correspondence should be addressed to Xiaojin Huang; [huangxj@tsinghua.edu.cn](mailto:huangxj@tsinghua.edu.cn)

Received 31 December 2016; Revised 12 April 2017; Accepted 26 April 2017; Published 30 May 2017

Academic Editor: Alejandro Clausse

Copyright © 2017 Jianghai Li et al. This is an open access article distributed under the Creative Commons Attribution License, which permits unrestricted use, distribution, and reproduction in any medium, provided the original work is properly cited.

High-temperature gas-cooled reactors (HTGR) can incorporate wireless sensor network (WSN) technology to improve safety and economic competitiveness. WSN has great potential in monitoring the equipment and processes within nuclear power plants (NPPs). This technology not only reduces the cost of regular monitoring but also enables intelligent monitoring. In intelligent monitoring, large sets of heterogeneous data collected by the WSN can be used to optimize the operation and maintenance of the HTGR. In this paper, WSN-based intelligent monitoring schemes that are specific for applications of HTGR are proposed. Three major concerns regarding wireless technology in HTGR are addressed: wireless devices interference, cybersecurity of wireless networks, and wireless standards selected for wireless platform. To process nonlinear and non-Gaussian data obtained by WSN for fault diagnosis, novel algorithms combining Kernel Entropy Component Analysis (KECA) and support vector machine (SVM) are developed.

## 1. Introduction

Wireless sensor network technology (WSN) can be employed in high-temperature gas-cooled reactors (HTGR) to achieve intelligent monitoring. Intelligent monitoring with WSN will not only reduce the direct cost of regular monitoring but also assist with various tasks, such as fault diagnosis and recovery, condition-based maintenance, and control of nuclear materials, which would optimize the operation and maintenance of the HTGR nuclear power plant (NPP).

WSN is a new technology in which interest is growing. Sensors with the wireless communication capability are able to cooperatively monitor physical or environmental conditions, such as temperature, pressure, sound, and vibration. A sensor can be a fully contained device with a sensing component, a radio transceiver, a microcontroller, and an energy source all in the same module. It can also be a conventional instrument attached to a wireless data transmitter, where sensed data are transmitted to a data processing center wirelessly. The WSN has been widely used in industry, agriculture, military, transportation, and other fields.

At present, regular monitoring of NPPs mainly employs wired connections between sensors and data processing centers. For example, in Instrumentation and Control (I&C) systems, instrument signals are transmitted by hard wires. Although the wired connection is assumed to be more reliable, it is costlier and increases the complexity of plant layout. A rough estimate of the cost of normal wiring in an NPP is around US \$2,000 per 0.3 m, whereas the cost of using wireless technology for the same application is less than US \$20 per 0.3 m [1]. Moreover, increasing the number of cables also increases the number of cable trays required, which occupy a lot of space and complicate design and construction.

Applying WSN in the monitoring part of equipment and processes in HTGR NPP can effectively alleviate the above problems. The replacement of some wired cables with wireless connections will create economic benefits for HTGR by cutting the cost of wiring, reducing the space required for cable trays, and shortening the period of design and construction for the cable tray layout.

A WSN can also enable higher levels of monitoring. With WSNs, massive and heterogeneous data about equipment

and processes can be gathered. These rich monitoring data offer brand new possibilities for better fault detection and diagnosis, more advanced maintenance, and more efficient management of nuclear materials.

To achieve such high levels of intelligent monitoring, three questions must be answered.

Q1. What are intelligent monitoring schemes for various applications? The monitoring scheme includes the selection of process variables and equipment parameters to be monitored, the placement of wireless sensors, and the power supply for sensors and transmitters.

Q2. How can large amounts of heterogeneous data be transmitted via the WSN? The wireless communication problems for intelligent monitoring in HTGR include the selection of appropriate communication protocols, as well as the electromagnetic compatibility concern and the security issue.

Q3. How should we deal with the large scale of data to realize intelligent monitoring?

This paper is organized as follows. The kind of data that should be monitored (see Q1) depends on different intelligent monitoring schemes for various applications. Three monitoring schemes in three scenarios are proposed in Section 2. The methods of transmitting data in Q2 are specified in wireless communication protocols. In Section 3, wireless protocols of WSNs are compared and some important issues are discussed. We also demonstrate specific data processing algorithms related with Q3 in Section 4. Conclusions are drawn in Section 5.

A preliminary version of this work has been published in [2] to deal with the intelligent monitoring for general NPPs. Two data processing algorithms of KPCA and SVM were proposed. In this paper, we focus on the intelligent monitoring for HTGR. We make more detailed monitoring schemes that are specific for HTGR. Additional material is supplemented to adequately address three major concerns of the wireless communication. We further develop the KECA-SVM algorithms for slow process fault diagnosis of HTGR.

## 2. Intelligent Monitoring Schemes for HTGR

Intelligent monitoring with rich information about processes and equipment will greatly benefit the safety and cost efficiency of HTGR. Currently, the number and types of monitoring variables are determined based on the aim of controlling performance during normal operation. Insufficient consideration is given to other aspects of the full life cycle of NPPs, such as off-normal operation, maintenance, and retirement. To realize the type of intelligent monitoring that can optimize the full life cycle of a NPP, massive and heterogeneous data are required [3]. Multiple types of data out of the scope of conventional monitoring can be incorporated into intelligent monitoring with a WSN, such as radio-frequency identification (RFID) data, video camera data, and microphone sensor data. Some examples will be discussed below to show how rich information could contribute to

advanced maintenance, fault diagnosis and recovery, and management of nuclear materials.

Condition-based maintenance requires comprehensive monitoring of equipment. At present, only a few critical parameters of equipment are monitored by I&C systems due to the limited number of wired input channels. The number of wired input channels is constrained not only by the cost of monitoring modules in the data center but also by the confined space occupied by sensor wiring [4]. The WSN can break the limitation of the cost and the space. The wireless sensors are able to collect abundant sensing data and send them to the data center via wireless channels. This can be achieved without significantly increasing the number of monitoring modules or expanding wiring space, since one access point can gather data from multiple sensors via wireless technology. For example, we can consider the task of monitoring the main helium blower of HTGR. In addition to critical parameters like rotational speed and the pressure rise, diverse information about the equipment, such as the vibration of the base, the surface temperature distribution, and even the operational noise, could help in assessing the need for maintenance. To gather this diverse information, a variety of wireless sensors could be positioned around the main helium blower motor. Several infrared thermometers placed above the blower can observe the temperature distribution of its surface. A number of vibration sensors laid on the base of the blower can measure its vibration in multiple dimensions. A microphone array deployed beside the blower can collect data on operational noise in an uninterrupted manner. All these heterogeneous observations would be sent to the data center to enable the real-time health monitoring of the main blower.

Another example shows fault diagnosis and recovery with wireless monitoring data. The feed water flow in a HTGR measured by a conventional flowmeter can be sent back to the process control system via wired cables or via a wireless transmitter. The wireless data serves as a diverse backup for the wired data. The backup data can verify the wired data to detect malfunctions of cables or monitoring modules. If the failure is caused by communication faults, regardless of whether this occurs in the wired network or in the wireless channel, the checksum transmitted along with the data will indicate the error. If the fault is identified in the wired network, the valid wireless data can be used in place of the faulty wired data to maintain continuous monitoring.

The third example demonstrates how the RFID technology and wireless networks can contribute to efficient management of spent fuel from HTGR. The canister-based dry spent fuel storage system is adopted in HTGR [5]. Each canister has a capacity of 40 000 spent fuel spheres and can be placed in the spent fuel storage building with concrete shields. In current design, the ID is carved on the cap of the canister and is read by the operator through cameras. However, cameras at fixed positions have difficulty reading the ID at the first stage of the canister transport, which reduces the efficiency of spent fuel management. RFID based on wireless networks provides an alternative for the conventional optical ID. An RFID tag is composed of memory, modulator, and wireless antenna. They can be attached on any nuclear material containers

or packages that require rigorous monitoring. Information about nuclear material can be recorded and updated on the RFID tags. Using an RFID reader, the information on tags can be read in a contactless way through the whole transport process of spent fuel canisters. Meanwhile, the positions of nuclear material can be localized and tracked by RFID tag-reader pairs. The up-to-date information retrieval and the localization by RFID can not only enhance the efficiency of nuclear material management but also reduce risk of nuclear material loss.

### 3. Wireless Transmission for the WSN of HTGR

To employ wireless technologies to transmit monitoring data in HTGR, three major concerns need to be considered comprehensively. They are wireless devices interference, cybersecurity of wireless networks, and wireless standards selected for wireless platform of HTGR.

For the first concern, wireless devices must be electromagnetically compatible (EMC) with the existing I&C systems. The power level of wireless sensors is usually below 20 mW. In the EMC standard of IEC 61000-4-3 [6] (GB/T 17626.3), note 4 in Section 5.2 states that “other systems operating in this frequency range, e.g. radio LANs operating at 2.4 GHz or higher frequencies, are generally very low power (typically lower than 100 mW), so they are much less likely to present significant problems.” Even so, in order to ensure that there is no interference by wireless devices, all the I&C systems, in particular the safety-related systems, should pass the susceptibility testing in the frequency range covering the wireless frequency band. The Regulatory Guide 1.180 [7] suggests that this susceptibility test operating envelope will remain the same as at lower frequencies than 2.4 GHz.

For the second point, cybersecurity is another major concern with using wireless sensors in NPPs. It is believed that unprotected wireless transmission in opening space makes the network platform vulnerable to external malicious cyber-attacks, such as spoofing and jamming. With the advanced technologies of encryption, authentication process, channel fault-tolerance, and security certification, the cybersecurity concern of wireless network can be significantly allayed [8]. Moreover, for the intelligent monitoring applications of the HTGR with inherent safety feature, the cyber-attacks pose little potential risk to the plant. In addition, it should be mentioned that the cybersecurity features cannot protect against attacks at the physical layer. The physical security requirement of the wireless platform should be the same as that of the wired I&C system.

For the third concern, the selection of wireless standards is the main task of wireless platform design. More and more applications have been or are going to be built on the wireless platform of NPPs, such as voice communication, personnel positioning, and radiation monitoring. The requirements of future wireless applications need to be taken into account in advance. Thus, the major criteria for the wireless platform of HTGR are listed as follows:

- (i) High bandwidth
- (ii) Lower RF power while covering a wide range
- (iii) Being scalable and extensible
- (iv) Widespread support by industry

The first criterion, high bandwidth, provides the possibility to accommodate high traffic applications such as voice and video. The second criterion intends to balance the emission restriction with the deployment cost. The third one and the fourth one consider the long-term utility of the wireless platform.

According to the result of our research, wireless standards which have been employed in NPPs in China include Wi-Fi, McWill, PHS, and TDD (Table 1). Some other potential wireless standards using IEEE 802.15.4 [1], such as ZigBee, WirelessHART, and ISA100, which have low data transmission rate, are not taken into consideration for the wireless platform of HTGR. Currently, the wireless applications are limited to voice communications. The great potential of wireless data communication for the intelligent monitoring has not been fulfilled yet. Only McWill and Wi-Fi technologies have the potential for the data communication. They have the capabilities of high bandwidth, high security, and terminal roaming handoff. However, McWill causes higher RF power and thus only allows one-way communication for mobile receivers in the nuclear island [9]. Wi-Fi technology with 2.4 GHz band meets all the above requirements of wireless applications in NPPs. The high bandwidth of communication, the openness of protocols, and the scalability of the systems make the Wi-Fi suitable for a variety of applications, such as wireless monitoring, emergency communications, and mobile operation.

### 4. Data Processing Algorithms for Intelligent Monitoring

In this section, we aim to provide solution based on WSN data for a particular fault diagnosis problem of HTGR, that is, slow process fault diagnosis. The slow process faults mainly refer to the faults that occur slowly over time, such as leakage and small broken pipe of helium gas. Unlike the failures of main components within the system, such as the main helium blower and turbine, these failures are not easily noticed due to the compensation control and the simple limit alarming. However, slow process faults can also lead to the degradation of reactor performance or even abnormal operational occurrence. The difficulties in slow process fault diagnosis, including fault detection and fault classification, are the nonlinear and non-Gaussian nature of the monitoring data obtained by WSN.

There have been many fault detection methods, such as PCA and its variants. PCA performs poorly for the nonlinear problem, as it assumes that the process data are linear. To overcome the shortcoming of the PCA, several nonlinear extensions of PCA were reported, like Kernel PCA (KPCA). KPCA was used to detect faults in two example systems in [10, 11]. The problem of fault detection was addressed in mechanical systems using a KPCA-based

TABLE 1: Comparison of wireless standards in NPPs.

Spec.	Tech.			
	McWill	Wi-Fi	PHS	TDD
Frequency band	1875–1805 MHz Need licenses	2.4 GHz Free band	1900–1920 MHz Need licenses	800 MHz Need licenses
Bandwidth	15.36 Mbps	300 Mbps	64/128 Kbps	64 Kbps
Transmitting power	Base station 30 W (outdoor) Base station 10 mW (indoor) Cellphone 2 W (outdoor) Cellphone 10 mW (indoor)	Base station 0.1 W (indoor) Base station 0.5 W (outdoor) Cellphone 0.1 W	Base station 10 mW Cellphone 10 mW	Base station 0.6–40 W Cellphone 1.8 W
Coverage (outdoor)	4 Km	0.5 Km	0.5 Km	5 Km
Mobility	120 Km/h	50 Km/h	40 Km/h	100 Km/h
Advancement	Better	Great	Normal	Good
Security	Encryption, group function, authorization, channel fault-tolerance, and security certification	Encryption, group function, authorization, channel fault-tolerance, and security certification	AI encryption	Authorization, P2P encryption
Industrial cluster	Scarcely	More than 300 alliance members	Weed out	TETRA/PDT/GT800/GoTa/iDEN
Functionality	Dispatcher voice/note/data/real-time video	Dispatcher voice/note/data/HD real-time video/location	Voice/note	Voice/note

method [12]. In [13], the methods of KPCA and kernel partial least analysis were used for fault diagnosis and process monitoring of a continuous annealing process and fused magnesium furnace. However, non-Gaussian information is usually included in the high-dimensional data of the industry process; these fault detection methods no longer fit well. In view of the nonlinear characteristics and non-Gaussian distributed data in HTGR, Kernel Entropy Component Analysis (KECA) algorithm for fault detection is demonstrated in Section 4.1.

For the fault classification problem, support vector machine (SVM), as a novel machine learning method based on statistical learning theory, has been widely employed [14–17], as it is very suitable for the nonlinear data with small samples and high dimension. It gradually takes the place of neural network by using structural risk minimization principle instead of empirical risk minimization (ERM) principle. There are previous works on applying SVM to fault classification in many industrial areas. Four fault types of power transformer were identified by the trained multilayer SVM classifier [14]. A hybrid two-stage one-against-all SVM approach was proposed for fault diagnosis of defective rolling element bearings [15]. An improved SVM classifier was developed for fault diagnosis of actual analog circuits [16]. Combining chaos particle swarm algorithm with SVM, a novel fault diagnosis method was applied to isolate wireless

sensor faults [17]. The KECA-SVM combining algorithm for the WSN data of HTGR is proposed in Section 4.2, which can overcome the nonlinear and non-Gaussian difficulties in slow process fault diagnosis.

*4.1. KECA Algorithms for Fault Detection.* As a new approach in reducing data dimension and detecting faults of HTGR, the Rényi quadratic entropy is first introduced by

$$H(p) = -\log \int p^2(\mathbf{x}) d\mathbf{x}, \quad (1)$$

where  $p(\mathbf{x})$  is the probability density function (PDF) of the data set  $D = \mathbf{x}_1, \dots, \mathbf{x}_N$ . Since the logarithm is a monotonic function, what we only need to consider is the quantity  $V(p) = \int p^2(\mathbf{x}) d\mathbf{x}$ . To estimate  $V(p)$  and then estimate  $H(p)$ , Parzen-window density estimation is given by

$$\hat{p}(\mathbf{x}) = N^{-1} \sum_{\mathbf{x}_t \in D} k_\sigma(\mathbf{x}, \mathbf{x}_t), \quad (2)$$

where  $k_\sigma(\mathbf{x}, \mathbf{x}_t)$  is the Parzen window, also known as the kernel function, which centers on  $\mathbf{x}_t$  with a width parameter  $\sigma$ . Here the most commonly used radial basis function is selected as the kernel function:

$$k(\mathbf{x}, \mathbf{x}') = \exp\left(-\frac{\|\mathbf{x} - \mathbf{x}'\|^2}{2\sigma^2}\right). \quad (3)$$

Using (2) and the convolution theorem for Gaussian kernel function, we have

$$\begin{aligned}\widehat{V}(p) &= \int \widehat{p}^2(\mathbf{x}) d\mathbf{x} \\ &= N^{-2} \sum_{\mathbf{x}_t \in D} \sum_{\mathbf{x}_{t'} \in D} \int k(\mathbf{x}, \mathbf{x}_t) k(\mathbf{x}, \mathbf{x}_{t'}) d\mathbf{x} \\ &= N^{-2} \sum_{\mathbf{x}_t \in D} \sum_{\mathbf{x}_{t'} \in D} k(\mathbf{x}_t, \mathbf{x}_{t'}) = N^{-2} \mathbf{1}^T \mathbf{K} \mathbf{1},\end{aligned}\quad (4)$$

where  $(t, t')$ th element of the  $N \times N$  kernel matrix  $\mathbf{K}$  is  $k(\mathbf{x}_t, \mathbf{x}_{t'})$  and  $\mathbf{1}$  is the  $N \times 1$  column vector whose element is 1. Thus, the Rényi quadratic entropy estimate can be compactly expressed as the form of kernel matrix.  $\mathbf{K}$  can be eigen-decomposed in the following form:

$$\mathbf{K} = \mathbf{E} \mathbf{D} \mathbf{E}^T, \quad (5)$$

where  $\mathbf{D}$  is the diagonal matrix consisting of eigenvalues  $\lambda_1, \dots, \lambda_N$  and  $\mathbf{E}$  is the matrix  $\mathbf{e}_1, \dots, \mathbf{e}_N$  whose column vectors are the corresponding eigenvectors. In the meantime, kernel matrix can be also written as the form of inner product matrix in kernel feature space:

$$\mathbf{K} = \Phi^T \Phi = \mathbf{E} \mathbf{D} \mathbf{E}^T, \quad (6)$$

where  $\Phi = \mathbf{D}^{1/2} \mathbf{E}^T$ . So  $\widehat{V}(p)$  can be rewritten as follows:

$$\widehat{V}(p) = N^{-2} \sum_{i=1}^N \left( \sqrt{\lambda_i} \mathbf{e}_i^T \mathbf{1} \right)^2. \quad (7)$$

Each item in the above equation contributes to the entropy estimate. That is to say, certain eigenvalues and corresponding eigenvectors will contribute more to the entropy estimate than other eigenvalues and eigenvectors. Thus, in KECA algorithm, the eigenvalues and corresponding eigenvectors which are the first  $l$  largest contribution to the entropy estimate are chosen. KECA can be interpreted as a data dimension reduction technique which projects  $\Phi$  onto a subspace  $U_l$  composed of those  $l$  principal axes contributing more to the Rényi entropy estimate. The data transformation is formulated as follows:

$$\Phi_{\text{eca}} = P_{U_l} \Phi, \quad (8)$$

where  $P_{U_l}$  is the loading matrix.

The  $l$ -dimensional matrix  $\Phi_{\text{eca}}$  in kernel feature space can be also expressed as follows:

$$\Phi_{\text{eca}} = \mathbf{D}_l^{1/2} \mathbf{E}_l^T, \quad (9)$$

where  $\mathbf{D}_l, \mathbf{E}_l$  are the matrices which consist of selected eigenvalues and corresponding eigenvectors, respectively.

Thereby, the new kernel matrix  $\mathbf{K}_{\text{eca}}$  generated by KECA algorithm can be written as follows:

$$\mathbf{K}_{\text{eca}} = \Phi_{\text{eca}}^T \Phi_{\text{eca}} = \mathbf{E}_l \mathbf{D}_l \mathbf{E}_l^T. \quad (10)$$

Therefore,  $-\log$  of the quantity  $\widehat{V}_l(p) = (1/N^2) \mathbf{1}^T \mathbf{K}_{\text{eca}} \mathbf{1}$  can be considered as the Rényi entropy estimation of some data set which is denoted as  $\mathbf{x}'_1, \dots, \mathbf{x}'_N$ .  $\widehat{V}_l(p)$  carries most of the information of the Rényi entropy estimation of the initial data set  $\mathbf{x}_1, \dots, \mathbf{x}_N$ . Accordingly, data transformation  $\mathbf{x} \rightarrow \mathbf{x}'$  in input space is produced so that the entropy of  $\mathbf{x}'_1, \dots, \mathbf{x}'_N$  and the entropy of  $\mathbf{x}_1, \dots, \mathbf{x}_N$  are closely approximate. This also reflects data transformation of KECA in input space.

In contrast to KPCA which performs data transformation and dimension reduction by selecting eigenvalues and corresponding eigenvectors of the kernel matrix merely based on the size of the eigenvalues, KECA chooses the eigenvalues based on the contribution to entropy estimate.

To apply KECA algorithm to condition monitoring and fault diagnosis of HTGR, monitoring statistical control charts need to be constructed to reflect the operating condition. Here, Hotelling  $T^2$  and SPE statistics are used to monitor the industrial process. Faults can be detected by judging whether  $T^2$  and SPE statistics exceed the respective confidence limit or not. Faults occur as long as SPE statistic exceeds the confidence limit. If  $T^2$  statistic exceeds the confidence limit and SPE statistic does not, working conditions may change.

The two measures are defined as follows. Hotelling  $T^2$  statistic, which represents the major variation of the sample to the model, is the standard quadratic sum of principal component score vectors:

$$T^2 = [t_1, t_2, \dots, t_R] \Lambda^{-1} [t_1, t_2, \dots, t_R]^T, \quad (11)$$

where  $R$  is the number of selected principal components.

SPE statistic, also known as the Q statistic, which represents the goodness of fit of the sample to the built model, is the error between the actual measured variable and the KECA model:

$$\text{SPE} = \|\Phi(\mathbf{x}) - \widehat{\Phi}_R(\mathbf{x})\|^2 = \sum_i^N t_i^2 - \sum_i^R t_i^2, \quad (12)$$

where  $\widehat{\Phi}_R(\mathbf{x})$  is the reconstructed feature vector with principal components in the feature space.

After constructing the monitoring statistics, the confidence limits of the two statistics need to be determined. However, the process variables are not necessarily mutually independent and obey Gaussian distribution. Hence, the traditional selected method of calculating the confidence limits is not applicable any longer in KECA. Here, KDE method is introduced to determine the confidence limits of the two statistics. The PDFs of  $T^2$  and SPE statistics based on sample data of the normal condition are first obtained. The area surrounded by the PDF curve and  $x$ -axis is 1. The statistical confidence  $\beta$  is selected to determine the confidence limits of  $T^2$  and SPE statistics. The confident limits of the two statistics can be formulated as follows:

$$\begin{aligned}\int_{T_{\text{lim}}^2}^{+\infty} \gamma_{T^2} &= 1 - \beta, \\ \int_{\text{SPE}_{\text{lim}}}^{+\infty} \gamma_{\text{SPE}} &= 1 - \beta.\end{aligned}\quad (13)$$

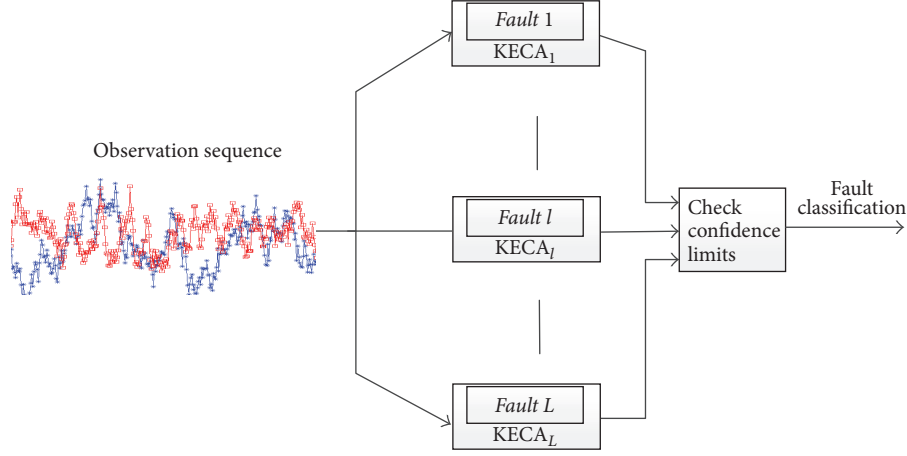


FIGURE 1: Architecture of the KECA-based fault detection algorithm.

The architecture of the KECA-based fault detection algorithm is shown in Figure 1.

**4.2. SVM Algorithms for Fault Classification.** Support vector machine (SVM) is adopted to identify the faults. For the classification of two-class samples, denote the training set as  $D = \{(\mathbf{x}_i, y_i) \mid i = 1, 2, \dots, n\}$ , where  $\mathbf{x}_i \in \mathbf{R}^n$  stands for  $n$  samples and  $y_i \in \{+1, -1\}$  their class values. Define two standard hyperplanes  $H_1 : \mathbf{w} \cdot \Phi(\mathbf{x}) + b = +1$  and  $H_2 : \mathbf{w} \cdot \Phi(\mathbf{x}) + b = -1$ , where  $\mathbf{w}$  is the weight vector and  $b$  the bias. The distance between two standard hyperplanes is called classification interval. The optimal hyperplane is a hyperplane  $H : \mathbf{w} \cdot \Phi(\mathbf{x}) + b = 0$  that can correctly separate the two-class samples and the classification interval has the maximum value. As a result, two standard hyperplanes include the samples that are closest to the optimal hyperplane. To maximize the classification interval,  $\|\mathbf{w}\|^2 = \mathbf{w}^T \mathbf{w}$  should be minimized because the distance between  $H_1$  and  $H_2$  is  $2/\|\mathbf{w}\|$ . To ensure that there is not any sample between  $H_1$  and  $H_2$ , the classification plane should satisfy the following constraint:

$$y_i [\mathbf{w} \cdot \Phi(\mathbf{x}_i) + b] \geq 1, \quad i = 1, 2, \dots, n. \quad (14)$$

To construct the optimal hyperplane when the sample is linearly inseparable, a nonnegative relaxation variable  $\xi_i \geq 0$  is introduced. Then the constraint of the classification plane is changed into

$$y_i [\mathbf{w} \cdot \Phi(\mathbf{x}_i) + b] \geq 1 - \xi_i, \quad i = 1, 2, \dots, n. \quad (15)$$

These samples which make the equality in (15) hold are called support vectors. To construct the optimal classification plane requires solving the following optimization problem:

$$\min \quad \frac{1}{2} \mathbf{w}^T \mathbf{w} + C \sum_{i=1}^n \xi_i, \quad (16)$$

$$\text{s.t.} \quad y_i [\mathbf{w} \cdot \Phi(\mathbf{x}_i) + b] \geq 1 - \xi_i, \quad i = 1, 2, \dots, n,$$

where  $C$  is the penalty parameter that compromises the minimum falsely separated samples and the maximum classification interval. By using Lagrange function, the above problem can be transformed into

$$\begin{aligned} L(\mathbf{w}, b, \xi, \alpha, \beta) = & \frac{1}{2} \mathbf{w}^T \mathbf{w} + C \sum_{i=1}^n \xi_i \\ & - \sum_{i=1}^n \alpha_i [y_i (\mathbf{w} \cdot \Phi(\mathbf{x}_i) + b) + \xi_i - 1] \\ & - \sum_{i=1}^n \beta_i \xi_i, \end{aligned} \quad (17)$$

where  $\alpha_i$  and  $\beta_i$  are Lagrange multipliers. By calculating partial derivatives with respect to  $\mathbf{w}$ ,  $\xi_i$ ,  $b$  and making them equal to zero, the following equations can be obtained:

$$\begin{aligned} \frac{\partial L}{\partial \mathbf{w}} = 0 & \implies \mathbf{w} = \sum_{i=1}^n \alpha_i y_i \Phi(\mathbf{x}_i), \\ \frac{\partial L}{\partial b} = 0 & \implies \sum_{i=1}^n \alpha_i y_i = 0, \\ \frac{\partial L}{\partial \xi_i} = 0 & \implies C - \alpha_i - \beta_i = 0. \end{aligned} \quad (18)$$

Since  $\alpha_i \geq 0$ ,  $\beta_i \geq 0$ , and  $C - \alpha_i - \beta_i = 0$ ,  $0 \leq \alpha_i \leq C$  can be obtained. Substituting (18) into (17) results in

$$\begin{aligned} L(\mathbf{w}, b, \xi, \alpha, \beta) \\ = \sum_{i=1}^n \alpha_i - \frac{1}{2} \sum_{i=1}^n \sum_{j=1}^n \alpha_i \alpha_j y_i y_j [\Phi(\mathbf{x}_i) \cdot \Phi(\mathbf{x}_j)]. \end{aligned} \quad (19)$$

Based on Mercer condition, inner product  $[\Phi(\mathbf{x}_i) \cdot \Phi(\mathbf{x}_j)]$  in feature space can be replaced by kernel function

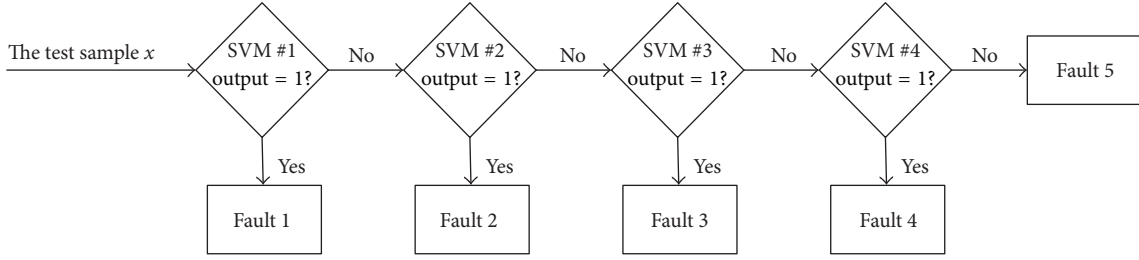


FIGURE 2: Architecture of the SVM-based fault classification algorithm.

$K(\mathbf{x}_i, \mathbf{x}_j)$ ; it can then be transformed into the dual quadratic programming problem as follows:

$$\begin{aligned} \max_{\alpha} \quad & \sum_{i=1}^n \alpha_i - \frac{1}{2} \sum_{i=1}^n \sum_{j=1}^n \alpha_i \alpha_j y_i y_j K(\mathbf{x}_i, \mathbf{x}_j), \\ \text{s.t.} \quad & \sum_{i=1}^n y_i \alpha_i = 0 \quad 0 \leq \alpha_i \leq C, \quad i = 1, 2, \dots, n. \end{aligned} \quad (20)$$

After working out  $\alpha_i$ , given the test samples  $\mathbf{x}$ , classification function of SVM classifier can then be written as follows:

$$\begin{aligned} f(\mathbf{x}) &= \text{sgn}[\mathbf{w} \cdot \Phi(\mathbf{x}) + b] \\ &= \text{sgn} \left[ \sum_{i=1}^n \alpha_i y_i K(\mathbf{x}_i, \mathbf{x}) + b \right], \end{aligned} \quad (21)$$

where  $\text{sgn}[\ ]$  is the sign function. The class to which  $\mathbf{x}$  belongs can be determined by the positive and negative sign of the classification function  $f(\mathbf{x})$ .

It can be known that SVM classifier is a typical two-class classifier. However, there are more than two kinds of faults in HTGR. As a result, multiclass SVM classifier should be adopted. Usually, there are two methods to construct multiclass SVM classifier. One is the multiclass classification algorithm put forward by Weston in 1998. This method reconstructs multiclass classification model and chooses the new objective function of optimization. But the objective function of this algorithm is very complicated due to many variables; it greatly increases the difficulty of solving optimization problem and decreases the classification accuracy. Another method is to combine several two-class classifiers.

The architecture of the SVM-based fault classification algorithm is shown in Figure 2. When constructing classifier  $m$ , the output of Class  $m$  samples is trained as 1 and the output of the rest of samples is trained as  $-1$ . The test sample  $x$  is first put into classifier 1. If the output of classification function  $f^1(x)$  is 1,  $x$  belongs to Class 1. Otherwise,  $x$  is put into classifier 2. If the output of  $f^2(x)$  is 1,  $x$  belongs to Class 2. Otherwise,  $x$  is put into classifier 3. The rest can be done in the same manner. When  $x$  is put into classifier  $k-1$ , if the output of  $f^{k-1}(x)$  is 1,  $x$  belongs to Class  $k-1$ . Otherwise,  $x$  belongs to Class  $k$ .

This paper is first proposing the algorithms combining KECA and SVM to solve the fault diagnosis problems of HTGR. The numerical experiments of KECA-SVM algorithm are expected to be performed in the future work.

## 5. Conclusion

The wireless sensor network can not only reduce the cost of regular monitoring but also enable the ability to achieve intelligent monitoring, which could enhance the economic competitiveness of HTGR. The intelligent monitoring schemes for three example applications of the condition-based maintenance, the fault diagnosis and recovering, and the management of spent fuel materials are proposed. Three major concerns about applying wireless technology in NPPs are addressed. By comparison, the Wi-Fi technology is promising to be the underlying platform for wireless data communication in HTGR. Statistical data processing algorithms, KECA-SVM-based algorithms for fault detection and identification, are developed. The numerical experiments of KECA-SVM algorithm are expected to be performed in the future work.

## Conflicts of Interest

The authors declare that there are no conflicts of interest regarding the publication of this paper.

## Acknowledgments

This paper is jointly supported by the National Natural Science Foundation of China (Grant no. 61502270) and the National S&T Major Project (Grant no. ZX06901).

## References

- [1] IAEA, *Advanced Surveillance, Diagnostic and Prognostic Techniques in Monitoring Structures, Systems and Components in Nuclear Power Plants*, International Atomic Energy Agency, 2013.
- [2] J. Li, X. Kang, Z. Long, J. Meng, and X. Huang, "The application of the wireless sensor network in intelligent monitoring of nuclear power plants," in *Nuclear Power Plants: Innovative Technologies for Instrumentation and Control Systems*, vol. 400, pp. 179–188, Springer, Singapore, 2016.
- [3] S. J. Qin, "Survey on data-driven industrial process monitoring and diagnosis," *Annual Reviews in Control*, vol. 36, no. 2, pp. 220–234, 2012.
- [4] H. M. Hashemian, "Wireless sensors for predictive maintenance of rotating equipment in research reactors," *Annals of Nuclear Energy*, vol. 38, no. 2-3, pp. 665–680, 2011.
- [5] Z. Zhang, Y. Dong, F. Li et al., "The shandong shidao Bay 200 MWe high-temperature gas-cooled reactor pebble-bed

- module (HTR-PM) demonstration power plant: an engineering and technological innovation,” *Engineering*, vol. 2, no. 1, pp. 112–118, 2016.
- [6] “International Electrotechnical Commission: Electromagnetic compatibility (EMC)—Part 4-3: Testing and measurement techniques—Radiated, radio-frequency, electromagnetic field immunity test (IEC 61000-4-3),” 2010.
- [7] United States Nuclear Regulatory Commission, *Guidelines for Evaluating Electromagnetic and Radio-Frequency Interference in Safety-Related Instrumentation and Control Systems (Regulatory Guide 1.180)*, 2003.
- [8] D. Trask, C. Jung, and M. MacDonald, “Cyber security for remote monitoring and control of small reactors,” in *Proceedings of the 19th Pacific Basin Nuclear Conference (PBNC '14)*, Vancouver, Canada, 2014.
- [9] S. Jiang, B. Chai, Y. Cao, S. Zhai, and X. Deng, “Study of the technical solution to the dedicated wireless communication system in nuclear power plant,” *Chinese Journal of Nuclear Science and Engineering*, vol. 30, pp. 275–279, 2010 (Chinese).
- [10] J. M. Lee, C. K. Yoo, S. W. Choi, P. A. Vanrolleghem, and I. B. Lee, “Nonlinear process monitoring using kernel principal component analysis,” *Chemical Engineering Science*, vol. 59, no. 1, pp. 223–234, 2004.
- [11] I. Elaissi, I. Jaffel, O. Taouali, and H. Messaoud, “Online prediction model based on the SVD-KPCA method,” *ISA Transactions*, vol. 52, no. 1, pp. 96–104, 2013.
- [12] V. H. Nguyen and J. C. Golinval, “Fault detection based on Kernel Principal Component Analysis,” *Engineering Structures*, vol. 32, no. 11, pp. 3683–3691, 2010.
- [13] Y. W. Zhang and C. Ma, “Fault diagnosis of nonlinear processes using multiscale KPCA and multiscale KPLS,” *Chemical Engineering Science*, vol. 66, no. 1, pp. 64–72, 2011.
- [14] L. V. Gan, H. Z. Cheng, H. B. Zhai, and L. X. Dong, “Fault diagnosis of power transformer based on multi-layer SVM classifier,” *Electric Power Systems Research*, vol. 7, no. 1, pp. 1–7, 2005.
- [15] K. C. Gryllias and I. A. Antoniadis, “A Support Vector Machine approach based on physical model training for rolling element bearing fault detection in industrial environments,” *Engineering Applications of Artificial Intelligence*, vol. 25, no. 2, pp. 326–344, 2012.
- [16] J. Cui and Y. Wang, “A novel approach of analog circuit fault diagnosis using support vector machines classifier,” *Measurement*, vol. 44, no. 1, pp. 281–289, 2011.
- [17] Z. Chenglin, S. Xuebin, S. Songlin, and J. Ting, “Fault diagnosis of sensor by chaos particle swarm optimization algorithm and support vector machine,” *Expert Systems with Applications*, vol. 38, no. 8, pp. 9908–9912, 2011.

## Research Article

# Dynamic Modeling and Control Characteristics of the Two-Modular HTR-PM Nuclear Plant

**Zhe Dong, Yifei Pan, Maoxuan Song, Xiaojing Huang, Yujie Dong, and Zuoyi Zhang**

*Institute of Nuclear and New Energy Technology, Collaborative Innovation Centre of Advanced Nuclear Energy Technology, Key Laboratory of Advanced Reactor Engineering and Safety of Ministry of Education, Tsinghua University, Beijing 100084, China*

Correspondence should be addressed to Zhe Dong; [dongzhe@mail.tsinghua.edu.cn](mailto:dongzhe@mail.tsinghua.edu.cn)

Received 5 December 2016; Revised 2 March 2017; Accepted 5 March 2017; Published 22 May 2017

Academic Editor: Enrico Zio

Copyright © 2017 Zhe Dong et al. This is an open access article distributed under the Creative Commons Attribution License, which permits unrestricted use, distribution, and reproduction in any medium, provided the original work is properly cited.

The modular high temperature gas-cooled reactor (MHTGR) is a typical small modular reactor (SMR) with inherent safety feature. Due to its high reactor outlet coolant temperature, the MHTGR can be applied not only for electricity production but also as a heat source for industrial complexes. Through multimodular scheme, that is, the superheated steam flows produced by multiple MHTGR-based nuclear supplying system (NSSS) modules combined together to drive a common thermal load, the inherent safety feature of MHTGR is applicable to large-scale nuclear plants at any desired power ratings. Since the plant power control technique of traditional single-modular nuclear plants cannot be directly applied to the multimodular plants, it is necessary to develop the power control method of multimodular plants, where dynamical modeling, control design, and performance verification are three main aspects of developing plant control method. In this paper, the study in the power control for two-modular HTR-PM plant is summarized, and the verification results based on numerical simulation are given. The simulation results in the cases of plant power step and ramp show that the plant control characteristics are satisfactory.

## 1. Introduction

With comparison to burning fossil fuels, there is nearly no greenhouse gas emission in nuclear fission reaction. Thus, nuclear fission energy is a crucial clean energy for giving basis products such as electricity, fresh water, and process heat and for addressing the challenges associated with global climate and environmental impact [1, 2]. Actually, nuclear energy may substitute the fossil in a centralized way and in a great amount with commercial availability and economic competitiveness [3]. After the successful development of small (tens of megawatts) light water reactors (LWRs) for propulsion by the US Navy, the commercial nuclear reactors began to be commissioned since the late 1950s. These early-stage nuclear reactors were the simply scaled up versions of the naval reactor with high power density [4]. Although the increase of the reactor size induced the economic competitiveness with those fossil plants, the complicated operational issues began to moderate the industry's confidence in the plant safety. More stringent safety requirements were then imposed,

which induced a complex layering of redundant safety and auxiliary systems to the original simple LWRs. The escalation of plant complexity contributed to the rapidly increasing costs, licensing periods, and construction delays. However, the plant safety still cannot be guaranteed satisfactorily. After the severe nuclear accidents, that is, Three Mile Island, Chernobyl, and Fukushima, the safety issues of nuclear reactors have become much more significant than before. Thus, there should be a novel reactor technology providing a satisfactory tradeoff between safety and economics.

Small modular reactors (SMRs) are those nuclear fission reactors whose electrical output power is less than 300 MW<sub>e</sub> [4–6]. Due to the low power density and large heat capacity, some SMRs even have the inherent safety feature which prevents SMRs from the hazards of core-melting, radiological release, and LOCA (Loss of Coolant Accident). With load-following function, SMRs can be incorporated with renewable energy sources to build hybrid energy systems (HESs) having the virtues such as persistent power supply and free refueling [1, 2]. By adopting multimodular operation strategy

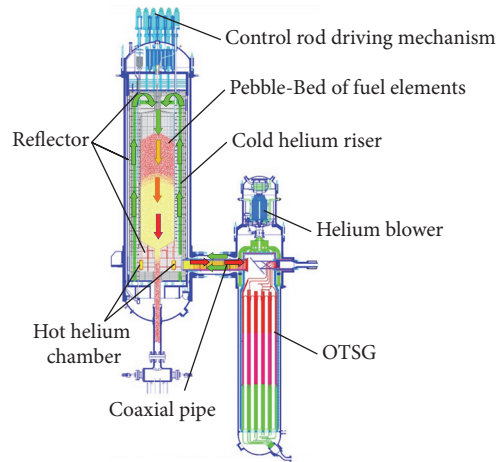


FIGURE 1: Composition of the MHTGR-based NSSS module.

[7], that is, multiple nuclear steam supplying system (NSSS) modules feeding steam to common thermal load equipment such as the turbine/generator set, the inherent safety feature of a SMR can be applicable to large-scale nuclear plants at any desired power ratings, which could be beneficial in providing electricity to remote areas without transmission or distribution infrastructure, in generating local power for a large population center and in being viable for specific applications such as heat sources for the industrial complexes. Furthermore, the SMRs can offer simpler, safer, and standardized modular design by being factory-built, requiring smaller initial capital investment, and having shorter construction period, and have been regarded by International Atomic Energy Agency (IAEA) as one of the active developing trends of nuclear energy.

Due to its inherent safety feature, the modular high temperature gas-cooled reactor (MHTGR, such as HTR-Module designed in Germany and MHTGR designed in US) has been seen as one of the best candidates for the next-generation nuclear plants. The MHTGR is a typical SMR which uses helium as coolant and graphite as moderator and structural material, and its inherent safety is determined by the low power density, strong negative temperature feedback effect, and slim reactor shape [8–10]. China began to study the MHTGR at the end of 1970s, and a 10 MW<sub>th</sub> pebble-bed high temperature gas-cooled reactor HTR-10, which was designed by the Institute of Nuclear and New Energy Technology (INET) of Tsinghua University, achieved its criticality in December 2000 and full power in January 2003 [11]. Then, six safety demonstration tests were done on the HTR-10, which manifested its inherent safety and self-stabilizing features [12]. Based on the experience of the HTR-10 project, a high temperature gas-cooled reactor pebble-bed module (HTR-PM) plant was then proposed, which consists of two pebble-bed one-zone MHTGRs with combined  $2 \times 250$  MW<sub>th</sub> power and adopts the operation scheme of two NSSS modules driving one steam turbine [13, 14]. Figure 1 shows that a NSSS module of the HTR-PM plant is composed of an MHTGR, a helically coiled once-through steam generator (OTSG), a

primary helium blower, and some connecting pipes. Figure 2 illustrates a simplified flow diagram of the entire two-modular HTR-PM plant. The HTR-PM plant is now in the stage of plant construction and commissioning. By incorporating more MHTGR-based NSSS modules, more large-scale multimodular high temperature gas-cooled nuclear plant can be realized.

Satisfactory plant dynamic behavior is important for realizing load-following function and for further forming HESs with fossil or renewable energy sources, which is given by not only the open-loop dynamics but also the control strategy. There have been some promising results in dynamical modeling and control design for entire nuclear plants. In the field of plant modeling, Han gave a mathematical model of pressurized water reactors for thermal-hydraulic analysis [15]. Fazekas et al. proposed a simple dynamic model for the primary circuit in VVER plants for controller design purposes [16]. Dong et al. presented a lumped parameter dynamic model for control design and verification for the NSSS of the nuclear heating reactors (NHRs) [17]. With comparison to the abundant results in reactor power-level regulation such as the linear control, nonlinear control, and intelligent method [18–20], there are still less results in the field of entire nuclear plant control. Shtessel proposed a sliding-mode plant control and state-observation strategy for space nuclear energy system TOPAZ II [21]. Huang et al. gave a multi-input-multioutput (MIMO) fuzzy-adapted recursive sliding-mode plant controller for an advanced boiling water reactor (ABWR) nuclear power plant [22]. In order to achieve safe, stable, and efficient operation of the HTR-PM plant, it is necessary to give the lumped parameter model of the main plant dynamics and to propose proper plant control strategy. It is worth noting that, due to the two-modular scheme, there is much difference between the modeling and control of the HTR-PM plant and that of those single-modular nuclear plant.

In this paper, both the dynamical modeling and control design method for HTR-PM plant are first summarized or reviewed, the realization of feedback loops and control

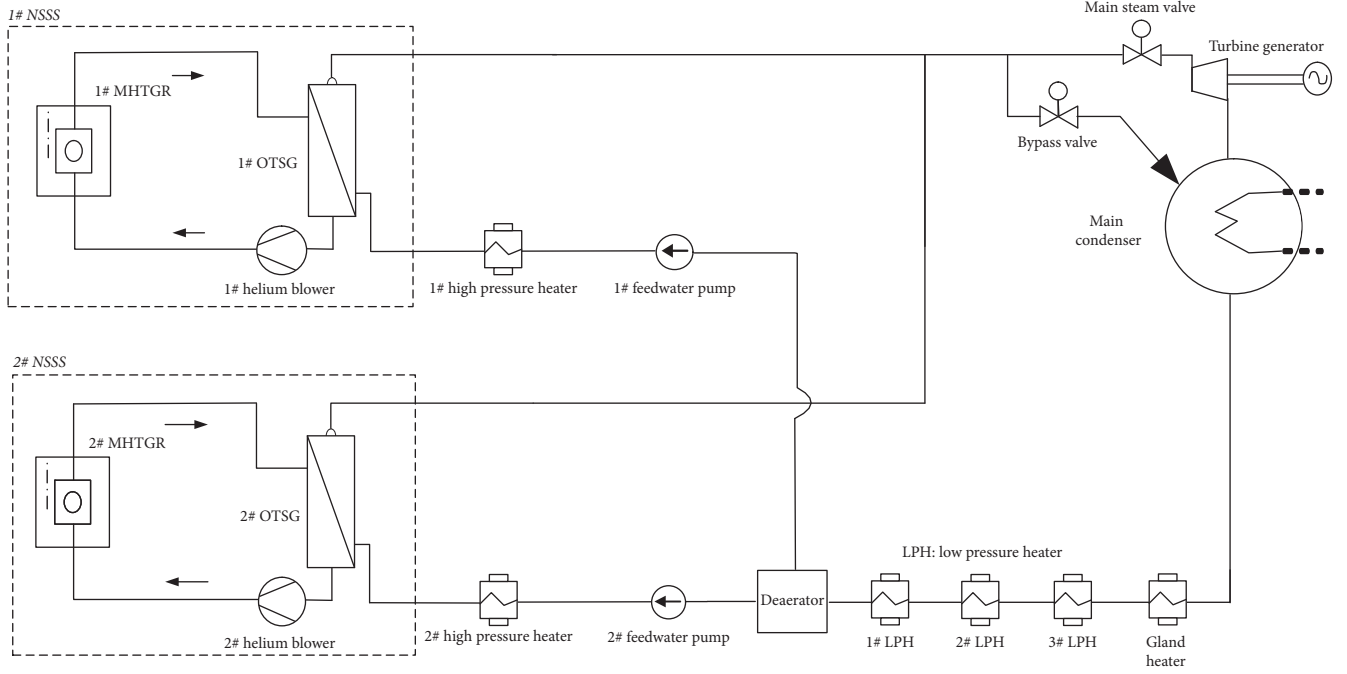


FIGURE 2: Simplified flow diagram for the HTR-PM plant.

laws are proposed, and then the verification results based upon numerical simulation are given, which shows the main transient performance of the HTR-PM plant is satisfactory for building HESs with the renewables.

## 2. Dynamical Modeling

In this section, the main parts of dynamic model of the HTR-PM plant, that is, the pebble-bed one-zone MHTGR, OTSG, fluid flow network (FFN) of the common secondary-loop system, and turbine/generator unit, are summarized from [23–26]. This model is proposed for control system design and verification, whose parameters are determined by the data collected from physical and thermal-hydraulic design.

**2.1. MHTGR.** From Figure 1, the cold helium enters the primary blower where it is pressurized before flowing into the cold gas duct. Then, the cold helium gets into the channels (called riser) inside the side reflector from bottom to top and passes through the pebble-bed (called downcomer) from top to bottom where it is heated to a high temperature about 750°C. The hot helium leaves the hot gas chamber inside the bottom reflector and flows into the OTSG primary side where it transfers the heat to the secondary feedwater. To guarantee the inherent safety feature, the MHTGR of the HTR-PM plant has a slim core shape. Relative to using a single node [23], it is more proper to divide the reactor core into  $N$  nodes along the axial direction [24]. The nodalization is shown in Figure 3, where the riser is some tubes in the side reflector through which helium can flow upward to the upper entry of the pebble-bed, and the downcomer is the volume gap among the

fuel elements inside the pebble-bed through which helium can flow down. Moreover, the pressure loss of the primary helium flow is very small with comparison to the primary pressure and is omitted here.

**2.1.1. Neutron Kinetics.** The nodalized neutron kinetics can be written as [24]

$$\begin{aligned}
 \frac{dn_{r,1}}{dt} &= \frac{\rho_1 - \beta - \alpha_{1,1}}{\Lambda_1} n_{r,1} + \frac{1}{\Lambda_1} \alpha_{1,2} n_{r,2} + \sum_{k=1}^6 \frac{\beta_k}{\Lambda_1} C_{r,1,k}, \\
 \frac{dn_{r,i}}{dt} &= \frac{\rho_i - \beta - \alpha_{i,i}}{\Lambda_i} n_{r,i} \\
 &\quad + \frac{1}{\Lambda_i} (\alpha_{i,i-1} n_{r,i-1} + \alpha_{i,i+1} n_{r,i+1}) \\
 &\quad + \sum_{k=1}^6 \frac{\beta_k}{\Lambda_i} C_{r,i,k}, \quad i = 2, \dots, N-1, \\
 \frac{dn_{r,N}}{dt} &= \frac{\rho_N - \beta - \alpha_{N,N}}{\Lambda_N} n_{r,N} + \frac{1}{\Lambda_N} \alpha_{N,N-1} n_{r,N-1} \\
 &\quad + \sum_{k=1}^6 \frac{\beta_k}{\Lambda_N} C_{r,N,k}, \\
 \frac{dC_{r,i,k}}{dt} &= \lambda_k (n_{r,i} - C_{r,i,k}), \\
 &\quad i = 1, \dots, N, \quad k = 1, 2, \dots, 6,
 \end{aligned} \tag{1}$$

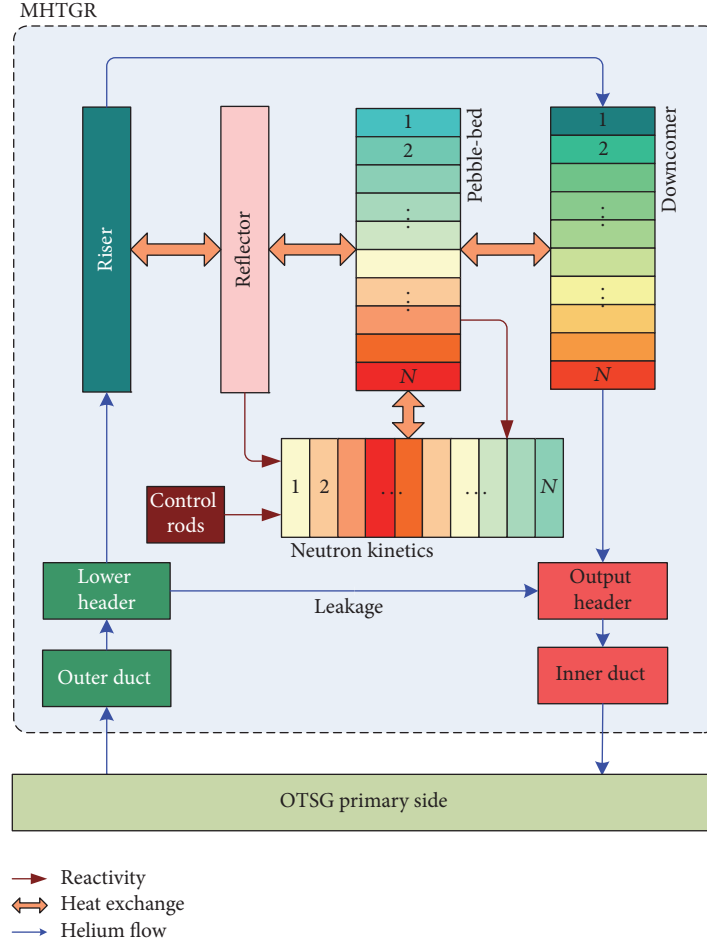


FIGURE 3: Nodalization of the MHTGR.

where  $i = 1, \dots, N$ ,  $n_{r,i}$  is the relative neutron flux of the  $i$ th node,  $C_{r,i,k}$  is the relative concentration of the  $k$ th delayed neutron group of the  $i$ th node,  $\alpha_{i,i}$  and  $\alpha_{i,j}$  ( $j = 1, \dots, N_i$ ) are the coupling coefficients corresponding to the  $i$ th node,  $N_i$  is the number of adjacent nodes of the  $i$ th node,  $\Lambda_i$  is the prompt neutron lifetime in the  $i$ th node,  $\rho_i$  is the reactivity of the  $i$ th node,  $\beta$  is the fraction of all the delayed neutrons in all the nodes, and  $\beta_k$  is the fraction of the  $k$ th delayed neutron group in every node.

The nodal reactivity feedback is expressed as function of the nodal fuel temperature  $T_{c,i}$  ( $i = 1, \dots, N$ ) and temperature of the reflector  $T_r$ . The total nodal reactivity is given as [24]

$$\rho_i = \rho_{r,i} + (\alpha_{f,i} + \alpha_{m,i})(T_{c,i} - T_{c0,i}) + \alpha_r(T_r - T_{r0}), \quad (2)$$

where  $\rho_{r,i}$  is the nodal reactivity provided by the control rods,  $\alpha_{f,i}$  and  $\alpha_{m,i}$  are, respectively, the reactivity coefficients of the fuel and moderator inside node  $i$ ,  $\alpha_r$  is the reactivity coefficient of the average reflector temperature, and  $T_{c0,i}$  and  $T_{r0}$  are, respectively, the initial temperature of the fuel inside node  $i$  and that of the reflector. Since the reflector is very thick, and since the metal core support structure is cooled by the cold helium with its temperature no more than 250°C, the

reactivity feedback induced by the support structure is omitted here, which has been verified by the MHTGR physical and thermal-hydraulic design.

Moreover, it can be derived that [24]

$$\alpha_{i,j} = \left( \frac{n_{j0}}{n_{i0}} \right) \frac{DA}{v \Sigma_{f,i} V d},$$

$$j = \begin{cases} 2, & i = 1 \\ i - 1, i + 1, & i = 2, \dots, N - 1 \\ N - 1, & i = N, \end{cases} \quad (3)$$

$$\alpha_{i,i} = \begin{cases} \frac{DA}{v \Sigma_{f,2} V d}, & i = 1, \\ \frac{DA}{v V d} \left( \frac{1}{\Sigma_{f,i-1}} + \frac{1}{\Sigma_{f,i+1}} \right), & i = 2, \dots, N - 1, \\ \frac{DA}{v \Sigma_{f,N-1} V d}, & i = N, \end{cases}$$

where  $A$  is the cross-sectional area of the active core region,  $V$  is the volume of every node,  $d$  is the height of every node,  $v$  is the fission number,  $\Sigma_{a,i}$  and  $\Sigma_{f,i}$  ( $i = 1, \dots, N$ ) are,

respectively, the macroabsorption and fission cross sections in the  $i$ th node.

### 2.1.2. Thermal Hydraulics

(1) *Pebble-Bed*. The thermal dynamics of  $i$ th node of the pebble-bed can be written as [24]

$$(1 - \varepsilon) \rho_{c,i} V C_{c,i} \frac{dT_{c,i}}{dt} = P_{0,i} n_{r,i} - K_{d,i} A_{d,i} (T_{c,i} - T_{d,i}) - K_{cr,i} A_{cr,i} (T_{c,i} - T_r) + \begin{cases} -K_{c,1} A (T_{c,1} - T_{c,2}), & i = 1, \\ -K_{c,i} A (T_{c,i} - T_{c,i+1}) + K_{c,i-1} A (T_{c,i-1} - T_{c,i}), & i = 2, \dots, N-1, \\ K_{c,N-1} A (T_{c,N-1} - T_{c,N}), & i = N, \end{cases} \quad (4)$$

where  $\rho_{c,i}$ ,  $C_{c,i}$ ,  $T_{c,i}$ , and  $P_{0,i}$  are, respectively, the density, specific heat, temperature, and rated power of fuel pile inside node  $i$ ,  $K_{d,i}$  and  $A_{d,i}$  are, respectively, the heat transfer coefficient and heat transfer area between the fuel pile and helium inside node  $i$ ,  $T_{d,i}$  is the temperature of the helium inside node  $i$ ,  $K_{cr,i}$  and  $A_{cr,i}$  are, respectively, the heat transfer coefficient and heat transfer area between the fuel pile in node  $i$  and the reflector,  $T_r$  is the temperature of the reflector,  $K_{c,i}$  ( $i = 1, \dots, N-1$ ) is the heat transfer coefficient between the fuel pile inside node  $i$  and that inside node  $i+1$ , and  $\varepsilon$  is the porosity of the pebble-bed.

(2) *Reflector*. To improve the heat capacity and to weaken the neutron leakage, the reflector of the MHTGR is very thick, which means that the thermal inertial of the reflector is so large that the dynamic response of the reflector is in different scale with that of the fuel elements and helium flow. Moreover, the side reflector is cooled by the cold helium flow injected into the reactor with a high speed. Therefore, for the simplicity of dynamic model, it is reasonable to regard the reflector as one nodal.

From Figure 3, there are two heat transfer processes with the reflector. This first one is the fission heat conducted from the fuel pile inside every node, which heats up the reflector. The second one is that the cold helium inside the riser cools down the reflector. The heat transfer about the reflector can be written as [24]

$$\rho_r V_r C_r \frac{dT_r}{dt} = \sum_{i=1}^N K_{cr,i} A_{cr,i} (T_{c,i} - T_r) - K_{ur} A_{ur} (T_r - T_u), \quad (5)$$

where  $\rho_r$ ,  $V_r$ , and  $C_r$  are, respectively, the density, volume, and specific heat of the reflector,  $K_{ur}$  and  $A_{ur}$  are the heat transfer coefficient and heat transfer area between the reflector and the coolant in the riser, and  $T_u$  is the average coolant temperature inside the riser.

(3) *Downcomer*. The cold helium enters the downcomer from its upper entry and flows downward to cool the pebble-bed. The heat is mainly transferred to the helium inside the downcomer, which can be described as [24]

$$V_i \frac{d\rho_{d,i}}{dt} = \begin{cases} W_u - W_{d,1}, & i = 1, \\ W_{d,i-1} - W_{d,i}, & i = 2, \dots, N, \end{cases}$$

$$\varepsilon V_i C_p \frac{d(\rho_{d,i} T_{d,i})}{dt} = K_{d,i} A_{d,i} (T_{c,i} - T_{d,i}) + \begin{cases} C_p (W_u T_u - W_{d,1} T_{d,1}), & i = 1, \\ C_p (W_{d,i-1} T_{d,i-1} - W_{d,i} T_{d,i}), & i = 2, \dots, N, \end{cases} \quad (6)$$

where  $\rho_{d,i}$  and  $W_{d,i}$  are, respectively, the density and flowrate of the helium inside node  $i$  of the downcomer and  $C_p$  is the helium specific heat at constant pressure. Then, substitute (6), the thermodynamics of the helium in the downcomer can be written as [24]

$$\varepsilon V_i \rho_{d,i} C_p \frac{dT_{d,i}}{dt} = K_{d,i} A_{d,i} (T_{c,i} - T_{d,i}) + \begin{cases} C_p W_u (T_u - T_{d,1}), & i = 1, \\ C_p W_{d,i-1} (T_{d,i-1} - T_{d,i}), & i = 2, \dots, N. \end{cases} \quad (7)$$

(4) *Riser*. In the channels of the riser, the cold helium flows upward to cool the reflector, and the heat transfer process can be described by [23, 24]

$$V_u \frac{d\rho_u}{dt} = (1 - \kappa) W_{lh} - W_u, \\ V_u C_p \frac{d(\rho_u T_u)}{dt} = C_p [(1 - \kappa) W_{lh} T_{lh} - W_u T_u] + K_{ur} A_{ur} (T_r - T_u), \quad (8)$$

where  $\rho_u$ ,  $W_u$ , and  $T_u$  are, respectively, the density, flowrate, and temperature of the helium inside the riser,  $W_{lh}$  and  $T_{lh}$  are, respectively, the flowrate and temperature of the helium inside the lower header, and  $\kappa$  is the leakage ration of the lower header. Substitute (8), the thermodynamics of the helium inside the riser can be written as

$$V_u \rho_u C_p \frac{dT_u}{dt} = C_p (1 - \kappa) W_{lh} (T_{lh} - T_u) + K_{ur} A_{ur} (T_r - T_u). \quad (9)$$

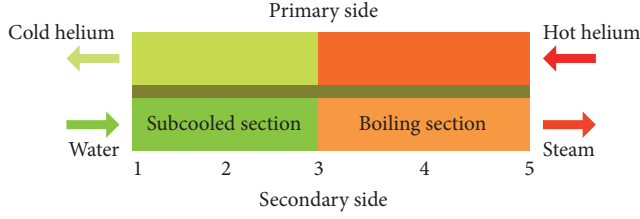


FIGURE 4: Nodalization scheme of the OTSG.

(5) *Lower Header*. The lower header is assumed to be a well-mixed chamber which has no heat exchange with the environment, and the thermodynamics corresponding to the lower header can be expressed as [23, 24]

$$V_{lh}\rho_{lh}\frac{dT_{lh}}{dt} = W_{lh}(T_{in} - T_{lh}), \quad (10)$$

where  $T_{in}$  is the temperature of the inlet cold helium,  $\rho_{lh}$ ,  $W_{lh}$ , and  $T_{lh}$  are, respectively, the density, flowrate, and temperature of the helium inside the lower header, and  $V_{lh}$  is the volume of the low header.

(6) *Outlet Header*. The output header is assumed to be a well-mixed chamber, and its dynamics can be given as [23, 24]

$$V_{oh}\rho_{oh}\frac{dT_{oh}}{dt} = \kappa W_{lh}(T_{lh} - T_{oh}) + W_{d,N}(T_{d,10} - T_{oh}), \quad (11)$$

where  $\rho_{oh}$ ,  $W_{lh}$ , and  $T_{oh}$  are, respectively, the density, flowrate, and temperature of the helium inside the outlet header and  $V_{oh}$  is the volume of the outlet header.

**2.1.3. MHTGR Dynamics.** The dynamic model of MHTGR is composed of neutron kinetics determined by (1)–(3) as well as thermal hydraulics given by (4), (5), (7), and (9)–(11). The dynamic behavior of this MHTGR model can be influenced by nodal number  $N$ , and an improper nodal number leads to the fluctuation of the responses. Actually, this model is only utilized for control design and verification and is not for physical and thermal-hydraulic design. The nodal numbers are determined by comparing the response

of this model with that of the model for physical and thermal-hydraulic design. When the error between responses is satisfactorily small, the corresponding nodal number is suitable. Here, the nodal number  $N$  is chosen to be 10. Based on the simulation results to be given in Section 4, it will be seen that there is no numerical fluctuation in the responses, and all the transience is determined by power-level maneuver which show that the nodal number is properly selected.

Since the dynamic model in this paper is tuned based upon the comparison with the model for reactor physical and thermal-hydraulic design, the stability of this model is also guaranteed by the model for reactor design. Moreover, it was shown in [27] that the MHTGR is open-loop globally asymptotically stable, and by the use of the shifted-entropy-based self-stability analysis method given in [27], it can be shown that the model coupled by neutron kinetics and thermal hydraulics are open-loop globally asymptotically stable.

**2.2. OTSG.** Since the OTSG can provide superheated steam which does not satisfy the one-to-one map from pressure to temperature, the OTSG is more proper for building multi-SMR-based nuclear plants. Therefore, the dynamic model of the OTSG is very crucial for studying behavior of the SMR-based plant and also for verifying the operation and control strategies. In this section, a moving-boundary model [25] is introduced for describing OTSG dynamics in the cases of generating saturated and superheated steam [26]. The nodalization of the OTSG is given in Figure 4.

**2.2.1. Secondary Side.** The dynamics of the OTSG secondary side is given by both the thermodynamics and pressure drops of the secondary fluid flow.

(1) *Thermodynamics.* The thermodynamics of the secondary side can be given by the following vector-valued nonlinear differential equation [26]:

$$E_s(\mathbf{x}_s)\frac{d\mathbf{x}_s}{dt} = \mathbf{f}_s(\mathbf{x}_s, \mathbf{u}_s), \quad (12)$$

where

$$\mathbf{x}_s = [l_{13} \ h_{s5} \ h_{s1} \ G_{s3}]^T,$$

$$\mathbf{u}_s = [G_{s1} \ h_{fw} \ Q_{s2} \ Q_{s4}]^T,$$

$$E_s(\mathbf{x}_s) = \begin{bmatrix} E_{s11}(\mathbf{x}_s) & 0 & \frac{1}{2}\rho_{s2}l_{13} & E_{s14}(\mathbf{x}_s) \\ E_{s21}(\mathbf{x}_s) & \frac{1}{2}\rho_{s4}l_{35} & 0 & E_{s24}(\mathbf{x}_s) \\ 0 & 0 & \tau_H & 0 \\ 0 & 0 & 0 & \tau_G \end{bmatrix},$$

$$E_{s11}(\mathbf{x}_s) = \frac{1}{2} \left[ \rho_{s3}(h_{s1} - h_{s3}) + (P_{s3} - P_{s1}) + l_{13} \left( 1 - \rho_{s2} \left. \frac{\partial h_{s3}}{\partial P_{s3}} \right|_{P_{s3}} \right) \left( \rho_{s2}g \sin \theta + F_{s2} \frac{G_{s2}^2}{A_{s2}^2} \right) \right],$$

$$\begin{aligned}
E_{s14}(\mathbf{x}_s) &= \frac{F_{s2}G_{s2}l_{13}^2}{2A_{s2}^2} \left( 1 - \rho_{s2} \left. \frac{\partial h_{s3}}{\partial P_{s3}} \right|_{P_{s3}} \right), \\
E_{s21}(\mathbf{x}_s) &= \frac{1}{2} \left\{ \rho_{s3} (h_{s3} - h_{s5}) + (P_{s5} - P_{s3}) + l_{35} \left[ \left( 2 - \rho_{s4} \left. \frac{\partial h_{s3}}{\partial P_{s3}} \right|_{P_{s3}} \right) \left( \rho_{s2} g \sin \theta + F_{s2} \frac{G_{s2}^2}{A_{s2}^2} \right) - \left( \rho_{s4} g \sin \theta + F_{s4} \frac{G_{s4}^2}{A_{s4}^2} \right) \right] \right\}, \\
E_{s24}(\mathbf{x}_s) &= l_{35} \left[ \left( 1 - \frac{1}{2} \rho_{s4} \left. \frac{\partial h_{s3}}{\partial P_{s3}} \right|_{P_{s3}} \right) \frac{F_{s2}G_{s2}l_{13}}{A_{s2}^2} + \frac{2F_{s4}G_{s4}l_{13}}{A_{s2}^2} \right], \\
\mathbf{f}_s(\mathbf{x}_s, \mathbf{u}_s) &= \left[ \frac{Q_{s2}}{A_{s2}} + \frac{1}{2} \left( \frac{G_{s1}}{A_{s1}} + \frac{G_{s3}}{A_{s3}} \right) (h_{s1} - h_{s3}) \frac{Q_{s4} + G_{s4} (h_{s3} - h_{s5})}{A_{s4}} \frac{h_{fw} - h_{s1}}{\tau_H} \frac{G_{s1} - G_{s3}}{\tau_G} \right]^T,
\end{aligned} \tag{13}$$

$g$  is the gravitational acceleration (N/m/s<sup>2</sup>), both  $\tau_G$  and  $\tau_H$  are given positive constants denoting inertial effect,  $h_{fw}$  is the enthalpy per unit mass (J/kg) of the feedwater flow,  $l_{ij}$  ( $i, j = 1, \dots, 5$  and  $i < j$ ) is the length between points  $i$  and  $j$  in Figure 4, and  $\rho_{si}$ ,  $G_{si}$ ,  $h_{si}$ ,  $Q_{si}$ , and  $A_{si}$  are, respectively, the flow density (kg/m<sup>3</sup>), flowrate (kg/s), enthalpy per unit mass (J/kg), heat flux from the primary side, and cross section (m<sup>2</sup>) of node  $i$  of the secondary side. Here,  $l_{13}$  is the length of the subcooled section,  $l_{35}$  is that of the boiling section, and  $h_{1s}$  is specific enthalpy of the feedwater. Due to the high speed of the steam flow, it is assumed that  $G_{s3} = G_{s4} = G_{s5}$ .

(2) *Pressure Drops*. The pressure drop of the fluid flow in the OTSG secondary side cannot be omitted, and the pressure of each node is given by [26]

$$\begin{aligned}
P_{s3} &= P_{s1} - \rho_{s2} g l_{13} \sin \theta - F_{s2} l_{13} G_{s2}^2, \\
P_{s5} &= P_{s3} - \rho_{s4} g l_{35} \sin \theta - F_{s4} l_{35} G_{s4}^2, \\
P_{s4} &= \frac{(P_{s3} + P_{s5})}{2}, \\
P_{s2} &= \frac{(P_{s1} + P_{s3})}{2},
\end{aligned} \tag{14}$$

where  $\theta$  is the helically coiled angle of the tubes,  $F_{si}$  ( $i = 2, 4$ ) is the friction factor of the two sections, and  $P_{s1}$  is the feedwater pressure.

2.2.2. *Tube Wall*. There is no flow inside the metal tube wall between the primary and secondary sides, and the dynamics of the tube wall are determined by its thermodynamics, which can be expressed as [26]

$$\begin{aligned}
\frac{dT_{m2}}{dt} &= \frac{Q_{p2} - Q_{s2}}{C_m \rho_m A_{m2} l_{13}} + \frac{T_{m4} - T_{m2}}{l_{15}} \frac{dl_{13}}{dt}, \\
\frac{dT_{m4}}{dt} &= \frac{Q_{p4} - Q_{s4}}{C_m \rho_m A_{m4} l_{35}} + \frac{T_{m4} - T_{m2}}{l_{15}} \frac{dl_{13}}{dt},
\end{aligned} \tag{15}$$

where  $Q_{p2}$  and  $Q_{p4}$  are, respectively, the heat flux from the primary helium flow to tube wall in the subcooled and boiling sections.

2.2.3. *Primary Side*. Since velocity of the primary helium flow is much higher than that of the two-phase flow inside the secondary side, the energy and temperature relationship of the primary side can be given by the following algebraic equation [26]:

$$\mathbf{A}_p(\mathbf{x}_s) \mathbf{x}_p = \mathbf{b}_p(\mathbf{x}_m, \mathbf{x}_p), \tag{16}$$

where

$$\begin{aligned}
\mathbf{x}_p &= [T_{p1} \ T_{p2} \ T_{p3} \ T_{p4}]^T, \\
\mathbf{A}_p(\mathbf{x}_m) &= \begin{bmatrix} 1 & -2 & 1 & 0 \\ 0 & l_{35} & -l_{15} & l_{13} \\ -C_p G_p & -K_{p2} l_{13} & C_p G_p & 0 \\ 0 & 0 & -C_p G_p & -K_{p4} l_{35} \end{bmatrix}, \\
\mathbf{b}_p(\mathbf{x}_m, \mathbf{x}_p) &= [0 \ 0 \ -K_{p2} l_{13} T_{m2} \ -K_{p4} l_{35} T_{m4} - C_p G_p T_{p5}]^T,
\end{aligned} \tag{17}$$

where  $G_p$  is the primary helium flowrate,  $C_p$  is the helium specific heat,  $T_{pi}$  is the helium temperature at point  $i$  ( $i = 1, \dots, 5$ ),  $K_{p2}$  and  $K_{p4}$  are the heat transfer coefficients between the primary side and tube wall of the subcooled and boiling sections, respectively, and  $K_{s2}$  and  $K_{s4}$  are, respectively, the heat transfer coefficients between the tube wall and secondary side of the subcooled and boiling sections.

2.3. *Secondary-Loop FFN*. After the hot helium leaves the reactor, it flows into the OTSG primary side where it transfers the heat to the secondary feedwater. By absorbing the heat of the primary loop, the feedwater is converted to the superheated steam in 571°C and about 13.9 MPa or so. The

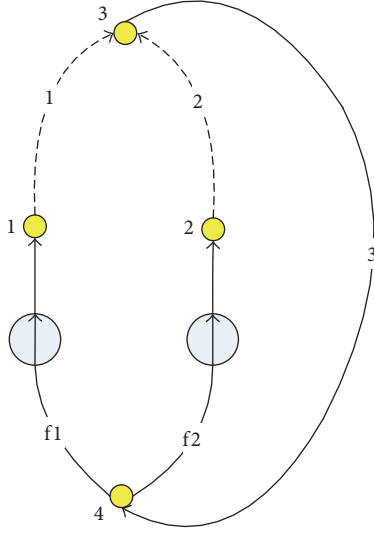


FIGURE 5: Fluid flow network of the secondary loop of the HTR-PM plant.

main steam flow at 13.24 MPa combined from the two NSSS modules then enters the steam turbine for producing electricity. The condensed flow is fed into the OTSG secondary side again after it goes through the grand heater, low pressure heaters (LPHs), deaerator, and high pressure heaters (HPHs). Thus, the hydraulics of the secondary-loop system can be modeled as the FFN shown in Figure 5, where branches  $f_1$  and  $f_2$  are the fan branches of which everyone has a feedwater pump, branches 1 and 2 denote the secondary side of the OTSGs corresponding to the first and second NSSS module respectively, and branch 3 contains the equipment of the plant secondary loop such as the steam turbine, condenser, low pressure heaters, and deaerator.

The flowrate dynamics of branches 1, 2, and 3 can be given as [28, 29]

$$\frac{d\mathbf{Q}}{dt} + \mathbf{K}\mathbf{Q}_D^2\mathbf{R} = \mathbf{K}\mathbf{H}, \quad (18)$$

where  $\mathbf{Q} = [Q_1, Q_2, Q_3]^T$ ,  $\mathbf{Q}_D^2 = [\text{diag}(\mathbf{Q})]^2$ ,  $\mathbf{K} = \text{diag}(K_1, K_2, K_3)$ ,  $\mathbf{R} = [R_1, R_2, R_3]^T$ ,  $\mathbf{H} = [H_1, H_2, H_3]^T$ , and  $Q_j$ ,  $R_j$ ,  $H_j$ , and  $K_j$  are the flowrate, resistance, pressure drop, and inertia coefficient of branch  $j$  ( $j = 1, 2, 3$ ), respectively.

Every FFN can be divided into a tree containing the fan branches and its complement, that is, the cotree whose branches are referred to as the links. From Figure 5, the branches with solid line, that is, branches 3,  $f_1$ , and  $f_2$ , constitute the tree of this FFN, and the branches with dashed line, that is, branches 1 and 2, are the links which constitute the cotree. Based on the network property, the pressure drops and the flowrates of the tree branches are not independent and obey the following algebraic equations given by Kirchhoff's voltage law (KVL) and Kirchhoff's current law (KCL) [28]:

$$\begin{aligned} [H_1 \ H_2]^T &= -[H_3 + H_{f_1} \ H_3 + H_{f_2}]^T, \\ [Q_3 \ Q_{f_1} \ Q_{f_2}]^T &= [Q_1 + Q_2 \ Q_1 \ Q_2]^T, \end{aligned} \quad (19)$$

where  $H_{f_j}$  is the pressure drop of fan branch  $j$  ( $j = 1, 2$ ) and can be further expressed as

$$H_{f_j} = -H_{d_j} + R_{f_j}Q_{f_j}, \quad j = 1, 2. \quad (20)$$

Then, based on (18) and (19), the hydraulics of the FFN shown in Figure 4 can be given by differential-algebraic system [29]:

$$\frac{d\mathbf{Q}_c}{dt} = -\mathbf{K}_c (\mathbf{R}_f \mathbf{Q}_c + \mathbf{Q}_{cD}^2 \mathbf{R}_c) + \mathbf{K}_c (\mathbf{H}_d - H_3 \boldsymbol{\eta}), \quad (21)$$

$$\bar{\mathbf{K}} H_3 = \mathbf{k}_c^T \mathbf{H}_d - \mathbf{k}_{fc}^T \mathbf{Q}_c - \mathbf{k}_c^T \mathbf{Q}_{cD}^2 \mathbf{R}_c + K_3 Q_3^2 R_3,$$

where  $\mathbf{Q}_c = [Q_1, Q_2]^T$ ,  $\mathbf{Q}_{cD}^2 = [\text{diag}(Q_1, Q_2)]^2$ ,  $\mathbf{k}_c = [K_1, K_2]^T$ ,  $\mathbf{k}_{fc} = [K_1 R_{f_1}, K_2 R_{f_2}]^T$ ,  $\bar{\mathbf{K}} = K_1 + K_2 + K_3$ ,  $\mathbf{K}_c = \text{diag}(K_1, K_2)$ ,  $\mathbf{R}_f = \text{diag}(R_{f_1}, R_{f_2})$ , and  $\boldsymbol{\eta} = [1 \ 1]^T$ .

**2.4. Model Integration.** The above dynamic models of the MHTGR, OTSG, and secondary-loop FFN can be integrated together with other commonly utilized models such as the turbine and the synchronous generator to form the dynamic model for the whole plant. Based upon this model, a simulation code for the dynamic behavior and control characteristics of the HTR-PM plant is developed under MATLAB/Simulink platform, and the composition of this Simulink model is shown in Figure 6. This model can incorporate the plant control laws proposed in the next section for giving the simulations of the operational and control characteristics of the HTR-PM plant, where the program modules named as "1# NSSS" and "2# NSSS" are used to simulate the dynamic behavior of the two NSSS modules, the program module named as "secondary-loop FFN" is used to simulate the thermal hydraulics for the secondary-loop FFN, the module "Secondary Thermal Feature" is used to simulate the thermodynamics of secondary-loop systems, and module "Generator" is used to simulate the electric generator dynamics. Furthermore, some important model parameters are given in Table 1.

### 3. Plant Power Control

Plant control is a key technique to provide safe, stable, and efficient operation for every nuclear plant and to balance the power supply and demand. Since the two NSSS modules of the HTR-PM plant are coupled together by the common secondary loop including the turbine/generator set, and since the side-by-side arranged MHTGR and OTSG of a NSSS module are tightly coupled with each other through the connecting pipes, it is more difficult to design a power control strategy for the two-modular HTR-PM plant than for those traditional single-modular traditional nuclear plants. Furthermore, the HTR-PM plant is essentially a large-scale and multi-input-multioutput (MIMO) nonlinear system whose complexity in its dynamics certainly leads to the complexity in its plant control strategy, while, in the practical engineering, a single control loop is usually utilized to regulate a single process parameter such as the nuclear power, primary flow, feedwater flow, helium temperature, and steam

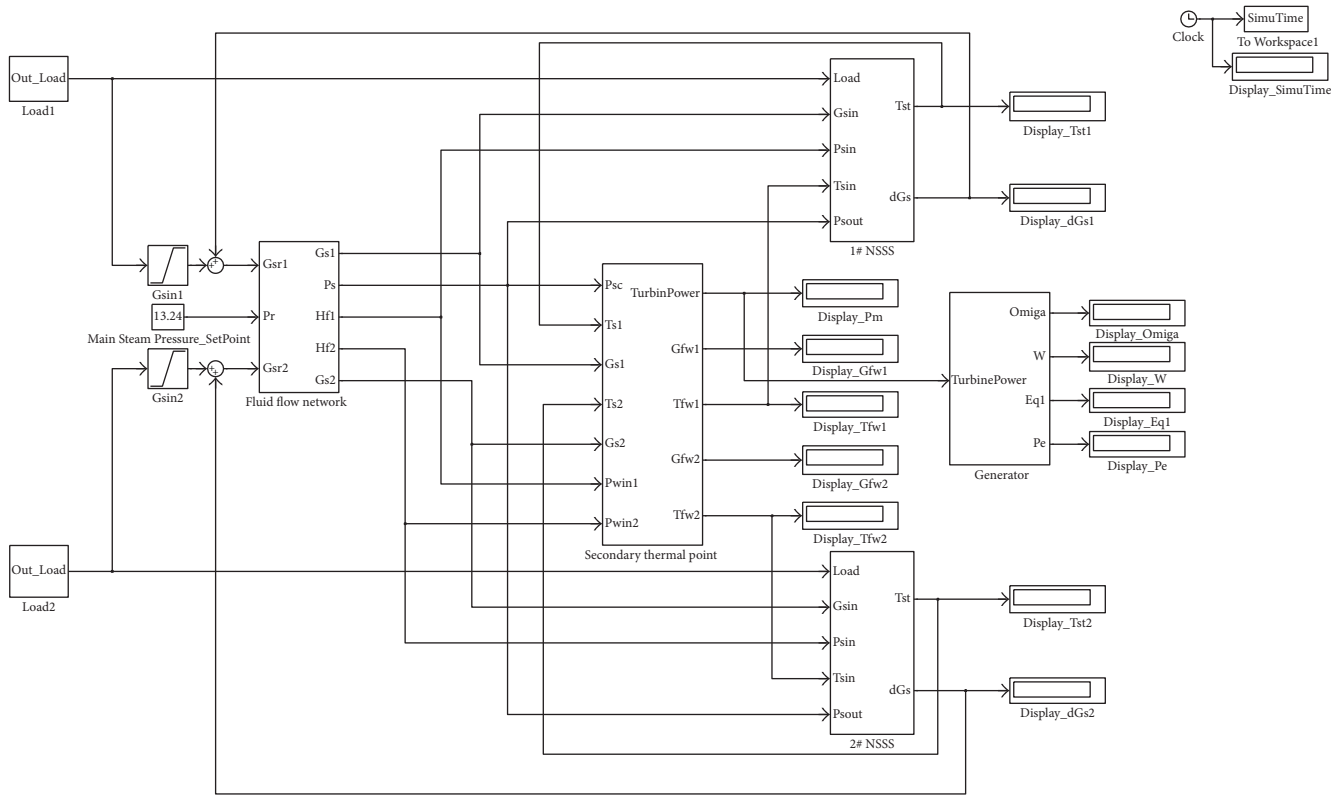


FIGURE 6: Composition of the SIMULINK code.

temperature. Since the combination of all these single control loops deeply affects the plant dynamic behavior, it is necessary to coordinate these control loops for satisfactory closed-loop stability as well as transient performance. In this section, the control design method is first reviewed, and the control realization including feedback loops and control laws is then given.

**3.1. Control Design Method.** The control design mainly lies in two aspects, that is, feedback loop design and control law design, which are tightly related to each other. There have been many process control system design approaches such as the relative gain analysis- (RGA-) based method. In this paper, both the feedback loops and control laws of HTR-PM control system are designed by the use of the physics-based NSSS control method proposed in [30–36] and module coordination control method proposed in [28, 29], which provide the globally asymptotic closed-loop stability through guaranteeing the convergence of Lyapunov functions determined by the shifted-ectropies of neutron kinetics and thermodynamics as well as the kinetic energy stored in secondary-loop FFN.

**3.1.1. NSSS Module Control.** Both the MHTGR and OTSG are complex nonlinear dynamic systems, and their dynamics are tightly coupled with each other due to their side-by-side arrangement. To improve both the steady and transient

performance, it is necessary to give proper control laws for the NSSS module composed of the MHTGR and OTSG by considering the nonlinear dynamics. The physics-based control (PBC) method is an effective way to design nonlinear reactor control laws by retaining or strengthening stable subdynamics and by cancelling or suppressing unstable subdynamics, which has been applied to the load-following control design for the PWR [30, 31], MHTGR [32–34], and OTSG [35]. Very recently, based upon the PBC method, a novel model-free MHTGR-based NSSS module control strategy was proposed in [36], which provides globally asymptotic stability (GAS) for the NSSS module if the feedwater temperature is constant and both the helium and feedwater flowrate are well regulated. This NSSS module control strategy can be realized by feedback loops given in Section 3.2.1 and simple control laws given in Section 3.3.1.

**3.1.2. Coordination Control of Multiple NSSS Modules.** Through the multimodular scheme, the inherent safety of the MHTGR is applicable to the large-scale plants with any desired power ratings. Module coordination control is one of the most important characteristics of the multimodular nuclear plants such as the HTR-PM with comparison to the control of those traditional single module nuclear plants. It has been revealed in [29] that the module coordination problem is essentially a flowrate-pressure regulation problem of the secondary-loop FFN. Moreover, based on the dissipation

TABLE 1: Main parameters of the dynamic model.

Parameter	Name	Unit	Value
$\Lambda_i$ ( $i = 1, \dots, 10$ )	Prompt neutron lifetime	s	$7.66e - 4$
$\beta$	Fraction of all the delayed neutrons	%	0.67
$\beta_1$	Fraction of 1st group delayed neutrons	%	0.0256
$\beta_2$	Fraction of 2nd group delayed neutrons	%	0.14
$\beta_3$	Fraction of 3rd group delayed neutrons	%	0.13
$\beta_4$	Fraction of 4th group delayed neutrons	%	0.27
$\beta_5$	Fraction of 5th group delayed neutrons	%	0.086
$\beta_6$	Fraction of 6th group delayed neutrons	%	0.017
$\lambda_1$	Decay constant of 1st group precursor	$s^{-1}$	0.0256
$\lambda_2$	Decay constant of 2nd group precursor	$s^{-1}$	0.14
$\lambda_3$	Decay constant of 3rd group precursor	$s^{-1}$	0.13
$\lambda_4$	Decay constant of 4th group precursor	$s^{-1}$	0.27
$\lambda_5$	Decay constant of 5th group precursor	$s^{-1}$	0.086
$\lambda_6$	Decay constant of 6th group precursor	$s^{-1}$	0.017
$A = [\alpha_{ij}]_{10 \times 10}$	Coupling coefficients		$\begin{bmatrix} 3.5 & 7.0 & & & & & & & & & \\ & 1.8 & 7.1 & 5.5 & & & & & & & \\ & & 2.2 & 6.9 & 3.9 & & & & & & \\ & & & 3.1 & 7.0 & 3.3 & & & & & \\ & & & & 3.7 & 7.0 & 2.9 & & & & \\ & & & & & 4.2 & 7.0 & 2.8 & & & \\ & & & & & & 4.5 & 7.0 & 2.6 & & \\ & & & & & & & 4.7 & 7.0 & 2.4 & \\ & & & & & & & & 5.0 & 7.0 & 2.2 \\ & & & & & & & & & 5.6 & 3.5 \end{bmatrix} \times 10^{-3}$
$\alpha_{f,i}$ ( $i = 1, \dots, 10$ )	Reactivity coefficient of fuel temperature	$\Delta K/K/^\circ C$	$-4.36e - 5$
$\alpha_{m,i}$ ( $i = 1, \dots, 10$ )	Reactivity coefficient of moderator temperature	$\Delta K/K/^\circ C$	$-0.94e - 5$
$\alpha_r$	Reactivity coefficient of reflector temperature	$\Delta K/K/^\circ C$	$1.49e - 5$
$\varepsilon$	Porosity of the pebble-bed		0.39

structure of the FFNs, it has also been proved in [29] that feedback loops given in Section 3.2.2 and control laws given in Section 3.3.2 can provide globally input-to-state stability (ISS) and satisfactory transient performance for the cotree flowrates and tree branch pressure drops for the secondary-loop FFN.

**3.2. Feedback Loops and Controller Functions.** All the feedback loops of the plant control system of the HTR-PM plant are shown in Figure 7. Since the feedback loops of the two NSSS modules are the same with each other, only those of the first NSSS module are illustrated. From Figure 2, we can see that the plant control system is constituted by the controllers for regulating the reactor nuclear power, primary helium flowrate, secondary feedwater flowrate, outlet helium temperature, steam temperature, reactor thermal power, and main steam pressure as well as the controller

for discharge and bypass. Based on their functions, these controllers can be classified to the layers of module control, module coordination, and supervisory as well as bypass and discharge.

**3.2.1. Module Control.** The layer of module control is composed of the controllers for regulating the nuclear power, helium flowrate, reactor outlet helium temperature, steam temperature, and NSSS output thermal power. The functions of these five controllers are given as follows.

(1) **Nuclear Power Controller.** It regulates the neutron flux by generating both the given direction and velocity signals that determine the control rod movement. These signals are utilized to drive the stepping motors belonging to the reactor control rod mechanism for realizing the given movement. The movement of the control rods induces satisfactory reactivity to the reactor, which guarantees the

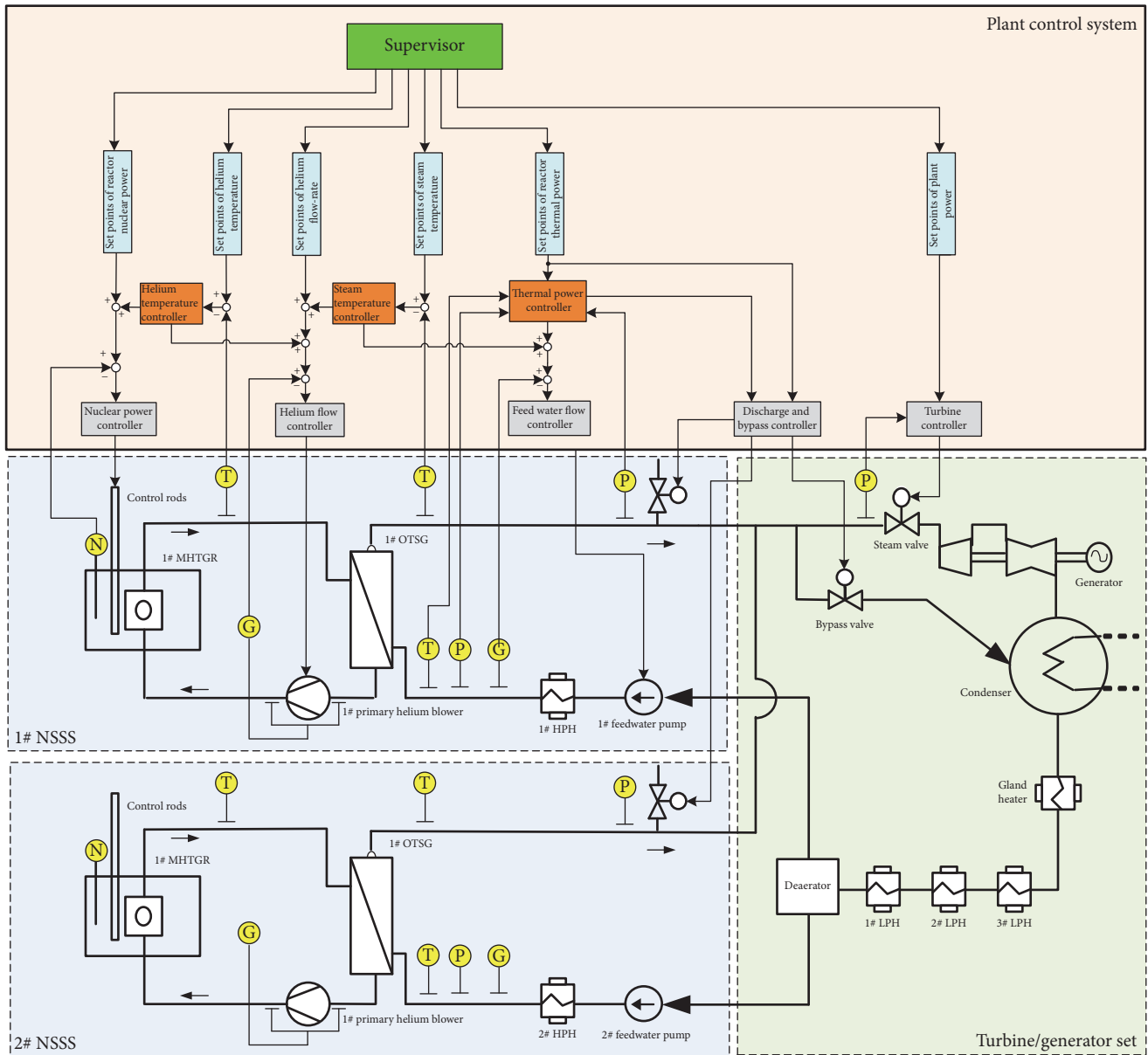


FIGURE 7: Composition of HTR-PM plant control system.

stability and transient performance of the reactor neutron flux.

(2) *Helium Flow Controller.* Satisfactory primary helium circulation is the precondition of transferring the heat produced by the fission reaction to the secondary loop for steam generation. In order to provide enough pressure header for the primary helium circulation, the helium flow controller gives the referenced frequency for the variable frequency driver (VFD) of the induction motor that drives the primary helium blower.

(3) *Feedwater Flow Controller.* It regulates the secondary feed-water flowrates of the OTSGs through adjusting the rotational speed of the feedwater pumps by their hydraulic couplings. It is worth noting that the feedwater flowrate controller is

responsible for the stability and transient performance of not only the NSSS modules but also the secondary-loop FFN of the HTR-PM plant.

(4) *Helium Temperature Controller.* It regulates the reactor outlet helium temperature by properly adjusting the set-points of the nuclear power controller and (or) helium flow controller. Specifically, if there is only modification of the referenced relative nuclear power, then the helium temperature controller and the nuclear power controller constitute a cascaded feedback loop, where the former one is in the outer loop as the major controller, and the latter one is in the inner loop as minor controller.

(5) *Steam Temperature Controller.* It regulates the outlet steam temperature of the OTSG by properly adjusting the

setpoints of the helium flowrate controller and (or) feedwater flowrate controller. Specifically, if its output is only the revision of the setpoints of the primary helium flowrate, then the steam temperature controller serves as the major regulator of the cascaded loop formed with the helium flow controller. Moreover, if its output is only the revision for the referenced feedwater flowrate, then the steam temperature controller and feedwater flow controller form a cascaded loop where the former one is the major regulator. In the power operation stage of the HTR-PM plant, the OTSG outlet steam temperature should be kept to be 571°C constantly.

(6) *Thermal Power Controller*. It is essentially a feedforward controller that gives the referenced feedwater flowrate based on both the setpoint of NSSS thermal power and the measurement of the temperatures and pressures of the feedwater and outlet superheated steam of each OTSG.

3.2.2. *Module Coordination*. The two NSSS modules of the HTR-PM plant are tightly coupled with each other through the common secondary-loop FFN. To regulate the feedwater flowrate of 1# NSSS module, it is necessary to adjust  $H_{d1}$  by revising the rotating speed of the pump. However, from model (21), the variation of  $H_{d1}$  influences not only the feedwater flowrate of 1# NSSS module but also pressure drop  $H_3$  which can be utilized to measure the main steam pressure. Then, from (21), the variation in  $H_3$  influences the dynamic behavior of the feedwater flowrate of 2# NSSS module, which induces the need of adjusting  $H_{d2}$  for keeping this feedwater flowrate. Therefore, regulating the feedwater flowrate of one NSSS module needs to adjust the rotating speeds of the two pumps, and each NSSS feedwater flowrate can influence the main steam pressure. The module coordination is just the flowrate-pressure control of the secondary-loop FFN.

It has been proved theoretically in [29] that the FFN flowrate regulation can be realized by distributed controllers of which each one only needs the measurement of the flowrate to be regulated. Thus, the NSSS feedwater flowrate controllers can well guarantee the stability and transient performance of the flowrates of the HTR-PM secondary-loop FFN shown in Figure 7. Moreover, in the power operation stage of the HTR-PM plant, the main steam pressure should be kept to be 13.24 MPa constantly. The stability of the main steam pressure is a basic operation requirement of the OTSG and also indicates the power balance between NSSS modules and the turbine/generator. Here, the main steam pressure of the HTR-PM plant is regulated by the turbine controller which provides the main steam pressure stability through adjusting the opening of the main steam valve. Thus, the collaboration of the NSSS feedwater flowrate controllers and the turbine controller realizes the flowrate-pressure regulation of the secondary-loop FFN, which achieves the function of NSSS module coordination and keeps the power balance between the NSSS modules and turbine.

3.2.3. *Supervisor*. The supervisor gives the setpoint of the thermal power for every NSSS module according to the requirement of the power grid and has no feedback regulation

function. Moreover, it also contains the map from the referenced NSSS thermal power to the referenced values of the NSSS process variables including the reactor nuclear power, primary helium flowrate, secondary feedwater flowrate, reactor outlet helium temperature, OTSG outlet steam temperature, and main steam pressure, which gives the setpoints of all the controllers. The supervisor can be viewed as an input-output (IO) interface between the power plant and the power grid so as to improve the power balance quality between the grid and plant.

3.2.4. *Bypass and Discharge*. The function bypass and discharge guarantee the operationability of the HTR-PM plant in some tough cases. The bypass controller opens the bypass valve so that the OTSG outlet steam flows into the condenser in the cases of load rejection, reactor startup, turbine bypass, and so forth. The function of the bypass controller is essentially providing a virtual load to compensate the large difference between the thermal inertias of the NSSS and turbine. The discharge controller opens the discharge valve if the pressure of the outlet steam is larger than its maximal value and closes the valve when the steam pressure is lower than a given value.

3.3. *Control Laws*. The control laws for the nuclear power, primary helium flowrate, feedwater flowrate, MHTGR outlet helium temperature, OTSG outlet steam temperature, and main steam pressure, which have the feedback regulation function, are all given in this subsection. These control laws can be classified into control laws for NSSS modules and those for module coordination.

3.3.1. *Module Control Laws*. The module control laws include the feedback regulation algorithms of the nuclear power, primary helium flowrate, feedwater flowrate, MHTGR outlet helium temperature, and OTSG outlet steam temperature, which are designed based on the physics-based NSSS control method proposed in [30–36].

(1) *Nuclear Power Control Law*. The nuclear power control laws is designed to be proportional-differential (PD) feedback regulation algorithm with the transfer function given by

$$G_N(s) = \frac{u_N(s)}{n_{r,e}(s)} = k_{n,p} + \frac{k_{n,d}s}{\tau_{n,d}s + 1}, \quad (22)$$

where positive scalars  $k_{n,p}$  and  $\tau_{n,d}$  are, respectively, the proportional and differential feedback gains,  $\tau_{n,d}$  is a small inertia time constant,  $u_N$  is the setpoint of the control rod speed signal used to drive stepping motors of the control rod driving mechanism, and  $n_{r,e}$  is the mismatch of the referenced relative nuclear power  $n_{r,r}$  from its actual value  $n_r$ ; that is,  $n_{r,e} = n_{r,r} - n_r$ . It is necessary to note that relative nuclear power is the normalized reactor neutron concentration, and the total thermal power is the outlet thermal power of the NSSS module. The steady values of the relative nuclear power is calibrated by that of total thermal power through experiment.

(2) *Helium Flow Control Law.* The feedback control of the primary helium flowrate adopts the proportional-integral (PI) law with its transfer function given by

$$G_{\text{HF}}(s) = \frac{u_{\text{HF}}(s)}{W_{\text{H,e}}(s)} = k_{\text{hf,p}} + \frac{k_{\text{hf,i}}}{s}, \quad (23)$$

where positive constants  $k_{\text{hf,p}}$  and  $k_{\text{hf,i}}$  are, respectively, the proportional and integral feedback gains,  $u_{\text{HF}}$  is the referenced rotating speed of the primary helium blower, and  $W_{\text{H,e}}$  is the error between the referenced and actual values of the primary helium flowrate.

(3) *Feedwater Flow Control Law.* The NSSS module feedwater flowrate is also regulated by PI control law, which is given by

$$G_{\text{FW}}(s) = \frac{u_{\text{FW}}(s)}{W_{\text{fw,e}}(s)} = k_{\text{fw,p}} + \frac{k_{\text{fw,i}}}{s}, \quad (24)$$

where positive scalars  $k_{\text{fw,p}}$  and  $k_{\text{fw,i}}$  are, respectively, the corresponding proportional and integral gains,  $u_{\text{FW}}$  is the driving signal of the hydraulic coupling, and  $W_{\text{fw,e}}$  is the error between the referenced and actual values of the feedwater flowrate.

(4) *MHTGR Outlet Helium Temperature Control Law.* The reactor outlet helium temperature is regulated by the lead-lag feedback law that is given by transfer functions:

$$G_{\text{HT1}}(s) = \frac{u_{\text{HT1}}(s)}{T_{\text{HO,e}}(s)} = \frac{k_{\text{ht1,p}} + k_{\text{ht,d}}s}{k_{\text{n,p}} + k_{\text{n,d}}s}, \quad (25)$$

$$G_{\text{HT2}}(s) = \frac{u_{\text{HT2}}(s)}{T_{\text{HO,e}}(s)} = -\left(k_{\text{ht2,p}} + \frac{k_{\text{ht,i}}}{s}\right),$$

where  $k_{\text{n,p}}$  and  $k_{\text{n,d}}$  are, respectively, the proportional and differential gains of the nuclear power control law, gains  $k_{\text{ht}j,\text{p}}$  ( $j = 1, 2$ ),  $k_{\text{ht,d}}$ , and  $k_{\text{ht,i}}$  are positive constants determining the lead-lag performance,  $u_{\text{HT1}}$  is the revision to the setpoint of the relative nuclear power,  $u_{\text{HT2}}$  is the revision to the referenced primary helium flowrate,  $T_{\text{HO,e}}$  is the error between the setpoint and measurement of the reactor outlet helium temperature.

(5) *OTSG Outlet Steam Temperature Control Law.* The OTSG outlet steam temperature of every NSSS module is regulated by PI feedback laws:

$$G_{\text{S1}}(s) = \frac{u_{\text{S1}}(s)}{T_{\text{S,e}}(s)} = k_{\text{s1,p}} + \frac{k_{\text{s1,i}}}{s}, \quad (26)$$

$$G_{\text{S2}}(s) = \frac{u_{\text{S2}}(s)}{T_{\text{S,e}}(s)} = -\left(k_{\text{s2,p}} + \frac{k_{\text{s2,i}}}{s}\right),$$

where positive constants  $k_{\text{s}j,\text{p}}$  and  $k_{\text{s}j,\text{i}}$  ( $j = 1, 2$ ) are, respectively, the proportional and integral feedback gains,  $u_{\text{S1}}$  is the revision of the setpoint of the primary helium flowrate,  $u_{\text{S2}}$  is the revision of the setpoint of the secondary feedwater flowrate, and  $T_{\text{S,e}}$  is the error between the setpoint and measurement of the OTSG outlet steam temperature.

3.3.2. *Module Coordination Laws.* The NSSS module coordination laws are just the flowrate-pressure feedback control laws for the secondary-loop FFN flowrates and pressure drop, which are designed based on the module coordination control method proposed in [28, 29].

(1) *FFN Flowrate Control Law.* As discussed in Section 3.1.2 and [28, 29], the flowrates of a FFN can be well regulated by controlling the flowrates of its cotree branches in a distributed way. From the structure of HTR-PM secondary-loop FFN shown in Figure 5, the OTSG secondary sides of the first and the second NSSS modules form branches 1 and 2 of this FFN which are just the cotree branches. Thus, from the graph properties of the FFN, all the branch flowrates can be well controlled or stabilized by regulating the feedwater flowrates of the OTSGs. Then, it is clear that OTSG feedwater flowrate control law (24) can realize the FFN flowrate control function, which means that flowrate control law (24) belongs to both the layers of module control and module coordination.

(2) *FFN Pressure Drop Control Law.* The pressure drop of the FFN tree branches (excluding the branches with pump) is also a crucial issue to guarantee the stability and operability. The pressure drop  $H_3$  of the HTR-PM secondary-loop FFN shown in Figure 5 can be measured by the main steam pressure which is regulated by the turbine control law with transfer function given by

$$G_{\text{SP}}(s) = \frac{u_{\text{SP}}(s)}{P_{\text{S}}(s)} = k_{\text{p,p}} + \frac{k_{\text{p,i}}}{s}. \quad (27)$$

Here, in (27), positive scalars  $k_{\text{p,p}}$  and  $k_{\text{p,i}}$  are, respectively, the proportional and integral gains,  $u_{\text{SP}}$  is the setpoint of the steam valve opening, and  $P_{\text{S,e}}$  is the mismatch of the referenced main steam pressure from its actual value.

3.3.3. *Parameters of Control Laws.* The plant control performance relies on the two aspects, that is, the performances of both the module control and module coordination. The former one is guaranteed by the physics-based NSSS control approach, and the latter one is provided by the FFN flowrate-pressure control method. All the control laws take the form as PI or PD feedback laws. For PI control laws, the proportional gain is larger, and the response is faster, but if it is too large, the control action will hit the saturation margin, which leads to the deterioration of closed-loop stability. Moreover, the integral gain is larger, and the transition period to the steady state is shorter, but the overshoot is larger. Usually, proportional gain is chosen not larger than 1.0, and the integral gain is chosen not larger than 0.1. For the PD law for nuclear power regulation, the proportional gain is chosen not larger than 0.5, and the differential gain is chosen not larger than 3.0.

## 4. Simulation Results with Discussions

In this section, the dynamic behavior of the HTR-PM plant in both the cases of power step and ramp are studied through the numerical simulation. This study is performed based on

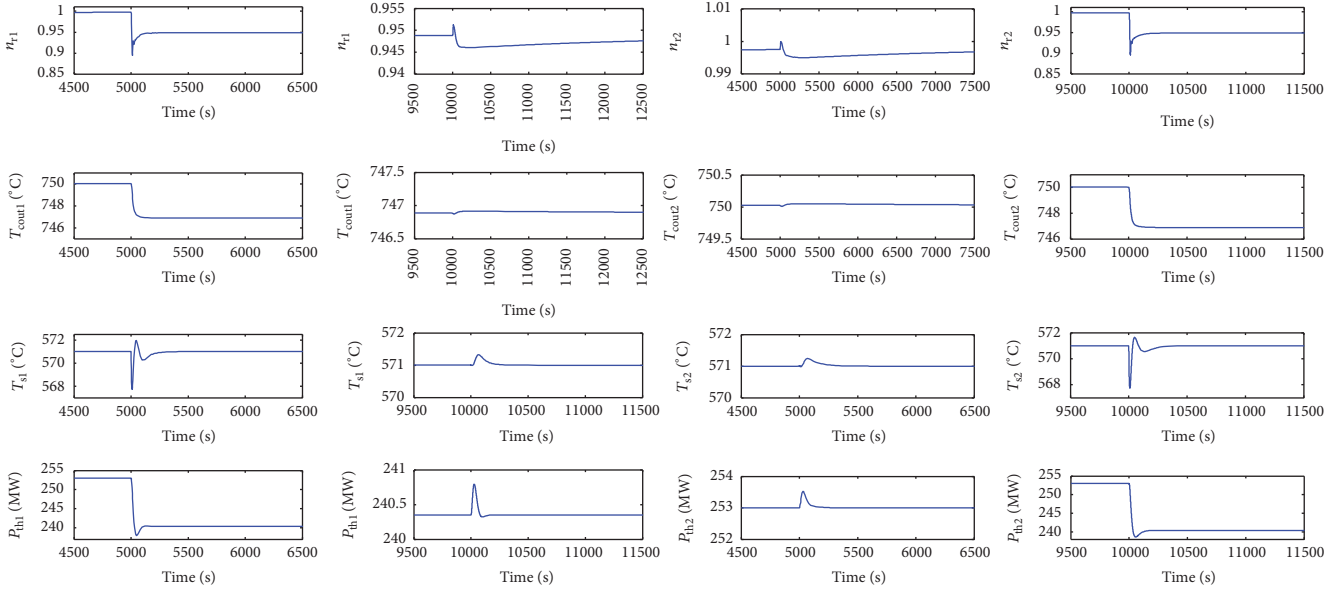


FIGURE 8: Responses of 1# and 2# NSSS in the case of power step-down:  $n_{ri}$ ,  $T_{counti}$ ,  $T_{si}$ , and  $P_{thi}$  are, respectively, the relative nuclear power, MHTGR outlet helium temperature, OTSG outlet steam temperature, and total thermal power of the  $i$ th NSSS,  $i = 1, 2$ .

the MATLAB/Simulink simulation code shown in Figure 6 that integrates both the plant model introduced in Section 2 and control strategy given in Section 3. Moreover, necessary discussions are also given in this section.

#### 4.1. Simulation Results

**4.1.1. Power Step.** The dynamic responses of the power step between 100% and 95% plant full power (PFP) are obtained through numerical simulation.

**(1) Power Step-Down.** Initially, the HTR-PM plant remains at the steady state of 100% PFP which means that the two NSSS modules are running at the 100% reactor full power (RFP). At 5000 s, the thermal power setpoint of the first (i.e., 1#) NSSS module steps down from 100% to 95% RFP, and then at 10000 s, the referenced thermal power of the second (i.e., 2#) NSSS module steps down from 100% to 95% RFP. The dynamic responses of the relative nuclear powers, reactor outlet helium temperatures, OTSG outlet steam temperatures, and thermal powers of 1# and 2# NSSS modules are given in Figure 8. The responses of flowrates  $Q_i$  ( $i = 1, 2, 3$ ), feedwater headers  $-H_{fk}$  ( $k = 1, 2$ ), and main steam pressure  $H_3$  are illustrated in Figure 9.

**(2) Power Step-Up.** Initially, the HTR-PM plant remains at the steady state of 95% PFP; that is, the two NSSS modules operate at 95% RFP. The thermal power setpoints of 1# and 2# NSSS modules step up from 95% to 100% RFP at 5000 s and 10000 s, respectively. The dynamic responses of the relative nuclear powers, reactor outlet helium temperatures, OTSG outlet steam temperatures, and thermal powers of 1# and 2# NSSS modules are given in Figure 10. The responses of  $Q_i$  ( $i = 1, 2, 3$ ),  $-H_{fk}$  ( $k = 1, 2$ ), and  $H_3$  are shown in Figure 11.

**4.1.2. Power Ramp.** The responses of the steady power ramp between 100% and 50% plant full power (PFP) are given by the simulation study.

**(1) Power Ramp-Down.** Initially, the HTR-PM plant remains at the steady state of 100% PFP; that is, the two NSSS modules operate at 100% RFP. At 5000 s, 1# NSSS module maneuvers from 100% to 50% RFP steadily in 10 minutes, and then at 10000 s, the referenced thermal power of 2# NSSS module changes steadily from 100% to 50% RFP in 10 minutes, which is just the power decrease process from 100% to 50% PFP of the HTR-PM plant. The responses of the relative nuclear powers, reactor outlet helium temperatures, OTSG outlet steam temperatures, and thermal powers of 1# and 2# NSSS modules are given in Figure 12. The responses of flowrates  $Q_i$  ( $i = 1, 2, 3$ ), feedwater headers  $-H_{fk}$  ( $k = 1, 2$ ), and main steam pressure  $H_3$  are illustrated in Figure 13.

**(2) Power Ramp-Up.** Initially, the HTR-PM plant remains at the steady state of 95% PFP; that is, the two NSSS modules operate at 95% RFP. At 5000 s and 10000 s, 1# and 2# NSSS modules, respectively, maneuver steadily from 50% to 100% RFP in 10 minutes, which is the process of HTR-PM power increase from 50% to 100% PFP. The responses of the relative nuclear powers, reactor outlet helium temperatures, OTSG outlet steam temperatures, and thermal powers of 1# and 2# NSSS modules are given in Figure 14. The responses of flowrates  $Q_i$  ( $i = 1, 2, 3$ ),  $-H_{fk}$  ( $k = 1, 2$ ), and  $H_3$  are illustrated in Figure 15.

**4.2. Discussions.** The variation of the plant power is realized by the successive power maneuver of 1# and 2# NSSS modules, and at most one NSSS module can be in the state of

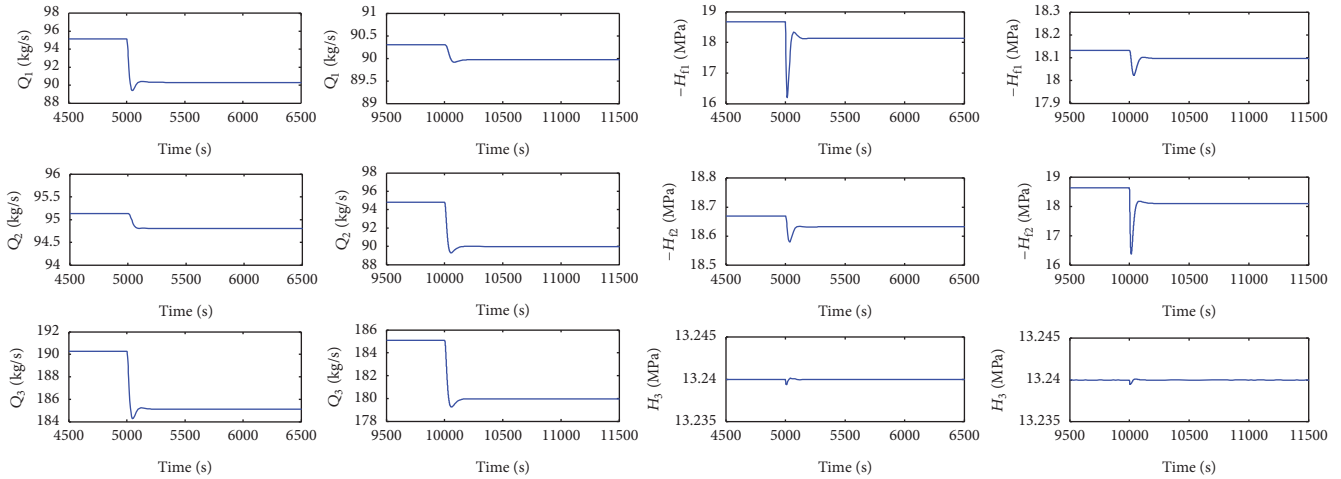


FIGURE 9: Responses of secondary-loop FFN flowrates and pressure drops in the case of power step-down.

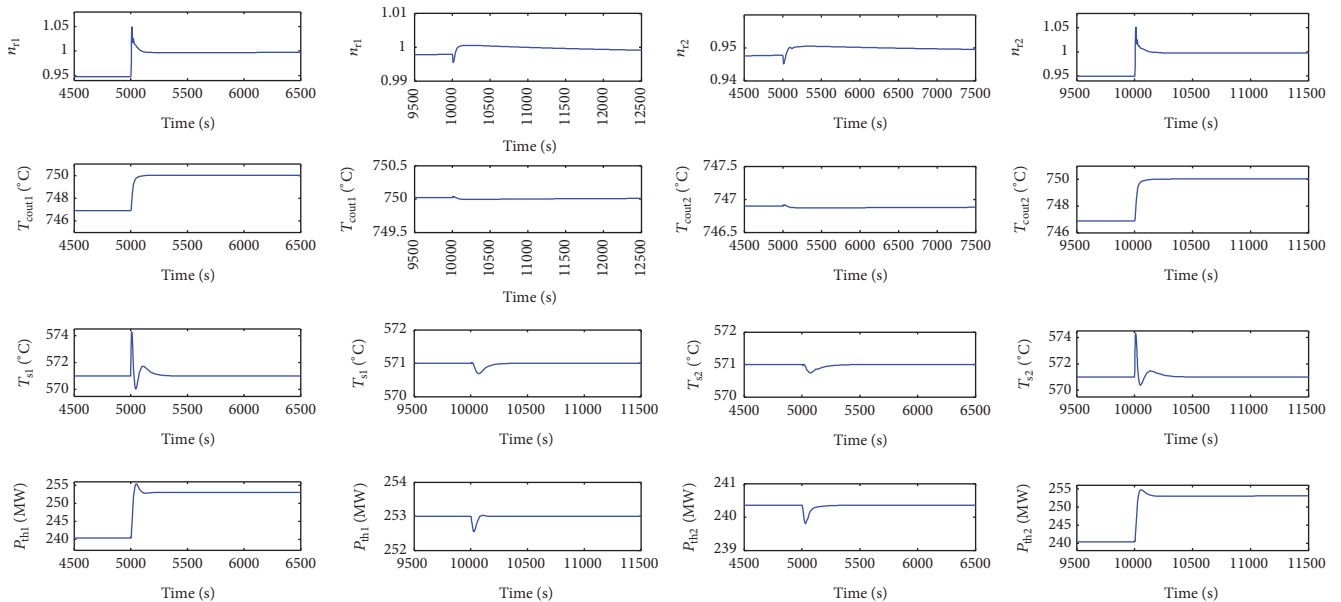


FIGURE 10: Responses of 1# and 2# NSSS in the case of power step-up:  $n_{ri}$ ,  $T_{counti}$ ,  $T_{si}$ , and  $P_{thi}$  are, respectively, the relative nuclear power, MHTGR outlet helium temperature, OTSG outlet steam temperature, and total thermal power of the  $i$ th NSSS,  $i = 1, 2$ .

power maneuver at any time. Generally, from Figures 8–15, the control laws for the modules and those for the module coordination guarantee satisfactory closed-loop stability and transient performance of the process variables of the NSSS modules as well as the secondary-loop FFN.

The variation of a NSSS power-level setpoint directly induces the variations of the setpoints of nuclear power, reactor outlet helium temperature, primary helium flowrate, and secondary feedwater flowrate of this NSSS, which enlarge the errors between the practical values and setpoints of these variables. These errors drive the nuclear power controller and helium temperature controller to insert or withdraw the control rods and drive the flowrate controllers to slow down or speed up the helium blower and feedwater pump. Due to

the negative feedback laws, the movement of control rods, helium blower, and feedwater pump can suppress the errors. Moreover, the variations of the flowrates and helium temperature induce the variations of steam temperature and main steam pressure, which drive the steam temperature controller to revise the setpoints of helium or feedwater flowrates for maintaining the steam temperature and drive the pressure controller to change the steam valve opening for keeping the main steam pressure. The variation of the steam valve opening can also reduce the feedwater flowrate of the other NSSS, which leads to the successive variations of steam temperature, helium temperature, fuel temperature, and nuclear power of the other NSSS. Then, the controllers of the other NSSS are active to suppress the errors of process

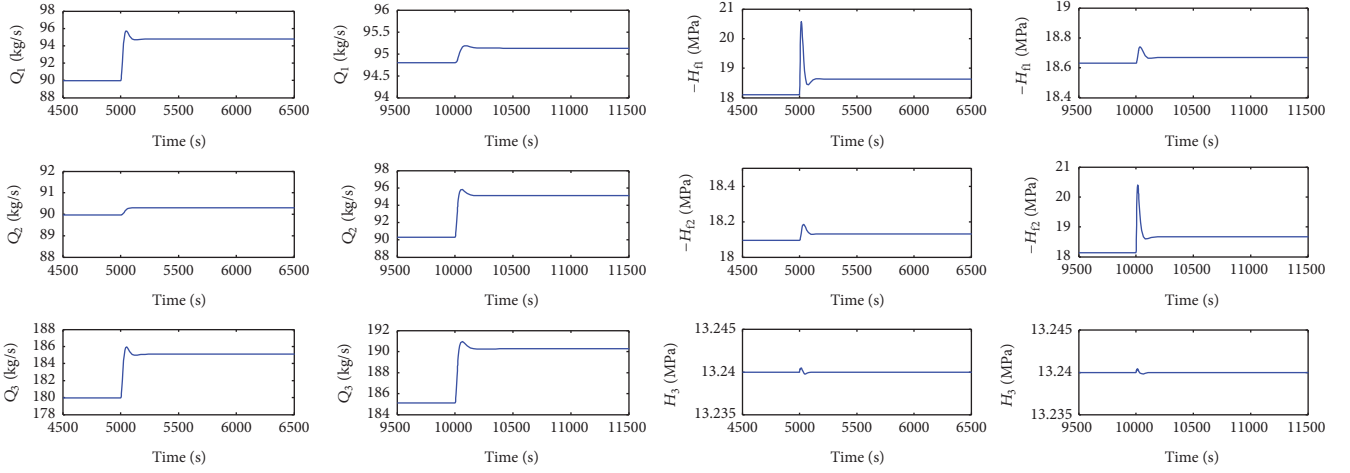


FIGURE 11: Responses of secondary-loop FFN flowrates and pressure drops in the case of power step-up.

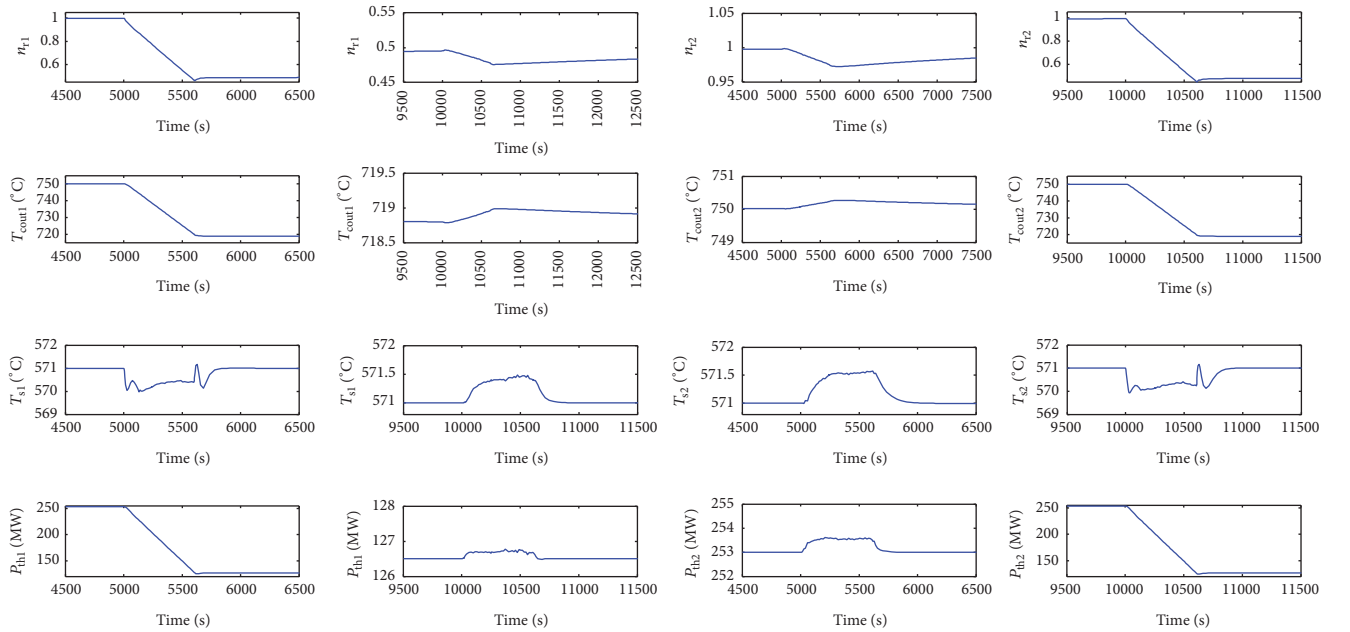


FIGURE 12: Responses of 1# and 2# NSSS in the case of power ramp-down:  $n_r$ ,  $T_{\text{count}}$ ,  $T_{\text{st}}$ , and  $P_{\text{th}}$  are, respectively, the relative nuclear power, MHTGR outlet helium temperature, OTSG outlet steam temperature, and total thermal power of the  $i$ th NSSS,  $i = 1, 2$ .

variables caused by the variation of steam valve opening. Furthermore, since the steam flow extracted from the turbine is equally distributed to the two HPHs, the power maneuver of one module changes feedwater temperatures of both two modules. To maintain the thermal powers, the setpoints of feedwater flowrates of the two modules should be adjusted by the thermal power controllers.

Specifically to the NSSS module control performance, we can clearly see from the simulations results illustrated in Figures 8–15 that simple module control laws (22)–(26) can guarantee satisfactory stability and transient performance for the NSSS modules in the cases of power-level maneuver and maintenance. Here, the expressions of these module control laws are given by guaranteeing proper dissipation feature for the NSSS module with its shifted-ectropy as the storage

function, which is the key idea of physics-based nuclear plant control method with the ability of giving simple control laws. These simulation results effectively show the feasibility of these module control laws which can be implemented and commissioned easily in the practical engineering.

Furthermore, the key difference between the HTR-PM plant and those single-modular nuclear plants is the module coordination control. There is a tight hydraulic coupling effect of the two NSSS modules that is induced by the common secondary-loop FFN. There is also coupling effect between the feedwater temperatures of the two NSSS modules, which is induced by the equal distribution of the steam flow extracted from the turbine to the two HPHs belonging to the two modules, respectively. Because of the existence of the hydraulic and thermal module coupling effects, when

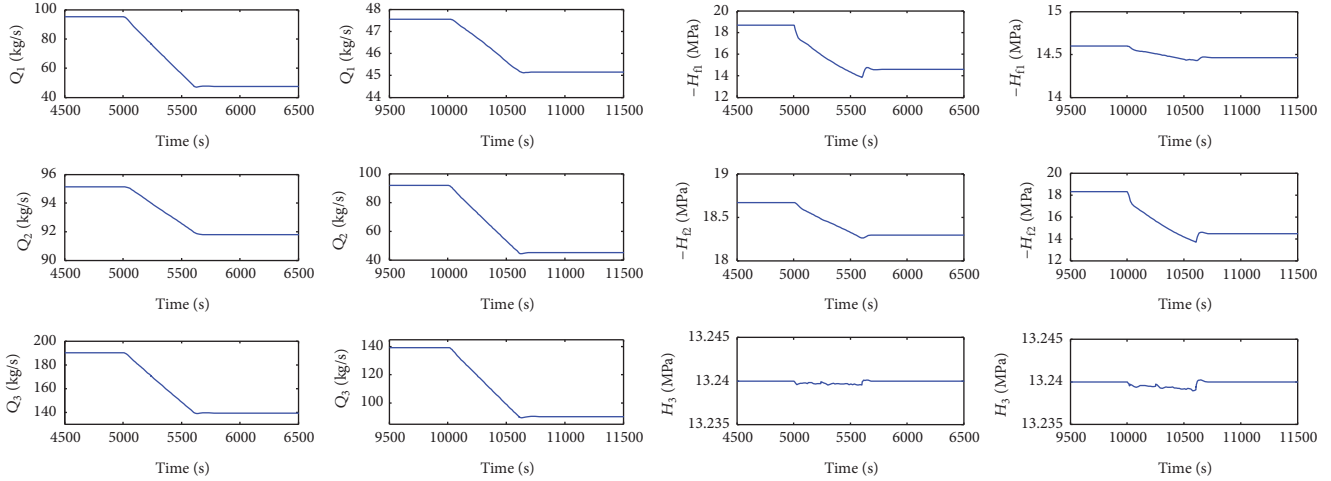
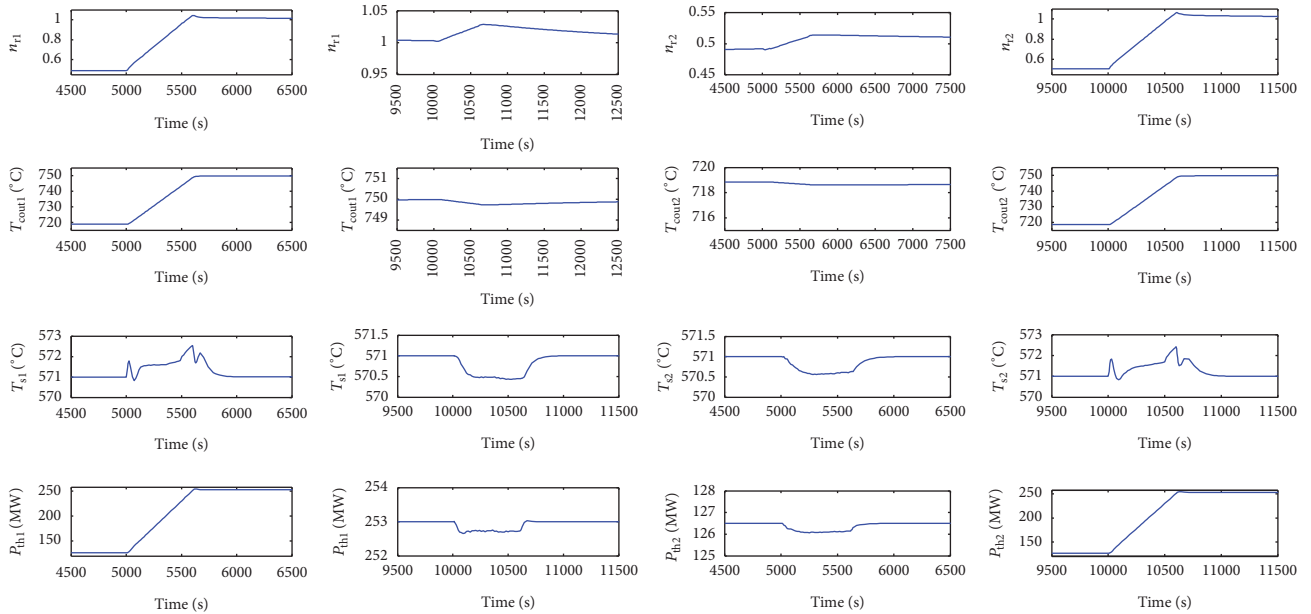


FIGURE 13: Responses of secondary-loop FFN flowrates and pressure drops in the case of power ramp-down.


 FIGURE 14: Responses of 1# and 2# NSSS in the case of power ramp-up:  $n_{ri}$ ,  $T_{counti}$ ,  $T_{si}$ , and  $P_{thi}$  are, respectively, the relative nuclear power, MHTGR outlet helium temperature, OTSG outlet steam temperature, and total thermal power of the  $i$ th NSSS,  $i = 1, 2$ .

one NSSS module is in the state of power maneuvering, both the feedwater flowrate and output thermal power of the other NSSS module must vary simultaneously if there is no control input. Due to the proper referenced feedwater flowrates given by thermal power controllers, and due to the effectiveness of the feedwater flowrate control law, both the secondary flowrates and thermal power of the two NSSS modules are statically decoupled with each other, which means that the steady values of the feedwater flowrates (outlet thermal power) of the two NSSS modules are decoupled with each other. For example, from columns 1 and 3 of Figures 8 and 10, the power step of 1# NSSS module does not influence the steady values of the feedwater flowrate and outlet thermal power of 2# NSSS module. Thanks to the plant

control strategy proposed in this paper, we can see from the simulation results that the power step and ramp of one NSSS module only induce small transient disturbance to the other module and do not induce steady-point perturbations of the secondary flowrate and thermal power. The feedback laws of the module coordinated control given by (24) and (27) are also simple for engineering implementation and conditioning.

In summary, the power maneuver of the HTR-PM plant can be realized by the plant control strategy given in Section 3 which has already been applied to the HTR-PM power control project. The numerical simulation results show that the HTR-PM plant is flexible enough for constituting HESS with those renewable energy sources such as the wind and

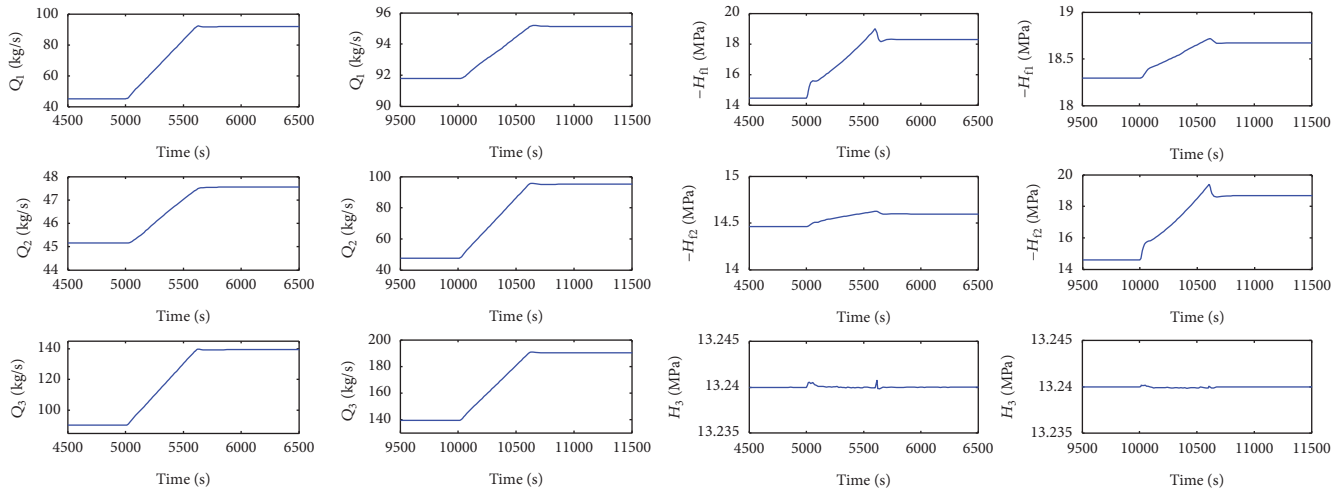


FIGURE 15: Responses of secondary-loop FFN flowrates and pressure drops in the case of power ramp-up.

solar. Moreover, the technical issues of integrating more NSSS modules are nearly the same with integrating two modules by allocating a pump to each NSSS module, implementing module control laws in Section 3.2.2 to each NSSS module and applying module coordination laws in Section 3.2.3 to the secondary FFN.

## 5. Conclusions

Due to its inherent safety feature and potential economic competitiveness, the modular high temperature gas-cooled reactor (MHTGR) has already been seen as one of the best candidates in building the next generation nuclear plants. Through the multimodular scheme, the inherent safety feature of the MHTGR can be applicable to the large-scale nuclear plants at any desired power ratings. Plant power control is the one of the crucial techniques for guaranteeing the safe, stable, and efficient operation of every nuclear plant, and the plant power control strategy of the traditional single-modular nuclear plants cannot be directly applied to multimodular plants. Thus, it is very necessary to study the plant power control of multimodular nuclear plants. Here, dynamic modeling, control strategy design, and performance verification are the three main aspects of plant power control studying, where the former one is the basis for the latter two. In this paper, the dynamical modeling of the main parts of the HTR-PM plant is first given, and the corresponding plant control strategy including the feedback loops and control laws is then proposed. By integrating the dynamic model and power control strategy for a simulation code in MATLAB/Simulink environment, numerical verification is performed. Simulation results in the cases of plant power step and ramp show that the plant control strategy provides satisfactory closed-loop stability and transient performance for the HTR-PM plant. The future work mainly lies in commissioning the power control system of the HTR-PM plant, which is implemented based on the control strategy given in this paper, practically for a practical verification.

## Conflicts of Interest

The authors declare that they have no conflicts of interest.

## Acknowledgments

This work is jointly supported by National S&T Major Project of China and Natural Science Foundation of China (NSFC) (Grant no. 61374045).

## References

- [1] H. E. Garcia, J. Chen, J. S. Kim et al., "Dynamic performance analysis of two regional nuclear hybrid energy systems," *Energy*, vol. 107, pp. 234–258, 2016.
- [2] M. Lykidi and P. Gourdil, "How to manage flexible nuclear power plants in a deregulated electricity market from the point of view of social welfare?" *Energy*, vol. 85, pp. 167–180, 2015.
- [3] W. Dazhong and L. Yingyun, "Roles and prospect of nuclear power in China's energy supply strategy," *Nuclear Engineering and Design*, vol. 218, no. 1–3, pp. 3–12, 2002.
- [4] D. T. Ingersoll, "Deliberately small reactors and the second nuclear era," *Progress in Nuclear Energy*, vol. 51, no. 4-5, pp. 589–603, 2009.
- [5] J. Vujić, R. M. Bergmann, R. Škoda, and M. Miletić, "Small modular reactors: simpler, safer, cheaper?" *Energy*, vol. 45, no. 1, pp. 288–295, 2012.
- [6] M. K. Rowinski, T. J. White, and J. Zhao, "Small and medium sized reactors (SMR): a review of technology," *Renewable and Sustainable Energy Reviews*, vol. 44, pp. 643–656, 2015.
- [7] D. D. Lanning, "Modularized high-temperature gas-cooled reactor systems," *Nuclear Technology*, vol. 88, no. 2, pp. 139–156, 1989.
- [8] H. Reutler and G. H. Lohnert, "The modular high-temperature reactor," *Nuclear Technology*, vol. 62, no. 1, pp. 22–30, 1983.
- [9] H. Reutler and G. H. Lohnert, "Advantages of going modular in HTRs," *Nuclear Engineering and Design*, vol. 78, no. 2, pp. 129–136, 1984.

- [10] G. H. Lohnert, "Technical design features and essential safety-related properties of the HTR-module," *Nuclear Engineering and Design*, vol. 121, no. 2, pp. 259–275, 1990.
- [11] Z. Wu, D. Lin, and D. Zhong, "The design features of the HTR-10," *Nuclear Engineering and Design*, vol. 218, pp. 25–32, 2002.
- [12] S. Hu, X. Liang, and L. Wei, "Commissioning and operation experience and safety experiments on HTR-10," in *Proceedings of the 3rd International Topical Meeting on High Temperature Reactor Technology*, Johannesburg, South Africa, October, 2006.
- [13] Z. Zhang and Y. Sun, "Economic potential of modular reactor nuclear power plants based on the Chinese HTR-PM project," *Nuclear Engineering and Design*, vol. 237, no. 23, pp. 2265–2274, 2007.
- [14] Z. Zhang, Z. Wu, D. Wang et al., "Current status and technical description of Chinese  $2 \times 250$  MW<sub>th</sub> HTR-PM demonstration plant," *Nuclear Engineering and Design*, vol. 239, no. 7, pp. 1212–1219, 2009.
- [15] G. Y. Han, "A mathematical model for the thermal-hydraulic analysis of nuclear power plants," *International Communications in Heat and Mass Transfer*, vol. 27, no. 6, pp. 795–805, 2000.
- [16] C. Fazekas, G. Szederkényi, and K. M. Hangos, "A simple dynamic model of the primary circuit in VVER plants for controller design purposes," *Nuclear Engineering and Design*, vol. 237, no. 10, pp. 1071–1087, 2007.
- [17] Z. Dong, X. Huang, J. Feng, and L. Zhang, "Dynamic model for control system design and simulation of a low temperature nuclear reactor," *Nuclear Engineering and Design*, vol. 239, no. 10, pp. 2141–2151, 2009.
- [18] R. M. Edwards, K. Y. Lee, and M. A. Schultz, "State feedback assisted classical control: an incremental approach to control modernization of existing and future nuclear reactors and power plants," *Nuclear Technology*, vol. 92, no. 2, pp. 167–185, 1990.
- [19] M. G. Na, I. J. Hwang, and Y. J. Lee, "Design of a fuzzy model predictive power controller for pressurized water reactors," *IEEE Transactions on Nuclear Science*, vol. 53, no. 3, pp. 1504–1514, 2006.
- [20] G. R. Ansarifard and H. R. Akhavan, "Sliding mode control design for a PWR nuclear reactor using sliding mode observer during load following operation," *Annals of Nuclear Energy*, vol. 75, pp. 611–619, 2015.
- [21] Y. B. Shtessel, "Sliding mode control of the space nuclear reactor system," *IEEE Transactions on Aerospace and Electronic Systems*, vol. 34, no. 2, pp. 579–589, 1998.
- [22] Z. Huang, R. M. Edwards, and K. Y. Lee, "Fuzzy-adapted recursive sliding-mode controller design for a nuclear power plant control," *IEEE Transactions on Nuclear Science*, vol. 51, no. 1, pp. 256–266, 2004.
- [23] H. Li, X. Huang, and L. Zhang, "A simplified mathematical dynamic model of the HTR-10 high temperature gas-cooled reactor with control system design purposes," *Annals of Nuclear Energy*, vol. 35, no. 9, pp. 1642–1651, 2008.
- [24] Z. Dong, X. Huang, and L. Zhang, "A nodal dynamic model for control system design and simulation of an MHTGR core," *Nuclear Engineering and Design*, vol. 240, no. 5, pp. 1251–1261, 2010.
- [25] H. Li, X. Huang, and L. Zhang, "A lumped parameter dynamic model of the helical coiled once-through steam generator with movable boundaries," *Nuclear Engineering and Design*, vol. 238, no. 7, pp. 1657–1663, 2008.
- [26] Z. Dong, "A differential-algebraic model for the once-through steam generator of MHTGR-based multimodular nuclear plants," *Mathematical Problems in Engineering*, vol. 2015, Article ID 370101, 12 pages, 2015.
- [27] Z. Dong, "Self-stability analysis of MHTGRs: a shifted-entropy based approach," *Nuclear Engineering and Design*, vol. 248, pp. 137–148, 2012.
- [28] Z. Dong, "Dissipation analysis and adaptive control of fluid networks," in *Proceedings of the American Control Conference (ACC '15)*, pp. 671–676, Chicago, Ill, USA, July 2015.
- [29] Z. Dong, M. Song, X. Huang, Z. Zhang, and Z. Wu, "Module coordination control of MHTGR-based multi-modular nuclear plants," *IEEE Transactions on Nuclear Science*, vol. 63, no. 3, pp. 1889–1900, 2016.
- [30] Z. Dong, J. Feng, X. Huang, and L. Zhang, "Power-level control of nuclear reactors based on feedback dissipation and backstepping," *IEEE Transactions on Nuclear Science*, vol. 57, no. 3, pp. 1577–1588, 2010.
- [31] Z. Dong, "Nonlinear state-feedback dissipation power level control for nuclear reactors," *IEEE Transactions on Nuclear Science*, vol. 58, no. 1, pp. 241–257, 2011.
- [32] Z. Dong, "Physically-based power-level control for modular high temperature gas-cooled reactors," *IEEE Transactions on Nuclear Science*, vol. 59, no. 5, pp. 2531–2549, 2012.
- [33] Z. Dong, "Power-level control for MHTGRs with time-delay in helium temperature measurement," *IEEE Transactions on Nuclear Science*, vol. 61, no. 3, pp. 1349–1359, 2014.
- [34] Z. Dong, "Model-free power-level control of MHTGRs against input saturation and dead-zone," *IEEE Transactions on Nuclear Science*, vol. 62, no. 6, pp. 3297–3310, 2015.
- [35] Z. Dong, X. Huang, and L. Zhang, "Saturated output feedback dissipation steam temperature control for the OTSG of MHTGRs," *IEEE Transactions on Nuclear Science*, vol. 58, no. 3, pp. 1277–1289, 2011.
- [36] Z. Dong, "Model-free coordinated control for MHTGR-based nuclear steam supply systems," *Energies*, vol. 9, no. 1, article 37, 2016.

## Research Article

# The Electric Current Effect on Electrochemical Deconsolidation of Spherical Fuel Elements

**Xiaotong Chen, Zhenming Lu, Hongsheng Zhao, Bing Liu, Junguo Zhu, and Chunhe Tang**

*Institute of Nuclear and New Energy Technology, Collaborative Innovation Center of Advanced Nuclear Energy Technology, Tsinghua University, Beijing 100084, China*

Correspondence should be addressed to Xiaotong Chen; [chenxiaotong@tsinghua.edu.cn](mailto:chenxiaotong@tsinghua.edu.cn) and Zhenming Lu; [sunmoon@tsinghua.edu.cn](mailto:sunmoon@tsinghua.edu.cn)

Received 30 December 2016; Revised 31 March 2017; Accepted 19 April 2017; Published 18 May 2017

Academic Editor: Robert Morris

Copyright © 2017 Xiaotong Chen et al. This is an open access article distributed under the Creative Commons Attribution License, which permits unrestricted use, distribution, and reproduction in any medium, provided the original work is properly cited.

For High-Temperature Gas-Cooled Reactor in China, fuel particles are bonded into spherical fuel elements by a carbonaceous matrix. For the study of fuel failure mechanism from individual fuel particles, an electrochemical deconsolidation apparatus was developed in this study to separate the particles from the carbonaceous matrix by disintegrating the matrix into fine graphite powder. The deconsolidated graphite powder and free particles were characterized by elemental analysis, X-ray photoelectron spectroscopy (XPS), X-ray diffraction (XRD), scanning electron microscopy (SEM), energy dispersive spectrometer (EDS), and ceramography. The results showed that the morphology, size distribution, and element content of deconsolidated graphite matrix and free particles were notably affected by electric current intensity. The electrochemical deconsolidation mechanism of spherical fuel element was also discussed.

## 1. Introduction

The fuel elements of High-Temperature Gas-Cooled Reactor (HTR) are spherical and have an overall diameter of 60 mm. A 5 mm thick unfueled matrix graphite shell comprises the outer portion of the sphere. The central, fueled region of the fuel element is 50 mm in diameter and is composed of 0.92 mm diameter tristructural isotropic- (TRISO-) coated fuel particles that are overcoated and pressed into a 50 mm diameter sphere [1]. The graphite matrix covered more than 95% weight of the fuel element. To study the irradiation behaviors of the spent fuel element, coated particles need to be separated and sampled from the matrix graphite from the inside out for further inspections of fission products distribution [2]. Therefore, the structural integrity of coated particles and the complete separation of coated particles from matrix graphite are two key issues for exact measurements. Intact coated particles consisting of silicon carbide (SiC) and outer/inner pyrolytic carbon (PyC) layers should be maintained, with graphite matrix and overcoating layers removed [3, 4]. Most practical methods of disintegration of HTR fuel elements studied in the past made use of the

fact that graphite forms so-called intercalation compounds with certain elements, accompanied by enlargement of the C-spacing of graphite lattice [5–7]. In this process graphite matrix is loosened to such an extent that it disintegrates into fine graphite powder to liberate the coated particles.

Electrochemical deconsolidation method is based on anodic oxidation of graphite in electrolytes including strong acids [8–10] and salt solution [11, 12]. Under the concentration gradient and electrostatic potential gradient, anions would transport towards anodic graphite matrix, with insertion into the graphite layer to form the well-known graphite intercalation compounds. Since the compounds are not stable, they could decompose naturally in the presence of water, resulting in the destruction of the graphite matrix [13, 14]. If the deconsolidation is conducted in strong acid, carbon oxidization caused by dissociated acid cations would also lead to the destruction of the graphite matrix. During the deconsolidation, the electric current is considered as one of main factors that affect the deconsolidation procedure. In this study, the electric current effect on the electrochemical deconsolidation of spherical fuel elements was investigated in  $\text{HNO}_3$  electrolyte. Unirradiated spherical graphite balls with

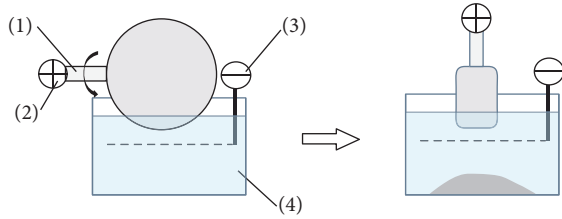


FIGURE 1: The electrochemical deconsolidation process.

ZrO<sub>2</sub> kernels produced by the similar processing of UO<sub>2</sub> fuel elements were used as the test samples in this work.

## 2. Experimental

The apparatus in this work contains electrolyzing cell, rotator (1), anode (2), Pt cathode (3), HNO<sub>3</sub> electrolyte (4), and DC electrolytic power supply and control system (Figure 1). The sample sphere is connected to a direct current source as well as a gear motor using a motor rod linker. The motor rod linker is only inserted about 4 mm into the unfueled portion of the sphere to avoid particle damage as a result of the deconsolidation process. The deconsolidation process involves two steps. In the first part of the deconsolidation process, the sample sphere rotates (1rpm) with the outer circumference submerged in electrolyte solution, leaving a 2 cm-cylinder in diameter at the end. In the second part of the process, the remaining cylinder is rotated by 90° and lowered into the electrolyte in discrete steps. The tested electric currents in this work are 2 A (2.4 V), 7 A (6.4 V), 10 A (8.5 V), and 13 A (10.7 V). Each step yields a sample of electrolyte solution, graphite matrix, and associated coated particles after a series of separation methods. Then unbonded particles are collected and packaged separately, providing a profile of fuel from the edge to the center of the sphere.

The deconsolidated powders were washed by SB-50 sonicator (Xinzhi, China) and dried by DHG-9030A (Yiheng, China). The samples were weighed by QUINTIX124-1CN (Sartorius, German). The X-ray diffraction (XRD) spectra of samples before and after deconsolidation were characterized by D8 X-ray diffractometer (Bruker, German); the X-ray photoelectron spectrometry (XPS) properties of samples were characterized by 250XI XPS instrument (Thermo, USA); the element contents of the samples were measured by Various ELIII element analysis instrument (Elementar, German); the scanning electron microscope (SEM) images were measured by S-3000N (Hitachi, Japan) equipped with energy dispersive spectrometer (EDS). The particle size was measured by Mastersizer 2000 laser particle size analyzer (Malvin, UK).

For elemental analysis, the deconsolidated samples were firstly sonicated by high purified water to remove HNO<sub>3</sub> and filtrated by vacuum for times until the filter liquor pH reached above 6.0. Afterwards, the samples were dried at 120°C in a vacuum drying oven for 6 h to remove H<sub>2</sub>O with the weights measured. Then the samples were dried at 120°C for another 0.5 h and weighed. Once the weights differences before and after drying were smaller than 0.2 mg, H<sub>2</sub>O was thought to be

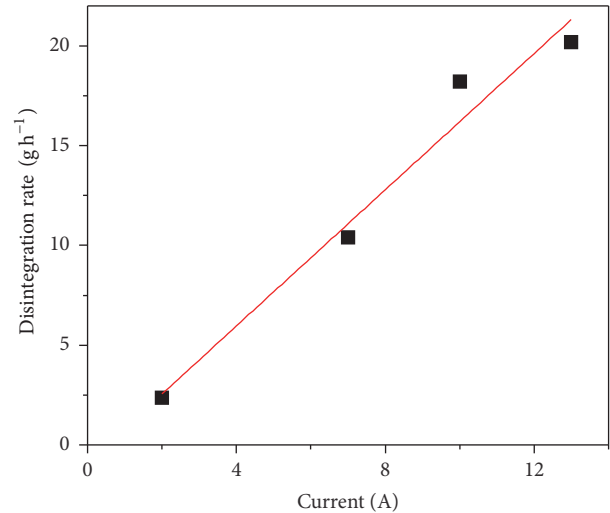


FIGURE 2: The electric current intensity effect on deconsolidation rate.  $R^2 = 0.96$ .

completely removed and the samples were sent for elemental analysis.

## 3. Results and Discussion

**3.1. The Electric Current Effect on Deconsolidation Rate.** The electric current effect on deconsolidation rate is shown in Figure 2. The deconsolidation rate is defined as the mass of disintegrated graphite fragments per hour. According to the results, a positive influence of current on the disintegration rate can be observed. It seems that a larger current leads to a faster disintegration rate. However, if the current is further increased to 20 A, the disintegration rate will deviate from the linear relationship (not shown in the figure), which might be caused by competitive H<sub>2</sub>O electrolyzation.

### 3.2. The Components of Graphite Matrix before and after Deconsolidation

**3.2.1. Elemental Analysis.** If collected after deconsolidation, the graphite fragments gain an obvious weight of around 7–15% compared to those before deconsolidation. To examine the component of samples, elemental analysis was carried out for C, H, N, and O contents (Table 1). Based on the mass balance, the difference between the overall mass and those of C, H, and N can be ascribed to the mass of O. According to the elemental analysis results, C is still the main component of the fragments. The slight change of N content indicates the formation of graphite-nitrate compounds, which are probably intercalation compounds. The O increasing from graphite matrix to deconsolidated samples indicates that graphite matrix might be oxidized to some degree during the chemical deconsolidation, which results in the weight gain.

**3.2.2. XPS Results.** Since elemental analysis result is a mean value of the bulk of the sample, we further used XPS to characterize the sample surface with extensive functionalization.

TABLE 1: The elemental analysis results before and after deconsolidation.

Sample	N% (mea.)	C% (mea.)	H% (mea.)	O% (calc.)	O/C
Graphite matrix	0.06	98.80	0.22	0.91	0.009
Deconsolidated by 2 A (2.4 V)	0.98	80.6	0.60	17.80	0.22
Deconsolidated by 7 A (6.2 V)	1.14	78.68	0.88	19.31	0.25
Deconsolidated by 10 A (8.5 V)	0.62	81.48	0.81	17.09	0.21
Deconsolidated by 13 A (10.7 V)	0.75	80.91	0.79	17.55	0.22

TABLE 2: XPS fitting results.

Sample	284.6 eV	286.8 eV	289.0 eV	O/C
Cont.	C-C(H)	C-O	O-C=O	
Graphite matrix	>99.8%	<0.1%	<0.1%	0.04
Deconsolidated by 2 A (2.4 V)	65.3%	29.8%	4.8%	0.39
Deconsolidated by 7 A (6.2 V)	73.2%	16.2%	10.5%	0.24
Deconsolidated by 10 A (8.5 V)	45.6%	37.5%	16.9%	0.59
Deconsolidated by 13 A (10.7 V)	60.9%	33.8%	5.2%	0.56

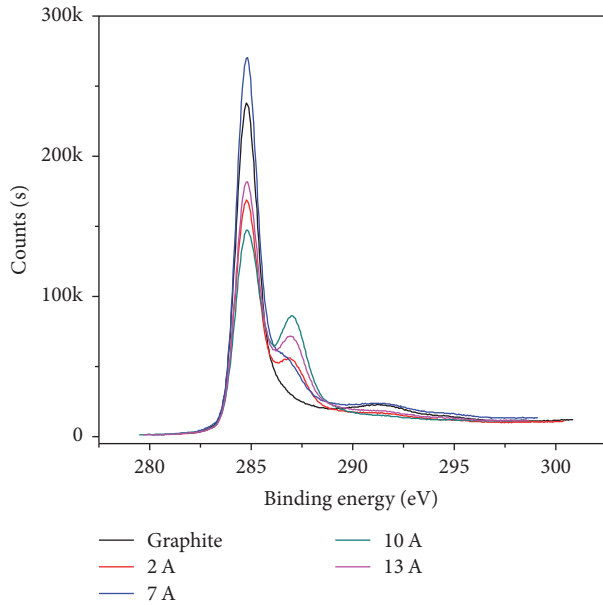


FIGURE 3: XPS results before and after deconsolidation.

XPS spectra for graphite before and after deconsolidation by different electric currents are shown in Figure 3. By means of deconvolution, one spectrum can be fit to three peaks at 284.6, 286.8, and 289.0 eV, separately [15], which can be assigned to C-C(H), C-O, and O-C=O peaks (Table 2). According to XPS results, the graphite crystal accounted for more than 99.8% before electrochemical treatment, which decreased from 65.3% to 45.6% if the current intensity increased from 2 A to 10 A. It is noted that the graphite proportion increased to 60.9% when the electric current further increased to 13 A, which is probably due to the discounted oxidation effect with decreasing O/C ratio at too rapid electrochemical rate (Table 2). Larger O/C calculated

from XPS results compared to those from elemental analysis results implies that more abundant graphite oxide was formed on the surface of graphite debris after deconsolidation.

**3.2.3. XRD Results.** The XRD results (Figure 4) also provide evidences about the formation of graphite oxide. The strong single peak at  $26.5^\circ$  can be attributed to 002 diffraction peak of graphite crystal [16], indicating a high graphitization degree and an ordered arrangement of micrographite crystal layers. During the deconsolidation, the formation of covalent bond between oxygen and carbon atoms enhances the spacing in graphite crystal along *c*-axial, and the peak at around  $12^\circ$  corresponds to the reflection of graphite oxides [17]. If we calculate the graphitization, *G* value, according to (1), a declined graphitization can be observed for deconsolidated samples compared to the matrix (Table 3). Since the deconsolidated samples are inhomogeneous mixture of various carbon species, the graphitization is not dependent on current but lies in the range of 0.80–0.89.

$$d_{002} = \frac{\lambda}{(2 \sin \theta)} \quad (1)$$

$$G = \frac{(0.3440 - d_{002})}{(0.3440 - 0.3354)}$$

[18], where  $\lambda$  is wavelength of the X-rays,  $d_{002}$  is distance between 002 planes, and  $\theta$  is the angle of incidence of the X-ray beam.

**3.3. The Current Intensity Effect on Particle Size of Graphite Matrix after Deconsolidation.** If we look further into the current intensity effect on the particle size of graphite matrix after deconsolidation (Figure 5), the following can be found: as the current increased from 2 A to 10 A, the particle size decreased from 365 nm to 148 nm, which was correspondent to the previous study [7, 19]; as the current further increased to 13 A,

TABLE 3:  $2\theta$  and  $G$  values of graphite powders produced by different deconsolidation currents intensities.

	$2\theta$ ( $^{\circ}$ )	$G$
Graphite matrix	26.54	0.95
Deconsolidated by 2 A (2.4 V)	26.46	0.83
Deconsolidated by 7 A (6.2 V)	26.48	0.86
Deconsolidated by 10 A (8.5 V)	26.50	0.89
Deconsolidated by 13 A (10.7 V)	26.44	0.80

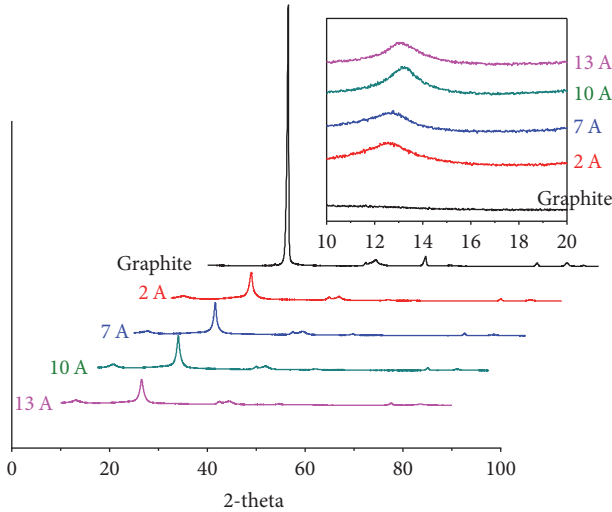


FIGURE 4: XRD results before and after deconsolidation.

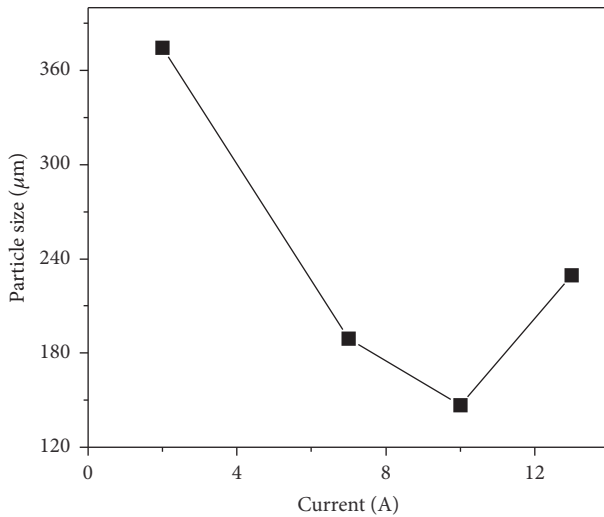


FIGURE 5: The current intensity effect on particle size after deconsolidation.

the particle size slightly increased to 240 nm. These results indicate that when the electric current is relatively small, larger deconsolidated particles are more likely to be formed caused by more graphite oxidation inside the bulk. In this case, the permeation rate of  $\text{H}_2\text{O}$  is faster than electrolysis

rate, and the latter is a rate-control step. Inversely, when the electric current becomes large enough, fine particles are more likely to be formed caused by more graphite oxidation on the interface. On one hand, both electrolysis rates of graphite matrix and  $\text{H}_2\text{O}$  become larger as current increases; on the other hand, the permeation rate of  $\text{H}_2\text{O}$  into graphite matrix would become smaller with increasing  $\text{H}_2\text{O}$  electrolysis rate. In this case, the permeation rate of  $\text{H}_2\text{O}$  is slower than electrolysis rate of graphite matrix, and the former becomes the control step. Therefore, 10 A is a turning point where the rate-control step changes from electrolysis rate-control to permeation rate-control. According to these results, the electric current range from 7 A to 13 A would be recommended, because the large difference in particle sizes between graphite fragments and TRISO-particles benefits better separation of deconsolidated graphite powders and TRISO-particles. However, the OPyC layer may be degraded or broken at higher currents, which will be discussed in additional analysis in Section 3.4.

The raw graphite matrix powder is composed of natural graphite, synthetic graphite, and resin binder in a certain proportion, which experience a series of high-temperature treatment to form graphite matrix [20]. The binder phenol resin is used to provide adhesion to mixture and helps to adhere the graphite matrix powder to TRISO-coated fuel particles during the overcoating process and will harden into a carbonaceous carbon during the subsequent carbonization process [21]. Compared to natural and synthetic graphite, the structure of carbonaceous graphite is not so ordered, so it is probably easier to be electrochemically oxidized. Also, micropore structure will be formed on the surface or in the bulk after manufacture processing due to powder compression and volatilization of light components in binder. According to SEM of the deconsolidated graphite sample (Figure 6), the graphite matrix surface is relatively smooth despite the porous structure, whereas the surface after deconsolidation becomes rough, displaying the shape of graphite raw materials. The electric current exerted little effect on the microstructure of the graphite. Since graphite microcrystalline is more ordered with higher reaction activation energy, it is reasonable to deduce that the carbonaceous carbon with turbostratic structure is easier to be broken in electrochemical process. During the electrolysis, the nitric acid electrolyte gradually infiltrated into the micropores of graphite matrix, and the electrochemical reaction would take place around micropore structure as well as on matrix surface. With much higher surface reaction capability due to large specific area of micropore structure, the expansion stress originated from

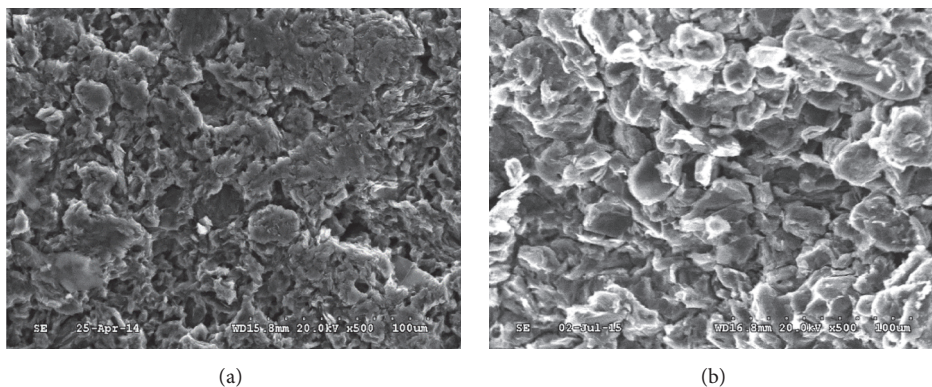


FIGURE 6: SEM images before (a) and after (b) deconsolidation.

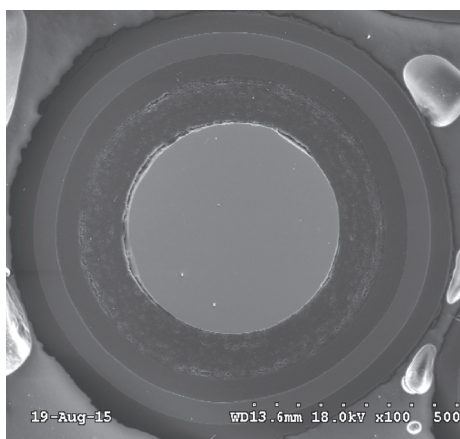


FIGURE 7: The ceramography of TRISO-particles deconsolidated by 7 A (6.2 V).

inner surface of micropores widened the  $c$ -spacing of the layer lattice of carbonaceous carbon, which was thought to be one of the main driving forces of deconsolidation.

**3.4. The Characterization of TRISO-Particles after Deconsolidation.** During the deconsolidation, it is critical to maintain intact structure of obtained TRISO-particles for further analysis. According to ceramography (Figure 7) and EDS characterization of TRISO-particle surface after deconsolidation (Figure S1, Supplementary Material available online at <https://doi.org/10.1155/2017/2126876>), Si (1.740 eV) was detected besides C (0.277 eV) and O (0.523 eV) if the samples are treated by large electric current like 10 A and 13 A, indicating that the outer PyC layer was broken and SiC layer was exposed. Moreover, the detected Si peak at 13 A is stronger than that at 10 A. Therefore, larger electric current might increase the breakage risk of PyC layer. Combining the above results for graphite fragments and TRISO-particles, the current of 7 A (6.2 V) is preferred in this study.

## 4. Conclusions

In this work, the effect of different electric current intensities on deconsolidation of spherical fuel element was studied. It

is shown that increased electric current improved deconsolidation rate. Particle size and components of deconsolidated graphite fragments were also related to the current intensity. According to the structure and surface analysis results, graphite oxide was produced after the deconsolidation, the content of which was also related to current intensities. The expansion stress originated from inner surface of micropores of carbonaceous carbon was thought to be one of the main driving forces of deconsolidation. Considering that larger electric current than 10 A would cause the breakage of OPyC layer and the exposure of SiC layer, the electric current of 7 A is preferred in this study.

## Disclosure

Part of this work has been presented on a paper in Embedded Topical 2016 ANS Winter Meeting.

## Conflicts of Interest

The authors declare that they have no conflicts of interest.

## Acknowledgments

This work is supported by National Natural Science Foundation of China 21405092, the National S&T Major Project (Grant no. ZX06901), Tsinghua University Initiative Scientific Research Program 2014z21025, and Nuclear Energy Development Project.

## References

- [1] C. Tang, Y. Tang, J. Zhu, Y. Zou, J. Li, and X. Ni, "Design and manufacture of the fuel element for the 10 MW high temperature gas-cooled reactor," *Nuclear Engineering and Design*, vol. 218, article 91, 2002.
- [2] C. Tang, Y. Tang, J. Zhu, X. Qiu, J. Li, and S. Xu, "Research and development of fuel element for Chinese 10 MW high temperature gas-cooled reactor," *Journal of Nuclear Science and Technology*, vol. 37, article 802, 2000.
- [3] G. D. Del Cul, B. B. Spencer, C. W. Forsberg et al., "Triso-coated fuel processing to support high-temperature gas-cooled

- reactors,” Oak Ridge National Laboratory Report ORNL/TM-2002/156, 2002.
- [4] M. Masson, S. Grandjean, J. Lacquement, S. Bourg, J. M. Delauzun, and J. Lacombe, “Block-type HTGR spent fuel processing: CEA investigation program and initial results,” *Nuclear Engineering and Design*, vol. 236, article 516, 2006.
- [5] E. Merz, “Destruction of graphite matrix by metallic cesium. Application for processing pyrocarbon-coated nuclear fuels,” *Nukleonik*, vol. 11, article 38, 1968.
- [6] R. L. Gray and C. Calif, “Method for disposing of radioactive graphite and silicon carbide in graphite fuel elements,” US, 5449505, 1995.
- [7] E. Merz, “On the disintegration of graphite by the formation of electrolytic graphite intercalation compounds,” *Kerntechnik*, vol. 12 article 341, 1970.
- [8] H. Bildstein and K. Knotik, “The use of oxidizing acid mixtures to disintegrate fuel inserts for gas-cooled high temperature reactor,” *Kerntechnik*, vol. 10 article 255, 1968.
- [9] N. E. Sorokina, N. W. Maksimova, and V. V. Avdeev, “Anodic oxidation of graphite in 10–98% HNO<sub>3</sub>,” *Inorganic Materials*, vol. 37, article 360, 2001.
- [10] V. V. Avdeev, O. A. Tverezovskaya, N. E. Sorokina et al., “Electrochemical study of the graphite-HNO<sub>3</sub> system,” *Inorganic Materials*, vol. 36, article 214, 2000.
- [11] L. F. Tian, M. F. Wen, and J. Chen, “Analysis of electrochemical disintegration process of graphite matrix,” *Electrochimica Acta*, vol. 56 article 985, 2010.
- [12] L. Tian, M. Wen, and J. Chen, “Studies on disintegrating spherical fuel elements of high temperature gas-cooled reactor by an electrochemical method,” *Journal of Nuclear Materials*, vol. 432 article 113, 2013.
- [13] L. Tian, M. Wen, L. Li, and J. Chen, “Disintegration of graphite matrix from the simulative high temperature gas-cooled reactor fuel element by electrochemical method,” *Electrochimica Acta*, vol. 54 article 7313, 2009.
- [14] N. Sorokina E, L. Monyakina A, N. Maksimova W et al., “Potentials of graphite mirate formation during spontaneous and electrochemical graphite intercalation,” *Inorganic Materials*, vol. 38 article 482, 2002.
- [15] S. Yumitori, “Correlation of C1s chemical state intensities with the O1s intensity in the XPS analysis of anodically oxidized glass-like carbon samples,” *Journal of Materials Science*, vol. 35, article 139, 2000.
- [16] F. Kang, T.-Y. Zhang, and Y. Leng, “Electrochemical behavior of graphite in electrolyte of sulfuric and acetic acid,” *Carbon*, vol. 35, article 1167, 1997.
- [17] Z. D. Han, J. Q. Wang, and J. Chin, “Cesium-133 NMR studies of crown ether-cesium (1+) complexes in high dielectric amide solvents,” *Inorganic Chemistry*, vol. 19, pp. 1366–1370, 2003.
- [18] M. Inagaki and Y. F. Kang, *Materials science and engineering of carbon: characterization*, Butterworth-Heinemann, 2016.
- [19] J. L. Fromm, “Recovery of valuable material from graphite bodies,” US, 2903402, 1959.
- [20] H. Zhao, T. Liang, J. Zhang, J. He, Y. Zou, and C. Tang, “Manufacture and characteristics of spherical fuel elements for the HTR-10,” *Nuclear Engineering and Design*, vol. 236, article 643, 2006.
- [21] X. W. Zhou, Z. M. Lu, J. Zhang et al., “Preparation of spherical fuel elements for HTR-PM in INET,” *Nuclear Engineering and Design*, vol. 263, article 456, 2013.

## Research Article

# A New Method to Measure Crack Extension in Nuclear Graphite Based on Digital Image Correlation

Shigang Lai,<sup>1</sup> Li Shi,<sup>2</sup> Alex Fok,<sup>3</sup> Haiyan Li,<sup>3</sup> Libin Sun,<sup>2</sup> and Zhengming Zhang<sup>2</sup>

<sup>1</sup>Zhejiang Electric Power Design Institute Co., Ltd., China Energy Engineering Group, Zhejiang, China

<sup>2</sup>Institute of Nuclear and New Energy Technology, Collaborative Innovation Center of Advanced Nuclear Energy Technology, Tsinghua University, Beijing, China

<sup>3</sup>Minnesota Dental Research Center for Biomaterials and Biomechanics, University of Minnesota, Minneapolis, MN, USA

Correspondence should be addressed to Li Shi; [shili@mail.tsinghua.edu.cn](mailto:shili@mail.tsinghua.edu.cn)

Received 30 December 2016; Revised 21 March 2017; Accepted 30 March 2017; Published 26 April 2017

Academic Editor: Leon Cizelj

Copyright © 2017 Shigang Lai et al. This is an open access article distributed under the Creative Commons Attribution License, which permits unrestricted use, distribution, and reproduction in any medium, provided the original work is properly cited.

Graphite components, used as moderators, reflectors, and core-support structures in a High-Temperature Gas-Cooled Reactor, play an important role in the safety of the reactor. Specifically, they provide channels for the fuel elements, control rods, and coolant flow. Fracture is the main failure mode for graphite, and breaching of the above channels by crack extension will seriously threaten the safety of a reactor. In this paper, a new method based on digital image correlation (DIC) is introduced for measuring crack extension in brittle materials. Cross-correlation of the displacements measured by DIC with a step function was employed to identify the advancing crack tip in a graphite beam specimen under three-point bending. The load-crack extension curve, which is required for analyzing the R-curve and tension softening behaviors, was obtained for this material. Furthermore, a sensitivity analysis of the threshold value employed for the cross-correlation parameter in the crack identification process was conducted. Finally, the results were verified using the finite element method.

## 1. Introduction

In the High-Temperature Gas-Cooled Reactor (HTGR) design, the fuel and control rods are contained and supported by graphite moderator bricks. Graphite is normally described as a brittle or quasi-brittle material with low fracture toughness [1]. Under irradiation, the material properties and dimensions of graphite change dramatically with the increase of dose [2, 3], which will create stresses high enough to cause brittle failure of the graphite components. As a result, the fuel and control rod channels may be breached, jeopardizing the operation and safety of HTGR. Therefore, it is important to consider the fracture behaviors of nuclear graphite at both the design and operation stages.

The fracture behaviors of brittle materials, including ceramic, concrete, rocks, and graphite, have been widely investigated [4–8]. Various failure criteria for nuclear graphite have been proposed and verified by experiments [9–11]. As the nonlinear fracture behavior of nuclear graphite is closely related to its grain size [1, 8], many researchers

have focused on the studies of crack initiation, propagation, and failure of graphite materials with different grain sizes. Su et al. [12] carried out three-point bend tests with single-edge-notched beams (SENB) to measure the tension softening curves and Fracture Process Zone (FPZ) of a fine-grain graphite. Similar tests were adopted for a coarse-grain graphite, NBG-18 [13]. Important fracture parameters, including the fracture toughness, FPZ, size effect, and R-curve, which can be used for evaluating crack resistance in quasi-brittle materials were obtained. The compact tension [14] and double torsion tests [15], which are able to produce relatively stable cracks, have also been used to investigate the crack extension of graphite. In such studies, one primary requirement was to detect and monitor crack initiation and propagation. However, the failure of graphite is usually associated with fast unstable crack initiation and propagation, making it difficult to capture the process [16]. To date, many techniques have been employed to identify the crack position and measure its extension in situ during loading. Although the load-displacement curve can be used

to determine the crack extension using the compliance of the cracked specimen [13], the compliance of the equipment and deviation of the material from linear-elastic behavior could introduce errors to the measurement. Another method for detecting crack extension is to measure the change in electric resistance between two electrodes placed on the opposite sides of the anticipated crack path [17]. When the crack propagates, the resistivity of the material will change accordingly. However, the results are sensitive to the environment since the resistivity of the sample is also a function of temperature and strain.

Consequently, noncontact imaging techniques have been developed for crack measurement. For example, Electronic Speckle Pattern Interferometry (ESPI) and X-ray micro-computed tomography (micro-CT) have been used to monitor crack growth in nuclear graphite [12, 15, 18]. ESPI can detect very small deformations on an object's surface but the measurement is affected by external disturbances such as mechanical vibrations. With micro-CT, the internal microcracks developed around the main crack were observed and the actual shape of the crack front was clearly revealed [18]. However, this method needed specially designed test equipment that could be fitted into the X-ray machine, and the scanning after each crack increment took a considerable amount of time to perform.

Digital image correlation (DIC) is an optical method which can also be used to measure the deformation and strain on an object's surface [19]. By analyzing a series of images recorded through a charge-coupled device (CCD) camera the whole displacement and strain fields can be calculated, from which the cracks on the material's surface can be identified. Compared to other methods, DIC has many advantages. For example, it is easy to set up, its measurement is in situ, full-field, and noncontacting, and it can be used to detect large deformation [20]. Moreover, it can be used for measurement at high temperatures, which is often required for studying nuclear graphite. Not surprisingly, DIC has been widely used as an alternative method to monitor in situ the crack growth within structural materials, including nuclear graphite and functionally graded materials [21–24].

Although DIC has been shown to be a powerful tool for measuring crack extension, the accuracy of its results is uncertain. In order to identify the crack tip, a commonly used method is to define a strain threshold,  $\epsilon_{th}$ , and the areas with strains higher than  $\epsilon_{th}$  are considered to be part of the crack [13–15]. The opening strain, which is an artificial strain caused by the crack opening displacement, was employed by Mostafavi et al. to visualize the cracks of different types of graphite [14]. A strain threshold of 1% was applied to the map of the maximum principal strain in their study. However, the position of the crack tip thus determined is rather sensitive to the value chosen for  $\epsilon_{th}$  and is greatly dependent on the resolution of the DIC results [19]. Additionally, methods using strains are not capable of identifying cracks on small specimens. Therefore, it is necessary to develop a less sensitive method for DIC that can be used to accurately identify the crack tip. In this study, the cross-correlation [25] algorithm was employed for the first time to process the displacement fields obtained from

TABLE 1: Material properties of NBG-18 [24].

Properties	Unit	Value
Mass density	kg/m <sup>3</sup>	1873.24
Modulus of elasticity	GPa	11.9
Poisson's ratio	—	0.21
Shear modulus of elasticity	GPa	4.92
Coefficient of thermal expansion	1/°C	$4.54 \times 10^{-6}$

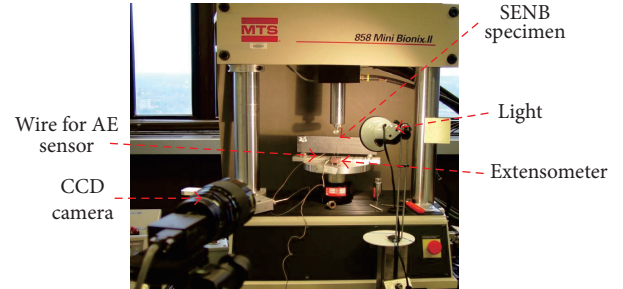


FIGURE 1: Setup of the three-point-bend test with a specimen in position.

DIC to identify the crack tip position in the specimens. A sensitivity analysis was conducted to test the convergence of this method. The results were verified through linear-elastic finite element (FE) simulations and good agreement between theory and experiment was achieved.

## 2. Experiments

Three-point-bend tests had previously been conducted using graphite single-edge-notched beams (SENB) and the full-field distributions of displacement and strain were obtained through DIC [13]. The results for one group of these specimens were analyzed using the cross-correlation technique presented in this study.

**2.1. Material and Specimens.** The test material was a pitch-coke, vibrationally molded, near isotropic nuclear grade graphite NBG-18 (SGL Carbon Group, Germany). Its main material properties are listed in Table 1.

The dimensions of the SENB specimen analyzed in this study were 45 mm length, 10 mm width, and 5 mm thickness. A prenotch was cut into the specimen with a diamond blade (Buehler diamond wafering blade, 102 mm × 0.3 mm). The specimen had an initial crack length-to-width ratio of 0.4, and the load span was 40 mm.

**2.2. Three-Point-Bend Test.** The specimen was tested in three-point bending using a universal MTS test machine (858 Mini Bionix II, MTS, US). The test setup is shown in Figure 1. A vertical displacement was applied to the specimen until it fractured completely. During loading, the notch mouth opening displacement was monitored continuously using an

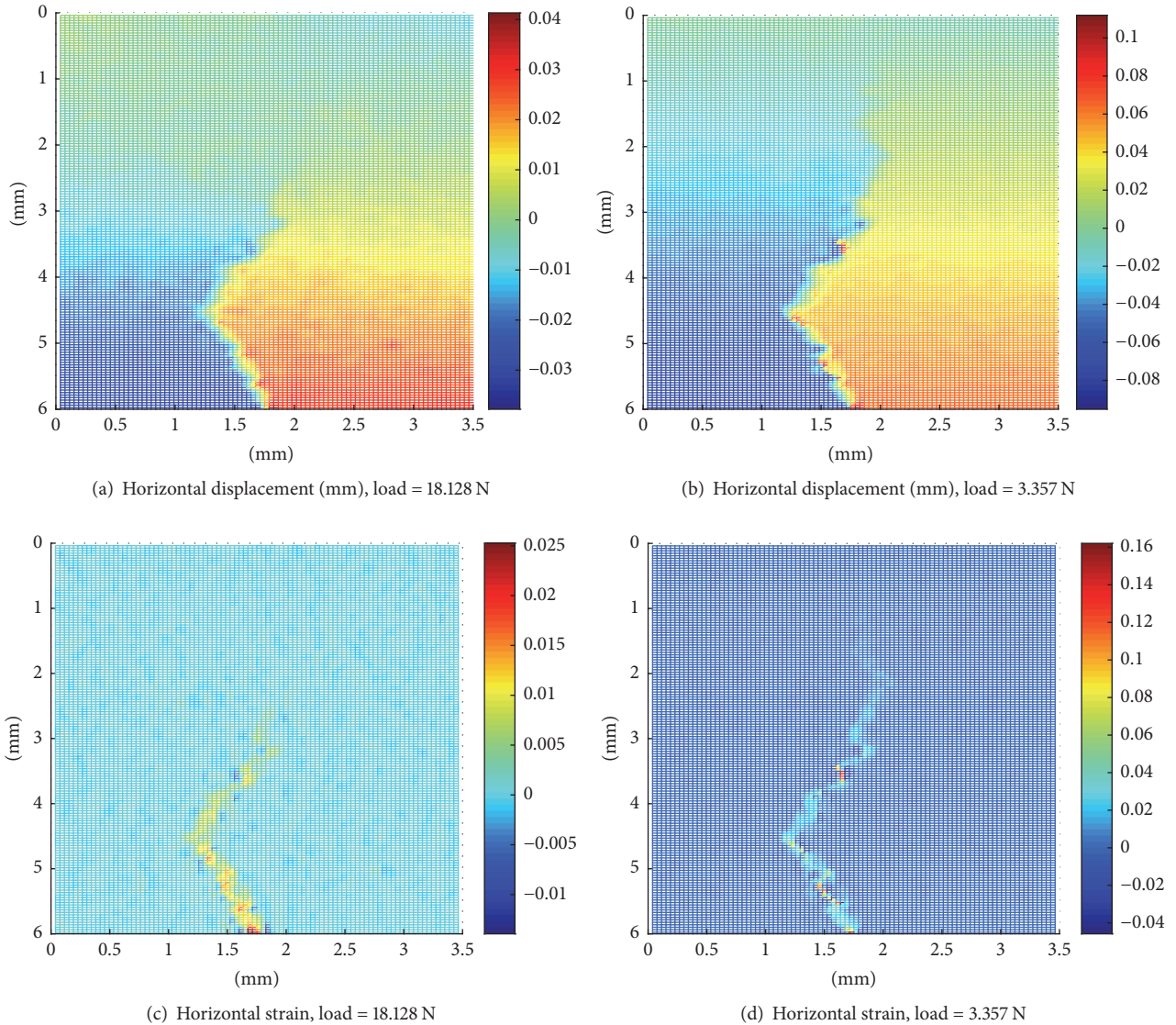


FIGURE 2: Strain and displacement fields from DIC analysis under different postpeak loads.

extensometer for feedback control purposes so that stable postpeak load-displacement data were obtained.

During loading, a CCD camera (Point Grey Grasshopper GRAS-20S4C-C, Point Grey Research, Inc.) was used to take a series of pictures of the front surface of the specimen at a frequency of 7.5 Hz (Figure 1). To ensure accuracy of the DIC results, the surface of the specimen facing the camera was sprayed with a white paint to produce more irregularly shaped speckles, which facilitated the tracking of the surface displacements. The camera started to record at the same time as the loading process began.

**2.3. Digital Image Correlation.** The images recorded during the loading process were then analyzed by proprietary image correlation software (DAVIS, LaVision). Whole-field displacement and strain distributions of the front surface of the specimens were obtained. Multiple interrogations were

used with a window size of  $64 \times 64$  pixels at an overlap of 50% with two passes, followed by the use of  $32 \times 32$ -pixel windows at an overlap of 75% with two passes.

Figure 2 shows the distributions of the horizontal displacement and strain under two different loads from the DIC analysis. The images were taken at the postpeak stage when the crack was extending. Since the crack propagated mainly along the vertical direction, only the horizontal displacement and strain were used for crack identification.

Figure 3 shows the horizontal displacements along different horizontal paths. It can be seen that the displacements on the left side of the beam's centerline are negative, and those on the right side are positive. Within the upper uncracked area (Path m3), the horizontal displacement is close to zero, whereas within the lower cracked area (Paths m1 and m2), there is a step change in the displacement curves at the position of the crack.

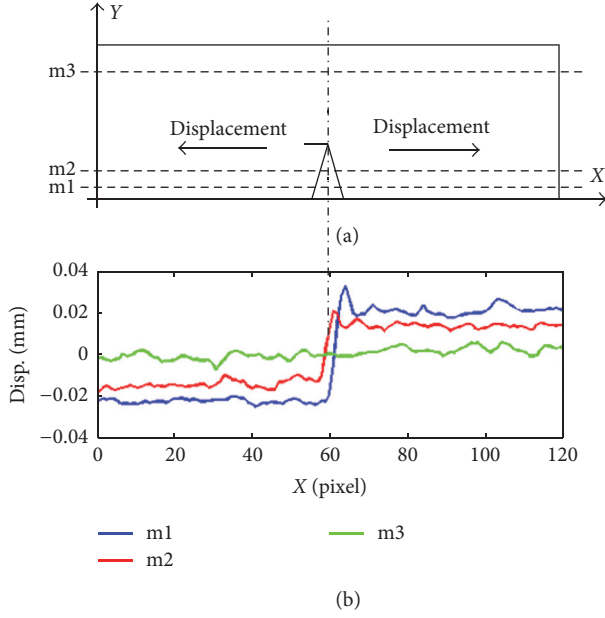


FIGURE 3: (a) Schematic diagram of SENB specimen under three-point bending showing the positions of Paths m1, m2, and m3; (b) horizontal displacement along Paths m1, m2, and m3.

### 3. Cross-Correlation Analysis

In signal processing, cross-correlation is a measure of similarity between two waveforms as a function of a varying time-lag applied to one of them. It is widely used to detect the time delay between two similar signals [25]. Cross-correlation is similar in nature to the convolution of two functions. As an example, consider two real valued functions  $f$  and  $g$  which are different only by an unknown shift along the  $x$ -axis. Cross-correlation can be used to find how much  $g$  must be shifted along the  $x$ -axis to make it identical to  $f$ . The procedure essentially slides the  $g$  function along the  $x$ -axis, calculating the summation of their product at each position. When the two functions match, the value of their cross-correlation is maximized. This is because when the peaks and troughs are aligned, they both make a large positive contribution to the summation [22].

For discrete functions  $f$  and  $g$ , the cross-correlation between them is defined as

$$(f \circ g)[n] \stackrel{\text{def}}{=} \sum_{\tau=-\infty}^{\infty} f[\tau] g[n + \tau], \quad (1)$$

where  $\tau$  is the discrete time-lag and  $f[n]$  and  $g[m]$  are the  $n$ th element of function  $f$  and the  $m$ th element of function  $g$ , respectively.

The cross-correlation method was used here to trace the crack in the graphite specimen under three-point bending based on the displacement distributions from the DIC analysis. The scientific software Matlab [26] was used for programming the method.

**3.1. Data Format.** Each displacement field data obtained through DIC is stored as a two-dimension matrix, as shown

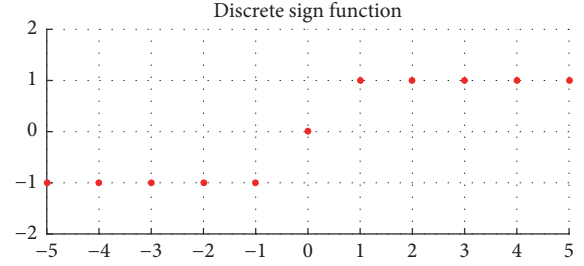


FIGURE 4: The G-function.

in Figures 2(a) and 2(b); the horizontal displacement at each sampling point was extracted and stored in the form of  $M$ -by- $N$  matrix:

$$U : U(m, n) \quad m = 1, 2, \dots, M; \quad n = 1, 2, \dots, N, \quad (2)$$

or

$$U = \begin{bmatrix} u_{11} & u_{12} & \cdots & u_{1N} \\ u_{21} & u_{22} & \cdots & u_{2N} \\ \vdots & \vdots & u_{ij} & \vdots \\ u_{M1} & u_{M2} & \cdots & u_{MN} \end{bmatrix}, \quad (3)$$

where component  $u_{ij}$  is the horizontal displacement in the  $i$ th row and  $j$ th column  $M$  and  $N$  are the total number of rows and columns, respectively, which are dependent on the resolution of the DIC analysis.

**3.2. Cross-Correlation Process.** Using each matrix  $U$  extracted from the DIC results, a cross-correlation procedure was conducted to accurately map out the crack and to measure its extension. The process included two steps:

*Step 1* (establishing the cross-correlation function  $R$  and crack position array  $P$ ). A discrete sign function  $G$  is defined in (4). As shown in Figure 4, the shape of the  $G$ -function is similar to the distribution of horizontal displacement along a horizontal path crossed by the crack (Figure 3(b)).

$$G(n) = \begin{cases} -1, & n \leq -1, \\ 0, & n = 0, \\ 1, & n \geq 1. \end{cases} \quad (4)$$

For the  $M$  rows of horizontal displacement, the cross-correlation function between the  $G$ -function and the matrix  $U$  was constructed as

$$R(m, \tau) = \sum_{\tau} U(m, n) G(n - \tau), \quad (5)$$

$$m = 1, 2, \dots, M; \quad n = 1, 2, \dots, N,$$

where  $R$  is the cross-correlation function,  $m$  is the row number,  $n$  is the column number, and  $\tau$  is an integer variable

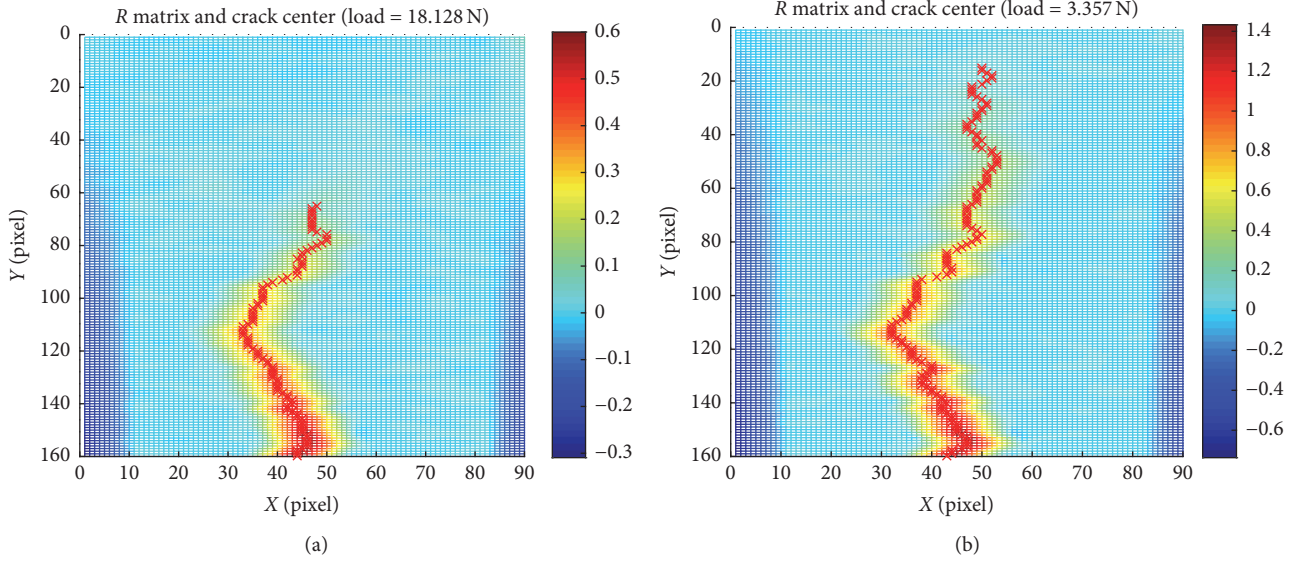


FIGURE 5: Maps of the cross-correlation function  $R$  and crack position  $P$  under (a) Load 1 (18.128 N) and (b) Load 2 (3.357 N).

representing the shift. Therefore, by shifting  $G$ , the closer it was in matching its step to that of a particular row of entries in  $U$ , the larger the corresponding value in the cross-correlation function  $R$  is. In this way, the dissimilarity between the cracked and uncracked areas was actually enlarged with the cross-correlation analysis. Note that the cross-correlation function  $R$  was also an  $M$ -by- $N$  matrix.

Along the  $m$ th row,  $R$  reached its maximum value where the shift in  $G$  matched its step with that in the horizontal displacement curve best. This coincided with the crack position. So the crack position was identified by finding the maximum value of  $R$  along each row. An array  $P$  was thus constructed to store the crack position (column number) in each row:

$$P(m) = n_{\max}, \quad m = 1, 2, \dots, M, \quad (6)$$

where  $n_{\max}$  is the column number with the maximum  $R$  in the  $m$ th row; that is,  $R(m, n_{\max}) = \max(R(m, n))$ . Figure 5 shows the maps of the matrix  $R$  and the array  $P$  (marked by red crosses) under the same Load 1 and Load 2 as in Figure 2.

*Step 2 (identification of the crack tip).* After obtaining the crack position array  $P$ , the next task was to accurately identify the crack tip. To do so, an array  $V$  was introduced to store the variance of the cross-correlation function  $R$  on each row:

$$V(m) = \text{Var}(R(m, n)). \quad (7)$$

The variance function was defined by the following equation:

$$\text{Var}(X) = E[(X - \mu)^2], \quad (8)$$

where  $X = [x_1, x_2, \dots, x_n]$  and  $\mu$  is the mean value of  $X$ .

With the variance array  $V$ , the dissimilarity between the cracked and uncracked areas was further enlarged. The crack

tip was then positioned by defining the cracked area as the area where  $V \geq V_{\text{th}}$ ,  $V_{\text{th}}$  being a threshold of  $V$  (see later). And the complete crack was fully captured by combining the crack position array  $P$  and the variance array  $V$  that defined the crack tip.

Figures 6(a) and 6(c) show the distributions of  $V$  along the vertical direction for images under Load 1 (18.128 N) and Load 2 (3.357 N), respectively. In Figure 6(a), the value of  $V(m)$  tends towards  $9 \times 10^{-4}$  as it enters the uncracked region. Figures 6(b) and 6(d) show the delineated cracks using a threshold for  $V$  of  $V_{\text{th}} = 9 \times 10^{-4} \text{ mm}^2$ .

*3.3. Crack Extension versus Load.* The above analysis was repeated for all the images and the crack extensions under different load levels were obtained, as shown in Figure 7. Each point on the curve represents the results from one DIC image. The curve shows that crack propagation started just before the peak load and the crack propagated steadily thereafter with a decrease in load.

*3.4. Sensitivity Analysis.* In the crack identification process, a threshold,  $V_{\text{th}}$ , for the variance was required to locate the crack tip. In order to study how much the results were dependent on  $V_{\text{th}}$ , a sensitivity analysis was conducted by measuring the crack extension with different  $V_{\text{th}}$ , as shown in Figure 8(a). It can be seen that as  $V_{\text{th}}$  decreased, the calculated crack length increased. But the results converged quickly, and when  $V_{\text{th}}$  was smaller than  $1.5 \times 10^{-3}$ , the curves were almost the same.

For comparison, the crack extension was also calculated using two other methods that were based on (1) the displacement field  $U$  without the cross-correlation analysis and (2) the strain fields. These two methods also required a threshold value for their respective parameters, displacement and strain, to identify the crack tip. The results are shown

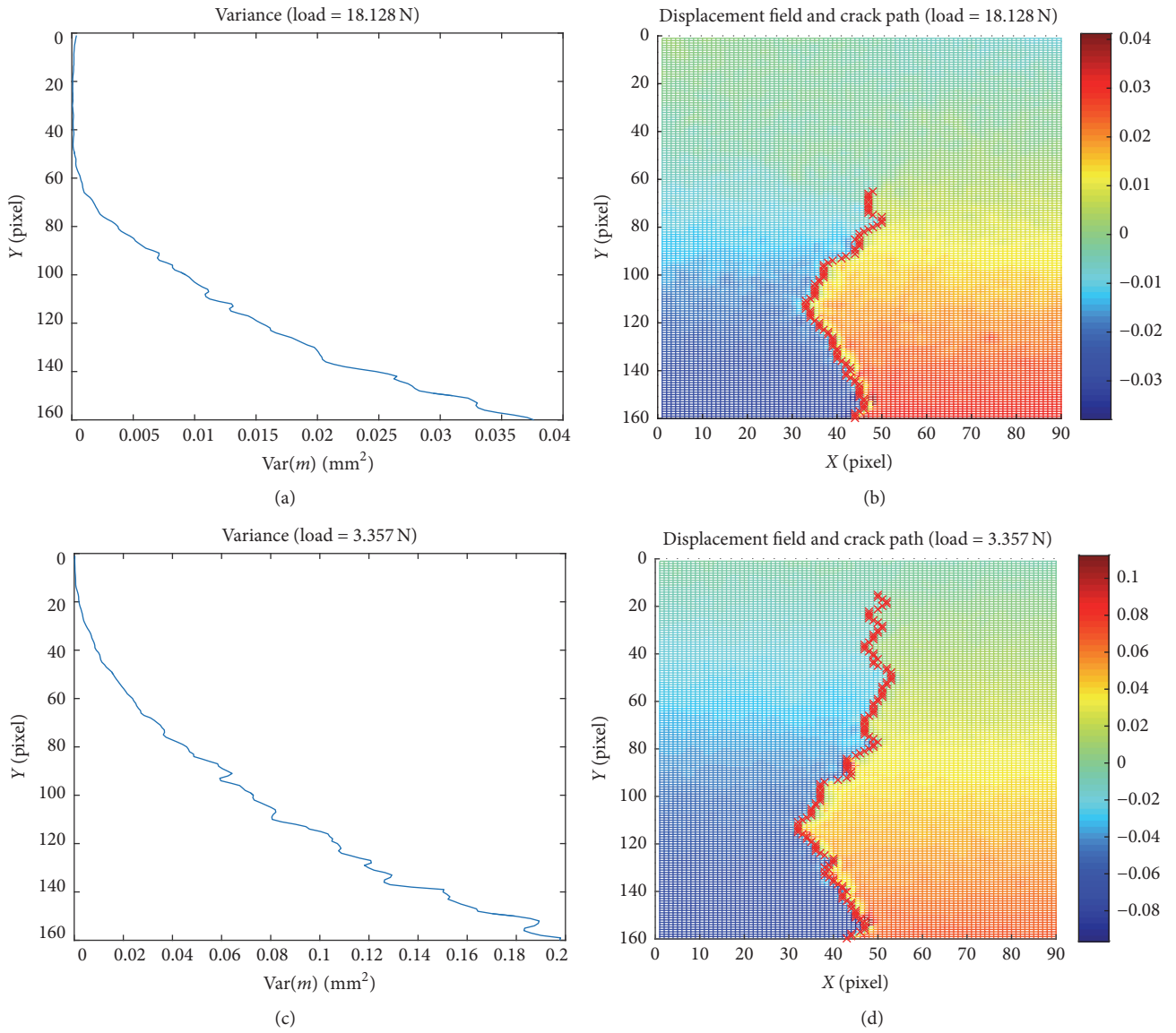


FIGURE 6: Distributions of  $V$  and delineated cracks on the displacement maps under different loads.

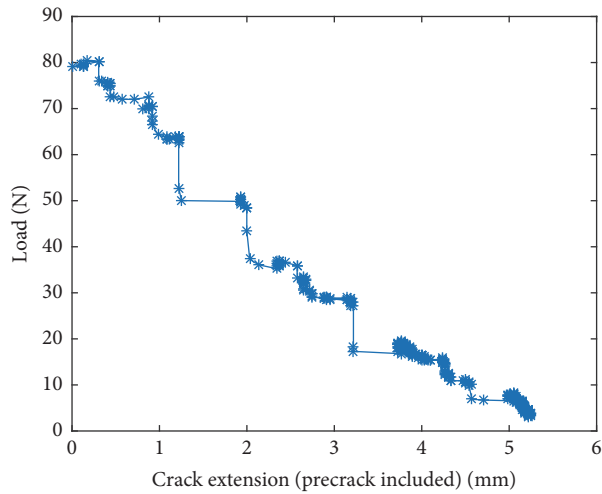


FIGURE 7: Load versus crack extension.

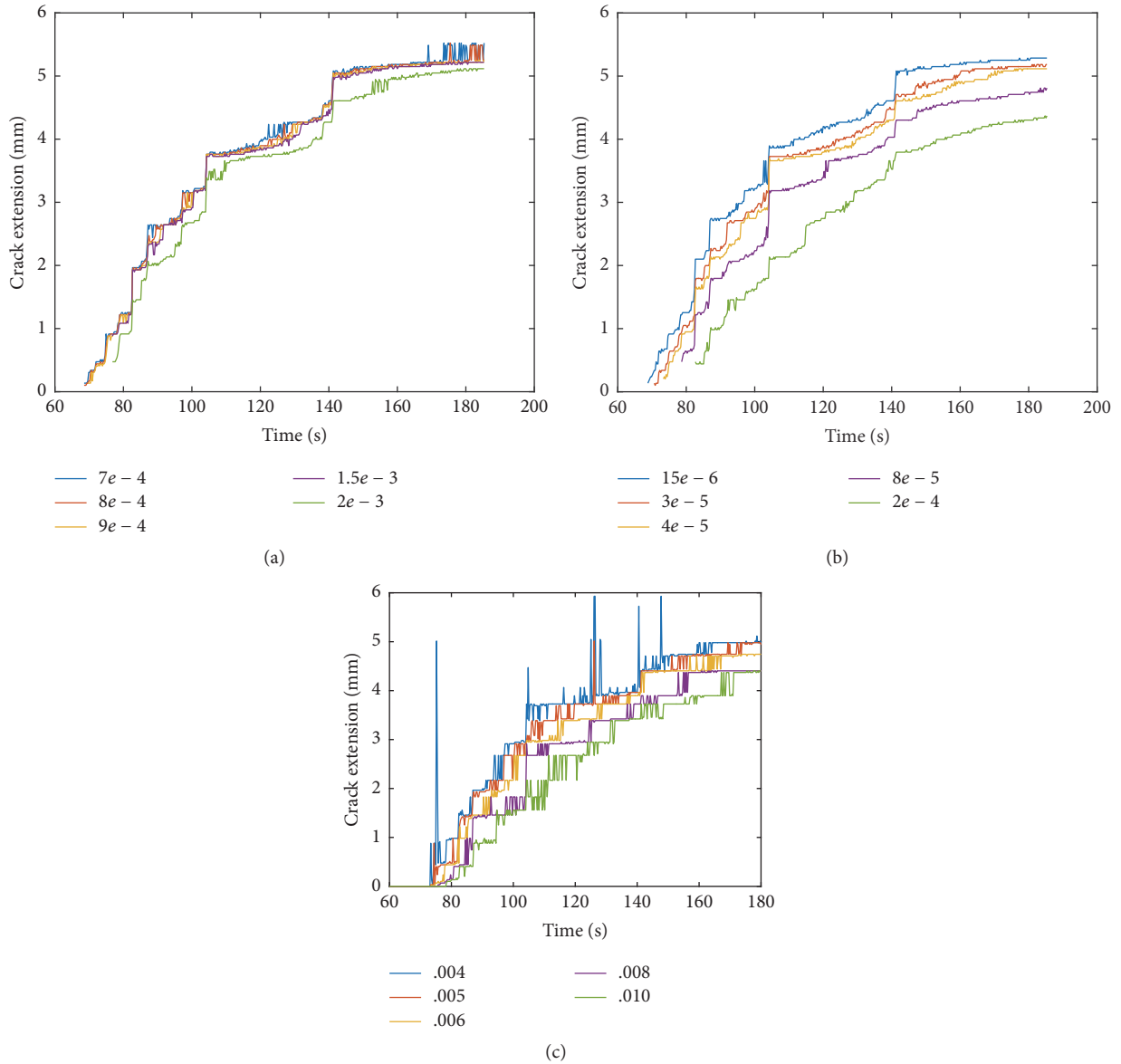


FIGURE 8: Crack extensions using different threshold parameters based on (a) displacement map with cross-correlation analysis, (b) displacement map without cross-correlation analysis, and (c) strain map without cross-correlation analysis.

in Figures 8(b) and 8(c). It can be seen that their speeds of convergence were much slower than that based on the cross-correlation of displacement functions, as shown in Figure 8(a), indicating that their results were more sensitive to the threshold.

#### 4. Verification with the Finite Element Method

In order to verify the results obtained from the cross-correlation process, the finite element (FE) method was used to predict the crack extension versus load for the same specimen. The dimensions of the specimen were given in Section 2.1.

Cracks with different lengths, from 0 mm to 5 mm, were considered in the FE analysis using ABAQUS. Figure 9(a)

shows one of the FE models with a crack of 1 mm long ahead the notch. The mesh around the crack tip was refined. Loading and supporting components were considered in the model and hard contacts were assumed between these components and the graphite specimens. The FE model contained 6904 8-node, plane-strain elements (CPE8) and 20939 nodes. The material was assumed to be linear-elastic, with the same parameters as those in Table 1.

The FE-predicted load-displacement curves (green) for different crack lengths were plotted together with one of the test results (blue) in Figure 9(b). It can be seen that with the increase of crack extension, the slopes of the green lines decreased, indicating a decrease in stiffness of the specimen. The loads corresponding to the different crack extensions were obtained from the intersection points between the

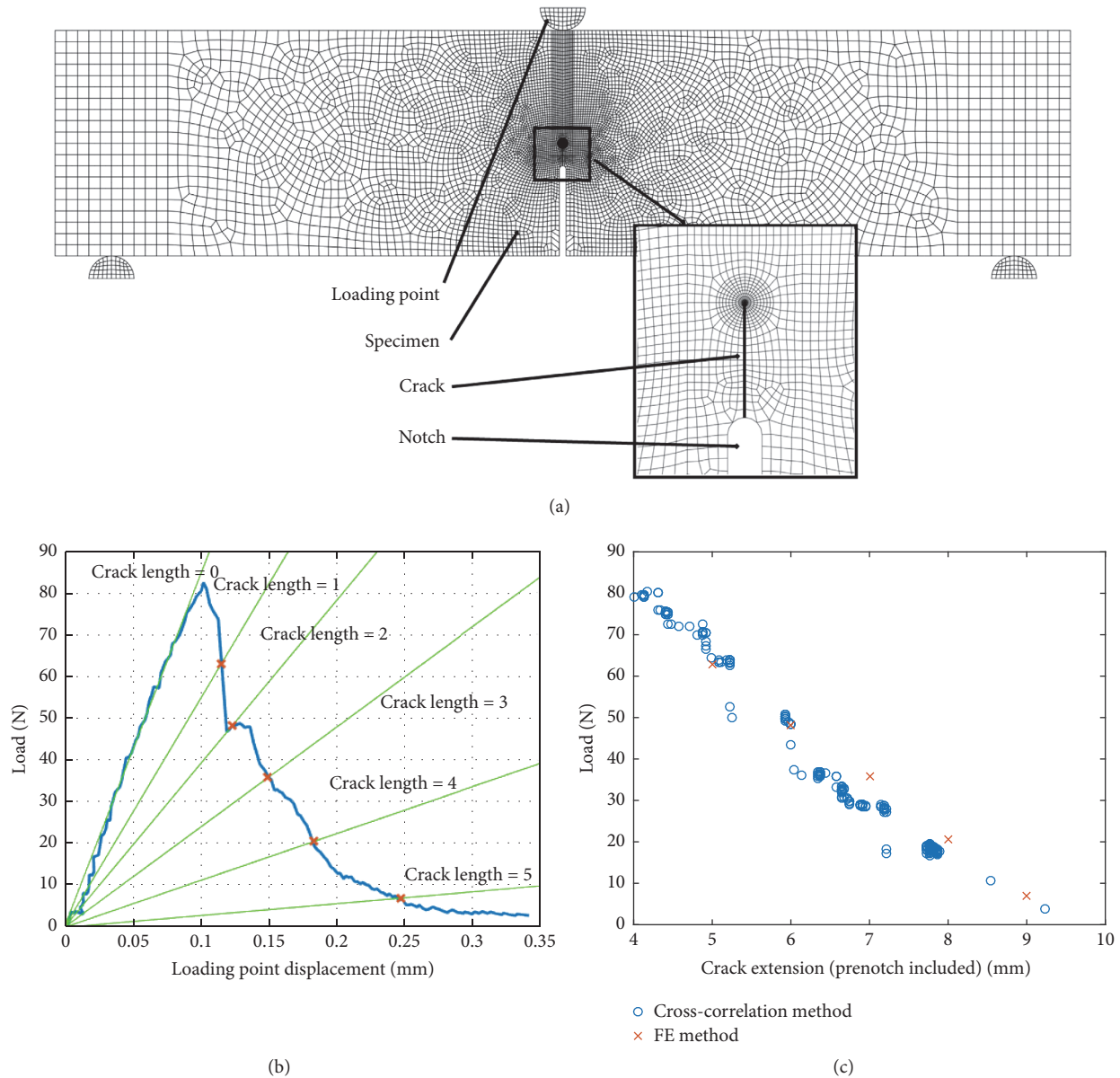


FIGURE 9: FE simulation: (a) FE model, (b) FE-predicted load-displacement curves (green) for models with different crack lengths intersecting with the experimental load-displacement curve (blue), and (c) FE and cross-correlation results for the load-crack extension curve.

experimental load-displacement curve and the FE-simulated load-displacement lines, as shown in Figure 9(b). The crack length as a function of load in the test can thus be estimated. The intersection points in the figure are listed in Table 2. The procedure is similar to that used by Hodgkins et al. to observe the microstructural damage and crack morphology in graphite [27]. In their study, the specimen was unloaded and reloaded during crack propagation and the crack length was calculated from the unloading compliance. In the present study, FE simulations were used instead to obtain the compliance of the cracked specimen.

Figure 9(c) shows the load versus crack extension behavior predicted by the FE analysis, together with those from the cross-correlation analysis. It can be seen that the two sets of

results agreed well with each other. The results given by the cross-correlation method were slightly lower than those from the FE simulation.

## 5. Discussion and Conclusion

Digital image correlation (DIC) has been widely used to monitor the failure of engineering materials because of its capability to provide in situ, full-field, and noncontacting deformation measurement.

In a DIC analysis, the displacement field is the primary result obtained directly from the correlation analysis of the raw images, while the strain field is a secondary result which is obtained through the differentiation of the displacement

TABLE 2: FE simulation results.

Crack extension/mm	Crack extension including prenotch	Loading point Disp./mm	Load/N
1	5	0.115	62.89
2	6	0.123	48.12
3	7	0.149	35.71
4	8	0.183	20.54
5	9	0.246	6.975

field. Therefore, the displacement field provides more detailed information on the crack profile than the strain field. However, unlike strain, the values of displacement could not be directly related to the crack. Therefore, a cross-correlation method was developed in this study to more accurately identify the tip of an advancing crack and measure its extension at different stages of loading from the displacement field.

The crack length identified is dependent on the threshold set for the parameter used in the identification, which may in turn depend on the material properties, specimen size, and loading conditions. This is reflected in the different strain thresholds,  $\varepsilon_{th}$ , employed in the literature. For the three-point bend test [13], as fracture occurred rapidly, the detected crack length was found to be very sensitive to  $\varepsilon_{th}$ . To find the proper  $\varepsilon_{th}$ , crack extension curves for different threshold values were compared and the one which could describe the experimental results best was adopted. Strain thresholds of 0.4% and 0.7% were chosen for large- and small-size specimens, respectively. Compared to the SENB specimen, compact tension and double torsion specimens were able to produce more stable crack growth and the measured crack length based on the strain map was less sensitive to  $\varepsilon_{th}$ . However, the selection of the threshold strain is still based on experience or trial and error, depending on the application. A threshold value of 1% was used to calculate crack length and 0.5% was chosen to identify microcracking in [14]. In a later study using the double torsion technique [15], the threshold strain for identifying microcracking was 0.35%, which was about twice the maximum predicted strain of the material assuming linear elasticity.

Similar to methods that are based on strain maps, a threshold for the variance  $V$  is also required in the cross-correlation method in order to locate the crack tip. However, the sensitivity analysis showed that the results with the cross-correlation analysis were much less dependent on the threshold adopted. As shown in Figure 8, the results based on the cross-correlation method converged fastest. In addition, the crack profile could be more accurately defined with this method, as shown in Figure 5.

The crack extension-load curve obtained with the cross-correlation method was verified through FE analysis. As shown in Figure 9(c), the crack extensions given by the FE simulations were slightly longer than those from the cross-correlation method. This was reasonable because the linear-elastic material behavior assumed in the FE model could result in a higher stiffness of the specimen, causing an overestimation of the load for a certain crack extension. In

reality, the stress-strain curve of graphite is slightly nonlinear and there is a Fracture Process Zone ahead of the crack tip which leads to inelastic behavior.

Based on the characteristics of the displacement distribution across a crack, a  $G$ -function (see (1)) was defined to enlarge the difference between the cracked and uncracked areas through cross-correlation. It should be noted that the  $G$ -function in (1) is only suitable for mode I cracks, such as those produced under tensile, three-point, and four-point bending tests. For specimens with other fracture modes, the aforementioned  $G$ -function should be revised according to the characteristics of the displacement distribution.

Although the cross-correlation method presented in this paper was developed to trace the single crack, it can be extended to identify multiple cracks in specimens under complex loading. For example, cross-correlation analyses along the  $x$ - and  $y$ -directions can be conducted jointly to map out crack trajectories in different directions.

In conclusion, the cross-correlation method developed in this study is a robust way to identify the path of an advancing crack based on DIC results. The main advantages of this method include the following: (1) the crack extension can be measured accurately; (2) the profile of the crack can be clearly identified; and (3) the results are less sensitive to the calculation parameters. The developed method will improve the current measurement of crack propagation of nuclear graphite and lead to a better understanding of its fracture behaviors, which is essential for the design and safe operation of HTGR.

## Nomenclature

CCD:	Charge-coupled device
DIC:	Digital image correlation
ESPI:	Electronic Speckle Pattern Interferometry
FE:	Finite element
FPZ:	Fracture Process Zone
HTGR:	High-Temperature Gas-Cooled Reactor
SENB:	Single-edge-notched beams
$U$ :	Displacement field
$V$ :	Variance array
$\varepsilon$ :	Strain
$\varepsilon_{th}$ :	Strain threshold.

## Conflicts of Interest

The authors declare that they have no conflicts of interest.

## Acknowledgments

This research was performed using funding received from the DOE Office of Nuclear Energy's Nuclear Energy University Programs. The authors would like to acknowledge Minnesota Dental Research Center for Biomaterials and Biomechanics (MDRCBB) for providing the testing devices and the Minnesota Supercomputing Institute (MSI) for providing the computing services.

## References

- [1] T. D. Burchell, Ed., *Carbon Materials for Advanced Technologies*, Elsevier, Amsterdam, Netherlands, 1999.
- [2] H. Matsuo, T. Saito, and Y. Sasaki, "Effects of high temperature neutron irradiation on dimension and thermal expansion coefficient of nuclear grade graphites," *Journal of Nuclear Science and Technology*, vol. 18, no. 11, pp. 863–869, 1981.
- [3] H. Matsuo and T. Saito, "Irradiation behaviors of nuclear grade graphite in commercial reactor, (I) dimensional change and thermal expansion," *Journal of Nuclear Science and Technology*, vol. 22, no. 2, pp. 139–146, 1985.
- [4] S. P. Shah, S. E. Swartz, and C. Ouyang, *Fracture Mechanics of Concrete: Applications of Fracture Mechanics to Concrete, Rock and Other Quasi-Brittle Materials*, John Wiley & Sons, 1995.
- [5] A. Bornhauser, K. Kromp, and R. F. Pabst, "R-curve evaluation with ceramic materials at elevated temperatures by an energy approach using direct observation and compliance calculation of the crack length," *Journal of Materials Science*, vol. 20, no. 7, pp. 2586–2596, 1985.
- [6] M. R. Ayatollahi, M. R. M. Aliha, and M. M. Hassani, "Mixed mode brittle fracture in PMMA—an experimental study using SCB specimens," *Materials Science and Engineering A*, vol. 417, no. 1–2, pp. 348–356, 2006.
- [7] F. Berto and P. Lazzarin, "Recent developments in brittle and quasi-brittle failure assessment of engineering materials by means of local approaches," *Materials Science and Engineering R: Reports*, vol. 75, no. 1, pp. 1–48, 2014.
- [8] A. Hodgkins, T. J. Marrow, M. R. Wootton, R. Moskovic, and P. E. J. Flewitt, "Fracture behaviour of radiolytically oxidised reactor coregraphites: a view," *Materials Science and Technology*, vol. 26, no. 8, pp. 899–907, 2010.
- [9] S. Sato, H. Awaji, K. Kawamata, A. Kurumada, and T. Oku, "Fracture criteria of reactor graphite under multiaxial stresses," *Nuclear Engineering and Design*, vol. 103, no. 3, pp. 291–300, 1987.
- [10] M. R. Ayatollahi, F. Berto, and P. Lazzarin, "Mixed mode brittle fracture of sharp and blunt V-notches in polycrystalline graphite," *Carbon*, vol. 49, no. 7, pp. 2465–2474, 2011.
- [11] P. Lazzarin, F. Berto, and M. R. Ayatollahi, "Brittle failure of inclined key-hole notches in isostatic graphite under in-plane mixed mode loading," *Fatigue and Fracture of Engineering Materials and Structures*, vol. 36, no. 9, pp. 942–955, 2013.
- [12] R. K. L. Su, H. H. Chen, S. L. Fok et al., "Determination of the tension softening curve of nuclear graphites using the incremental displacement collocation method," *Carbon*, vol. 57, pp. 65–78, 2013.
- [13] H. Li, J. Li, G. Singh, and A. Fok, "Fracture behavior of nuclear graphite NBG-18," *Carbon*, vol. 60, pp. 46–56, 2013.
- [14] M. Mostafavi, M. J. J. Schmidt, B. J. Marsden, and T. J. Marrow, "Fracture behaviour of an anisotropic polygranular graphite (PGA)," *Materials Science and Engineering A*, vol. 558, pp. 265–277, 2012.
- [15] T. H. Becker, T. J. Marrow, and R. B. Tait, "Damage, crack growth and fracture characteristics of nuclear grade graphite using the Double Torsion technique," *Journal of Nuclear Materials*, vol. 414, no. 1, pp. 32–43, 2011.
- [16] R. Moskovic, P. J. Heard, P. E. J. Flewitt, and M. R. Wootton, "Overview of strength, crack propagation and fracture of nuclear reactor moderator graphite," *Nuclear Engineering and Design*, vol. 263, pp. 431–442, 2013.
- [17] B. Stalder, P. Béguelin, and H. H. Kausch, "A simple velocity gauge for measuring crack growth," *International Journal of Fracture*, vol. 22, no. 2, pp. R47–R50, 1983.
- [18] A. Hodgkins, T. J. Marrow, P. Mummery, B. Marsden, and A. Fok, "X-ray tomography observation of crack propagation in nuclear graphite," *Materials Science and Technology*, vol. 22, no. 9, pp. 1045–1051, 2006.
- [19] DANTEC, "Measurement Principles—Digital Image Correlation (DIC)," 2012.
- [20] R. Lichtenberger and H. Schreier, "Non-contacting measurement technology for component safety assessment," in *Proceedings of the 6th International Symposium and Exhibition on Sophisticated Car Occupant Safety Systems (AIRBAG '02)*, Karlsruhe, Germany, 2002.
- [21] J. Abanto-Bueno and J. Lambros, "Investigation of crack growth in functionally graded materials using digital image correlation," *Engineering Fracture Mechanics*, vol. 69, no. 14–16, pp. 1695–1711, 2002.
- [22] S. J. Orfanidis, *Optimum Signal Processing*, McGraw-Hill, New York, NY, USA, 2007.
- [23] M. R. Ayatollahi and M. Moazzami, "Digital image correlation method for calculating coefficients of Williams expansion in compact tension specimen," *Optics and Lasers in Engineering*, vol. 90, pp. 26–33, 2017.
- [24] R. Markgraaff, *Relationship between the natural frequencies and fatigue life of NBG-18 graphite [M.S. thesis]*, North-West University, Potchefstroom, South Africa, 2010.
- [25] Wikipedia, "Cross-correlation," 2013.
- [26] MathWorks, "Matlab the language of Technical Computing," 2013.
- [27] A. Hodgkins, J. Marrow, P. Mummery, A. Fok, and B. J. Marsden, "Crack propagation resistance and damage mechanisms in nuclear graphite," in *Fracture of Nano and Engineering Materials and Structures: Proceedings of the 16th European Conference of Fracture, Alexandroupolis, Greece, July 3–7, 2006*, E. E. Gdoutos, Ed., pp. 891–892, Springer, Dordrecht, The Netherlands, 2006.

## Research Article

# Research on the Computed Tomography Pebble Flow Detecting System for HTR-PM

Xin Wan,<sup>1,2</sup> Ximing Liu,<sup>1,2</sup> Jichen Miao,<sup>1,2</sup> Peng Cong,<sup>1,2</sup> Yuai Zhang,<sup>1,2</sup> and Zhifang Wu<sup>1,2</sup>

<sup>1</sup>Institute of Nuclear and New Energy Technology, Tsinghua University, Beijing 100084, China

<sup>2</sup>Key Laboratory of Nuclear Detection and Measurement Technology, Beijing 100084, China

Correspondence should be addressed to Zhifang Wu; zhifang.wu@tsinghua.edu.cn

Received 26 December 2016; Revised 21 March 2017; Accepted 4 April 2017; Published 24 April 2017

Academic Editor: Robert Morris

Copyright © 2017 Xin Wan et al. This is an open access article distributed under the Creative Commons Attribution License, which permits unrestricted use, distribution, and reproduction in any medium, provided the original work is properly cited.

Pebble dynamics is important for the safe operation of pebble-bed high temperature gas-cooled reactors and is a complicated problem of great concern. To investigate it more authentically, a computed tomography pebble flow detecting (CT-PFD) system has been constructed, in which a three-dimensional model is simulated according to the ratio of 1:5 with the core of HTR-PM. A multislice helical CT is utilized to acquire the reconstructed cross-sectional images of simulated pebbles, among which special tracer pebbles are designed to indicate pebble flow. Tracer pebbles can be recognized from many other background pebbles because of their heavy kernels that can be resolved in CT images. The detecting principle and design parameters of the system were demonstrated by a verification experiment on an existing CT system in this paper. Algorithms to automatically locate the three-dimensional coordinates of tracer pebbles and to rebuild the trajectory of each tracer pebble were presented and verified. The proposed pebble-detecting and tracking technique described in this paper will be implemented in the near future.

## 1. Introduction

Pebble dynamics is important for the safe operation of pebble-bed high temperature gas-cooled reactor (PB-HTGR). Several countries have done many experiments on pebble flow according to their PB-HTGR modules separately, such as the United States, South Africa, Germany, and China. However, most of these experiments were done in two-dimensional (2D) models or limited to phenomenological methods like visual observation. In the United States, a 180° half-model with an open window for visual inspection and data collection was built according to the ratio of 1:10 with the actual size of PBMR [1]. In Germany, experiments were done based on AVR. Transparent glass pebbles of different colors were immersed in a special liquid, and the marked pebbles were tracked through the refractivity relationship between the transparent wall and the special liquid [2]. In China, a 2D experimental platform was built as the proportion of 1:5 with HTR-PM and colored pebbles were also used in the observation [3, 4]. Since the results obtained by 2D models are different from the physical truth and phenomenological methods are easy

to be influenced by human factors, a three-dimensional (3D) model and a more objective experimental method are needed.

Kadak and Bazant [1] from MIT used an imaging method in their research with the help of a radioactive tracer pebble inside a 3D model and two collimated scintillation detectors to locate the tracer pebble. This technique is called radioactive particle tracking (RPT), which was firstly introduced and implemented at Australian Atomic Energy Commission in 1973 [5]. Shehata [6] from NCSU and Khane et al. [7] from Missouri S&T also adopted RPT in their research. Shehata used three collimated detectors while Khane et al. used as much as sixteen noncollimated detectors to track one pebble. The major defect of the RPT technique is that usually only one radioactive pebble can be tracked at the same time. To investigate different pebble trajectories, the initial position of the radioactive pebble needs to be changed manually. Radioprotection from the radioactive tracer pebble inside the model and radioactive waste disposal are serious problems to solve as well. Laufer and Buster [8] from UC Berkeley designed an X-ray pebble recirculation experimental system (X-PREX), in which X-ray radiography was utilized. Both the

translational and rotational motion of pebbles in a 3D model were tracked using special plastic pebbles with thin tungsten wires inserted through one central axis. Tungsten wires can be resolved by X-ray imaging due to their larger attenuation coefficients compared to plastic; thus the coordinates of pebbles were acquired through special image processing algorithms. They have obtained important experimental results in a small cylindrical test tube with the inner diameter of 5.5 pebble diameters. However, when the test tube is bigger and the number of tracer pebbles is larger, the projection images of tungsten wires will be overlapped too much to accurately distinguish them from each other.

In our study, multislice helical computed tomography (MSCT) is introduced to research pebble dynamics. CT can get the cross-sectional images of an object, thus providing a way to learn the object's internal structure without damaging it. CT has been widely used in different application fields for decades, and, as a revolutionary progress of regular CT, MSCT plays an increasingly important role in aspects of medical diagnosis and some industrial nondestructive testing (NDT). Considering its feature of translational scan along objects, MSCT is perfectly suitable for investigating pebble trajectories in the core. A CT pebble flow detecting (CT-PFD) system has been constructed in Tsinghua University with a 3D simulated model built as the ratio of 1:5 with the core of HTR-PM and an eight-slice helical CT scanning equipment. The 2D cross-sectional images and 3D stereoscopic images of pebbles at any position and any time during the discharging process can be obtained using the system. A few special tracer pebbles will be mixed in the core with many other background pebbles. Tracer pebbles' trajectories can be reconstructed through some image postprocessing algorithms, which will be introduced below.

Section 2 introduces the design and detecting principle of the CT-PFD system. They are demonstrated by a verification experiment using the existing CT equipment in our lab. Section 3 presents our research on the realization of the whole pebble-detecting procedure. Algorithms to automatically locate the 3D coordinates of tracer pebbles and to rebuild the trajectory of each tracer pebble were presented and verified. The last section is a comprehensive summary of this paper.

## 2. CT Pebble Flow Detecting (CT-PFD) System

**2.1. System Design.** The simulated core is a cylindrical container made of polymethylmethacrylate (PMMA) with a charging inlet above and a discharging outlet below, as shown in Figure 1. Its structure and sizes are designed according to the core of HTR-PM [9], as shown in Table 1. The inner diameter of the container is 600 mm, the external diameter is 650 mm, and the height is 2,200 mm. The container is set in the center of the system, while the radiation source and the detector are arranged in a turntable around it. Two marble pillars support the turntable and serve as its translational orbit. During the inspection, the turntable rotates around the stationary container while it translates along the pillars, which makes the scan path of the radiation source a helix.

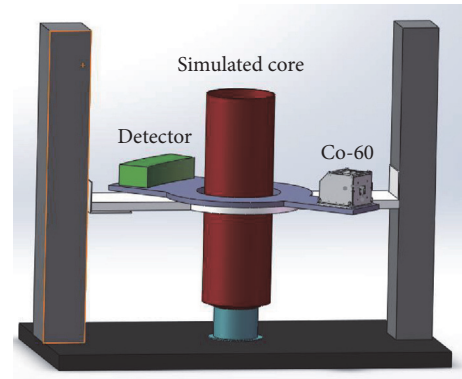


FIGURE 1: Sketch of the CT-PFD system.



FIGURE 2: Current view of the CT-PFD system.

Power is transmitted through a slip ring. Signal and data are transmitted by a wireless network. The CT-PFD system is still under construction, and Figure 2 is its current view.

The radioactive cobalt-60 (Co-60) is chosen as the radiation source for its high radiant energy, low cost, and convenience; it is free of electricity, high pressure, or refrigeration. Two kinds of gamma photons with energy of 1.17 MeV and 1.33 MeV are emitted by Co-60 and pass through the simulated core after collimation. An eight-slice linear array detector is designed to receive the rays coming out from the simulated core. Each row has 460 CsI (TI) scintillator units, which transform gamma photons to electrical charges. The electrical signal is scaled and finally uploaded to computers for further processing and image reconstruction.

Collimators and an extra radiation catcher, made of tungsten alloy with high density to increase radiation-shielding effectiveness, are set on the turntable together with the radiation source and the detector. The whole CT-PFD system is installed in a concrete room, separated from the main control room where operators stay. A safety interlock system,

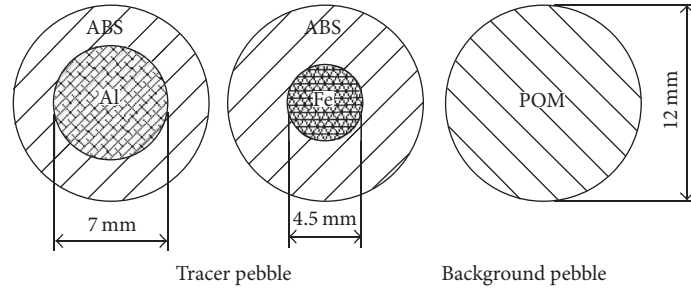


FIGURE 3: Tracer pebble and background pebble.

TABLE 1: Design parameters of the HTR-PM and the simulated core.

Parameters	HTR-PM	Simulated core
Core diameter (mm)	3,000	600
Core height (mm)	11,000	2,200
Pebble diameter (mm)	60	12

a dose monitoring system, and a video surveillance system are applied to prevent radiation accidents from happening.

**2.2. Pebble-Detecting Principle.** There are two kinds of simulated pebbles in our experimental design, background pebbles, and tracer pebbles. Their diameters are both 12 mm and mass is identical to make sure that they will share the same motion law. Background pebbles are made of a homogeneous material, a plastic called POM (density:  $1.42 \text{ g/cm}^3$ ). Tracer pebbles are coated with the light material ABS (density:  $1.05 \text{ g/cm}^3$ ) outside and filled with a heavy material inside. The inner diameter of a tracer pebble depends on the filler's material. For example, the inner diameter of an iron-kernel pebble is 4.5 mm and 7 mm for an aluminum-kernel pebble (Figure 3), which can be calculated according to the condition of equal mass. CT images represent the radioactive attenuation coefficient distributions of the reconstructed cross sections of the measured objects. And it is known that the radioactive attenuation coefficient of a material is approximately proportional to its density for the gamma rays of Co-60. So the heavy kernels of tracer pebbles can be resolved in the CT images due to their substantially higher densities compared to the plastic materials around.

Compared with aluminum tracer pebbles, the advantage of iron tracer pebbles is that their density difference between background pebbles is greater, which makes them easier to be distinguished. But due to their smaller internal diameters, better spatial resolution is needed for the CT system. Iron tracer pebbles should be preferred when the spatial resolution is good enough.

During pebble detection experiments, two kinds of pebbles will be put into the simulated core simultaneously and unloaded from the outlet. When the simulated core is filled with pebbles, the total unloading time is about 22 hours. Since the height of the simulated core is 2200 mm, the average velocity of pebble flow is about 1.67 mm/min. It is a quite



FIGURE 4: CT equipment in our lab.

small value compared to the diameter of pebbles. The rotating speed of the CT-PFD system is 1 minute per turn, and the translational increment of the helical CT in the vertical direction is 40 mm if the pitch equals 1. It means that the system can get the cross-sectional images of the simulated core at the speed of 40 mm per minute, during which pebbles move downward for only 1.67 mm on average. The CT-PFD system scans the simulated core along the vertical direction, reconstructs the cross-sectional images of pebbles, tracks and locates tracer pebbles by image processing algorithms, and then turns back for another track.

**2.3. Verification Experiment.** The design parameters and detecting principle were tested preliminarily using the existing CT equipment in our lab (Figure 4). It is a fan-beam CT with a single-slice linear array detector composed of 448  $\text{CdWO}_4$  scintillator units. A turntable in the middle of the CT system supports the measured object and provides both rotational and translational motion. Helical scan was achieved by letting the turntable rotate and translate synchronously while the radiation source and the detector keep still. Since there is only one row of detector, the system operated in this way is equivalent to a single-slice CT.

Simulated pebbles used here were also identical in size (their diameter is 12 mm) but not identical in mass, since they were originally designed for the 2D phenomenological experiments [3, 4]. Background pebbles were made of glass. Tracer pebbles were filled with iron and coated with paraffin. Tracer pebbles with three kinds of inner diameters were mixed with many background pebbles in a pot (Figure 5).



FIGURE 5: Pebbles used in the verification experiment.

TABLE 2: Experimental parameters.

Parameters	Value
Number of detector units	448
Width of detector units (mm)	2.6
Collimated width (mm)	3.0
Distance of source-rotating center (mm)	858.5
Distance of source-detector (mm)	1316.0
Pixel size of CT images (mm)	0.4
Dimension of CT images	1024 * 1024
Inner $D$ of tracer pebble 1 and 2 (mm)	7.0
Inner $D$ of tracer pebble 3 (mm)	4.7
Inner $D$ of tracer pebble 4 and 5 (mm)	4.0

$D$ : diameter.

Note that pebbles here were static. The aim of this experiment is to test if tracer pebbles can be recognized and extracted from background pebbles based on the system design. The inner diameters of tracer pebbles and other experimental parameters are shown in Table 2.

The pot was scanned under three kinds of helical pitches ( $P$ ), 0, 1, and 2. It has been proven that the linear interpolation (LI) algorithm is effective enough for the system to reconstruct images with high quality in our previous work [10]. So a classical LI algorithm named 360LI for single-slice CT was used to reconstruct cross-sectional images of pebbles. The results are shown in the left column of Figure 6. Five tracer pebbles can be clearly distinguished when  $P$  is 0 and 1, but only four tracer pebbles can be distinguished when  $P$  is 2. By adjusting the gray contrast of the three figures manually, we got figures of tracer pebbles (their heavy kernels actually) in the right column. All five tracer pebbles with clear edges were extracted from the background when  $P$  is 0 and 1 while only three clear tracer pebbles can be extracted when  $P$  is 2.

The verification experiment demonstrates that tracer pebbles can be detected and tracked using the CT-PFD system and that the helical scan pitch should not be too

large to guarantee image quality. A helical pitch within 1~1.5 should be chosen for the CT-PFD system according to the experimental results and relative literature knowledge [11].

The experimental results also tell us that the spatial resolution of the CT system is good enough to distinguish iron tracer pebbles from background pebbles. The CT-PFD system has similar spatial resolution with the CT system used in the verification experiment. So iron tracer pebbles are chosen in the CT-PFD system without additional tests for aluminum tracer pebbles.

### 3. Algorithms and Discussion

Images of tracer pebbles in the right column of Figure 6 were obtained by adjusting gray contrast manually. In the CT-PFD system, special algorithms are needed to extract and locate tracer pebbles automatically from CT images and rebuild pebble trajectories afterwards. Based on CT images obtained in the verification experiment, the extraction algorithm, location algorithms and trajectory-rebuilding algorithm were researched and discussed.

**3.1. Extraction Algorithm.** Extracting tracer pebbles from the background is an image segmentation problem, in which the global threshold technique is a classical and simple method. A threshold should be decided firstly to turn a gray-scale image to a binary image. There are many kinds of global threshold segmentation approaches like the bimodal method [12] and the Otsu [13] method. They are both histogram dependent techniques and assume that an image can be partitioned into a foreground and a background. The bimodal method chooses the value in the valley between two peaks of the histogram as the threshold. The Otsu method calculates the threshold by finding the maximum interclass variance of the foreground and background. However, neither of them is suitable to extract tracer pebbles. The reason is that the number of tracer pebbles is too small to be counted as a separate class compared to background pebbles and the image background.

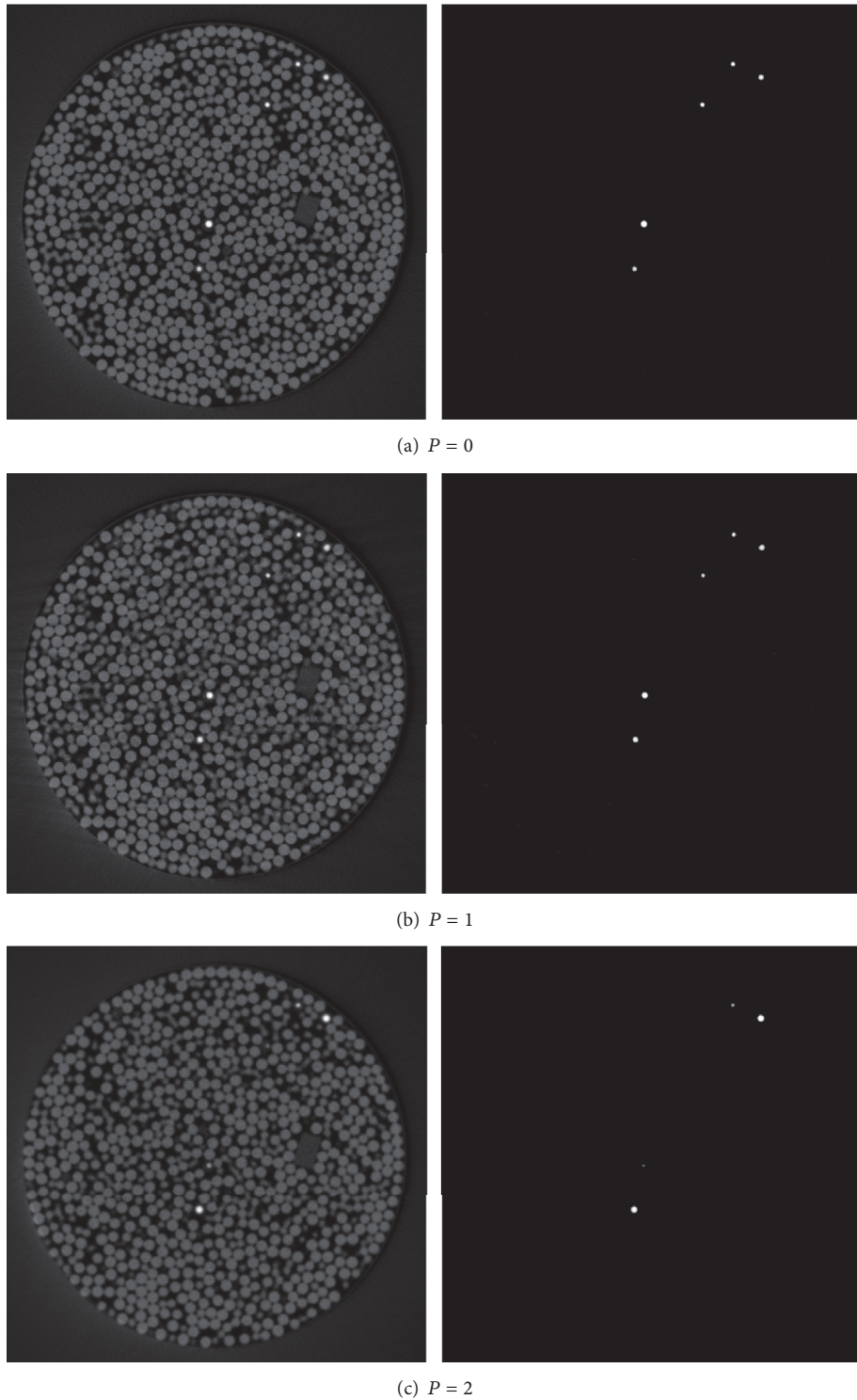


FIGURE 6: CT images in three different pitches (the left side) and the corresponding images after adjusting gray contrast manually (the right side).

Figure 7 shows the histogram of the image in Figure 6(b), left, in which two peaks represent the counts of the image background and background pebbles and are nearly one magnitude order higher than the count of tracer pebbles in the gentle end. Based on this feature, we transformed

the histogram by substituting a value with the ratio of it and its adjacent value, as shown in Figure 8. The abscissa values are the ratios and the ordinate values are the gray-scale indexes. We can find that there is a prominent peak value, which is the threshold we need. Partitioning the image in

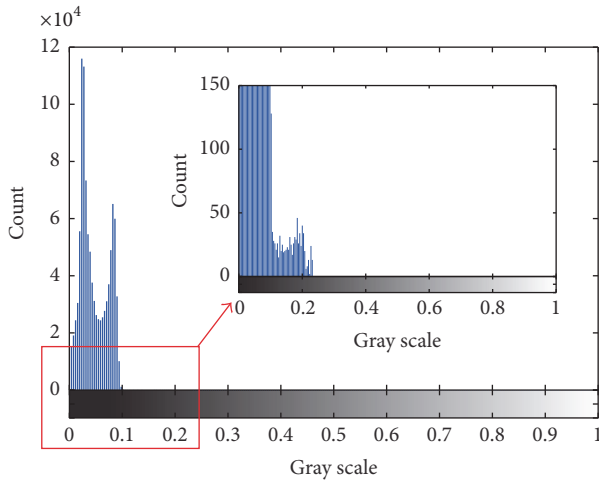


FIGURE 7: The histogram of the image in Figure 6(b), left.

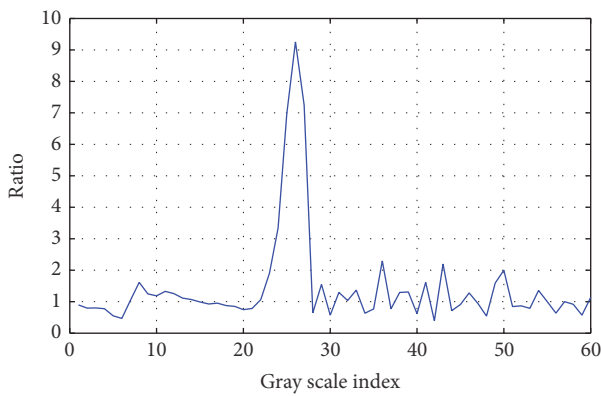


FIGURE 8: The transformed histogram.

Figure 6(b), left, by this threshold, we got Figure 9, image of the extracted five tracer pebbles that is similar to Figure 6(b), right.

This method can be used to extract tracer pebbles automatically from CT images. It has been tested in CT images reconstructed from many other positions of the pot and proved to be effective.

**3.2. Location Algorithms.** Once tracer pebbles are extracted, we need to acquire their locations, that is, their 3D coordinates. The horizontal coordinates ( $X$  and  $Y$ ) can be obtained by searching for the center coordinates of each tracer pebble in Figure 9. The vertical coordinate ( $Z$ ) is more difficult to determine, since we can only get the positions of pebbles' cross sections according to the location of the image rather than the real coordinates of spheres' centers. Special algorithm is needed to calculate the vertical coordinates of tracer pebbles.

**3.2.1. Horizontal Coordinates.** Since the cross sections of pebbles are circles, pebbles' horizontal coordinates can be obtained by circle detection methods like circular Hough transform. Considering that there are only several circular



FIGURE 9: Tracer pebbles extracted by threshold segmentation.

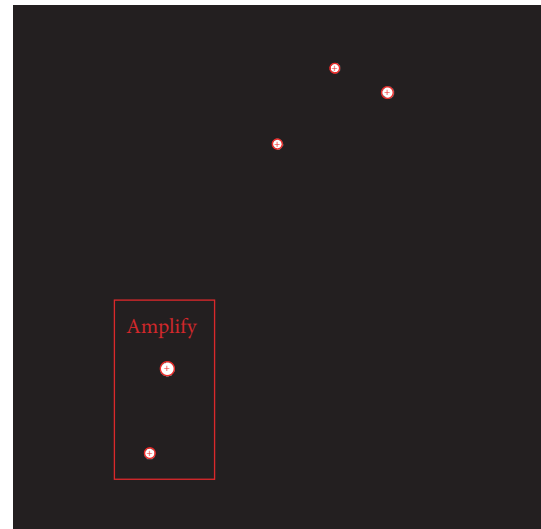


FIGURE 10: Circular detection.

regions in the extracted image, simpler connected domain detection is used here. In a binary image, a rectangular grid is called 4 or 8 connected domain if the central pixel has the same property with the adjacent 4 or 8 pixels. The connected domain is effective to judge if pixels of an image area belong to the same object. There are five connected domains in Figure 9, representing five tracer pebbles, respectively. For each connected domain, we search for the centroid according to the mean value of all pixels and calculate the equivalent radius according to the domain's area. This algorithm is called circular detection. The centroid and the equivalent radius were marked on each tracer pebble and two pebbles were amplified, as shown in Figure 10.

The result of circular detection is not bad visually. However, after the image was amplified, we found that this algorithm is good for a regular circle but inaccurate for an irregular circle (Figure 11). The reason is that this method is based on statistical average calculation, which will bring error to the location of the centroid for an irregular circle.

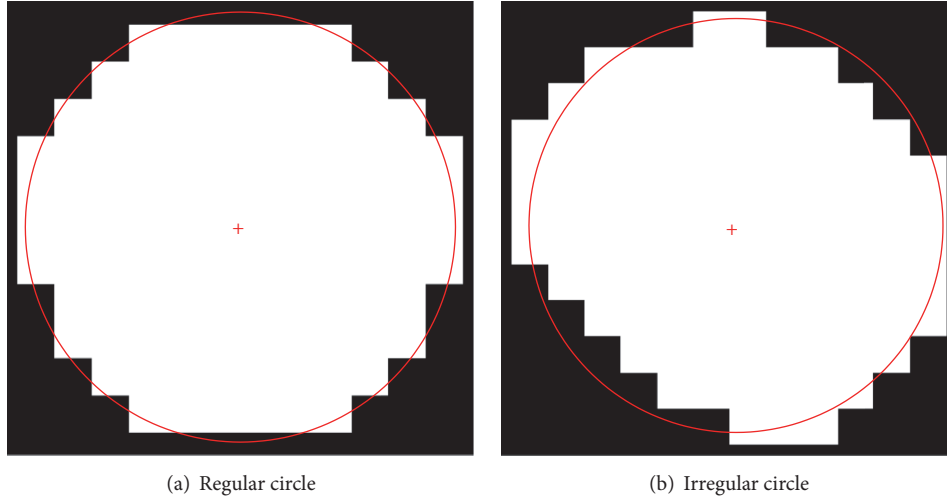


FIGURE 11: Circular detection.

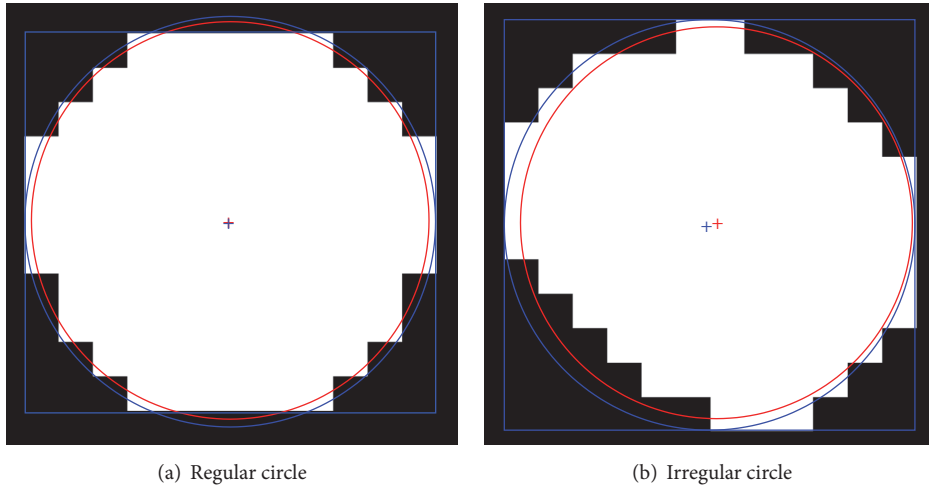


FIGURE 12: Rectangular detection (the blue line).

But in the extracted images, tracer pebbles are not always regular because of noise, artifacts, or image segmentation errors. Considering this problem, we adopted an alternative algorithm called rectangular detection. This method searches for the minimum rectangle that contains each connected domain and then takes the central point of the rectangle as the circle's center and the longer side as its diameter. The result is shown in Figure 12, in which the red lines are results obtained by circular detection and the blue lines are results obtained by rectangular detection. When the circle is regular, their results are similar. But when the circle is irregular, rectangular detection is more accurate to restore the real edges of tracer pebbles and thus more precise to locate them.

**3.2.2. Vertical Coordinate.** The same tracer pebble may appear in adjacent CT images simultaneously, since the spacing between images needs to be smaller than pebbles' inner diameter to avoid omission during detection. This phenomenon leads to duplicate detection that needs to be

eliminated but also provides a way to calculate the accurate vertical coordinates of tracer pebbles.

As mentioned above, for the eight-slice helical CT in the CT-PFD system, the translational increment of the radiation source is 40 mm when the helical scan pitch is 1. Many images within the scan range can be reconstructed when the detecting system turns a circle, during which tracer pebbles move only 1.67 mm in the vertical direction and hardly move in the horizontal direction. So the positions of tracer pebbles in adjacent CT images are almost invariable. Based on this fact, a criterion was established to help eliminate duplicate detection. It can be written as follows:

$$\sigma = \left( \frac{x_2 - x_1}{x_1} \right)^2 + \left( \frac{y_2 - y_1}{y_1} \right)^2 < \delta, \quad (1)$$

where  $(x_1, y_1)$  and  $(x_2, y_2)$  are the horizontal coordinates of two tracer pebbles detected in adjacent images. If the variance  $\sigma$  of these two pebbles is smaller than the set value  $\delta$ , we take them as the same pebble.

Now assume that a pebble is captured in two adjacent CT images, whose vertical coordinates are  $z_1$  and  $z_2$ , respectively ( $z_1$  is on top of  $z_2$ ). The section radii of the pebbles detected from these two images are  $r_1$  and  $r_2$ . The real inner radius of tracer pebbles in CT images is  $r_0$ , which can be calculated according to the relationship between the pebble inner diameter and the pixel size. There exists a relationship between the two cross sections of the pebble: if  $r_2 > r_1$ , cross section 1 must be in the upper hemisphere of the pebble; if  $r_2 < r_1$ , cross section 2 must be in the lower hemisphere of the pebble. So the vertical coordinate of the tracer pebble,  $z$ , can be calculated as the equations below:

$$\begin{aligned} z &= z_1 - \Delta z_1, & r_2 > r_1; \\ z &= z_2 + \Delta z_2, & r_2 < r_1; \\ \Delta z_1 &= \sqrt{(r_0^2 - r_1^2)}; \\ \Delta z_2 &= \sqrt{(r_0^2 - r_2^2)}. \end{aligned} \quad (2)$$

The procedure of determining the vertical coordinate of a tracer pebble in the current extracted image can be described as follows. Firstly, get its horizontal coordinates and section radius by processing the extracted image using the rectangular detection algorithm. The vertical coordinate is assigned the position of the CT image temporarily. Then search in the upper image to find if there exists a duplicated detection of this pebble using (1). If the answer is yes, compare their section radii and calculate the final vertical coordinate using (2). If no, wait for the comparison with the lower extracted image and the number of tracer pebbles being detected plus one. The following block flow diagram (Figure 13) describes the whole location process of tracer pebbles. The process is terminated when all tracer pebbles are detected or the detection time is longer than the set value.

**3.2.3. Validation.** This location method is only suitable for tracer pebbles with identical inner diameter, which is not fulfilled for pebbles in the verification experiment. Furthermore, in the verification experiment, tracer pebbles were distributed in the pot without calibrating their positions, which means that CT images acquired in the verification experiment are not appropriate for verifying the location algorithms. Alternatively, a simple test model consisting of five balls with precise 3D coordinates in a cylindrical container was simulated, as shown in Figure 14(a). Their diameter was set to the inner diameter of an iron-kernel pebble, that is, 4.5 mm. Five cross-sectional images of the cylinder were intersected with the spacing of 2.5 mm, as shown in Figures 14(b)–14(f), which were simplified forms of CT images after extraction. There were  $343 * 343$  pixels in each image with the pixel size of 0.47 mm.

In the simulated extracted images, there were 9 pebbles overall, meaning that duplicate detection happened. Five images were processed according to the procedure in Figure 14. The judgment condition  $\delta$  in (1) was specified as 0.0001. Table 3 shows the reconstructed 3D coordinates obtained from the extracted images and the original values.

TABLE 3: The reconstructed and original 3D coordinates of five balls.

Ball	Parameters	X/mm	Y/mm	Z/mm
1	O	1.26	20.64	-4.76
	R	1.19	20.56	-5.00
	$\epsilon$	0.07	0.08	0.24
2	O	-1.20	-20.76	-6.12
	R	-1.19	-20.70	-6.26
	$\epsilon$	0.01	0.06	0.14
3	O	0.87	1.21	-10.18
	R	0.94	1.17	-10.01
	$\epsilon$	0.07	0.04	0.17
4	O	19.41	0.33	-10.26
	R	19.32	0.37	-10.01
	$\epsilon$	0.09	0.04	0.25
5	O	-19.65	-0.57	-12.54
	R	-19.57	-0.62	-12.51
	$\epsilon$	0.08	0.05	0.03

O: the original values; R: the reconstructed values;  $\epsilon$ : the absolute errors.

Their absolute errors were also calculated. We can find that most of these errors are smaller than a half pixel size (0.235 mm). Errors of the vertical coordinates are larger than that of the horizontal coordinates because of calculating errors or calibration failures during the process of duplicate detection elimination. Although images used here were not reconstructed by the CT-PFD system, the results do prove that the location algorithms are effective enough to rebuild the 3D coordinates of tracer pebbles in the simulated core, because there is no great difference between CT images after the extraction process (Figure 9) and simulated images here (Figure 14) except some noise or pixel defects.

**3.3. Trajectory-Rebuilding Algorithm.** The 3D coordinates of tracer pebbles obtained from CT images in different time steps are disordered. For each tracer pebble, an algorithm is needed to search for its coordinates in every time step, which act as the points on its trajectory. Based on the analyses above, it can be inferred that only several minutes are needed to track and locate all tracer pebbles for each time step, during which their horizontal positions change a little. Results in some references like [1] also provide a priori information that lateral diffusion or mingle between pebble flow is quite small. So the parameter  $\sigma$  in (1) can be used to match different tracer pebbles as well. For each tracer pebble in the current time step, calculate its  $\sigma$  with every tracer pebble in the earlier time step. When the value of  $\sigma$  between some two pebbles is the smallest, these two pebbles are considered as the same one. This method is called trajectory-rebuilding algorithm.

To verify the algorithm, pebble flow of five tracer pebbles with 60 trajectory points was simulated. Pebbles' diameters were 4.5 mm and were arranged as a cross with the spacing of 30 mm. The time increment was 5 min. The average velocities between two time steps were random numbers in normal

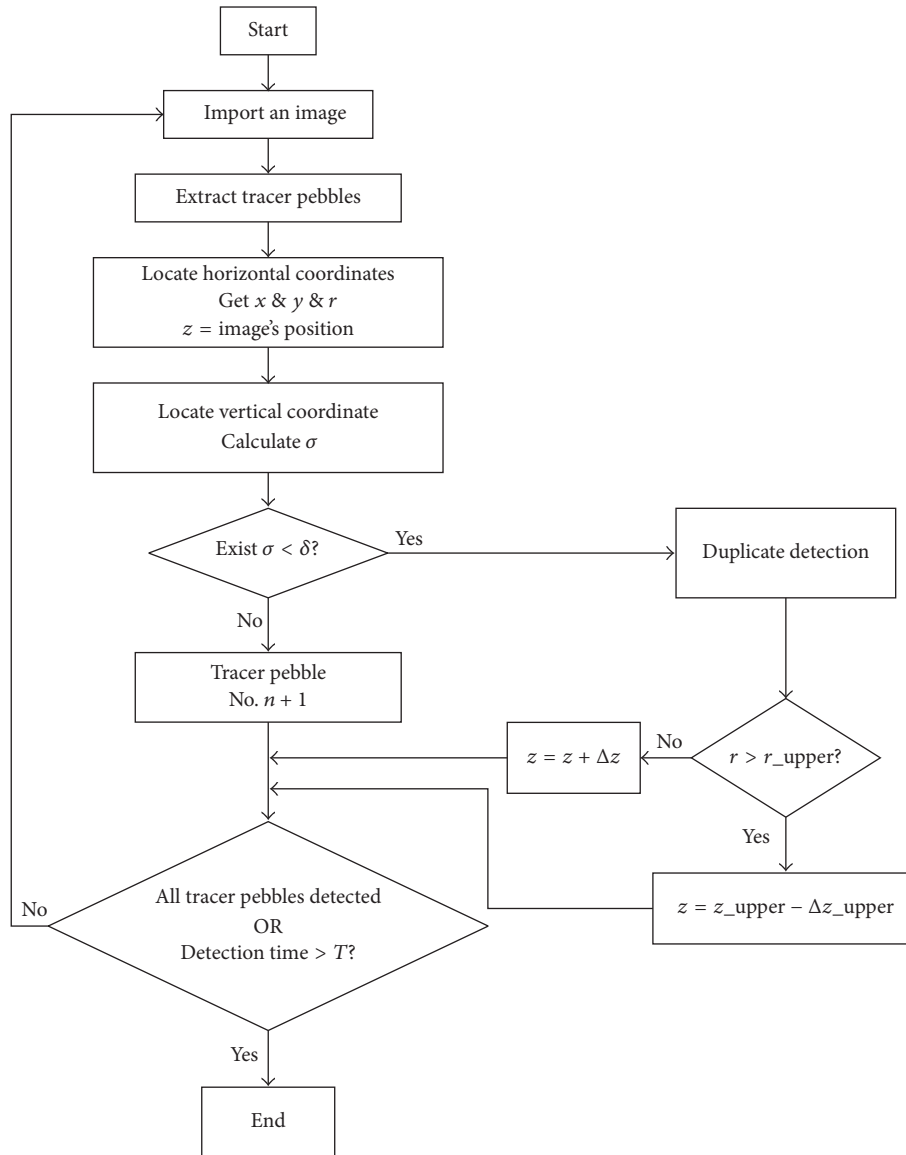


FIGURE 13: Block flow diagram of the location procedure.

distribution. In the vertical direction, the mean velocity was 1.67 mm/min. In the horizontal direction, the mean velocity was 0 in the first 50 points. Centripetal movement was added in the last 10 points, which represented pebble flow in the conical region. Simulated trajectories in three views are shown in Figure 15.

Then CT images of tracer pebbles after the extraction process were simulated in 60 time steps according to their coordinates in Figure 15. Since only the horizontal coordinates are needed when calculating  $\sigma$ , it is reasonable to neglect the process of locating the vertical coordinates. It is assumed that all tracer pebbles were captured in the same image in a time step. The simulated extracted images are shown in Figure 16.

We can find that the positions of tracer pebbles changed continuously in 60 images of Figure 16. But the variation

is very small between two adjacent images. First, pebbles' coordinates in 60 images were obtained by the location algorithms. Then these coordinates were allocated to each tracer pebble by the trajectory-rebuilding algorithm. Pebbles were differentiated from each other successfully. Their restored streamlines in the horizontal plane are shown in Figure 17. Figure 18 shows the absolute errors; that is,  $|x - x_0| + |y - y_0|$  between the restored horizontal coordinates  $(x, y)$  and the original value  $(x_0, y_0)$ . The errors are quite small, meaning that no fault occurred during the rebuilding process.

After the trajectories of tracer pebbles were acquired, a three-dimensional display program is designed to show pebbles' motion process, which provides a clear observation of pebble flow. Figure 19 shows several screenshots of the 3D display process of pebble flow.

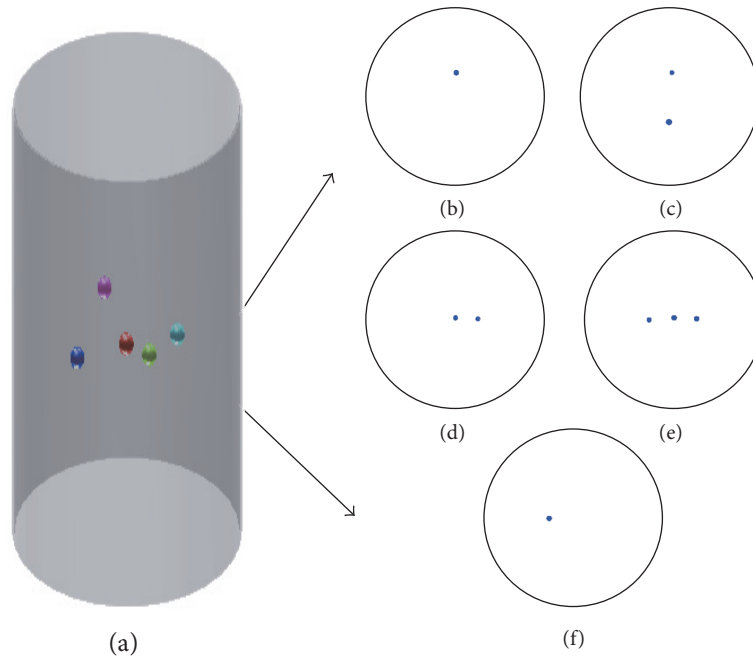


FIGURE 14: Simulated balls and their simulated extracted images.

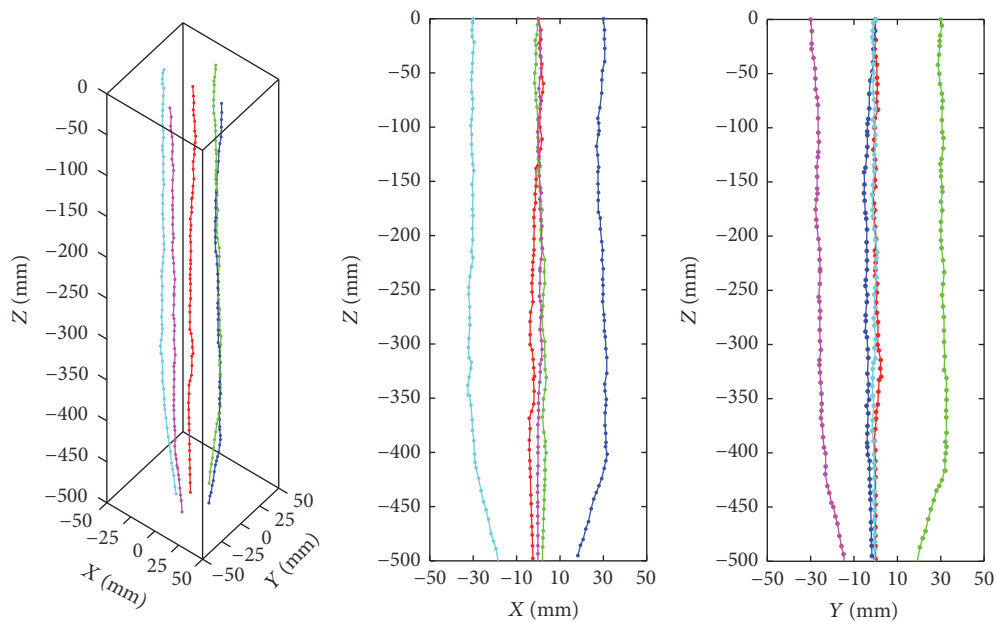


FIGURE 15: Simulated trajectories of five tracer pebbles.

#### 4. Conclusions and Discussion

In this paper, the CT-PFD system for 3D experimental investigation of pebble dynamics in the HTR-PM was presented. By special designed tracer pebbles and a multislice helical CT facility, trajectories of tracer pebbles can be detected and tracked. The design and pebble-detecting principle of the CT-PFD system were verified by the existing CT equipment in our lab and proved to be effective to capture tracer pebbles. Then the extraction algorithm to segment tracer pebbles from CT

images, the location algorithms to rebuild their 3D coordinates, and the trajectory-rebuilding algorithm to acquire each pebble's trajectory were studied. The effectiveness of these algorithms was demonstrated using images obtained from the verification experiment and simulation models. The CT-PFD system is under construction and will be put into use soon, which can provide a powerful research platform for 3D experimental investigation of pebble dynamics in the HTR-PM.

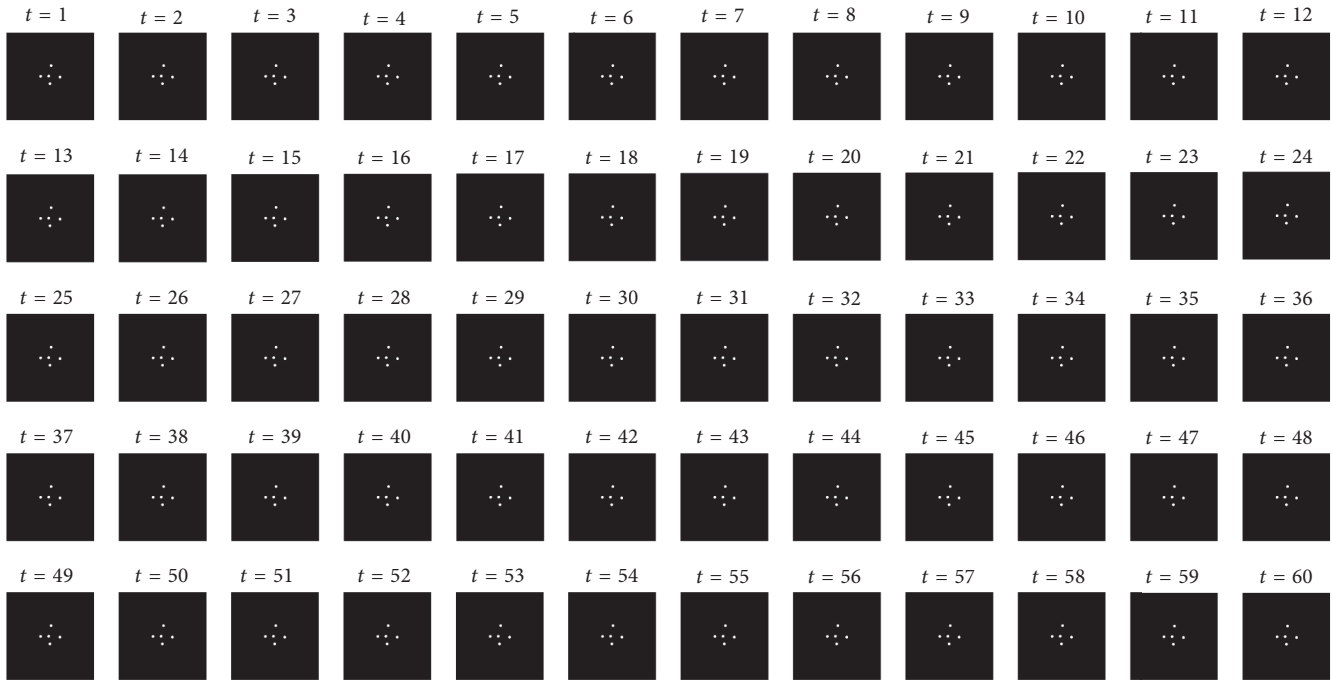


FIGURE 16: Simulated extracted images of five tracer pebbles.

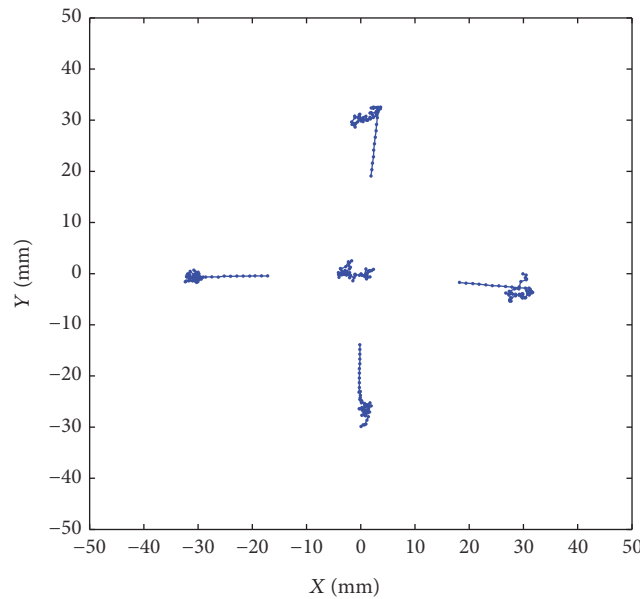


FIGURE 17: The restored streamlines in the horizontal plane.

The fluid, pebbles' materials, and structure of the simulation model in the CT-PFD system could be replaced or changed according to practical demand. The type of the fluid does not affect the validity of the CT-PFD system. Helium, air, or some other fluids are feasible, because the densities of these fluids are much smaller than that of pebbles. As long as we distinguish tracer pebbles from the background (including the fluid, background pebbles, and the wall of the

container) of CT images, we can locate and track them. In our future work, we will choose helium to better simulate the environment in the HTR-PM. Pebbles' materials can also be different. The system requires only a density difference between tracer pebbles and background pebbles. We can coat the pebbles with graphitized carbon without altering their internal structures to simulate the surface conditions of graphite pebbles in the HTR-PM. The system has no special

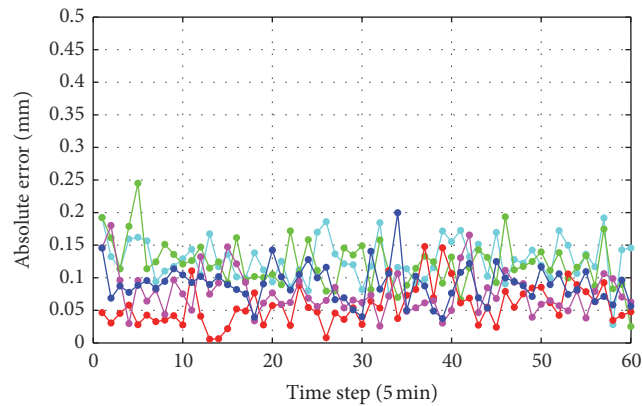


FIGURE 18: The absolute errors of the restored coordinates.

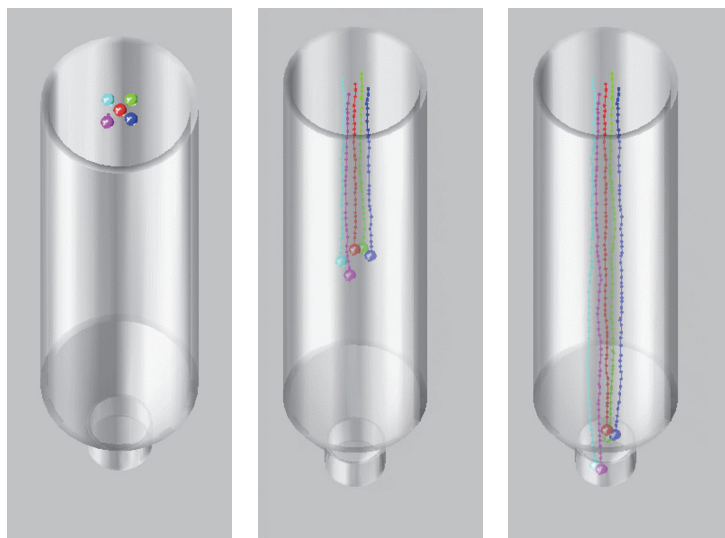


FIGURE 19: Screenshots of the 3D display process of pebble flow.

requirements for the structure of the simulation model, so the model might be designed as the structure of some conceptual reactor cores in future.

### Conflicts of Interest

The authors declare that they have no conflicts of interest.

### References

- [1] A. C. Kadak and M. Z. Bazant, "Pebble flow experiments for pebble bed reactors," in *Proceeding of the 2th International Topical Meeting on High Temperature Reactor Technology*, p. 22, Beijing, China, 2004.
- [2] V. D. Decken and G. Lange, *Pebble Bed Mechanics: AVR-Experimental High Temperature Reactor*, vol. 154, Association of German Engineers VDI-Society for Energy Technologies, Düsseldorf, Germany, 1990.
- [3] S. Y. Jiang, X. T. Yang, Z. W. Tang et al., "Experimental and numerical validation of a two-region-designed pebble bed reactor with dynamic core," *Nuclear Engineering and Design*, vol. 246, pp. 277–285, 2012.
- [4] X. Z. Zhang, X. T. Yang, Y. J. Zhang et al., "Experiments of two-region pebble dynamics of two-dimension core in HTR," *Nuclear Power Engineering*, vol. 31, Supplement 1, p. 57, 2010.
- [5] F. C. Gatt, *Flow of spheres and near spheres in cylindrical vessels, part IV*, Australian Energy Commission, Lucas Heights, New South Wales, Australia, 1973.
- [6] A. H. Shehata, *A new method for radioactive particle tracking [Phd dissertation]*, Graduate Faculty of North Carolina State University, 2005.
- [7] V. Khane, I. A. Said, and M. H. Al-Dahhan, "Experimental investigation of pebble flow dynamics using radioactive particle tracking technique in a scaled-down Pebble Bed Modular Reactor (PBMR)," *Nuclear Engineering and Design*, vol. 302, pp. 1–11, 2016.
- [8] M. Laufer and G. Buster, "X-ray pebble recirculation experiment (X-PREX) design and initial experimental results," Report UCBTH-15-002, Department of Nuclear Engineering, UC Berkeley, Berkeley, Calif, USA, 2014.
- [9] Y. Zheng, L. Shi, and Y. Wang, "Water-ingress analysis for the 200-MWe pebble-bed modular high temperature gas-cooled reactor," *Nuclear Engineering and Design*, vol. 240, no. 10, pp. 3095–3107, 2010.

- [10] X. Wan, J. C. Miao, X. M. Liu et al., "Research on reconstruction method for pebble-detecting CT system," in *Proceedings of the 8th International Topical Meeting on High Temperature Reactor Technology*, Las Vegas, Nev, USA, 2016.
- [11] G. Wang and M. W. Vannier, "Optimal pitch in spiral computed tomography," *Medical Physics*, vol. 24, no. 10, pp. 1635–1639, 1997.
- [12] S. U. Lee, S. Y. Chung, and R. H. Park, "A comparative performance study of several global thresholding techniques for segmentation," *Computer Vision, Graphics and Image Processing*, vol. 52, no. 2, pp. 171–190, 1990.
- [13] N. Otsu, "A threshold selection method from gray-level histograms," *Automatica*, vol. 11, no. 23–27, pp. 23–27, 1975.

## Research Article

# Physical Analysis of the Initial Core and Running-In Phase for Pebble-Bed Reactor HTR-PM

Jingyu Zhang,<sup>1</sup> Fu Li,<sup>2</sup> and Yuliang Sun<sup>2</sup>

<sup>1</sup>*School of Nuclear Science and Engineering, North China Electric Power University, Beijing 102206, China*

<sup>2</sup>*Institute of Nuclear and New Energy Technology, Tsinghua University, Beijing 100084, China*

Correspondence should be addressed to Jingyu Zhang; [popnt@163.com](mailto:popnt@163.com)

Received 19 December 2016; Revised 9 March 2017; Accepted 23 March 2017; Published 16 April 2017

Academic Editor: Rafael Miró

Copyright © 2017 Jingyu Zhang et al. This is an open access article distributed under the Creative Commons Attribution License, which permits unrestricted use, distribution, and reproduction in any medium, provided the original work is properly cited.

The pebble-bed reactor HTR-PM is being built in China and is planned to be critical in one or two years. At present, one emphasis of engineering design is to determine the fuel management scheme of the initial core and running-in phase. There are many possible schemes, and many factors need to be considered in the process of scheme evaluation and analysis. Based on the experience from the constructed or designed pebble-bed reactors, the fuel enrichment and the ratio of fuel spheres to graphite spheres are important. In this paper, some relevant physical considerations of the initial core and running-in phase of HTR-PM are given. Then a typical scheme of the initial core and running-in phase is proposed and simulated with VSOP code, and some key physical parameters, such as the maximum power per fuel sphere, the maximum fuel temperature, the refueling rate, and the discharge burnup, are calculated. Results of the physical parameters all satisfy the relevant design requirements, which means the proposed scheme is safe and reliable and can provide support for the fuel management of HTR-PM in the future.

## 1. Introduction

Modular high-temperature gas-cooled reactor (HTGR) is a kind of safe and advanced nuclear energy system, which can efficiently provide electric power and high-temperature process-heat. On February 15, 2008, Chinese State Council approved the implementation plan of HTGR demonstration project. The goal is to build a 200 MW<sub>e</sub> demonstration plant, named high-temperature gas-cooled reactor-pebble-bed module (HTR-PM), as the first one meeting the safety standards of Generation-IV reactors in the world [1].

At present, the physical design of the equilibrium core of HTR-PM has been finished by Institute of Nuclear and New Energy Technology (INET) of Tsinghua University, which includes that the fuel spheres with 8.5% enrichment are adopted, pass through the core for 15 times, and reach the average discharge burnup of 90000 MWd/tU. The emphasis in work is transferred to determine the scheme of the initial core and running-in phase.

From the initial core with fresh fuel, HTR-PM needs to take years of continuous refueling and burnup to reach the stable equilibrium core. Spending this time safely is

the important research content of in-core fuel management and is an actual technical problem in pressing need of solution. There are many possible schemes for the initial core and running-in phase, and many factors need to be considered in the process of scheme evaluation and analysis. Before HTR-PM, some design schemes of pebble-bed reactors have been proposed, including THTR-300 [2] from Hochttemperatur-Kernkraftwerk GmbH in Germany, HTR-10 [3] from Tsinghua University in China, HTR-Module [4] from Siemens AG in Germany, and PBMR [5] from PBMR (Pty) Ltd. in South Africa. Although the detailed design schemes of the initial core and running-in phase are different from each other, the common experience of these pebble-bed reactors shows that the fuel enrichment and the ratio of fuel spheres to graphite spheres are important.

In this paper, the physical model and simulation tool of HTR-PM are described in Section 2. The physical considerations of the initial core and running-in phase are, respectively, described in Sections 3 and 4. Then a typical scheme of the initial core and running-in phase is proposed and analyzed in Section 5. In the last section, a comprehensive comment is presented.

TABLE 1: Main design parameters of HTR-PM.

Parameters	Units	Values
Reactor total thermal power	$MW_{th}$	$2 \times 250$
Active core diameter	m	3
Equivalent active core height	m	11
Primary helium pressure	MPa	7
Helium temperature at reactor inlet/outlet	$^{\circ}C$	250/750
Uranium loading per fuel sphere	g	7
Enrichment of fresh fuel spheres	%	8.5
Diameter of fuel spheres	cm	6
Number of fuel spheres in one reactor core		420,000
Average discharge burnup	GWd/tU	90

## 2. Physical Model and Simulation Tool

*2.1. Physical Model.* The main technical parameters of HTR-PM are presented in Table 1.

HTR-PM uses helium as coolant and graphite as moderator as well as structural material. Its spherical fuel elements contain thousands of very small “coated particles” which are embedded in the graphite matrix. The pebble-bed design allows fuel spheres to constantly pass the core by gravity from an up direction to a down direction, which ensures that the operation mode of continuous fuel loading and discharging is available without shutting down the reactor.

HTR-PM adopts the cylindrical single zone core. The ceramic structures surrounding the reactor core consist of the inner graphite reflector and outer carbon brick layers, as shown in Figure 1. The whole ceramic internals are installed inside a metallic core barrel, which itself is supported by reactor pressure vessel (RPV). The metallic core barrel and the RPV are protected against high temperature from the core by the cold helium borings of the side reflector, which act like a shielding temperature screen.

HTR-PM adopts multipass refueling strategy. The fuel spheres drop into the reactor core from the central fuel loading tube and are discharged through a fuel extraction pipe at the core bottom. Subsequently, the discharged fuel spheres pass the burnup measurement facility one by one. Depending on their burnup, either they will be discharged and transported into the spent fuel storage tank when having reached their designed burnup, or they will be reinserted into the reactor to pass the core once again.

*2.2. Simulation Tool.* VSOP [6] code is developed by the Institute for Safety Research and Reactor Technology, Juelich Research Center, Germany. The code has been widely used for the design of the high-temperature reactor (HTR) with spherical fuel elements, such as THTR-300 and HTR-Module in Germany, PBMR in South Africa, and HTR-10 in China. The application of the code includes the setup of the reactor and of the fuel element, processing of cross sections, neutron spectrum evaluation, neutron diffusion calculation in two or three dimensions, fuel depletion, fuel shuffling, reactor control, and thermal hydraulics of steady states and transients. The code can simulate the reactor operation from the initial core towards the equilibrium core.

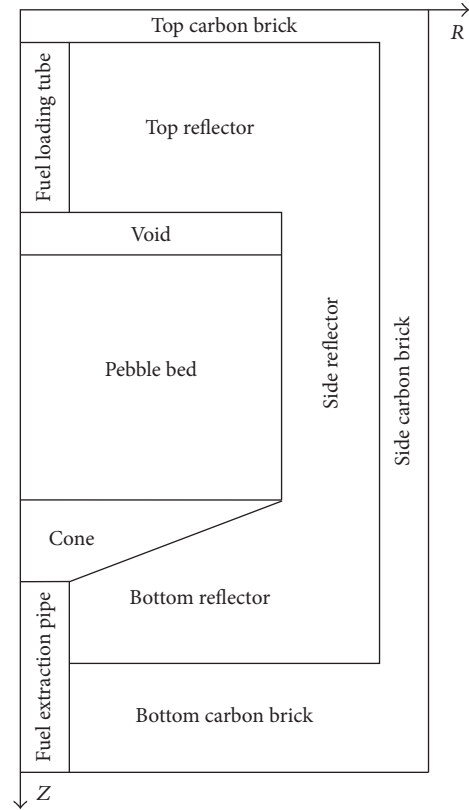


FIGURE 1: Geometric structure of HTR-PM core.

In VSOP code, to simulate the multipass refueling strategy of pebble-bed reactor, the reactor core is divided into different channels along the radial direction and different layers along the axial direction. Thus, lots of material regions are produced, which are the basic unit of neutron spectrum calculation. Then, each material region is divided into different fuel batches, which are the basic unit of fuel burnup calculation and fuel shuffling, and the number of fuel batches in material region is chosen as the designed times of fuel cycles. When the reactor is running, at the bottom of the core, the fuel batches with highest burnup will be discharged, and other fuel batches will be sent back to the top of the core, and meanwhile the bathes of fresh fuel will be loaded at the top of the core to keep the total quantity of fuel spheres stable. In the middle of the core, the fuel batches of each material region will be shuffled down to its neighbouring material region along the channel. Through the above method, the multipass refueling strategy of pebble-bed reactor can be well simulated. More detailed information can be seen in [6, 7].

Through the long-term validation and verification in the 10  $MW_{th}$  high-temperature gas-cooled test reactor (HTR-10) as well as continuous updating by INET [8], VSOP code is thought to be capable of satisfying the requirements of HTR-PM physical design.

## 3. Physical Considerations of the Initial Core

*3.1. Loading Patterns of the Initial Core.* The initial core is defined as the core that contains only the fresh fuel spheres,

TABLE 2: The key physical parameters of typical volume fractions of fuel spheres in the initial core.

Volume fraction of fuel spheres	Fuel enrichment needed (%)	Maximum power per fuel sphere (kW/FS)	Maximum fuel temperature (°C)
1/15	21.30	16.39	3401
5/15	5.10	3.30	1093
10/15	3.45	1.66	978
14/15	3.10	1.18	951

maybe with some graphite spheres, and that can reach the full power.

Due to the accumulation of fission products and the deep burnup of fuel spheres, in the equilibrium core, the average fuel enrichment over the core in HTR-PM is only 4.58%, although the enrichment of fresh fuel spheres loaded in the core is 8.5%. For the initial core almost without burnup, if only the fresh fuel spheres with 8.5% enrichment are loaded, the excess reactivity will be too big to control. To avoid this situation, some absorber balls containing boron need to be added in the core, or the quantity of fissile fuel in the core needs to be decreased, which can be achieved through adding some graphite spheres or decreasing the enrichment of the fuel spheres. As a result, the possible loading patterns of the initial core are formed as follows. (1) Fuel spheres with 8.5% enrichment or lower enrichment and graphite spheres are adopted; (2) fuel spheres with 8.5% enrichment or lower enrichment and absorber balls are adopted; (3) fuel spheres with 8.5% enrichment or lower enrichment and graphite spheres as well as absorber balls are adopted; (4) only fuel spheres with very low enrichment are adopted.

To determine the loading pattern of the initial core of HTR-PM, some important factors need to be considered, which are as follows.

- (1) Enrichment of fuel spheres: if the initial core and equilibrium core both load the fuel spheres with 8.5% enrichment, the processes of fuel purchase, manufacture, and management can be simplified, according to the THTR-300 and HTR-10 experiences. Considering the requirement of excess reactivity control, not many fuel spheres will be loaded, which increases the power per fuel sphere and is disadvantageous for safety. HTR-Module and PBMR recommend adopting low-enrichment fuel spheres in the initial core, which can increase the quantity of fuel spheres in the core and decrease the power per fuel sphere. So, in HTR-PM, the low-enrichment fuel spheres are adopted.
- (2) Absorber balls: another way to increase the quantity of fuel spheres loaded in the core and to decrease the power per fuel sphere is loading some absorber balls. In THTR-300 and HTR-Module, a small quantity of absorber balls is adopted. Unfortunately, experience of manufacture and application of absorber balls is lacking in China. Moreover, considering the big movement randomness of the small quantity of absorber balls in the core will increase the difficulty of fuel management; the absorber balls are not expected in the initial core of HTR-PM.

- (3) Graphite spheres: the enrichment of fuel spheres loaded in the initial core can be increased if some graphite spheres are added, which can decrease the difference of enrichment between the initial core and equilibrium core to make the running-in phase more smooth and can avoid discharging fuel spheres at the beginning of running-in phase to improve the fuel utilization. In THTR-300 and HTR-10, significant amount of graphite spheres is loaded in the initial core, and this is also recommended by HTR-Module and PBMR. So, in HTR-PM, the graphite spheres are planned to be used.

*3.2. Physical Characteristics of the Initial Core.* HTR-PM adopts the scheme of mixing low-enrichment fuel spheres with graphite spheres as its loading pattern for the initial core, in which the ratio of fuel spheres to graphite spheres needs to be determined. In Table 2, the key physical parameters of several typical volume fractions of fuel spheres in the initial core are given.

From Table 2, the following physical characteristics can be seen. (1) If the volume fraction of fuel spheres in the initial core is very low, the enrichment of fuel spheres needs to be very high to keep the reactor critical, even higher than 8.5% adopted in the equilibrium core, which is unpractical. Besides this, the small value of volume fraction of fuel spheres in the initial core means that there are few fuel spheres to share the operation power, causing big values of power per fuel sphere and fuel temperature, which is not safe. Considering these problems, the volume fraction of fuel spheres in the initial core should be as high as possible. (2) When the volume fraction of fuel spheres in the initial core is very high, the enrichment of fuel spheres needs be very low. In the subsequent running-in phase, if the fuel spheres with 8.5% enrichment adopted in the equilibrium core are directly added to replace the discharged fuel spheres with low enrichment, the difference of enrichment will cause big value of power per fuel sphere in the running-in phase, considering the fact that the fuel spheres with high enrichment will produce more power. To avoid this situation, one or more kinds of fuel spheres with medium enrichment are needed, but this could bring additional problems for fuel purchase, manufacture, and management. From these respects, the volume fraction of fuel spheres in the initial core should be as low as possible. (3) In conclusion, if the volume fraction of fuel spheres in the initial core is medium, the above advantages and disadvantages can be well balanced, and good physical characteristics can be expected.

#### 4. Physical Considerations of the Running-In Phase

There are some basic considerations for the refueling patterns of the running-in phase of HTR-PM.

- (1) The process of replacing the graphite spheres and the process of replacing the low-enrichment fuel spheres loaded in the initial core should be separated, which is beneficial for stabilizing the running-in phase and simplifying the operation of the fuel handling and storage system (FHSS). This is recommended by HTR-Module and PBMR.
- (2) The process of replacing the graphite spheres with fuel spheres should be performed at the beginning of running-in phase, which can quickly increase the quantity of fuel spheres in the core and thus decrease the power per fuel sphere and can avoid discharging fuel spheres at the beginning of running-in phase to improve fuel utilization. This is performed in THTR-300 and HTR-10 and is recommended by HTR-Module and PBMR.
- (3) For simplifying the processes of fuel purchase, manufacture, and management, it is better to use as few kinds of fuel spheres in enrichment as possible in the running-in phase. In HTR-Module, three kinds of fuel spheres are recommended, including the low-enrichment fuel spheres loaded in the initial core, the medium-enrichment fuel spheres used in the running-in phase, and the high-enrichment fuel spheres adopted in the equilibrium core.
- (4) In the running-in phase, the times of fuel cycles should be as many as possible, which can smooth the power distribution and burnup distribution along the axial direction of the core [9], but the refueling rate should be controlled in the capability of FHSS.

#### 5. Physical Analysis of a Typical Scheme of the Initial Core and Running-In Phase

*5.1. Description of the Scheme.* Based on the above physical considerations of the initial core and running-in phase, a typical scheme for HTR-PM is proposed as follows.

- (1) The initial core is made up of the fuel spheres with 4.1% enrichment and the graphite spheres. The volume fraction of fuel spheres in the core is 7/15.
- (2) The running-in phase is divided into three continuous processes. In the first process, 3/8 of the graphite spheres are replaced by the fuel spheres with 4.1% enrichment. When the first process is ended, the volume fraction of fuel spheres in the core is improved to 10/15. In the second process, the remaining graphite spheres are replaced by the fuel spheres with 4.1% enrichment. When the second process is ended, they are full of fuel spheres with 4.1% enrichment in the core. The last process includes 15 fuel cycles. In each cycle, 1/15 of the fuel spheres with 4.1% enrichment are

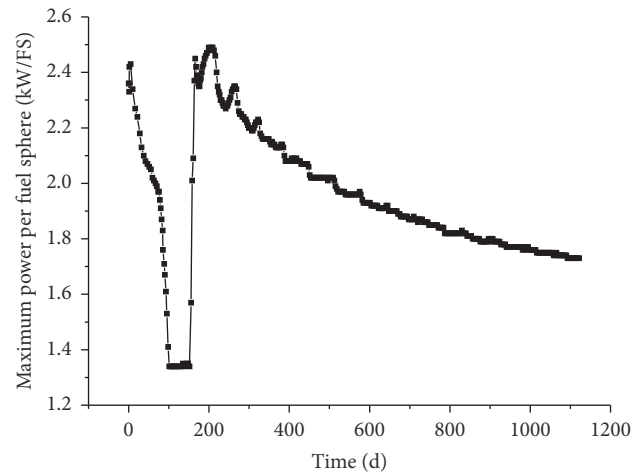


FIGURE 2: Maximum power per fuel sphere changing with time.

replaced by the fuel spheres with 8.5% enrichment. When this process is ended, they are full of fuel spheres with 8.5% enrichment in the core, and the status is close to the equilibrium core.

*5.2. Physical Characteristics of the Scheme.* The above scheme is simulated with VSOP code, and the key physical parameters, such as the maximum power per fuel sphere, the maximum fuel temperature, the refueling rate, and the discharge burnup, are calculated.

Results of the maximum power per fuel sphere in the running-in phase are shown in Figure 2.

In the running-in phase, the maximum power per fuel sphere reaches 2.49 kW/FS, which is higher than that in the equilibrium core (1.81 kW/FS), but there is still some margin compared with the safety limit value (3.5 kW/FS).

There are two obvious peak values of the maximum power per fuel sphere in the running-in phase. The first one appears at the beginning of running-in phase. That is mainly because the fuel spheres loaded in the core are very few at that time, and the peak value becomes smaller along with adding fuel spheres. The second peak value appears at the time of adding the fuel spheres with 8.5% enrichment. That is mainly because the enrichment of the new added fuel spheres is much higher than the depleted fuel spheres, which means the new added fuel spheres share a great part of operation power.

Results of the maximum fuel temperature in the running-in phase are shown in Figure 3.

In the running-in phase, the maximum fuel temperature reaches 1022°C, which is higher than that in the equilibrium core (932°C), but there is still some margin compared with the safety limit value (1200°C).

Results of the refueling rate in the running-in phase are shown in Figure 4.

In the running-in phase, the refueling rate is controlled in the capability of FHSS, that is, lower than 12000 FS/d. It can be seen that, at the beginning of running-in phase, the refueling rate is very high, which is because the fissile fuel loaded in the core is much less than that in the equilibrium

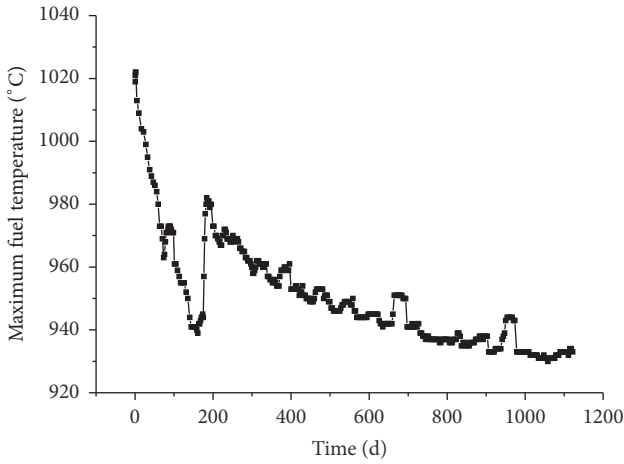


FIGURE 3: Maximum fuel temperature changing with time.

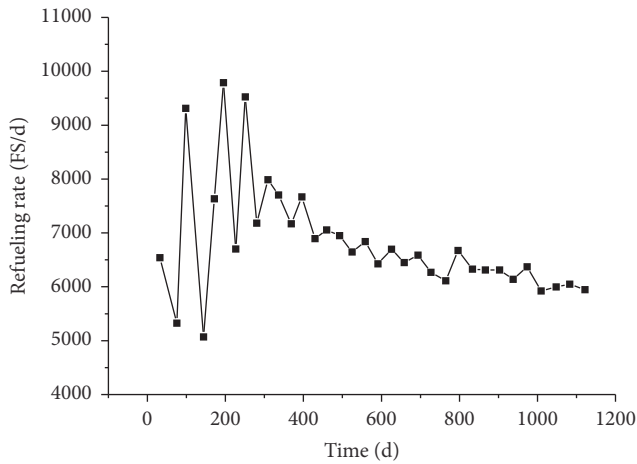


FIGURE 4: Refueling rate changing with time.

core. It makes the reactivity decrease with burnup faster than that in the equilibrium core, and thus higher refueling rate is needed to maintain normal operation of the reactor. And at the beginning of running-in phase, the refueling rate fluctuates widely, which is because the power distribution and burnup distribution along the axial direction of the core have not been flattened well during this period. But, with the development of the running-in phase, the composition and burnup in the core are getting more and more well-distributed, resulting in smaller fluctuation of the refueling rate.

Results of the discharge burnup in the running-in phase are shown in Figure 5.

In the running-in phase, the discharge burnup is lower than the safety limit value (100000 MWd/tU). At 143.9 days, all the graphite spheres are discharged, and then the depleted low-enrichment fuel spheres start to be discharged and the initial discharge burnup is 16281 MWd/tU. The discharge burnup climbs to 57342 MWd/tU with operation of the reactor. At 1118.2 days, all of the depleted low-enrichment fuel spheres are discharged, and then the depleted high-enrichment fuel

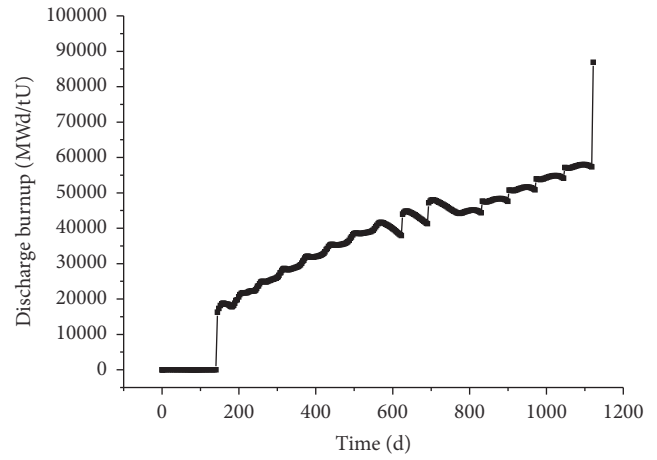


FIGURE 5: Discharge burnup changing with time.

spheres start to be discharged and the discharge burnup is close to that in the equilibrium core (90000 MWd/tU).

The uncertainty quantification of the calculation results of VSOP code for HTR-PM design has been performed by INET, involving the uncertainties from nuclear data, pebble flow [10], filling fraction of pebble bed [11], uranium loading per fuel sphere, and some thermal-hydraulic parameters. The corresponding influence on the key physical parameters, such as  $k_{eff}$ , power density, power peak, axial offset of power (AO), fuel temperature, and fuel burnup, is detailedly evaluated. The results show that the maximum uncertainty for the situation of normal operation is less than 1.0% [12].

As to this paper, the calculation results of VSOP code for the proposed scheme of the initial core and running-in phase are 10%~20% lower than the safety limit values. So, after taking the corresponding uncertainties into account, the safety margins are still enough.

## 6. Conclusions

In this paper, some physical considerations for the fuel management of the initial core and running-in phase of HTR-PM are given, including the advantages and disadvantages of different loading patterns of the initial core and different refueling patterns of the running-in phase. Then a typical scheme of the initial core and running-in phase of HTR-PM is proposed, in which one kind of graphite sphere and two kinds of fuel spheres in enrichment are used. Firstly, the graphite spheres are replaced by low-enrichment fuel spheres through two fuel cycles. When all the graphite spheres are discharged, the low-enrichment fuel spheres start to be replaced by high-enrichment fuel spheres through fifteen fuel cycles. When all the low-enrichment fuel spheres are discharged, the running-in phase is ended and the equilibrium core is established. The above scheme of the initial core and running-in phase is simulated with VSOP code, and some key physical parameters, such as the maximum power per fuel sphere, the maximum fuel temperature, the refueling rate, and the discharge burnup, are calculated. Results of the physical parameters all satisfy the relevant design requirements, which

means the proposed scheme is safe and reliable. In the future, more detailed physical analysis of the scheme will be performed, especially for the accident conditions.

### Conflicts of Interest

The authors declare that there are no conflicts of interest regarding the publication of this paper.

### Acknowledgments

The authors would like to express their gratitude for the support by National Natural Science Foundation of China (Project 11605058 and Project 11375099) and Chinese National S&T Major Project ZX06901.

### References

- [1] Z. Zhang, Z. Wu, D. Wang et al., "Current status and technical description of Chinese  $2 \times 250$  MWth HTR-PM demonstration plant," *Nuclear Engineering and Design*, vol. 239, no. 7, pp. 1212–1219, 2009.
- [2] R. Bäumer, I. Kalinowski, E. Röhler, J. Schöning, and W. Wachholz, "Construction and operating experience with the 300-MW THTR nuclear power plant," *Nuclear Engineering and Design*, vol. 121, no. 2, pp. 155–166, 1990.
- [3] Z. Wu, D. Lin, and D. Zhong, "The design features of the HTR-10," *Nuclear Engineering and Design*, vol. 218, no. 1–3, pp. 25–32, 2002.
- [4] G. H. Lohnert, "Technical design features and essential safety-related properties of the HTR-module," *Nuclear Engineering and Design*, vol. 121, no. 2, pp. 259–275, 1990.
- [5] J. F. M. Slabber and E. J. Mulder, "Loading of the PBMR initial core and the transition into the equilibrium core," in *Proceedings of the International Congress on Advances in Nuclear Power Plants (ICAPP '05)*, Seoul, Republic of Korea, May 2005.
- [6] H. J. Rütten, K. A. Haas, H. Brockmann, and W. Scherer, *V.S.O.P. (99/05) Computer Code System for Reactor Physics and Fuel Cycle Simulation*, Forschungszentrum Jülich GmbH, 2005.
- [7] Z. Wu and X. Jing, "Fuel management of HTR-10," *Journal of Tsinghua University (Science and Technology)*, vol. 41, no. 4–5, pp. 120–123, 2001 (Chinese).
- [8] International Atomic Energy Agency, "Evaluation of high temperature gas cooled reactor performance: benchmark analysis related to the PBMR-400, PBMM, GT-MHR, HTR-10 and the ASTRA critical facility," Tech. Rep. IAEA-TECDOC-1694, 2013.
- [9] B. Ling and Y. Yang, *Theory of Nuclear Reactor Engineering*, Atomic Press, Beijing, China, 1982 (Chinese).
- [10] H. Chen, L. Fu, G. Jiong, S. Ximing, and W. Lidong, "Quantitative analysis of uncertainty from pebble flow in HTR," *Nuclear Engineering and Design*, vol. 295, pp. 338–345, 2015.
- [11] H. Chen, L. Fu, G. Jiong, and W. Lidong, "Uncertainty and sensitivity analysis of filling fraction of pebble bed in pebble bed HTR," *Nuclear Engineering and Design*, vol. 292, pp. 123–132, 2015.
- [12] C. Hao, *Uncertainty analysis in modeling of pebble bed HTR [ph.D. dissertation]*, Tsinghua University, Beijing, China, 2014 (Chinese).

## Research Article

# Source Term Analysis of the Irradiated Graphite in the Core of HTR-10

**Xuegang Liu, Xin Huang, Feng Xie, Fuming Jia, Xiaogui Feng, and Hong Li**

*Institute of Nuclear and New Energy Technology, Collaborative Innovation Center of Advanced Nuclear Energy Technology, Key Laboratory of Advanced Reactor Engineering and Safety of Ministry of Education, Tsinghua University, Beijing 100084, China*

Correspondence should be addressed to Feng Xie; [fxie@tsinghua.edu.cn](mailto:fxie@tsinghua.edu.cn)

Received 31 December 2016; Accepted 20 March 2017; Published 6 April 2017

Academic Editor: Robert Morris

Copyright © 2017 Xuegang Liu et al. This is an open access article distributed under the Creative Commons Attribution License, which permits unrestricted use, distribution, and reproduction in any medium, provided the original work is properly cited.

The high temperature gas-cooled reactor (HTGR) has potential utilization due to its featured characteristics such as inherent safety and wide diversity of utilization. One distinct difference between HTGR and traditional pressurized water reactor (PWR) is the large inventory of graphite in the core acting as reflector, moderator, or structure materials. Some radionuclides will be generated in graphite during the period of irradiation, which play significant roles in reactor safety, environmental release, waste disposal, and so forth. Based on the actual operation of the 10 MW pebble bed high temperature gas-cooled reactor (HTR-10) in Tsinghua University, China, an experimental study on source term analysis of the irradiated graphite has been done. An irradiated graphite sphere was randomly collected from the core of HTR-10 as sample in this study. This paper focuses on the analytical procedure and the establishment of the analytical methodology, including the sample collection, graphite sample preparation, and analytical parameters. The results reveal that the Co-60, Cs-137, Eu-152, and Eu-154 are the major  $\gamma$  contributors, while H-3 and C-14 are the dominating  $\beta$  emitting nuclides in postirradiation graphite material of HTR-10. The distribution profiles of the above four nuclides are also presented.

## 1. Introduction

The high temperature gas-cooled reactor (HTGR) has some remarkable advantages, such as inherent safety, higher power efficiency, and wide diversity of heat utilization [1]. Nowadays HTGR is being accepted as one of the most promising nuclear reactors in the future nuclear market. However, the actual development of HTGR still highly relies on the comprehensive understanding of the philosophy of HTGR from all aspects. The source term of the radionuclides resulting from the HTGR operation plays significant roles in reactor safety, environmental release, waste management, and disposal. HTGR features its huge inventory of nuclear graphite in the HTGR core acting as reflector, moderator, or structure materials. The contaminated graphite becomes a special kind of radioactive waste, which is completely different from that in traditional pressurized water reactor (PWR). With the growing application of HTGR, the source term analysis of the irradiated graphite in the HTGR core has been highlighted.

While the nuclear grade graphite has excellent chemical, structural, and neutronic properties for HTGR utilization [2], the utilization of graphite in core leads to the generation of many types of radioactive nuclides in the graphite material. Theoretically, the graphite can retain radionuclides such as H-3, C-14, and Cl-36, corrosion/activation products (Co-57, Co-60, Mn-54, Ni-59, Ni-63, Na-22, etc.), fission products (Cs-134, Cs-137, Sr-90, Eu-152, Ce-144, etc.), and a small amount of uranium and transmutation elements (Pu-238, Pu-239, Am-241, Am-243, etc.). Some of these radionuclides arise from the activation of impurities which were integral with the original graphite components. The other radionuclides come from offsite locations of the core and migrate to the graphite carried around the circuit in the coolant gas [3, 4]. Practically, the radionuclides in graphite will vary greatly with graphite quality, reactor operating history, fuel element performance, and so forth. An examination by Fachinger et al. [5] indicated that the main  $\gamma$  nuclides in the carbon dust in AVR pipe components were Co-60, Cs-137, and Eu-154. Wenzel et al.

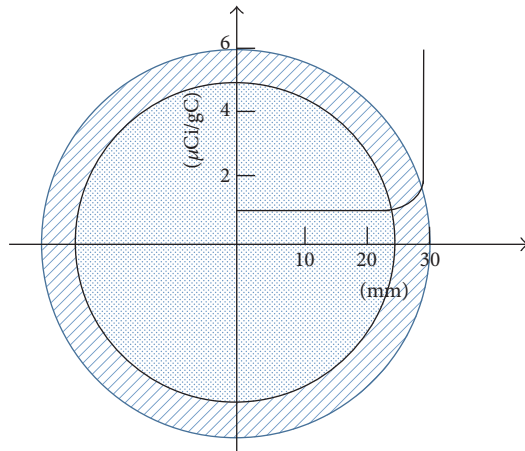


FIGURE 1: C-14 profile in a spent AVR sphere.

[6] determined the C-14 in the graphite matrix of spent AVR fuel element and agreed with the C-14 profile in a spent AVR sphere as published in a previous literature [7] (see Figure 1). Some other literatures [8–10] have introduced the progress of fundamental studies on the behaviors of H-3, Cs, or I in the HTGR system. Besides, some research results on irradiated graphite material used in British Magnox reactors are also useful as [11–13].

In China, a high temperature gas-cooled reactor pebble bed module (HTR-PM) demonstration power plant is under construction in Shandong Province [14]. The reality needs deeper understanding on the characterization of the irradiated graphite material in such type of HTGR. Thanks to the construction and operation of HTR-10, a 10 MW test reactor of the same type, some genuine graphite materials are available and suitable for the above research. A project was proposed with the purpose of mastering the irradiated graphite in pebble bed HTGR, in which the HTR-10 was chosen as a reference reactor. As part of a whole project, this paper will focus on the sample preparation, analytical procedure, and methodology. Some postirradiation graphite sphere are discharged from the reactor core. Samples are collected at different positions of spherical radius, prepared, and measured with different analytical devices, that is, the multi-channel  $\gamma$  counter, liquid scintillation counter, and total  $\alpha/\beta$  counter. The analytical results are presented.

## 2. HTR-10 and Irradiated Graphite Element

The 10 MW high temperature gas-cooled test reactor (HTR-10) was constructed in the late 1990s and realized the first criticality in December 2000. In 2003, HTR-10 firstly succeeded in connecting to the grid with full design capacity. Since then, a number of experiments have been done based on the reactor. Being exposed to the radiation resulted from the above operations, the graphite materials in the core of HTR-10 have been good test subjects for the source term analysis.

The core of HTR-10 is designed to hold large amount of spherical fuel elements, which are 60 mm in diameter and contain about 12000 of TRISO-coated fuel particles homogeneously distributed in graphite matrix. Before the fueling of the spherical fuel elements, the core was piled with graphite spheres of the same size. During the first starting period, graphite spheres were replaced by spherical fuel elements to reach criticality. When the reactor is in a steady state operation, a fuel handling system makes provision for online refueling by allowing fuel sphere circulation. Considering the behaviors of the graphite sphere, we regard them as the most ideal ones for source term analysis due to the following reasons. (1) Graphite spheres were exposed to the genuine radiation of HTR-10, with almost the same neutron flux and energy spectrum. (2) Materials and manufacturer of the graphite spheres are the same as fuel elements, making them good alternatives to study the properties of graphite matrix in irradiated fuel elements without high radiation from fuel particles. (3) Due to the probabilistic release, it is possible to have a series of graphite spheres with different exposure in the core. Some of them might be staying even longer than fuel elements. (4) Controlled by the fuel handling system, graphite spheres can be discharged from the core or reloaded to the core for higher exposure. All operations can be handled very easily without any negative impact on safe operation of the reactor. But, on the other hand, it should be noted that the probability distribution of staying time in the core makes it difficult to know the exposure history of a specific graphite sphere. In this paper, a postirradiation graphite sphere was collected from the storage tank. We do not know how long it stayed in the core and total exposure it received.

## 3. Experimental Works

Figure 2 shows the experimental program. The whole analysis procedure consists of six major steps. After a prompt measurement on mass, the surface dose rate, and  $\gamma$  multichannel spectrum (Step 1), the selected graphite sphere was fixed in a drilling machine. A hollow drilling tool with 9 mm inner diameter was used to drill a penetrating hole through the center of the sphere. A cylindrical graphite sample was prepared in Step 2 (see Figures 3 and 4). To learn the source term of samples in different radius location, the cylindrical graphite was then fixed in a grinder machine. A series of graphite powder samples were prepared in Step 3. Each powder sample which represents the component of graphite in a specific radius was spread on a stainless steel disk to form a flat circular sample with 40 mm diameter. The flat circular sample was then analyzed with multichannel  $\gamma$  detector and total  $\alpha/\beta$  analyzer (Step 4). The graphite sample on the stainless steel disk was then put into a combustion vessel full with oxygen. The gas ( $\text{CO}_2$  and water vapour) was adsorbed with NaOH solution. The purpose of Step 5 is to convert C-14 and H-3 in the solid graphite into a solution for consequential analysis. In Step 6, the above aqueous sample was analyzed with titration to measure the total carbon in solution and liquid scintillation counter (LSC) to measure the activity of C-14 and H-3.

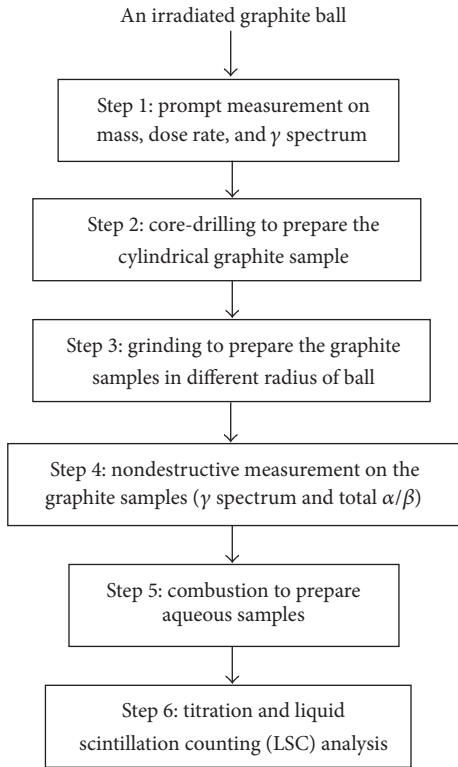


FIGURE 2: The experimental program on source term analysis of an irradiated graphite sphere.



FIGURE 3: The graphite sphere with a penetrating hole after drilling.

## 4. Results and Discussions

**4.1. The Measurement of the Irradiated Graphite Sphere.** The selected postirradiation graphite sphere was weighed as 208.82 g. The dose rate at the very surface of the sphere was about  $25.2 \pm 0.5 \mu\text{Sv/h}$ . The multichannel  $\gamma$  spectrum is shown in Figure 5, which exhibits the most distinct four nuclides: Co-60, Eu-152, Eu-154, and Cs-137. Although, due to the special shape of the graphite sphere, it is difficult to calibrate the detective efficiency of each peak of spectrum, the results are very useful to evaluate the external exposure of the irradiated graphite materials.

**4.2. Combustion of Graphite Powders.** In order to measure the C-14 and H-3 with LSC, a combustion process was developed

TABLE 1: Distribution ratios of nuclide after graphite combustion.

Nuclides	Distribution ratio (%)		
	In residue	In NaOH aqueous solution	In off-gas
H-3	<1%	~95%	~5%
C-12	<1%	>99%	<1%
C-14	<1%	>99%	<1%
Co-60	~100%	BKG	BKG
Cs-137	~100%	BKG	BKG
Eu-152	~100%	BKG	BKG
Eu-154	~100%	BKG	BKG

BKG: background.



FIGURE 4: The cylindrical graphite sample prepared after drilling.

to convert the graphite powder into the aqueous solution. The powder sample was firstly weighed and put into the crucible of an Oxygen Combustion Apparatus [15] (see Figure 6). After the oxygen inflation and ignition, most graphite powder was burned except for a very small amount of residues left on the crucible bottom. The gasified substance may be absorbed by NaOH solution in the beaker or exist in the gas. When the vent valve was released slowly and carefully, the off-gas in the vessel can pass through a series of adsorber bottles to trap all concerned components for analysis. As a result, all radionuclides originally in the graphite powder will be transferred to three possible destinations as solid residue, NaOH solution, and the off-gas adsorption solution.

**4.2.1. Combustion Conditions.** No doubt, the final destination of each nuclide relies on the combustion conditions to some extent. A stable and quantitative distribution among the flows is desirable for our task. Through a series of systematic experiments and optimization, the combustion conditions were finally chosen as follows: (1) 0.1 to 0.2 gram of graphite powders in the crucible; (2) 10 mL of NaOH with the concentration of 3 to 4 mol/L; (3) >20 atm of oxygen in the vessel; (4) >20 min of ageing after combustion with some gentle shaking.

**4.2.2. Behaviors of the Certain Nuclides in Combustion.** The stable carbon and C-14 were measured by titration and LSC, respectively. The H-3 was also measured by LSC, while  $\gamma$  emitting nuclides were detected by multichannel  $\gamma$  detector. The distribution ratios of the above nuclides are shown in Table 1.

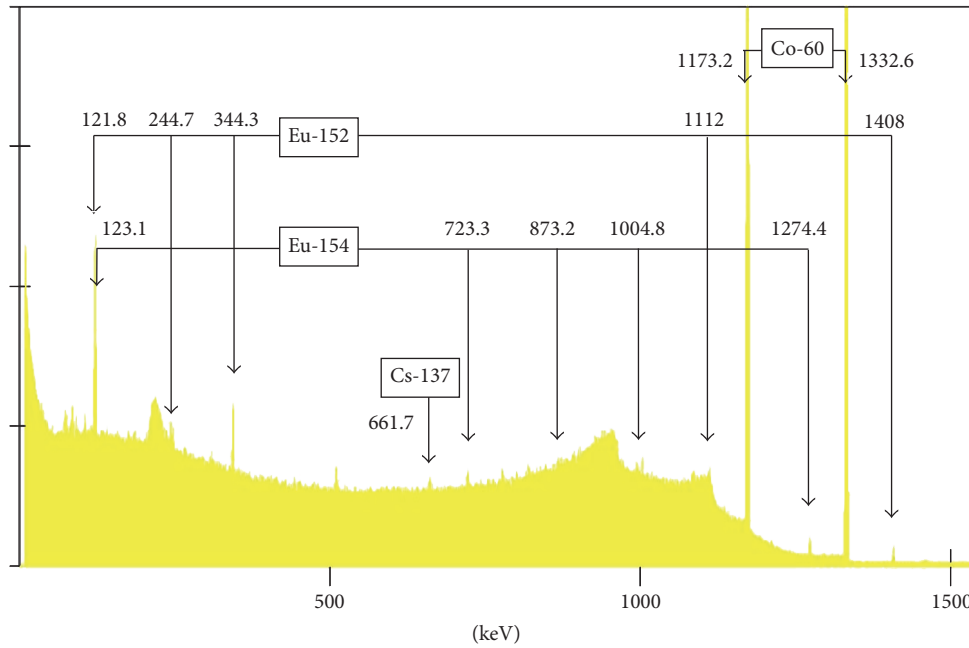


FIGURE 5: The multichannel  $\gamma$  spectrum of the irradiated graphite sphere.

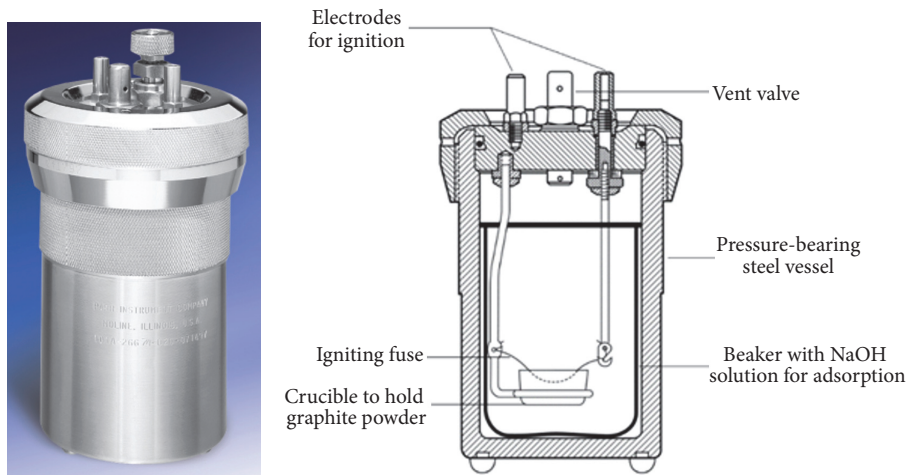


FIGURE 6: The oxygen combustion apparatus and structure schematic.

Because all  $\gamma$  emitting nuclides in graphite belong to metal elements, they will remain in the crucible after combustion. As an evidence, Figure 7 shows the comparison of  $\gamma$  spectrums between NaOH aqueous solution and the residual powder. Therefore, no disturbance from  $\gamma$  radionuclides needs to be considered in the LSC analysis on NaOH solution samples. Almost all carbon, both stable and radioactive, was found to be adsorbed in NaOH solution. Because a small portion of H-3 was lost in the off-gas, the analytical result of H-3 in NaOH solution will be lower than the fact. However, such kind of deviation is acceptable in the case of source term analysis.

#### 4.3. Distribution Profile of Radionuclides in the Graphite Sphere

4.3.1. *The Distribution of  $\gamma$  Emitting Nuclides.* Figures 8 and 9 show the distribution profiles of Co-60/Cs-137 and Eu-152/Eu-154 in the graphite sphere, respectively.

Among all  $\gamma$  emitting nuclides, Co-60 has the highest activity in the irradiated graphite sphere. The distribution of Co-60 implies a much higher activity on the spherical surface than the interior. And the activities of Co-60 inside of the sphere have no distinct dependence on the distance to the center. According to the present study, the distributions of

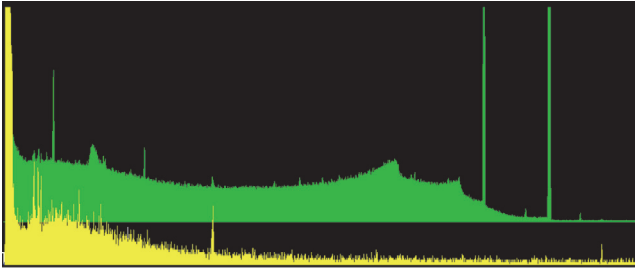


FIGURE 7: The comparison of  $\gamma$  spectrums between NaOH aqueous solution and graphite residue (the green for the residual powder, the yellow for the NaOH solution).

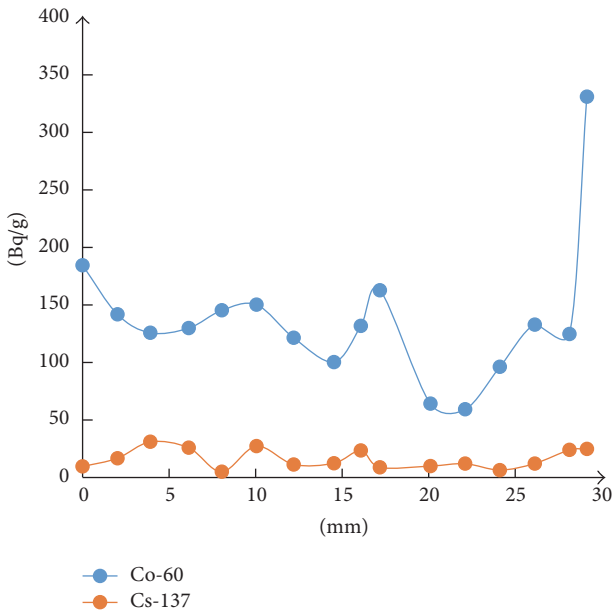


FIGURE 8: Distribution profiles of Co-60 and Cs-137 activities at different spherical radii in the selected graphite sphere.

Cs-137, Eu-152, and Eu-154 in the sphere showed weak or no correlative effect on the radius. The different distribution between Co-60 and fission products (Cs-137, Eu-152, and Eu-154) may be explained by their generation mechanisms. The Co-60 inside of the graphite sphere might come from the neutron activation of the impurity (mainly Co-59), while the surface might be contaminated by the dusts in the primary coolant circuit. For Cs-137, Eu-152, and Eu-154, the mechanism is supposed to be neutron activation of the impurity (trace of uranium, possibly). Certainly, much more work has to be done to investigate the generation mechanisms of the above nuclides.

4.3.2. *The Distribution of  $\beta$  Emitting Nuclides.* Figure 10 shows the total  $\beta$  count per gram of graphite at different radial locations. Figure 11 shows the dependence of H-3 and C-14 specific activity on the distance to the spherical center. Both figures indicate that  $\beta$  emitting nuclides, H-3 and C-14, are uniformly distributed in the graphite sphere.

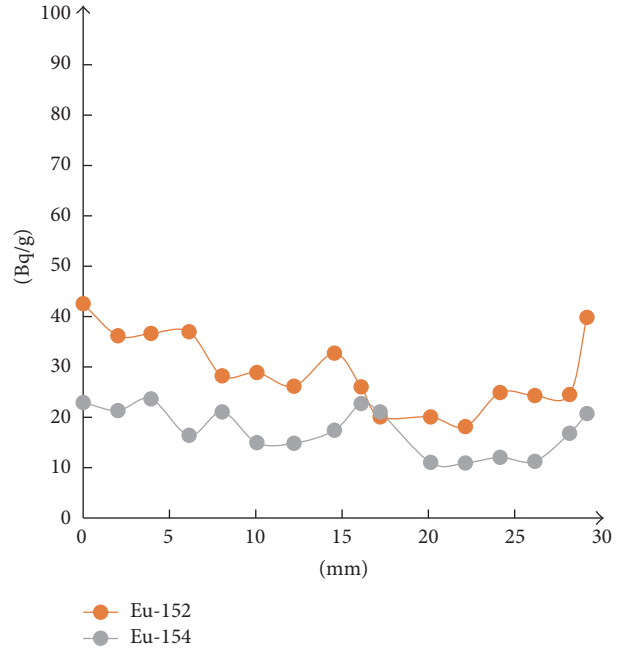


FIGURE 9: Distribution profiles of Eu-152 and Eu-154 activities at different spherical radii in the selected graphite sphere.

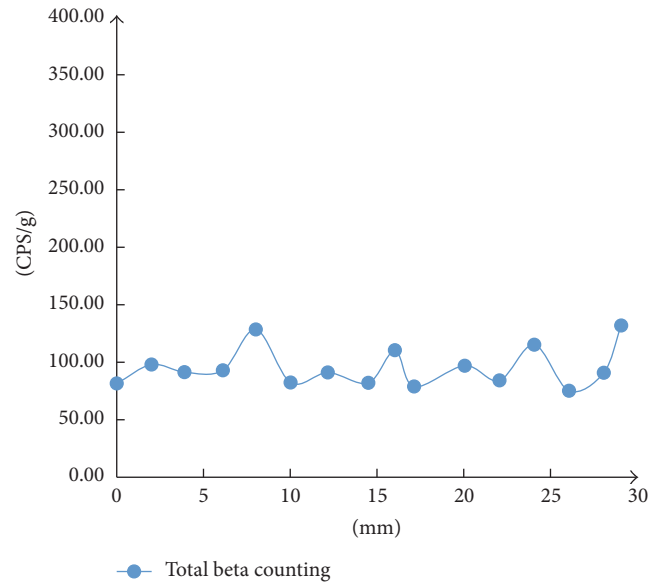


FIGURE 10: Total  $\beta$  count per gram of graphite at different spherical radii.

## 5. Conclusion and Remarks

Based on operation of HTR-10, an investigation on the source term of irradiated graphite was conducted. Some initial work has been completed to establish an experimental analysis procedure to measure the radionuclides in the irradiated graphite sphere. In this paper, the procedure was used successfully to analyze one randomly selected irradiated graphite sphere

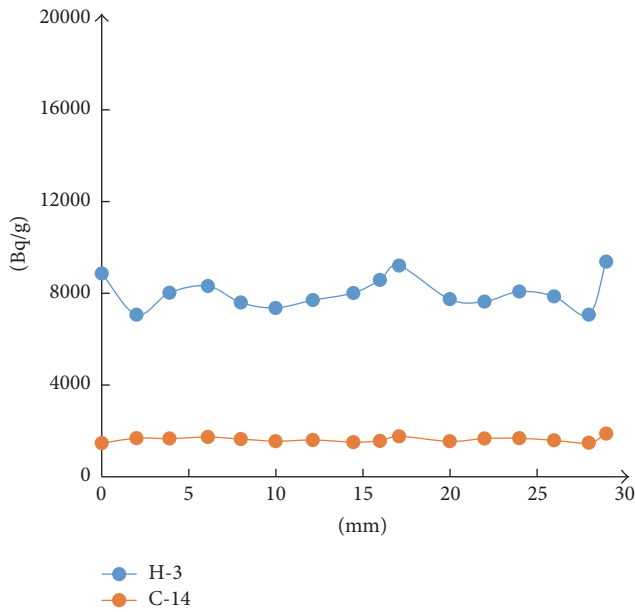


FIGURE 11: Profile of H-3 and C-14 specific activity at different spherical radii.

discharged from HTR-10. The results show that Co-60, Cs-137, Eu-152, and Eu-154 are major contributors of  $\gamma$  radiation. H-3 and C-14 are the most important  $\beta$  emitting nuclides in graphite. Except for Co-60, which indicated a sharp rise on the surface, the distributions of other radionuclides were almost uniform from the outer surface to the spherical center.

It shall be noted that this paper is focusing on the analytical procedure rather than obtaining a result or predicting the mechanism of radionuclides generation or immigration. Due to the uncertainty of graphite sphere sampling, any one of them is incapable of representing all graphite spheres in the core. To understand the source term, analysis of a large number of irradiated spheres seems essential.

## Conflicts of Interest

The authors declare that they have no conflicts of interest regarding the publication of this paper.

## Acknowledgments

This work was supported by the National Natural Science Foundation of China (no. 11575099), the National Science and Technology Major Project of the Ministry of Science and Technology of China (Grant no. 2011ZX06901), and the Beijing Natural Science Foundation (no. 2163051).

## References

[1] H. Sekimoto, S. Shiozawa, Y. Tsuchie et al., "Perspective of HTGR and its commercial development," in *Proceedings of the International Seminar*, IAEA-SR-218/219, pp. P322–P327, Cairo, Egypt, May 2001.

[2] T. D. Burchell, "Graphite: properties and characteristics," *Comprehensive Nuclear Materials*, vol. 2, pp. 285–305, 2012.

[3] A. J. Wickham, "UK Nuclear Graphite Decommissioning," 2008.

[4] A. N. Jones and B. J. Marsden, "Review of the characterisation of nuclear graphites in UK reactors scheduled for decommissioning," Tech. Rep. IAEA-TECDOC-1647, 2010.

[5] J. Fachinger, A. Kummer, G. Caspary et al., "Examination of dust in AVR pipe components," in *Proceedings of the 4th International Topical Meeting on High Temperature Reactor Technology (HTR '08)*, pp. 591–602, Washington, DC, USA, October 2008.

[6] U. Wenzel, D. Herz, and P. Schmidt, "Determination of  $^{14}\text{C}$  in spent HTGR fuel elements," *Journal of Radioanalytical Chemistry*, vol. 53, no. 1-2, pp. 7–15, 1979.

[7] P. C. Schmidt, "Alternativen zur Verminderung der C-14-Emission bei der Wiederaufbereitung von HTR-Brennelementen," KFA-Bericht Jül-1567, und Diss. RWTH Aachen, 1975.

[8] H. Li, C. Yang, C. Fang, and B. Feng, "Experimental study on the adsorption and desorption of tritium in the graphite materials for HTR-PM," *Progress in Nuclear Energy*, vol. 85, pp. 676–681, 2015.

[9] L. M. Carter, J. D. Brockman, J. D. Robertson, and S. K. Loyalka, "Diffusion of cesium and iodine in compressed IG-110 graphite compacts," *Journal of Nuclear Materials*, vol. 476, pp. 30–35, 2016.

[10] K. L. Walton, T. K. Ghosh, D. S. Viswanath, S. K. Loyalka, and R. V. Tompson, "Adsorption of iodine on graphite in High Temperature Gas-Cooled Reactor systems: a review," *Progress in Nuclear Energy*, vol. 73, pp. 21–50, 2014.

[11] M. P. Metcalfe and R. W. Mills, "Radiocarbon mass balance for a Magnox nuclear power station," *Annals of Nuclear Energy*, vol. 75, pp. 665–671, 2015.

[12] R. W. Mills, Z. Riaz, and A. W. Banford, "Nuclear data issues in the calculation of C-14 and Cl-36 in irradiated graphite," in *Proceedings of the European Nuclear Conference (ENC '12)*, Manchester, UK, 2012.

[13] T. Lansdell and M. Newland, "Magnox reactor graphite characterisation stage 2—final active analysis stage," Babcock Report TSG(11)0801, 2012.

[14] Z. Zhang, Y. Dong, F. Li et al., "The Shandong Shidao Bay 200 MWe high-temperature gas-cooled reactor pebble-bed module (HTR-PM) demonstration power plant: an engineering and technological innovation," *Engineering*, vol. 2, no. 1, pp. 112–118, 2016.

[15] "1108 Oxygen Combustion Vessel Operating Instruction Manual. Parr Instrument Company," <http://www.parrinst.com>.

## Research Article

# Adsorption Behaviors of Cobalt on the Graphite and SiC Surface: A First-Principles Study

Wenyi Wang,<sup>1,2,3</sup> Chuan Li,<sup>1,2,3</sup> Jianzhu Cao,<sup>1,2,3</sup> and Chao Fang<sup>1,2,3</sup>

<sup>1</sup>Institute of Nuclear and New Energy Technology, Tsinghua University, Beijing 100084, China

<sup>2</sup>Collaborative Innovation Center of Advanced Nuclear Energy Technology, Beijing 100084, China

<sup>3</sup>The Key Laboratory of Advanced Reactor Engineering and Safety, Ministry of Education, Beijing 100084, China

Correspondence should be addressed to Chao Fang; [fangchao@tsinghua.edu.cn](mailto:fangchao@tsinghua.edu.cn)

Received 19 October 2016; Revised 13 February 2017; Accepted 12 March 2017; Published 20 March 2017

Academic Editor: Arkady Serikov

Copyright © 2017 Wenyi Wang et al. This is an open access article distributed under the Creative Commons Attribution License, which permits unrestricted use, distribution, and reproduction in any medium, provided the original work is properly cited.

Graphite and silicon carbide (SiC) are important materials of fuel elements in High Temperature Reactor-Pebble-bed Modules (HTR-PM) and it is essential to analyze the source term about the radioactive products adsorbed on graphite and SiC surface in HTR-PM. In this article, the adsorption behaviors of activation product Cobalt (Co) on graphite and SiC surface have been studied with the first-principle calculation, including the adsorption energy, charge density difference, density of states, and adsorption ratios. It shows that the adsorption behaviors of Co on graphite and SiC both belong to chemisorption, with an adsorption energy 2.971 eV located at the Hollow site and 6.677 eV located at the hcp-Hollow site, respectively. Combining the charge density difference and density of states, it indicates that the interaction of Co-SiC system is stronger than Co-graphite system. Furthermore, the variation of adsorption ratios of Co on different substrate is obtained by a model of grand canonical ensemble, and it is found that when the temperature is close to 650 K and 1700 K for graphite surface and SiC surface, respectively, the Co adatom on the substrate will desorb dramatically. These results show that SiC layer in fuel element could obstruct the diffusion of Co effectively in normal and accidental operation conditions, but the graphite may become a carrier of Co radioactivity nuclide in the primary circuit of HTR-PM.

## 1. Introduction

Cobalt-60 (<sup>60</sup>Co) is a kind of long half-life  $\gamma$ -ray radionuclide and it could be generated through activation reaction of impurities (<sup>59</sup>Co and <sup>60</sup>Ni) in the material of fuel elements and metal/nonmetal reactor internals of High Temperature Reactor-Pebble-bed Modules (HTR-PM). The behavior of <sup>60</sup>Co is important for the safety analysis and radiation protection design in HTR-PM and has attracted a lot of attentions. In the fuel element of HTR-PM, <sup>60</sup>Co in porous pyrolytic carbon (buffer layer) and dense inner pyrolytic carbon (IPyC) of TRISO fuel particle will diffuse and interact with silicon carbide (SiC) of TRISO fuel particle [1], which is considered to possibly influence the performance of SiC. In the primary circuit of HTR-PM, <sup>60</sup>Co on the surfaces of fuel elements, graphite reflectors, graphite reactor internals, and metal reactor internals will adsorb on the graphite dust, which is generated through abrasion or corrosion effect

when the fuel elements flow in the primary circuit and is playing a significant role in contributing to the source term of HTR-PM [2]. It is reported that, in the end of lifetime of HTR-PM, the radioactivity of <sup>60</sup>Co in the primary circuit will be accumulated to  $8.6 \times 10^{10}$  Bq [3], while the activity concentration of other radionuclides is at least two orders of magnitude lower than that of <sup>60</sup>Co.

It is known that the study of interaction between Co and reactor material is essential but it is difficult to obtain the experimental result. Fortunately, the first-principle calculation, a powerful tool to study on an atomic scale, provides a way to research the above issue [4–7]. Based on the density functional theory (DFT) [8], the first-principle calculation is implemented in the Vienna Ab initio Simulation Package (VASP) by the group of Kresse et al. [9–11], which could be used to study the atom-material interaction in microlevel [12–14]. A number of theoretical studies about the adsorption behaviors using first-principle calculations, especially

for the graphite [15–19] and SiC nanotubes [20–27], have been published. Ancilotto and Toigo have performed first-principles total-energy calculations to study the adsorption of potassium on graphite [15]. Electronic structure calculations based on spin-polarized DFT with the generalized gradient approximation (GGA) and ultrasoft pseudopotentials are used to investigate the interaction between H atoms and a graphite surface [16]. The single Co atom adsorbed on some graphite materials also is discussed [28–31]. Wehling et al. have researched the orbitally controlled Kondo effect of Co adatoms on graphene [28]. Rudenko et al. have researched the adsorption of Co on graphene and analysis of the electron correlation effects from a quantum chemical perspective [29].

However, there is few works on the adsorption/desorption of Co on graphite/SiC and the mechanism of interaction is also not clear. In this work, the behavior of Co adsorbed on graphite and SiC surface with DFT will be studied, including the charge density difference (CDD) and the density of states (DOS). Furthermore, the mechanism of adsorption will also be discussed. At last, the variation of adsorption ratios of Co will be given by a model of grand canonical ensemble, which is significant for understanding the adsorption of Co on graphite and SiC macroscopically.

## 2. Method of Calculation

*2.1. The Construction of Graphite and SiC Micromodel.* The first-principle calculation is also known as ab initio calculation; it has been performed based on DFT as implemented in the VASP code and employed the projector augmented wave (PAW) pseudo-potential [32] and GGA-PBE exchange-correlation functional [33] to describe the interaction of electron-ion. Since a large number of basis functions are usually required to describe the electronic wave functions appropriately, it is very demanding to use the first-principles pseudo-potential method to calculate the carbon properties [15]. To simplify the calculations, we choose a single, isolated graphite monolayer with  $6 \times 6$  primitive cells (Figure 1(a)), by using a  $K$ -point mesh of  $1 \times 1 \times 1$ , as the substrate to calculate the adsorption energy. According to the anisotropic character of bonding in graphite, the coupling between adjacent graphite layers is much weaker than the in-plane coupling between carbon atoms [14, 34, 35]. This means that the electronic properties of a monolayer can usually provide a reasonable picture of the electronic properties of the infinite crystal [36]. As shown in Figure 1(b), graphite is here represented by graphene; there are three different adsorption sites on the graphene including Top (T), Bridge (B), and Hollow (H). SiC used in TRISO fuel particle of fuel element in HTR-PM is  $\beta$ -SiC and the corresponding structure is diamond cubic crystal. Different from pure diamond, there are four silicon atoms surrounding carbon in each SiC crystal. Therefore, the interaction between adjacent atoms in a crystal is very strong and makes the structure of SiC especially stable, which is conducive to SiC to block the activation products diffuse from the fuel particle. The supersurface of SiC(001) lattice with  $3 \times 3 \times 1$  primitive cells (Figure 2(a)) and the  $K$ -point mesh as  $2 \times 2 \times 1$  are employed to calculate the adsorption energy. The four kinds of adsorptive sites are

including Top (T), Bridge (B), hcp-Hollow (hH), and fcc-Hollow (fH) as shown in Figure 2(b).

*2.2. Adsorption Energy.* The adsorption energy of Co is defined as

$$E_{\text{ads}} = E_{\text{Co-sub}} - (E_{\text{sub}} + E_{\text{Co}}), \quad (1)$$

where  $E_{\text{ads}}$ ,  $E_{\text{sub}}$ ,  $E_{\text{Co}}$ , and  $E_{\text{Co-sub}}$  are the energies of the adsorption, substrate, a single Co atom, and the Co-substrate system, respectively.  $E_{\text{sub}}$ ,  $E_{\text{Co}}$ , and  $E_{\text{Co-sub}}$  could be obtained by the first-principle calculations directly, and then  $E_{\text{ads}}$  could be obtained from (1). There are two influencing factors that need to be considered which may affect the value of  $E_{\text{ads}}$ . One is the adsorptive sites and the other is the height between the adatom and substrate. The adsorption energies at different heights of different adsorptive sites are calculated firstly and after obtaining the most suitable position which located at the height corresponding to the largest adsorption energy, the total system will be relaxed to obtain the value of  $E_{\text{ads}}$  and obtain the optimum adsorptive site and height. It should be mentioned that the “-” sign of  $E_{\text{ads}}$  represents the direction of energy change, and the adsorption energy is only related to the absolute value of  $E_{\text{ads}}$ . Meanwhile, the CDD and the DOS could be obtained and are employed to analysis. The CDD is defined as the difference between the total charge density and the atomic charge densities [20]. It shows the visual image of electron transfer between nuclide and substrate directly. As suggested by Khantha et al. [37], the redistribution of the charge density indicates that the interaction potential between the adatom and substrate is composed of two distinct contributions: a screened Coulomb interaction resulting from the charge transfer between the adatom and substrate atoms and a van der Waals type interaction [38, 39]. The equilibrium position of an adatom above graphite/SiC is largely determined by the charge redistribution that takes place in this short-separation region. DOS shows the distributions of electrons in each energy level, which are helpful to understand the behaviors of atom absorbed/desorbed on material in microlevel. Fermi energy level  $E_F$  could also be obtained in the abovementioned process. The relative position of the Fermi level in the DOS shows the occupation of the states and the features of bonding [39, 40]. If atom is absorbed on the surface of substrate, the peaks of the state for both adatom and substrate compared to  $E_F$  will be shifted. Supposing that the DOS is changed, the adsorption behavior between the adatom and substrate is chemisorption. Otherwise, it is physisorption. If the energy state of atom has a left shift, this means that the atom acquires electrons. Then its energy decreases, so that the peak width of state will become wider and more occupied. If the energy state shifted towards right, the atom will lose electrons.

What should be emphasized here is  $E_{\text{ads}}$ , CDD, DOS, and  $E_F$  are obtained in the condition of 0 K with DFT method, but the temperature condition of the fuel element and primary circuit of HTR-PM is below 1000 K under normal operation and below 1850 K under accident operation. It is necessary to point out that the energy of electron is not sensitive to the temperature at the range of  $T \sim 10^3$  K [41], so the results

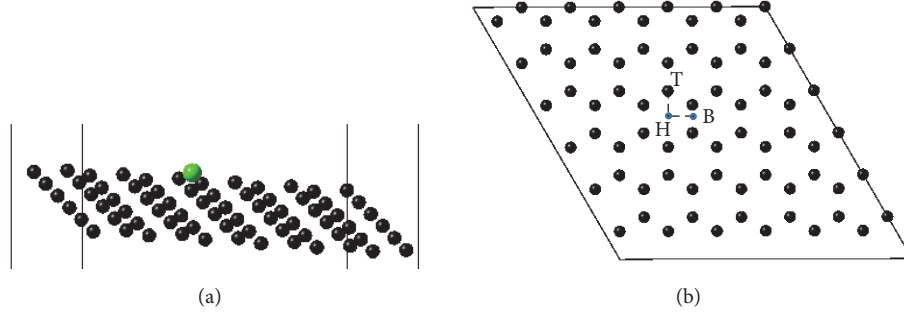


FIGURE 1: (a) The supersurface of Co on graphite. (b) The three adsorption sites on the graphite surface, where T, B, and H represent the Top, Bridge, and Hollow positions.

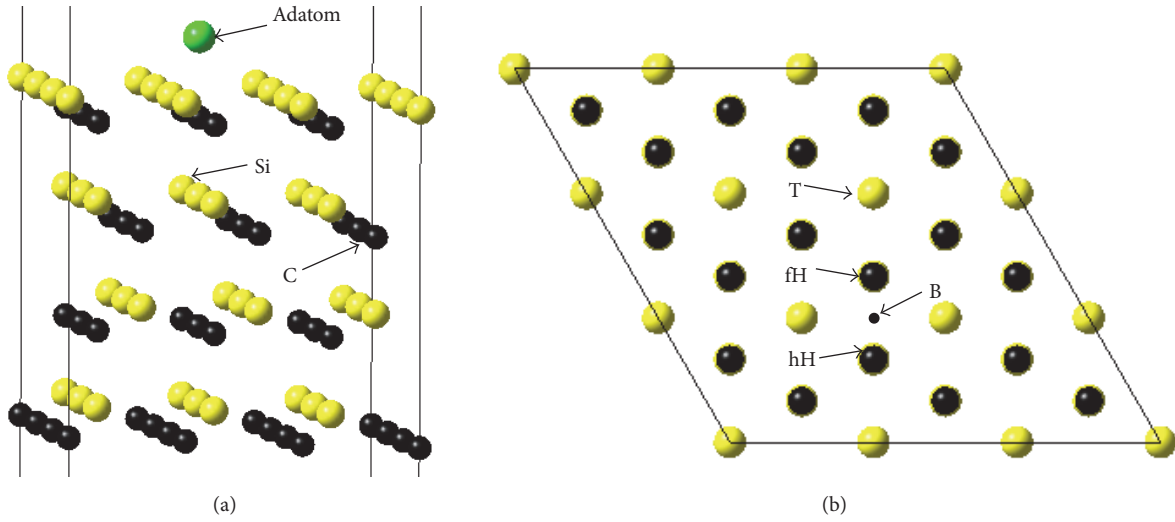


FIGURE 2: (a) The supersurface of Co on SiC. (b) The adsorption sites on the SiC surface, where T, B, and H represent the Top, Bridge, and Hollow positions.

obtained by DFT can be applied to study the interaction between Co and graphite and SiC of HTR-PM.

**2.3. Adsorption Ratio.** The adsorbed nuclide atoms on substrate and separate nuclide atoms will form a dynamic equilibrium system. According to literatures [14, 42], a model of grand canonical ensemble is considered to describe this system and calculate the balanced adsorption ratio of Co on the graphite and SiC. In this model, the substrate materials adsorbing Co atoms are considered as an open system, and the separate Co atoms in circumstance (i.e., the coolant in the primary circuit of HTR-PM and the gas interlayer between SiC and IPyC of TRISO fuel particle) are treated as particle and gas source. On the theory of the statistic physics, the relation between the number of adsorbed Co atoms  $\bar{N}$  and the total adsorptive centers  $N_0$  is given by

$$\bar{N} = \frac{N_0}{1 + e^{(E_{\text{ads}} - \mu)/K_b T}}, \quad (2)$$

where  $\mu$  is the chemical potential of Co atom,  $K_b$  is Boltzmann's constant, and  $T$  is the temperature of the circumstance. So the adsorption ratio can be defined as

$$\theta = \frac{\bar{N}}{N_0}. \quad (3)$$

Because the concentration of radioactive products is very low [42], the ideal gas model can be employed to deal with nuclide gas source directly. If an equilibrium state is achieved in the reactor, the chemical potentials of nuclide atoms in the open system will be identical to those of gas source. Therefore, according to the ideal gas model, the chemical potential of Co can be written as follows:

$$\mu = K_b T \ln \left[ n \left( \frac{h^2}{2\pi m K_b T} \right)^{3/2} \right], \quad (4)$$

where  $n$  is the density of the nuclide in the circumstance,  $m$  is the atomic mass of Co, and  $h$  is the Planck constant.

Combined with (2), (3), and (4), the adsorption ratio is accessible to obtain as

$$\theta = \frac{1}{1 + (1/n) (2\pi m K_b T / h^2)^{3/2} e^{E_{\text{ads}}/K_b T}}. \quad (5)$$

It is seen from (5) that only three parameters of  $n$ ,  $T$ , and  $E_{\text{ads}}$  are undetermined. The numerical value of  $n$  and  $T$

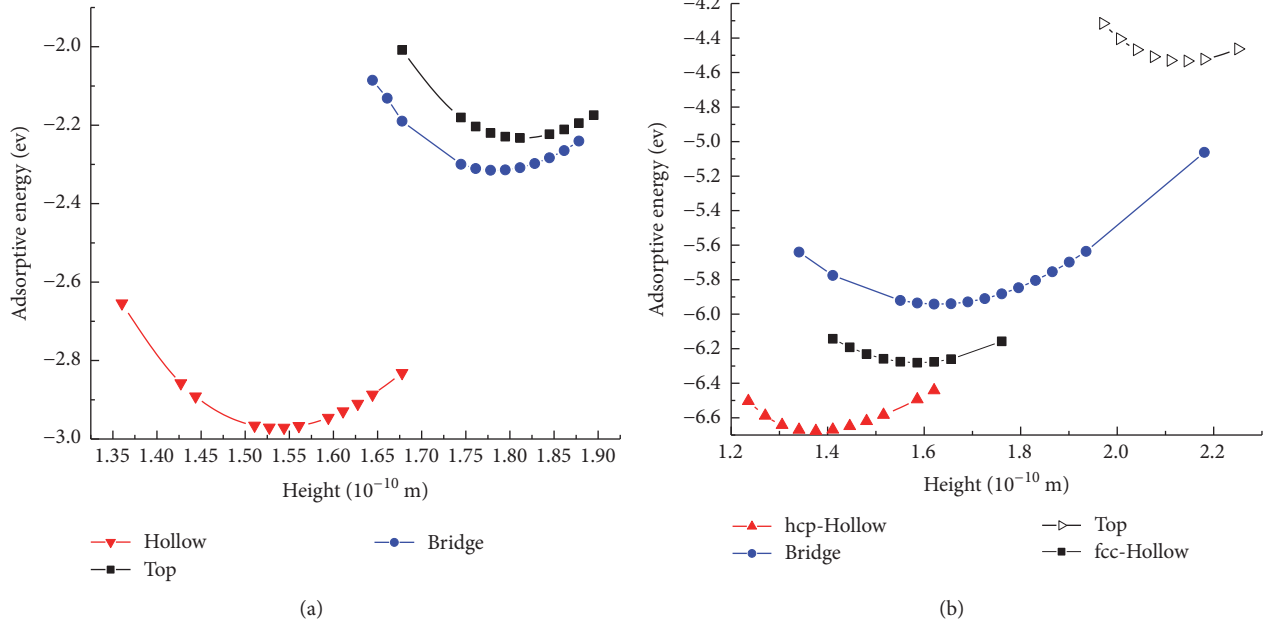


FIGURE 3: The variations of adsorption energies at different sites with different height. (a) The Co adatom at graphite. (b) The Co adatom at SiC.

of circumvents in HTR-PM can be determined by either calculation or experimental measurement and  $E_{\text{ads}}$  can be obtained from (1).

### 3. Results and Discussion

**3.1. Adsorption Energy.** In order to obtain the most stable adsorptive site, the adsorption energy with different adsorptive sites has been calculated. For each adsorptive site, the adsorption energy depends on the height between the adatom and substrate and there exists a maximum value which could be considered as the exact adsorption energy of corresponding site. Figure 3 shows the variations of adsorption energies of Co on graphite and SiC at different sites with different height.

The adsorption energies of Co on graphite and SiC at different adsorptive sites are listed in Tables 1 and 2. To different substrate, the adsorption energies and the most stable adsorptive sites of Co are different. It shows that the most stable sites for Co-graphite and Co-SiC system are Hollow and hcp-Hollow with the adsorption energies 2.971 eV and 6.677 eV, respectively. These results indicate that the interaction of Co-SiC system is stronger than Co-graphite system.

**3.2. Analysis of Electronic Structure.** To identify the adsorption behavior of the Co adatom on different substrates, the electronic structure of the two systems should be analyzed. Figure 4 shows the optimized stable configurations and their corresponding CDD for the Co-graphite system and Co-SiC system. The blue areas represent the decreases of charge density and the yellow areas represent the increase of charge density. Even though there is no obvious electron transfer

TABLE 1: The adsorption energies at different adsorptive sites for the Co adatom on graphite.

Adsorption sites	$E_{\text{ads}}$ (eV)	$d_{\text{Co-SiC}}$ (Å)
Bridge (B)	-2.315	1.778
Top (T)	-2.233	1.811
Hollow	<b>-2.971</b>	1.544

TABLE 2: The adsorption energies at different adsorptive sites for the Co adatom on SiC.

Adsorption sites	$E_{\text{ads}}$ (eV)	$d_{\text{Co-SiC}}$ (Å)
Bridge (B)	-5.942	1.621
Top (T)	-4.533	2.146
fcc-Hollow	-6.281	1.586
hcp-Hollow	<b>-6.677</b>	1.376

between Co and graphite in Figure 4(a), the adsorption behavior of the Co-graphite system could be considered as chemisorption due to its high adsorption energy in Table 1, while in Figure 4(b) there are a lot of yellow areas that appeared between Co and SiC surface, which suggests that a strong chemical bond is formed in this area. This result indicates that the Co has a stronger interaction with SiC than graphite. The result also coincides with the abovementioned adsorption energies of these two systems.

In order to understand the deep features of interactions between the adatom and substrates, the DOS for single Co atom, the substrate of graphite and SiC, and the Co-substrate system are calculated. It should be mentioned that the  $K$ -point meshes to integrate the Brillouin zone have been changed to  $2 \times 2 \times 2$  and  $4 \times 4 \times 1$  for the DOS calculation

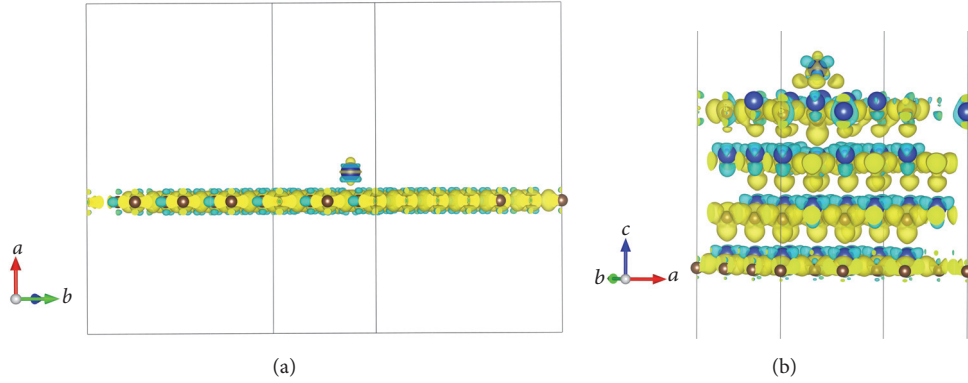


FIGURE 4: The CDD of Co at different substrate. (a) The Co adatom at graphite. (b) The Co adatom at SiC.

of Co-graphite system and Co-SiC system, respectively. The results of DOS are shown in Figure 5. When the Co adsorbed on graphite and SiC surface, the positions of Co adatom are different. In the following discussion, different systems and different positions corresponding to the adsorption state are used in the calculation of isolated Co atom for Co-graphite and Co-SiC, respectively, which makes the DOS of Co have some differences in these two systems.

Figures 5(a) and 5(b) give a comparison of DOS for the Co-graphite system, the isolated graphite substrate, the isolated Co atom, and the adsorbed Co adatom. For isolated Co atom, the peaks of the  $d$ -state nearly locate at  $E_F$  and that of  $s$ -state locate at the right of  $E_F$ . When the Co atom is adsorbed on the graphite surface, the peaks of the  $d$ -state have a left shift towards a lower energy than  $E_F$  and have evident broadenings owing to adsorption interaction. It is also found that the peak of the  $s$ -state shifts slightly right and the peak intensity becomes too weak to be identified when the Co atom is adsorbed on the graphite surface. Combining the above results and total DOS of graphite, it is feasible to know that the interaction between Co and graphite is very strong and there are electrons transferring on the interactive interface, which is the direct evidence of chemisorption. The situation of the Co-SiC system, as shown in Figures 5(c) and 5(d), is a little different. When the Co atom is adsorbed on the SiC surface, the peak intensities of the  $s$ -state become too weak to recognize and there are only shifts and broadenings of the peaks of  $d$ -state. Remarkably, although most of the peaks of  $d$ -state move to the left, there is still right shift, which indicates that Co adatom not only gains partial electrons from SiC but also loses electrons to SiC. These results could be explained from the view of electrochemistry that the electronegativity of Co is close to Si and there exists resonance between the  $d$ -state of Co adatom and SiC surface when the partial electron transferring turns out. That is to say, due to the orbital hybridization, the adsorptive behavior between Co and SiC is also chemisorption. Based on the electronic analysis, it presented that the interaction between Co and SiC is stronger than that between Co and graphite significantly.

**3.3. Adsorption Ratio.** The adsorption ratio, as shown in (4), is determined by three parameters  $n$ ,  $T$ , and  $E_{\text{ads}}$ . Among them,  $E_{\text{ads}}$  can be obtained from (1) by the first-principle

calculation, the temperature  $T$  is variational, and the density of Co ( $n$ ) in circumstance could be obtained by experiment or theoretical calculations. Considering that the adsorption conditions of  $^{60}\text{Co}$  on graphite and SiC surface are different in HTR-PM, the density of  $^{60}\text{Co}$  used for calculation is not the same. Based on the experimental data, the density of  $^{60}\text{Co}$  in the primary circuit could be set to be  $2.4 \times 10^{10} \text{ m}^{-3}$  [3]. The density of  $^{60}\text{Co}$  on the surface of the SiC was calculated according to the content of  $^{59}\text{Co}$  impurity in the graphite matrix, and the calculated result was  $6.33 \times 10^{14} \text{ m}^{-3}$ . In order to investigate the trend of adsorption ratio varying with temperature  $T$ , the adsorption ratios of Co adatom on graphite and SiC surface calculated by (4) are shown in Figure 6. It can be easily noted that the adsorption ratio of the Co decreases exponentially with the increase of temperature.

According to Figure 6, there exists an inflexion point while the adsorption ratio varies with the temperature. When the temperature is close to 650 K and 1700 K for graphite surface and SiC surface, respectively, the adsorption ratio of Co decreases dramatically. The temperature at the inflexion point is suggested to be defined as the critical temperature,  $T_c$ . If the temperature is lower than  $T_c$ , most or even all of Co will be absorbed on the substrate surface. If the temperature is higher than  $T_c$ , it stands for the idea that the Co on the substrate will have a lot of transitions from absorption to desorption.

In HTR-PM, the average temperature of the fuel element and the primary circuit under normal operation is usually less than 1000 K, and the maximum design value of temperature under accident conditions is about 1850 K. From these data, it shows that Co could be adsorbed well on the surface of SiC in the normal operating temperature range and only at the highest temperature in supposed accidents, Co will be desorbed and diffused from the SiC surface. For graphite, Co is susceptible to a large amount of desorption and diffusion from the graphite surface whether in normal operation or accident conditions. As a result, the Co absorbed on SiC surface performed a better adsorption behavior than on graphite surface. Therefore, SiC could block the diffusion of Co, while graphite could not if the temperature is higher than 650 K.

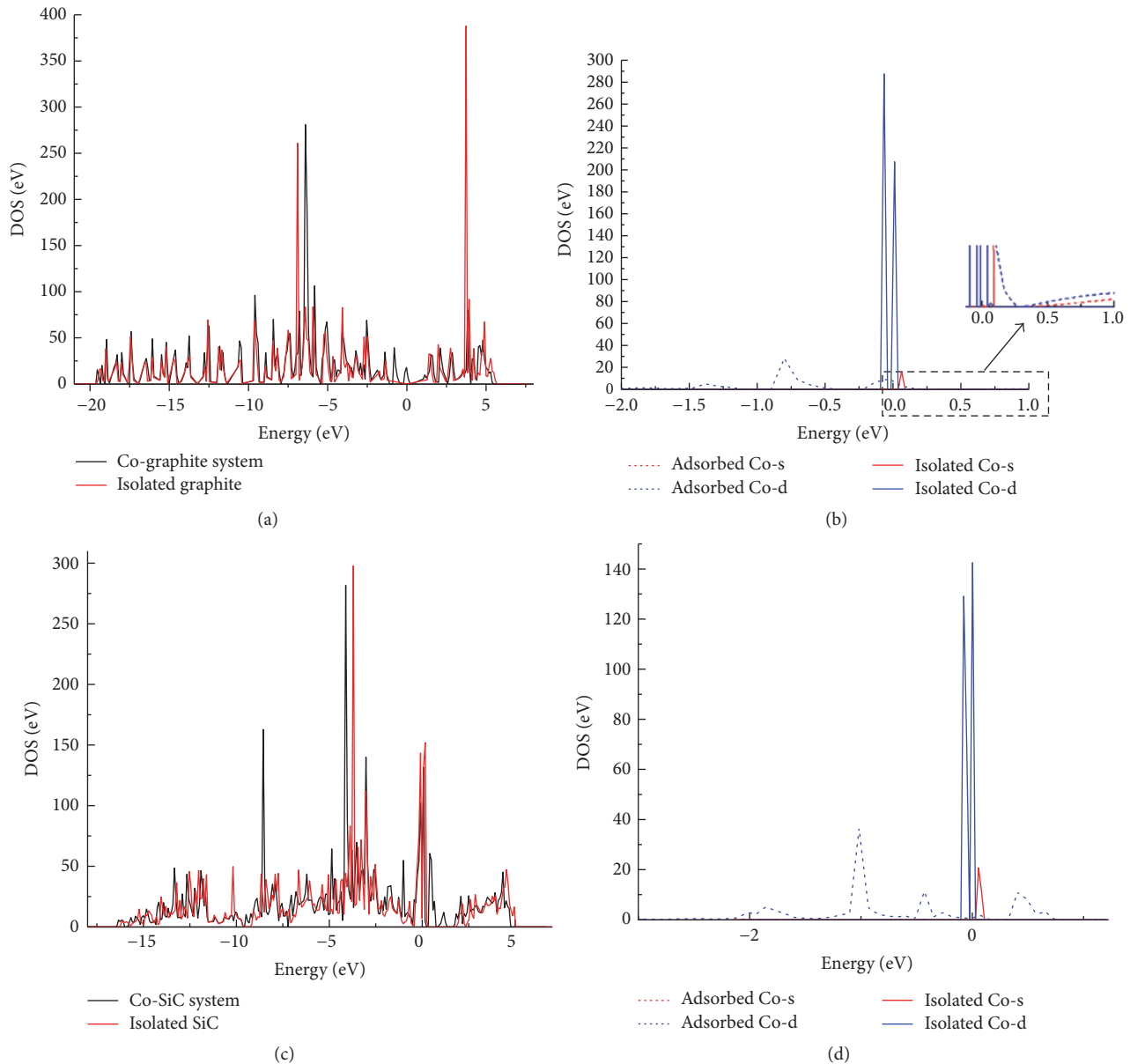


FIGURE 5: A comparison of DOS with Co: (a) the Co-graphite system and the isolated graphite substrate, (b) the isolated Co atom and the adsorbed Co adatom on the graphite, (c) the Co-SiC system and the isolated SiC substrate, and (d) the isolated Co atom and the adsorbed Co adatom on the SiC. (The number on the abscissa axes indicates the energy difference between the electronic state and the Fermi energy.)

#### 4. Conclusion

In this paper, the first-principles DFT theory was used to study the adsorption behavior of Co on graphite and SiC surface in HTR-PM. The adsorption energies corresponding to different adsorptive site and height were calculated, and the adsorption energy for Co on graphite and SiC surface is 2.971 eV and 6.677 eV, respectively. In order to know the underlying physical nature of the adsorption behavior of Co, we have analyzed the electronic structure of the adsorption system by CDD and DOS. The results suggested that the adsorptive behavior of the two systems belongs to chemisorption. All of these results could be used to explain the result of adsorption energy from different aspects; the source term

from the microscopic mechanism has been analyzed; it helps us to understand the adsorption behavior of the Co more clearly. In addition, combining the adsorption energy obtained by the first-principle calculation, the adsorption ratio was derived with different temperature and the density of Co in HTR-PM. The critical temperature for graphite surface is 650 K, and for SiC surface it is 1700 K.

In a conclusion, the adsorption performance of Co on the SiC surface was better than that on the graphite surface. In the primary circuit of HTR-PM, the Co adatom seems to be easily desorbed from the graphite surface. Compared with graphite, SiC could suppress the diffusion of Co effectively for both the normal operation and the accident conditions in the fuel elements. The results of adsorption ratios can also be

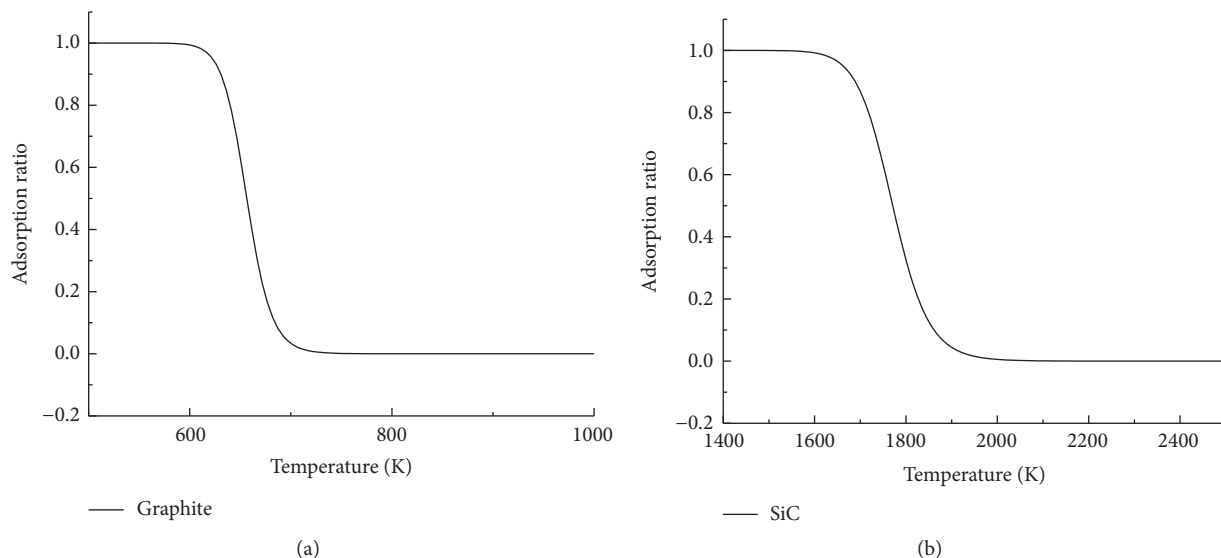


FIGURE 6: Variation of adsorption ratio with temperature for Co atom on (a) graphite and (b) SiC.

used for nuclear safety evaluation of Co release in the normal operation and the supposed accident of the HTR-PM.

### Conflicts of Interest

The authors declare that there are no conflicts of interest regarding the publication of this paper.

### Acknowledgments

This work was supported by the National Science and Technology Major Project of the Ministry of Science and Technology of China (Grant no. ZX06901).

### References

- [1] International Atomic Energy Agency, "Fuel performance and fission product behaviour in gas cooled reactors," Tech. Rep. IAEA-TECDOC-978, International Atomic Energy Agency, Vienna, Austria, 1997.
- [2] C. Yang, C. Fang, and J. Cao, "The design and thermohydraulics study of the HTR-10 high temperature helium experimental loop," *Progress in Nuclear Energy*, vol. 77, pp. 329–335, 2014.
- [3] L. Yuanzhong and C. Jianzhu, "Fission product release and its environment impact for normal reactor operations and for relevant accidents," *Nuclear Engineering and Design*, vol. 218, no. 1–3, pp. 81–90, 2002.
- [4] D. M. Riffe, G. K. Wertheim, and P. H. Citrin, "Alkali metal adsorbates on W(110): ionic, covalent, or metallic?" *Physical Review Letters*, vol. 64, no. 5, pp. 571–574, 1990.
- [5] B. N. J. Persson and H. Ishida, "Depolarization and metallization in alkali-metal overlayers," *Physical Review B*, vol. 42, no. 5, pp. 3171–3174, 1990.
- [6] K. Horn, A. Hohlfeld, J. Somers, T. Lindner, P. Hollins, and A. M. Bradshaw, "Identification of the s-derived valence-electron level in photoemission from alkali-metal adlayers on aluminum," *Physical Review Letters*, vol. 61, no. 21, pp. 2488–2491, 1988.
- [7] G. M. Lamble, R. S. Brooks, D. A. King, and D. Norman, "Determination of an adlayer bonding transition by surface extended X-ray-absorption fine-structure spectroscopy: Cesium adsorbed on Ag(111)," *Physical Review Letters*, vol. 61, no. 9, pp. 1112–1115, 1988.
- [8] W. Kohn and L. J. Sham, "Self-consistent equations including exchange and correlation effects," *Physical Review*, vol. 140, no. 4, pp. A1133–A1138, 1965.
- [9] G. Kresse and J. Furthmüller, "Efficient iterative schemes for ab initio total-energy calculations using a plane-wave basis set," *Physical Review B*, vol. 54, no. 16, pp. 11169–11186, 1996.
- [10] G. Kresse and J. Furthmüller, "Efficiency of ab-initio total energy calculations for metals and semiconductors using a plane-wave basis set," *Computational Materials Science*, vol. 6, no. 1, pp. 15–50, 1996.
- [11] G. Kresse and J. Hafner, "Ab initio molecular dynamics for liquid metals," *Physical Review B*, vol. 47, no. 1, pp. 558–561, 1993.
- [12] X. Luo, C. Fang, X. Li, W. Lai, and T. Liang, "Adsorption behaviors of Cs and I atoms on the graphite surface by the first-principles," *Journal of Nuclear Materials*, vol. 441, no. 1, pp. 113–118, 2013.
- [13] X.-F. Luo, C. Fang, X. Li, W.-S. Lai, L.-F. Sun, and T.-X. Liang, "Adsorption and electronic structure of Sr and Ag atoms on graphite surfaces: a first-principles study," *Chinese Physics Letters*, vol. 30, no. 6, Article ID 066801, 2013.
- [14] X. Luo, C. Fang, X. Li, W. Lai, L. Sun, and T. Liang, "Study of interaction between radioactive nuclides and graphite surface by the first-principles and statistic physics," *Applied Surface Science*, vol. 285, pp. 278–286, 2013.
- [15] F. Ancilotto and F. Toigo, "First-principles study of potassium adsorption on graphite," *Physical Review B*, vol. 47, no. 20, pp. 13713–13721, 1993.
- [16] X. Sha and B. Jackson, "First-principles study of the structural and energetic properties of H atoms on a graphite (0001) surface," *Surface Science*, vol. 496, no. 3, pp. 318–330, 2002.
- [17] Y. Ferro, F. Marinelli, and A. Allouche, "Density functional theory investigation of the diffusion and recombination of H

- on a graphite surface," *Chemical Physics Letters*, vol. 368, no. 5-6, pp. 609–615, 2003.
- [18] S. D. Chakarova-Käck, E. Schröder, B. I. Lundqvist, and D. C. Langreth, "Application of van der Waals density functional to an extended system: adsorption of benzene and naphthalene on graphite," *Physical Review Letters*, vol. 96, no. 14, Article ID 146107, 2006.
- [19] S. D. Chakarova-Käck, Ø. Borck, E. Schröder, and B. I. Lundqvist, "Adsorption of phenol on graphite(0001) and  $\alpha$ - $\text{Al}_2\text{O}_3$  (0001): nature of van der Waals bonds from first-principles calculations," *Physical Review B*, vol. 74, no. 15, Article ID 155402, 2006.
- [20] T. Meng, C.-Y. Wang, and S.-Y. Wang, "First-principles study of a single Ti atom adsorbed on silicon carbide nanotubes and the corresponding adsorption of hydrogen molecules to the Ti atom," *Chemical Physics Letters*, vol. 437, no. 4–6, pp. 224–228, 2007.
- [21] G. Gao, S. H. Park, and H. S. Kang, "A first principles study of  $\text{NO}_2$  chemisorption on silicon carbide nanotubes," *Chemical Physics*, vol. 355, no. 1, pp. 50–54, 2009.
- [22] E. Bekaroglu, M. Topsakal, S. Cahangirov, and S. Ciraci, "First-principles study of defects and adatoms in silicon carbide honeycomb structures," *Physical Review B*, vol. 81, no. 7, Article ID 075433, 2010.
- [23] E. F. Rosso and R. J. Baierle, "First principles study about Fe adsorption on planar SiC nanostructures: monolayer and nanoribbon," *Microelectronic Engineering*, vol. 126, pp. 37–41, 2014.
- [24] Y.-L. Shi, J.-M. Zhang, and K.-W. Xu, "Structural and electronic properties of SiC nanotubes filled with Cu nanowires: a first-principles study," *Physica E: Low-Dimensional Systems and Nanostructures*, vol. 54, pp. 319–325, 2013.
- [25] L. Wang, "Adsorption of formaldehyde (HCOH) molecule on the SiC sheet: a first-principles study," *Applied Surface Science*, vol. 258, no. 17, pp. 6688–6691, 2012.
- [26] P. V. Bui, K. Inagaki, Y. Sano, K. Yamauchi, and Y. Morikawa, "Adsorption of hydrogen fluoride on SiC surfaces: a density functional theory study," *Current Applied Physics*, vol. 12, no. 3, pp. S42–S46, 2012.
- [27] M. Şimşek and S. Aydın, "First-principles study of thiophene on  $\beta$ -SiC (0 0 1)-(2 $\times$ 1) surface," *Physica B: Condensed Matter*, vol. 406, no. 14, pp. 2880–2884, 2011.
- [28] T. O. Wehling, A. V. Balatsky, M. I. Katsnelson, A. I. Lichtenstein, and A. Rosch, "Orbitally controlled Kondo effect of Co adatoms on graphene," *Physical Review B*, vol. 81, no. 11, Article ID 115427, 2010.
- [29] A. N. Rudenko, F. J. Keil, M. I. Katsnelson, and A. I. Lichtenstein, "Adsorption of cobalt on graphene: electron correlation effects from a quantum chemical perspective," *Physical Review B*, vol. 86, no. 7, pp. 3305–3307, 2012.
- [30] D. Krychowski, J. Kaczkowski, and S. Lipinski, "Kondo effect of a cobalt adatom on a zigzag graphene nanoribbon," *Physical Review B*, vol. 89, no. 3, Article ID 035424, 2014.
- [31] H. Johll, H. C. Kang, and E. S. Tok, "Density functional theory study of Fe, Co, and Ni adatoms and dimers adsorbed on graphene," *Physical Review B*, vol. 79, no. 24, Article ID 245416, 2009.
- [32] G. Kresse and D. Joubert, "From ultrasoft pseudopotentials to the projector augmented-wave method," *Physical Review B*, vol. 59, no. 3, pp. 1758–1775, 1999.
- [33] J. P. Perdew, K. Burke, and M. Ernzerhof, "Generalized gradient approximation made simple," *Physical Review Letters*, vol. 77, no. 18, pp. 3865–3868, 1996.
- [34] H. Ishida and R. E. Palmer, "Electronic structure and phase transitions of submonolayer potassium on graphite," *Physical Review B*, vol. 46, no. 23, pp. 15484–15489, 1992.
- [35] S. Srivastava and J. Almlöf, "Chemisorption of aluminum atoms on a graphite surface: cluster convergence and effects of surface reconstruction," *Surface Science*, vol. 274, no. 1, pp. 113–119, 1992.
- [36] S. B. Trickey, F. Müller-Plathe, G. H. F. Diercksen, and J. C. Boettger, "Interplanar binding and lattice relaxation in a graphite dilayer," *Physical Review B*, vol. 45, no. 8, pp. 4460–4468, 1992.
- [37] M. Khantha, N. A. Cordero, L. M. Molina, J. A. Alonso, and L. A. Girifalco, "Interaction of lithium with graphene: an ab initio study," *Physical Review B*, vol. 70, no. 12, Article ID 125422, 2004.
- [38] Y. Andersson, E. Hult, H. Rydberg, P. Apell, B. I. Lundqvist, and D. C. Langreth, "Van der Waals interactions in density functional theory," in *Electronic Density Functional Theory*, pp. 243–260, Springer, Berlin, Germany, 1998.
- [39] Y. Mao, J. Yuan, and J. Zhong, "Density functional calculation of transition metal adatom adsorption on graphene," *Journal of Physics Condensed Matter*, vol. 20, no. 11, Article ID 115209, 2008.
- [40] R. Pentcheva and M. Scheffler, "Initial adsorption of Co on Cu (001): a first-principles investigation," *Physical Review B*, vol. 65, no. 15, Article ID 155418, 2002.
- [41] J. X. Fang and D. Lu, *Solid Physics*, Shanghai Scientific and Technical Publishers, Shanghai, China, 1980.
- [42] C. Fang, J.-Z. Cao, and Y.-J. Dong, "Study of adsorption on graphite and its mechanism of radionuclides in primary circuit of HTR-10 with Ab initio theory," *Atomic Energy Science and Technology*, vol. 46, no. 1, pp. 391–396, 2012.

## Research Article

# 3D Nondestructive Visualization and Evaluation of TRISO Particles Distribution in HTGR Fuel Pebbles Using Cone-Beam Computed Tomography

Gongyi Yu, Yi Du, Xincheng Xiang, Yuan Liu, Ziqiang Li, and Xiangang Wang

*Institution of Nuclear and New Energy Technology, Tsinghua University, Beijing 100084, China*

Correspondence should be addressed to Xiangang Wang; wangxiangang@tsinghua.edu.cn

Received 27 December 2016; Accepted 26 February 2017; Published 7 March 2017

Academic Editor: Robert Morris

Copyright © 2017 Gongyi Yu et al. This is an open access article distributed under the Creative Commons Attribution License, which permits unrestricted use, distribution, and reproduction in any medium, provided the original work is properly cited.

A nonuniform distribution of tristructural isotropic (TRISO) particles within a high-temperature gas-cooled reactor (HTGR) pebble may lead to excessive thermal gradients and nonuniform thermal expansion during operation. If the particles are closely clustered, local hotspots may form, leading to excessive stresses on particle layers and an increased probability of particle failure. Although X-ray digital radiography (DR) is currently used to evaluate the TRISO distributions in pebbles, X-ray DR projection images are two-dimensional in nature, which would potentially miss some details for 3D evaluation. This paper proposes a method of 3D visualization and evaluation of the TRISO distribution in HTGR pebbles using cone-beam computed tomography (CBCT): first, a pebble is scanned on our high-resolution CBCT, and 2D cross-sectional images are reconstructed; secondly, all cross-sectional images are reconstructed to form the 3D model of the pebble; then, volume rendering is applied to segment and display the TRISO particles in 3D for visualization and distribution evaluation. For method validation, several pebbles were scanned and the 3D distributions of the TRISO particles within the pebbles were produced. Experiment results show that the proposed method provides more 3D than DR, which will facilitate pebble fabrication research and production quality control.

## 1. Introduction

High-temperature gas-cooled reactor (HTGR) is one of the six candidates of the Generation IV nuclear systems which attract many countries' interests. One of the important safety features of the HTGR is the robust fission product retention capabilities of the fuel elements [1]. One of the important features of the HTGR is the improved safety of fuel elements. The Chinese High-Temperature Reactor Pebble-bed Module (HTR-PM) uses pebbles as fuel elements, which may enclose more than ten thousand tristructural isotropic (TRISO) particles in a single pebble [2]. The TRISO particle is the first and most important barrier to retain fission products [1, 2]. The distribution of TRISO particles within the pebbles is an important factor for the safety and fuel performance evaluation of the pebbles, because nonuniform distribution of particles causes nonuniform distribution of temperature gradient and produces thermal expansions within a pebble. It is therefore important to evaluate the particle distributions

within a pebble to be certain that the nonuniformity of the distributions does not exceed certain criteria.

Fabrication of pebbles is a very complicated process [2–4]. Firstly, TRISO particles and graphite powder are completely mixed and prepressed to form a ball with a silicone rubber mold. Secondly, a graphite ball with TRISO particles is formed in the fuel zone by cold quasi-isostatic pressing. Thirdly, the 5 mm graphite layer is pressed outside the fuel zone to form the nonfuel zone to provide protection for the TRISO particles. And finally, after the process of lathing, the heat treatments of carbonization, and high-temperature purification, the fuel pebble is formed. Figure 1 illustrates the structure of a pebble. A large number of TRISO particles are distributed randomly in a graphite matrix in the inner part of the pebble, which is about 50 mm in diameter. The outer part of the pebble is a layer of graphite that does not contain any fuel.

To visualize the particle distribution, X-ray Nondestructive Testing (NDT), such as the X-ray digital radiography

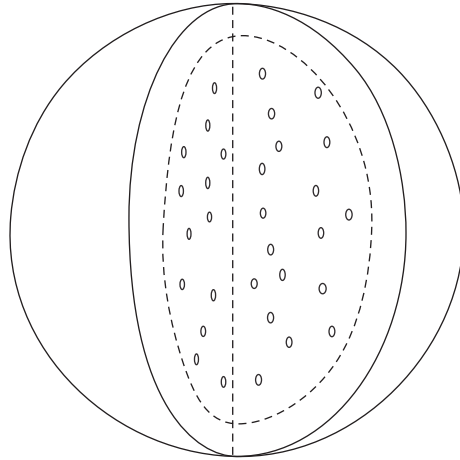


FIGURE 1: Scheme of a pebble.

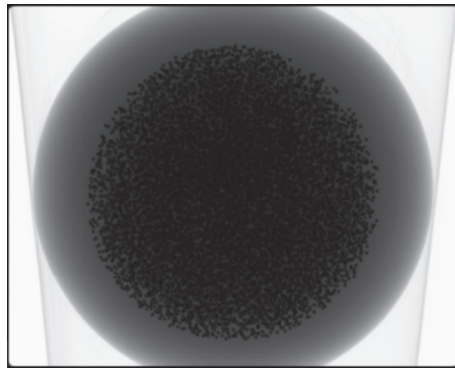


FIGURE 2: Raw DR of a fuel pebble.

(DR), is conventionally used at INET, Tsinghua University, because it is fast and penetrating. Figure 2 shows a digital radiography of a fuel pebble with the particles indicated by the black dots. These features make it convenient to evaluate parameters such as the size of the nonfuel zone [4–6].

Although DR can provide a preliminary evaluation of the particle distribution, DR is only a 2D projection of the 3D distribution of the TRISO particles. Particles overlap each other, which leads to a confusing image in a 2D projection. Moreover, the cracks or other structures with small effective cross section parallel to the direction of X-ray cause even more confusion in the DR image. For the DR method, well-distributed TRISO particles in the fuel zone cannot produce clear images. For example, we could not find the cutting edge of TRISO in Figure 3. In the 2D image produced by the DR method, the intensities of the particles depend on the thickness that X-ray penetrates instead of the number of particles in a certain volume.

The TRISO particles are desired to be uniformly distributed within the pebble so that they do not touch each other. The TRISO particles, however, are often distributed nonuniformly because they are not fully mixed when packing together into a pebble during the fabrication process.

Destructive methods such as the sample-slice-polish method are a conventionally used option to assess particle distributions. The sample is sliced and the section polished to take a photographic picture of the cross section in 2D. This method is straightforward to implement and the image can be in high resolution. It is, however, time-consuming, labor-intensive, operator-dependent, and not intrinsically a 3D method [7, 8]. More importantly, this method requires the pebbles to be cut into slices and causes difficulties in dust control. An alternative nondestructive method is therefore desired. The conventionally used DR method, however, cannot reliably assess the particle distribution due to the aforementioned disadvantages [7]. It is therefore important to develop a new nondestructive method for this purpose.

In this work, we used 3D cone-beam CT to acquire 3D tomographic images of particle distributions within pebbles. This method provides more valuable information to assess pebble quality [9].

## 2. Method

Cone-beam CT reconstructs 3D slices from 360° projections. The scheme of 3D cone-beam CT is shown in Figure 4, which

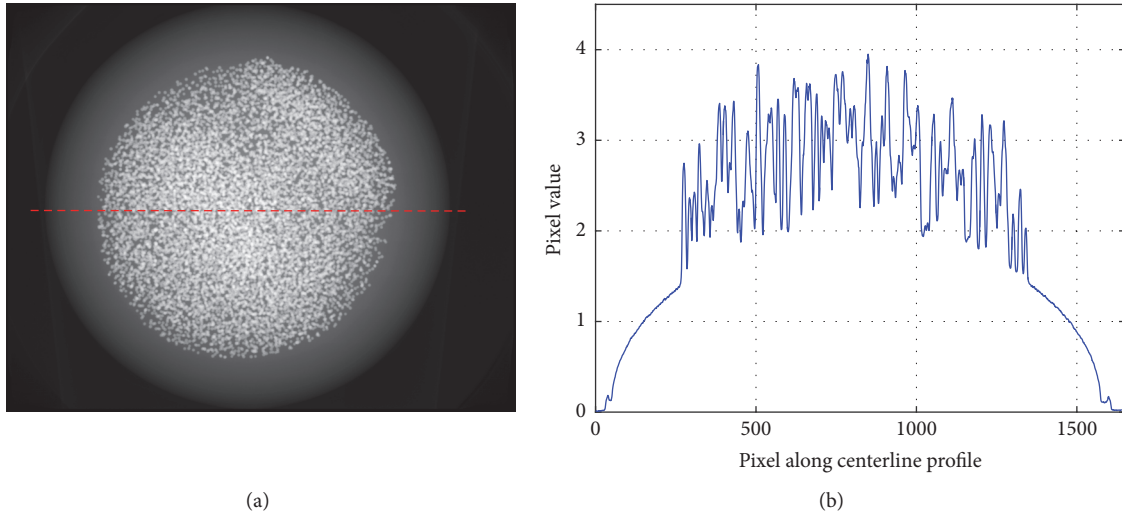


FIGURE 3: (a) DR of a fuel pebble and (b) its centerline profile marked in (a).

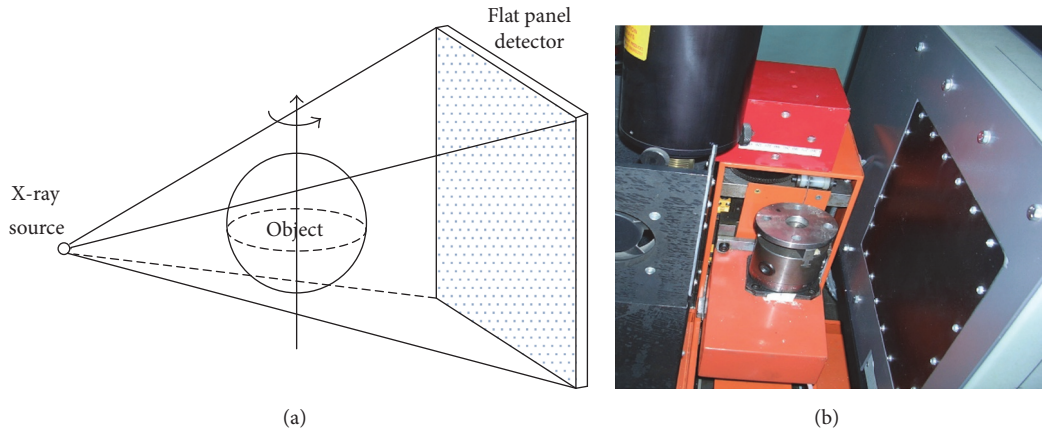


FIGURE 4: Scheme of flat panel based 3D cone-beam CT system and facility.

has good spatial resolution, efficient scanning, and effective X-ray utilization [9]. The system uses a 160 kVp microfocus X-ray generator and a flat panel detector. The X-ray tube is *HOMX-161 microfocus tube by Philips*. The voltage and current of the X-ray tube for pebble imaging are 140 kV and 0.2 mA, respectively. *The focus spot is about 20~50 μm*. The flat panel detector is PaxScan 2520 by Varian. The detector has 1920 × 1536 pixels with a pitch of 127 μm × 127 μm. The distance between the source and the detector is about 75 cm and the source-object distance is 25 cm. The equivalent pixel size of the slice is about 80 μm [9, 10].

A series of projections are acquired while scanning, and the time varies from 10 to 30 minutes per pebble. Slices are reconstructed with the 3D CBCT reconstruction algorithm, and the time may vary from 5 to 10 minutes if accelerated by GPUs. The reconstruction algorithm we used is fast FDK [11], which is in-house programmed in *Visual Studio 2012*. The flow chart for the visualization process is shown in Figure 5. A fuel pebble is scanned with CT, and the reconstruction

with acquired projections is simultaneously performed while scanning.

As a key step for 3D evaluation, the TRISO particle distribution is displayed in a 3D view by using visualization rendering. With visualization rendering, a complex 3D structure can be demonstrated in a more intuitive way. Surface rendering and volume rendering are two typical visualization methods. Surface rendering extracts polygonal mesh of an iso-surface from three-dimensional voxels. Volume rendering, such as ray-casting, works on the basis of pixel and it presents more details.

With TRISO particles displayed in a 3D and intuitive way, it becomes much easier for fuel experts to judge the TRISO distribution as good or bad, accepted or rejected. In addition, the CT modality and NDT staff establish qualified slices.

In this work, two HTR-PM pebbles were scanned to demonstrate feasibility using the 3D cone-beam CT with an angle step of 0.5 degrees, and hence 720 projections were made for each pebble. The scanning took about 20

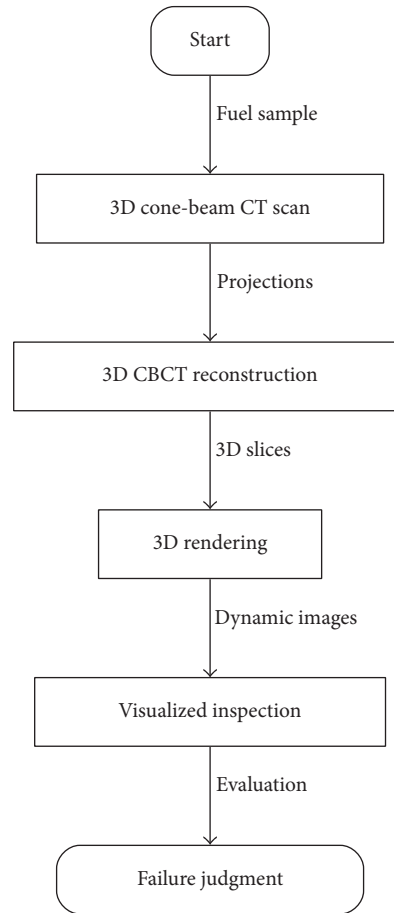


FIGURE 5: 3D visualized inspection process.

minutes, and the reconstruction was done simultaneously. 3D rendering and animation were processed using the ray-casting module in *Amira* (version 5.4).

### 3. Experimental Result and 3D Visualization Evaluation

Slices were reconstructed with the FDK algorithm and the central slice is shown in Figure 6. The distribution of TRISO particle is shown in 2D. Three slices in  $X$ ,  $Y$ , and  $Z$  directions are shown, respectively.

Figure 7 is a 3D volume rendering of TRISO in a pebble. The particles can be individually identified, and the space distribution is clear.

### 4. Discussion

To conveniently inspect the uniformity of TRISO distribution, several attributes, such as color, transparency, illumination, and perspective, could be set in the rendered images as shown in Figure 8.

Animation is also applicable as shown in Figure 9 and in the *Supplementary Material* (available online at

<https://doi.org/10.1155/2017/3857075>). With expert evaluation, aggregation phenomena could be observed easily. By using this tool, experts can identify any suspected defect regions from any view and the associated possible causes due to the fabrication process. The results provided by this method can therefore help optimize the manufacture process [12]. The results also provide information about the initial conditions of the pebbles for the fuel performance evaluations.

### 5. Conclusions

As the first layer of HTGR intrinsic safety system, the fuel pebble is fabricated in a complicated processing chain. For production QA (quality assurance) and QC (quality control), each process parameter of fuel element should be carefully defined and evaluated. The images generated by X-ray DR are two-dimensional and not well qualified to evaluate the 3D TRISO particle distribution.

This study provides a viable CBCT-based nondestructive method to visualize and evaluate the TRISO distribution in three dimensions. Experiment results showed that 3D cone-beam CT provides detailed 3D information compared to DR, which helps experts to individually evaluate each fuel

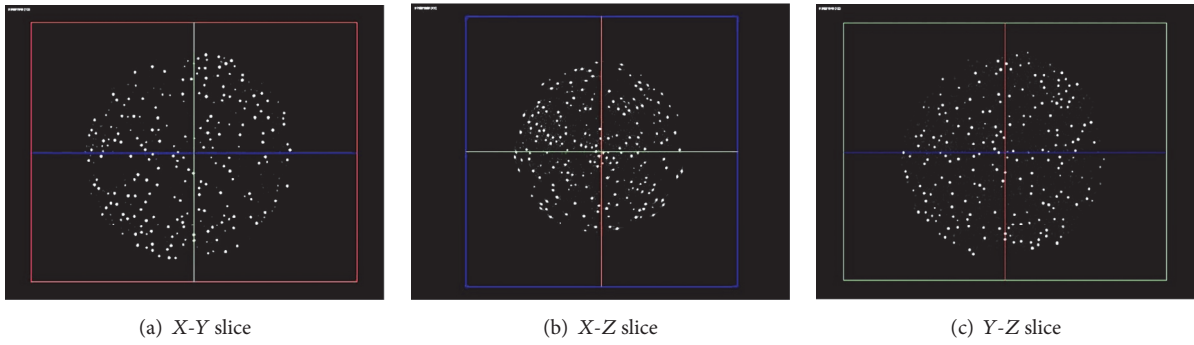


FIGURE 6: Distribution of TRISO particles in 2D.

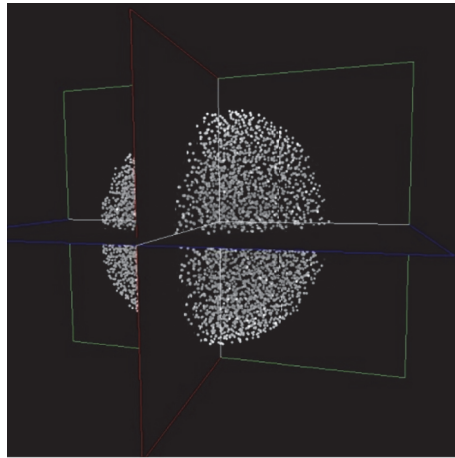


FIGURE 7: 3D visualization of TRISO particles in a pebble.

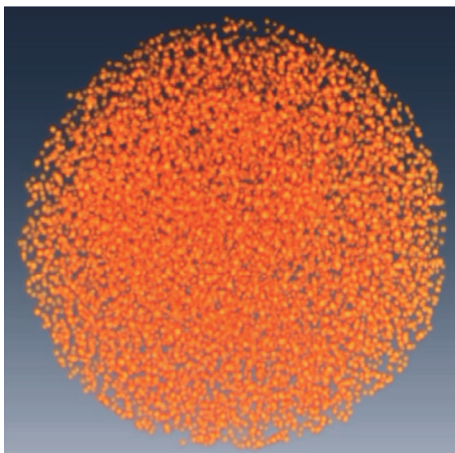


FIGURE 8: Adjustable 3D visualization of particles in a pebble.

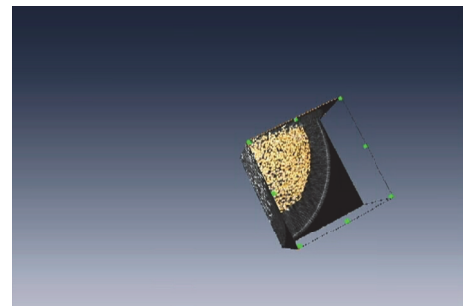


FIGURE 9: Illustration of animated 3D visualization of 3D slices of fuel element.

element slice. Experts can also visualize 3D data animatedly by the volume rendering technique, which helps the expert to evaluate the TRISO distribution or fabrication defects (e.g., cracks) in a more direct way. It also helps in aggregation or some other complicated circumstances, such as process optimization and quality control.

Work is in progress to provide statistical evaluations for the particle distributions within a pebble and modeling based on the 3D slices, and the results will be reported separately.

**Conflicts of Interest**

The authors declare that there are no conflicts of interest regarding the publication of this paper.

## Acknowledgments

This paper is partially supported by the National Natural Science Foundation of China (61171115, 61571262, and 11575095) and the National Key Research and Development Program (2016YFC0105406).

## References

- [1] International Atomic Energy Agency and Nuclear Power Technology Development Section, "Advances in high temperature gas cooled reactor fuel technology," IAEA-TECDOC 1674, International Atomic Energy Agency (IAEA), 2012.
- [2] Z. Zhang, Z. Wu, D. Wang et al., "Current status and technical description of Chinese  $2 \times 250 \text{ MW}_{th}$  HTR-PM demonstration plant," *Nuclear Engineering and Design*, vol. 239, no. 7, pp. 1212–1219, 2009.
- [3] Z. Xiangwen, L. Zhenming, Z. Jie et al., "Preparation of spherical fuel elements for HTR-PM in INET," *Nuclear Engineering and Design*, vol. 263, pp. 456–461, 2013.
- [4] K. Verfondern, H. Nabielek, and J. M. Kendall, "Coated particle fuel for high temperature gas cooled reactors," *Nuclear Engineering and Technology*, vol. 39, no. 5, pp. 603–616, 2007.
- [5] M. Yang, R. Li, J. Duan et al., "Analysis of DR testing blind zone of spherical fuel elements for 10 MW high-temperature gas-cooled reactor," *NDT & E International*, vol. 60, pp. 77–86, 2013.
- [6] J. Li and Z. Zhang, "X-ray real-time image detection of the fuel-free zone of spherical fuel elements," *Physics Examination and Testing*, vol. 3, pp. 41–43, 2000.
- [7] D. Yi, X. Wang, X. Xiang, and L. Bing, "Automatic X-ray inspection for the HTR-PM spherical fuel elements," *Nuclear Engineering and Design*, vol. 280, pp. 144–149, 2014.
- [8] D. Tisseur, J. Banchet, P.-G. Duny, M.-P. Vitali, G. Peix, and J.-M. Létang, "Quality control of High Temperature Reactors (HTR) compacts via X-ray tomography," in *Proceedings of the International Congress on Advances in Nuclear Power Plants. The Nuclear Renaissance at Work (ICAPP '07)*, pp. 2353–2359, Nice Acropolis, France, May 2007.
- [9] L. Zhang, "Determine the homogeneity of UO<sub>2</sub> distribution in HTGR fuel element by X-ray tomography," *Nuclear Power Engineering*, vol. 13, no. 2, pp. 63–68, 1992.
- [10] P. R. Hania, B. Janssen, A. V. Fedorov et al., "Qualification of HTR pebbles by X-ray tomography and thermal analysis," *Nuclear Engineering and Design*, vol. 251, pp. 47–52, 2012.
- [11] X. Wang, Z. Guo, Y. Peng, C. Zhang, and J. Tian, "Fast 3-D reconstruction of CT images using a geometric parameter table," *Journal of Tsinghua University*, vol. 42, no. 5, pp. 655–658, 2002.
- [12] International Atomic Energy Agency, "High temperature gas cooled reactor fuels and materials," Tech. Rep. IAEA-TECDOC-CD—1645, International Atomic Energy Agency (IAEA), Vienna, Austria, 2010.